Exploring the Electrocatalytic Ability of 3d Transition Metal Complexes for Hydrogen Evolution and Carbon Dioxide and Nitrite Reduction Reactions

Somayeh Norouziyanlakvan

Thesis submitted to the University of Ottawa in partial Fulfillment of the requirements for the Doctor of Philosophy in Chemistry

Department of Chemistry
Faculty of Science
University of Ottawa

For my parents, who taught me to be hardworking and ambitious.

~~~
~~~

Acknowledgements

I'd like to acknowledge the many people whose mentorship, teaching, collaboration, commiseration, support, and friendship made my time at uOttawa both productive and enjoyable. The last four years have been extraordinary, and it would be impossible to thank everyone who has made them that way, so the following is a necessarily incomplete list.

First and foremost, thanks to my supervisor, Prof. Darrin Richeson, for his commitment to my development as an independent scientist and for always having my best interests in mind. Thanks also to the members of my Qualifying Exam and Dissertation Committees, Professors Tom Baker, Abdel. Sayari, Dr. Aona Luca and Dr. Kathrine Marczenko. Special thanks to Wendy Pell who was always there for us to support us. I appreciate the invaluable assistance from Dr. Jeffery Ovens, Dr. Sharon Curtis, and Dr. Peter Pallister for their guidance in complex characterization and analysis.

Special thanks go out to the amazing friends I've made over the course of my academic career: Jonathan Ferguson, Josh Brown, Sarah Osterholm, Patrick Berro, and Vincent Morrin. You made my life easier and more fun.

To my parents, who have raised me strong and ambitious. I owe you everything for the opportunity and support to pursue what I want from this life, for that I will always be grateful.

Lastly, I can't say enough Thank-you's to Mohammad, my husband, who has always supported me, especially in the last few years. Thank you for the love and kindness you have never stopped giving to me since we've crossed paths.

Abstract

This research delves into the realm of molecular homogeneous catalysts, specifically focusing on 3d metal complexes, Ni in particular, for electrochemical processes involving CO_2 and nitrite reduction, as well as H_2 production. The investigation highlights the use of non-innocent ligands and their influence on catalytic activity, solubility, and complex efficiency and use of water both as solvent and proton source. Through experimental investigation and computational analysis, the study aims to enhance the understanding of catalytic mechanisms, metal-ligand interactions, and the role of metal in enhancing catalytic efficiency and selectivity.

List of Abbreviations

CPE	Controlled Potential Electrolysis
CV	Cyclic Voltammetry
LSV	Linear Sweep Voltammetry
DFT	Density Functional Theory
PCM	Polarizable Continuum Model
XRD	X-ray diffraction
TCD	Thermal Conductivity Detector
ESI	Electro Spray Ionisation
EI	Electron Impact
UV	Ultraviolet Light
FT-IR	Fourier transform Infrared
NMR	Nuclear Magnetic Resonance
MET	Multiple Electron Transfer
PCET	Proton Coupled Electron Transfer
HER	Hydrogen Evolution Reaction
HEC	Hydrogen Evolution Catalyst
NO_2RR	Nitrite Reduction Reaction
CO_2RR	Carbon dioxide Reduction Reaction
SOMO	Singly Occupied Molecular Orbital
LUMO	Lowest Unoccopied Molecular Orbital
HOMO	Highest Occupied Molecular Orbital
FE	Faradaic Efficiency
TOF	Turn Over Frequency
TON	Turn Over Number
WE	Working Electrode
RE	Reference Electrode
CE	Counter Electrode
GC	Glassy Carbon
Pt	Platinum

Ag	Silver
Fc	Ferrocene
NHE	Normal Hydrogen Electrode
SHE	Standard Hydrogen Electrode
SCE	Saturated Calomel Electrode
TFA	Trifluoroacetic acid
PHEN	Phenol
Me	Methyl
iPr	Isopropyl
Ph	Phenyl
TBAHFP	Tetrabutylammonium Hexafluorophosphate
MOPS	(3-(N-morpholino)propanesulfonic acid)
$CDCl_3$	Deuterated chloroform
Ar	Aryl
vs.	Versus
V	Volt
s	Second
h	Hour
t	Time
Å	Angstrom
°	Degree
η	Overpotential
μ	Micro
δ	Delta
E_p	Peak Potential
E_o	Onset Potential
E	Potential
$E_{1/2}$	Half-Wave Potential
E^o	Standard Potential
i	Current
M	Molar

mM	Millimolar
ppm	Parts per million
tbp	trigonal bipyramidal
sp	square-based pyramidal

Table of Contents

Table of Figures

Table of Tables

Table of Schemes

Chapter 1: Introduction

With society's energy demands dramatically increasing over the past few decades and the industrialization of chemical processes in order to meet these needs, there has been an upward spike in waste production, greenhouse gas emissions, and human-made nitrogen. Two problems in particular that garner widespread attention across the globe are the emission of CO_2, a thermodynamically stable greenhouse gas that contributes to global warming, and the formation of nitrates and nitrites from excess nitrogen arising from fertilizer runoff which pollutes waterways and contributes to an increase in an excess of nitrogen in the global nitrogen cycle.[1-3] Because of this, there have been widespread efforts to develop methods of mitigating and reversing the damage done to the Earth's environment from these industrial chemical processes[4-8]. Due to the thermodynamic stability of H_2O, CO_2 and NO_2^-, scientists have looked towards the development of innovative catalytic systems to transform these molecules into other useful products[9, 10].

Electrocatalysis plays a vital role in finding solutions to the production of reliable, affordable, and environmentally friendly energy, fuels, and chemicals—hydrogen, carbon monoxide, and ammonia, to name a few. For this reason, electrocatalyst development has generated increasing interest across disciplines, attracting chemists, physicists, surface scientists, materials scientists, and electrical and chemical engineers.

1.1. Molecular homogeneous electrocatalysts

Inorganic complexes are a promising subset of the many catalysts capable of electrochemical reduction of different molecules [11-14]. Molecular homogeneous catalysts offer clear advantages in the elucidation of detailed catalytic mechanisms including the detection of active intermediates. However, they sometimes suffer from low solubility in aqueous media and low stability.[15] Much of the foundational work in molecular homogeneous catalysis used precious metals that have limited abundance on Earth. While these elements possess properties that make them practical to

use as catalyst centers, recent efforts are focused on implementing more Earth-abundant metals.[16-18] This push has led to increasing studies of 3d transition metal complexes, in particular of nickel, copper, and iron. In addition to investigating new metal centers, different ligands are necessary to exploit the full potential of these molecules as efficient catalysts. This has led to research centered on increasingly complex ligands.

1.2. Non-innocent ligands

The properties of a metal complex as a whole are the result of interactions of the metal center with its surrounding ligands. In traditional approaches, the steric and electronic properties of the ligands are used to control the performance of the catalyst, but classically the role of the ligand was assigned a spectator role in the reactivity that takes place at the metal center. The central idea of an alternate view is that the metal and the ligand can cooperate in a synergistic manner, and their interplay facilitates the chemical process. In this light, complexes based on so-called "redox non-innocent" ligands offer interesting prospects to uncover new catalytic reactions. In other words, ligands can participate in the redox process. Such species can offer a unique opportunity to modify the reactivity of transition metal complexes.[15, 19-21] Four main strategies can be distinguished in this context: (i) Modification of the Lewis acidity of the metal by reduction/oxidation of the ligand, which strongly influences the substrate affinity as well as the energy profile of subsequent reactions; (ii) An "electron-reservoir" function of the redox active ligand, which allows the metal to store electrons on the ligand in elementary steps, generating excess electron density and accept electron density from the ligands in elementary steps generating deficiencies, in all cases avoiding uncommon oxidation states of the metal; (iii) the generation of reactive ligand-radicals that actively participate in the making and breaking of chemical bonds during catalysis; (iv) (radical-type) activation of the substrates or modification of the substrate reactivity in cases where the

substrate itself acts as a redox non-innocent ligand. Speaking more generally, redox non-innocent ligands can either participate in the catalytic cycle by (A) accepting/releasing electrons (strategies I and II) or by (B) forming/breaking chemical bonds of the substrate (strategies III and IV) (Figure 1.1)[19].

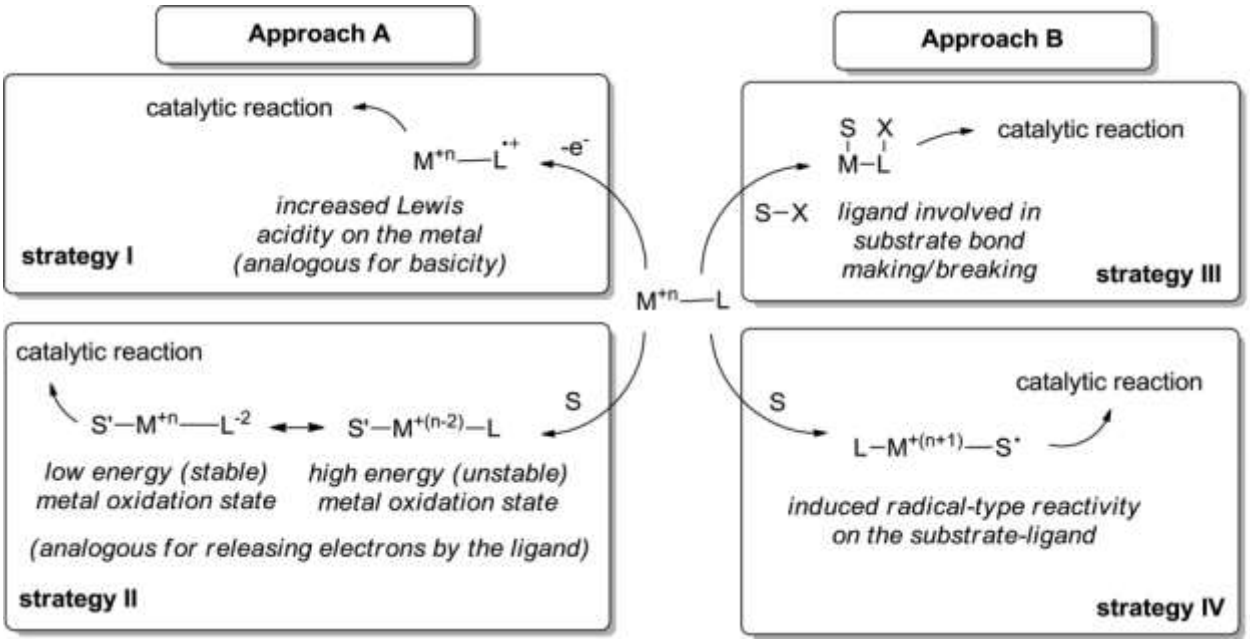

Figure 1.1. General representation of four main strategies of using redox non-innocent ligands in catalysis. (Bruin, Chem. Soc. Rev., 2021, 50, 6720–6733, Used with permission from Royal Society of Chemistry).

In this thesis the aim is on exploring new homogeneous electrocatalysts for different environmentally relevant targets and improving the solubility and stability of the catalyst by focussing on the ligand modifications. The targeted applications of these electrocatalysts are presented below.

To enhance comprehension of the terms and experiments discussed in this thesis, a concise introduction also provided on fundamental electrochemical tests and catalysis evaluation approaches.

1.3. Fundamental to electrocatalysis:

1.3.1 Electrochemistry Tests:[22, 23]

- **Cyclic voltammetry**

Cyclic voltammetry (CV) is a powerful and popular electrochemical technique commonly employed to investigate the reduction and oxidation processes of molecular species. CV is also invaluable to study electron transfer-initiated chemical reactions, which includes catalysis.

Figure 1.2 depicts a typical cyclic voltammogram. The x-axis represents a parameter that is imposed on the system, here the applied potential (E), while the y-axis is the response, here the resulting current (i) passed. The arrow indicates the direction in which the potential was scanned to record the data. The arrow indicates the beginning and sweep direction of the first segment. A crucial parameter included in the caption is the scan rate (υ). It indicates that during the experiment the potential was varied linearly at the speed (scan rate) of 100 mV per second.

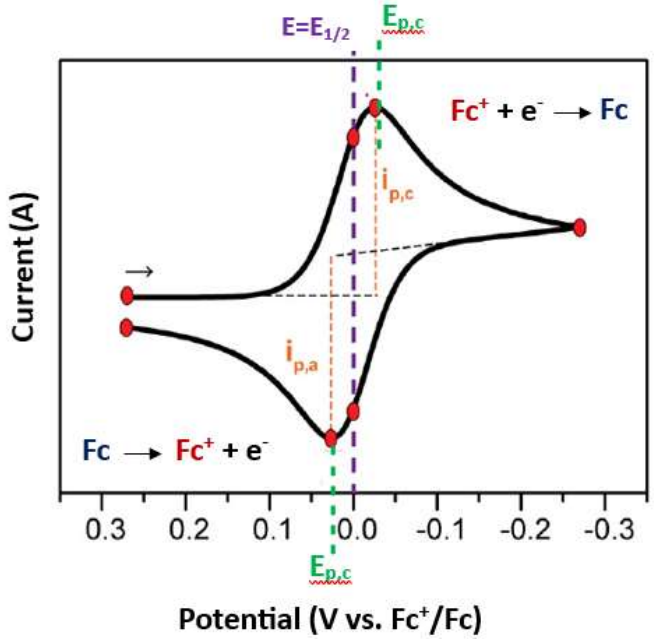

Figure 1.2. Voltammogram of the reversible reduction of a 1 mM Fc^+ solution to Fc (Ferrocene = $[Fe(C_5H_5)_2]$). Voltammogram recorded in 0.25 M $[NBu_4]$ $[PF_6]$ CH_3CN solution at υ = 100 mV/s with a 3 mm glassy carbon working electrode, 3 mm glassy carbon counter electrode, and a silver wire pseudo reference electrode.

Reversibility and irreversibility:

Consider the equilibrium between ferrocenium (Fc^+) and ferrocene (Fc). This equilibrium is described by the Nernst equation (equation 1.1). The Nernst equation relates the potential of an electrochemical cell (E) to the standard potential of a species (E^o) and the relative activities of the oxidized (Ox) and reduced (Red) analyte in the system at equilibrium.

$$E = E^O + \frac{RT}{nF} ln \frac{(Ox)}{(Red)} = E^O + 2.3026 \frac{RT}{nF} log_{10} \frac{(Ox)}{(Red)} \quad (1.1)$$

In the equation, F is Faraday's constant, R is the universal gas constant, n is the number of electrons, and T is the temperature. The Nernst equation provides a powerful way to predict how a system will respond to a change of concentration of species in solution or a change in the electrode potential. In application of the Nernst Equation to the one-electron reduction of Fc^+ to Fc, the activities are replaced with their concentrations, which are more experimentally accessible, the standard potential E^o is replaced with the formal potential $E^{o\prime}$, and n is set equal to 1: (1.2)

$$E = E^{O\prime} + \frac{RT}{nF} ln \frac{(Fc^+)}{(Fc)} = E^{O\prime} + 2.3026 \frac{RT}{nF} log_{10} \frac{(Fc^+)}{(Fc)}$$

The formal potential is specific to the experimental conditions employed and is often estimated with the experimentally determined $E_{1/2}$ value.

To illustrate, if a potential of $E = E^{o\prime} \approx E_{1/2}$ is applied to our example Fc^+ solution, the Nernst equation predicts that Fc^+ will be reduced to Fc until $[Fc^+] = [Fc]$, and equilibrium is achieved.

If the reduction process is chemically and electrochemically reversible, the difference between the anodic and cathodic peak potentials, called peak-to-peak separation (ΔE_p), is 57 mV at 25 °C (2.22 RT/F), and the width at half max on the forward scan of the peak is 59 mV.

Chemical reversibility is used to denote whether the analyte is stable upon reduction and can subsequently be reoxidized. Analytes that react in homogeneous chemical processes upon

reduction (such as ligand loss or degradation) are not chemically reversible. Electrochemical reversibility refers to the electron transfer kinetics between the electrode and the analyte. When there is a low barrier to electron transfer (electrochemical reversibility), the Nernstian equilibrium is established immediately upon any change in applied potential. By contrast, when there is a high barrier to electron transfer (electrochemical irreversibility), electron transfer reactions are sluggish and more negative (positive) potentials are required to observe reduction (oxidation) reactions, giving rise to larger ΔE_p. Often electrochemically reversible processes where the electron transfers are fast and the processes follow the Nernst equation are referred to as "Nernstian."

Importance of the Scan Rate:

The scan rate of the experiment controls how fast the applied potential is scanned. Faster scan rates lead to a decrease in the size of the diffusion layer; as a consequence, higher currents are observed. For electrochemically reversible electron transfer processes involving freely diffusing redox species, the Randles−Sevcik equation (equation 1.3) describes how the peak current i_p (A) increases linearly with the square root of the scan rate υ (Vs^{-1}), where n is the number of electrons transferred in the redox event, A (cm^2) is the electrode surface area (usually treated as the geometric surface area), D_o ($cm^2\ s^{-1}$) is the diffusion coefficient of the oxidized analyte, and C^0 (mol cm^{-3}) is the bulk concentration of the analyte.

$$i_p = 0.446nFAC^0\left(\frac{nF\upsilon D_0}{RT}\right)^{1/2}$$

The Randles−Sevcik equation can give indications as to whether an analyte is freely diffusing in solution. As analytes can sometimes adsorb to the electrode surface, it is essential to assess whether an analyte remains homogeneous in solution prior to analyzing its reactivity. In addition to

verifying that the analyte is freely diffusing, the Randles−Sevcik equation may be used to calculate diffusion coefficients.

- **Linear Sweep Voltammetry**

Linear sweep voltammetry (LSV) is a simple electrochemical technique which is similar to cyclic voltammetry, but rather than linearly cycling over the potential range in both directions, it involves only a single linear sweep from the lower potential limit to the upper potential limit. This is particularly useful for irreversible systems where a reverse sweep would not reveal any more information. By linearly sweeping the potential while measuring current, LSV identifies electrochemical reactions, assesses catalyst activity and stability, determines reaction kinetics, and screens and optimizes electrocatalysts.

- **Controlled Potential Electrolysis**

Controlled potential bulk electrolysis (CPE) is widely used to determine the overall number of electrons involved in an electrode process. It is also used to prepare a sufficient quantity of the reaction products to enable them to be identified by conventional analytical techniques.

The objectives of a CPE experiment are to ascertain the stability and product selectivity of a given homo- or heterogeneous electrocatalyst. The typical setup involves three electrodes: the reductive/oxidative transformation of interest occurs at the working electrode, which is held at a constant desired potential versus a calibrated reference electrode. The circuit is completed by a counter electrode, where the oxidative/reductive half-reaction occurs. Catalyst stability is typically determined by observing the current passed as a function of time—a steady current usually indicates that the catalyst is stable under the specified conditions, while decreases or increases in current over time suggest catalyst decomposition or activation, respectively. Evaluating product

selectivity is done by passing a large amount of charge and quantifying the resulting products. An important metric in this regard is the Faradaic efficiency (FE) for a given product.

1.3.2 Evaluation approaches:[24]

- **Overpotential**

Under the standard conditions the potential needed for a reaction follows Nernst equation (E^o). However, the practical catalytic processes require a greater applied potential to overcome the kinetic barriers resulting from some adverse issues, such as high activation energy and poor energy efficiency. The difference between Nernst potential (E^o) and the required potential to drive the electrocatalytic reaction is the corresponding overpotential (η) of the catalyst. Thus, the applied potential (E or $E_{uncorrected}$) can be expressed as $E = E^o + \eta$.[25]

- **Stability**

Stability is another crucial parameter to be evaluated for the potential practical applications of an electrocatalyst. There are two electrocatalytic methods for the stability measurements: repetitive cyclic voltammetry (CV) or linear sweep voltammetry (LSV) and galvanostatic or potentiostatic electrolysis. The voltammetric method is comparing the changes in overpotential before and after a certain cycling run by conducting CV or LSV in the region including the onset potential. A small change of the overpotential after multiple potential cyclings indicates that the electrocatalysis is stable.

- **Faradaic Efficiency**

Faradaic efficiency, the efficiency with which the electrons provided by an external circuit participate in catalytic reaction, is another important parameter to assess the performance of an electrocatalyst. In electrocatalytic reactions, Faradaic efficiency is defined as the ratio of the experimental to theoretical amount of product generated. The theoretical amount of generated

product is calculated from monitoring the actual amount of product generated from electrolysis and comparing it with the theoretical value allow us to determine the Faradaic efficiency (equation 1.4).

$$FE_{prod} = nF \times \frac{mol_{prod}}{Q}$$

where n is the number of electrons required to convert one molecule of reactant to product, F is Faraday's constant, mol_{prod} is the number of moles of product generated, and Q is the total charge passed during the CPE experiment. If more than one product is generated, a FE may be determined for each product, where the total FE should be close to 100%.

- **Turnover Frequency**

To evaluate and screen an active catalyst candidate for a reaction of interest from other catalysts, the intrinsic site activity or site efficiency of the catalyst is often determined unbiased by the number of active sites per weight or volume of the catalyst. In 1968, Michel Boudart first proposed to evaluate the catalytic rate of a catalyst in terms of turnover frequency (TOF), i.e., the number of molecules reacting per site per second.[26] Recently, the TOF was redefined as the total number of molecules transformed into a desired product per catalytic site per time unit.[27] Currently, the most used method to estimate TOF values of a electrocatalytic reaction is based on $TOF = \frac{jA}{4nF}$, where A is the area of the working electrode and n is the number of moles of the active materials that is calculated using the electrochemically active surface area of the catalyst.[28] However, it is not easy to precisely access the TOF value for most solid-state catalysts, especially for some emerging complex ones, because not all of the surface atoms in a catalyst are catalytically active or equally accessible. Although the calculated TOF is relatively imprecise, it still offers a useful way of comparing the catalytic activities among various catalysts, especially within a similar system.

- **Turnover Number**[29]

Turnover number (TON) specifies the maximum use that can be made of a catalyst for a special reaction under defined reaction conditions by the number of molecular reactions or reaction cycles occurring at the reactive center up to the decay of activity. In this respect, the TON represents the maximum yield of products attainable from a catalytic center. The TON results from multiplication of the turnover frequency (TOF) [$time^{-1}$] and the lifetime of the catalyst [time].

1.4 Hydrogen Evolution Reaction (HER):

Over the past century, worldwide energy demand has continued to increase rapidly due to global development and growth in population. The energy demand is expected to grow from 16 Terawatt (TW) in 2010 to 23 TW in 2030, and even up to 30 TW in 2050.[30] According to the statistics recently released, 79.5% of the total energy consumed was from conventional energy sources (such as coal, petroleum oil, and natural gas), whereas the renewable energy sources including hydropower, wind, biopower, and solar photovoltaics provided only 20.5% of global energy consumption in 2016. The heavy dependence on fossil fuels has inevitably caused their rapid depletion, as well as the accompanying detrimental environmental issues and global warming. Therefore, there is an urgency to develop renewable and clean alternatives that can resolve the current problems and sustain long-term development.

Molecular hydrogen gas (H_2) is one of the most attractive fuels. H_2 has the highest gravimetric energy density, and its only combustion byproduct is pollution-free water, making it an excellent energy carrier and a potential candidate for future low-carbon energy systems.[31] However, most of the H_2 is currently produced by steam reforming of fossil resources. This production route not only consumes fossil fuels with low conversion rate but also emits CO_2.[31, 32] To this end, a clean, renewable, and efficient technique for H_2 generation without adding further problems is the key. The kinetic and thermodynamic barriers to H_2 formation provide significant chemical challenges, necessitating the development of efficient and inexpensive catalysts that can promote H^+ reduction with high activity, low overpotential and good durability. Reactions are often accelerated by utilizing proton-coupled electron transfer (PCET), which integrates the motions of electrons and protons to avoid high-energy intermediates. To date, platinum performs best among catalysts able

to produce H_2, through water splitting. However, due to its scarcity and cost, there has been wide interest in finding alternatives made of non-noble transition metals.[33]

In biological systems, the [FeFe] and [Ni-Fe] hydrogenase enzymes regulate the activity of electro-catalytic hydrogen production by precisely positioned proton-relay groups in the second coordination sphere.[34] The pendent amine built in the active site of [Fe-Fe] hydrogenase has been shown to assist in proton transfer and facilitate hydrogen bond formation.[32, 35] With turnover rates of up to 104 s^{-1}, thermostability, and low overpotentials, hydrogenases have been studied as templates for the synthesis of new organometallic and coordination complex catalysts. Inspired by the biological system, chemists have designed several classical model complexes similar to that of hydrogenase to improve the catalytic activity. Unfortunately, due to their intricate architectures, there has not yet been precise agreement on how they function. Moreover, from a theoretical point of view, the size and composition of their active sites make them challenging to study.[35]

Literature review on HER with molecular electrocatalyst:

In terms of solubility, the complexes reported for HER can operate in either aqueous media or organic media. From a sustainability perspective, exploring HER catalysts that are soluble in water or use water as the proton source is more challenging. There are a limited number of reported electrocatalysts that are active for HER in neutral water.[31, 34]

In an early study, Darensbourg and co-workers reported two diiron thiolate clusters (Figure 1.3- **1** and **2**) for electrocatalytic reduction of acetic acid to H_2 in acetonitrile and water–acetonitrile solutions at ca. -1.7 V vs. SHE (Standard Hydrogen Electrode) on a glassy carbon electrode.[36] Although controlled potential electrolyses in mixed water–acetonitrile solutions are not reported, cyclic voltammograms of **1** and **2** with acetic acid in water–acetonitrile mixtures led to positive shifts of all redox potentials and higher catalytic current relative to the redox potentials in pure

acetonitrile solutions. Sun and co-workers reported similar findings for analogous diiron azadithiolates (**3** and **4**).[37]

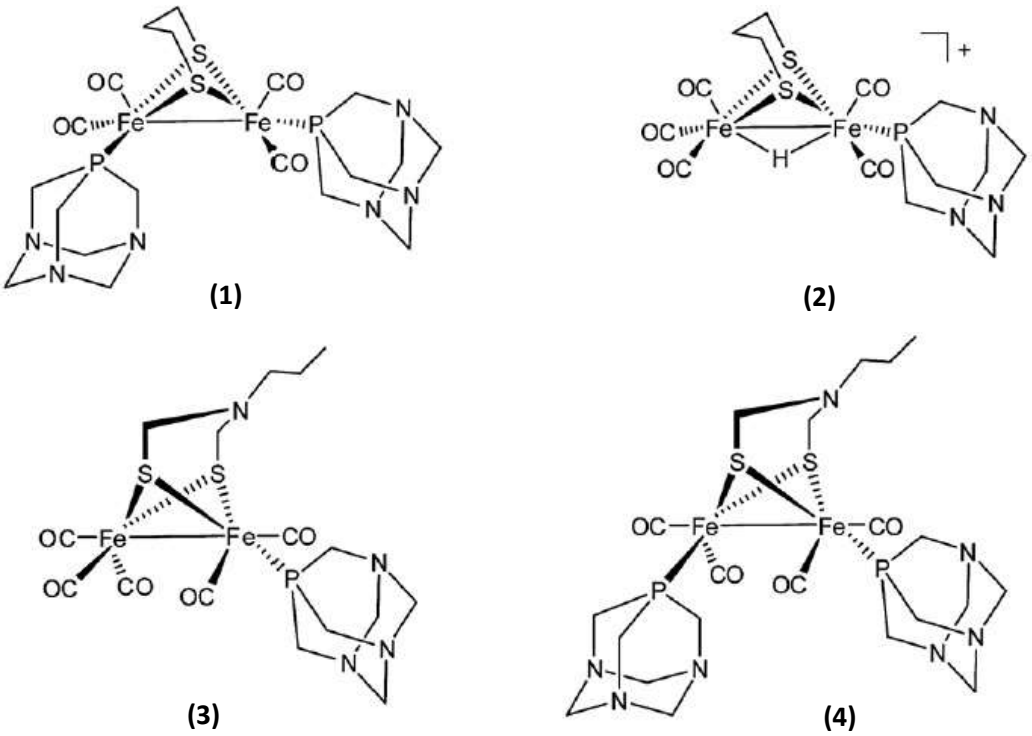

Figure 1.3. Structures of some of Fe base HECs (Chang, Chem. Soc. Rev., 2013, 42, 2388-2400, Used with permission from Royal Society of Chemistry).

In another early study, Fisher and Eisenberg reported that Ni tetraazamacrocycle (**5**) is a competent electrocatalyst for proton reduction at -1.46 V vs. SHE in 2:1 water–acetonitrile mixtures on a Hg electrode (Figure 1.4-**5**).[38] Sauvage and co-workers later reported that two Ni(II) complexes supported by 1,4,8,11-tetraazacyclotetradecane ($[Ni(cyclam)]_2^+$, **6**) and its bis-macrocyclic analog ($[Ni_2(biscyclam)]_4^+$, **7**) show catalytic activity toward proton reduction in neutral water on a Hg pool electrode.[39] Controlled potential electrolysis at -1.26 V vs. SHE reveals that **7** is a better hydrogen evolution catalyst than **6** and can achieve TONs reaching 100, presumably due to the

close proximity of two Ni centers and the ability to form Ni hydride intermediates. Electrocatalytic hydrogen generation by Ni bis(phosphine) complexes (**8-15**) has also been heavily investigated in recent years, most notably in elegant work from the Dubois laboratories. [40, 41]

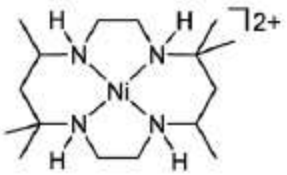

(5)

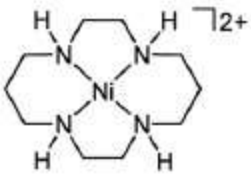

(6)

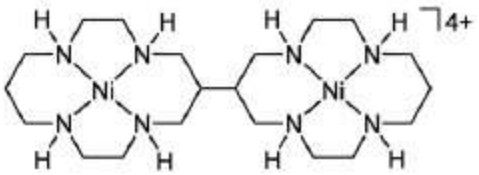

(7)

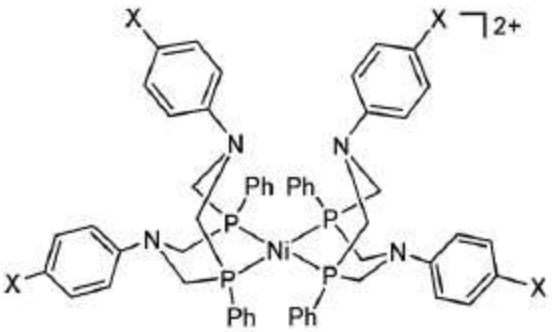

X= CF3 **(8),** Br **(9),** $CH_2P(O)(OEt)_2$**(10),** H **(11),**
Me **(12),** OM**e (13),** C_6H_{13} **(14)**

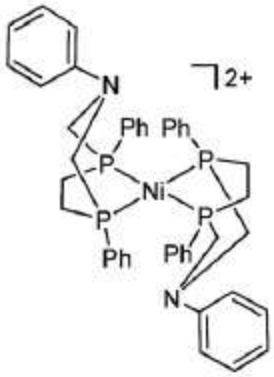

(15)

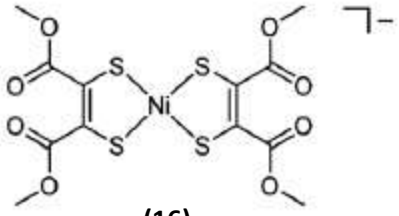

(16)

(17)

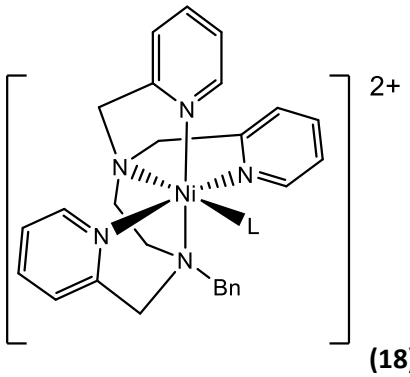

(18)

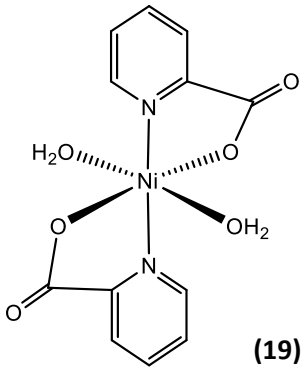

(19)

Figure 1.4. Structure of some Ni base HECs.

Recently, a family of Ni bis(phosphine) complexes $[(Ni(PPh_2NC_6H_4X_2)_2]_2^+$, was reported to have enhanced electrocatalytic activity when water was added to acidic acetonitrile solutions.[42] Catalyst **10**, where X $=CH_2P(O)(OEt_2)_2$, exhibits a TOF of 500 s^{-1} at an overpotential of 320 mV in pure acetonitrile on a glassy carbon electrode; addition of water leads to a TOF of 1850 s^{-1} at an overpotential of 370 mV. A new variant of $[Ni(P_2N_2)_2]_2^+$, catalyst **14**, has also been found to reduce protons in acidic ionic liquid–water solutions with a TOF of >4 $x10^{-4}$ s^{-1} at an overpotential of 400 mV. A similar trend was discovered for $[Ni(PPh_2NPh)_2]_2^+$ (**15**), where TOFs of 33000 s^{-1} and 106 000 s^{-1} were achieved in pure acetonitrile and 1.2 M of water in acetonitrile, respectively, at -0.49 V vs. SHE (Figure 1.4).[43] This remarkable rise in catalytic activity was attributed to the ability of water to enhance the rate of formation of the endo isomer, which allowed a second N–H stabilization. Other derivatives of Ni bis(phosphines) have been examined for proton reduction activity under water-compatible conditions.[44]

Similar to its Co(II) dithiolene analogues[45], Ni(II) dithiolene (**16**) was reported by Sarkar and co-workers to catalyze the reduction of tosic acid to H_2 in 0.2 M $NaClO_4$ in water at -0.5 V vs. SHE on a glassy carbon electrode coated with **16**.[46] Crabtree, Brudvig, and Batista et al. described Ni(II) complexes supported by diiminopyridine (**17**) for reducing water at pH 1 at -1.1 V vs. SHE on a vitreous carbon electrode at 95% Faradaic efficiency[47] (Figure 1.4).

In a 2014 report, a series of nickel complexes containing N5-pentadentate (**18**)[46] ligands were studied for electrochemical H_2 production in neutral water. The complexes varied with different amine-to-pyridine ratios and the one with a diamine/tripyridine ligand displayed a TON of up to 308000 over 60 h electrolysis at -1.25 V vs. SHE, with a Faradaic efficiency of approx. 91%. The most recent paper with these polypyridine ligands was reported in 2020 by Chen et al. They used a diamine/tripyridine ligand on Ni(II)"$[(bztpen)M(H_2O)]_2^+$ (bztpen=N-benzyl-N,N',N'-tris(2-

pyridylmethyl)ethylenediamine)" (**19**). In this paper the researchers added a "binding group" to the pyridine ligand to provide a second coordination sphere effect. The structure is a Ni (II) in a distorted octahedral coordination with two sites occupied by water molecules. Hydrogen evolution occurs at -1.25 V vs SHE.[47]

1.5 CO_2 as a Greenhouse Gas & Its Reduction

The Earth faces a dangerous problem as the monumental amount of CO_2 emitted into the atmosphere increases along with the further acidification of oceans due to them being one of the largest sinks of atmospheric CO_2 on Earth. Competition for the decreasing fossil fuel reserve is also increasing, leading to one of the world's largest sources of energy becoming increasingly expensive and eventually unattainable.[11, 48] In contrast, CO_2 does have the potential to be an abundant and renewable C1 feedstock with a variety of applications. Thus, the catalytic conversion of this thermodynamically stable compound to useful fuels could be helpful and provide an avenue for further scientific innovation. Although it is important to note that the amount of CO_2 emission is very high, and scalability of this method might be a limited.

The reduction pathway of CO_2 has many endpoints; most commonly ending in the production of carbon monoxide (CO), methanol, formaldehyde, or formic acid (HCOOH).[49] Due to the extremely strong C=O bond, with a bond energy of 750 kJ/mol, the reduction of this abundant yet thermodynamically stable compound is known to be challenging. The use of electrochemical reduction to pursue the one electron reduction of CO_2 to CO_2^- faces a potential of -2.14 V (vs SCE) which is not a favourable route. Other methods of CO_2 reduction employ the use of a proton donor to assist with multiple electron transfer (MET) reactions. From the table below, we see that use of a proton donor for MET is more favourable with respect to the one-electron-reduction pathway.[50, 51]

Table 1.1. Reduction Potentials of Common CO_2 Reduction Reactions (E^o (V vs SCE)).

$CO_2 + 2H^+ + 2e^- \rightarrow CO + H_2O$	-0.77 V
$CO_2 + 8H^+ + 8e^- \rightarrow CH_4 + 2H_2O$	-0.48 V
$CO_2 + 2H^+ + 2e^- \rightarrow HCOOH$	-0.85 V

Although the reduction potential of these reactions has become more positive, and thus more favourable, when related to Gibb's free energy ($\Delta G = -(nFE^o)$), these reactions are nonspontaneous.

The use of homogeneous molecular catalysts as a method to reduce the energy required to overcome the activation barrier, and thus reduce the overpotential of the CO_2 reduction reactions, has become widespread as scientists aim for carbon neutrality. These molecular catalysts serve to overcome the kinetic barrier by promoting proton coupled electron transfer (PCET) (Figure 1.5) and activating CO_2. PCET occurs through the transfer of electrons from one atom to another, so instead of reducing at -2.14 V (vs SCE) in single electron reduction, or -0.77V (vs SCE) in MET for CO_2 to CO, a catalyst would be reduced at a much lower potential and would transfer electrons directly to CO_2 thereby reducing it for a fraction of the energy cost. Catalysts allow for CO_2 to bind to the metal center leading to intramolecular electron and proton transfer which is quicker and requires less energy.[51]

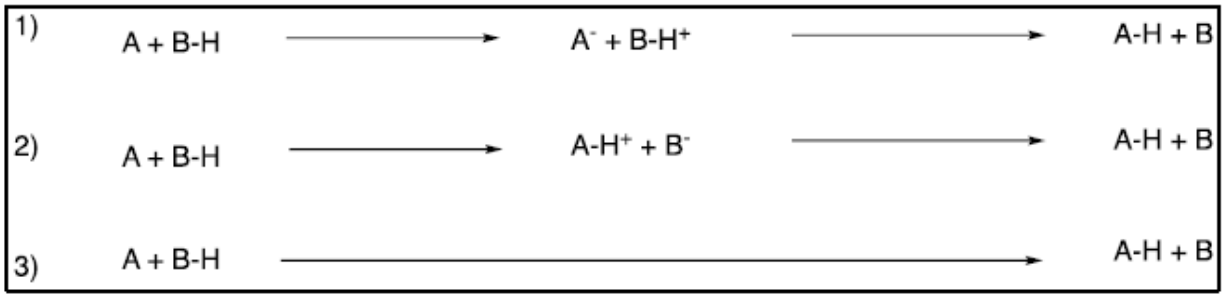

Figure 1.5. Depiction showing the different pathways between 1) electron transfer, 2) proton transfer, and 3) proton-coupled electron transfer (PCET). PCET occurs in essentially one step as opposed to discrete electron and proton transfer mechanisms which occur in two.

Literature review on CO_2 reduction with molecular electrocatalyst:

Despite the long history of electrochemical CO_2 reduction, the field still attracts much interest and the motivations for the research are typically the possibility to reduce the greenhouse effect by lowering the CO_2 concentration in the atmosphere, the generation of fuels from CO_2, and the transformation of CO_2 into building blocks for the production of chemicals.

Transition-metal complex catalysts for CO_2 electrochemical reduction based on earth-abundant metals with the various classes of ligands (polypyridyl, phosphine, cyclam, and aza-macrocyclic ligands, as well as porphyrins, phthalocyanines, and related macrocycles) and metals (Ni, Co, Mn, Fe), have been significantly investigated.[15] A few of these complexes are shown in Figure 1.6. The most frequently studied family of homogeneous Mn and Re catalysts for CO_2 electroreduction is represented by complexes of the type fac-[M(bpy)$(CO)_3$X] (with X = Br, Cl). [52] The fac-[Re(bpy)-$(CO)_3$Cl] complexes and bpy-substituted derivatives are known to be highly active for CO_2-to-CO conversion since early reports published by Lehn et al.[53] and Meyer et al.[54] in the 1980s. However, due to the importance of more sustainable methods and materials for CO_2 reduction, the focus has recently shifted from Re toward the bpy−Mn tricarbonyl congeners. The first study on the electrocatalytic activity of [Mn(bpy)$(CO)_3$Br] complexes (**20**) reported in 2011 by Chardon-Noblat et al.[55] They showed that compared to the Re analogues, the reduction proceeded at a significantly lower overpotential (approximately 0.4 V less). It was also demonstrated that in contrast to their Re congeners, the use of Mn complexes requires the addition of a proton source such as water.

Fe complexes belong to the more frequently studied catalysts for CO_2 electroreduction, although the reported examples are restricted mostly to porphyrins,[56] cyclopentadienone complexes[57] and Fe carbonyl clusters.[58, 59] Among these Fe catalysts, the porphyrin complexes are the best-characterized systems, and the progress made in terms of ligand optimization is truly remarkable.

Recently, cofacial Fe porphyrin dimers (**21**) have shown excellent catalytic performances for CO production.[60] In all of these cases, weak Brönsted acids such as water, trifluoroethanol, and phenol strongly enhance catalysis, and Lewis acids exert the same effect.

Cyclam-based complexes constitute the most frequently studied group of Ni catalysts for CO_2 electroreduction. On the basis of the pioneering work of Eisenberg et al.[61] and Sauvage et al.[62] in the 1980s, the Ni cyclam system (**23**) represents a remarkable case in which the selectivity of CO_2 reduction can be directed by choice of the electrolyte system: While CPE in water (pH 4 to 5) gives CO in high TON and FE, it leads preferentially to formic acid in aprotic solvents, with FEs of up to 75% and CO as byproduct.

There are only a few examples known in which Co complexes constitute efficient homogeneous catalysts for CO_2 electroreduction. For example, in an report by Peters et al.[63] they had a combined synthetic/electrocatalytic study of the macrocycle complex $[Co(III)N_4H(Br)_2]Br$ (**22**), the authors found that in CO_2-saturated wet acetonitrile, CO can be generated at −2.0 V vs. $Ag/AgNO_3$ with a FE of up to 45% (along with 30% H_2) using this catalyst.

While Cu is a well-studied heterogeneous electrocatalyst for CO_2 electroreduction,[64-66] only a handful of successful applications of Cu catalysts in homogeneously catalyzed reactions have been reported. These cases comprise Cu(II) complexes with ligands based on cyclam,[67] salicylaldimine,[68] carbonate,[69] and 2-hydroxy-1- naphthaldimine.[70] Promising results have also been obtained with dinuclear complexes bridged by phosphanylbipyridine ligands (**25**), whereby a selective formation of CO has been observed in aprotic electrolytes.[71] An outstanding case was reported by Bouwman et al. with the dinuclear complex $[Cu_2(L\text{-}L)]^{2+}$.

Among the 3d metals, perhaps not surprisingly, Zn is nearly absent from the metals that have been used for CO_2 reduction. The key obstacle to using Zn is that is found almost exclusively in the 2+

oxidation state and this redox innocence blocks its ability to undergo the fundamental of oxidative addition and reductive elimination steps typical of homogeneous catalyzed reactions. As an example from the rare number of Zn catalysts, The square planar Zn(II) thiosemicarboazone complex ("Zn(DMTH)") (**24**) is reported to convert CO_2 to formate via a methoxide complex, Zn(HDMTH)(OCH_3), which can insert CO_2 yielding a methylcarbonate species. This carbonate can be subsequently reduced to HCO_2^- by chemical or electrochemically generated hydride sources.[72]

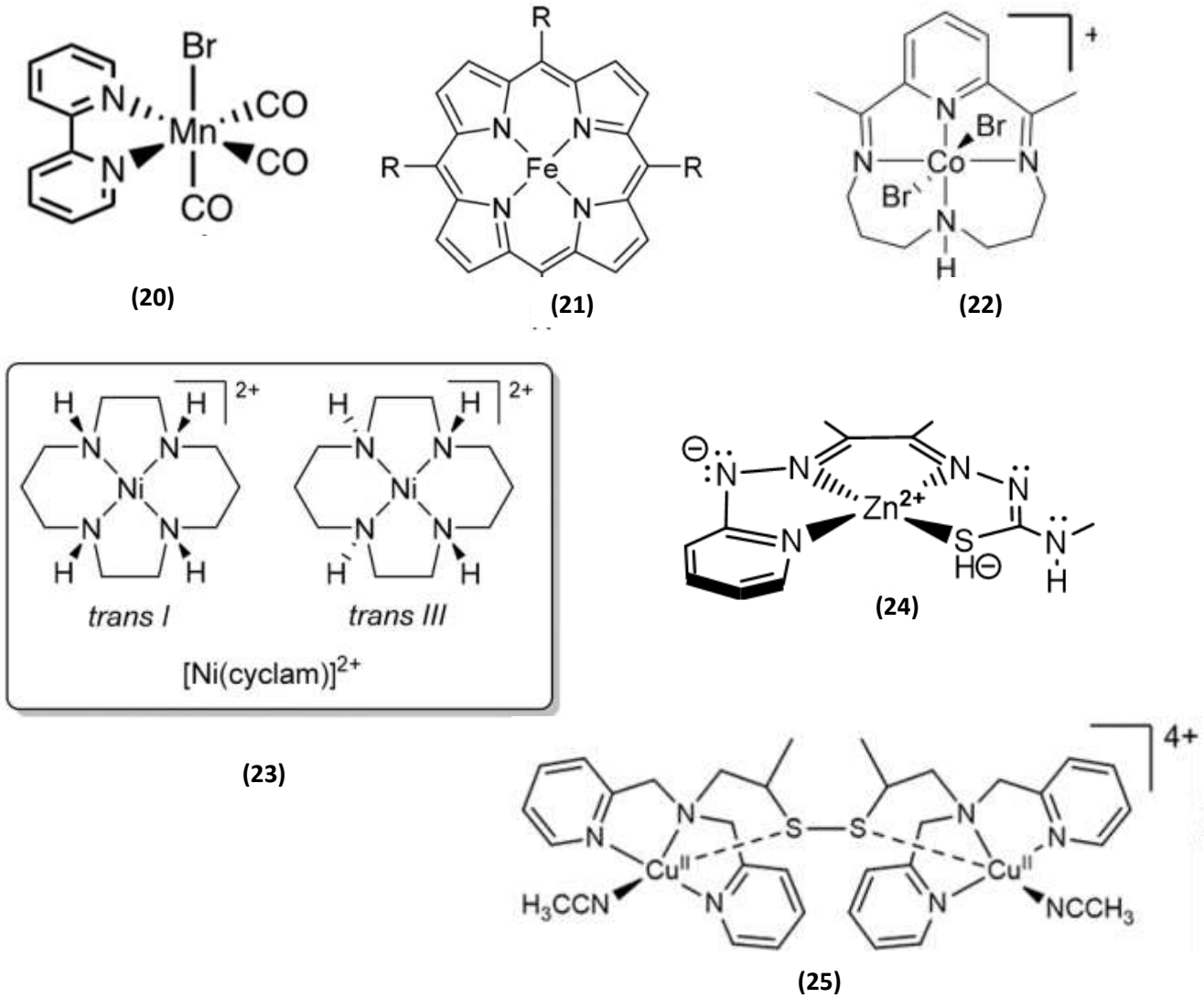

Figure 1.6. Some of the first-row metal complexes active for CO_2 reduction. (Roemelt, Chem. Rev. 2018, 118, 9, 4631–4701. Used with permission from American Chemical Society).

1.6 Nitrate and Nitrite as Water Contaminants and their Reduction

Nitrogen is one of the most abundant elements in organisms.[73] The nitrogen cycle is a basic element cycle in the biosphere.[74] The interference of anthropogenic activities, including overfertilization and factory emissions, has caused an imbalance in the global nitrogen cycle, inducing a threat to the environment and public health. Nitrites, although typically short-lived, can cause diseases such as brown blood disease which leads to the poisoning and accelerated death of fish if they experience prolonged exposure to high concentration. However, nitrite poisoning is not exclusive to aquatic life. When nitrite concentrations are high enough in the human body to enter the blood stream, it can oxidize hemoglobin leading to a condition called methemoglobinemia, which prevents the hemoglobin from delivering oxygen to cells.[75, 76] There are other potential harmful results of high nitrite levels in the body such as birth defects, thyroid disease, and colon cancer. Conventional biological, physical, and chemical treatments of nitrate and nitrite have been applied over the past decades. Because of these effects, governments and scientists have invested resources into methods to mitigate the amount of nitrogen oxyanions that may end up in lakes and our drinking water. Biological denitrification uses microorganisms for the transformation and removal of nitrate and nitrite under an appropriate growth environment for the bacteria. But the sludge that is produced and the possible generation of pathogenic bacteria are limitations on the widespread application of biological denitrification. As for physical-removal approaches, such as reverse osmosis and ion exchange, they focus on displacement, rather than elimination. Thus, the generated secondary-nitrate containing brine requires post-treatment with an additional cost. Chemical reduction is another way to convert nitrite into some desirable products selectively.[77] The driving forces for chemical reduction can be divided into heat, light, and electrical energy.[78] Among them, the electrochemical reduction of nitrite is considered a

promising way because of the use of the green electron as the reductant, the ambient operation conditions, and the lack of secondary treatment needed. This process is beneficial for converting nitrite into harmless dinitrogen from the point of environmental protection, or into recyclable ammonia from the point of ‘‘turning waste into wealth’’ (Figure 1.7).[79, 80] To design and synthesize efficient electrocatalysts for the reduction of nitrate, a fundamental understanding of its reaction mechanisms is necessary.

$$NO_2^- + 2H^+ + e^- \longrightarrow NO(g) + H_2O$$

$$2NO_2^- + 6H^+ + 4e^- \longrightarrow N_2O(g) + 3H_2O$$

$$NO_2^- + 8H^+ + 6e^- \longrightarrow NH_4^+ + 2H_2O$$

$$2NO_2^- + 12H^+ + 10e^- \longrightarrow N_2(g) + 6H_2O$$

Figure 1.7. Generic depiction of the electrochemical reduction of NO_2^- to various products.

Nitrite reduction is a complicated multi-electron-transfer process, which involves many nitrogen-containing species from +3 to -3 valence states. Dinitrogen and ammonia/ammonium, the most thermodynamically stable products, have been studied intensively.[79, 81]

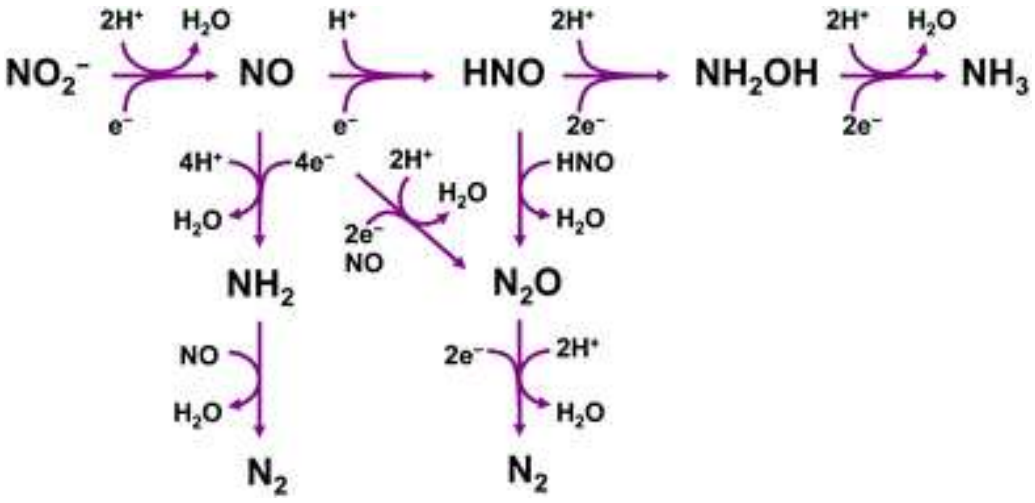

Figure 1.8. The pathway of electrochemical nitrite reduction to different products. (Chem. Commun., 2022, 58, 2777-2787). Used with permission from Royal Society of Chemistry).

To make the electrochemical reduction of NO_2^- more efficient, transition metal complexes are being employed as a method of not only reducing this harmful chemical, but also to elucidate the mechanisms of these transformations. Depending on the catalyst, several products are available, and are often in competition. Also, depending on the pH of the solution, the formation of certain products may be favoured over others (Figure 1.8).[82, 83] For instance, the reduction of protons, a hydrogen evolution reaction (HER), is pH dependent and often in competition with nitrate and nitrite electroreduction reactions. It has been shown that in acidic media, HER can lower the Faradaic efficiency of the nitrate/nitrite reduction reaction. Additionally, Xing et al.[84] demonstrated that in alkaline media (lower availability of H^+), the reduction of nitrate halts at NO_2^- whereas in acidic media (higher availability of H^+) nitrite reduction is favoured and leads to reduction products such as NH_4^+, N_2, N_2O, etc. Thus, the use of buffer systems in nitrate and nitrite reduction reactions is a necessity to control the pH of the system and aid in revealing mechanistic insights towards pH dependent product formation.

Literature review on nitrite reduction using molecular catalysts:

The search for homogeneous molecular electrocatalysts for the reduction of nitrite is a thriving field that has been focused on Fe(III), Co(III), and Cu(II) compounds (Figure 1.9). The Co(III) cyclam complex, $[Co(cyclam)Cl_2]^+$, provided an early report for electrocatalytic reduction at -1.5V vs. SCE to yield hydroxylamine as the principal product with activity only observed at a mercury pool working electrode and in basic solution.[85] More recent reports of a Co(III) cyclam analog having an unsaturated α-diimine ligand framework, **A**, electrocatalytically reduced nitrate to ammonia with 88% efficiency.[86, 87] These same workers reported that Co(III) complex of a neutral tetraazamacrocylic ligand containing the redox non-innocent di(imino)pyridine moiety, **D**, transformed nitrite under electrocatalytic and acidic (1.46V vs SCE, pH = 6.40) conditions to yield

ammonium with 88% FE. Experimental and computational studies suggested that the ligand plays an important role in the redox chemistry.[88] By contrast, porphyrin complexes, [Co(2-TMPyP)][89] (2-TMPyP =tetrakis(N-methyl-2 pyridyl)porphine) (**B**) and [Fe(H_2O)(TPPS)$]_3$] (TPPS = (meso-tetrakis(p-sulfonatophenyl)porphyrin)), (**E**) reduced NO_2^- to NH_3 and NH_2OH in acidic media. Side products of N_2O and hydroxylamine appeared depending on the reaction conditions. A bio-inspired Co(III) metallotripeptide complex, **C**, showed electrocatalytic reduction of nitrite at -0.90V vs. SCE using a Hg electrode in a slightly acidic buffered aqueous solution (pH = 7.2). The product was ammonia with a turnover number after 5.5 hours of greater than 3500. The Fe(III) complex, **F**, displaying a macrocyclic pentadentate ligand, which also included a di(imino)pyridine group, reduced NO_2^- to NH_2OH and NH_4^+ in a buffered aqueous solution at pH 7.2 and -0.98V vs. Ag/AgCl. In the absence of buffer this catalyst displayed little activity. Several Cu (II) complexes supported by tripodal N-coordinating ligands, such as **G**, have been demonstrated to reduce nitrate. The common product from these reductions was NO and the required electrochemical potentials and Faradaic yields depend on the features of the ligand framework and solution pH.

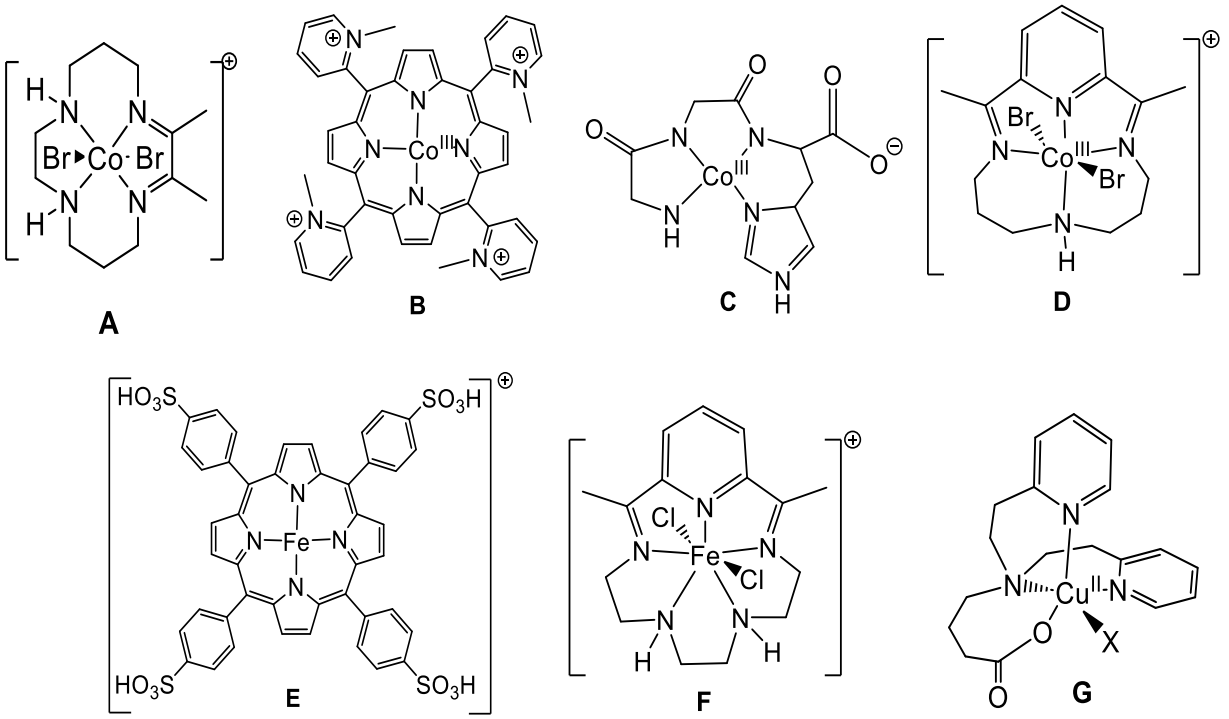

Figure 1.9. Selected recent molecular electrocatalyst for nitrite reduction.

1.7 Scope and Content of this Thesis

This thesis consists of seven chapters each of which focus on a broadly targeted area of electrocatalysis using earth abundant metals complexes to promote sustainability. Specifically, Chapters 2, 3, and 4 focus on the production of H_2 from neutral water as proton source. Chapter 5 focuses on the reduction of CO_2 gas to value-added products, and Chapters 6 and 7 on the reduction of nitrite to useful chemical building blocks in aqueous solution. Each of these areas presents a significant challenge that society faces with respect to improving the overall quality of the environment and human health.

Chapters 2, 3, and 4 present results on electrocatalysis using water as a renewable and green proton source and solvent to generate H_2. The electrocatalysts are Ni(II) complexes with pincer non-innocent ligands. In Chapter 2 we present two [Ni(κ^3-2,6-{Ph_2PNR}$_2$(NC_5H_3)Br_2] (Ni(II)PN^3P)

complexes and study their HER using electrochemical and computational experiments. In the next two Chapters [Ni(κ^3-2,6-{RPhNCR'}$_2$(NC_5H_3)Br_2] (Ni(II)DIMPY) complexes with different substituents on the ligand were used and electrochemical studies in both organic and aqueous solution using different proton sources in the range of different pKa were explored. As a part of these projects, we investigated the mechanism for the hydrogen generation by this catalyst in both aqueous and organic solution, using acetonitrile and TFA as the proton donor.

Chapter 5 explored application of electroreduction of CO_2 by employing a Zn complex bearing PN^3P pincer ligands. The approach behind this endeavour was to use a redox innocent metal center with a redox non-innocent ligand and study the role of ligand in the catalysis.

In Chapters 6 and 7 in a new endeavour for our group, reduction of nitrite (NO_2^-) in neutral aqueous solution was explored using a Ni complex with a DIMPY core. Part of this project was to elucidate the nitrite reduction mechanism to help understand part of the nitrogen cycle. The work from Chapter 6 was extended in Chapter 7 to investigating the effect of small changes in the ligand backbone on the catalyst performance.

Chapter 2: Electrocatalytic H_2 Generation from Water Relying on Cooperative Ligand Electron Transfer in "PN^3P" Pincer-Supported Ni(II) Complexes.

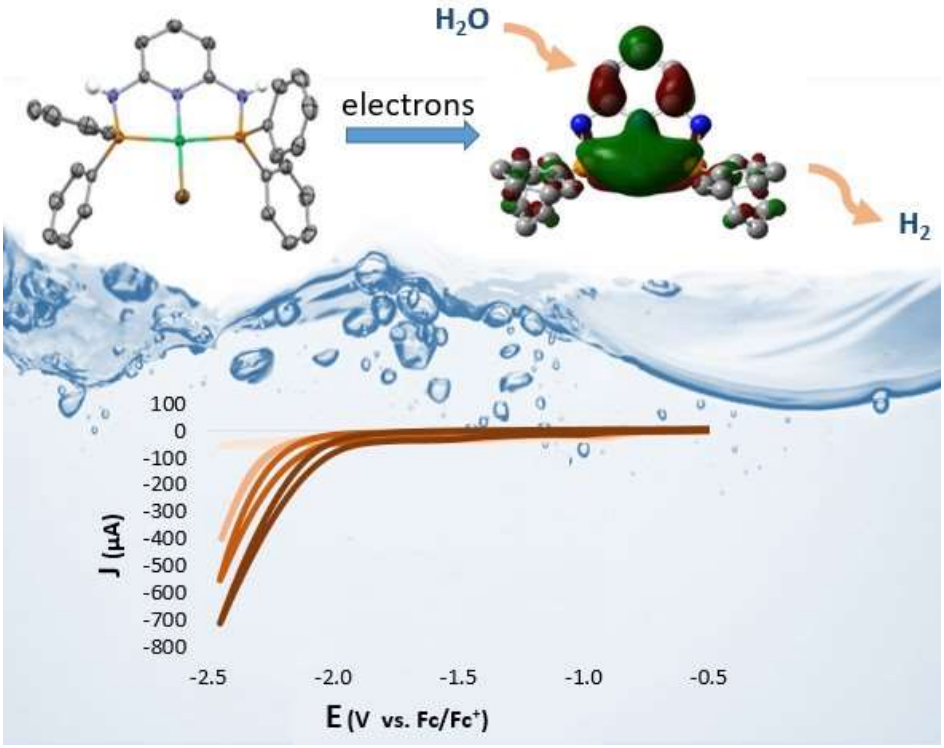

2.1. Preamble and Context

This work has been published in Chemistry a European Journal and can be accessed at https://doi.org/10.1002/chem.202102031 ["Norouziyanlakvan, S., Rao, G.K., Ovens, J., Gabidullin, B. and Richeson, D., 2021. Electrocatalytic H_2 Generation from Water Relying on Cooperative Ligand Electron Transfer in "PN^3P" Pincer-Supported NiII Complexes. Chemistry–A European Journal, 27(54), pp.13518-13522."].

This manuscript was prepared by Dr. Darrin Richeson (DR) and Somayeh Norouziyan (SN). DFT computations and their analysis were performed by DR with feedback from SN.

2.2. Abstract

Water represents the most sustainable source for H_2 production and the efficient electrocatalytic production of H_2 from mixed water/acetonitrile solutions using two new air-stable nickel(II) pincer complexes, [Ni(κ^3-2,6-{Ph_2PNR}$_2$(NC_5H_3)Br_2] (R = H **2.1**, Me **2.2**) is reported. Hydrogen generation from H_2O/CH_3CN solutions initiates at -2 V vs. $Fc^{+/0}$ and bulk electrocatalysis studies showed that the catalyst functions with an excellent Faradaic efficiency and a turnover frequency of 210 s^{-1}. A DFT computational investigation of the reduction behaviour of **2.1** and **2.2** revealed the correlation of H_2 formation with charge donation from electrons originating in a reduced ligand-localized orbital. As a result, these catalysts are proposed to proceed by a novel mechanism involving electron/proton transfer between a Ni(0) species bonded to an anionic PN^3P ligand ("L^-/Ni(0)") and a Ni(I)-hydride ("Ni-H"). Furthermore, these catalysts are capable to reduce phenol and acetic acid, more active proton sources, at lower potentials that correlate with the substrate pKa.

2.3 Introduction

Dihydrogen, the simplest of molecules, represents an ideal, environmentally innocent energy source that affords water as the sole product of oxidation. In order to enable sustainable production of H_2, it is crucial to discover and interrogate electrocatalysts based on earth-abundant metals. Furthermore, water represents the optimal substrate for the generation of hydrogen, and viable catalytic processes directly using water as the hydrogen source are desirable. The report that tetraazamacrocycle (cyclam) complexes of Co and Ni could generate H_2 from neutral water under electrochemical conditions was a starting point for the discovery of a wide range of metal complexes that can reduce protons to hydrogen[31, 38, 90-92]. The majority of these species perform in polar organic solvents and require the presence of acids as a hydrogen source even with

electrocatalysis in aqueous solution. In general, complexes that are capable of catalyzing hydrogen evolution from simple water as a proton source are still rare[31, 90-92]. While many of these reports focus on the important performance parameters of catalysts requiring acid as substrate, the lower environmental and economic impacts, as well as revealing fundamental features that would allow the use of water as a substrate, clearly inspires attention and motivates discovery of new earth-abundant catalysts and mechanisms.

Nickel is an attractive metal center for designing new H_2 generation catalysts due to its abundance and ability to form complexes with a range of accessible oxidation states and flexible coordination behavior[91]. Added stimulus comes from the appearance of Ni as a component in hydrogenase enzymes[93]. These features provide motivation to explore and design ligand scaffolds that would enable Ni complexes as hydrogen evolution catalysts.

Cyclam (1,4,8,11 -tetraazacyclotetradecane) complexes of Ni(II)[19] were the first report of a Ni complex that was able to produce hydrogen from water, at -1.55 V vs SCE. Since then, a number of Ni complexes with different types of ligands have been reported for Hydrogen Evolution Reactions (HER) using both water and acids as the proton source. Most of these are applied to proton reduction from acids (both organic and inorganic), neutral aqueous sources for hydrogen are much more rare. Nickel N4 and N5-pyridine containing macrocyclic complexes[39], diimine–dioxime complexes[94, 95], the pyridinediimine complex[47], the dithiolene complex[96, 97], thiolate complexes[98-100], and nickel complexes with amine-containing diphosphine ligands[42, 43, 101], are examples of complexes that are active for HER using water as proton source.

An example of a family of Ni electrocatalytic complexes with amine-containing diphosphine ligands (**A**) was reported by Dubois et al. , achieving a turnover frequency (TOF) of 106 000 s^{-1}

for H_2 production[43]. These complexes are among the most developed Ni-based Hydrogen Evolution Catalysts (HECs) and feature bis(diphosphine) ligation. They show a CV-derived TOF > 105 s^{-1}, in the presence of strong acids. A few other nickel-phosphines have been studied electrochemically but rarely with H_2O present. One exception is the functionalized diphosphine complex[102] shown in Figure 2.1. Controlled Potential Electrolysis (CPE) in aqueous H_2SO_4 (pH 1.0) using a Glassy Carbon (GC) foam WE at E_p = −0.60 V vs NHE (-1.25 V vs $Fc^{+/0}$) gave 92−105% Faradaic efficiency (FE) with a TON of 7−9 after 18 h. Despite showing good stability, the metrics are modest when compared with DuBois-type complexes.

Another example of HER from neutral water is diimine–dioxime complexes (**B**) reported in 2017 by Zhan et al. Two pyridine derivatives give Ni-based HECs that operate in neutral aqueous media and catalytic events were observed upon addition of acetic acid. CPE formed H_2, with a GC working electrode at E_p = −1.45 V vs Ag/AgCl in aqueous phosphate solution (pH 7.0) giving respective FE $_{H2}$ values of 91% and 88% over 1 h (no TON_{H2} reported).[103, 104]

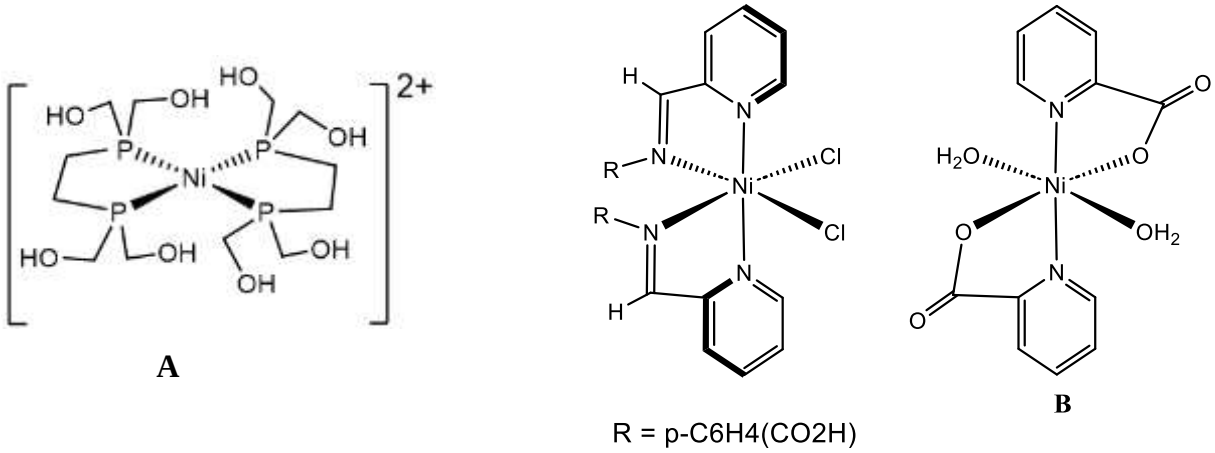

Figure 2.1. Selected Ni complexes that are active electrocatalysts for HER.

In most of these reports ligands are considered innocent and metal has the main role in catalysis undergoing two reductions and one step of protonation to generate a metal hydride which then releases H_2. There are a only few reports in which the ligands are non-innocent and cooperate in

HERs.

Some examples include Ni(II) dithiolate and nickel porphyrin electrocatalysts having ligand centered redox and proton transfer capabilities[105-107]. Remarkably, the concept of using redox active ligands for hydrogen evolution has been expanded to include metal-free redox active thiosemicarbazone and redox non-active Zn(II) complexes of this species[108, 109]. Notably, all these examples employ acid as the proton/hydrogen source. Recently, complexes of Ni(II) and N-benzyl-N,N',N'-tris(2-pyridylmethyl)ethylenediamine ligands have been reported as efficient catalysts for H_2 evolution from water at -2.09 V vs. $Fc^{+/0}$.[110, 111] This reduction was assigned to Ni(I/0) reduction couple and a ligand centered reduction at -2.6 V.

Strong electron donating anionic PNP pincer ligands, are among these non innocent ligands which contain unsaturated bonds and have been widely studied by the Huang group[112, 113]. In one example replacing the CH_2 groups with NH spacers in the pyridine-based PN^3 complexes can result in diverse catalytic activities and different thermodynamic and kinetic properties through deprotonation and reprotonation of the NH group[112]. In another example by this group, in 2018, a dearomatized PN^3P*-nickel hydride complex was reported for the nickel-catalyzed hydrosilylation of CO_2 to methanol[114].

Our efforts to reveal new Ni catalysts for the production of hydrogen from water began with the choice of N,N′-bis(diphenylphosphino)-2,6-diaminopyridine species (2,6-{Ph_2PNR}$_2$(NC_5H_3; R = H (**2.1**), Me (**2.2**)) as ligands. These "PN^3P" neutral pincer ligands offer tunablity of steric and electronic properties and are known to support catalysts for a variety of reactions[115]. In the case of R = H, the PN^3P ligand has been demonstrated to display non-innocence through deprotonation and "dearomatization" of the backbone during catalysis.[113, 114, 116] Furthermore, the Richeson

group has previously demonstrated PN^3P-supported Co complexes as efficient electrocatalysts for H_2 formation.[117]

This chapter reports two air-stable Ni(II)-PN^3P pincer complexes that perform electrocatalytic hydrogen evolution from mixed water/acetonitrile solutions. We found, through a combination of empirical and computational observations, that the PN^3P ligand acts an electron reservoir for this transformation. A Ni complex with bidentate PN^2 ({κ^3-(Ph_2PNMe)(NC_5H_3)Br_2) (**2.3**) ligand was also synthesized with the aim of studying the effects of symmetrical and unsymmetrical ligands on the catalysis.

2.4 Results and Discussion

2.4.1 Synthesis and Structural Analysis

Ready access to the PN^3P and PN^2 complexes of Ni(II) was provided by direct reaction of the appropriate ligand and a suspension of anhydrous $NiBr_2$ in toluene for overnight at room temperature (Scheme 2.1). All three complexes were stable under ambient conditions and could be stored for months with no obvious decomposition. NMR spectroscopic analysis indicated that complex **2.1** and **2.2** possessed symmetrically coordinated ligands as exemplified by a single NMR resonance for the N-H groups, and symmetrical pyridyl and phenyl substituents in the ^1H NMR. Additionally, the ^{31}P NMR spectra displayed single resonances. Complex **2.3**, as expected, showed an unsymmetrical bidentate structure supported by ^{1}HNMR showing four hydrogen resonances for the pyridyl group. This complex displayed a single ^{31}P NMR resonance at 51.0. The formulae were confirmed by elemental analysis.

Scheme 2.1. Reaction scheme for preparing complexes **2.1**, **2.2**, and **2.3**.

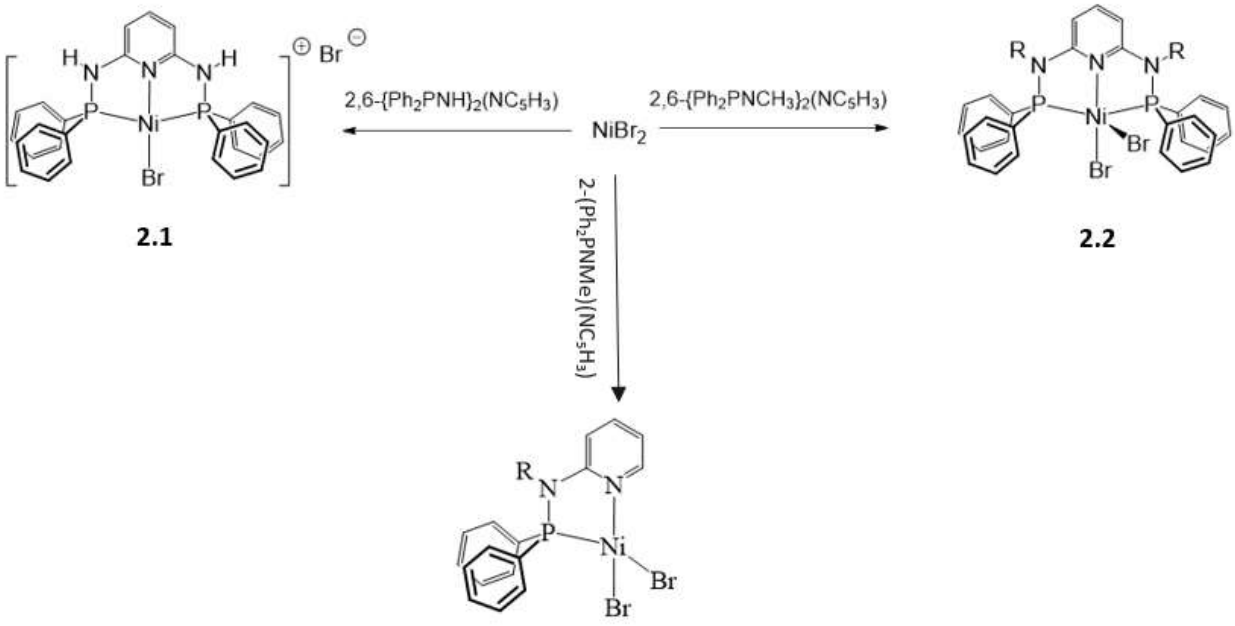

The molecular structures for compounds **2.1, 2.2, 2.3** were obtained through single crystal X-ray analysis. Compound **2.1**, [Ni{κ^3-$(Ph_2PNH)_2(NC_5H_3)$Br]t$^+$ Br$^-$ displayed a four-coordinate square planar Ni(II) cation (**2.1**$^+$) with a bromide counter anion. The result of the X-ray analysis is displayed in Figure 2.2 and Tables A1-A2. The crystal structure also contained co-crystallized water molecules. The Ni coordination sphere consists of a planar tridentate "PN^{3}P" neutral pincer ligand and a bromo ligand that is in the *trans* position relative to the coordinated N pyridyl center. The structure of **2.1**$^+$ compares favorably with the reported structures of [Ni(2,6-{Ph_2PNH}$_2$(NC_5H_3)Cl]Cl,[118] [Ni(2,6-{tBu_2PNH}$_2$(NC_5H_3)Br]Br[119] and Ni(2,6 {iPr_2PNH}$_2$($NC_3N_2H_2(NMe_2)$)Cl]Cl[120].

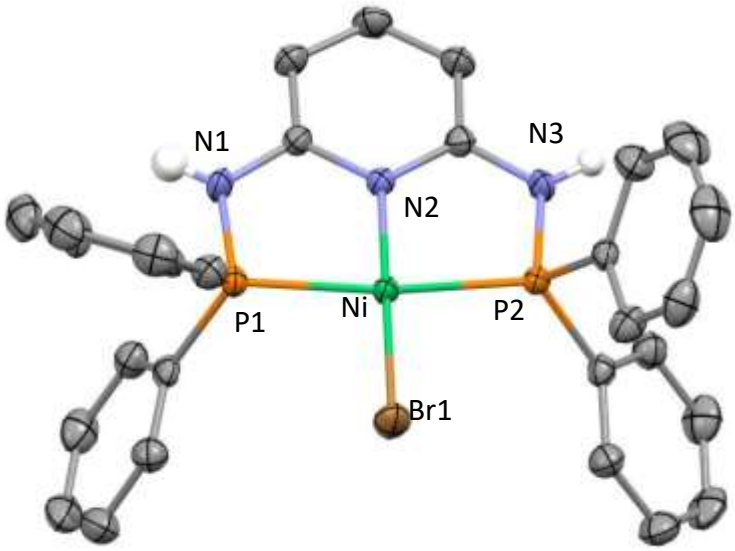

Figure 2.2. Structural representation of the cation of compound $[Ni\{\kappa^3\text{-}(Ph_2PNH)_2(NC_5H_3)Br]^+Br^-$ (**2.1**$^+$) obtained from single crystal X-ray diffraction analysis. The carbon bonded H atoms, bromide counter anion and co-crystallized water molecules have been omitted for clarity.

In contrast, complex **2.2**, $[Ni(2,6\text{-}\{Ph_2PNMe\}_2(NC_5H_3)Br_2]$, presents an asymmetric unit with a monomeric five-coordinate Ni(II) with distorted square pyramidal geometry, an unprecedented geometry with the PN^3P ligand. The ligand is coordinated to Ni in a planar tridentate fashion through the nitrogen and two phosphorus centers, occupying three basal positions of the square pyramid. One bromo ligand, Br1, occupies the remaining basal position, *trans* to the pyridyl N center, with Br2 filling an apical position, perpendicular to this plane with the average angle between Br2 and the other four coordinated centers of 97.4°. This apical Br(2)-Ni(1) distance is much longer (2.7961(9) Å) than the basal Br(1)-Ni(1) length (2.3100(6) Å) (Table A.3, A4). Interestingly, this Ni(1)-Br(1) distance is similar to the analogous Ni-Br distance in complex **2.1** (2.2741(4) Å). Furthermore, the Ni-P bond distances in **2.2** (P(1)-Ni(1) 2.1432(9) Å, P(2)-Ni(1) 2.1687(9) Å) are similar to those in **2.1** (i.e. 2.1705(5) Å, 2.1686(5) Å) and the Ni(1)-N(2) distance 1.911(2) Å is slightly longer than the corresponding Ni-N distance in **2.1** at 1.8857(15) Å. These

data suggest that **2.2** is related to **2.1** with an additional weak apical coordination of a bromide anion, Br(2), to Ni.

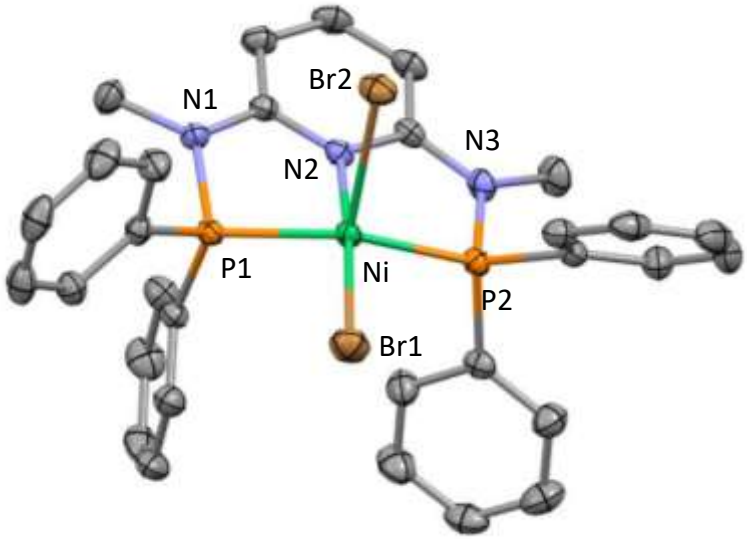

Figure 2.3. Structural representation of [Ni{κ^3-$(Ph_2PNMe)_2(NC_5H_3)Br_2$] (**2.2**). Hydrogen atoms omitted for clarity.

The single crystal X-ray analysis revealed a four coordinate Ni(II) center for [Ni{κ^2-$(Ph_2PNMe)(NC_5H_3)Br_2$] (**2.3)** with a planar coordinated bidentate PN^2 neutral pincer and two bromo ligands as shown in Figure 2.4. The Br(1) ligand (Br_{pl}) is in the same plane as the pincer ligand and *trans* to the coordinated pyridyl nitrogen, N2. The Br2 ligand (Br_{ax}) is perpendicular to this plane and the angle between Br(2) and Ni center is 93°. This axial bromo ligand has a longer bond length (Br(1)-Ni(1) , 2.3371(16)) compared with the bromo ligand in the plane, Br(2)-Ni(1), 2.3101(16)). In addition, the Ni-P bond distance is much longer P(1)-Ni(1) 2.107(3)Å than the Ni(1)-N(1) distance 1.935(8) Å (Table A5, A6)

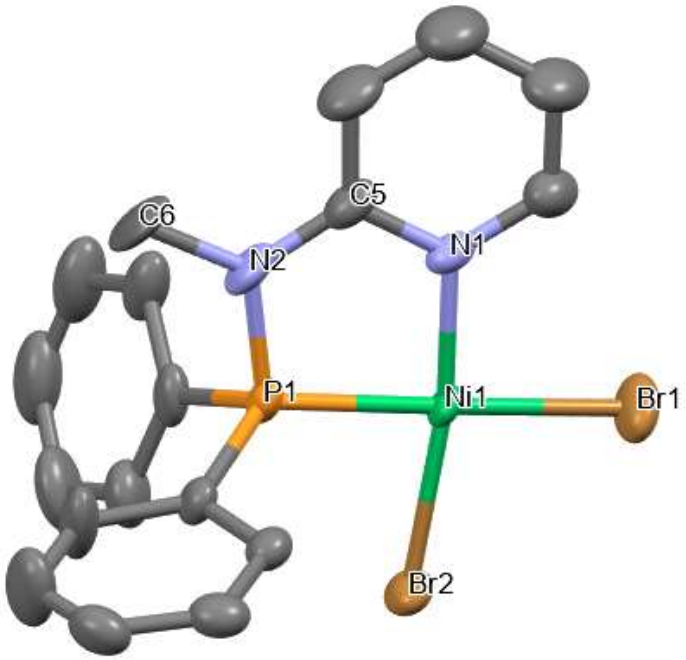

Figure 2.4. Structural representation of [Ni{κ^2-(Ph_2PNMe)(NC_5H_3)Br_2] (**2.3**). Hydrogen atoms omitted for clarity.

Initial experiments showed that complex **2.3** does not display promising electrochemistry as a catalyst toward HER; therefore, this chapter will focus on the reactivity of complexes **2.1** and **2.2** with only a few experiments with complex **2.3** for comparison purposes.

2.4.2 Electrochemistry and Electrocatalysis

Cyclic voltammetric scans of 1.0 mM solutions of these Ni complexes in dry acetonitrile, with 100 mM tetrabutylammonium hexafluorophosphate (TBAHFP) supporting electrolyte using a glassy carbon (GC) working electrode, a Platinum (Pt) counter electrode and a pseudo-reference electrode Silver (Ag) wire, under N_2 atmosphere, under cathodic potentials, are shown in Figure 2.5 for complexes **2.1**, **2.2**, and in Figure 2.6 for complex **2.3**. All potential measurements are referenced to the reversible ferrocene couple ($Fc^{+/0}$, $E_{1/2}$ = 0.55 V ΔE_p = 100mV). Both complexes exhibited similar profiles with three reduction events. The first peak was a reversible reduction at $E_{1/2}$ = -0.93 V (**2.1**, ΔE_p = 100mV) and $E_{1/2}$ = -0.89 V (**2.2,** ΔE_p = 100mV). This ΔE_p value is higher than

the ideal number of 0.059V, but it is close to the ΔE_p that we measured for the $Fc^{0/+}$ redox reactions in the same solvent system. This difference is attributed to the resistance in the electrochemical cell (Figure 2.A15). In order to find the resistant value of the system, an Electrochemical Impedance Spectroscopy (ESI) experiment was performed with 1mM **2.1** in CH_3CN solution with 0.28M water and the resistant value was measured Z_{re} = 200.6 Ω. at -2V.

A second reduction was irreversible at -1.4V (**2.1**) and -1.32V (**2.2**), respectively. Both complexes displayed a third irreversible reduction at -2.49 V for **2.1** and -2.57 V for **2.2** (Figure 2.5). Complex **2.3** showed a bit different behavior, showing two small redox peaks between -0.4 and -0.8V, two reduction peaks at -1.25V and -2.75V (Figure 2.6). A CV scan of CH_3CN alone was performed and it was observed that the solvent reduction by GC electrode happens at E_{onset} (E_o)=-2.6V. As it is shown in Figure 2.7 the third peak of complex **2.1** and **2.2** appears at a potential just before the CH_3CN reduction. In the case of complex **2.3,** the last peak overlaps with the solvent reduction peak.

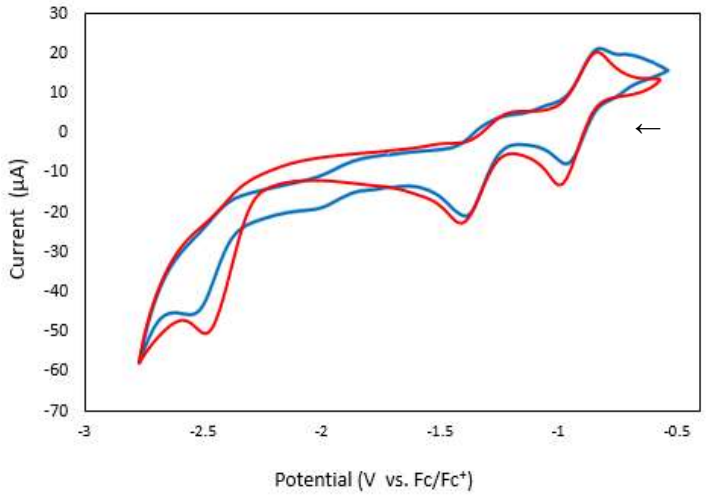

Figure 2.5. CV of complexes **2.1** (red) and **2.2** (blue) (1.0 mM) under N_2, in 0.1 M tetrabutylammonium hexafluorophosphate (TBAHFP) solution in CH_3CN and scan rate was 100 mV/s. The arrow indicates initial scan direction. (Open circuit potential approx. -0.6V).

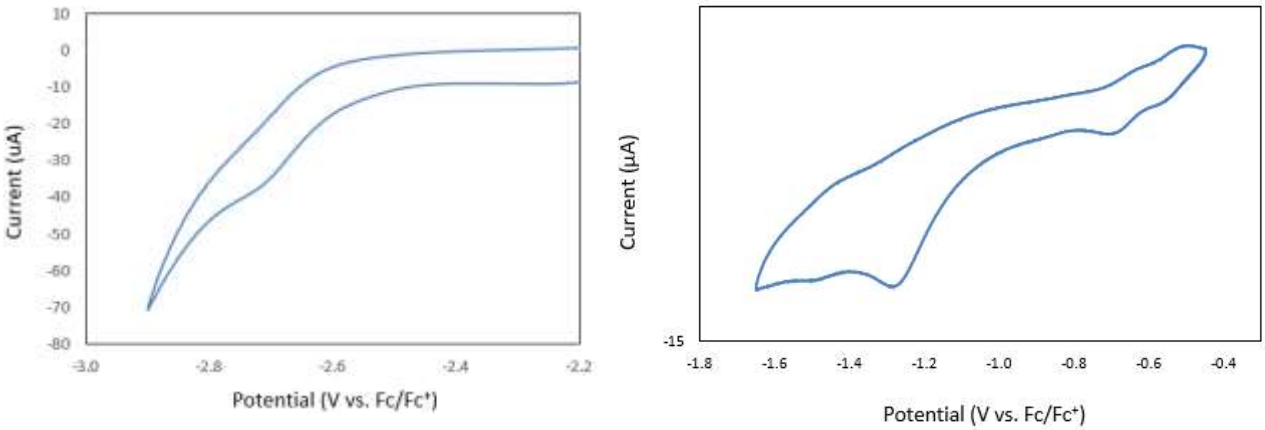

Figure 2.6. Cyclic voltammograms for complex **2.3** [Ni(2,6-{Ph_2PNMe}(NC_5H_3)Br_2].

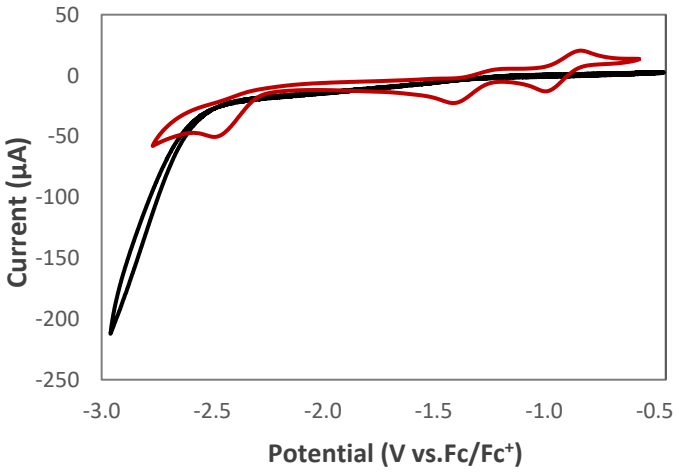

Figure 2.7. Cyclic voltammograms for complex **2.1** (red) and CH_3CN alone (black).

All of these reduction events displayed a linear dependence of the current intensity versus the square root of the scan rate, consistent with freely diffusing species, according to the Randles-Sevcik equation (Figures 2.8-2.10). The Randles-Sevcik formula indicates that species are freely diffusing in solution if the plots of currents vs. $v^{1/2}$ result in a linear relationship. Deviations from linearity in such plots may suggest adsorption of species on the electrode surface or even the occurrence of thin-layer diffusion.[22]

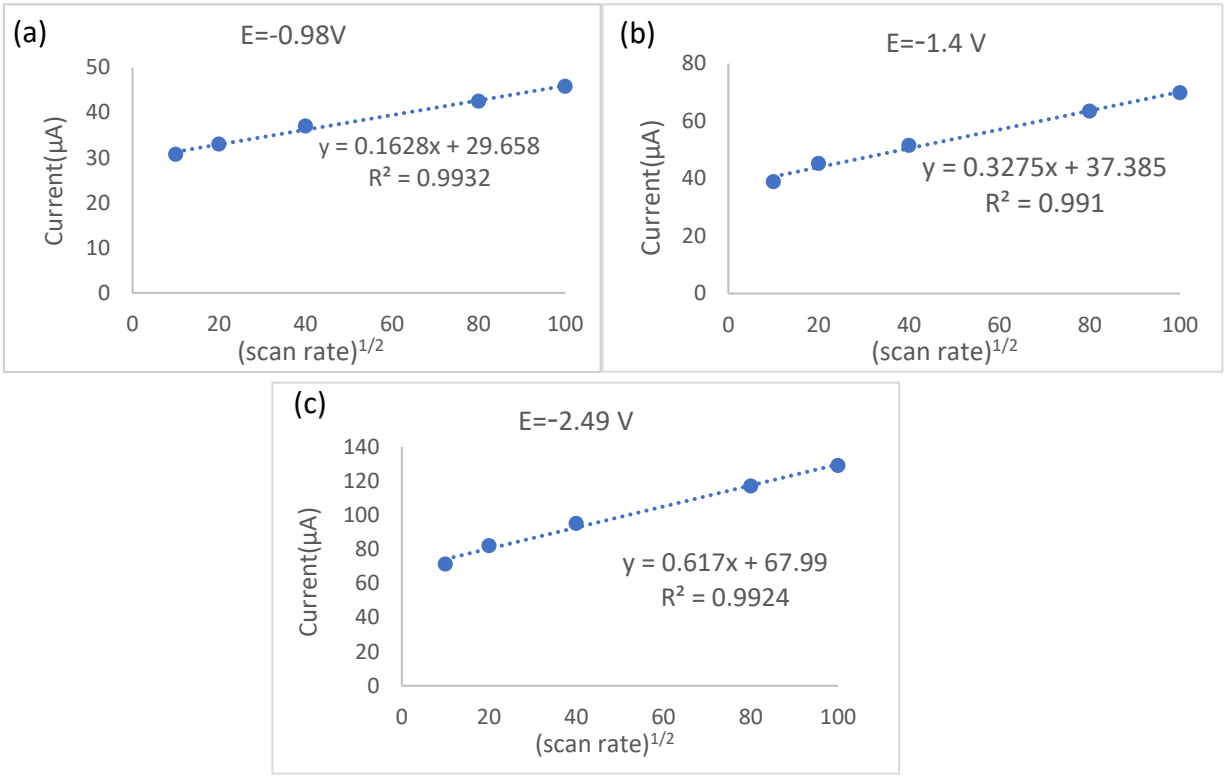

Figure 2.8. Plots of scan rate1/2 versus current for the (a) first at -0.98 V, (b) second at -1.4 V, and (c) third at -2.49 V reduction peaks of $[Ni(2,6\text{-}\{Ph_2PNH\}_2(NC_5H_3)Br]^+Br^-$ (**2.1**). All potentials are referenced to Fc/Fc^+ in CH_3CN.

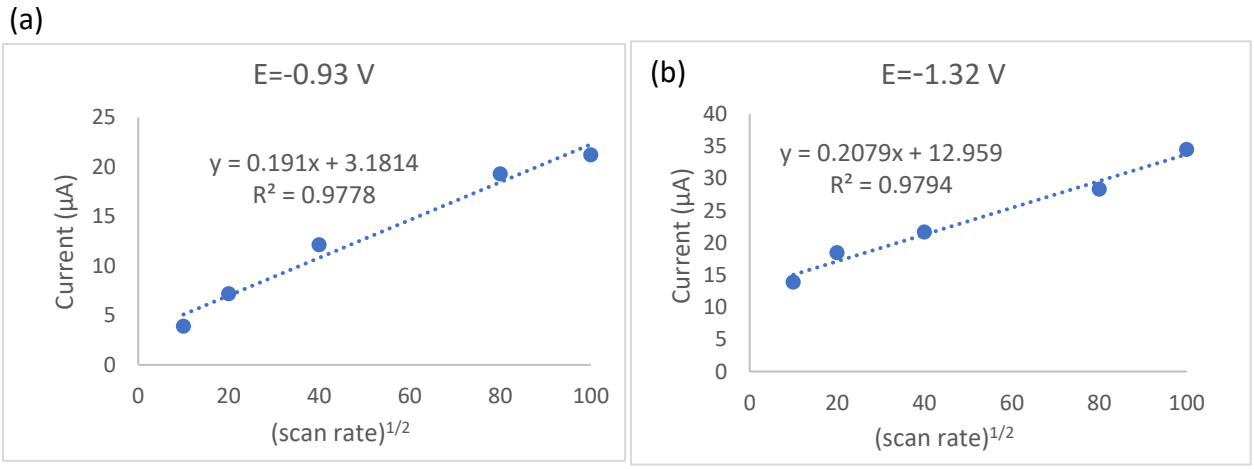

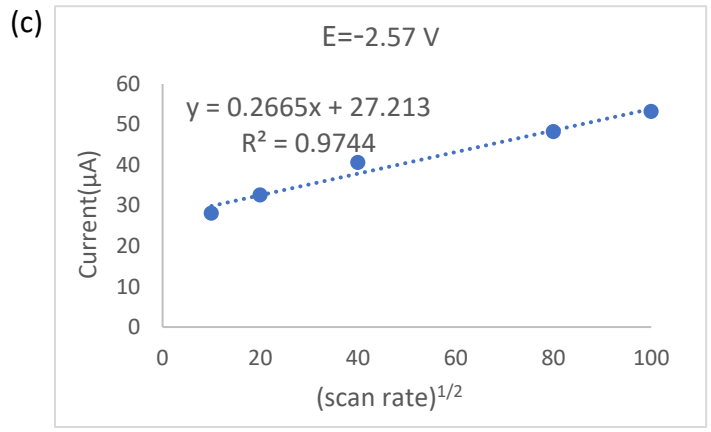

Figure 2.9. Plots of scan rate $^{1/2}$ versus current for the (a) first at -0.93 V, (b) second at -1.32 V, and (c) third at -2.57 V reduction peaks of [Ni(2,6-{Ph_2PNMe}$_2$(NC_5H_3)Br_2] (**2.2**). All potentials are referenced to Fc/Fc^+ in CH_3CN.

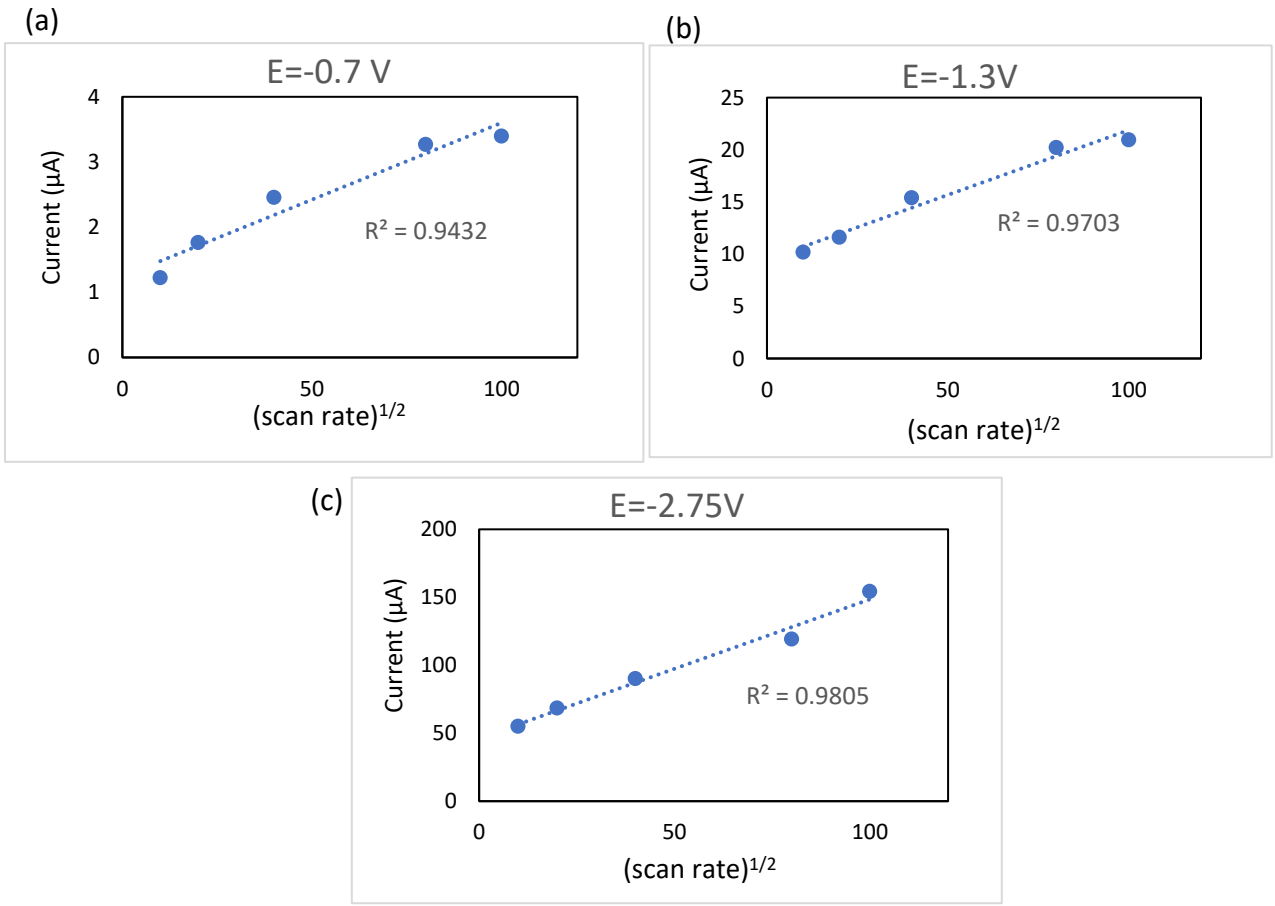

Figure 2.10. Plots of scan rate$^{1/2}$ versus current for the (a) first at -0.7 V, (b) second at -1.3 V, and (c) third at -2.75 V reduction peaks of [Ni(2,6-{Ph_2PNMe}(NC_5H_3)Br_2] (**2.3**). All potentials are referenced to Fc/Fc^+ in CH_3CN.

The first indications that these Ni complexes were active electrocatalytically for water reduction were seen in the voltametric behavior of these complexes in H_2O/CH_3CN mixtures. Figure 2.11 and 2.12 displays the reduction behavior of **2.1, 2.2** and **2.3** in the absence and presence of water. As it is clear, by adding water there was a catalytic enhancement observed at around the third reduction peak of complexes **2.1** and **2.2**, which showed increasing current when the concentration of water in the solution was increased. It is worth noting that the enhancement for a specific [H_2O] was more with complex **2.1** compared to complex **2.2**. In the absence of catalyst (Figure 2.11, dark blue dashed curve), there were no indications of enhanced current with added water which indicates that the catalysis depends on the presence of Ni complexes in the electrochemical cell. In the cyclic voltammograms, a shift toward more positive potentials was observed as the concentration of water increased which displays a Nernstian behavior as shown by a linear relationship of the log[H_2O] *vs*. E_o (Figure 2.11.c). In this plot, the onset potentials were defined by using a fixed threshold current value of 70μA, the corresponding voltage value was defined as E_o. Regarding complex **2.3**, after addition of water an enhancement was seen at E_o=-2.75V which correlated with the third peak of this complex. However, at this voltage there is a substantial current due to reduction of the solvent and of water by the GC electrode. As a result, is would be difficult to determine the effect of the catalyst. For these reasons, we decided not to further investigate the behavior of complex **2.3** for water reduction.

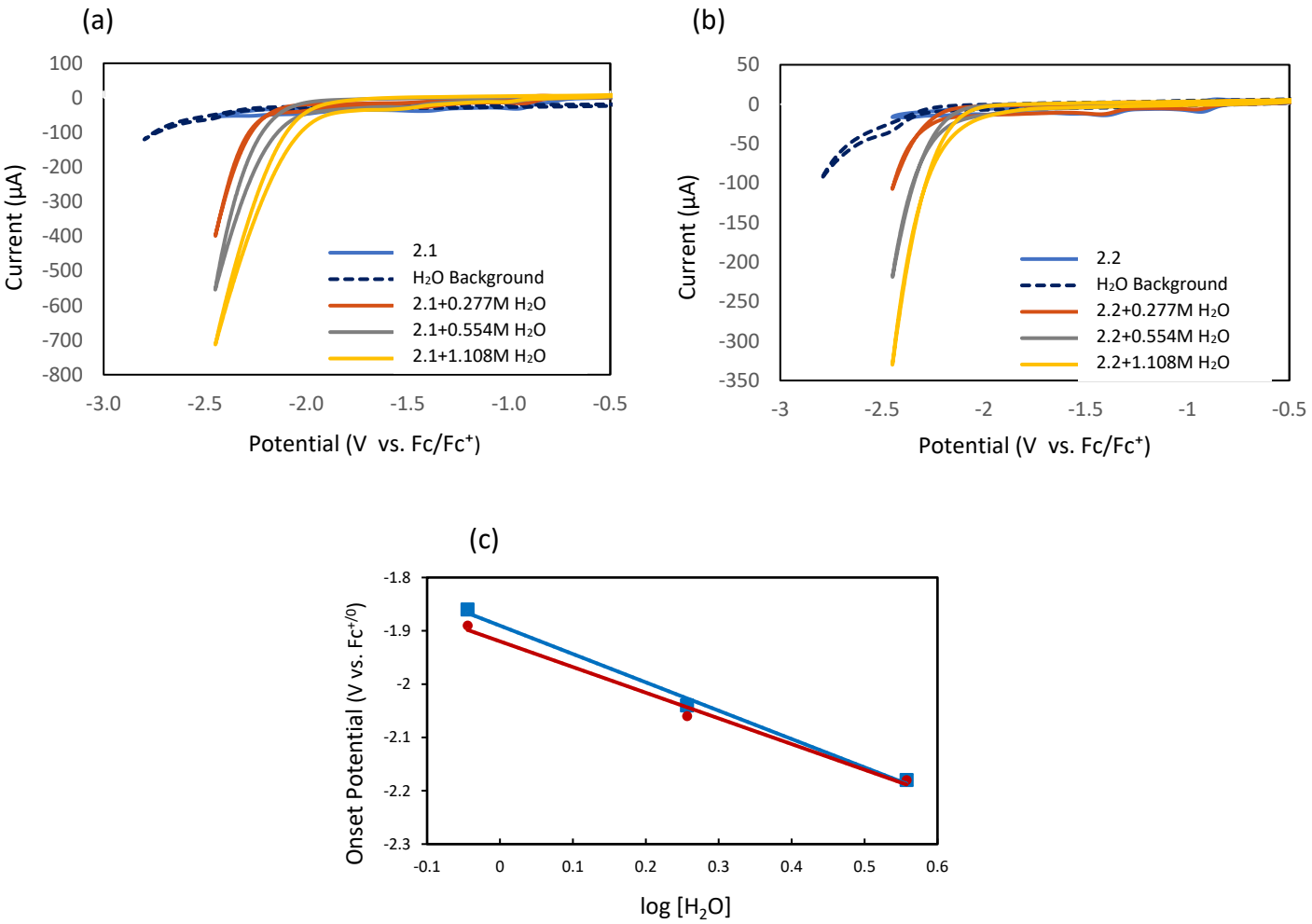

Figure 2.11. Cyclic voltammograms for (a) [Ni(2,6-{Ph_2PNH}$_2$(NC_5H_3)Br]$^+$Br$^-$ (**2.1**), (b) [Ni(2,6-{Ph_2PNMe}$_2$(NC_5H_3)Br_2] (**2.2**) (1.0 mM) under N_2 with different amounts of added water in CH3CN. In all cases, solution contained 0.1 M tetrabutylammonium hexafluorophosphate (TBAHFP) supporting electrolyte, scan rate was 100 mV/s using a glassy carbon (GC) working electrode and a Pt counter electrode. A background, showing the reduction of water in the absence of catalyst is shown in dark blue in each figure. Figure (c) shows the linear dependence of the E_{onset} for compound **2.1** as red circles and compound **2.2** as blue squares.

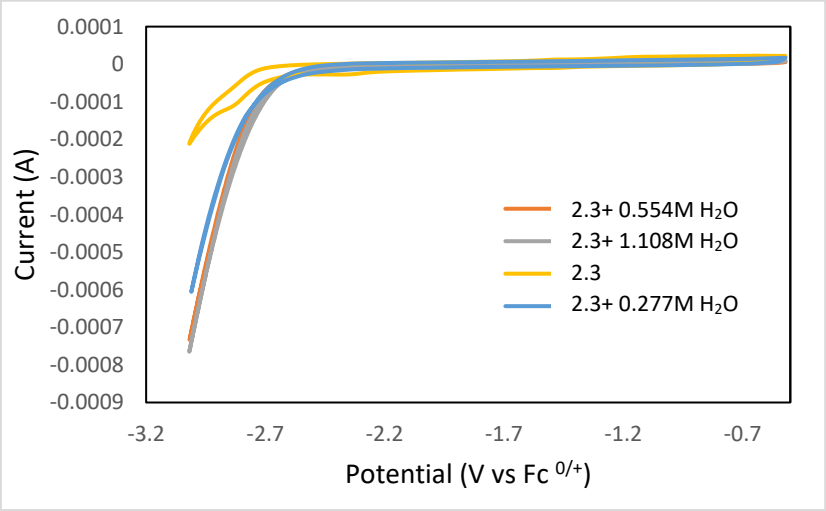

Figure 2.12. Cyclic voltammogram for [Ni(2,6-{Ph_2PNMe}(NC_5H_3)Br_2] (**2.3**) (1.0 mM) under N2 with different amounts of added water in CH_3CN. In all cases, solution contained 0.1 M tetrabutylammonium hexafluorophosphate (TBAHFP) supporting electrolyte, scan rate was 100 mV/s using a glassy carbon (GC) working electrode and a Pt counter electrode. A background, showing the reduction of water in the absence of catalyst is shown in dark blue in each figure.

To investigate the effect of adding water on the other reduction events of complexes **2.1** and **2.2**, each of these two reductions were isolated in the presence of different amounts of added water. It is clear that these reduction peaks were unchanged with added water, confirming that the catalytic current enhancement is associated with the third reduction of the complex (Figure 2.13, 2.14).

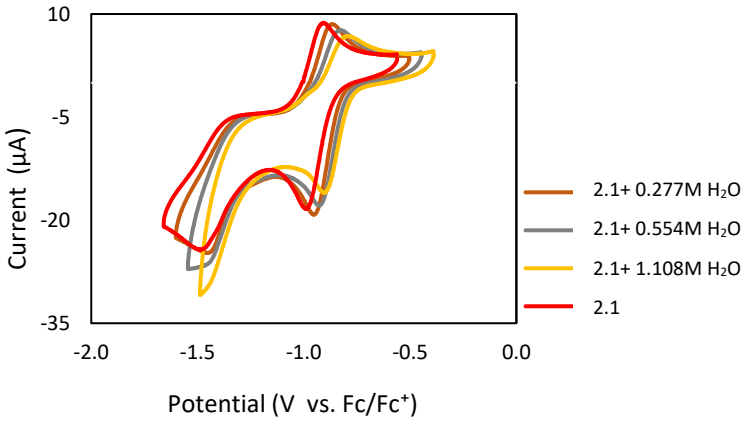

Figure 2.13. Cyclic voltammograms for complex **2.1** [Ni(2,6-{Ph_2PNH}$_2$(NC_5H_3)Br]$^+Br^-$ showing the first reduction at –0.98 V and the second reduction at -1.4 V in the presence of different concentrations of added H_2O.

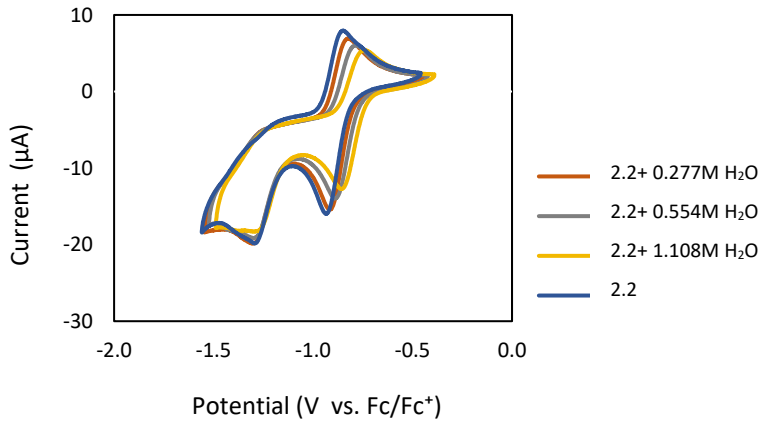

Figure 2.14. Cyclic voltammograms for complex **2.2** [Ni(2,6-{Ph_2PNMe}$_2$(NC_5H_3)Br_2] reduction at 0.93 V and the second reduction at -1.32 V in the presence of different concentrations of added H_2O.

Several experiments were carried out to confirm the stability and homogeneous nature of the catalysis observed for complexes **2.1** and **2.2**. Linear Sweep Voltammetry (LSV) measurements substantiated the operationally homogeneous catalytic behavior of **2.1** and **2.2** (Figure 2.15). Repeated scans of a catalyst solution (1 mM Ni complex, 0.5M water in CH_3CN) gave reproducible catalytic scans. After electrolytic reaction, the electrode was removed, rinsed, and immersed in fresh electrolyte/water solution containing no Ni complex and no catalytic response was observed. Furthermore, a CV of a sample of **2.1**, previously subjected to bulk electrolysis at -2.5 V *vs*. $Fc^{+/0}$ for 1 hr, displayed the original three reduction peaks of the complex.

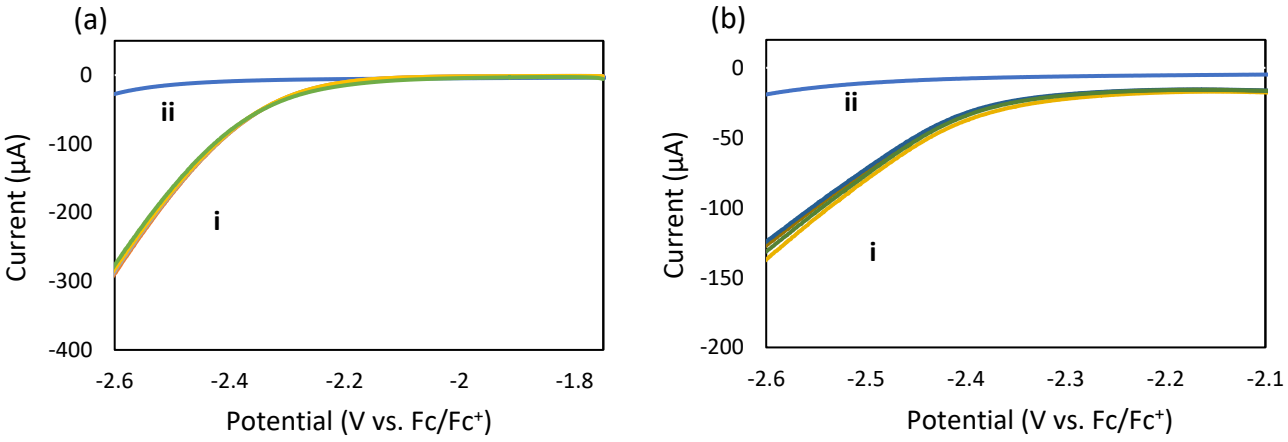

Figure 2.15. Linear Sweep Voltammetry measurements used to demonstrate that the working electrode surface remains clean during catalysis. Scans are shown for (a) [Ni(2,6-{Ph_2PNH}$_2$(NC_5H_3)Br]Br (**2.1**) and (b) [Ni(2,6-{Ph_2PNMe}$_2$(NC_5H_3)Br_2] (**2.2**). In each case (i) shows repeated linear scans of a solution containing 1 mM of Ni complex with 0.5M water in 0.1M TBAHFP in CH_3CN. The electrode was removed, rinsed with clean solvent and placed in a fresh solution containing no Ni complex, 0.5M water and 0.1M TBAHFP in CH_3CN. Scan rate = 100 mV/s.

The effect of varying the concentration of added water on the catalytic current, i_c, was also explored. Due to the reduction of solvent, we were not able to achieve a cathodic potential that allowed the observation of maximum catalytic peak current in the data. However, we did measure the increase in i_c relative to the peak current in the absence of water (i_p) at a fixed voltage of -2.55 V (Figure 2.16.a). The ratio of i_c to i_p, as a function of [H_2O] is shown in Figure 2.16.b. At low concentrations, a linear increase in the current ratio was observed with increasing water concentration. When the [H_2O] is sufficiently large that it remains constant, the catalytic current changed from first to zero order as observed in Figure 2.16. In this substrate concentration-independent region the current ratio can be approximated by equation 2.1 with R being the ideal gas constant, T the absolute temperature, F the Faraday constant and v the scan rate used in the cyclic voltammetry measurement in units of V/s.[7],[25] Since two electrons are used in the formation of H_2, n has a value of 2.

$$\frac{i_c}{i_p} = \left(\frac{n}{0.4463}\right)\sqrt{\frac{RTk}{Fv}} \qquad (2.1)$$

This analysis allows the calculation of *k*, a value which represents the number of times a catalyst molecule produces a molecule of H_2 per second, or the turnover frequency (TOF) of this catalyst under these conditions. With a scan rate of 0.1V/s the saturation current ratio was measured to be 29 giving a TOF of 210 s^{-1}

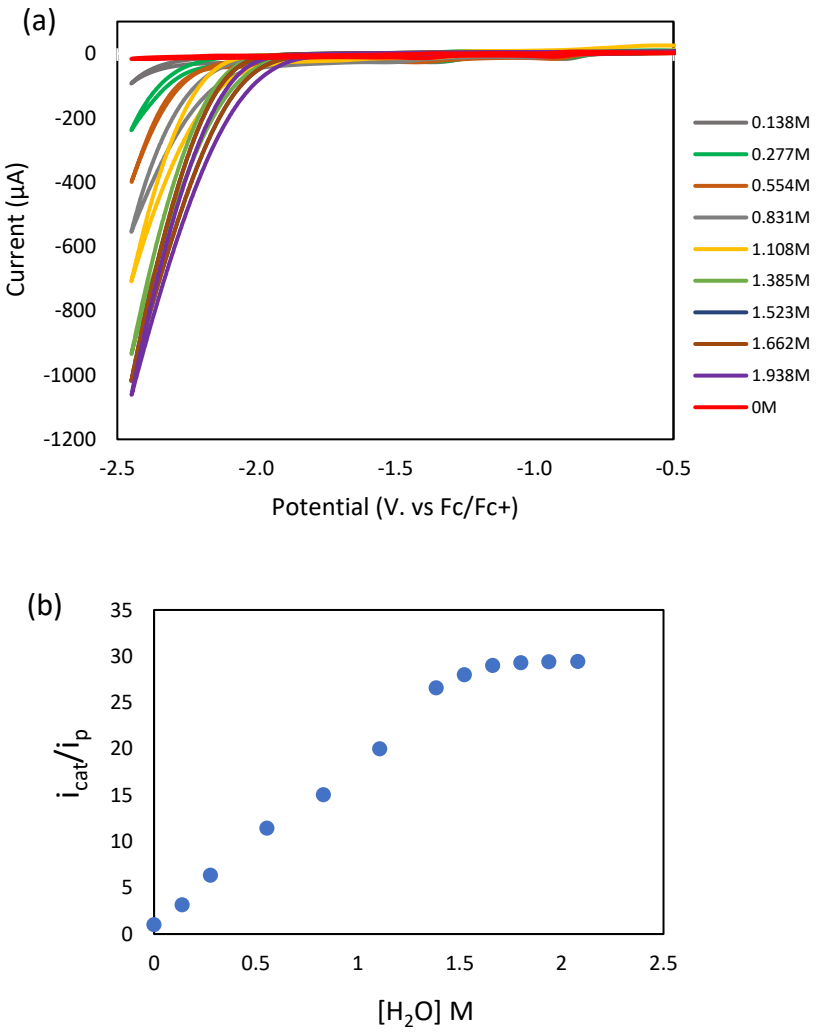

Figure 2.16. (a) Cyclic voltammograms of [Ni(2,6-{Ph_2PNMe}$_2$(NC_5H_3)Br_2] (**2.2**) (1 mM) in the absence of water and with varying concentrations of water in CH_3CN with 0.1 M

tetrabutylammonium hexafluorophosphate (TBAHFP) supporting electrolyte at 100 mV/s using a glassy carbon (GC) working electrode. (b) Corresponding plot of i_{cat}/i_p vs water concentration**.**

Quantitative confirmation of H_2 generation was obtained through bulk electrolysis experiments using either **2.1** or **2.2** as a catalyst for generating H_2 from H_2O/CH_3CN at -2.55 V vs $Fc^{+/0}$ with a glassy carbon electrode having a surface area of 1.38 cm^2. The reaction headspace was analyzed by gas chromotagraphy and confirmed dihydrogen evolution with 88% Faradaic efficiency (Table 2.1, Figure 2.17). As the concentration of H_2O increased, higher amounts of H_2 were measured with both complexes. For example, using **2.1** as the catalyst, with 0.138M water in the solution, 25μmol of H_2 were obtained, this amount rises to 125μmol when 1.108M H_2O was added to the solution as the substrate, although the FE dropped by 2% to 85%. Furthermore, with **2.1** more product was measured compared to with **2.2**. At longer electrolysis time also higher amount of H_2 was produced by both **2.1** and **2.2**.

Table 2.1. Selected bulk electrolysis data for hydrogen generation with various concentrations of water using compounds **2.1** and **2.2** after 2 hours experiment. Measurements were in acetonitrile at -2.55 V vs. $Fc^{+/0}$ using a glassy carbon working electrode. Values were determined using gas chromatographic analysis.

Compound + water	**i_c**	**H_2 (μmol)**	**charge**	**1/2 μmol of electron**	**Faradaic efficiency (%)**
2.1 + 0.138M H_2O (100μl)	300	25	5.5	28.7	87
2.1 + 0.277M H_2O (200μl)	450	56	12.6	65.1	86
2.1 + 0.415M H_2O (300μl)	550	81	18.4	95.3	85

2.1 + 0.554M H_2O (400µl)	650	102	22.4	115.9	88
2.1 + 0.830M H_2O (600µl)	750	125	28	145.3	86
2.1 + 1.108M H_2O (800µl)	850	138	31.3	162.4	85
2.2 + 0.138M H_2O (100µl)	75	18	4.1	21.2	85
2.2 + 0.277M H_2O (200µl)	130	40	8.8	45.5	88
2.2 + 0.415M H_2O (300µl)	200	65	14.1	73	89
2.2 + 0.554M H_2O (400µl)	260	83	18.4	95.4	87
2.2 + 0.830M H_2O (600µl)	310	106	24.1	124.7	85
2.2 + 1.108M H_2O (800µl)	360	116	26.3	136.5	85

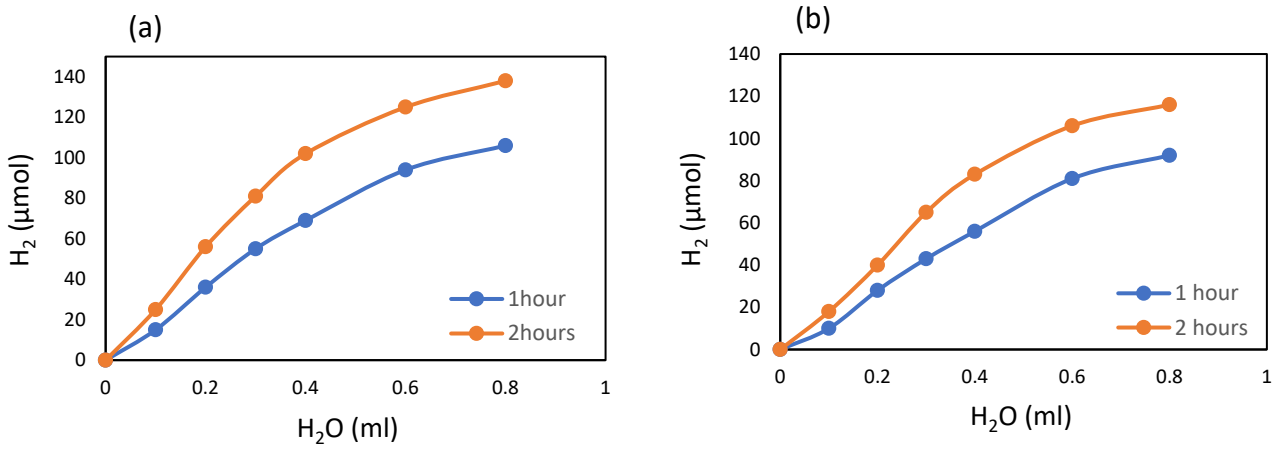

Figure 2.17. Graph of the H_2 production versus added H_2O for bulk electrolysis in (a) **2.1** and (b) **2.2** at two different periods of time.

As part of our continuing investigation of this catalyst system we explored the effect of changing the substrate for catalytic H_2 generation. The ability to employ either phenol or acetic acid as substrate was confirmed through appearance of catalytic currents in the presence of catalysts **2.1** and **2.2** as shown in Figures 2.18 and 2.19. As expected, the catalytic onset potential and current correlated with pK_a values of phenol (**2.1,** E_{onset} = -1.7V; $E_{cat/2}$ = -1.95V; pK_a = 29.14) and acetic acid (**2.1,** E_{onset} = -1.25V; $E_{cat/2}$ = -1.83V; pK_a = 23.51) in acetonitrile.[26] The lower the pKa and thus the stronger acidity of the substrate led to more accessible protons in the solution and the less energy is needed for productive reaction.

The overpotential for reduction of these substrates can be calculated using equations 2.2 and 2.3. With catalyst **2.1**, the overpotentials were calculated to be 200 and 410 mV for phenol and acetic acid, respectively.

overpotential = $\eta = E_{cat/2} - E_{H^+}$ (2.2)

$E_{H^+} = -0.028\ V - 0.05916\ V \times pKa$ (2.3)

These catalytic reductions appear to correlate most closely with the second reduction of the Ni complex and suggest that these substrates follow a more conventional Ni(II/0) mechanism for H_2 generation.

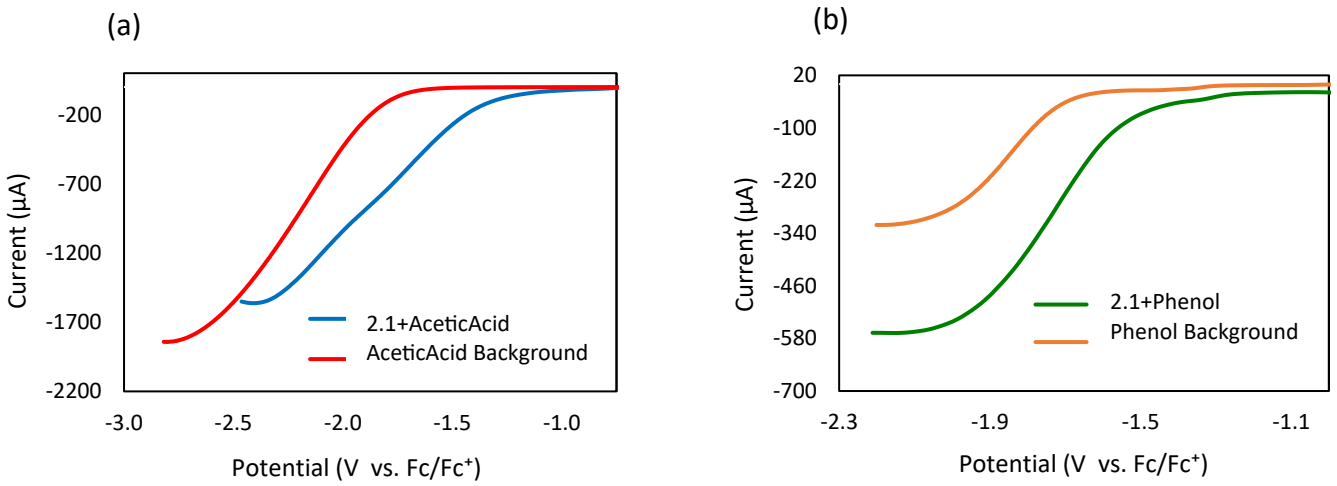

Figure 2.18. (a) Linear Sweep voltammograms for acetic acid in the absence (red) and presence (blue) of [Ni(2,6-{Ph_2PNH}$_2$(NC_5H_3)Br_2] (**2.1**) (1.0 mM), (b) Linear Sweep voltammograms for phenol in the absence (orange) and presence (green) of [Ni(2,6-{Ph_2PNH}$_2$(NC_5H_3)Br_2] (**2.1**) (1.0 mM).

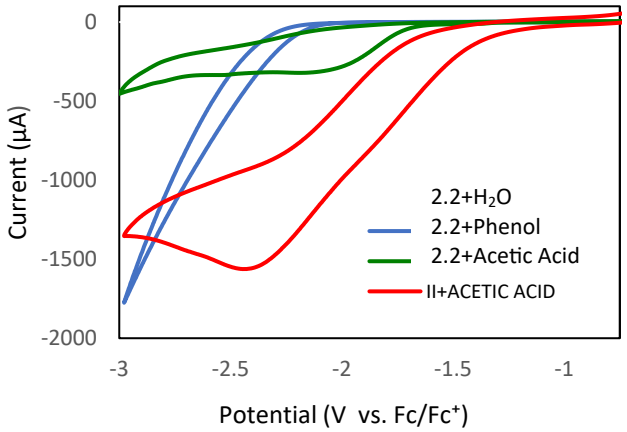

Figure 2.19. Cyclic voltammograms for [Ni(2,6-{Ph_2PNMe}$_2$(NC_5H_3)Br_2] (**2.2**) (1.0 mM) under N_2 in presence of different proton sources in CH_3CN with 0.1 M tetrabutylammonium hexafluorophosphate (TBAHFP) supporting electrolyte at 100 mV/s using a glassy carbon (GC) working electrode. Red = 0.55M acetic acid, Green = 0.55M phenol, and Blue = 0.55M water.

2.4.3 Computational Results

The similarity of the electrochemical features of **2.1** and **2.2**, along with the structural features noted above, encouraged our investigation of these species by computation.

Significant insights into the electronic structure and proposed nature of the reduction behavior of **2.1** and **2.2** were delivered through a DFT computational investigation using the B3LYP functional and def2TZVP basis set and employing the IEFPCM model for solvation with acetonitrile. This investigation began with an optimization of the cation $[Ni(\kappa^3\text{-}2,6\text{-}\{Ph_2PNMe\}_2NC_5H_3)Br]^+$ (**2.1**$^+$) of **2.1**. The computational results for **2.1**$^+$ produced an excellent match with the experimental structure (Figures 2.20, A.1, Tables A.7, A.8). Notably, the analogous optimization process on **2.2** in acetonitrile led to spontaneous dissociation of the apical Br^- to produce the analogue of **2.1**$^+$, $[Ni(\kappa^3\text{-}2,6\text{-}\{Ph_2PNMe\}_2NC_5H_3)Br]^+$ (**2.2**$^+$). The cation **2.2**$^+$ was optimized to yield a comparable structure of **2.1**$^+$ (Figures A.8, Tables A.12, A.13) and this is consistent with the observation of similar electrochemistry seen for the two Ni species. These structures form a starting point for exploring the reduction events for these two complexes and as expected, both displayed distorted square planar d^8 Ni(II) centers with filled Ni-centered dxy, dxz, dyz and dz^2 σ non-bonding MOs and an empty $dx^2\text{-}y^2$-centered σ^* orbital as the LUMO (Figures A.2, A.9)

By employing the same computational optimization parameters, we were able to obtain a logical and consistent set of structures for the sequential addition of three electrons to these cations. Focusing on $[Ni(\kappa^3\text{-}2,6\text{-}\{Ph_2PNMe\}_2NC_5H_3)Br]^+$ (**2.1**$^+$), addition of the first electron yielded a square planar neutral species (**2.1**) (Figure A.3, A.4, Table A.9) where this electron was added to a $dx^2\text{-}y^2$-based orbital to give a SOMO which displayed similar σ^* character as seen in **2.1**$^+$. Mayer bond analysis indicated an overall decrease in bond order compared with **2.1**$^+$ with the largest effect on Ni-Br. As a result, we interpret the first reduction wave as a Ni(II)/Ni(I) couple. The

addition of the next electron converted **2.1** to **2.1**$^{-}$. This electron was again added to the orbital with dx^2-y^2 character (Figures A.5, A.6, Table A.10) and thus we assigned this irreversible wave to a Ni(I)/Ni(0) couple and complex **2.1**$^{-}$ as an 18 electron species. By filling the σ* MO, not surprisingly, this reduction produced an optimized structure with substantial changes that included deviation of the Ni(0) center from square planar geometry, an increase in Ni-Br bond length and decrease in bond order (Table 2.2). Finally, the addition of an electron to **2.1**$^{-}$, led to a spontaneous and anticipated loss of bromide anion to yield a planar T-shaped complex [Ni(κ^3-2,6-{Ph_2PNH}$_2$$NC_5H_3$)]$^{-}$ (**A**$^{-}$) (Figure 2.21, Figure A.7, Table A.11). Examination of the electronic structure of this anion confirmed four Ni-centered dxz, dz^2, dxz, dxy occupied orbitals that were essentially non-bonding and an occupied σ* orbital that was about 70% Ni dx^2-y^2 in character (Figure 2.22). The additional electron was determined to reside in a ligand localized SOMO that was about equally dispersed on the ligand P centers and py moiety with less than 10% of the density on Ni as shown in Figure 2.21. Following this process with the analogous complex **2.2**$^{+}$ led to a parallel set of results at each reduction step (Figures A.10-A.13, Tables A.14-A.15).

Figure 2.20. Overlay of experimental and optimized structures for complex **2.1**$^{+}$, [Ni(κ^3-2,6 {Ph_2PNH}$_2$$NC_5H_3$)Br]$^{+}$

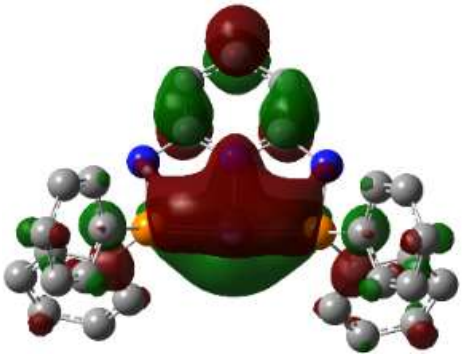

Figure 2.21. Representation of the SOMO (viewed perpendicular to the molecular plane) obtained from the computational optimization of [Ni(κ^3-2,6-{Ph_2PNH}$_2$$NC_5H_3$)]$^-$ (**A**$^-$) using the B3LYP functional and def2TZVP basis set and IEFPCM model for solvation in acetonitrile.

Table 2.2. Summary of Ni-centered bonding for [Ni(κ^3-2,6-{Ph_2PNH}$_2$$NC_5H_3$)Br]$^-$ (**2.1**$^-$). Values for bond length, overlap populations and Mayer bond order indices are from the B3LYP/def2TZVP/IEFPCM(acetonitrile) optimization.

Bond	Length(Å)	Overlap Population	Mayer Bond order
Ni-Br	2.735	0.07	0.26
Ni-P	2.141	0.34	1.13
Ni-N	2.017	0.12	0.31

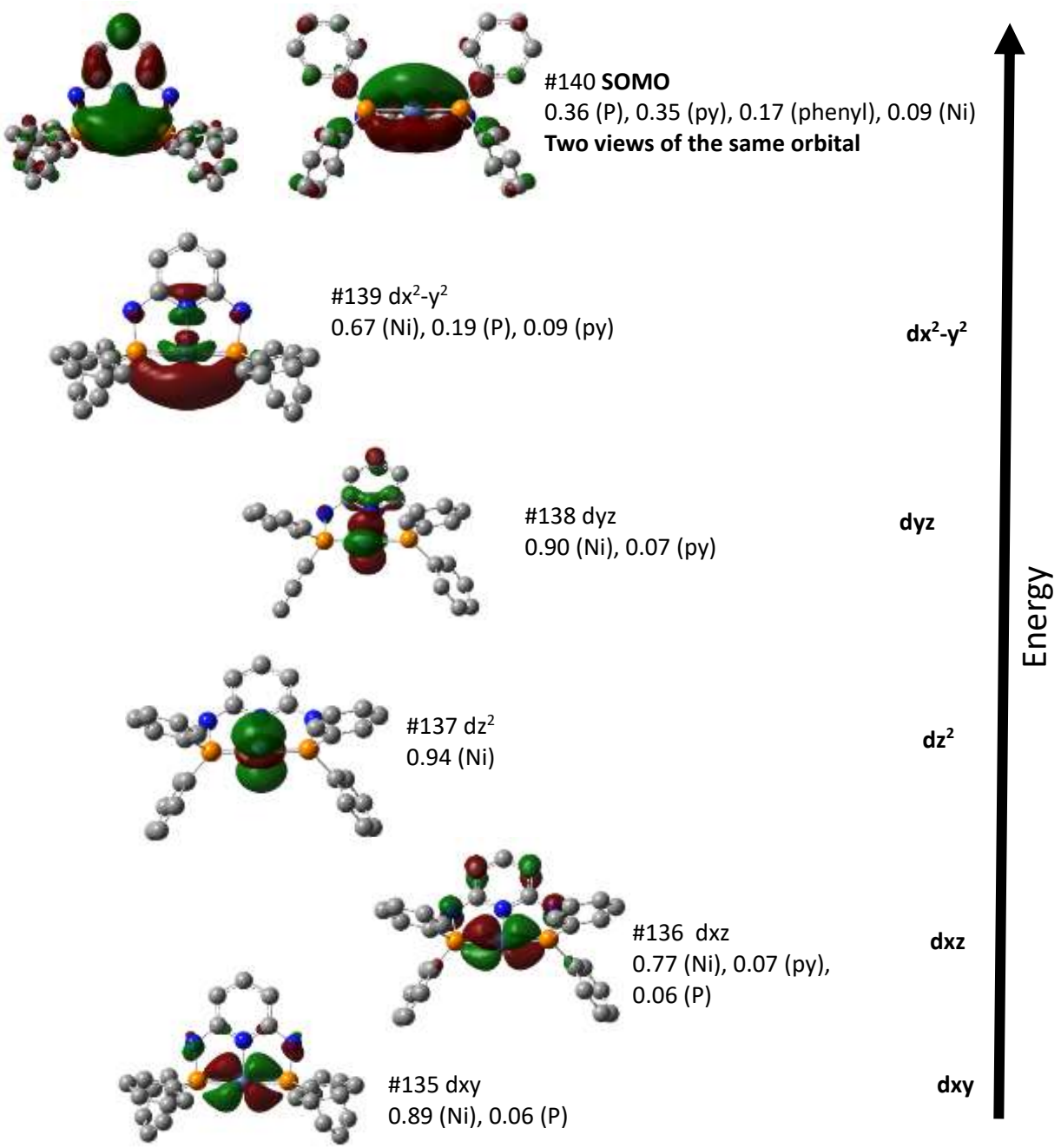

Figure 2.22. Selected, Ni-centered molecular orbitals and the SOMO obtained from the computational optimization of $[Ni(\kappa^3\text{-}2,6\text{-}\{Ph_2PNH\}_2NC_5H_3)]^-$ (**A**$^-$) using the B3LYP functional, def2TZVP basis set and IEFPCM model for solvation in acetonitrile.

Experimental and computational data point to a key role for the ligand in any proposed mechanism for the electrocatalytic generation of H_2 from water using either Ni complex **2.1** or **2.2**. The redox activity of this class of pincer ligands and their ability to undergo one electron transfer with first row metals is an open question in the literature.[29],[30] A CV measurement of the ligands in CH_3CN using a glassy carbon (GC) working electrode did display an irreversible reductions at approximately -2.55 V vs $Fc^{+/0}$ (Figure 2.23). Importantly, bulk electrolysis measurements with the ligands did not produce any measurable hydrogen gas.

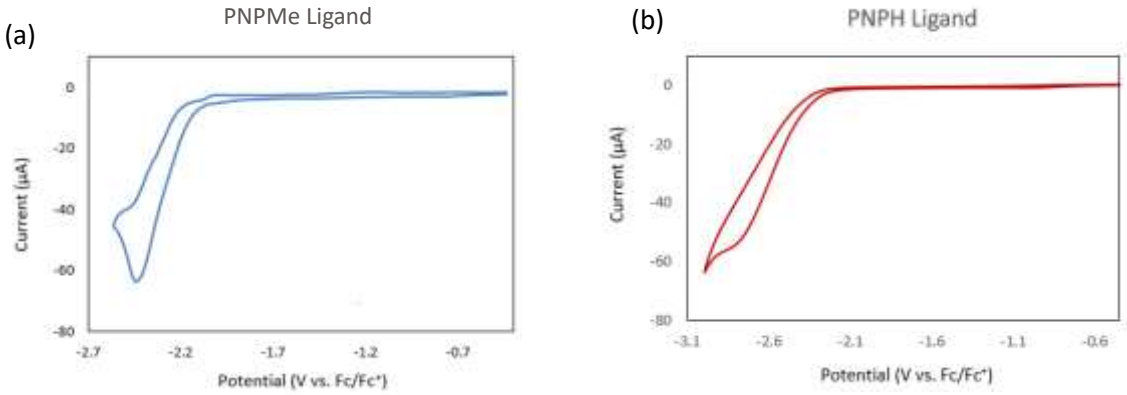

Figure 2.23. Cyclic voltammograms for ligands (a) (2,6-{Ph_2PNMe}$_2$(NC_5H_3) and (b) 2,6-{Ph_2PNH}$_2$(NC_5H_3) in CH_3CN with 0.1 M tetrabutylammonium hexafluorophosphate (TBAHFP) supporting electrolyte at 100 mV/s using a glassy carbon (GC) working electrode.

2.4.4. Proposed mechanism

A proposed mechanism for the catalytic behavior of these Ni complexes is summarized in Figure 2.24. For simplicity, the scheme is presented and discussed based on **2.1** but is entirely analogous for **2.2**. Hydrogen formation is correlated with the reduction at -2.6 V and computations have identified this species as a d^{10} Ni(0) species with an anionic ligand, $\mathbf{A}^-$. A first step in hydrogen formation is likely a proton transfer from H_2O to $\mathbf{A}^-$. In order to explore the structure of this

proposed species, a set of DFT (B3LYP/def2TZVP/IEPCM) optimizations were carried out for the addition of a proton to several locations in **A**$^-$. The lowest energy species corresponded to loss of one electron each from the ligand anion and Ni(0) and the formation of a Ni(I) hydride, ("**Ni-H**")(Figures 2.25, Figures A.14, Table A.16) Reaction of this complex with water would lead to hydrogen release and formation of a Ni(0) complex ("**Ni-OH**$^-$") under the reducing conditions employed for the reaction. This intermediate species is the analogue of the Ni(0) complex **2.1**$^-$ and was computationally optimized (Figure 2.26, Table A.17). By analogy to **2.1**$^-$, **Ni-OH**$^-$ could undergo reduction with hydroxide loss to return to **A**$^-$ and close the catalytic cycle.

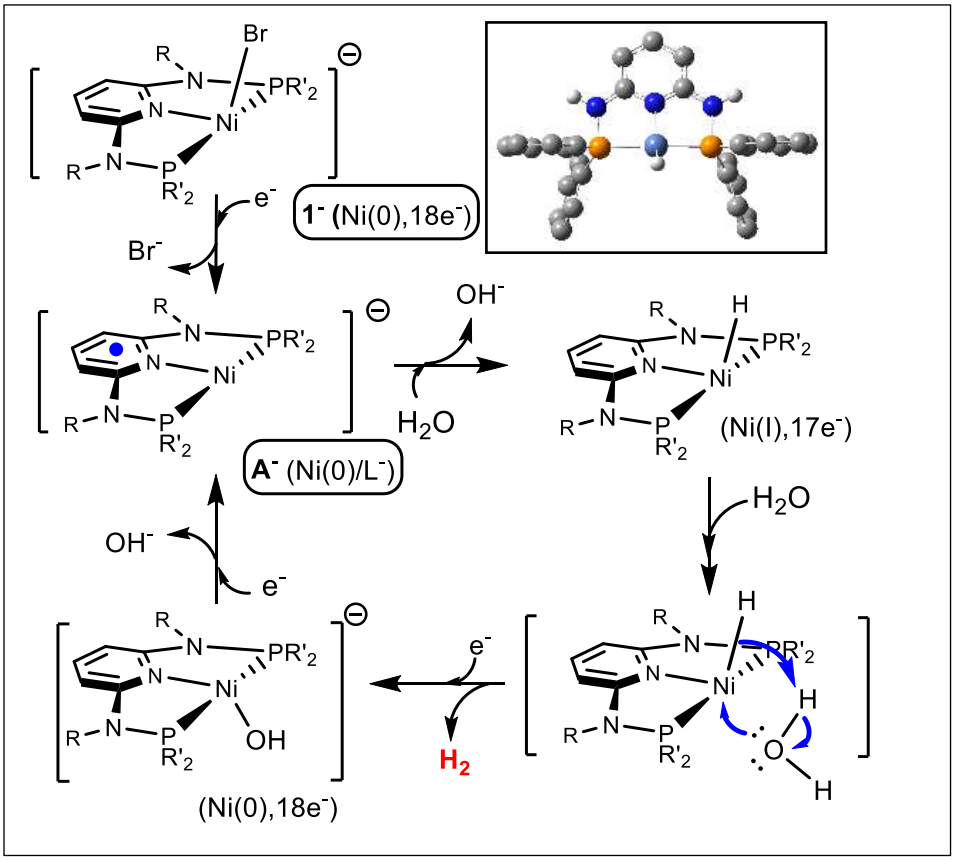

Figure 2.24. Proposed mechanism for the reduction of water and formation of H_2 from complex [Ni(κ^3-2,6-{Ph_2PNH}$_2$$NC_5H_3$)]$^-$ (**A**$^-$). The optimized (DFT, B3LYP, def2TZVP) structure of Ni-H complex is shown.

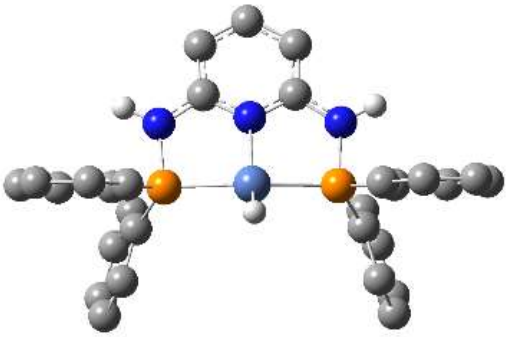

Figure 2.25. DFT optimized structure for the neutral complex [Ni(κ^3-2,6-{Ph_2PNMe}$_2$$NC_5H_3$)H] (**Ni-H**), the proposed hydride intermediate in the catalytic cycle, using the B3LYP functional and def2TZVP basis set with solvation with acetonitrile modeled with the IEFPCM model. Hydrogen atoms on the carbon centers have been eliminated for clarity. Frequency analysis confirmed that the optimized structure was a minimum with no imaginary frequencies.

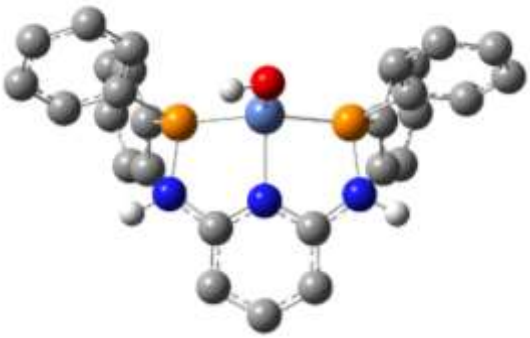

Figure 2.26. DFT optimized structure for the anionic complex [Ni(κ^3-2,6-{Ph_2PNMe}$_2$$NC_5H_3OH$]$^-$ (**Ni-OH**$^-$), a proposed intermediate in the catalytic cycle, using the B3LYP functional and def2TZVP basis set with solvation with acetonitrile modeled with the IEFPCM model. Hydrogen atoms on the carbon centers have been eliminated for clarity. Frequency analysis confirmed that the optimized structure was a minimum with no imaginary frequencies.

2.5 Conclusion:

In order to bring electrocatalytic hydrogen production into the sustainable realm, earth abundant metal catalysts should function with water as the substrate. These newly reported hydrogen generating catalysts of Ni(II) are robust, air stable and electrocatalytically reduce water to hydrogen with excellent Faradaic efficiency. Computations supplemented our understanding of a

unique ligand-based electron transfer with the cooperativity of the PN^3P ligand as an electron reservoir as a requirement for successful catalysis.

The framework of these catalysts is amenable to ligand variations and we continue to explore suitable ligand modifications to tune catalyst performance, reduce reduction potentials and improve solubility in water. Extended studies including elucidation of the mechanism by DFT are in progress. These results inspire the synthesis and characterization of new compounds that will both provide insight into the mechanisms of and replace precious metal catalysts in hydrogen production and application.

2.6 Experimental Section:

General:

Reagents and analytical grade solvents were purchased from Strem Chemicals or Sigma Aldrich and used without further purification. The ^{1}H, $^{13}C\{^{1}H\}$ and $^{31}P\{^{1}H\}$ NMR spectra were recorded at 400, 100 and 162 MHz respectively with chemical shifts reported in ppm using the residual protons of the NMR solvent as internal standards.

The two ligands, 2,6-$\{Ph_2PNH\}_2(NC_5H_3)$ and 2,6-$\{Ph_2PNCH_3\}_2(NC_5H_3)$ were prepared by literature methods.[117]

Synthesis of [Ni(2,6-$\{Ph_2PNH\}_2(NC_5H_3)Br]Br$ (2.1):

In a nitrogen filled glovebox, 0.5 mmol (0.238 g) of 2,6-$\{Ph_2PNH\}_2(NC_5H_3)$ was dissolved in 5mL of dichloromethane. To this solution was added 0.5 mmol (0.1093 g) of nickel (II) bromide suspended in 5 mL of acetonitrile. The reaction mixture was stirred for 16 hours. The solvent was removed to give 0.25 g (72% yield) of orange solid **2.1**. Single crystals of this complex were grown by slow diffusion of hexane into a concentrated solution of complex **2.1** in dichloromethane.

^{1}H NMR (600 MHz, $CDCl_3$): δ = 7.40-7.46 (m, 8H), 7.30-7.35 (m, 16H), 6.5 (m, 2H).

$^{31}P\{^{1}H\}$ NMR (162 MHz, $CDCl_3$): δ = 65.

$^{13}C\{^{1}H\}$ NMR (152 MHz, $CDCl_3$): δ = 101.16 (t, J = 4.1 Hz), 128.6 (t, J = 3.3 Hz), 129 (t, J = 5.6 Hz), 132.2 (s), 132.9 (t, J = 6.6 Hz), 142.0 (s), 161.7 (t, J = 10 Hz).

Elemental analysis calculated for $C_{29}H_{25}Br_2N_3P_2Ni$: C, 50.05; H, 3.62; Br, 22.96; N, 6.04; Ni, 8.43; P, 8.90. Found: C, 50.29; H, 3.82; N, 6.08.

Synthesis of [Ni(2,6-$\{Ph_2PNCH_3\}_2(NC_5H_3)Br_2$] (2.2):

In a nitrogen filled glovebox, 0.5 mmol (0.253 g) of **2,6-$\{Ph_2PNCH_3\}_2(NC_5H_3)$** was dissolved in 5mL of dichloromethane. To this solution was added 0.5 mmol (0.1093 g) of nickel (II) bromide

suspended in 5 mL of acetonitrile. The mixture was stirred for 16 hours. The solvent was removed to give 0.28 g (78% yield) of purple solid **2.2**. Single crystals of this complex were grown by slow diffusion of hexane into a concentrated solution of the complex **2.2** in dichloromethane.

^{1}H NMR (600 MHz, $CDCl_3$): δ = 8.05-8.1 (t, 1H, J=8.2 Hz) 7.85-7.90 (m, 8H) 7.66-7.7 (t, 4H, J=8.2 Hz), 7.56-7.62 (t, 8H, J=8.2 Hz), 6.73-6.77 (d, 2H, J=8.3 Hz), 3.11 (s, 6H, CH_3).

^{31}P{^{1}H} NMR (162 MHz, $CDCl_3$): δ = 95.8.

^{13}C{^{1}H} NMR (152 MHz, $CDCl_3$, 25ºC): δ = 34.72 (d, J = 14.5 Hz), δ = 101.16 (dd, J = 3.5 Hz), 125.5 (t, J = 29 Hz), 129.6 (t, J = 5.9 Hz), 133.3 (s), 133.6 (t, J = 6.5 Hz), 145.5 (d, J = 16.3 Hz), 161.8 (t, J = 11.3 Hz).

Elemental Analysis calculated for $C_{31}H_{29}Br_2N_3P_2Ni$: C, 51.43; H, 4.04; N, 5.80. Found: C, 51.22; H, 4.35; N, 5.48.

Synthesis of [Ni(2,6-{Ph_2PNCH_3} (NC_5H_3)Br_2] (2.3):

0.5 mmol (0.1093 g) of nickel (II) bromide was measured and added to 0.5 mmol (0.139 g) of the PN-Me ligand. The ligand and the nickel (II) bromide were dissolved in 5 mL of toluene each in the glovebox. The solutions were mixed together in a round bottom flask and stirred for 16 hours. The solution was then filtered, and the product was collected. Yield (80%).

^{1}HNMR (400 MHz, $CDCl_3$, 25°C): δ = 3 (s, 3H, J = 73 Hz), 6.7 (s, 1H, J=90 Hz), 7.35−8 (m, 12 H, J=30-40 Hz), 8.35 (s, 1H, J=35 Hz).

^{31}P{^{1}H} NMR (162 MHz, $CDCl_3$, 25°C): δ = 51.0.

^{13}C{^{1}H} NMR (152 MHz, $CDCl_3$, 25ºC): δ = 34.5 (s, J = 9.5 Hz), 111 (d, J = 11 Hz), 117.7 (s, J = 10 Hz), 128.5 (dd, J = 8 Hz), 131.3 (dd, J = 6.7 Hz), 134.8 (s, J = 15.6 Hz), 135.3 (dd, J = 6.5 Hz), 141.26 (s, J = 11.5 Hz), 153.3 (s, J = 9.5 Hz), 160.7 (s, J = 9.2 Hz).

X-ray Crystallography: The crystals of [Ni(2,6-{Ph_2PNH}$_2$(NC_5H_3)Br]Br (**2.1**) and [Ni(2,6-{Ph_2PNCH_3}$_2$(NC_5H_3)Br_2] (**2.2**) were mounted on thin glass fibers using paraffin oil. Prior to data collection crystals were cooled to 200.15 °K. Data were collected on a Bruker Smart or Kapa ApexII single crystal diffractometer equipped with a sealed tube Mo source (wavelength 0.71073 Å) and an ApexII CCD detector. Raw data collection and processing were performed with the Apex3 software package from Bruker. Initial unit cell parameters were determined from 60 data frames from select ω scans collected at the different sections of the Ewald sphere. Semi-empirical absorption corrections based on equivalent reflections were applied.[121] Systematic absences in the diffraction data-set and unit-cell parameters were consistent with the assigned space group. The initial structural solution was determined using ShelxT direct methods, and refined with full-matrix least-squares procedures based on F^2 using ShelXle.[122] Hydrogen atoms were placed geometrically and refined using a riding model. All scattering factors are contained in several versions of the ShelXL program library, with the latest version used being v.6.12 at the time of this writing.

Electrochemistry: Electrochemical experiments were carried out in a single or double compartment cells, with 50 mL approximate volumes, using a VersaSTAT 3 (Princeton Applied Research) potentiostat. Samples were prepared in a glovebox, sealed, removed from the glovebox and connected to a Schlenk line and maintained under a nitrogen atmosphere. A conventional three electrode system was employed consisting of a glassy carbon working electrode (diameter = 0.3 cm), a Pt wire as the auxiliary electrode, and an Ag wire as a pseudo-reference electrode. At the completion of a voltammetry measurement, ferrocene was added as a reference compound and potentials were referred to the redox potential of ferrocenium ion (Fc^+)/ferrocene (Fc) as an internal standard. Dried acetonitrile was purchased from Sigma Aldrich and stored on molecular sieves in

the glovebox. Tetrabutylammoniumhexafluorophosphate, $[(n\text{-}Bu)_4N]PF_6$ (TBAHFP), the supporting electrolyte, was crystallized two times with ethanol, dried under vacuum at 90 °C for 24 h before used and stored in a glovebox. The typical concentration of catalyst was 1 mM in each experiment.

Bulk electrolysis measurements (controlled potential coulometry) was carried out with an H cell arrangement. In these experiments, the working electrode was a glassy carbon electrode with an area of 1.38 cm^2.

Computational Details: Optimized structures were obtained from density functional theory (DFT) computations using the Gaussian 09 package.[123] The B3LYP functional and def2TZVP basis set was used for all atoms. All optimizations used the IEFPCM model for solvation with acetonitrile as the solvent. Frequency analysis confirmed that the optimized structures were minima with no imaginary frequencies. The initial optimization for complex **2.1** began with the experimental X-ray structure as input. Optimizations for the subsequent three reduction steps to generate **2.1, 2.1**$^-$ and **A**$^-$ began with the optimized structure from the preceding species. The canonical molecular orbitals were generated using the GaussView program and shown with isovalues of 0.03. The Chemissian program was used to generate the fragment orbital compositions.

3 Chapter 3: Electrocatalytic hydrogen production from neutral water using an aqueous Ni(II) pincer complex

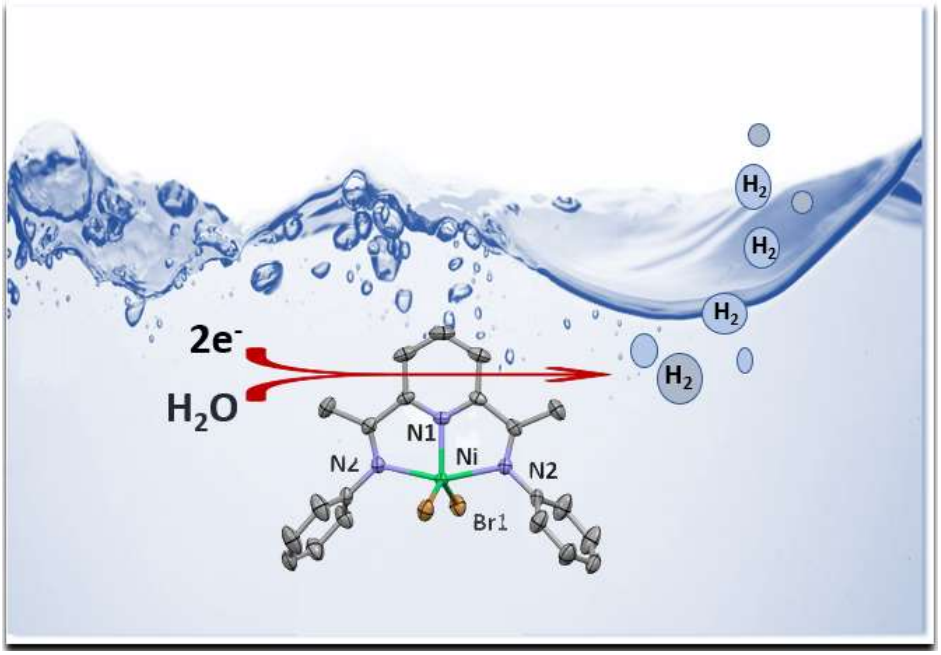

3.1. Preamble and Context:

This project is a collaboration work between Somayeh Norouziyan (SN) and a master's student, Jonathan Ferguson (JF). It was initiated by SN; SN performed the complex synthesis, NMR and SC-XRD characterizations, all the electrochemical measurements (CVs, LSV, and the first CPE) that indicated catalytic behavior. JF contributed to this project performing the controlled potential coulometry experiments, gas analysis, product characterization and quantification. DFT computations and their analysis were performed by Dr. Darrin Richeson (DR) with feedback from both SN and JF. This work has been published in Catalysis Science and Technology and can be accessed at https://doi.org/10.1039/d2cy01504h. ["Norouziyanlakvan, S., Ferguson, J. and Richeson, D., 2022. Electrocatalytic hydrogen production from neutral water using an aqueous Ni (II) pincer complex. Catalysis Science & Technology, 12(24), pp.7494-7500."]. The manuscript was prepared by DR, SN, and JF.

3.2 Abstract:

Water is the exemplary source for sustainable H_2 production and provides an ideal solvent for this electrocatalytic reaction. In neutral pH, aqueous saline solution, the Ni^{II} diminopyridiine precatalyst, [Ni(k^3-2,6-{PhNCMe}$_2$(NC_5H_3))Br_2 **3.1**, electrocatalytically produced H_2 with an onset voltage of -1.0 V (387 mV overpotential) versus Ag/AgCl. In anhydrous acetonitrile solution, trifluoroacetic acid supplied protons for H_2 production with an overpotential of 555 mV. Computational analysis (DFT) provided insight into the identities of the catalysts and supported the non-innocent role of the ligand in the reduction chemistry. Mechanistic propositions for these observations, also supported computationally, suggest proton transfer to the dz^2-based orbital of the reduced Ni(I) complex to generate a square planar Ni(II). A second proton transfer lead to formation of a Ni(II) dihydrogen complex.

3.3 Introduction

Energy consumption in today's rapidly expanding economy and worldwide population is a topic of increasing significance. While energy demands have been largely met through fossil fuel combustion, it is now established that the resulting greenhouse gases that are emitted into the atmosphere are a leading cause of climate change and harmful to life on Earth. Hydrogen can provide a clean source of energy that could address these issues. The electrocatalytic hydrogen evolution reaction (HER) using water as the substrate, could provide a sustainable and green approach to providing renewable energy.

In this context, researchers strive to discover and evaluate efficient catalysts for HER with a particular focus on employing earth-abundant metal complexes for this goal. While some hydrogen evolution catalysts require large negative potentials and acidic conditions to operate, there are reported molybdenum, cobalt and nickel complexes that are capable of hydrogen generation at less negative potentials.[31, 124-127] Unfortunately, most of these catalysts are only soluble in organic solvents or utilize organic acids to achieve H_2 production. A more sustainable approach and a challenging ongoing effort targets hydrogen generation catalysts that are soluble in water and require no additional proton sources. There are a limited number of reported electrocatalysts that are active for HER in neutral water. [46, 47, 102, 128-132] Long. et al. reported a molybdenum-oxo catalyst for generating hydrogen from water without any added acid addition or organic cosolvents with a high turnover number (TON).[32] In 2011, Chang. et al. reported a cobalt complex supported by a pentadentate polypyridyl ligand "$PY5Me_2$" which showcases a 100% Faradaic efficiency and high stability and activity for the HER from neutral water. In 2012, Peters and co-workers established that a Co(III)\(II) tetraazomacrocycle containing a pyridine donor catalyzes hydrogen

evolution at -0.69 V vs. SHE with 92% Faradaic efficiency and a TON of 17 in pH 2.2 phosphate buffer on a glassy carbon plate electrode.[96]

Scheme 3.1. Catalysts bearing the $PY5Me_2$ ligand used for HER.

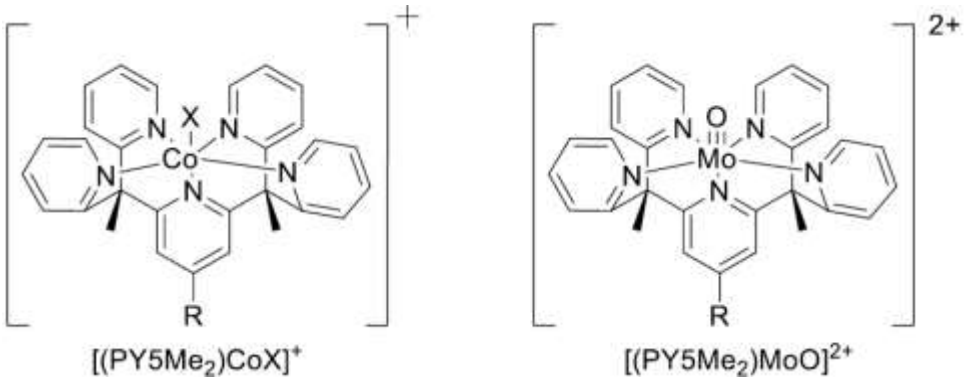

$[(PY5Me_2)CoX]^+$ $[(PY5Me_2)MoO]^{2+}$

We were attracted to developing nickel complexes for the HER in an aqueous environment partly due to the role of Ni in hydrogenase enzymes as well as their documented activity as hydrogen evolution catalysts.[133, 134] With appropriate design, we envisioned compatibility of Ni complexes as water soluble catalysts. In Table 3.1 the reported aqueous Ni complexes for HER application are shown. Although these complexes are active HER catalysts in water, most of them need acidic media. Indeed, the number of catalysts, not only with Ni but also with other metals, that are active at neutral pH is very small.

Diiminopyridines ligands are well-known pincer ligands that support a wide range of metal complexes and are established as non-innocent ligands, which are capable of operating as an electron reservoir allowing their metal complexes to exhibit high catalytic activity and selectivity.[135] Nickel complexes of these ligands are well-known and are often stable in aqueous solution. Furthermore, there are reports that nickel diiminopyridine complexes are effective catalysts for H_2 production. However, these reports are either in organic solvents or acidic aqueous media.[47, 136, 137]

This chapter reports on the HER activity of a simple Ni(II) diminopyridiine complex in neutral pH, aqueous saline solution. This compound operates at potentials as low as -1.0 V *versus* Ag/AgCl electrode. As part of an examination of the versatility of this catalysis we further demonstrate that this species can generate hydrogen from acidic acetonitrile solutions.

Table 3.1. Structures of reported nickel catalysts for the hydrogen evolution reaction in aqueous solutions.

catalyst	E (V vs. NHE)	WE	pH	Proton Source	TOF (h^{-1})	reference
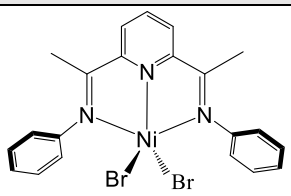	-0.89	GC	7	Water	1	This work
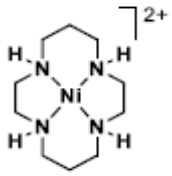	-1.26	Hg	2-10	water		[39]
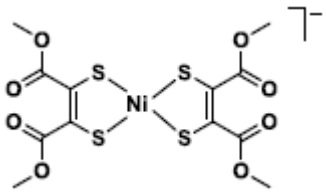	-0.5	GC		TsOH		[46]
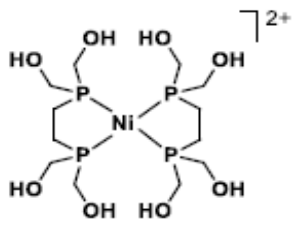	-0.6	carbon foam rod	1	H_2SO_4	6.7×10^6	[138]
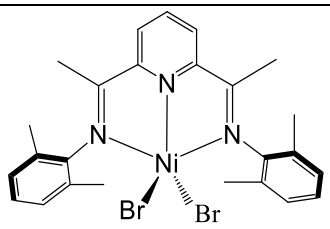	-0.8	RVC	1	HCl	65	[47]

3.4 Results and Discussion

The target complex [Ni(κ^3-2,6-{PhNCMe}$_2$(NC_5H_3)Br_2] (**3.1**) was readily prepared by adding $NiBr_2$ to a room temperature toluene solution of the diiminopyridine ligand, 2,6-{PhNCMe}$_2$(NC_5H_3). The reaction solution gradually became orange over several hours. The precipitated product was removed by filtration and recrystallized from CH_2Cl_2 (Figure 3.1). Although previously reported, this compound was not structurally characterized but was proposed to be a five-coordinate high spin Ni(II) species.[139] Single crystal X-ray analysis confirmed this proposition showing [Ni(κ^3-2,6-{PhNCMe}$_2$(NC_5H_3)Br_2] (**3.1**) to be a trigonal bipyramidal Ni(II) center displaying a neutral planar tridentate diminopyridine and two bromo ligand as shown in Figure 3.1. The bonding parameters were similar and consistent with other related structurally characterized species including a dichloro analogue, [Ni(κ^3-2,6-{PhNCMe}$_2$(NC_5H_3)Cl_2] (Table B.1, B.2).[137]

Figure 3.1. Reaction scheme for the preparation of [Ni(κ^3-2,6-{PhNCMe}$_2$(NC_5H_3)Br_2] (**3.1**). Representation of the single crystal XRD structure of **3.1** with selected atoms labeled and hydrogens atoms omitted for clarity.

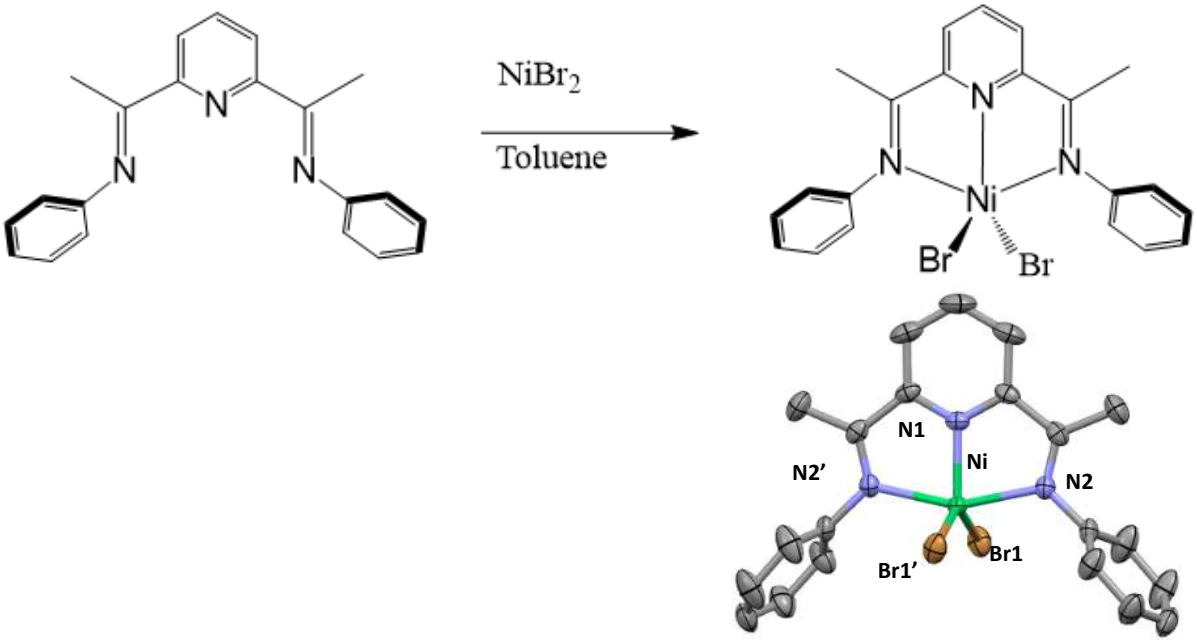

While in the solid state compound **3.1** was paramagnetic, consistent with a five coordinate Ni(II) center, diiminopyridine Ni(II) dihalo complexes are documented to autoionize in polar solvents to yield low spin diamagnetic, square planar d^8 species.[47, 137, 140] In fact, compound **3.1** displayed a diagnostic NMR spectra indicative of a symmetrical ligand coordinated with the structure $[Ni(\kappa^3\text{-}2,6\text{-}\{PhNCMe\}_2(NC_5H_3)Br]^+$ (**3.1'**$^+$) as schematically represented in Figure 3.2. Support for these observations came when attempts to computationally optimize structure **3.1** (DFT, B3LYP, def2-TZVP) using the PCM model for solvation in acetonitrile resulted in spontaneous dissociation of one of the Br^- ligands and rearrangement of the Ni center to a square planar geometry. As a result, the dissociated bromide was removed, which resulted in an optimized cationic square planar d^8 complex **3.1'**$^+$ (Figure 3.3, Table 3.2). In coordinating solvents such as water, these cationic Ni complexes are known to undergo a subsequent ligand substitution reaction of the bromo ligand by water to yield square planar Ni aquo species $[Ni(\kappa^3\text{-}2,6\text{-}\{PhNCMe\}_2(NC_5H_3)(OH_2)]^{2+}$, **3.1'(OH$_2$)$^{2+}$** (Figure 3.2).[47] This aquo complex was also successfully optimized to a minimum, confirmed by frequency calculations, yielding a structure that is the complement of **3.1**$'^+$ (Figure 3.4, Table 3.3). These results support that in polar/coordinating solvents **3.1** is a precursor to square planar Ni(II) species.

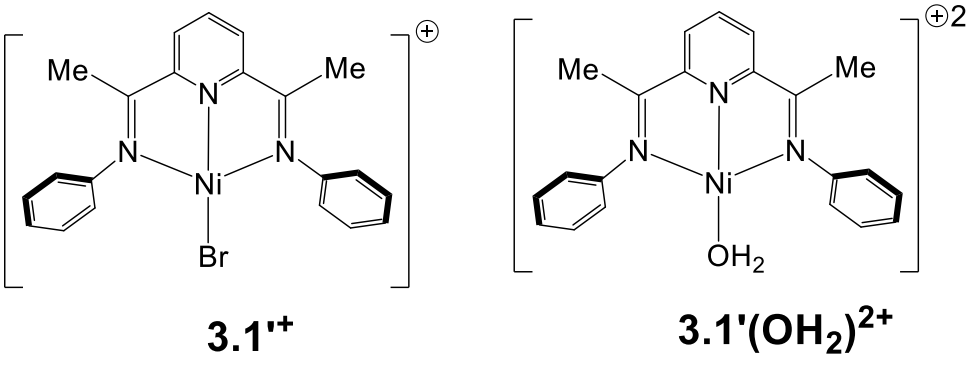

3.1'$^+$ **3.1'(OH$_2$)$^{2+}$**

Figure 3.2. Structural figures for compounds **3.1**$'^+$ and **3.1'(OH$_2$)$^{2+}$.**

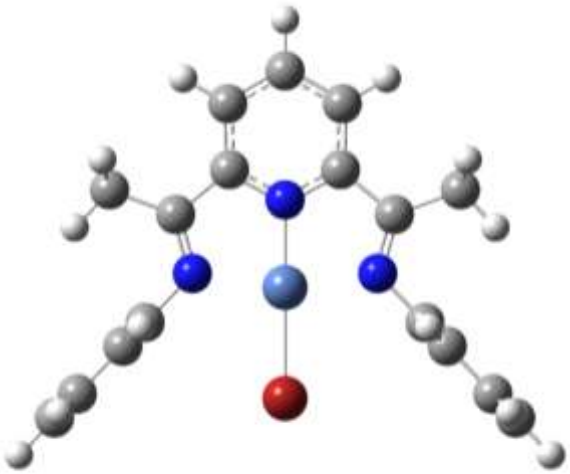

Figure 3.3. Computationally optimized $[Ni(\kappa_3\text{-}2,6\text{-}\{PhNCMe\}_2(NC_5H_3)Br]^+$ (**3.1'**$^+$) (DFT, B3LYP, def2-TZVP) using the PCM model for solvation in acetonitrile.

Table 3.2. Selected bonding parameters for computationally optimized $[Ni(\kappa^3\text{-}2,6\text{-}\{PhNCMe\}_2(NC_5H_3)Br]^+$ (**3.1'**$^+$)

Bond	Length(Å)	Overlap Pop	Mayer Bond Order
$Ni\text{-}N_{py}$	1.847	0.20	0.68
$Ni\text{-}N_{imine}$	1.976	0.26	0.65
Ni-Br	2.339	0.34	1.00

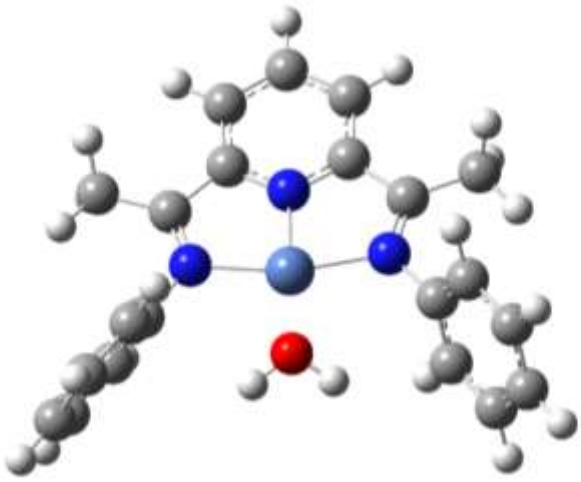

Figure 3.4. Computationally optimized $[Ni(\kappa^3\text{-}2,6\text{-}\{PhNCMe\}_2(NC_5H_3)(OH_2)]^{2+}$ (**3.1'(OH$_2$)$^{2+}$**) (DFT, B3LYP, def2-TZVP, PCM in water).

Table 3.3. Selected bond parameters for computationally optimized [Ni(κ^3-2,6-{PhNCMe}$_2$NC$_5$H$_3$)(OH$_2$)]$^{2+}$ (**3.1'(OH$_2$)$^{2+}$**)

bond	Length(Å)	Mayer Bond order
Ni-N_{py}	1.820	0.73
Ni-N_{imine}	1.948	0.68
Ni-N_{imine}	1.947	0.68
Ni-O	1.932	0.38

To see if the exchange between bromide ligand and water in aqueous media is in-situ, we investigated any changes in ^{1}H NMR and UV-VIS spectra of this complex in aqueous and organic solvent. As shown in Figure 3.5, the Me group of **3.1** has a peak at 2.35ppm in chloroform, however, in D_2O there are two peaks for Me at 2.18 and 2.06 ppm, suggesting that there might be a mixture of compounds in the aqueous solution, one could be the complex with one bromide (**3.1'**$^+$), the other coordinated with water (**3.1'(OH$_2$)$^{2+}$**). By adding 0.1M KBr in the D_2O solution of **3.1**, only one peak shows up with almost the same chemical shift observed in $CDCl_3$, suggesting that by adding KBr in the solution the bromo cation species was favored. In addition, by adding D_2O to a $CDCl_3$ solution of **3.1**, a new peak shows up which we attribute to complex **3.1** with substituted D_2O as ligand. Furthermore, the similarity between the UV-vis spectra of 0.1 mM complex **3.1** in CH_3CN and this complex with 100mM KBr in water support the in-situ generation of **3.1'**$^+$ in H_2O (Figure 3.6).

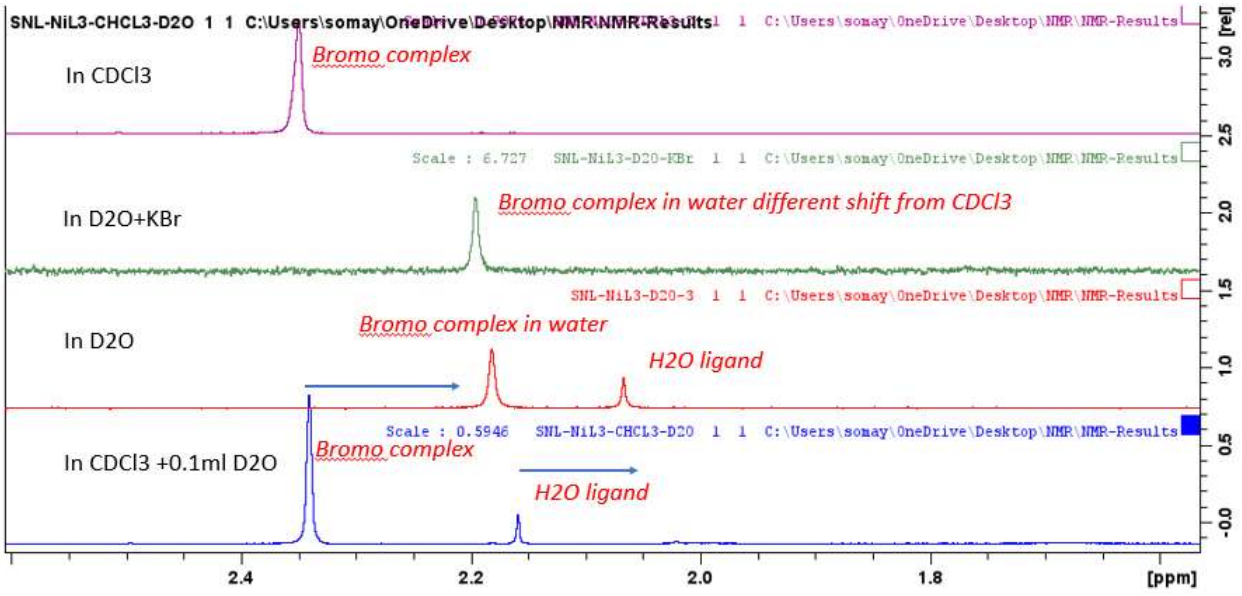

Figure 3.5. ^{1}H NMR spectra of [Ni(κ^3-2,6-{PhNCMe}$_2$(NC_5H_3)Br_2] in $CDCl_3$ (purple), in D_2O with added KBr (green), in D_2O (red), in $CDCl_3$ with added D_2O.

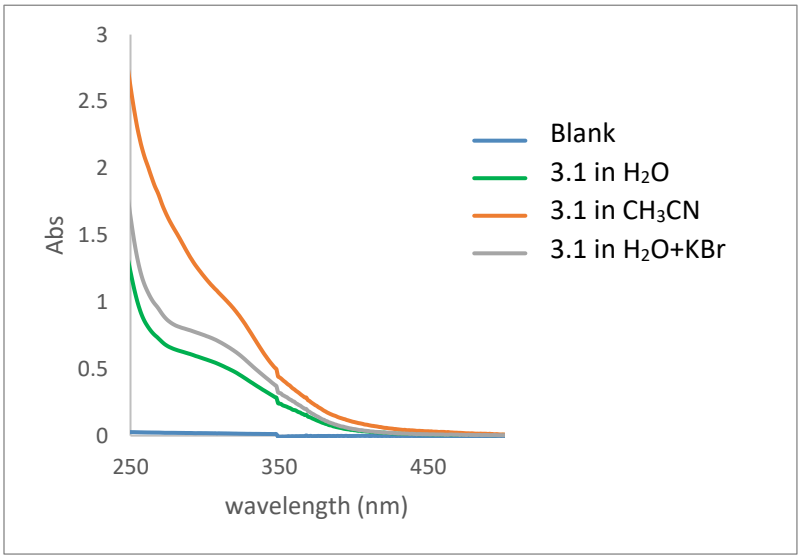

Figure 3.6. UV-vis spectra of 0.1 mM. [Ni(κ^3-2,6-{PhNCMe}$_2$(NC_5H_3)Br_2] in different solvents.

3.4.1 Electrochemical Characterization

The initial electrochemical characterization was performed on a 1mM solution in anhydrous acetonitrile with 0.1M Bu_4NPF_6 as the supporting electrolyte and using a glassy carbon (GC) working electrode, Pt counter electrode, and an Ag pseudo-reference electrode, which was externally referenced to the $Fc^{+/0}$ couple. The resulting cyclic voltammogram (CV) is displayed in Figure 3.7. As shown in the blue trace, **3.1'**$^{+}$ displayed two reversible reduction events with E_o = -0.75V and -1.15 V versus. $Fc^{+/0}$. Both redox events displayed a linear relationship of the square root of scan speed ($v^{1/2}$) versus current (i) consistent with a diffusion-controlled process[22] (Figure 3.8)

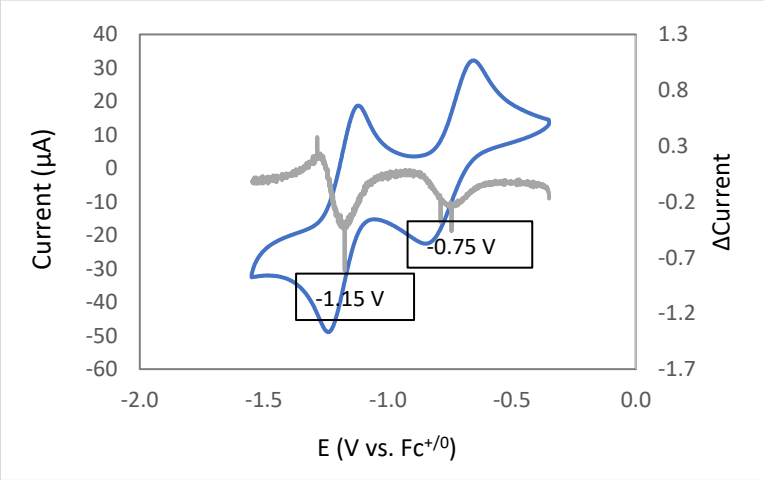

Figure 3.7. Cyclic voltammogram of **3.1** (1 mM) in presence of TBAHFP (100 mM) in CH_3CN using a GC working electrode. Potentials are referenced to $Fc^{+/0}$.

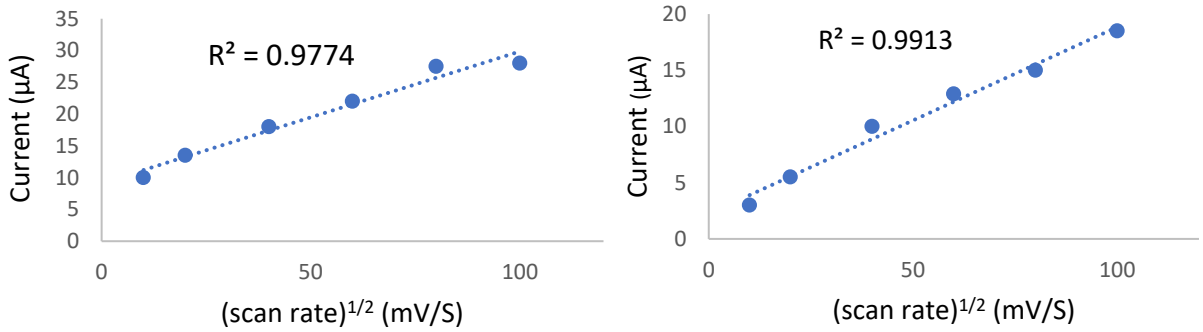

Figure 3.8. Plots of scan rate$^{1/2}$ versus current for the (a) first at -0.8V, (b) second at -1.2 V, reduction peaks of (**3.1**$^{'+}$).

All of these observations are consistent with reported electrochemical characterization of related diiminopyridine Ni(II) species. The first reduction has been assigned to addition of an electron to a ligand centered orbital while the second electron is placed in a metal centered (d_{x2-y2}) orbital.[47, 137] These results were confirmed by a computational optimization of the doubly reduced species, [Ni(κ^3-2,6-{PhNCMe}$_2$(NC_5H_3)Br]$^-$ (**3.1'**$^-$), which further confirmed the triplet ground state of this species. The two SOMOs of **3.1'**$^-$ (Figure 3.9) consist of a ligand centered MO that is a π* orbital delocalized across the pyridyl (48%) and imine (40%) moieties. The metal centered SOMO is σ* in nature and dominated by Ni d_{x2-y2} (41%) with a large Br p_y (19%) component.

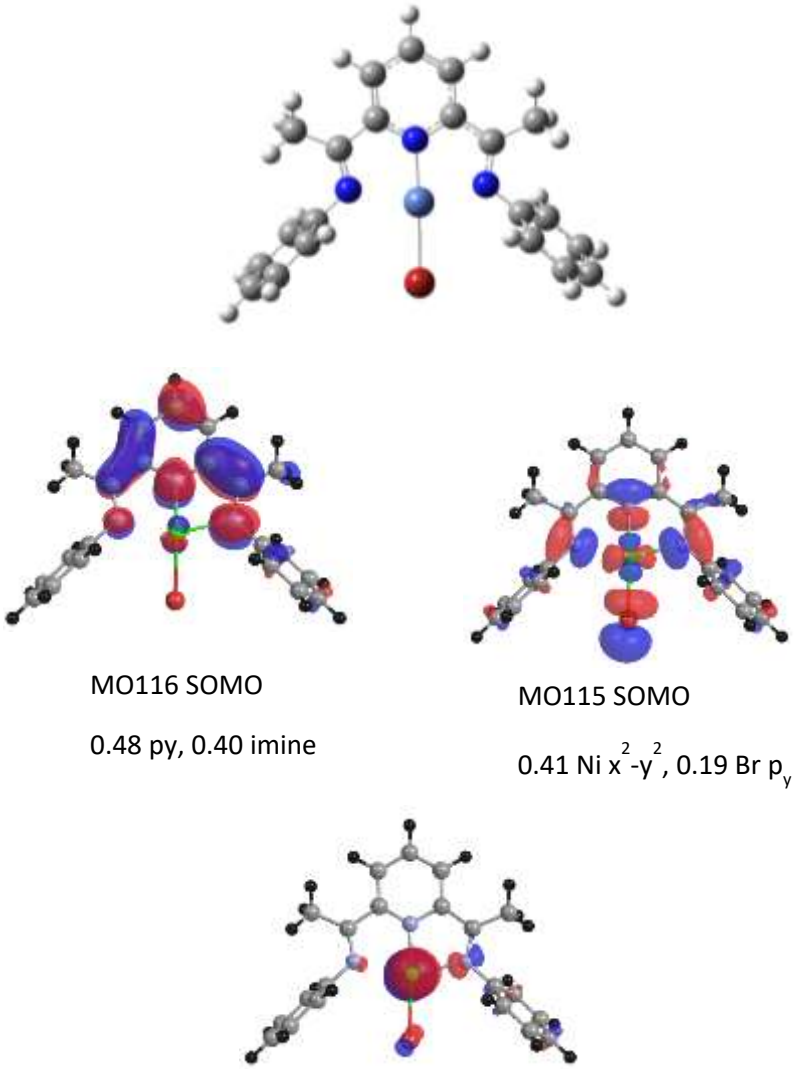

Figure 3.9. Computationally optimized [Ni(κ^3-2,6-{PhNCMe}$_2$(NC_5H_3)Br]$^-$ (**3.1'**$^-$) Both the singlet and triplet states of were successfully optimized to confirmed minima and the triplet state was determined to be lower in energy than the singlet state by 9 kcal/mole. Representations and fragment allocation of the two singly occupied molecular orbitals (SOMO) and a d_{z2} localized lone electron pair (MO112) for the DFT optimized [Ni(κ^3-2,6-{PhNCMe}$_2$(NC_5H_3)Br]$^-$ (**3.1'**$^-$) in the triplet state (DFT, B3LYP, def2-TZVP) using the PCM model for solvation in acetonitrile. The orbitals are rendered using the Chemissian software with an isosurface of 0.03.

A central goal of our efforts is to employ water as a sustainable and greener solvent and this prompted the electrochemical characterization of the aquo complex [Ni(κ^3-2,6-

{PhNCMe}$_2$(NC$_5$H$_3$)(OH$_2$)]$^{2+}$, **3.1'(OH$_2$)$^{2+}$** that would be generated by dissolving **3.1** in water. A CV of an aqueous solution of **3.1** (1mM) with KBr (100mM) supporting electrolyte under cathodic potentials is shown in Figure 3.10. Identical measurements were obtained in water and in aqueous phosphate buffer (pH=7). Here, two irreversible reduction events along with a single oxidation were observed. In order to more accurately assign the onset potentials for these reductions the maximum rate of electron transfer was determined by the method of first principles, which allowed their assignments of -0.95 V and -1.05 V versus. Ag/AgCl (Figure B.1).[141]

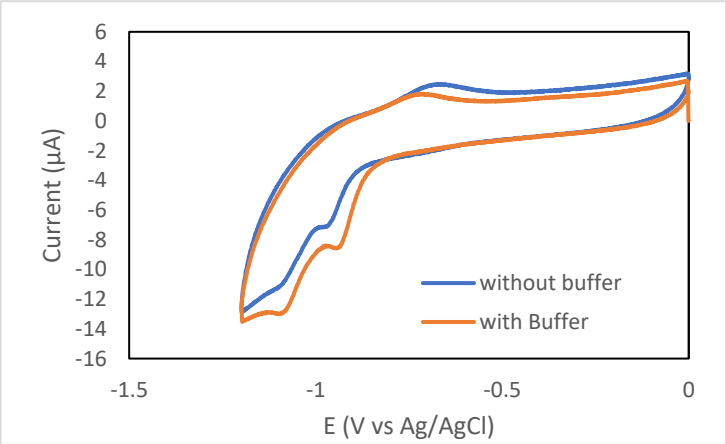

Figure 3.10. Cyclic voltammogram of Ni(κ^3-2,6-{PhNCMe}$_2$(NC$_5$H$_3$)(OH$_2$)]$^{2+}$, **3.1'(OH$_2$)$^{2+}$** (1mM) in an aqueous phosphate buffer at pH 7 (orange) and without buffer (blue). Supporting electrolyte was 100mM KBr, Measurement used a glassy carbon (GC) working electrode, Pt counterelectrode and Ag/AgCl reference electrode.

Significantly, the two reductions follow the Randles–Ševčík equation, yielding a linear relation for i versus $v^{1/2}$ consistent with a homogeneous diffusion-controlled process at the electrode/solution interface (Figure 3.11).

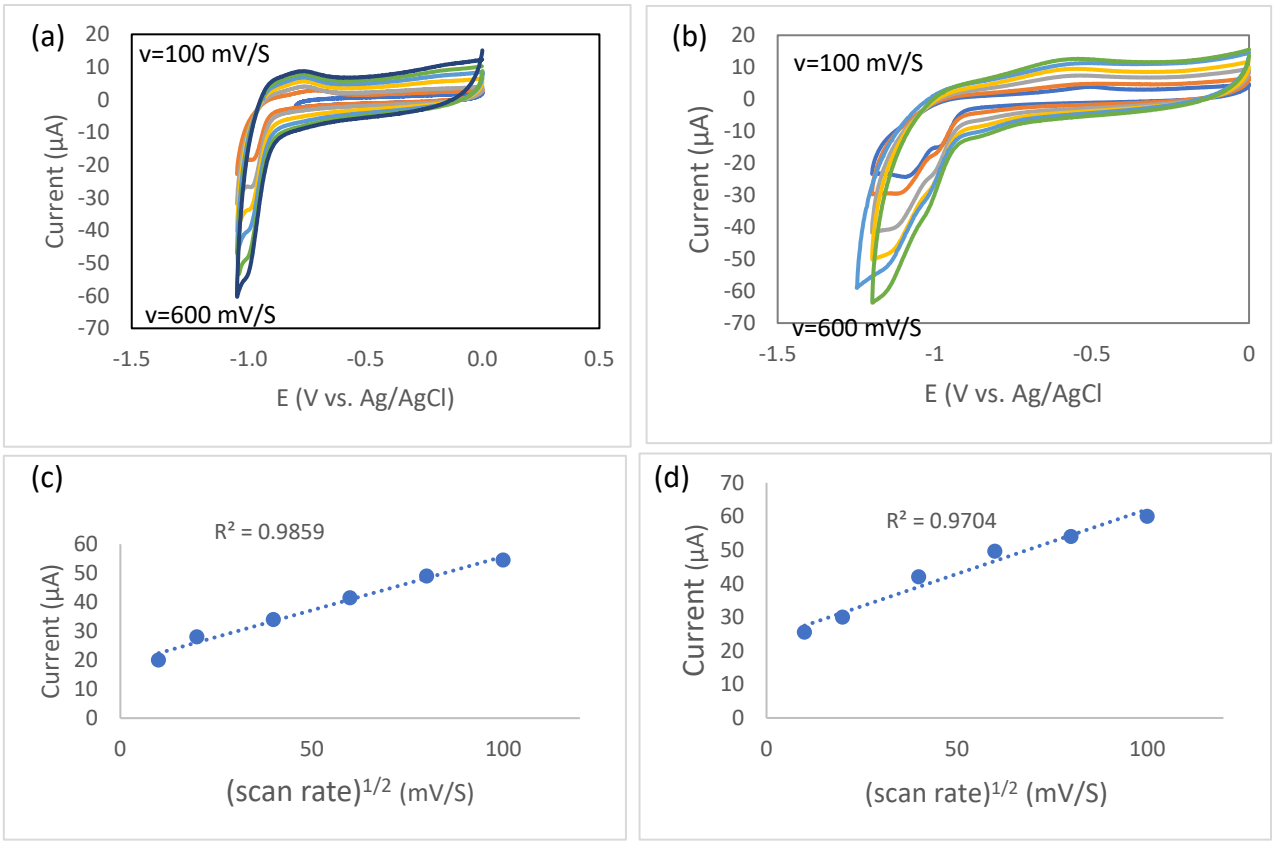

Figure 3.11. Cyclic voltammogram of complex $[Ni(\kappa^3\text{-}2,6\text{-}\{PhNCMe\}_2(NC_5H_3)(OH_2)]^{2+}$ (**3.1'(OH$_2$)$^{2+}$**) (1mM) at different scan rates in presence of 0.1M KBr in 0.3M phosphate buffer pH=7 for a) the first reduction, b) the first and the second reductions. Plots of scan rate$^{1/2}$ versus current for the first reduction (c) and the second reduction (d) at half wave potential. All potentials are referenced to Ag/AgCl.

The nature of the doubly reduced aquo species (**3.1'(OH$_2$)**) was examined through a computational optimization using the B3LYP functional, def2-TZVP basis set with the PCM solvation model in water. Frequency analysis validated that this led to a minimum structure (Figure B.2). As observed for **3.1'**$^{+}$, the lower energy electronic state for **3.1'(OH$_2$)** was the triplet by approximately 7 kcal/mole. The frontier orbitals of **3.1'(OH$_2$)** are shown in Figure 3.10 and were dominated by five metal centered d orbitals and two π^*orbitals of the ligand. The two singly occupied molecular orbitals (SOMOs) are constituted from the Ni d_{x2-y2} that was σ^* in nature and a π^* ligand centered

on pyridyl and imine groups. The next four lower energy molecular orbitals (MO 98-101) were Ni centered d_{xy} d_{yz}, d_{xz} and d_{z2}, respectively, and consistent with a square planar ligand field. This interpretation suggests that the starting Ni(II) species, $[Ni(k^3\text{-}2,6\text{-}\{PhNCMe\}_2NC_5H_3)(OH_2)]^{2+}$ (**3.1'(OH$_2$)$^{2+}$**), was reduced to a formally d^9 Ni(I) complex bearing a negatively charged diiminopyridine ligand, $[Ni(k^3\text{-}2,6\text{-}\{PhNCMe\}_2NC_5H_3)(OH_2)]$ (**3.1'(OH$_2$)**). The reduced complex displayed, as expected, slightly decreased Mayer bond orders and increased bond distances compared to the original cation, **3.1'(OH$_2$)$^{2+}$** (Figure 3.12, Table B.4).

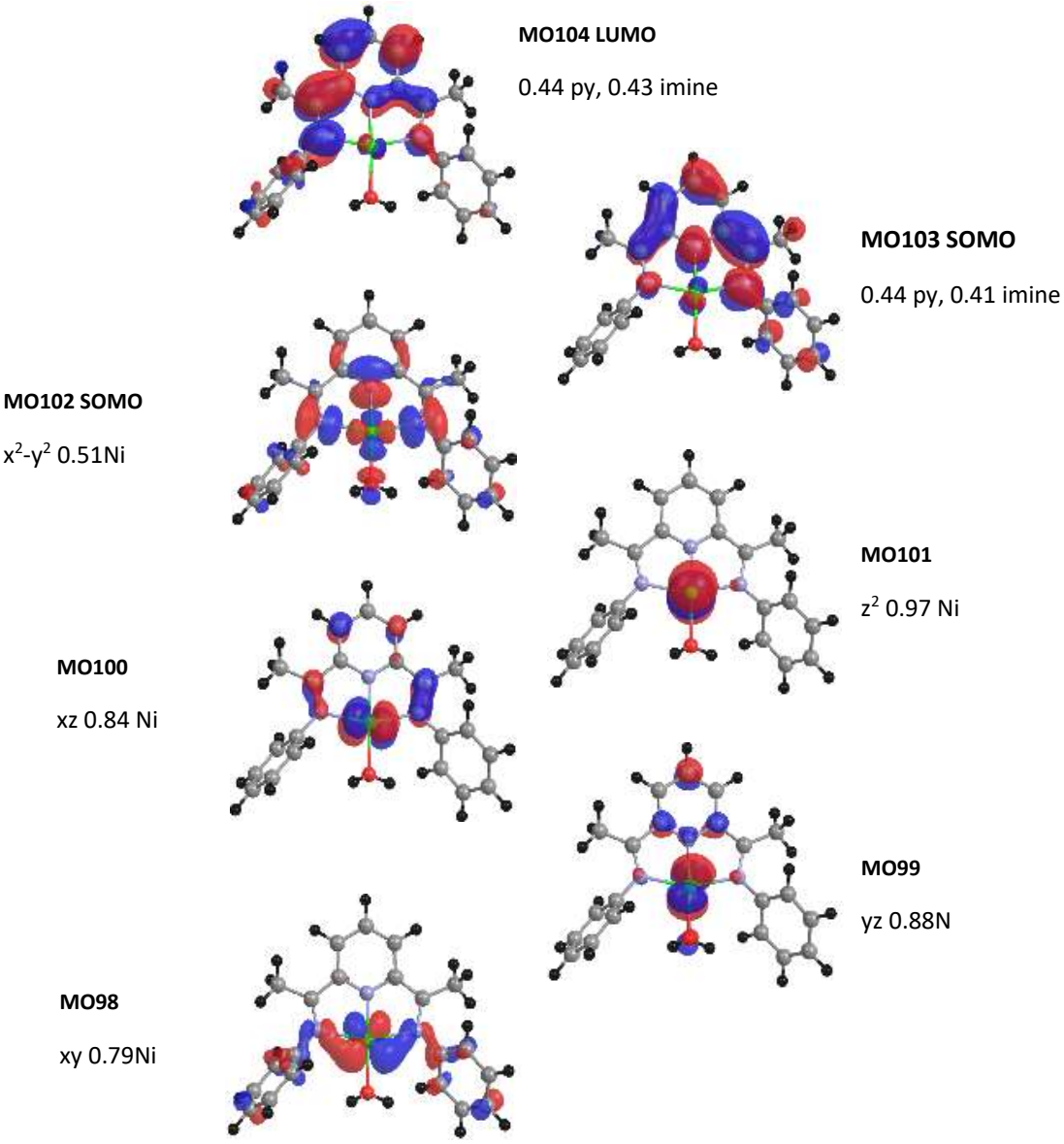

Figure 3.12. Frontier molecular orbitals obtained for the optimization of [Ni(κ^3-2,6-{PhNCMe}$_2$NC$_5$H$_3$)(OH$_2$)] (**3.1'(OH$_2$)**), the second reduction of (**3.1'(OH$_2$)$^{2+}$**). Obtained using the B3LYP functional, def2TZVP basis set and PCM model for solvation in water. Major fragment orbital contributions were visualized using the Chemissian program using a 0.03 isosurface.

3.4.2 Electrocatalytic H_2 Production

The prospective for **3.1** as a precatalyst for electrocatalytic H_2 generation was initiated in nonaqueous polar solvents. Dissolution in acetonitrile (CH_3CN), led to the cationic species [Ni(κ^3-2,6-{PhNCMe}$_2$(NC_5H_3)Br]$^+$ (**3.1'$^+$**). Based on literature reports that related complexes were capable of reducing acidic protons to hydrogen, we were pleased to reveal the reduction capability of **3.1'$^+$** with trifluoracetic acid (TFA) as the proton source in CH_3CN. As seen in Figure 3.13, the addition of TFA to acetonitrile solution of **3.1'$^+$** triggers a large catalytic wave under cathodic scan at E =-1.2V versus $Fc^{+/0}$.

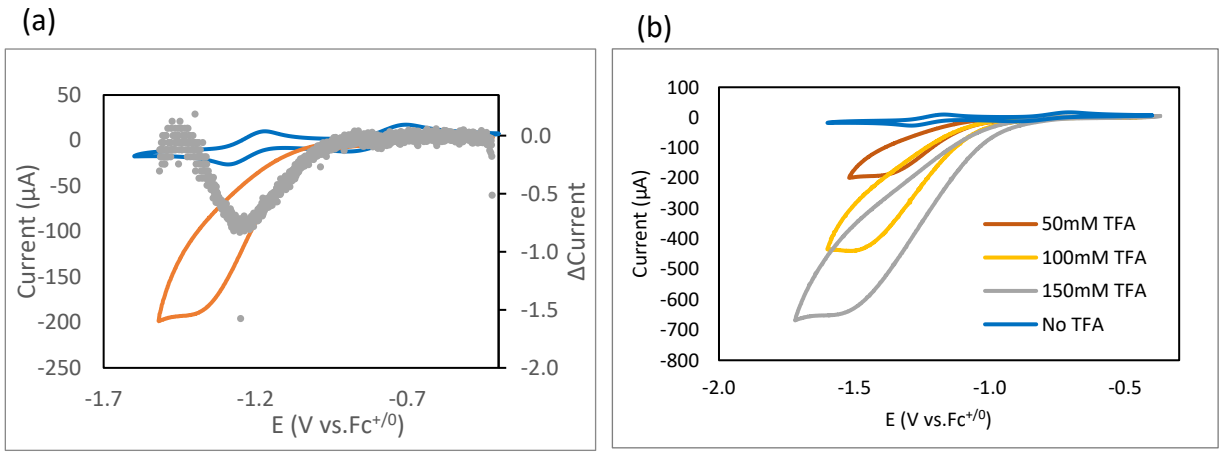

Figure 3.13. Cyclic voltammograms of **3.1'$^+$** (1mM) in presence of TBAHFP (100mM) in CH_3CN using a GC working electrode a) without (blue) and with 50mM TFA (orange), b) with various concentrations of trifluoroacetic acid (TFA). Potentials were referenced $Fc^{+/0}$.

The overpotential for this process can be determined by first calculating the theoretical proton reduction potential value, $E^T_{1/2}$, in acetonitrile, obtained from equation 3.1, and subtracting this

value from the experimental onset potential.[142, 143] For TFA in acetonitrile, the *pKa* value is 12.7 and the homoconjugation constant, K_c is $10^{3.7}$, ε_D is the relative diffusion rate of products to reactants, C^0 is the concentration of proton source, and $C^0_{H_2}$ is the maximum concentration of H_2 in solution. Using these values the $E^T_{1/2}$ is -645 mV with corresponding to overpotential of 555 mV for **3.1'**$^+$.

$$E^T_{1/2} = E^0_{H^+/H_2} - \left(\frac{2.303RT}{F}\right)pK_a + e_D + \left(\frac{RT}{2F}\right)ln(K_c^2 C^0 C^0_{H_2}) \qquad (3.1)$$

The effect of increasing TFA concentration on the catalytic current, i_{cat}, and the TFA concentration dependence of i_{cat}/i_p were also determined. A plot of catalytic current (i_{cat}) as a function of acid concentration revealed an initial linear acid concentration dependence that begins to plateau at ~0.5M TFA where the reaction shifts to a pseudo-zero order rate indicative of saturation conditions (Figure 3.14). This relationship can be expressed using equation 3.2 where TOF is the catalyst turnover frequency, R being the ideal gas constant, T the absolute temperature, F the Faraday constant and v the scan rate used in the cyclic voltammetry measurement in units of V/s.[40] In the case of **3.1'**$^+$ at n = 100 mV/s the TOF for hydrogen production from TFA at -1.2 V of 639 s^{-1}.

$$\frac{i_{cat}}{i_p} = \frac{2}{0.446}\sqrt{\frac{RT(TOF)}{Fv}} \qquad (3.2)$$

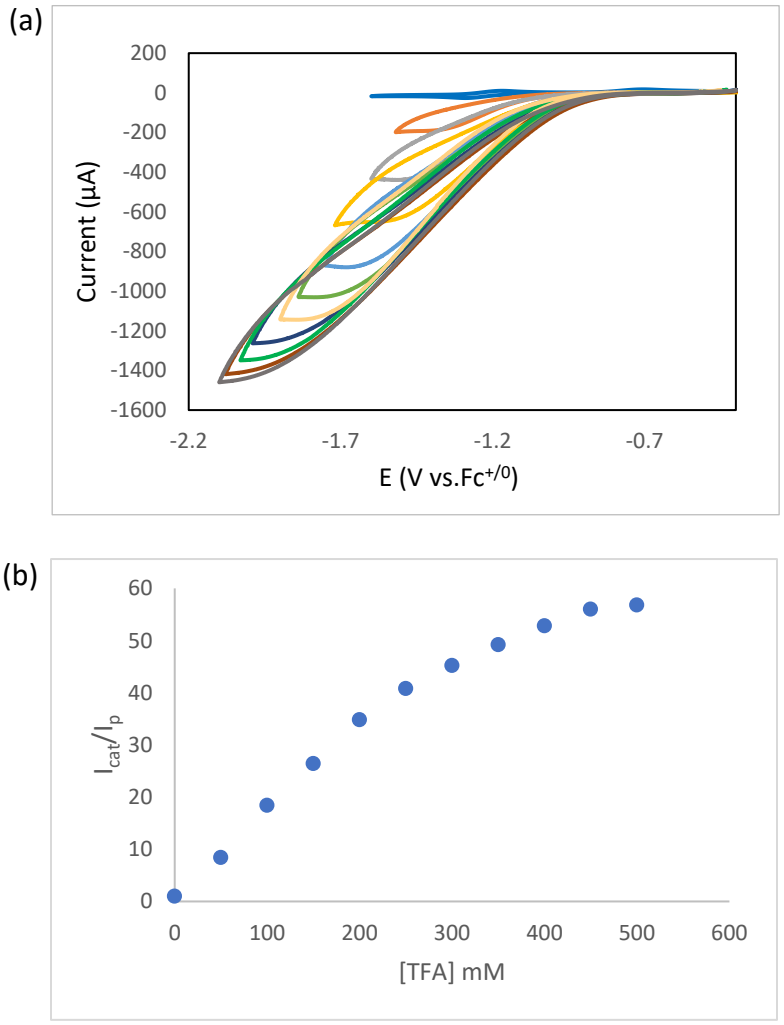

Figure 3.14. a) Cyclic voltammograms of $[Ni(\kappa^3\text{-}2,6\text{-}\{PhNCMe\}_2(NC_5H_3)Br]^+$ (**3.1'**$^+$) in the absence of TFA and with varying concentrations of TFA in CH_3CN with 0.1 M tetrabutylammonium hexafluorophosphate (TBAHFP) supporting electrolyte at 100 mV/s using a glassy carbon (GC) working electrode. (b) Corresponding plot of i_{cat}/i_p vs TFA concentration.

A controlled potential electrolysis (CPE) experiment demonstrated that under these conditions and over 2 hours, **3.1'**$^+$ catalytically produced 512µmol of H_2 with an 85% Faradaic efficiency.

Water, which represents the quintessential and sustainable source for H_2 production, also provides an ideal solvent for the electrocatalytic reaction. Therefore, we initiated an exploration of the ability of $Ni(\kappa^3\text{-}2,6\text{-}\{PhNCMe\}_2NC_5H_3)(OH_2)]^{2+}$ (**3.1'(OH$_2$)$^{2+}$**) for electrocatalytic hydrogen

generation in aqueous solutions. Clearly the consumption of protons from water would lead to an increase in hydroxide ions and an increase in solution pH. This was documented by two experiments. First, the pH of a controlled potential coulometry experiment with **3.1'$(OH_2)^{2+}$** was monitored for 2 hours and showed a steady increase of pH from 6.5 to 7.2. while in the presence of buffer this value stays almost constant (Figure 3.15). Second, the current response during a controlled potential electrolysis was monitored for both buffered (0.3M phosphate, pH 7) and unbuffered solutions of **3.1'$(OH_2)^{2+}$**. The buffered solution displayed a substantial increase in current compared to the unbuffered system (Figure 3.16). Importantly, the presence of buffer had no significant effect on the CV behavior of **3.1'$(OH_2)^{2+}$** (Figure 3.10).

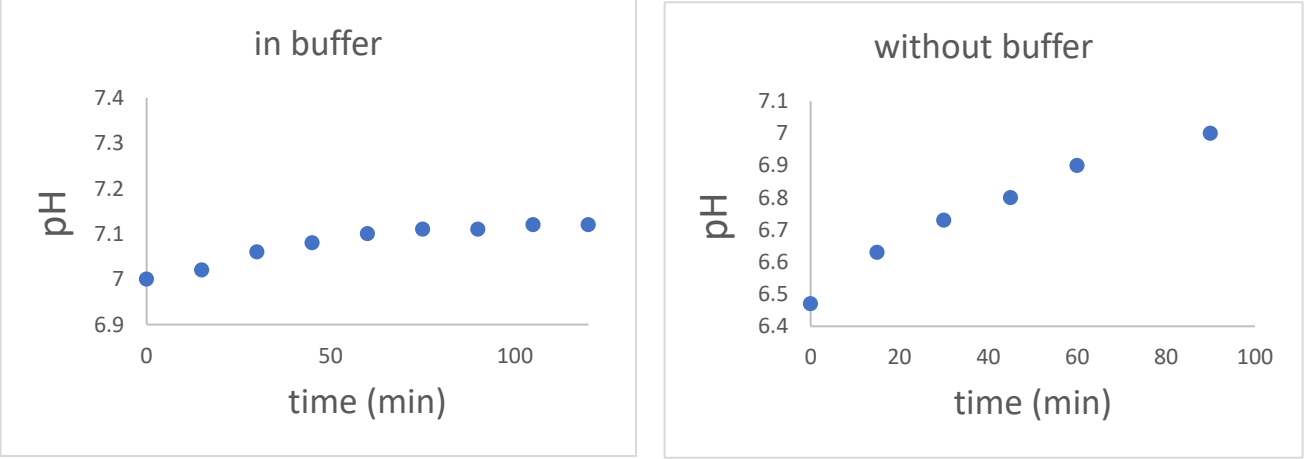

Figure 3.15. Plot of pH change during electrolysis a) in presence of phosphate buffer pH 7 b) absence of buffer. Both Solutions contain 1mM **3.1'$(OH_2)^{2+}$** and 0.1 M KBr in aqueous solution and the CPE was done at –1.2 V vs. Ag/AgCl.

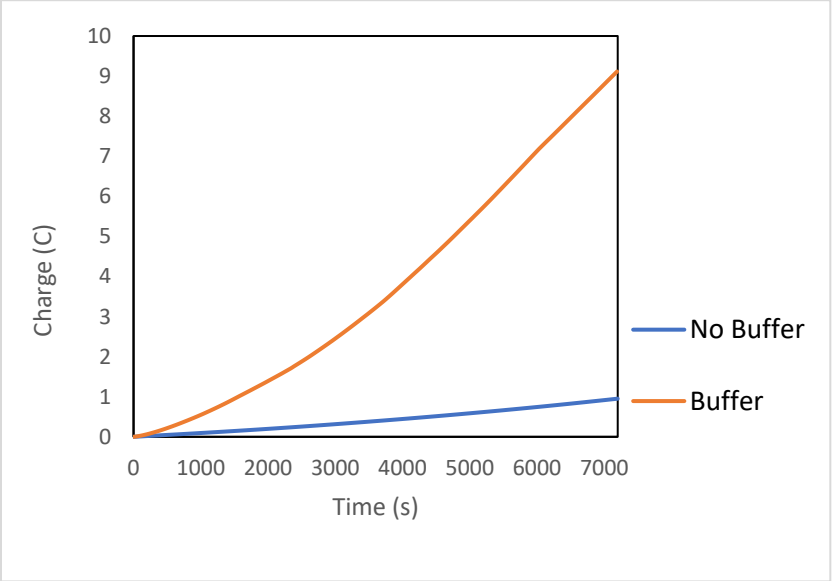

Figure 3.16. Controlled potential electrolysis of 1mM of **3.1'$(OH_2)^{2+}$** at –1.2 V vs. Ag/AgCl (0.1 M KBr) of an aqueous solution with (orange) and without (blue) phosphate buffer at pH = 7.

Electrocatalytic hydrogen production with **3.1'$(OH_2)^{2+}$** was confirmed by coulometry in buffered (pH 7) saline (KBr) solution at -1.1 V versus Ag/AgCl. The effect of using a buffered solution resulted in a significant quantitative effect for H_2 production leading to a ten-fold increase in H_2 and an improvement in Faradaic efficiency to 96% (Table 3.4). In the absence of **3.1'$(OH_2)^{2+}$**, a potential of -1.7V versus Ag/AgCl was required to get a current response (Figure 3.17, Figure B.3). The relation between applied reduction voltage and charge transfer was measured between -1.0 and -1.2 V (Figure 3.18). The combination of these observations with the CPE analysis in Table 3.4, indicated that catalytic H_2 formation from $[Ni(\kappa^3\text{-}2,6\text{-}\{PhNCMe\}_2NC_5H_3)(OH_2)]^{2+}$ (**3.1'$(OH_2)^{2+}$**) occurred at ≥-1.0V versus Ag/AgCl.

Table 3.4. Summary of data collected from CPE experiment.

Entry	[catalyst]	E (V vs. Ag/AgCl)	time (h)	solution	µmol H_2	FE (%)
1	1 mM	-1.1V	2	No Buffer	4.43	89
2	0.5 mM	-1.1V	2	0.3M Phosphate Buffer	34.74	76

3	1 mM	-1.1V	2	0.3M Phosphate Buffer	45.43	96
4	1 mM	-1.1V	18	0.3M Phosphate Buffer	415	28
5	1 mM	-1.0V	2	0.3M Phosphate Buffer	2	63
6	1 mM	-1.2V	2	0.3M Phosphate Buffer	110	78

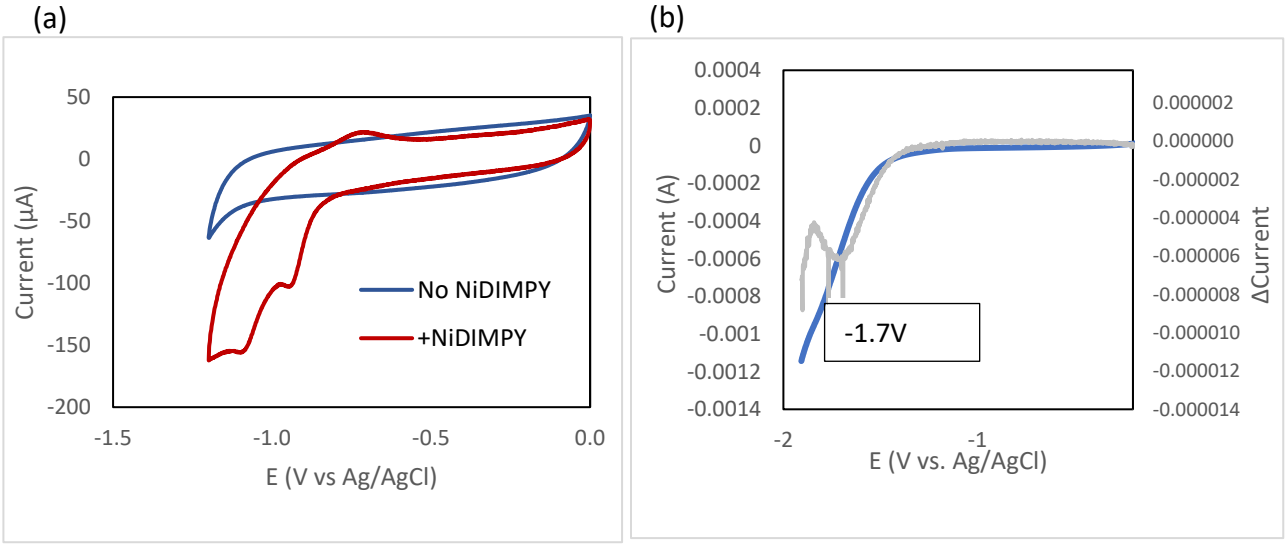

Figure 3.17. A comparison of cyclic voltammograms with (red) and without (blue) **3.1'$(OH_2)^{2+}$** in 100mM KBr in 0.3M phosphate buffer pH=7. Measurements used a glassy carbon (GC) working electrode, Ag/AgCl reference electrode. b) LSV of a solution in the absence of **3.1'$(OH_2)^{2+}$**). The gray markers represent application of the method of first principles to the blue curve. Minima denote inflection points in the catalytic curve and indicate the associated onset potential and current enhancement at the GC electrode.

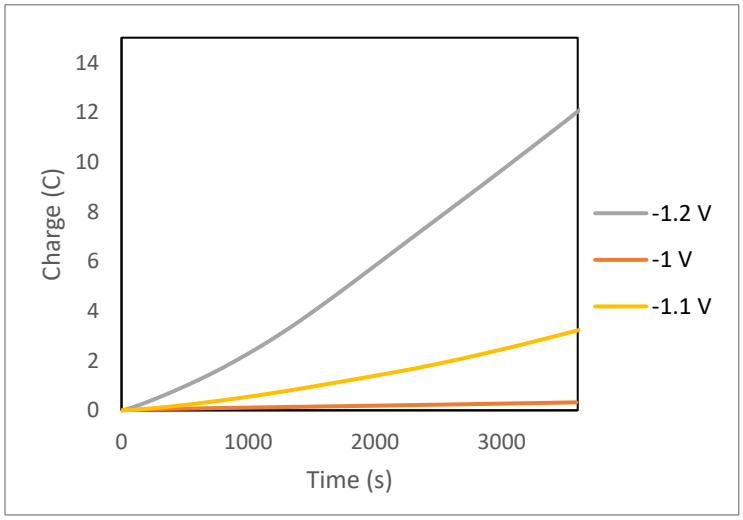

Figure 3.18. Controlled potential electrolysis of 1mM **3.1'(OH$_2$)$^{2+}$** (0.1 M KBr, phosphate buffer pH = 7) at different potentials at vs. Ag/AgCl.

Using the value of $E^{o}_{H^+/H_2}$ = 0.613 mV versus Ag/AgCl for water at pH = 7, a series of measurements for charge transfer (current) at various applied potentials was performed over the course of 2 min electrolysis using a 0.5mM **3.1'(OH$_2$)$^{2+}$** (Figure 3.19). This data is essentially a direct measure of the overpotential for hydrogen generation by **3.1'(OH$_2$)$^{2+}$** in water and provided a value of 0.387 mV, consistent with an applied potential of -1.0 V.

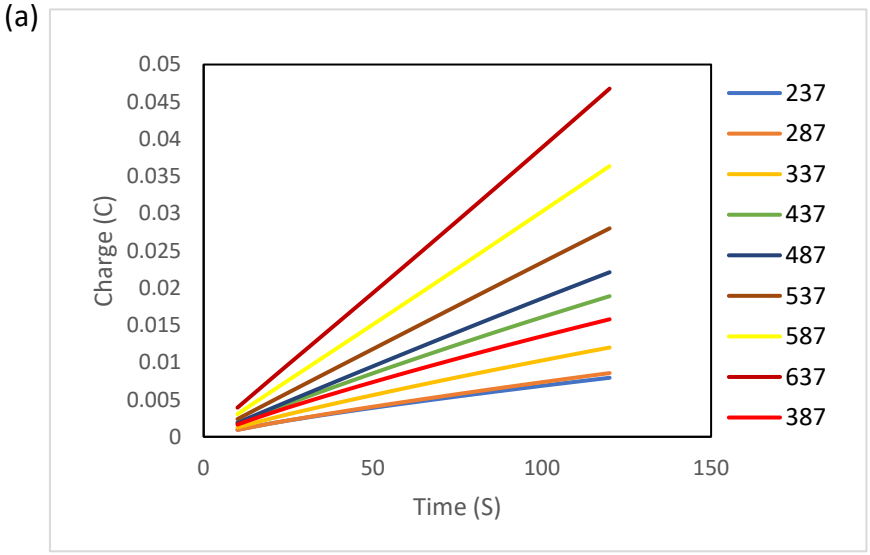

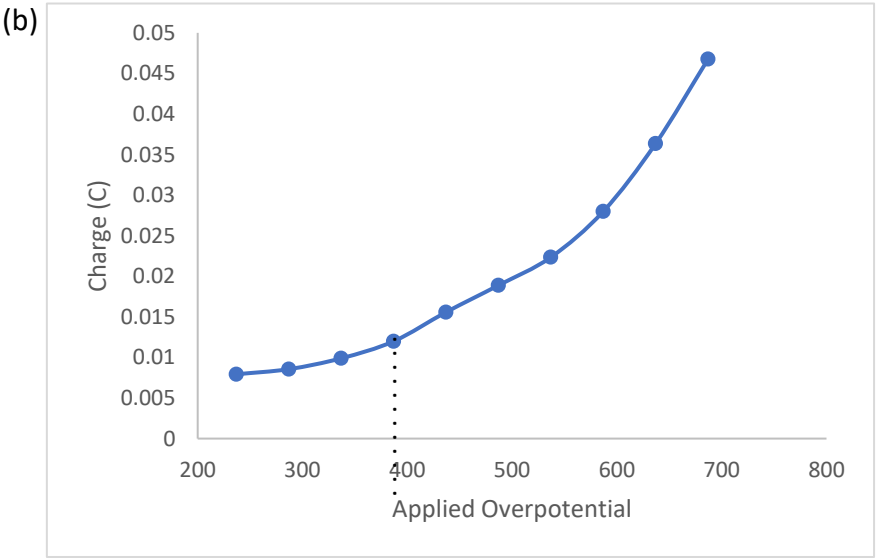

Figure 3.19. Using value of $E^{o}_{H^+/H_2}$ = 0.613 mV versus. Ag/AgCl for water at pH=7. a) Charge build up versus times and (b) the accumulated charge for controlled potential electrolysis of 0.5 mM solution of (**3.1'$(OH_2)^{2+}$**) in 0.1 M KBr and phosphate buffer pH=7. The enhancement starts from overpotential=0.387 V.

The homogeneous behavior of **3.1'$(OH_2)^{2+}$** was further supported by several control experiments. Repeated linear sweep voltammetry measurements of the catalyst/substrate systems were carried out to confirm catalytic current enhancement. Following these sweeps, the electrode was removed, carefully rinsed with clean solvent, and placed into a fresh solution containing substrate but no catalyst. Voltammetry measurements on these catalyst-free systems did not exhibit any electrochemical events, indicating that the catalyst had not deposited on the electrode surface following electrolysis (Figure 3.18). These measurements indicated that the catalyst had not transformed during electrolysis.

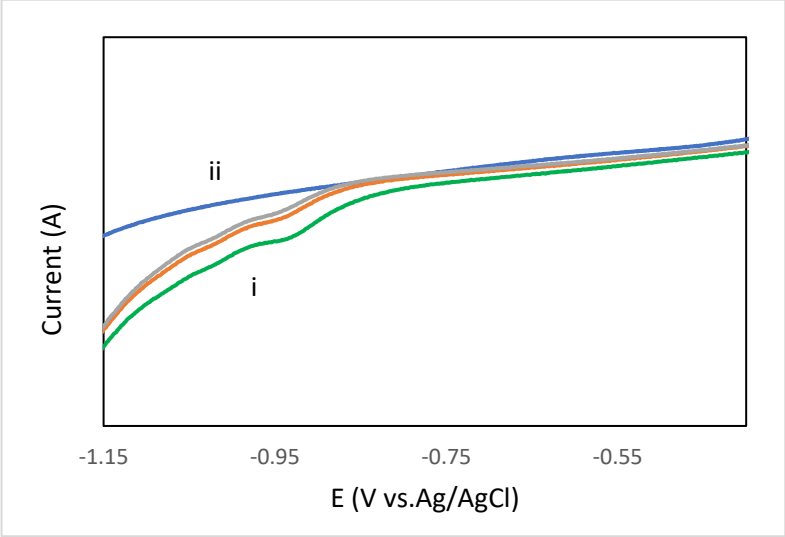

Figure 3.20. Linear Sweep Voltammetry measurements used to demonstrate that the working electrode surface remains clean during catalysis. Scans are shown for **3.1'$(OH_2)^{2+}$** (i) shows repeated linear scans of a solution containing 1 mM of (**3.1'$(OH_2)^{2+}$**) complex in 0.1M KBr in phosphate buffered solution. (ii) Shows a scan after the electrode was removed, rinsed with clean solvent and placed in a fresh solution containing no Ni complex.

Finally, CV measurements on aqueous solutions of **3.1** (0.5 to 1mM) with 100 mM KBr showed an increase in peak current with an increase in nickel concentration, which is consistent with a homogeneous system. (Figure 3.21)

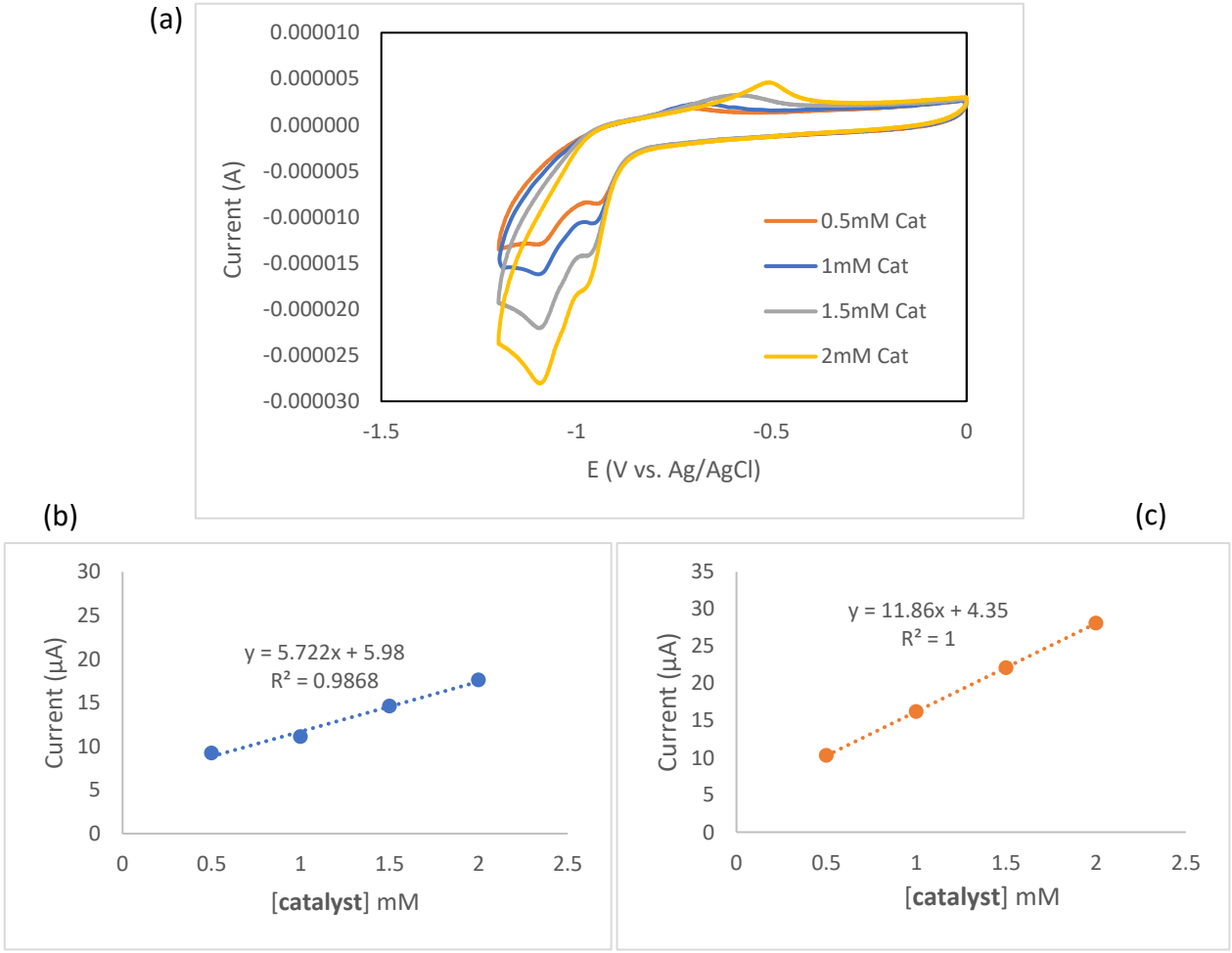

Figure 3.21. a) Cyclic voltammogram in presence of different concentration of complex [Ni(κ^3-2,6-{PhNCMe}$_2$(NC_5H_3)(OH_2)]$^{2+}$ (**3.1'$(OH_2)^{2+}$**) with 100mM KBr in 0.3M phosphate buffer pH=7, using a glassy carbon (GC) working electrode, Ag/AgCl reference electrode. Dependence of current to the concentration of (**3.1'$(OH_2)^{2+}$**) at the b) first reduction and at the c) second.

The durability of (**3.1'$(OH_2)^{2+}$**) for electrocatalytic hydrogen generation was investigated by long-term controlled potential electrolysis. Current could be sustained over the course of 18 h as shown in (Figure 3.22) which suggests that this catalyst is highly stable under these conditions.

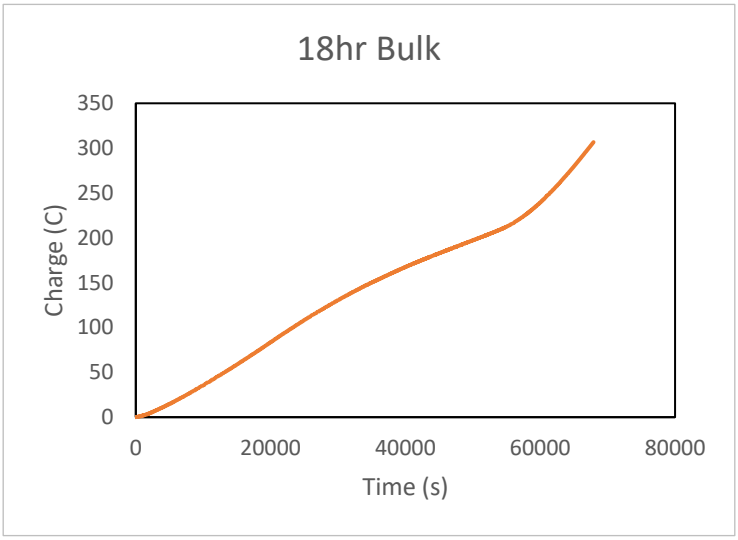

Figure 3.22. Controlled potential electrolysis of 1mM **3.1'(OH$_2$)$^{2+}$** at –1.2 V vs. Ag/AgCl (0.1 M KBr, phosphate buffer pH=7).

3.4.3 Proposed Mechanism for H_2 Production from Water

A proposed mechanism for the catalytic H_2 generation by **3.1'(OH$_2$)$^{2+}$** is presented in Figure 3.24. Computations provided additional support for this proposition with [Ni(κ^3-2,6-{PhNCMe}$_2$(NC_5H_3)Br_2] (**3.1**) as a precatalyst. As shown in Figure 3.24, the square planar d^8 complex [Ni(κ^3-2,6-{PhNCMe}$_2$(NC_5H_3)(OH_2)]$^{2+}$ (**3.1'(OH$_2$)$^{2+}$**) arises from the dissolution of **3.1** in water. The production of H_2 at -1.1 V versus Ag/AgCl correlates with the second reduction of **3.1'(OH$_2$)$^{2+}$** and computations supported that this doubly reduced species is a triplet state with the frontier orbitals shown in Figure 3.23.

At this stage the **3.1'(OH$_2$)** is an electron-rich, basic complex that can abstract a proton from water. The highest energy lone electron pair is a nonbonding pair in a Ni-centered d_{z2} orbital (Figure 3.22, MO 101). Addition of a proton to this site would lead to a cationic species [Ni(κ^3-2,6-{PhNCMe}$_2$(NC_5H_3)(OH_2)(H)]$^+$, shown as **A** in equation 3.3.

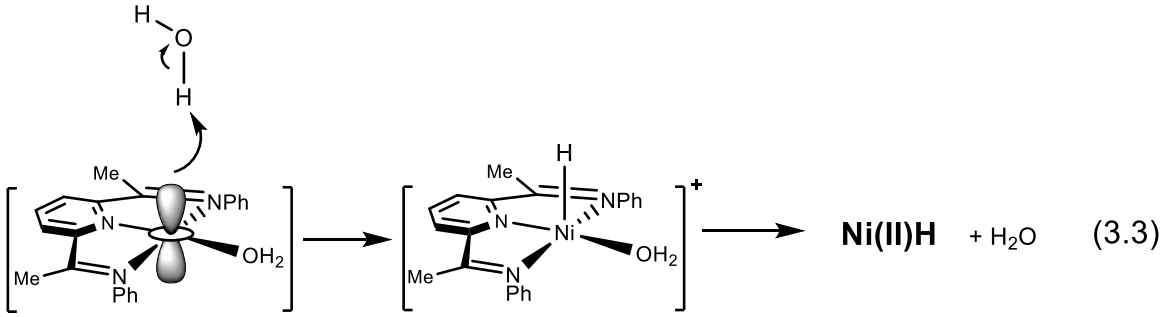

Attempts to carry out a computational optimization for the proposed species **A** using B3LYP/def2TZVP and modeling with water solvation, spontaneously led to a rearrangement with loss of the coordinated aquo ligand and formation of square planar hydride species, [Ni(κ^3-2,6-{PhNCMe}$_2$$NC_5H_3$)H]$^+$ (**Ni(II)H**) (Figure B.4). This proposed species has the Ni center in a divalent oxidation state and a d^8 configuration. A molecular orbital analysis (Figure B.5) confirmed that the HOMO is Ni-centered and largely d_{z2} in character with the LUMO derived from a π^* MO on the pyridyl and imine groups. The remaining metal d-centered orbitals reflect the ligand field splitting expected for a square planar Ni.

With the highest energy electron pair in a d_{z2}-based MO, proton abstraction from water could be envisioned as the next reaction step. Once again, addition of a proton to Ni along this z-axis with an attempted computational optimization (B3LYP/def2TZVP/PCM(water)) of such a proposed species resulted in a smooth impromptu molecular rearrangement to a minimum energy structure as a dihydrogen complex, [Ni(κ^3-2,6-{PhNCMe}$_2$$NC_5H_3$)($H_2$)]$^+$ (**Ni(II)(H_2)**) (Figure B6-B7).

Simple substitution by water and release of H_2 from **Ni(II)(H_2)** regenerates the Ni^{II}, d^8 starting material, **3.1'(OH_2)$^{2+}$**, to close the cycle.

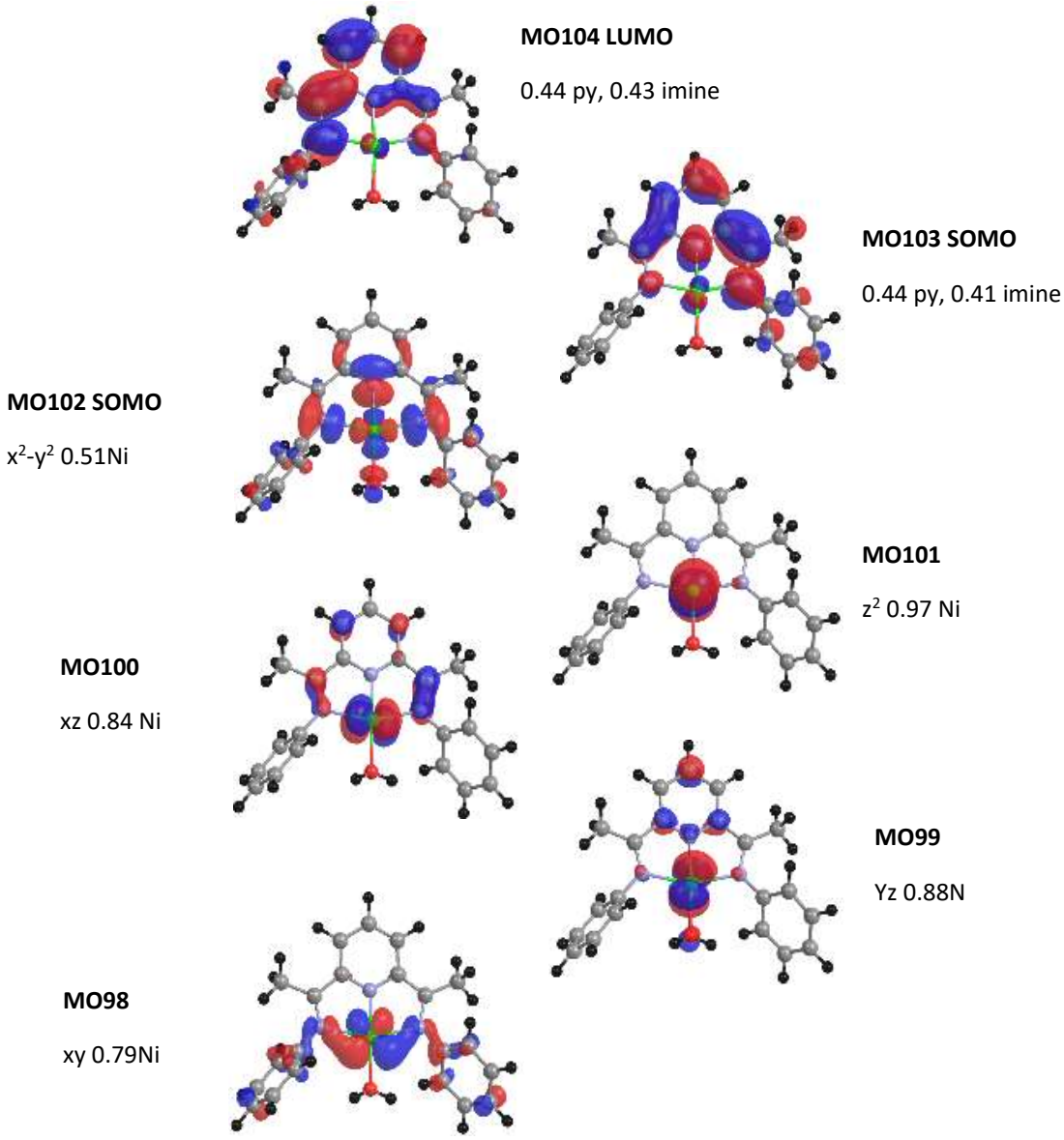

Figure 3.23. Frontier molecular orbitals obtained for the optimization of [Ni(κ^3-2,6-{PhNCMe}$_2$NC$_5$H$_3$)(OH$_2$)] **3.1'(OH_2)** , the second reduction of **3.1'(OH_2)$^{2+}$**. Obtained using the B3LYP functional, def2TZVP basis set and PCM model for solvation in water. Major fragment orbital contributions were visualized using the Chemissian program using a 0.03 isosurface.

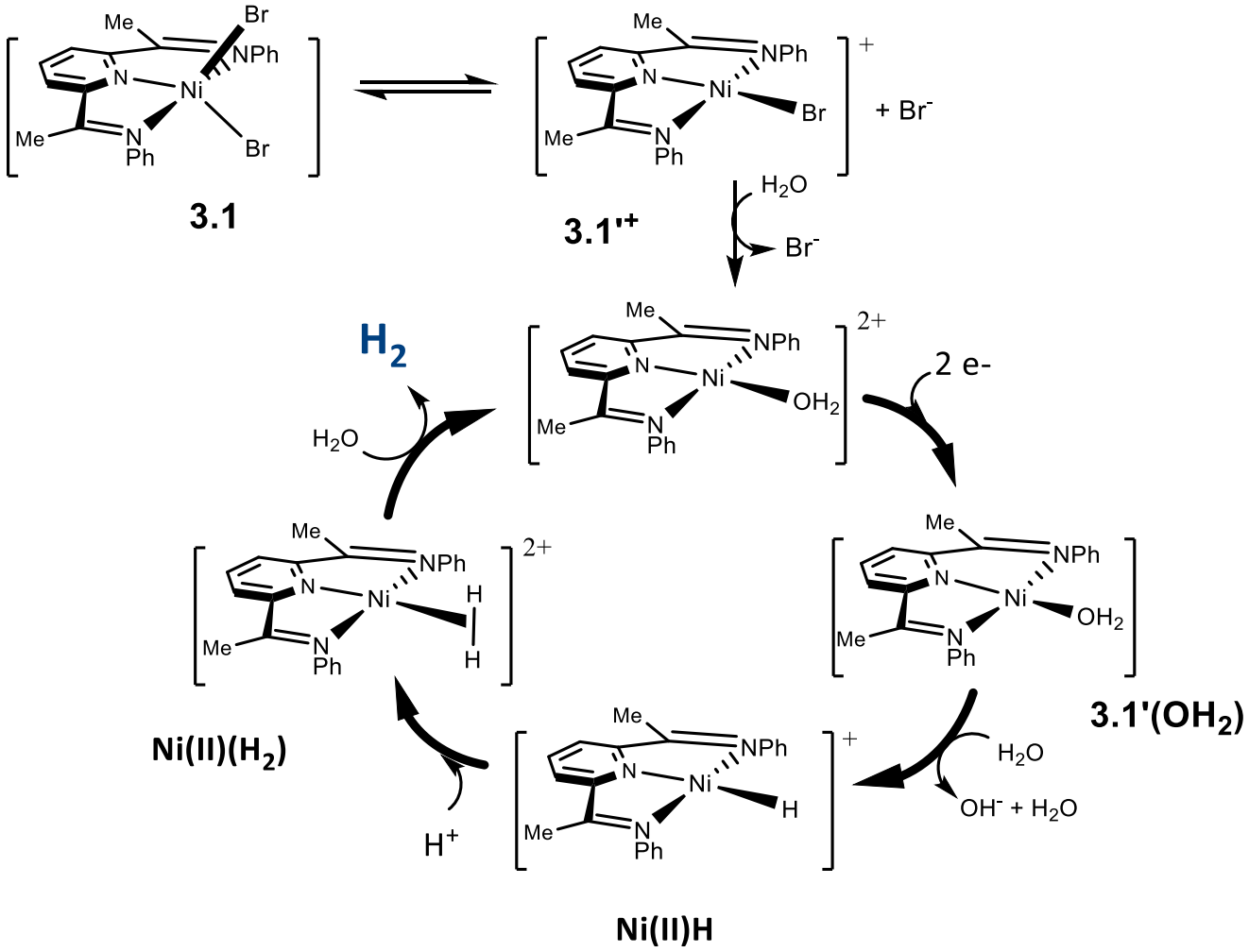

Figure 3.24. A computationally supported (B3LYP/def2TZVP/PCM(water)) proposed mechanism for the electrocatalytic hydrogen evolution from $[Ni(\kappa^3\text{-}2,6\text{-}\{PhNCMe\}_2(NC_5H_3)(OH_2)]^{2+}$ with H_2O as the substrate and solvent.

3.4.4 Proposed Mechanism for H_2 Production from TFA in Acetonitrile

A computational analysis informed our proposed mechanism and suggested some key differences from the reaction observed in water. The results of this analysis are presented in Figure 3.25. Again, starting from $[Ni(\kappa^3\text{-}2,6\text{-}\{PhNCMe\}_2(NC_5H_3)Br_2]$ (**3.1**) as a precatalyst, the square planar d^8 complex $[Ni(\kappa^3\text{-}2,6\text{-}\{PhNCMe\}_2(NC_5H_3)Br)]^+$ (**3.1'**$^+$) arises from the dissolution of **3.1** in

acetonitrile. The production of H_2 at -1.2V versus $Fc^{+/0}$ corresponds to the second reduction of **3.1'**$^{+}$ and computations supported that this doubly reduced species is a triplet state with SOMO orbitals shown in Figure 3.9.

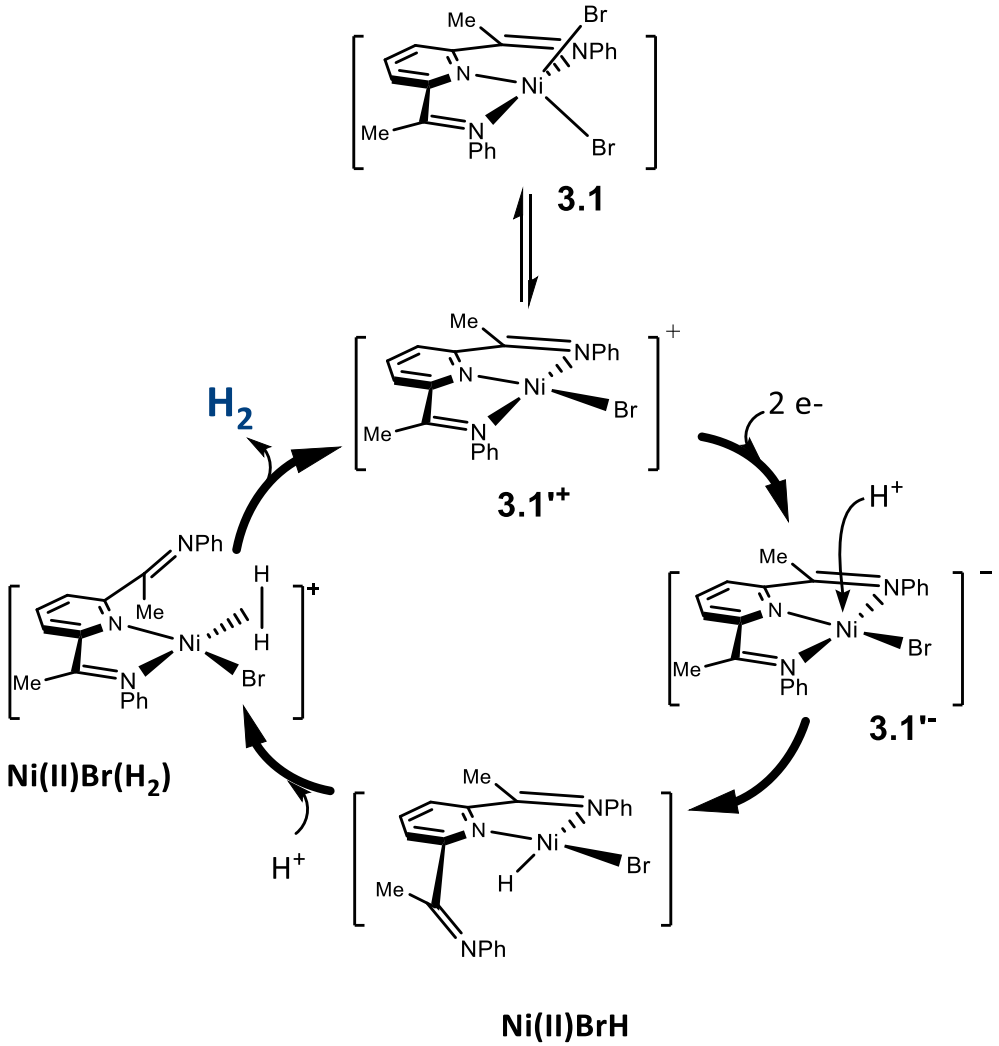

Figure 3.25. A computationally supported (B3LYP/def2TZVP/PCM(acetonitrile)) proposed mechanism for the electrocatalytic hydrogen evolution from $[Ni(\kappa^3\text{-}2,6\text{-}\{PhNCMe\}_2(NC_5H_3)Br]^+$ with TFA as the substrate and acetonitrile as the solvent.

This electron-rich, basic complex highest energy lone electron pair is a nonbonding pair in a Ni-centered dz^2 orbital (Figure 3.9, MO 112). Addition of a proton to this site and allowing the complex to freely optimize using B3LYP/def2TZVP resulted in a ready rearrangement releasing

one of the pincer ligand arms and formation of square planar hydride species, [Ni(κ^2-2,6-{PhNCMe}$_2$NC$_5$H$_3$)BrH] (**Ni(II)BrH**) (Figure B.8). This proposed species has the Ni center in a divalent oxidation state and a d^8 configuration. The addition of a second proton to Ni, along this z-axis, followed by a computational optimization (B3LYP/def2TZVP/PCM(acetonitrile)) resulted in the smooth uninitiated rearrangement to yield a minimum energy structure as a dihydrogen complex, [Ni(κ^2-2,6-{PhNCMe}$_2$NC$_5$H$_3$)Br(H$_2$)]$^+$ (**Ni(II)Br(H$_2$)**) (Figure B.9). After the formation of the proposed dihydrogen complex, simple coordination of the free imine arm would release H_2 and regenerate the starting species to complete this cycle.

3.5 Conclusion

This report has revealed some fundamental and practical features for electrocatalytic hydrogen generation from water employing a unique, air-stable Ni species. This Ni (II) complex, [Ni(κ^3-2,6-{PhNCMe}$_2$(NC$_5$H$_3$)Br$_2$] (**3.1**), was demonstrated to be a competent pre-catalyst for H_2 production with neutral water as a substrate and solvent. Furthermore, this was expanded to include the use of **3.1** in nonaqueous (acetonitrile) with TFA as a substrate. These experimental results were supported by DFT computational analysis, which revealed the important role of the ligand as electron reservoir in the reduction step as well as parallel but different reaction paths for the two hydrogen formation pathways. Our continuing explorations focus on the effects of ligand variation on this process and on expanded efforts to use water as a substrate and solvent.

3.6 Experimental Section

General Methods. Reactions were performed in a glovebox under a nitrogen atmosphere, with the exception of ligand synthesis, which was performed using standard Schlenk techniques under a flow of N_2. All solvents were sparged with nitrogen and then dried by passage through a column

of activated alumina using an apparatus purchased from Anhydrous Engineering. Deuterated solvents were dried using activated molecular sieves. All other chemicals were purchased from Sigma-Aldrich and used without further purification. Dried acetonitrile was purchased from Sigma-Aldrich and stored on molecular sieves in a glove-box.

Synthesis of [Ni(κ^3-2,6-{PhNCMe}$_2$(NC_5H_3)Br_2] (3.1)

$NiBr_2$ powder (34 mg, 0.160 mmol) was added to a clear yellow solution of ligand (100 mg, 0.165 mmol) in a 10ml toluene. The reaction mixture was allowed to stir for 4 hours, gradually becoming orange. A fine pink-orange powder was separated by filtration and washed with 5 x 2 mL hexanes, and allowed to dry under vacuum to produce **3.1** in 88% yield. Purple block-like crystals suitable for X-ray analysis were grown by diffusion of saturated dichloromethane solution in hexanes. Elemental analysis calculated (%) for $C_{21}H_{19}N_3Br_2Ni$: C 47.42; H 3.60; N 7.90. Found C 47.73; H 3.88; N 7.61. ^{1}H NMR (152 MHz, $CDCl_3$); δ (ppm) 8.25 (d, 2 H, Py-Hm), 8.14 (t, 1 H, Py- Hp), 7.15-7.32 (m, Ph, 10 H), and 2.35 (s, CH_3, 6 H).

X-ray Crystallography: The crystal of (**3.1**) was mounted on thin glass fibers using paraffin oil. Prior to data collection crystals were cooled to 200.15 K. Data were collected on a Bruker Smart ApexII single crystal diffractometer equipped with a sealed tube Mo source (wavelength 0.71073 Å) and an ApexII CCD detector. Raw data collection and processing were performed with the Apex3 software package from Bruker. Initial unit cell parameters were determined from 60 data frames from select ω scans collected at the different sections of the Ewald sphere. Semi-empirical absorption corrections based on equivalent reflections were applied. Systematic absences in the diffraction data-set and unit-cell parameters were consistent with the assigned space group. The initial structural solution was determined using ShelxT direct methods, and refined with full-matrix least-squares procedures based on F2 using ShelXle.5 Hydrogen atoms were placed geometrically

and refined using a riding model. All scattering factors are contained in several versions of the ShelXL program library, with the latest version used being v.6.12 at the time of this writing.

DFT Calculations

Computations were performed with the Gaussian software package. Initial molecular structures were created from crystal structures. Structural optimization was completed using the B3LYP functional with the def2-TZVP basis set. Frequency calculations on stable geometries verified there were no had no imaginary frequencies confirming minimum energy structures. The molecular orbitals from these computations were analyzed using the Chemissian software package.

Electrochemistry

All cyclic voltammetry experiments were carried out in a single compartment cell of approximately 50 mL volume under nitrogen. Samples were prepared in open air, sealed, connected to a Schlenk line and purged with a nitrogen atmosphere before measurement. Measurements were carried out using a VersaSTAT 3 (Princeton Applied Research) potentiostat. A conventional three electrode system was employed consisting of a glassy carbon electrode (diameter = 0.4 cm) was used as the working electrode, a Pt wire as the counter electrode, and an Ag/AgCl electrode was used as a reference electrode. For bulk electrocatalytic reduction experiments, a glassy carbon rod (diameter = 0.4 cm; length 2 cm) was used as the working electrode, a coiled Pt wire as the auxiliary electrode, referenced to an Ag/AgCl electrode.

For experiments in water, a 0.3M aqueous phosphate buffer with pH=7 was used. Dry potassium bromide (KBr) was used as the supporting electrolyte. For the experiments in acetonitrile, dry CH_3CN was used as solvent, TBAHFP as supporting electrolyte. In these non-aqueous reactions, a silver wire was used as pseudo-reference electrode and ferrocene added and used as an internal reference. The typical concentration of catalyst was 1 mM in each experiment.

First principles of the enhancements were computed to demonstrate the inflection point as a minimum value. Hydrogen production was measured using an Agilent 7820A gas chromatograph equipped with a thermal conductivity detector (TCD) using an Agilent select permanent gases column. The amount of H_2 was determined using a calibration curve.

Chapter 4: Elucidating Two Distinct Pathways for Electrocatalytic Hydrogen Production Using Ni (II) Pincer Complexes

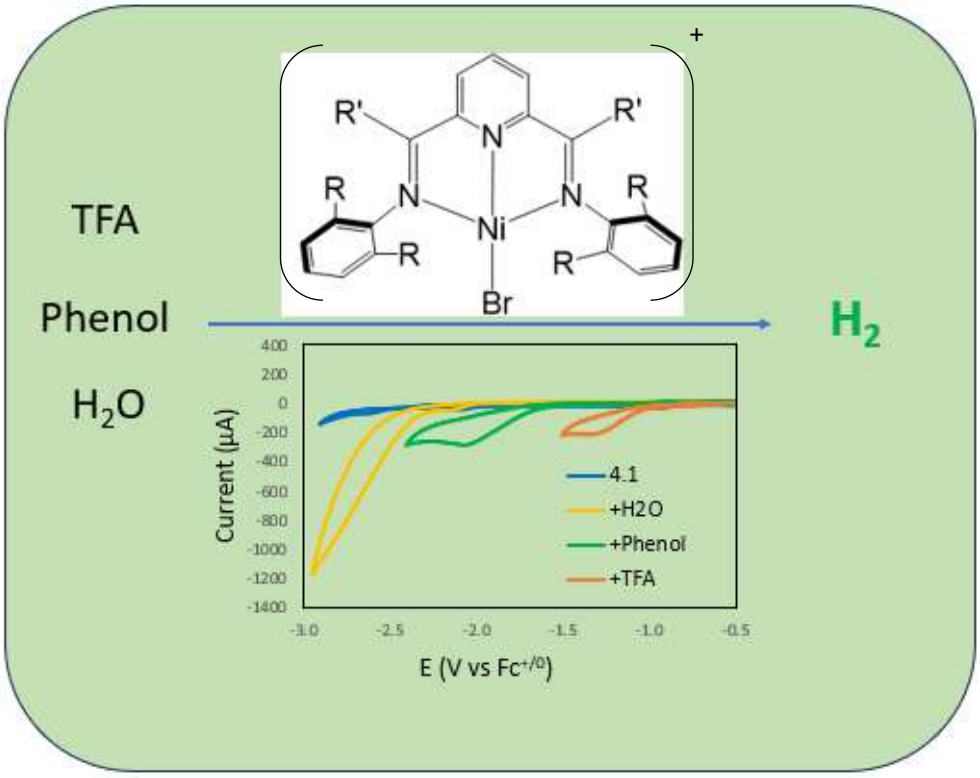

4.1. Preamble and Context

This chapter is a continuation of the work to the previous chapter. In this chapter we use a bulkier substituents on the Ni(II) DIMPY complex and study the effect of change in the substrate to the HER mechanism. DFT computation is done by Dr. Darrin Richeson. The manuscript for this project is under preparation.

4.2. Abstract

Efforts to catalyze sustainable H_2 production are essential, and this study explores the electrocatalytic capabilities of two Ni complexes incorporating non-innocent diiminopyridine ligands, Ni (2,6-{[($R_2C_6H_3$)N]CR'}($2C_5H_3$)Br_2 (R = Me(**4.1**), iPr (**4.2**), R' = Me (**4.1**), Ph (**4.2**)). Using various proton sources including trifluoroacetic acid (TFA), phenol (PHEN), and water (H_2O). Cyclic voltammetry (CV) and controlled potential electrolysis (CPE) reveal electrocatalysis occurring at three different potentials and associated with different reduction processes for **4.1** and **4.2**. Specifically, reduction with the stronger acids (e.g., TFA) proceeds at the second reduction through a Ni(II)/Ni(0) ligand-assisted metal-centered reduction, while proton sources with higher pKa values (e.g., PHEN) generate hydrogen at the third reduction via a ligand-centered reduction, Ni(0)L/Ni(0)$L^{-\bullet}$ pathway. This study contributes insights into the electrocatalytic mechanisms for sustainable H_2 production using non-innocent ligands with diverse proton sources.

4.3.Introduction

Growing environmental damages caused by anthropogenic climate change, coupled with the depletion of fossil fuel reserves has generated intense research interest into the catalytic production of clean burning and sustainable fuel sources such as hydrogen, an energy dense fuel source that has a sole combustion product of water[144]. Noble metals, like platinum, are known to effectively catalyse the reduction of water to produce hydrogen gas[90]. However, such catalysts, due to overall low abundance and high cost, do not provide an environmentally balanced avenue. Compounds composed of economical, earth abundant metals are essential for the practical application of H_2 generating electrocatalysts[31, 145]. Furthermore, molecular complexes[43, 146] for hydrogen

generation are attractive due to the ability to modify supporting ligands and more directly probe mechanisms.

For molecular catalysts, the overpotential and the reaction rate of Hydrogen Evolution Reaction (HER) are related to metal center reduction and metal hydride formation but in general, these two processes are deleteriously coupled. On the one hand, the modification of the catalysts with electron-withdrawing or bulkier substituents would reduce the electron density on the metal center, lowering the overpotential and making the compound more easily reduced. On the other hand, the low electron density on the metal center discourages its protonation, which lowers the rate of metal hydride formation with resulting decrease in the reaction rate of HER. Consequently, rational design of a molecular catalyst for HER with both low overpotential and a high reaction rate remains a challenge[47, 97, 147].

The properties of a metal complex as a whole are the result of the interactions of the metal center with its surrounding ligands.[148] Non-innocent ligands in metal complexes can operate as an electron reservoir and usually exhibit high catalytic activity and controllability in catalytic reactions[97, 149, 150]. Assuming that non-innocent ligands such as diiminopyridine may be able to store electrons for redox reactions and this may have an effect on the metal complex reducing "strength".

While water is the ideal hydrogen source for use in these catalytic systems, exploring substrates across a range of pKa values would allow for further exploration into the functionality of these complexes and elucidate important fundamental features of their catalytic mechanism.[151] For example, proton reduction electrocatalysts generally operate more efficiently for H_2 in more acidic environments. Elucidating mechanistic differences for H_2 generating electrocatalysts on substrates of different acid strength will inform the trajectory of future research and direct catalyst selection

based on the target environment. Studies of some first row-based hydrogen evolution catalysts performed in organic media have shown that the pKa of the proton donor and even added buffer can influence the catalyst performance and kinetics of hydride formation. In one study in our group by Josh Brown, it was shown that the two [Co(κ^3-2,6-{Ph_2PNR}$_2$(NC_5H_3))Br_2] R = H, Me, complexes are functional catalysts for efficient H_2 production at two different cathodic potentials. Using acidic substrates, hydrogen is produced at a potential corresponding to the first reduction of the catalysts. More negative potentials were required for substrates with larger pKa values.[152] In another report with Co(II) dimethylglyoximato complexes, the pathway for H_2 formation was influenced by the applied potential and the acid strength of the proton source.[153]

Herein, we demonstrate that the design of Ni complexes with suitable non-innocent diiminopyridine ligands can lead to efficient catalysts for HER. In particular, we report on catalyst variation and alternative hydrogen sources by examining the catalytic abilities of [Ni(II)(2,6-{[($iPr_2C_6H_3$)N]CPh}($2C_5H_3N$)Br_2] (**4.1**) and [Ni(II)(2,6-{[($Me_2C_6H_3$)N]CMe}($2C_5H_3N$)Br_2 (**4.2**) with trifluoroacetic acid (TFA), phenol (PHEN), and water (H_2O).

4.4.Results and Discussion

The direct reaction of the neutral tridentate ligands, 2,6-{[($R_2C_6H_3$)N]CR'}$_2C_5H_3N$ (R = iPr (L1), Me (L2); R'=Ph (L2), Me (L2)) with Ni(II) bromide at room temperature, in toluene, under nitrogen led to direct synthesis of [Ni(κ^3-2,6-{[($R_2C_6H_3$)N]CR'}$_2C_5H_3N$ Br_2] (R = iPr (**4.1**), Me (4.2); R'=Ph (**4.1**), Me (**4.2**)). An instant color change was noted upon mixing and the corresponding product was isolated by filtration.

Scheme 4.1. Reaction scheme for the preparation of [Ni(κ^3-2,6-{[(iPr$_2$C$_6$H$_3$)N]CPh}$_2$C$_5$H$_3$N Br$_2$] (**4.1**) and [Ni(κ^3-2,6-{[(Me$_2$C$_6$H$_3$)N]CMe}$_2$C$_5$H$_3$N Br$_2$] (**4.2**).

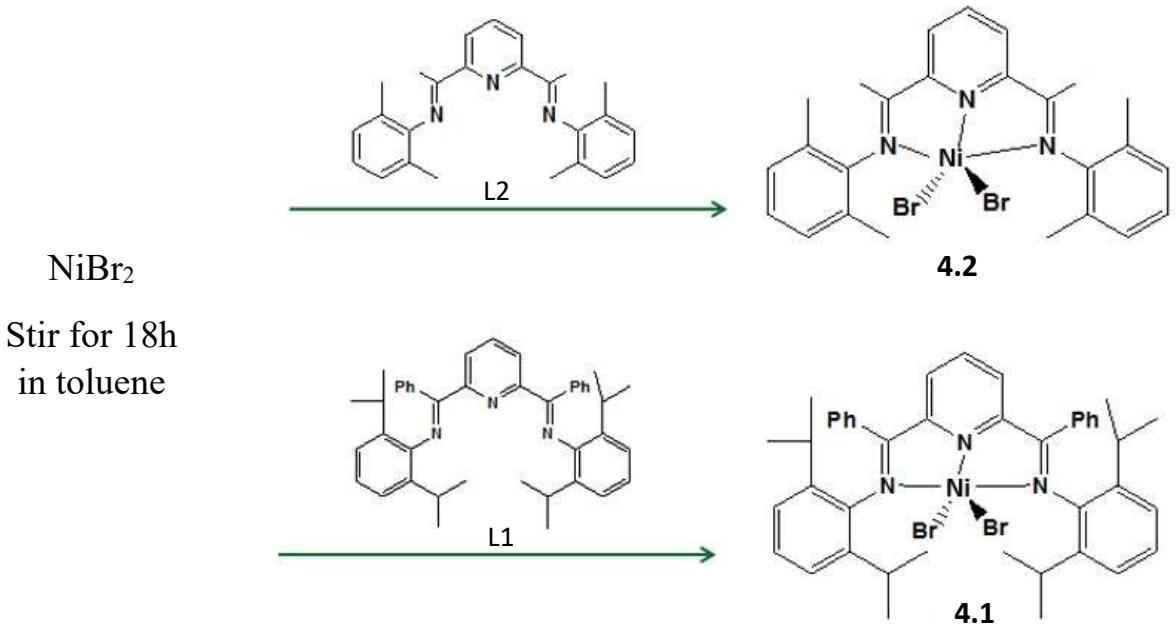

These complexes can be crystallized from CH_2Cl_2 and single crystal X-ray structure determinations confirmed that both complexes exhibits a trigonal bipyramidal high spin Ni(II) center displaying a neutral planar tridentate diminopyridine and two bromide ligand as shown in Figure 4.1.

Compound **4.1** has the formula of 2,6-{[(iPr$_2$C$_6$H$_3$)N]CPh}$_2$C$_5$H$_3$NNi(II)(Br)$_2$]. The 2,6-diisopropylphenyl substituents on the coordinated imine nitrogen centers lie orthogonal to the basal plane of the complex. The two angles involving the pyridyl and bromide, [N(1)-Ni(1)-Br(1) = 88.7°(3)] and [N(1)-Ni(1)-Br(2) = 152.5°(3)] are supportive of the distorted square pyramidal geometry (Table 4.1, 4.2). Compound **4.2** has similar structure and geometry with the two angles involving the pyridyl and bromide, [N(1)-Ni(1)-Br(1) = 155.6°(3)] and [N(1)-Ni(1)-Br(2) = 90.7°(3)] (Table 4.3). The two common limiting ideal geometries for five coordinate species are trigonal bipyramidal (tbp) and square-based pyramidal (sp) metal environments and the

assignment of tbp or sp metal coordination geometry can be made using a simple quantitative measure derived from calculation of structural index parameter, τ.[154, 155] Application of this approach yielded τ parameter 0.02 for **4.1** and 0.08 for **4.2** indicating that the coordination geometry of **4.1** and **4.2** was best be described as distorted square-based pyramidal (sp) with the basal plane was defined by the nitrogen donors of the bis(imino)pyridine ligand and one of the bromides identified as Br2 in **4.1** and Br1 in **4.2**. The pseudo-apical position is occupied by the bromo ligand labelled Br1 in **4.1** and Br2 in **4.2**.

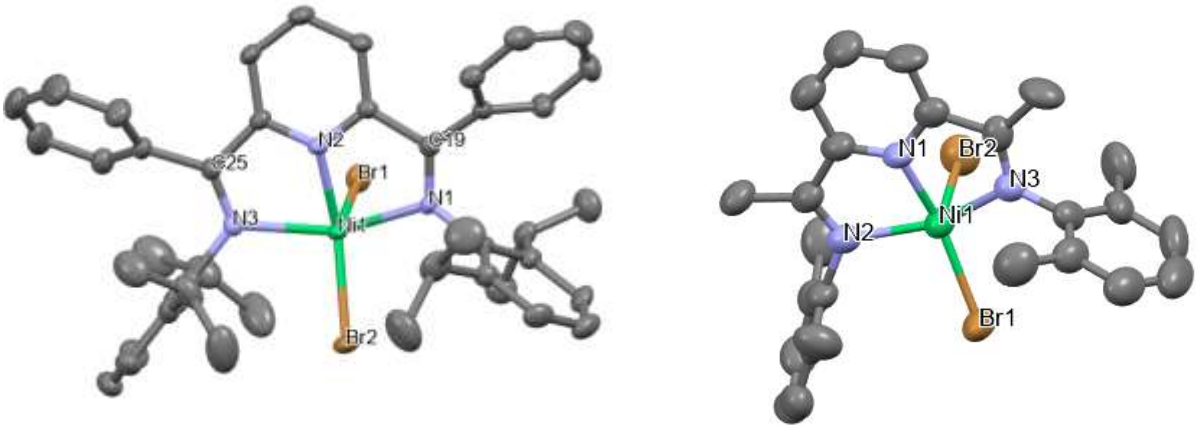

Figure 4.1. Structural representation of (**4.1**) (left) and (**4.2**) (right). Hydrogen atoms omitted for clarity.

Table 4.1. Crystal data and structure refinement for (**4.1**).

Compound	
Empirical formula	$C_{44}H_{48}Br_2Cl_2NiN_3$
Formula weight	908.28
Temperature(K)	203(2)
λ (Å)	0.71073
Crystal system	Triclinic
Space group	P -1
a (Å)	9.5281(6)

b (Å)	9.7700(6)
c (Å)	13.6689(9)
α (deg)	93.325(2)
β (deg)	107.463(2)
γ (deg)	114.273(2)
V (Å3)	1082.15(12)
Z	1
p (calc) (Mg/m3)	1.394
Mu (mm-1)	2.451
R1a	0.0812
wR2b	0.1797

Table 4.2. Selected Bond lengths [Å] and angles [°] for (**4.1**)

Bond lengths [Å]		**Bond angles [°]**	
Br(1)-Ni(1)	2.451 (2)	N(1)-Ni(1)-N(2)	77.2(5)
Ni(1)-N(1)	1.99(1)	N(1)-Ni(1)-N(3)	76.9(4)
Ni(1)-N(2)	2.17(1)	N(2)-Ni(1)-N(3)	151.2(4)
N1(i)-N(3)	2.20(1)	Br(2)-Ni(1)-Br(1)	118.75(8)
Ni(1)-Br(2)	2.348(2)	C(7)-N(2)-Ni(1)	114.1(9)
N(1)-C(1)	1.34(2)	C(20)-N(2)-Ni(1)	126.1(9)
N(2)-C(7)	1.29(2)	C(21)-N(3)-Ni(1)	127.1(9)
N(2)-C(20)	1.45(2)	C(5)-N(1)-Ni(1)	117.4(9)
N(3)-C(6)	1.28(2)	C(1)-N(1)-Ni(1)	117.4(9)
N(3)-C(21)	1.46(2)	Br(1)-Ni(1)-N(2)	95.2(3)
C(5)-N(1)	1.32(2)	Br(2)-Ni(1)-N(2)	97.7(3)

Table 4.3. Crystal data and structure refinement, selected Bond lengths [Å] and angles [°] for (**4.2**)

compound	**4.2**
Formula	$C_{26}H_{29}Br_2Cl_2N_3Ni$
a (Å)	18.677(2)
b (Å)	8.137(1)
c (Å)	20.489(3)
α [°]	90.00
β [°]	112.772(5)
γ [°]	90.00

Bond Distance [Å]	
Ni(1)-N(2)	2.141(9)
Ni(1)-N(3)	2.127(9)
Ni(1)-N(1)	1.95(1)
Ni(1)-Br(2)	2.440(3)
Bond Angles [°]	
Br(1)-Ni(1)-N(1)	155.6(3)
N(2)-Ni(1)-N(3)	150.3(4)

In the solid state both of these Ni complexes were paramagnetic, consistent with a five coordinate Ni(II) center. However, diiminopyridine Ni(II) dihalo complexes are documented to autoionize in polar solvents to yield low spin diamagnetic, square planar d^8 species.[47, 137] In fact, in solution compounds **4.1** and **4.2** displayed diagnostic ^{1}H NMR spectrum, indicative of low spin diamagnetic, square planar d^8 species with symmetrical ligand coordination for $[Ni(\kappa^3\text{-}2,6\text{-}\{iPr_2C_6HNCPh\}_2(NC_5H_3)Br]^+$ (**4.1'**$^+$) and $[Ni(\kappa^3\text{-}2,6\text{-}\{Me_2C_6HNCMe\}_2(NC_5H_3)Br]^+$ (**4.2'**$^+$) as schematically represented in Figure 4.2. Support for these observations came when attempts to computationally optimize structure **4.1** (DFT, B3LYP, def2-TZVP) using the PCM model for solvation in acetonitrile resulted in spontaneous dissociation of one of the Br^- ligands and rearrangement of the Ni center to a square planar geometry. As a result, the dissociated bromide was removed, which resulted in an optimized cationic square planar d^8 complex **4.1'**$^+$ (Figure 4.2).

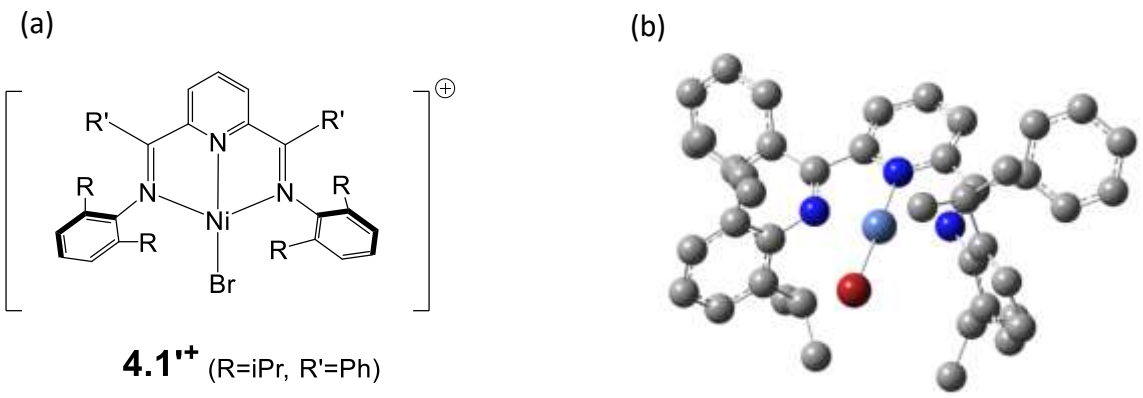

Figure 4.2. a) Structural figures for compounds **4.1**'$^{+}$, b) optimized structure of **4.1**'$^{+}$.

4.4.1. Electrochemical Characterization

Electrochemical characterizations were performed for both complexes in acetonitrile using a glassy carbon (GC) working electrode, platinum (Pt) counter electrode, and a silver (Ag) wire pseudo-reference electrode, under N_2 atmosphere. After completing the CV, ferrocene was added to the solution and voltages were referenced to the reversible ferrocene/ferrocenium ($Fc^{0/+}$) redox couple. The resulting cyclic voltammograms for **4.1** and **4.2** are displayed in Figure 4.3.

Both complexes displayed three reversible reduction events before -2.3V, to be exact, at $E_{1/2}$=-0.4V, -0.8V, -2V for **4.1** and at $E_{1/2}$= -0.5V and -1.15V and -1.88V for complex **4.2** (all potentials are referenced to $Fc^{0/+}$). According to the literature and our computations reported in Chapter 3 (see Figures 3.9, Figure B.4-B.9), the first reduction can be assigned to addition of an electron to a ligand-centered orbital while the second electron is placed in a metal-centered (d_{x2-y2}) orbital. Based on the calculations presented in this chapter, the third reduction peak is attributed to addition of an electron into an orbital associated with the ligand, as illustrated in Figure 4.4. As we previously performed calculations for the initial and secondary reduction of the complex [Ni(κ^3-2,6-{C_6HNCMe}$_2$(NC_5H_3)Br]$^+$ (**3.1**) in chapter 3, we have opted to persist with this same complex and explore the third reduction process for these NiDIMPY complexes. Figure 4.4 shows the third reduced species, [Ni(κ^3-2,6-{PhNCMe}$_2$(NC_5H_3)H] (**Ni(H)**), after protonation. The LUMO of

Ni(H) consist of a ligand centered MO that is a π* orbital delocalized across the pyridyl (47%) and imine (44%) moieties. The SOMO is also a π* orbital with the highest contribution from ligand with 44% of this orbital on the pyridyl group, 45 % on over the two imine moieties and only 7% contribution from Ni orbitals. The metal centered HOMO is σ* in nature and dominated by Ni d_{z2} (91%).

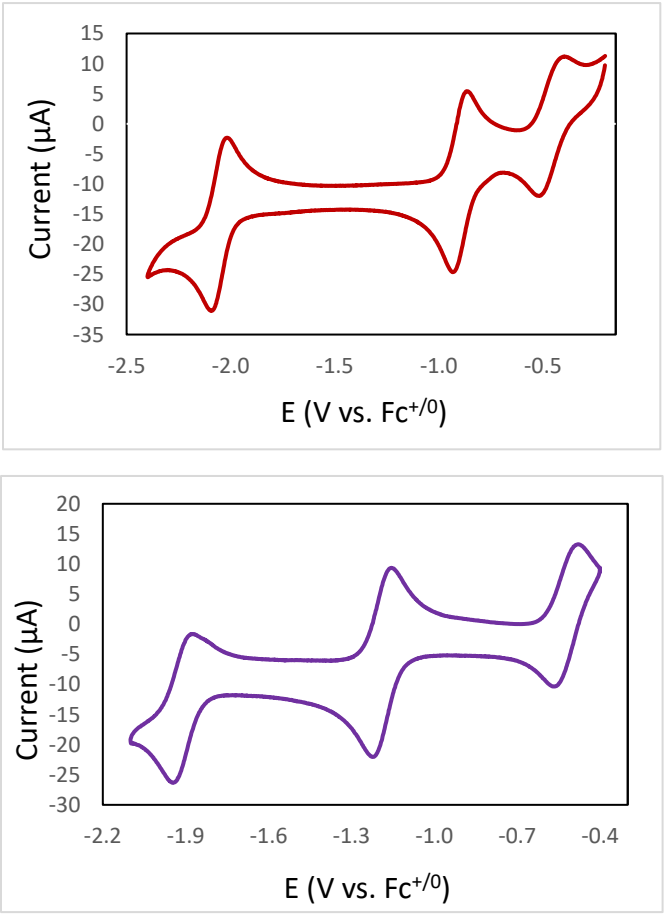

Figure 4.3. Cyclic voltammogram of 1mM of **4.1**(red) and **4.2** (purple) in 0.1M TBAHFP in acetonitrile with scan rate of 100 mV/s, under N_2.

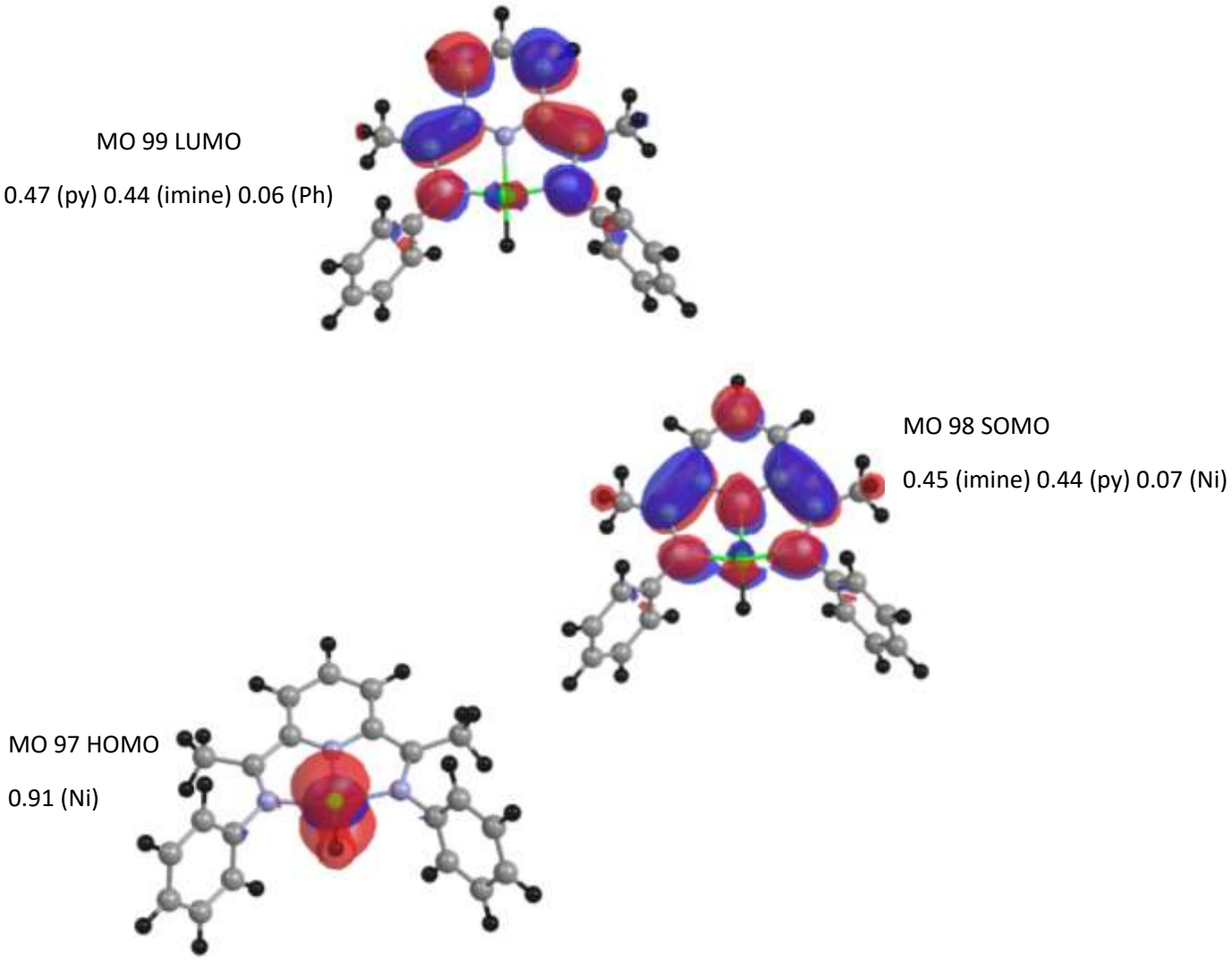

Figure 4.4. Computationally optimized [Ni(κ^3-2,6-{PhNCMe}$_2$(NC_5H_3)H] (**Ni(I)H**). Representations and fragment allocation of the LUMO, SOMO, and HOMO of **Ni(I)H**, (DFT, B3LYP, def2-TZVP) using the PCM model for solvation in acetonitrile. The orbitals are rendered using the Chemissian software with an isosurface of 0.03.

These redox events were further examined using varied scan rates and a plot of (scan rate)$^{1/2}$ versus current displayed a linear relationship consistent with a diffusion-controlled process (Figure 4.5).

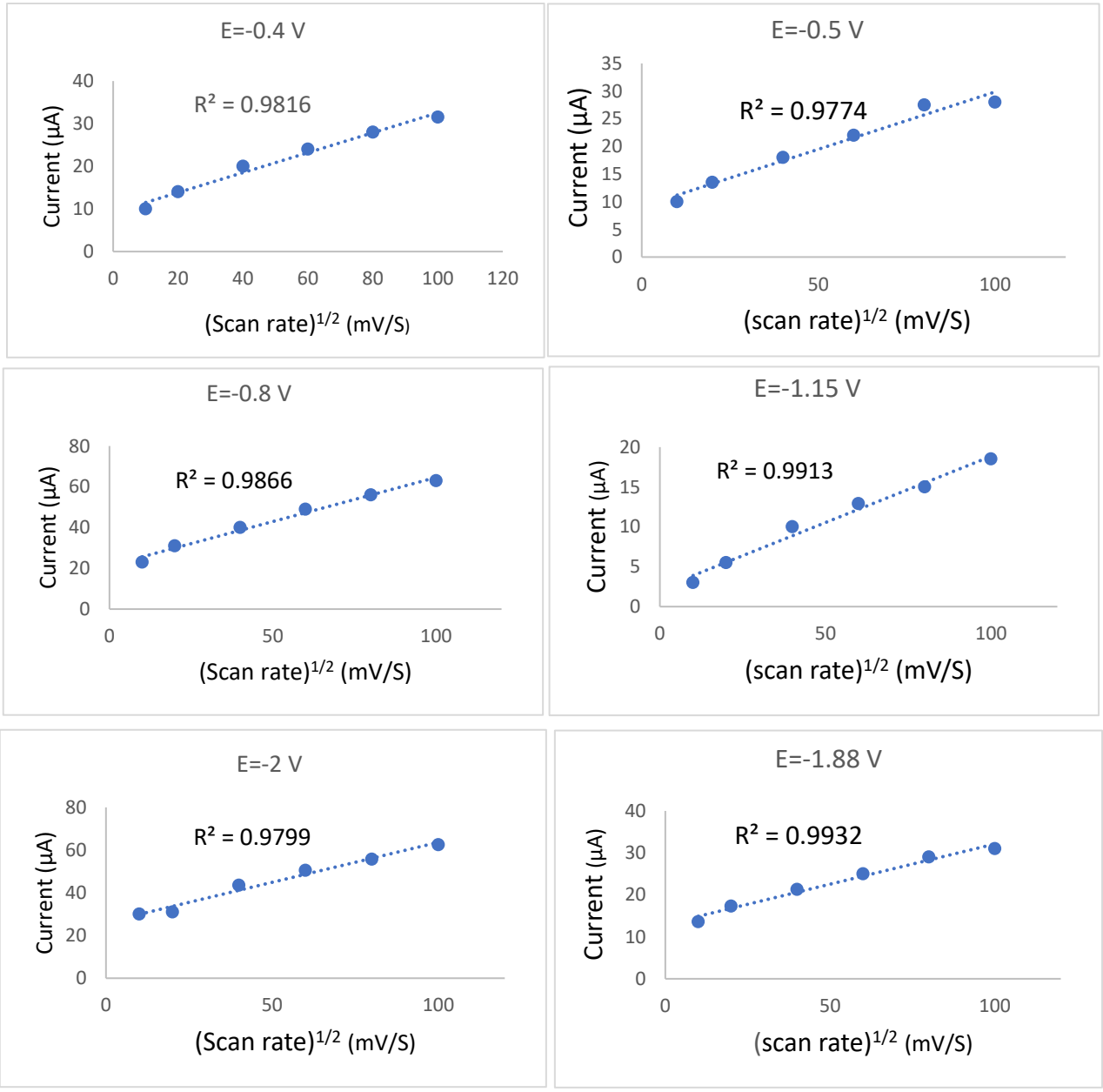

Figure 4.5. Plots of scan rate$^{1/2}$ versus current for complex **4.1** (left) and complex **4.2** (right). All potentials are referenced to Fc/Fc^{+} in CH_3CN.

4.4.2. Catalysis:

Here we examine the HER activity of these Ni complexes with variation of the hydrogen source using trifluoroacetic acid (TFA), phenol (PHEN) and water (H_2O). This began by examining the addition of TFA to 1.0 mM solutions of **4.1** and **4.2**. As seen in Figure 4.6, both complexes

exhibited significant current enhancement at the second redox event in the presence of TFA, indicative of catalysis. This enhancement also increases with increasing concentrations of TFA in the solution. Furthermore, the corresponding return oxidation events were absent, as expected for redox catalysis.[23] The onset potential for the catalytic event was determined by identifying the inflection point, which corresponds to the region on the curve where the rate of electron transfer is maximized, before the reaction kinetics are controlled by the diffusion of substrate towards the electrode.[28] The derivatives were determined by the method of first principles (Figure 4.6.a and Figure 4.7.a). For complex **4.1** the onset potential for the reduction of TFA was determined to be -1.13 V vs $Fc^{0/+}$. This value was only 30mV beyond the reversible redox event for **4.2**. It is worth noting that in the absence of catalyst, TFA reduction by GC was measured at E_{onset} (E_o)= -1.7 V which is with much higher overpotential compared to when a catalyst is used (Figure 4.8).

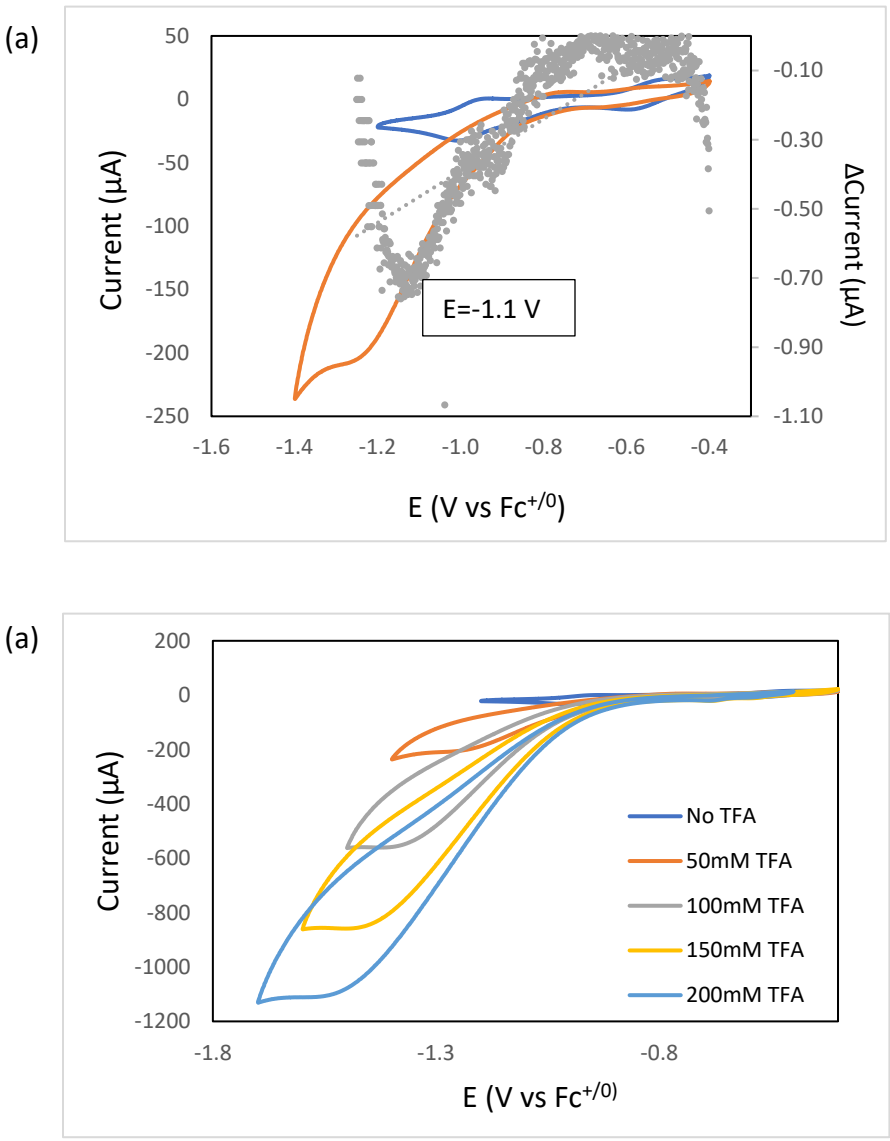

Figure 4.6. Cyclic voltammogram of complex (**4.1**) (1mM) in presence of 100 mM TBAHFP in CH_3CN using a glassy carbon (GC) working electrode a) in the absence of TFA (blue) and with 50 mM of TFA (orange), gray curve shows the inflection point. b) in the absence of TFA and with varying concentrations of TFA.

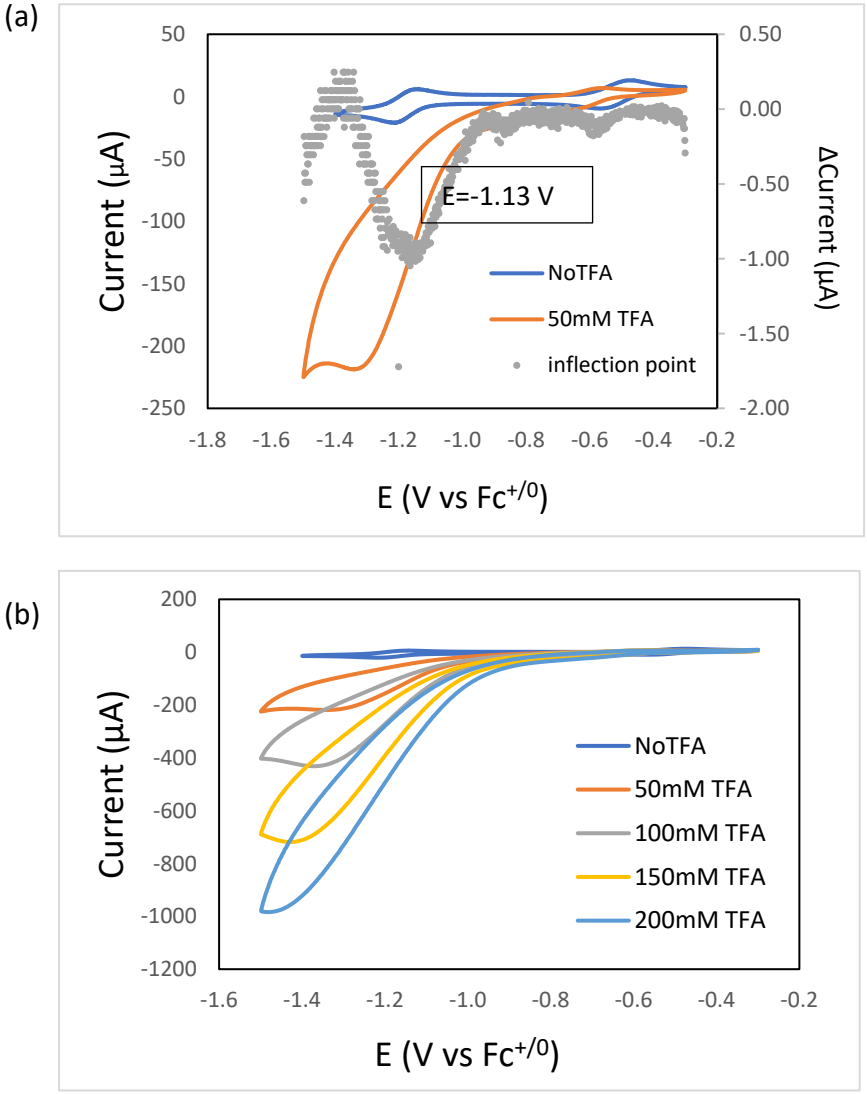

Figure 4.7. Cyclic voltammogram of complex (**4.2**) (1mM) in presence of 100 mM TBAHFP in CH_3CN using a glassy carbon (GC) working electrode a) in the absence of TFA (blue) and with 50 mM of TFA (orange), gray curve shows the inflection point. b) with varying concentrations of TFA.

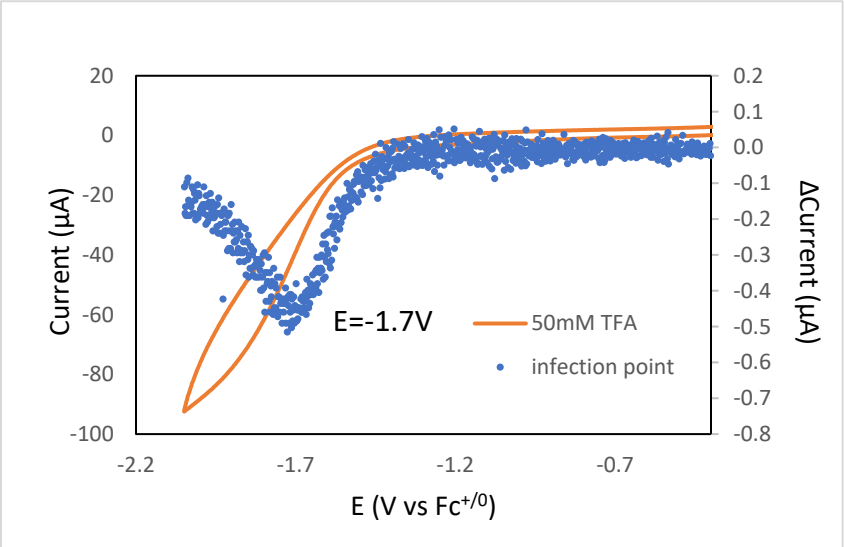

Figure 4.8. Orange Curve – cyclic voltammogram demonstrating the enhancements related to the reduction of the TFA by the glassy carbon electrode. Solution contains 0.1M TBAHFP, and 50 mM TFA. The CV was performed at a scan rate of 100 mV/s.

Scan rate dependence measurements were run on complex **4.1** and **4.2** under catalytic conditions consisting of 1 mM catalyst and 50 mM TFA (Figure 4.9). The plot of the square root of the scan-rate vs. peak current displayed a linear relationship, which is consistent with a diffusion-controlled process.

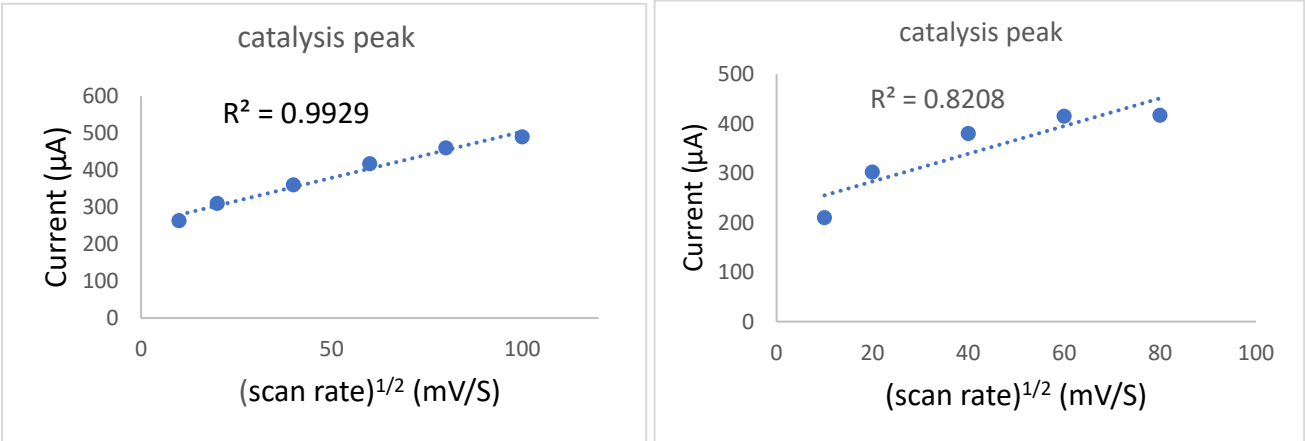

Figure 4.9. Plots of scan rate$^{1/2}$ versus current for the catalysis peak after addition of 50mM TFA at -1.1V with **4.1** (left), at -1.13 V with **4.2** (right).

Homogeneous catalysis behavior of **4.1** and **4.2** was supported by several control experiments. Repeated linear sweep voltammetry measurements of the catalyst/substrate systems were carried out to confirm catalytic current enhancement. Following these sweeps, the electrode was removed, carefully rinsed with clean solvent, and placed into a new solution containing only substrate. Voltammetry measurements on these catalyst free systems did not exhibit any electrochemical events, indicating that the catalyst had not deposited on the electrode. In addition, following bulk electrolysis measurements, CV measurements were performed on the reaction mixture. These measurements displayed no new redox events and current enhancements occurred at identical potentials before and after bulk electrolysis was performed. These measurements indicated that the catalyst had not transformed during electrolysis (Figure 4.10).

(a)

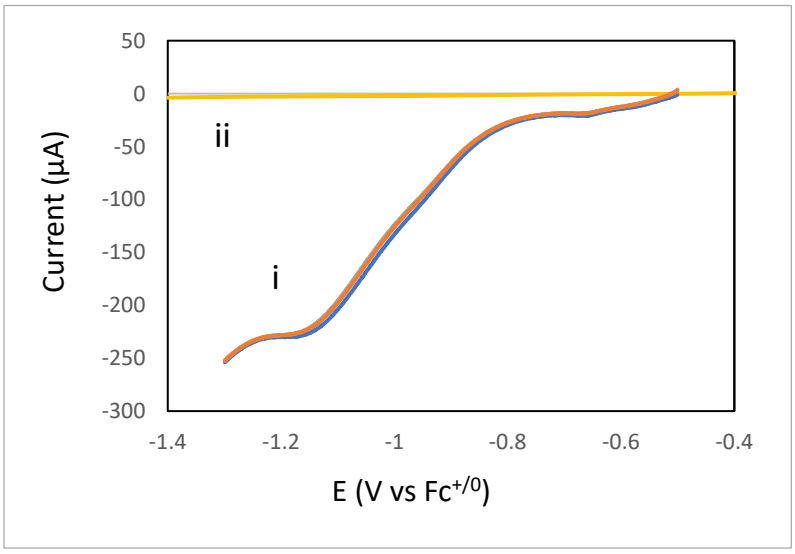

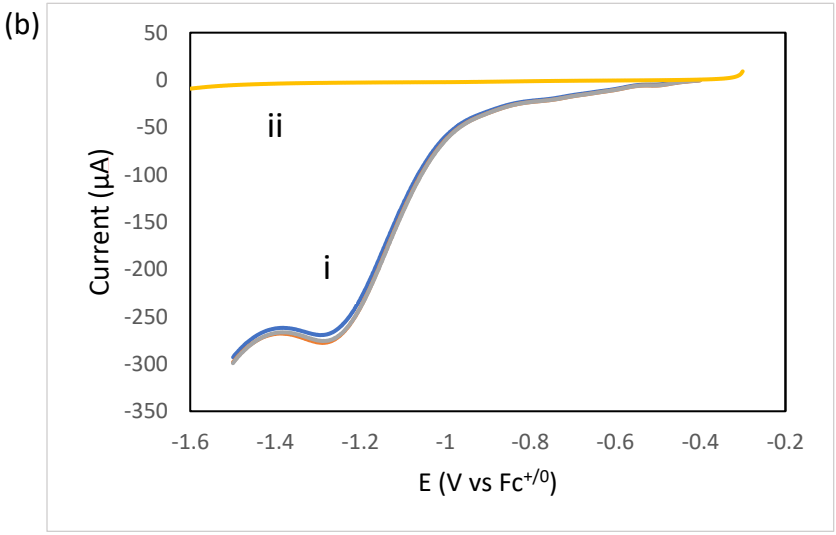

Figure 4.10. Linear Sweep Voltammetry measurements used to demonstrate that the working electrode surface remains clean during catalysis. Scans are shown for (a) $NiBr_2$-2, 6-Bis{1-[(2,6-diisopropylphenyl)imino]-benzyl}pyridine (**4.1**) and (b) $NiBr_2$-2,6-Bis[1-(2,6-dimethylphenylimino)ethyl]pyridine (**4.2**). In each case (i) shows repeated linear scans of a solution containing 1 mM of Ni complex with 0.5M TFA in 0.1 M TBAHFP in CH_3CN. The electrode was removed, rinsed with clean solvent and placed in a fresh solution containing no Ni complex, 0.5 M water and 0.1M TBAHFP in CH_3CN. Scan rate = 100 mV/s.

Using the onset potential, the overpotential for TFA reduction with catalyst **4.1** was determined. Homoconjugation is known to be a factor leading to an underestimation of the overpotential when dealing with high acid concentrations in acetonitrile. This occurs when the conjugate base interacts through the proton of the acid at the surface of the electrode, effectively decreasing the apparent pKa and decreasing the potential required to reduce the protons. Accounting for homoconjugation can be achieved by considering the association constant for the formation of the homoconjugation product and the concentration of H_2 dissolved in the acetonitrile when computing the theoretical reduction potential. The theoretical reduction potential can be calculated using equation 4.1. In this equation, $E^o{}_{H^+/H2}$ is the potential required to produce hydrogen in acetonitrile, pKa is for the proton source, ε_D is the relative diffusion rate of products to reactants, K_c is the rate constant for the formation of the homoconjugation product (103.7 for TFA)[142, 143], C_0 is the concentration of

proton source, and C^{o}_{H2} is the maximum concentration of H_2 in solution. The overpotential is then calculated by taking the difference between the onset potential and the computed theoretical reduction potential. For complex **4.1**, the overpotential for TFA reduction was determined to be 355mV. Complex **4.2** was slightly less effective and operated at an overpotential of 385mV.

$$E^{T}_{1/2(AH/AHA^{-})} = E^{o}_{H^{+}/H_2} - \frac{2.303RT}{F}pK_a + \varepsilon_D + \frac{RT}{2F}\ln(K_c^2 C_0 C^{o}_{H_2}) \qquad (4.1)$$

Having established the onset potential and corresponding overpotentials for TFA with each catalyst, the performance and efficiencies of each catalyst were evaluated. The effects of changing TFA concentration are displayed in Figure 4.11.a for 1mM of **4.1**. The current enhancement at the inflection point of -1.13 V vs $Fc^{0/+}$, increases, approximately linearly, until saturation is reached. Evaluating the current enhancement values (i_{cat}) at -1.13 V relative to the acid-free reduction current for **4.1** (i_p) against the acid concentration gave the results displayed in Figure 4.11.b. Initially, the enhanced current increased linearly until saturation was achieved at approximately 0.425 M TFA. This data can be used to evaluate reaction rates of the overall catalytic cycle. When the reaction rate becomes independent of the acid concentration, a saturated rate is achieved, and the reaction shifts to a pseudo-zero-order rate. This relationship can be expressed in terms of turnover frequency (TOF) using equation 4.2.[40] A similar set of experiments were also performed with catalyst complex **4.2**, yielding analogous observations (Figure 4.12). Using this approach, catalyst **4.1** exhibited a TOF for hydrogen production from TFA at -1.1V of 1897 s^{-1} while **4.2** gave a TOF at -1.13V of 2134 s^{-1} (Table 4.4, 4.5).

$$\frac{i_{cat}}{i_p} = \frac{2}{0.446}\sqrt{\frac{RT(TOF)}{Fv}} \qquad (4.2)$$

Bulk electrolysis using 1 mM of **4.1** at a potential of -1.1 V vs $Fc^{0/+}$ yielded hydrogen gas with a Faradic efficiency of 91%. This number was slightly higher (92%) when complex **4.2** was used as the catalyst at -1.13 V. Blank experiments omitting catalyst produced no hydrogen gas (Table 4.4, 4.5).

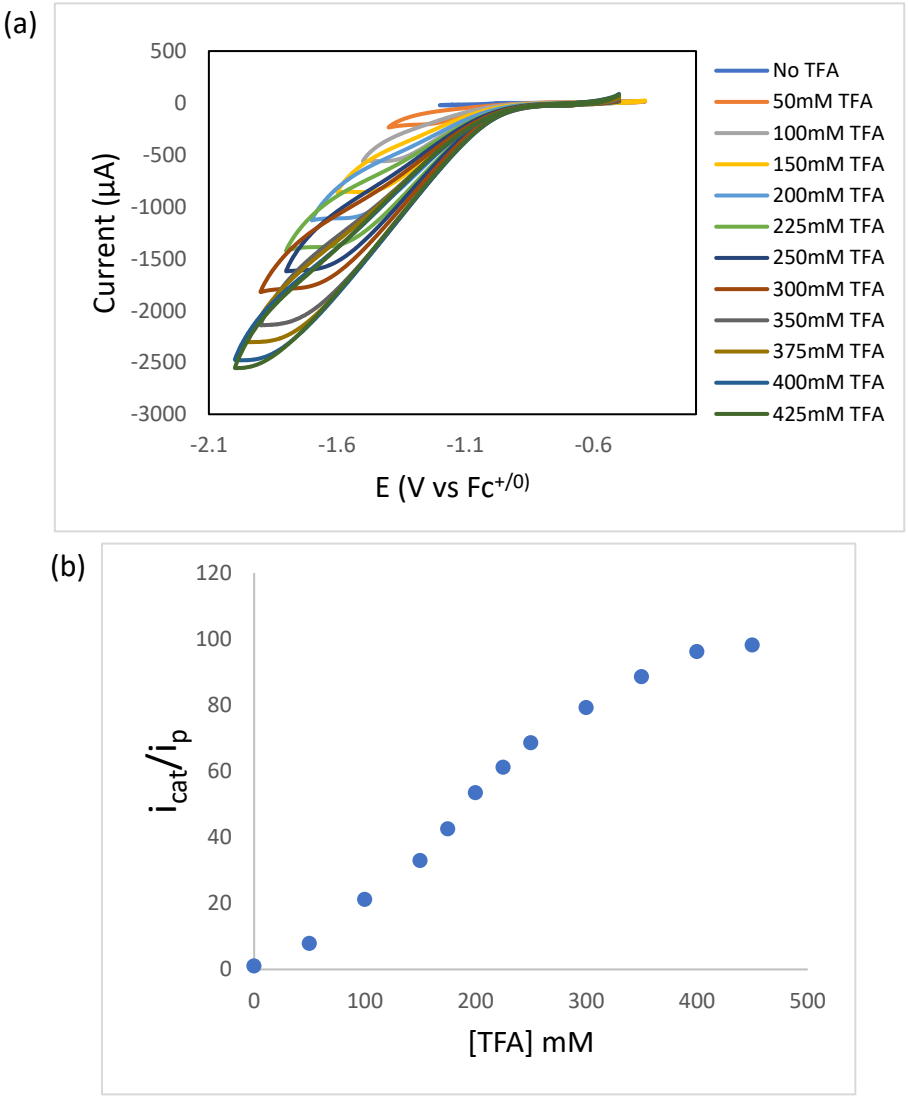

Figure 4.11. a) Cyclic voltammograms of $NiBr_2$-2,6-Bis{1-[(2,6-diisopropylphenyl)imino]-benzyl}pyridine (**4.1**) in the absence of TFA and with varying concentrations of TFA in CH_3CN with 0.1 M tetrabutylammonium hexafluorophosphate (TBAHFP) supporting electrolyte at 100 mV/s using a glassy carbon (GC) working electrode. (b) Corresponding plot of i_{cat}/i_p vs TFA concentration**.**

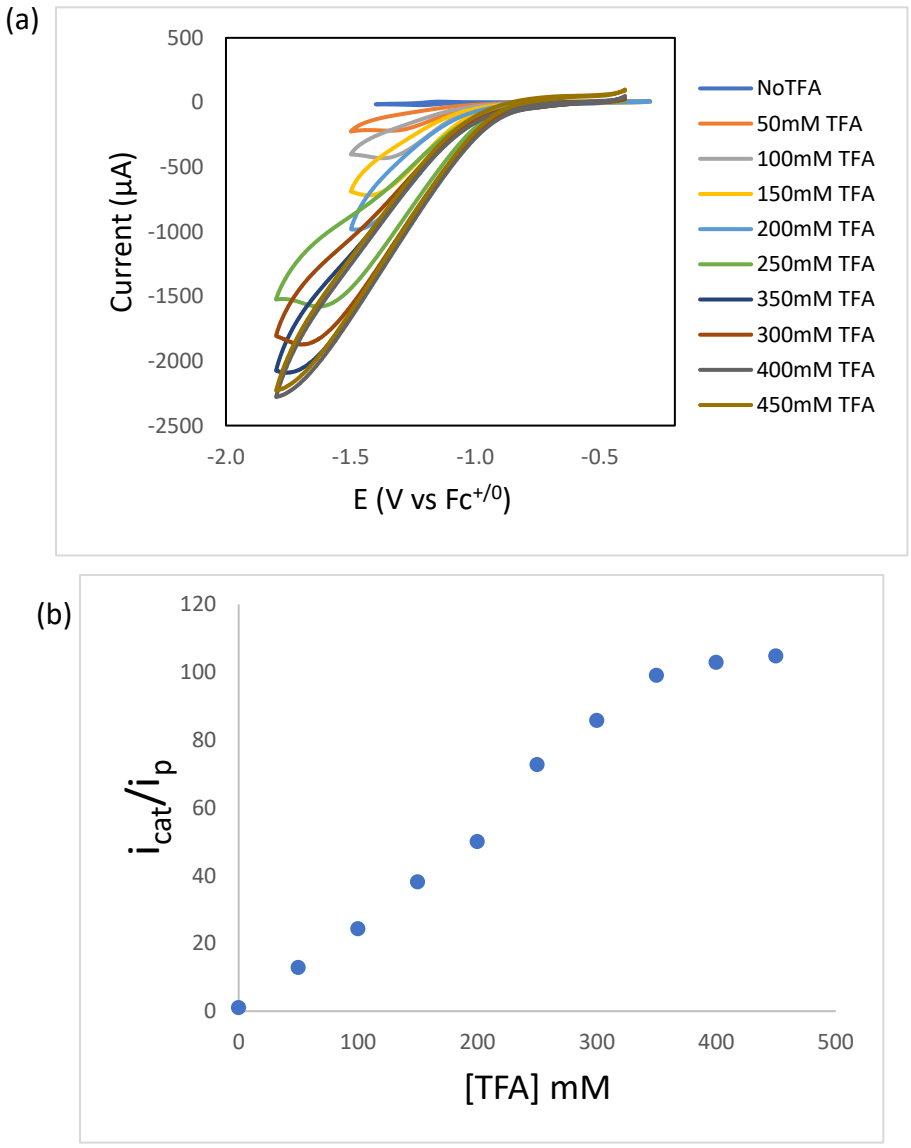

Figure 4.12. a) Cyclic voltammograms of $NiBr_2$-2,6-Bis[1-(2,6-dimethylphenylimino)ethyl]pyridine (**4.2**) in the absence of TFA and with varying concentrations of TFA in CH_3CN with 0.1 M tetrabutylammonium hexafluorophosphate (TBAHFP) supporting electrolyte at 100 mV/s.

With a pKa in acetonitrile of 29.14, phenol (PHEN) is considerably less acidic than TFA (pKa = 12.7). The catalytic H_2 generation from PHEN was next explored using a parallel set of conditions and analysis. The catalytic enhancement in reduction for complexes **4.1** and **4.2** (Figure 4.13, 4.14) was clearly observed and using the inflection points in these curves, the onset potentials for PHEN reduction were determined to be -1.85V for **4.1** and -1.8V for **4.2**. This correlates with the third

reduction of catalysts **4.1** and **4.2**. Using equation 4.1 and a Kc of 1 for PHEN[156, 157], for the formation of the homoconjugation product, these values correspond to overpotentials of 13mV for complex **4.1** and almost 0 for **4.2**. The effect of increasing PHEN concentration on the catalytic current, $i_{cat,}$ and the PHEN concentration dependence of i_{cat}/i_p were also measured for both **4.1** and **4.2** (Figure 4.16, 4.17). The application of equation 4.2 to this data led to catalytic turnover frequencies for hydrogen production from TFA of 52 s^{-1} and 104 s^{-1} for **4.1** and **4.2**, respectively. The discrepancy in the performance between TFA and PHEN is as expected based on the pKa of the acids and suggests a protonation reaction is the rate limiting step of the catalytic cycle. Moreover, in the absence of catalyst, reduction of phenol by GC was measured at E_o=-2.45V (Figure 4.14). Bulk electrolysis using 1mM of **4.1** and **4.2** at the onset potential yielded hydrogen gas with a Faradic efficiency 87% and 83%, respectively. Blank experiments omitting catalyst produced no hydrogen gas (Table 4.4, 4.5).

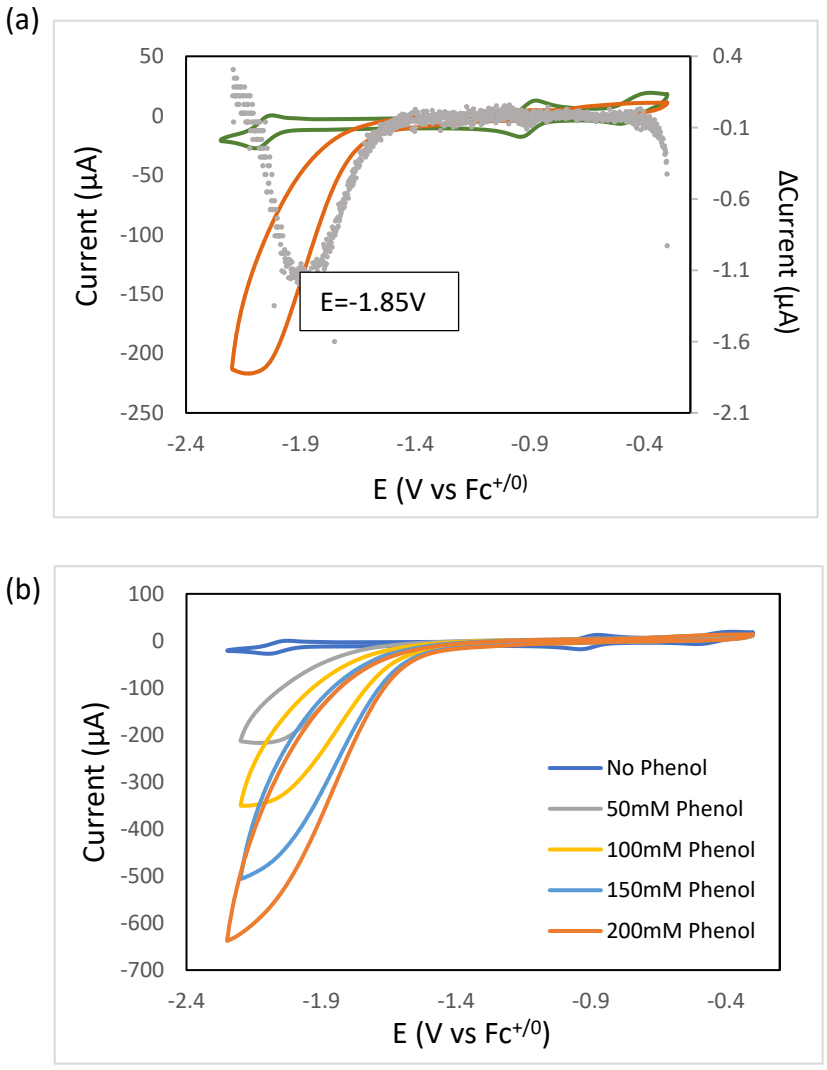

Figure 4.13. Cyclic voltammogram of complex $NiBr_2$-2, 6-bis{1-[(2,6-diisopropylphenyl)imino]-benzyl}pyridine (**4.1**) (1 mM) in presence of 100 mM TBAHFP in CH_3CN using a glassy carbon (GC) working electrode. a) in the absence of phenol (green) and with 50mM of phenol (orange), gray curve shows the inflection point. b) in the absence of phenol and with varying concentrations of phenol.

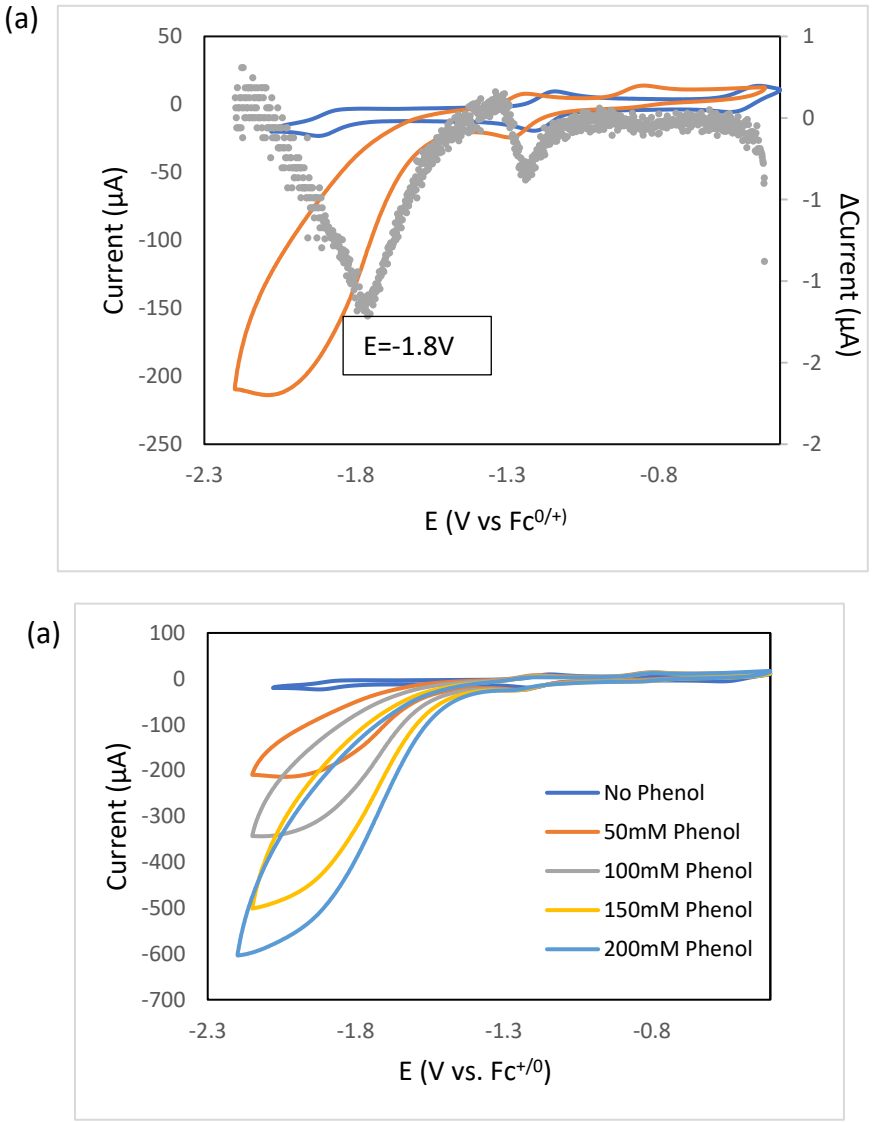

Figure 4.14. Cyclic voltammogram of complex $NiBr_2$-2,6-Bis[1-(2,6-dimethylphenylimino)ethyl]pyridine (**4.2**) (1 mM) in presence of 100mM TBAHFP in CH_3CN using a glassy carbon (GC) working electrode, a) in the absence of phenol (blue) and with 50 mM of phenol (orange), gray curve shows the inflection point. b) in the absence of phenol and with varying concentrations of phenol.

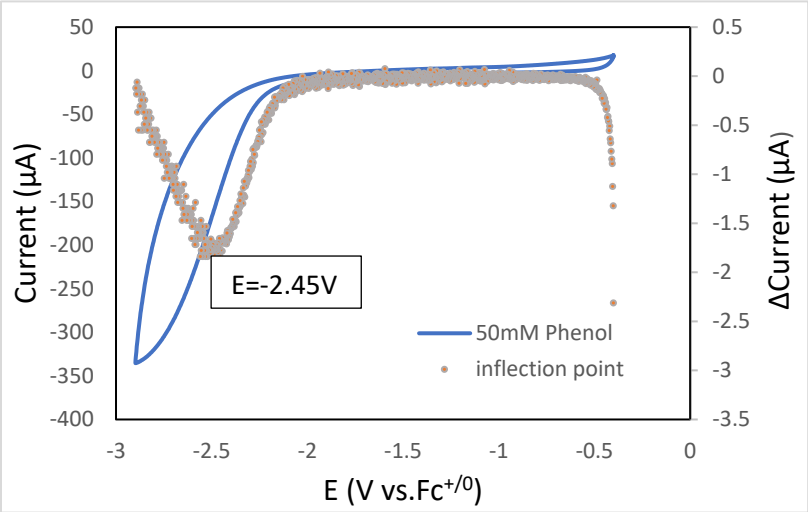

Figure 4.15. blue curve-cyclic voltammogram demonstrating the enhancements related to the reduction of phenol by the glassy carbon electrode. Solution contains 0.1 M TBAHFP, and 50 mM phenol. The CV was performed at a scan rate of 100 mV/s. Gray markers – First principles of blue curve representing the change in current enhancements. Minima denote an inflection point in the curve, indicating the associated onset potential and current enhancement for its respective phenol concentration.

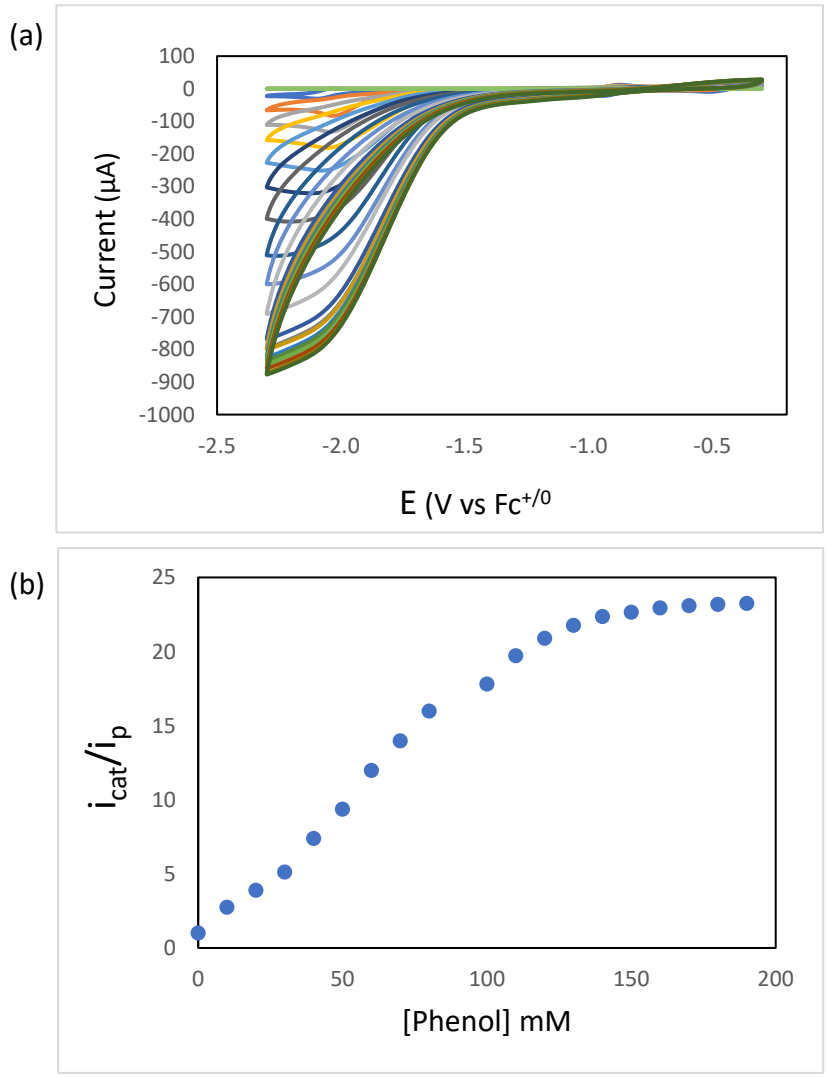

Figure 4.16. a) Cyclic voltammograms of $NiBr_2$-2,6-bis{1-[(2,6-diisopropylphenyl)imino]-benzyl}pyridine (**4.1**) in the absence of phenol and with varying concentrations of phenol in CH_3CN with 0.1 M tetrabutylammonium hexafluorophosphate (TBAHFP) supporting electrolyte at 100 mV/s using a glassy carbon (GC) working electrode. (b) Corresponding plot of i_{cat}/i_p vs phenol concentration**.**

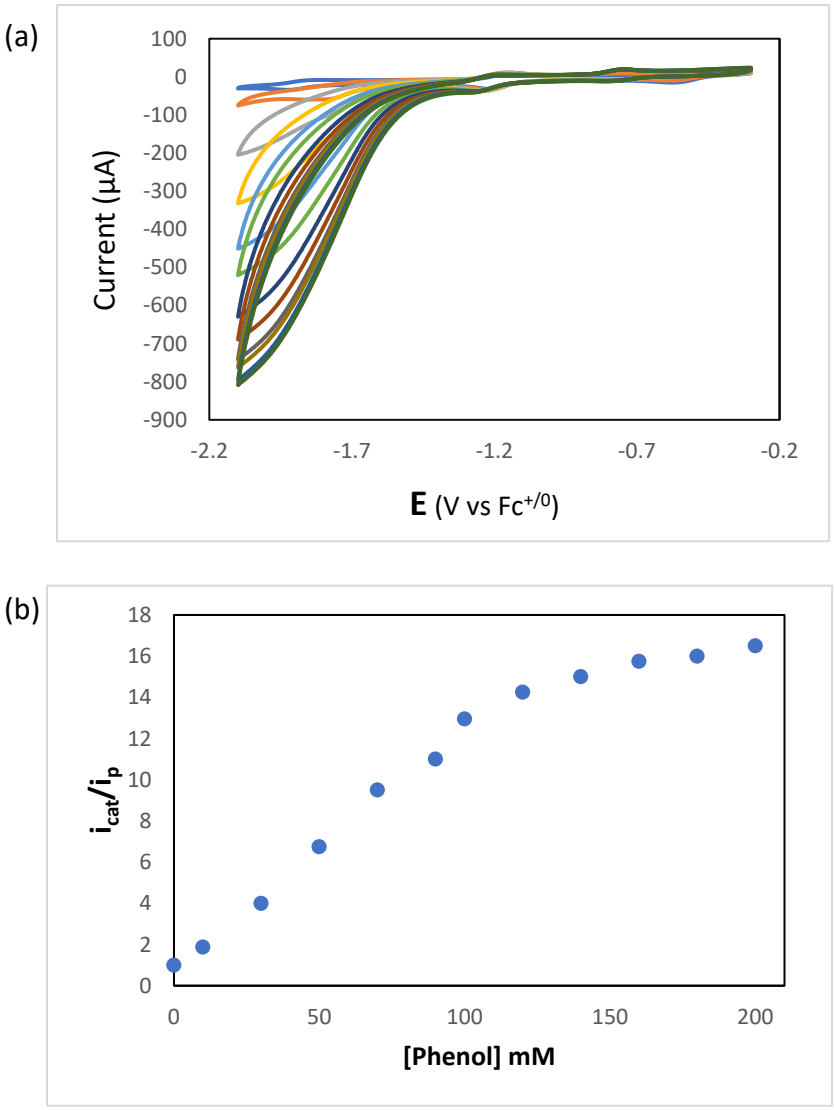

Figure 4.17. a) Cyclic voltammograms of $NiBr_2$-2,6-Bis[1-(2,6-dimethylphenylimino)ethyl]pyridine (**4.2**) in the absence of phenol and with varying concentrations of phenol in CH_3CN with 0.1 M tetrabutylammonium hexafluorophosphate (TBAHFP) supporting electrolyte at 100 mV/s using a glassy carbon (GC) working electrode. (b) Corresponding plot of i_{cat}/i_p vs phenol concentration**.**

After having explored acid and phenol as substrates for hydrogen production with catalysts **4.1** and **4.2**, a proton source with larger pKa was targeted. Water as the most ideal proton source with pKa of 32 in CH_3CN was chosen. We wished to expand the analysis to a substrate that would function as a hydrogen source at the next reduction event if there were any. Therefore, we scanned

a new CV of complex **4.1** and **4.2** to more negative voltages. A new reversible peak was observed at E_p=-2.6 V in **4.1** and E_p=-2.3 V in **4.2** (Figure 4.17.a, 4.18.a). As expected, when water was the proton source, catalyst **4.1** showed enhancement at E_O= -2.63 V (overpotential=624 mV) while with **4.2** this occurred at -2.6 V (overpotential = 594 mV), these values correlate with the fourth reduction peak for both complexes (Figures 4.17.b, 4.18.b). Note that following the fourth reduction, a decrease in the oxidation potential of the third redox peak is observed, especially in complex **4.2**. This phenomenon is ascribed to the decomposition of the catalyst or solvent occurring at lower voltages. This time, complex **4.1** displayed a smaller saturation in i_{cat}/i_p than **4.2** which corresponded to a lower TOF of 28 s^{-1} compared to the TOF of 237 s^{-1} for **4.2** (Figures 4.19, 4.20). Bulk electrolysis using 1 mM of **4.1** and **4.2** at the onset potential yielded hydrogen gas with a Faradic efficiency of 75% and 71%, respectively. Blank experiments omitting catalyst produced a few micromoles of hydrogen gas. The reported FE is after subtraction from the background (Table 4.4, 4.5).

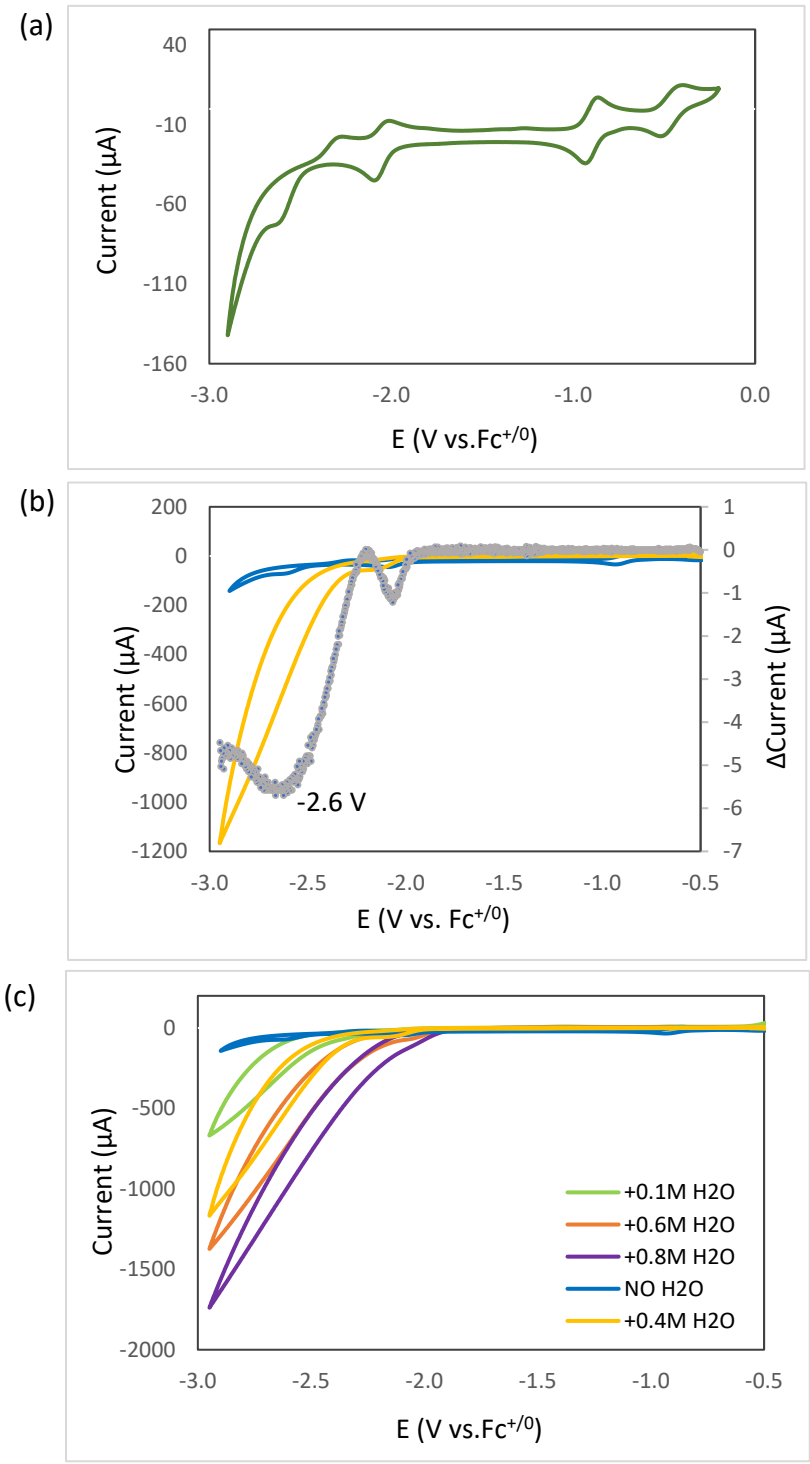

Figure 4.18. Cyclic voltammograms for (**4.1**) (1.0 mM) under N_2 a) until -2.5V in CH_3CN with 0.1 M tetrabutylammonium hexafluorophosphate (TBAHFP) supporting electrolyte at 100 mV/s using a glassy carbon (GC) working electrode, b) in the absence (blue) and presence of H_2O (0.4 M) (yellow) and inflection point (gray), c) in the absence and presence of different concentrations of H_2O.

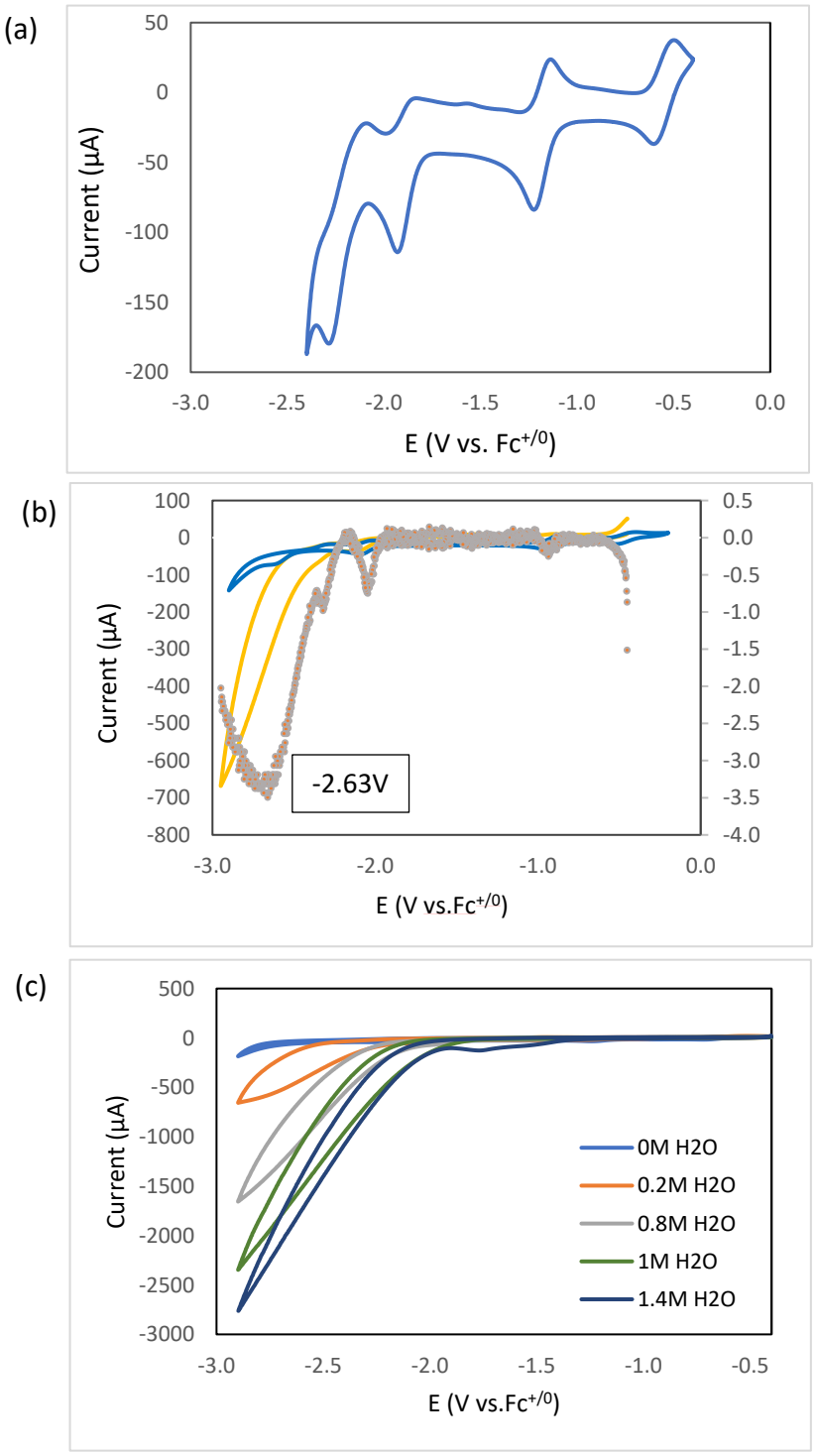

Figure 4.19. Cyclic voltammograms for (**4.2**) (1.0 mM) under N_2 a) until -2.5 V in CH_3CN with 0.1 M tetrabutylammonium hexafluorophosphate (TBAHFP) supporting electrolyte at 100 mV/s using a glassy carbon (GC) working electrode, b) in the absence (blue) and presence of H_2O (0.2 M) (yellow) and inflection point (gray), c) in the absence and presence of different concentrations of H_2O.

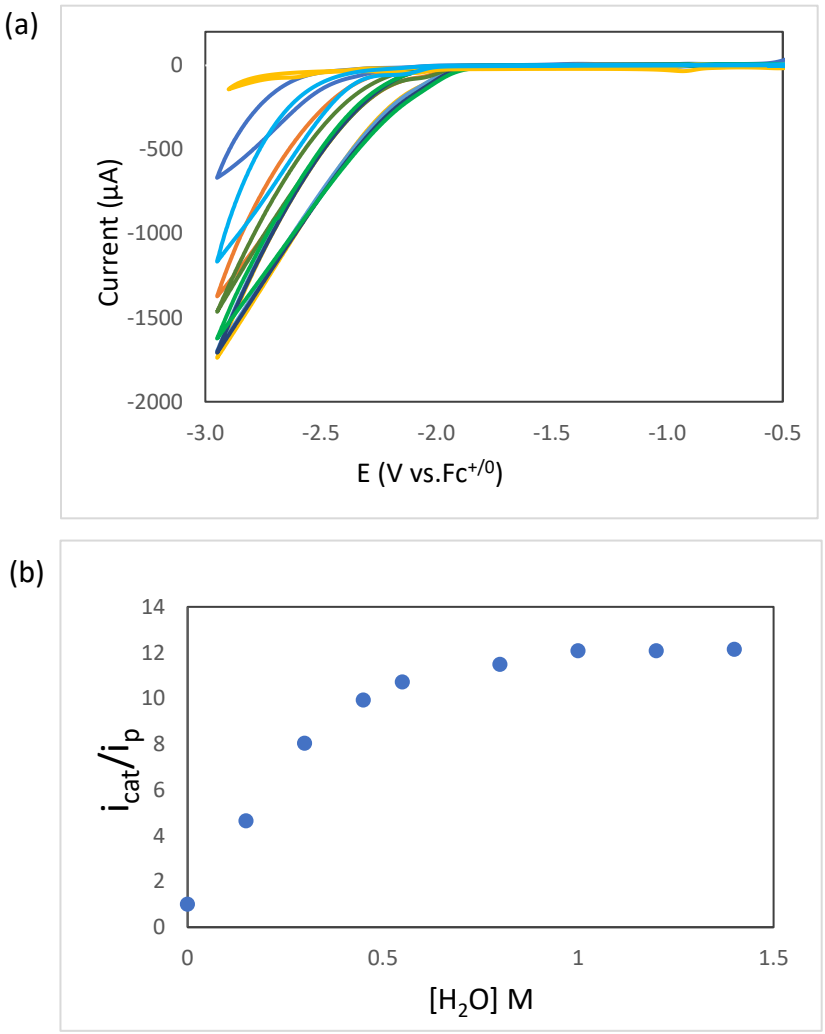

Figure 4.20. a) Cyclic voltammograms of (**4.1**) in the absence of H_2O and with varying concentrations of H_2O in CH_3CN with 0.1 M tetrabutylammonium hexafluorophosphate (TBAHFP) supporting electrolyte at 100 mV/s using a glassy carbon (GC) working electrode. (b) Corresponding plot of i_{cat}/i_p vs H_2O concentration**.**

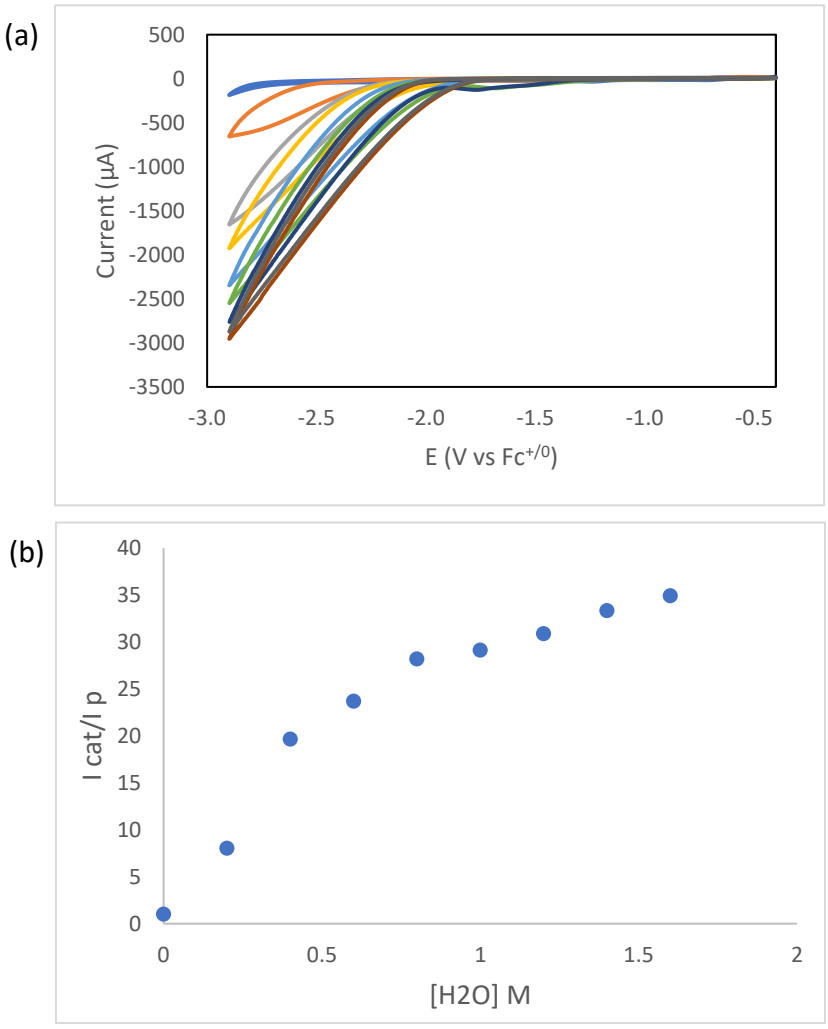

Figure 4.21. a) Cyclic voltammograms of (**4.2**) in the absence of H_2O and with varying concentrations of H_2O in CH_3CN with 0.1 M tetrabutylammonium hexafluorophosphate (TBAHFP) supporting electrolyte at 100 mV/s using a glassy carbon (GC) working electrode. (b) Corresponding plot of i_{cat}/i_p vs H_2O concentration**.**

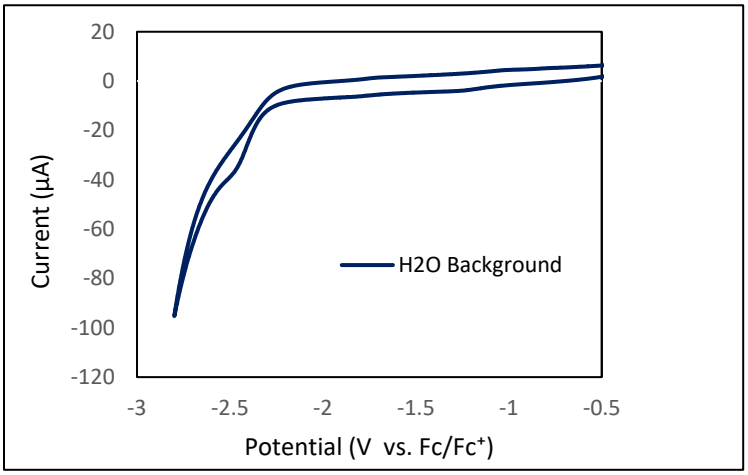

Figure 4.22. Cyclic voltammogram demonstrating the enhancements related to the reduction of H_2O by the glassy carbon electrode. Solution contains 0.1M TBAHFP, and 50 mM H_2O. The CV was performed at a scan rate of 100 mV/s.

Table 4.4. Catalytic capability data for 1 mM of **4.1**. Potentials and turnover frequencies determined through cyclic voltammetry with increasing acid concentration. Faradaic efficiencies were determined in 2 hour controlled potential coulometry experiments using a gas chromatogram for hydrogen detection.

Substrate	**E_o (V)**	**Overpotential (V)**	**TOF (s^{-1})**	**Faradaic efficiency**
Trifluoroacetic acid	-1.1	0.355	2134	91%
Phenol	-1.85	0.013	52	87%
Water	-2.6	0.594	28	75%

Table 4.5. Catalytic capability data for 1 mM of **4.2**. Potentials and turnover frequencies determined through cyclic voltammetry with increasing acid concentration. Faradaic efficiencies were determined in 2 hour controlled potential coulometry experiments using a gas chromatogram for hydrogen detection.

Substrate	**E_o (V)**	**Overpotential (V)**	**TOF (s^{-1})**	**Faradaic efficiency**
Trifluoroacetic acid	-1.13	0.385	1897	92%

Phenol	-1.7	≈0	104	83%
Water	-2.63	0.624	237	71%

Our observations unequivocally demonstrate that hydrogen generation from [Ni(κ^3-2,6-{[($R_2C_6H_3$)N]CR'}$_2C_5H_3N$ Br_2] (R = iPr, R'=Ph (**4.1**); R = Me, R'= Me (**4.2**)) occurs at three distinct potentials, which appear to correlate with the acidity of the substrate. The lower the pKa of the substrate, the more facile the protonation of the metal center and the faster the formation of the metal hydride. It is noteworthy that the ligand plays a crucial role as an electron reservoir and this may influence the reducing "strength".

Overall, the Faradaic efficiency values for both complexes across all three substrates showcase similar values, underscoring a great performance in the hydrogen evolution reaction (HER), especially when trifluoroacetic acid (TFA) is employed as the substrate. A comparative analysis of turnover frequency (TOF) between the two Ni complex reveals that complex **4.1** exhibits a heightened TOF with TFA, accompanied by lower values with the other two substrates. The TFA reduction, occurring at the second reduction peak and involving a metal-based reduction, benefits from the lower electron density around nickel (Ni) in **4.1** (due to having electron withdrawing groups), expediting the metal reduction and thereby accelerating the overall reaction. In the case of PHEN reduction which is occurring at the third CV peak that was shown, to be a ligand-based process, the observed slower HER rate in **4.1** with a bulkier ligand could suggest the necessity for ligand "rearrangements" crucial for the reaction. Alternatively, it raises the possibility that the ligand may be retaining electrons from the initial reduction, making it more challenging to undergo further reduction. Regarding water as the substrate, the absence of evidence regarding the character of the fourth peak precludes any meaningful discussion about its characteristics.

Trial for chemical reduction of compound 4.2:

In order to study the mechanism of this catalysis, we tried to chemically reduce complex **4.2** using a strong reducing agent. This experiment was performed in the glove box, in anhydrous THF. After addition of 1 equivalent of 1.0 M $Li(BEt_3H)$ as the reducing agent, the solution immediately turned from yellow to green. The product was separated by solvent evaporation in the glovebox. The resulting green powder was found to be very air sensitive and reactive. According to the literature and our DFT observation, the first reduction is expected to be a ligand centered reduction resulting in a paramagnetic Ni(II) complex. An Electron Paramagnetic Resonance spectroscopy (EPR) test was conducted to validate the product, but no discernible peaks were observed in the spectrum, indicating that the obtained product is a diamagnetic compound. One potential explanation is that the product may have undergone reactions with air or solvent prior to the test. Another factor to consider is the temperature of the test tube, which was at room temperature; it might have been more appropriate to conduct the test at lower temperatures. The product also exhibited a diagnostic ^{1}HNMR spectrum, once again showing that the obtained product is diamagnetic. However, the spectrum featured numerous peaks that proved challenging to assign. Additionally, Electrospray Ionization (ESI)-mass spectroscopy and Electron Impact (EI)-mass spectroscopy were employed in an effort to identify the molecular weight of the product. Two masses were observed, one at m/z 923 (with ESI) and the other at m/z 312 (with EI). Regrettably, no viable structure corresponding to these molecular weights could be identified.

4.4.3. Mechanism

A proposed mechanism for complex **3.1** until the second reduction in CH_3CN was reported in Chapter 3, Figure 3.25. A potential mechanism for H_2 generation that involved the third reduction of the same complex **3.1** was also examined using computations (DFT, B3LYP, def2-TZVP) and

employing the PCM model for solvation in acetonitrile (Figure 4.22). After the addition of the first two electrons to this complex, a square planar Ni(0) species supported by a tridentate diiminopyridine ligand and a bromide anion is formed ($\mathbf{A}^-$). Attempts at optimization of the complex after addition of a third electron were unsuccessful due to dissociation of a bromide anion during the optimization. Removing the coordinated bromide also did not lead to a successful optimization. Finally, replacing the bromide ligand in $\mathbf{A}^-$ with a coordinated acetonitrile (the reaction solvent) did yield a fully optimized complex with no imaginary frequencies. This resulted in a Ni(-I) complex **NiMeCN** shown in Figure 4.23. Protonation of this complex and computational optimization led to **Ni(I)H** that had undergone loss of coordinated CH_3CN to yield the square planar species represented in Figure 4.23. The addition of a second proton was explored and computations showed a spontaneous loss of H_2. Coordination of Br^- would then close the cycle to regenerate **A**.

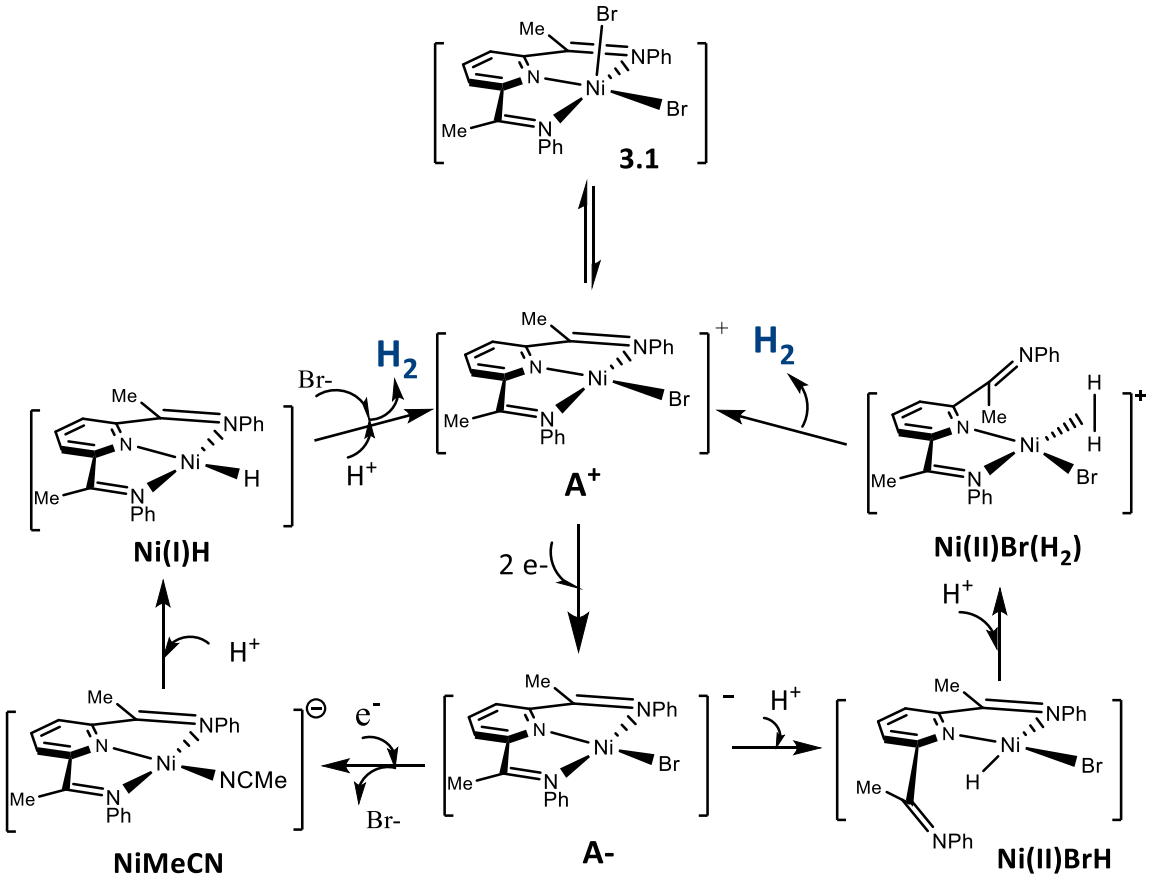

Figure 4.22. A computationally supported (B3LYP/def2TZVP/PCM(acetonitrile)) proposed mechanism for the electrocatalytic hydrogen evolution from $[Ni(\kappa^3\text{-}2,6\text{-}\{PhNCMe\}_2(NC_5H_3)Br]^+$ with TFA as the substrate and acetonitrile as the solvent.

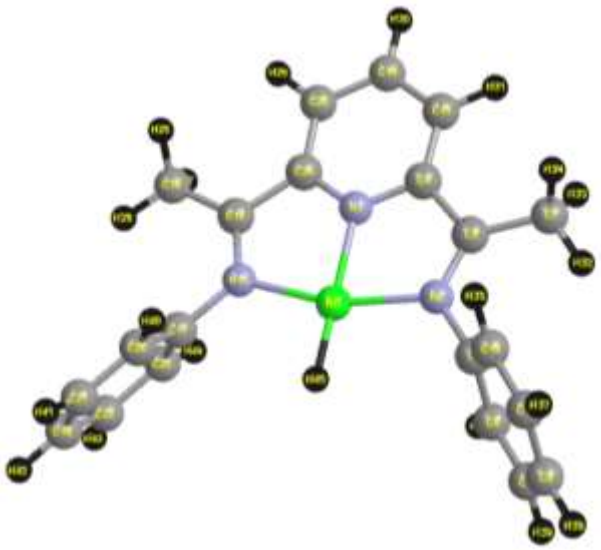

Figure 4.23. The structure obtained for the optimization of [Ni(κ^2-2,6-{PhNCMe}$_2$NC$_5$H$_3$)(H)] (**Ni(I)H**), Obtained using the B3LYP functional, def2TZVP basis set and PCM model for solvation in acetonitrile. This species was obtained after the protonation of [Ni(κ^3-2,6-{PhNCMe}$_2$(NC$_5$H$_3$)CH$_3$CN] (**NiCH$_3$CN**) as described in the text.

Table 4.6. Selected bond parameters for computationally optimized [Ni(κ^3-2,6-{PhNCMe}$_2$NC$_5$H$_3$)H] (**Ni(I)H**).

bond	Length(A)	OverlapPop	Bond order
Ni-N2	1.927	0.26	0.66
Ni-N3	1.851	0.17	0.61
Ni-N15	1.927	0.26	0.66
Ni-H45	1.500	0.34	0.89

Figure 4.24. The structure obtained for the optimization of [Ni(κ^2-2,6-{PhNCMe}$_2$NC$_5$H$_3$)(H)$_2$] (**Ni(H$_2$)**), Obtained using the B3LYP functional, def2TZVP basis set and PCM model for solvation in acetonitrile. This species was obtained after the protonation of [Ni(κ^3-2,6-{PhNCMe}$_2$(NC$_5$H$_3$)H] (**Ni(I)H**) as described in the text.

This combination of computational and experimental results suggests these Ni complexes operate with two distinct mechanisms depending on the substrate employed. Both routes begin with the two electro reduction of the Ni(II), d^8 starting material to yield a square planar Ni(0) species. With stronger acids, complex **A**$^-$ accepts a proton from the substrate to yield a square planar hydride species (**Ni(II)BrH**). Subsequent addition of a second proton results in a dihydrogen complex (**Ni(II)Br(H$_2$)**). Coordination of a free imine arm releases H$_2$, regenerating the initial species and completing the cycle.

On the other hand, with weakly acidic substrates such as phenol, complex **A**$^-$ is not sufficiently basic to abstract a proton from the substrate. Thus, a third reduction is necessary which yields an anionic Ni(0)L$^{-\cdot}$ intermediate. This more basic complex can now abstract a proton to produce **Ni(I)H**. This species can undergo a bimolecular reductive elimination to close the cycle.

4.5.Conclusion

In summary, this study unveils fundamental and practical aspects of electrocatalytic hydrogen generation using two air-stable Ni species, specifically Ni(2,6-{[($R_2C_6H_3$)N]CR'}($2C_5H_3$)Br_2 (R = Me(**4.2**), iPr (**4.1**), R' = Me (**4.2**), Ph (**4.1**)). These species, previously established for their efficacy with neutral water as both substrate and solvent, are now investigated with various substrates featuring diverse pKa values, shedding light on the underlying mechanism. The Ni(II) complexes serve as efficient catalysts for H_2 production at two distinct cathodic potentials, with acidic substrates yielding hydrogen corresponding to the second reduction of the pincer-supported Ni(II) catalysts. Experimental findings align with DFT computational analysis, suggesting two distinct electrocatalytic proton reduction pathways: a Ni(II)/Ni(0) homolytic route for stronger acids and lower reduction potentials, and a Ni(0)L/Ni(0)$L^{-\cdot}$ heterolytic pathway for sources with higher pKa values. Crucially, the introduction of electron-withdrawing substituents significantly amplifies the catalytic rate during metal-based reduction processes. On the other hand, the utilization of bulkier substituents exerts a decelerating effect on the rate of reactions involving ligand-based reduction.

4.6.Experimental Section

General:

Reagents and analytical grade solvents were purchased from Strem Chemicals or Sigma Aldrich and used without further purification. The ^{1}H and $^{13}C\{^{1}H\}$ NMR spectra were recorded at 162 and 76 MHz respectively with chemical shifts reported in ppm using the residual protons of the NMR solvent as internal standards.

X-ray Crystallography: The crystals of $NiBr_2$-2,6-bis[(1-phenylimino)ethyl]pyridine (**4.1**) and $NiBr_2$-2, 6-bis{1-[(2,6-diisopropylphenyl)imino]-benzyl}pyridine (**4.2**) were mounted on thin glass fibers using paraffin oil. Prior to data collection crystals were cooled to 200.15 K. Data were collected on a Bruker Smart ApexII single crystal diffractometer equipped with a sealed tube Mo source (wavelength 0.71073 Å) and an ApexII CCD detector. Raw data collection and processing were performed with the Apex3 software package from Bruker. Initial unit cell parameters were determined from 60 data frames from select ω scans collected at the different sections of the Ewald sphere. Semi-empirical absorption corrections based on equivalent reflections were applied. Systematic absences in the diffraction data-set and unit-cell parameters were consistent with the assigned space group. The initial structural solution was determined using ShelXT direct methods, and refined with full-matrix least-squares procedures based on F^2 using ShelXL.[122] Hydrogen atoms were placed geometrically and refined using a riding model. All scattering factors are contained in several versions of the ShelXL program library, with the latest version used being v.6.12 at the time of this writing.

Electrochemistry: Electrochemical experiments were carried out in a single or double compartment cell, with 40 mL approximate volumes, using a VersaSTAT 3 (Princeton Applied Research) potentiostat. Samples were prepared in a glovebox, sealed, removed from the glovebox

and connected to a Schlenk line and maintained under a nitrogen atmosphere. A conventional three electrode system was employed consisting of a glassy carbon working electrode (diameter = 0.3 cm), a Pt wire as the auxiliary electrode, and an Ag wire as a pseudo-reference electrode. Ferrocene was added as a reference compound and potentials were referred to the redox potential of ferrocenium ion (Fc^+)/ferrocene (Fc) as an internal standard. Dried acetonitrile was purchased from Sigma Aldrich and stored on molecular sieves in the glovebox. Tetrabutylammoniumhexafluorophosphate, $[(n\text{-}Bu)_4N]PF_6$ (TBAHFP), the supporting electrolyte, was crystallized two times with ethanol, dried under vacuum at 90 °C for 24 h before use and stored in a glovebox. The typical concentration of catalyst was 1 mM in each experiment.

Figure 4.25. Produced H_2 gas bubbles in the electrochemical cell after CPE shown in Table 4.4, row1.

SYNTHESIS:

Synthesis of 2,6-bis{[2,6-di(isopropyl)phenyl)imino]benzyl}pyridine (L1)[158]:

A mixture of 2,6-dibenzoylpyridine (5.0 g, 17.4 mmol), 2,6 diisopropylaniline (7.5 g, 38.3 mmol), and p-toluenesulfonic acid (0.2 mg) in toluene (50 mL) were placed in a round bottom flask equipped with a Dean–Stark trap. Under a nitrogen atmosphere, the reaction mixture was heated to reflux in an oil bath at 140˚C for 48 h then cooled to room temperature and the solvent was removed under vacuum to give a dark yellow oil. Hexanes were added and a small quantity of a white solid was removed by filtration. The filtrate was removed under vacuum yielding a dark yellow oil. Methanol (~400 mL) was added to this oil and the mixture was stirred for several minutes, causing the product to precipitate as a yellow solid which was filtered off and rinsed with methanol. The filtrate was reduced to about half the initial volume under vacuum, and then placed in a refrigerator, causing additional product to precipitate, which was filtered off and rinsed with methanol. The product was obtained as a yellow powder. Yield: 7.2 g (68%). ^{1}H NMR (d6-dimethyl sulfoxide, 76 MHz) δ 7.82 (br t, 1 H, py, p CH), 7.55–7.20 (br m, 12 H, Ar–H), 6.94 (br s, 6H, Ar–H), 2.90 (m, 4H, iPr), 1.00 (d, 24H, iPr) ppm.

2,6-bis[1-(2,6-dimethylphenylimino)ethyl]pyridine (L2)[159]: 2,6-Dimethylaniline (6.4 mL, 51.7 mmol) was added to a solution of 2,6-diacetylpyridine (2.81 g, 17.2 mmol) in absolute methanol (50 mL). After the addition of several drops of formic acid, the reaction mixture was refluxed for 24 h and then allowed to cool down to room temperature. The crude product precipitated as a yellow powder and the pure ligand was obtained in 85% yield (5.4 g) upon recrystallization from methanol. ^{1}H NMR (76 MHz, $CDCl_3$): δ -8.56 (d, J -7.8 Hz, 2 H, Py-Hm), 7.95 (t, J -7.8 Hz, 1 H, Py- Hp), 7.11-6.95 (m, 6 H, Ar-H), 2.27 (s, 6 H, N-CMe), 2.07 (s, 12 H, CMe) ppm.

Synthesis of $NiBr_2$-2, 6-bis{1-[(2,6-diisopropylphenyl)imino]-benzyl}pyridine (4.1)[159]: $NiBr_2$ powder (34 mg, 0.160 mmol) was added to a clear yellow solution of 2,6-Bis{[2,6-di(isopropyl)phenyl)imino]benzyl}pyridine (136 mg, 0.165 mmol) in 6 mL of toluene. The reaction mixture was allowed to stir for 4 hours, gradually becoming brown. Solution was then held at -20°C overnight, over which time a brown precipitate formed. Solution was filtered, washed with 5 x 2 mL hexanes, and allowed to dry under vacuum. A brown powder was isolated in 78% yield. Brown needle-like crystals suitable for X-ray analysis were grown from saturated dichloromethane solution by diffusion of hexanes.

^{1}H NMR (162 MHz, $CDCl_3$) δ 7.91 (br t, 1 H, py, p CH), 7.27–7 (br m, 12 H, Ar–H), 6.94 (br s, 6H, Ar–H), 2.76 (m, 4H, iPr), 1.15 (d, 24H, iPr) ppm.

Synthesis of NiB_2,6-bis[1-(2,6-dimethylphenylimino)ethyl]pyridine (4.2)[159]: $NiBr_2$ powder (34 mg, 0.160 mmol) was added to a clear yellow solution of 2,6-bis[1-(2,6-dimethylphenylimino)ethyl]pyridine (65mg, 0.160 mmol) in 6 mL of toluene. The reaction mixture was allowed to stir for 14 hours, gradually becoming orange. Solution was then held at -20°C overnight, over which time a pink precipitate formed. Solution was filtered, washed with 5 x 2 mL hexanes, and allowed to dry under vacuum. A pink powder was isolated in 85% yield. purple plate-like crystals suitable for X-ray analysis were grown by diffusion of saturated dichloromethane solution in hexanes.

^{1}H NMR (162 MHz, $CDCl_3$): δ 8.6 (d, J -7.7 Hz, 2 H, Py-Hm), 7.97 (t, J -13 Hz, 1 H, Py- Hp), 7.4-6.9 (m, 6 H, Ar-H), 2.28 (s, 6 H, N-CMe), 2.06 (s, 12 H, CMe) ppm.

The molecular structure of compound (**4.1**) was obtained through single crystal X-ray analysis. The single crystal X-ray analysis revealed a five coordinate Ni(II) center with a planar coordinated tridentate DIMPY ligand. The unit cells obtained for compound (**4.2**) matched with the data base.

Chapter 5: Electrocatalytic Reduction of CO_2 and H_2O with Zn(II) Complexes Through Metal-Ligand Cooperation

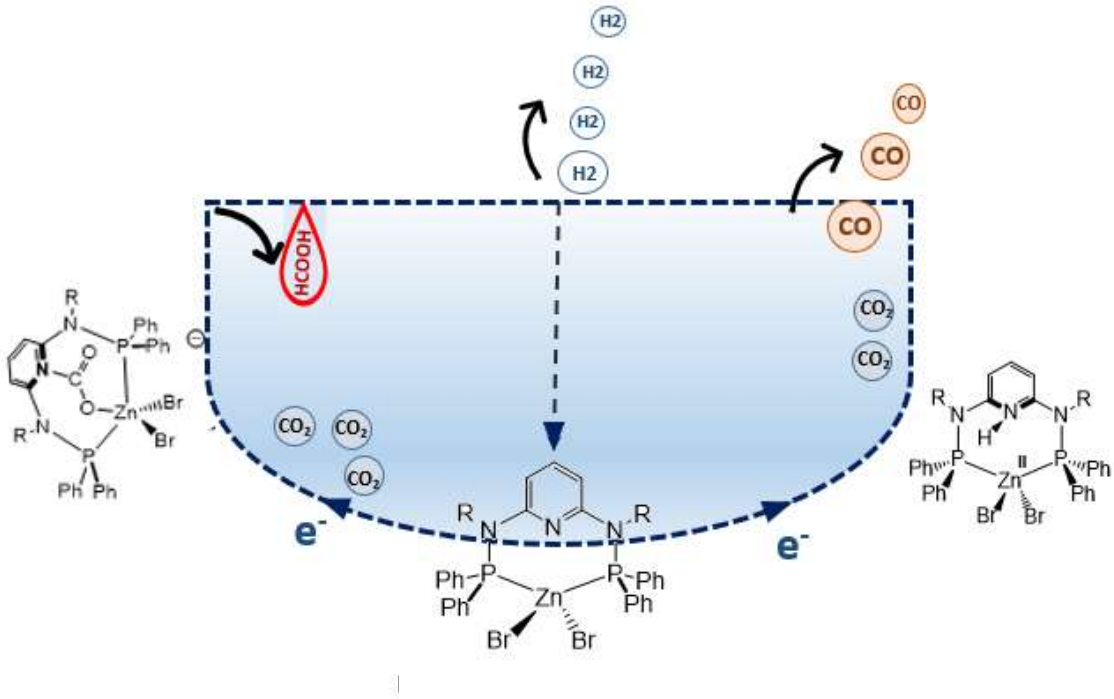

5.1. Preamble and Context

This chapter is based on a project that was initiated by Patrik Berro (PB), a master student in the lab. He worked on CO_2 reduction using complex **5.1** and **5.2**. I had a small contribution on this project performing background controlled potential coulometry experiments, gas analysis, product characterization and quantification, and all figures related to those tasks. This work has been published in Chemical Communication and can be accessed at https://doi.org/10.1039/D1CC03887G, [Berro, P., Norouziyanlakvan, S., Rao, G.K., Gabidullin, B. and Richeson, D., 2021. Electrocatalytic reduction of CO_2 to CO and HCO_2^- with Zn (ii) complexes displaying cooperative ligand reduction. Chemical Communications, 57(73), pp.9292-

9295.]. This manuscript was prepared by Dr. Darrin Richeson (DR), PB and Somayeh Norouziyan (SN).

As a continuation of this study, SN added complex **5.3** to these Zn pincer complexes and studied electroreduction of CO_2 using this catalyst as a comparison to the reported complexes. Furthermore, SN studied HER activity of all three compounds which would be a good comparison with NiPN^{3}P complexes reported in chapter II. This work has been accepted to Chemistry-a European Journal and can be accessed at https://doi.org/10.1002/chem.202303147, [Norouziyanlakvan, S., Berro, P., Rao, G., Gabidullin, B. and Richeson, D., 2024. Electrocatalytic Reduction of CO_2 and H_2O with Zn (II) Complexes Through Metal-Ligand Cooperation. Chemistry–A European Journal, p.e202303147.]. Computations and their analysis were performed by DR with feedback from SN. The manuscript was prepared by DR and SN.

5.2. Abstract

Air and water stable zinc(II) complexes of neutral pincer bis(diphenylphosphino)-2,6-di(amino)pyridine ("PN^{3}P") ligands and the bidentate analogous (diphenylphosphino)-2,(amino)pyridine ("PN^2") are reported. These compounds, [Zn(κ^3-2,6-{Ph_2PNR}$_2$(NC_5H_3)Br_2] (R = Me, **5.1**; R = H, **5.3**), were shown to be capable of electrocatalytic reduction of CO_2 at -2.3 V vs. $Fc^{+/0}$ to CO and HCO_2H with **5.1** and only CO for **5.3**, in mixed water/acetonitrile solutions. These complexes also electrocatalytically generate H_2 from water in acetonitrile solutions, at the same potential, with Faradaic efficiencies up to 90%. DFT computations support a proposed mechanism involving the first reduction of **5.1** or **5.3** occurring at the PN^{3}P ligand. Furthermore, through computational analysis, a mechanism involving metal-ligand cooperation of a Lewis acidic Zn(II) and a basic ligand was suggested. The Zn complex with the bidentate ligand [Zn(κ^2-

2{Ph_2PNR}(NC_5H_3)Br_2] (**5.2**) did not show catalytic behavior for CO_2 reduction. However, it was active for H_2 generation from water.

5.3. Introduction

The existential threat of climate change provides a strong incentive to reveal new approaches to balance the carbon cycle and to exploit underdeveloped carbon-free energy sources. In this regard, the electro- and photocatalytic reduction of CO_2 and catalysts for the hydrogen evolution reaction (HER) employing a broad assortment of homogeneous transition-metal complexes (e.g., Mn-, Fe-, Co-, Ni-, Cu-, Ru-, and Re-based complexes), are active fields of exploration.[160-162] From a sustainability perspective, an essential feature of a successful catalyst would be the implementation of earth-abundant elements and the search for such catalytic complexes is an active field of research.[31, 90, 163, 164] Among the 3d metals, complexes of Zn present attractive targets due to the low cost, relatively high abundance, and low toxicity of this metal.[165, 166] On the other hand, Zn complexes are found almost exclusively in the redox inactive, divalent oxidation state and as a result lack the ability to undergo the fundamental redox steps typical of homogeneous catalyzed reactions.[167] The literature reveals that Zn complexes have documented roles in catalyzed reactions for the capture and insertion of CO_2 [168-170] and $ZnBr_2$ has been shown to accelerate the reaction of PEt_3/CH_2I_2 with CO_2 to form CO.[171] Specifically, complexes **A-C** represent exceptional Zn-based catalysts for CO_2 reduction. The hydride complex [κ^3-Tptm]ZnH (Tptm = tris(2-pyridylthio)methyl), **A**, is a catalyst for the hydrosilylation of CO_2.[172] The Zn(II) thiosemicarbazone complex **B** ("Zn(DMTH)") converts CO_2 to formate via a methoxide complex, Zn(HDMTH)(OCH_3), which inserts CO_2 to yield a methylcarbonate species. Subsequent reduction leads to HCO_2^- via chemically or electrochemically generated hydride sources.[72] The electrochemical proton reduction to hydride was key to this transformation. Complex **C** is a

homogeneous Zn-centered catalyst for electrocatalytic CO_2 reduction. This pyridylphosphine complex displayed an irreversible one-electron reduction at −2.03 V *vs.* $Fc^{+/0}$ with current enhancement observed under a CO_2 atmosphere.[173] Bulk electrolysis of this system led to CO

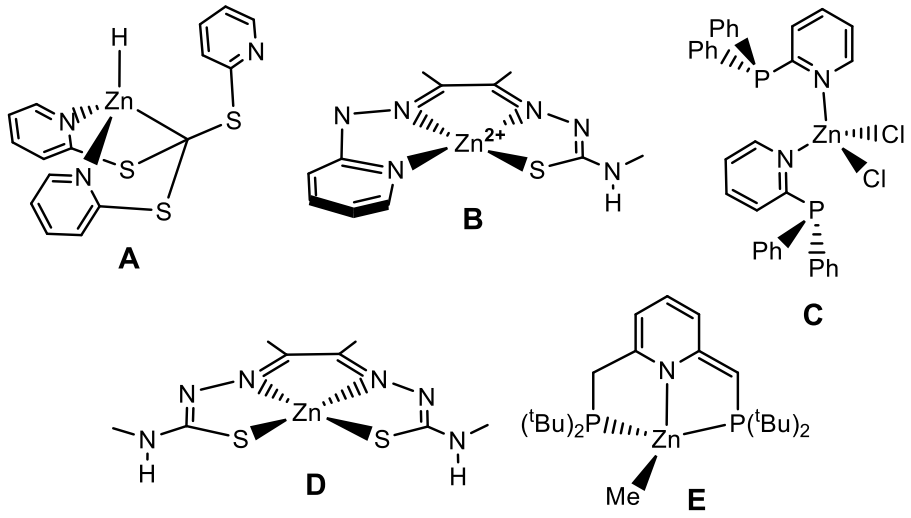

formation as documented by mass spectrometery and IR spectrocopy. The activation of CO_2 by the non-coordinated P center of the ligand was proposed as a step in this transformation.

Not surprisingly, some of these complexes were active for catalytic hydrogen production. For example, **A** catalytically generated H_2 from triphenylsilane.[172] Furthermore, complexes **B** and **D** generated H_2 electrocatalytically from acetic acid through ligand-centered pathways.[108, 109] The proposed mechanism for this process involved ligand protonation by acetic acid to yield active catalysts, which displayed catalytic reduction currents in acetonitrile at −3.29 V and −2.3 V and *vs.* $Fc^{+/0}$, for **B** and **C** respectively. These observations represent rare and interesting examples of electrocatalytic H_2 production with redox inactive metal complexes that rely on a ligand centered process.[109, 174, 175] A recent report for complex **E**, demonstrated the unique ability of this Zn(II) complex to heterolytically cleave and form H-H bonds.[176] The metal-ligand cooperation (MLC)

mechanism for this process involved activation across the metal and ligand and was applied to catalytic hydrogenation of imines and ketones.

The role of MLC with Zn and bis(diphenylphosphino)-2,6-di(methylamino)pyridine ("PN^3P") **5.1** and ("PN^2") **5.2** pincers was recently reported for electrocatalytic CO_2 reduction by the Richeson group.[177] In particular, the air-stable Zn(II) complex, [Zn(κ^2-2,6-{Ph_2PNMe}$_2$(NC_5H_3)Br_2] (**5.1**) was reported to electrocatalytically reduce CO_2 to yield CO/HCO_2H in mixed water/acetonitrile solutions. However, [Zn(κ^2-2,6-{Ph_2PNMe}(NC_5H_3)Br_2] (**5.2**) did not catalyze CO_2 reduction.

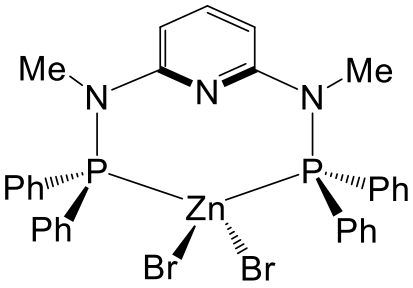

5.1

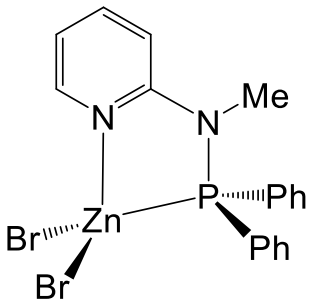

5.2

We now expand on these results with a new Zn complex **5.3** for CO_2 reduction using water as a proton source. We also reveal details on the prospective application of these Zn complexes for the generation of H_2 from neutral water thereby contributing to other reported complexes of Mn(I),[132] Co(II),[117] and Ni (II)[178] with non-innocent ligand scaffolds that display electrocatalytic HER with water as a substrate.

5.4. Results and Discussion

5.4.1. Synthesis and characterisation

The direct reaction of $ZnBr_2$ with the relative neutral pincer ligand, N,N′-bis(diphenylphosphino)-2,6-di(methylamino)pyridine ("PN^3P"), N-(diphenylphosphino)-2-methylaminopyridine ("PN^2"), and N,N′-bis(diphenylphosphino)-aminopyridine ("PN^3P"), yielded colorless Zn complexes of

5.1, **5.2** and **5.3,** respectively (Scheme 5.1) that were purified by crystallization from CH_2Cl_2. Complex **5.1** displayed ^{1}H, ^{13}C and ^{31}P NMR spectra consistent with a symmetrical coordination of the ligand to Zn. In particular, a single proton resonance for the N-Me groups as well as symmetrical signals for the pyridyl and the PPh_2 moieties were observed. For complex **5.2** the ^{1}H and ^{13}C NMR spectra gave resonances and intensities consistent with a single environment for the ligand. Evidence for coordination of the PPh_2 group was given by the ^{31}P NMR resonance at δ 27.7ppm, an upfield shift from the free ligand at δ 51.0ppm. Complex **5.3** is related to **5.1** by replacement of the NMe moieties with NH groups.[177] The characterization of **5.3** through spectroscopic and single crystal diffraction methods compared well with **5.1**. For example, the ^{1}H NMR spectrum of compound **5.3** was similar to that of **5.1** with the expected absence of the N-Me resonance. Furthermore, the ^{31}P NMR spectrum of **5.3** displayed a single resonance at 22.6 ppm while the analogous signal for **5.1** appeared at 22.5 ppm.

5.4.2. XRD characterizations

Single crystal X-ray diffraction analysis of compound **5.1** showed the potentially tridentate ligand binds to Zn only through the two phosphine groups that flank the central pyridyl group while the pyridyl-N(2) center remained beyond bonding distance to Zn at 2.680 Å. This group is directed toward the Zn(II) center, likely due to steric restraints and electrostatic forces (Figure 5.1). Selected bonding parameters are given in Table C.1-C.2. Single crystal X-ray diffraction analysis of compound **5.3** revealed that the asymmetric unit exhibited two molecules of formula [Zn(2,6-$\{Ph_2PNH\}_2(NC_5H_3)Br_2$] with very similar bonding parameters and one of these molecules is shown in Figure 5.2. Complex **5.3** displayed a four coordinate Zn(II) center constituted with a bidentate PN^3P ligand and two bromide ligands. Selected bonding parameters are given in Table C.4-C.5. This complex displayed symmetrical Zn-P distances with bond distances in-line with

reported Zn bond distances (**5.1**).[179, 180] In particular, the average Zn-P distance of 2.4461 Å is similar to those observed in **5.1**, however, for **5.3** the pyridyl group is oriented slightly closer to the Zn with Zn-N distances of 2.472(4) Å and 2.525(4) Å compared to the Zn-Npy distance of 2.68 Å in **5.1**. These Zn-N distances are well beyond typical bond distances. For comparison the Zn-Npy distances in **A** were 2.076(3) Å and 2.078(2) Å[181], those for **C** were 2.061(4) Å, 2.067(4) Å.[173] The orientation of the pyridyl group differentiates the two Zn-Br sites with Br(1) oriented "trans" to the Npy and Br(2) at 90 degrees to Br(1) and the Npy center. In spite of this distortion it is noteworthy that an average for the bonding angles around Zn in the complexes **5.1** and **5.3** are 109.3 and 109.4, which resemble a distorted pseudo-tetrahedral Zn coordination geometry. The coordination environment in complex **5.2** consists of a bidentate planar diphenylaminopyridine ("PN") ligand and two bromide ligands. Overall, this yields distorted tetrahedral Zn(II) centers. The PN ligand forms an essentially planar five-membered chelate ring, consisting of the P-N-C-N ligand skeleton bonded to the Zn center with the ligand plane bisecting the Br-Zn-Br plane. The asymmetric unit gave Zn-N distances of 2.067(4) Å and 2.091(4) Å (average = 2.08 Å) and Zn-P distances of 2.4030(13) Å and 2.4045(13) Å) (average = 2.40 Å) and these distances are comparable to reported bond distances (Figure 5.3, Table C.1, C.3).

Scheme 5.1. Synthetic scheme and structural representation for compound Zn(2,6-{Ph_2PNH}$_2$($Me_2NC_5H_3$)Br_2] (**5.1**) and [Zn(2,6-{Ph_2PNH}$_2$(NC_5H_3)Br_2] (**5.3**)

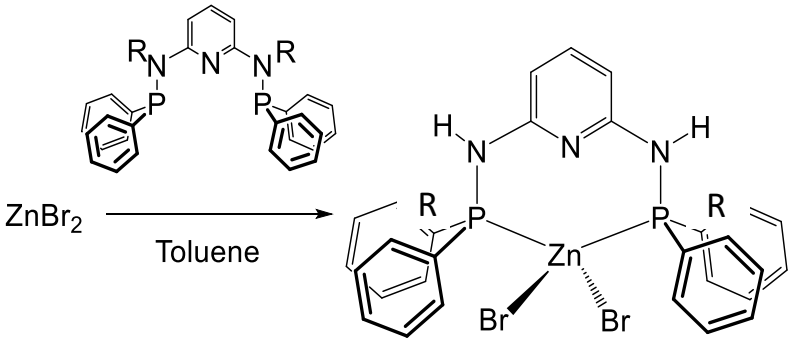

5.1 (R=CH_3)
5.3 (R=H)

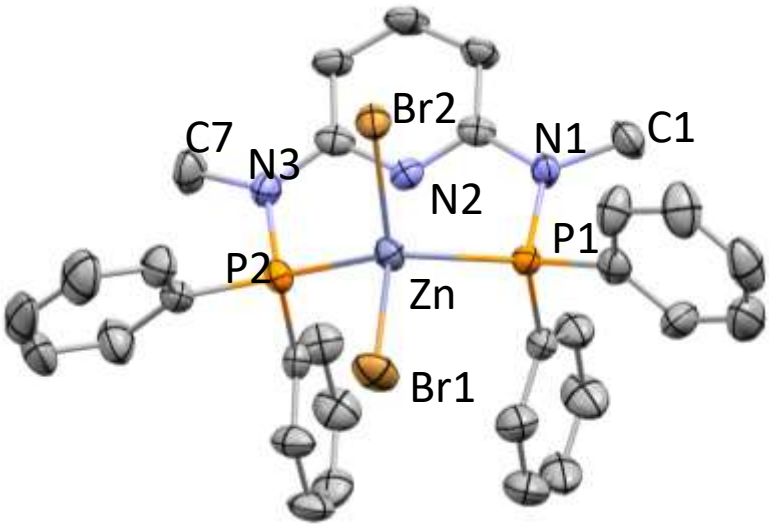

Figure 5.1. Structural representation for one of the two unique molecules of the compound [Zn(2,6-{Ph_2PNCH_3}$_2$(NC_5H_3)Br_2] (**5.1**) in the asymmetric unit. The hydrogen atoms bonded to carbon as well as co-crystallized solvent are omitted for clarity.

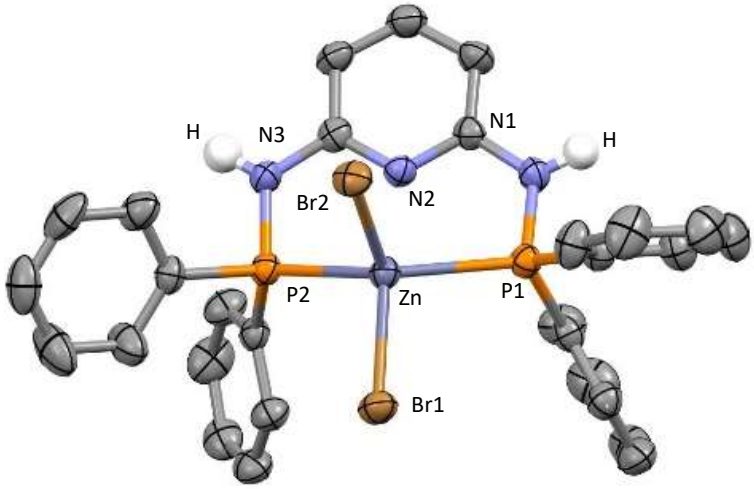

Figure 5.2. Structural representation for one of the two unique molecules of the compound [Zn(2,6-{Ph_2PNH}$_2$(NC_5H_3)Br_2] (**5.3**) in the asymmetric unit. The hydrogen atoms bonded to carbon as well as co-crystallized solvent are omitted for clarity.

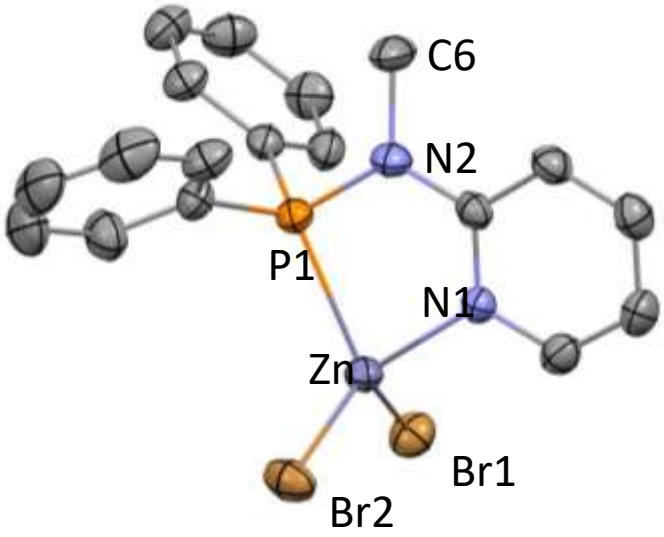

Figure 5.3. Structural representation for the compound [Zn(2-{Ph_2PNMe}(NC_5H_3)Br_2] (**5.2**) obtained from single crystal X-ray analysis. Only one of the two molecules in the asymmetric unit is shown. Hydrogen atoms are omitted for clarity.

5.4.3. Electrochemical characterisation

The fundamental electrochemical characterization of these Zn complexes began by performing cyclic voltammetry (CV) measurements, at cathodic potentials, on a 1.0 mM acetonitrile solution of **5.1**, **5.2** and **5.3** under N_2 using a glassy carbon (GC) working electrode, a Pt counter electrode and Ag pseudo-reference electrode. All potentials were referenced to the ferrocene ($Fc^{+/0}$) redox couple. The relationship of **5**.**1**, **5.2,** and **5.3** can be seen in the overlay of the CV's shown in Figure 5.4. These measurements revealed for **5.1** two irreversible reduction peaks at -2.32 and -2.62 V with the CV for complex **5.2** displaying two irreversible reductions at -2.28V and -2.68V and for complex **5.3** two irreversible reductions at -2.3V and -2.74V. Overall, from looking at Figure 5.2, it seems that all three catalysts have a similar reduction pattern. The first reduction for all three happens very close together, but the second reduction of complex **5.1** happens relatively at less negative voltages.

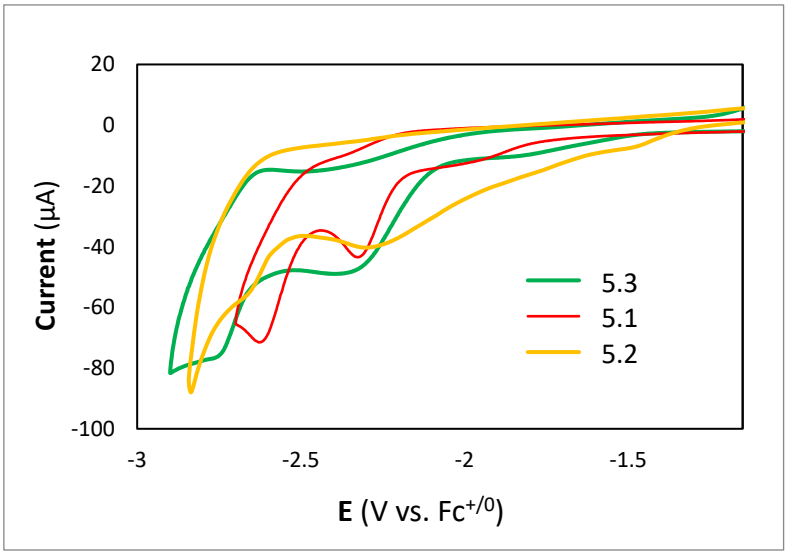

Figure 5.4. Overlay of the Cyclic Voltamograms of complexes [Zn(2,6-{Ph_2PNMe}$_2$(NC_5H_3)Br_2] (**5.1**, red) and [Zn(2-{Ph_2PNMe}(NC_5H_3)Br_2] (**5.2**, yellow) [Zn(2,6-{Ph_2PNH}$_2$(NC_5H_3)Br_2] (**5.3**, green) in CH_3CN with tetrabutylammonium hexafluorophosphate (TBAHFP) supporting electrolyte using a GC working electrode, a Pt counter electrode under N_2.

For all three complexes, the reduction peaks displayed a linear variation of the square root of the voltammogram scan rate versus current (i) as expected for freely diffusing species according to the Randles–Ševčík equation (Figure 5.5).

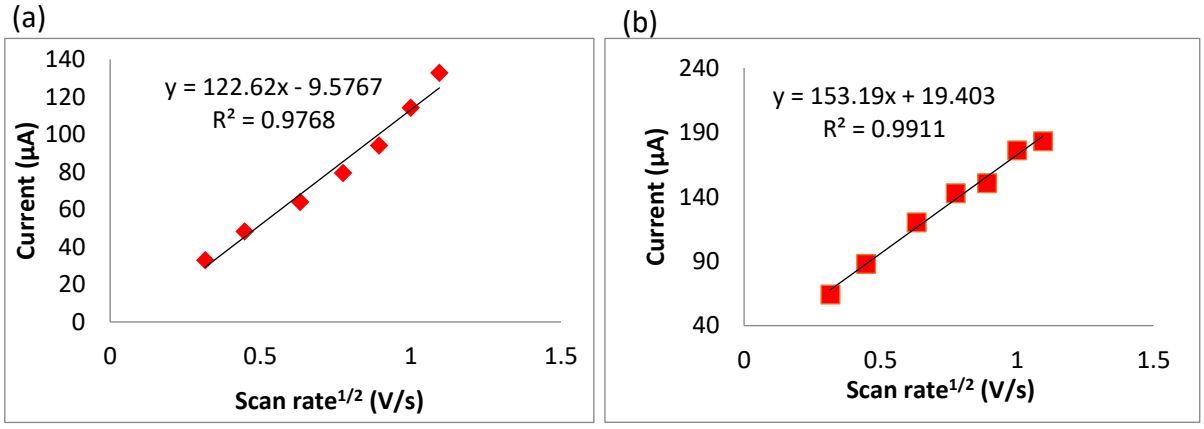

(c)

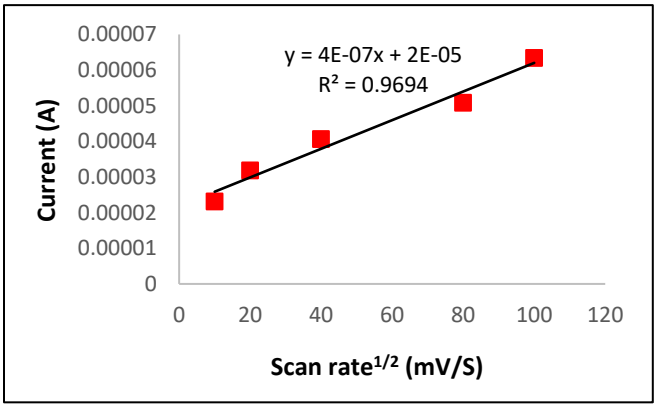

Figure 5.5. The current (i) versus (scan rate)$^{1/2}$ dependence of the first reduction for compound (a) **5.1**, (b) **5.2**, (c) **5.3**.

To analyze the reduction behavior more clearly, a computational study of **5.2** and **5.3** and their reduction products was undertaken. The results for the DFT optimization of [Zn(2,6-{Ph_2PNMe}$_2$(NC_5H_3)Br_2] (**5.1**) have been previously reported.[177] According to these computations the frontier orbitals of **5.1** displayed little contribution from Zn, with the HOMO being a π molecular orbital of the ligand that was largely localized on the py and NMe groups with the fragment orbital allocation of 0.51 (py), 0.27 (NMe). The LUMO was also ligand localized and mostly π in nature localized on the pendant Ph groups (56%) with some py contribution (22%). The lowest energy, unoccupied, orbital with substantial Zn contribution was 0.2283 Hartrees (6.21eV) above the HOMO and was clearly σ antibonding with Zn s orbital. (Figure 5.6) The lowest energy, unoccupied, orbital with substantial Zn contribution (MO 194) was clearly σ antibonding with 51% Zn s orbital (Figure C.1).

An analogous approach was taken with [Zn(2-{Ph_2PNMe}(NC_5H_3)Br_2] **(5.2)** and [Zn(2,6-{Ph_2PNH}$_2$(NC_5H_3)Br_2] (**5.3**). Starting from the crystallographic parameters, optimization was performed with the B3LYP functional, def2TZVP basis set and using the PCM model for solvation with acetonitrile. Frequency analysis confirmed by the absence of imaginary values that the resulting structure was a minimum.

Computational optimizations of **5.2** yielded frontier orbitals that displayed little contribution from Zn, with the π-type HOMO essentially localized on the py and NMe groups and the LUMO is of π character with the majority localized on the py portion of the ligand (Figure 5.7) The lowest energy, unoccupied, orbital with substantial Zn contribution (MO 134) was clearly σ antibonding with 73% Zn s orbital (Figure C.2).

The optimization yielded a structure for **5.3** that reproduced the experimental structure and is presented in Figure 5.8. Compared to the experimental geometry, the computational model displayed slightly shorter Zn-Br bond distances and slightly longer Zn-P distances. In general the computational results for **5.3** were closely parallel to those reported for **5.1.** As with **5.1**, the optimized structure of **5.3** provided frontier orbitals that displayed little contribution from Zn.[177] For example, the HOMO consisted of a π molecular orbital of the ligand that was largely localized on the py and NH groups with the fragment orbital allocation approximately 50% (py), and >25% NH groups (Figure. 5.8(c)). Similarly, the LUMOs for these two compounds were also ligand localized and mostly π in nature. The largest contributions arise from the pendant Ph groups (≈60%) with some py contribution (≈15%) (Figure 5.8(b)). The lowest energy, unoccupied, orbital with substantial Zn contribution (MO 186) was 6.15eV above the HOMO and was clearly σ antibonding with 56% Zn s orbital (Figure C.3). A summary of computed Zn-centered bonding from the optimization of **5.3** is shown in Table C.6.

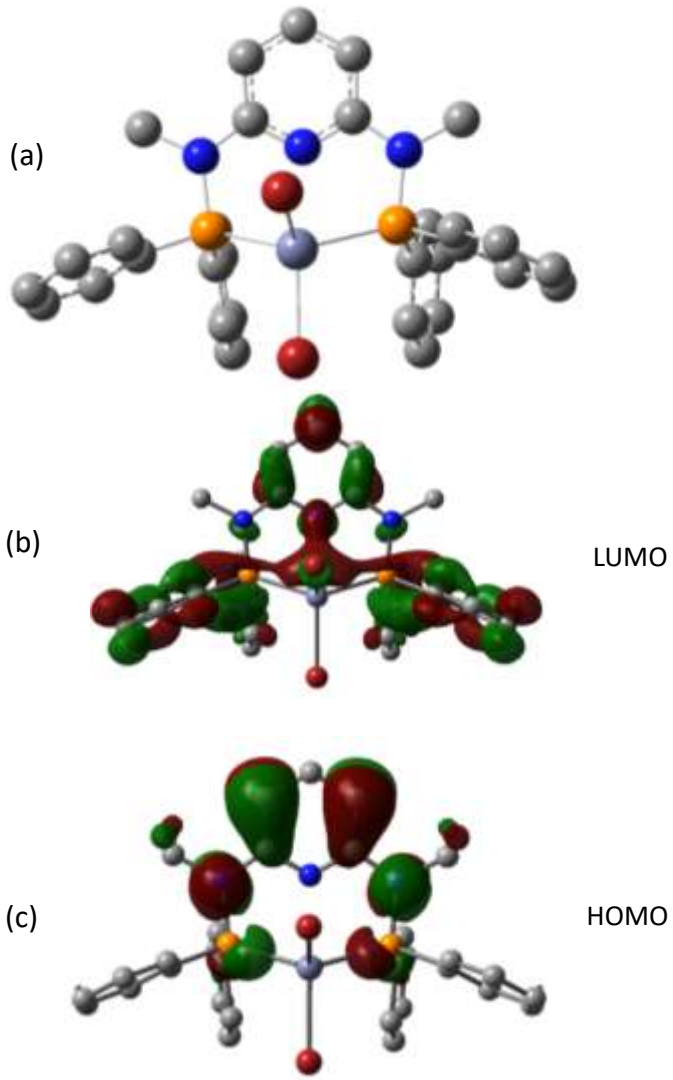

Figure 5.6. (a) DFT optimized structure of [Zn(2,6-{Ph_2PNH}$_2$(NC_5H_3)Br_2] (**5.1**) using the B3LYP functional and def2TZVP basis set in acetonitrile (PCM). Hydrogen atoms eliminated for clarity (b) The LUMO (MO 184) for [Zn(2,6-{Ph_2PNMe}$_2$(NC_5H_3)Br_2] (**5.1**). The major fragment orbital contributions were Ph (0.56), py (0.22), P (0.13) with only 0.06 (Zn). (c) The HOMO (MO 183) [Zn(2,6-{Ph_2PNMe}$_2$(NC_5H_3)Br_2] (**5.1**). The major fragment orbital contributions are 0.51 (py), 0.27 (NMe), 0.09 (Ph) and 0.07 (P).

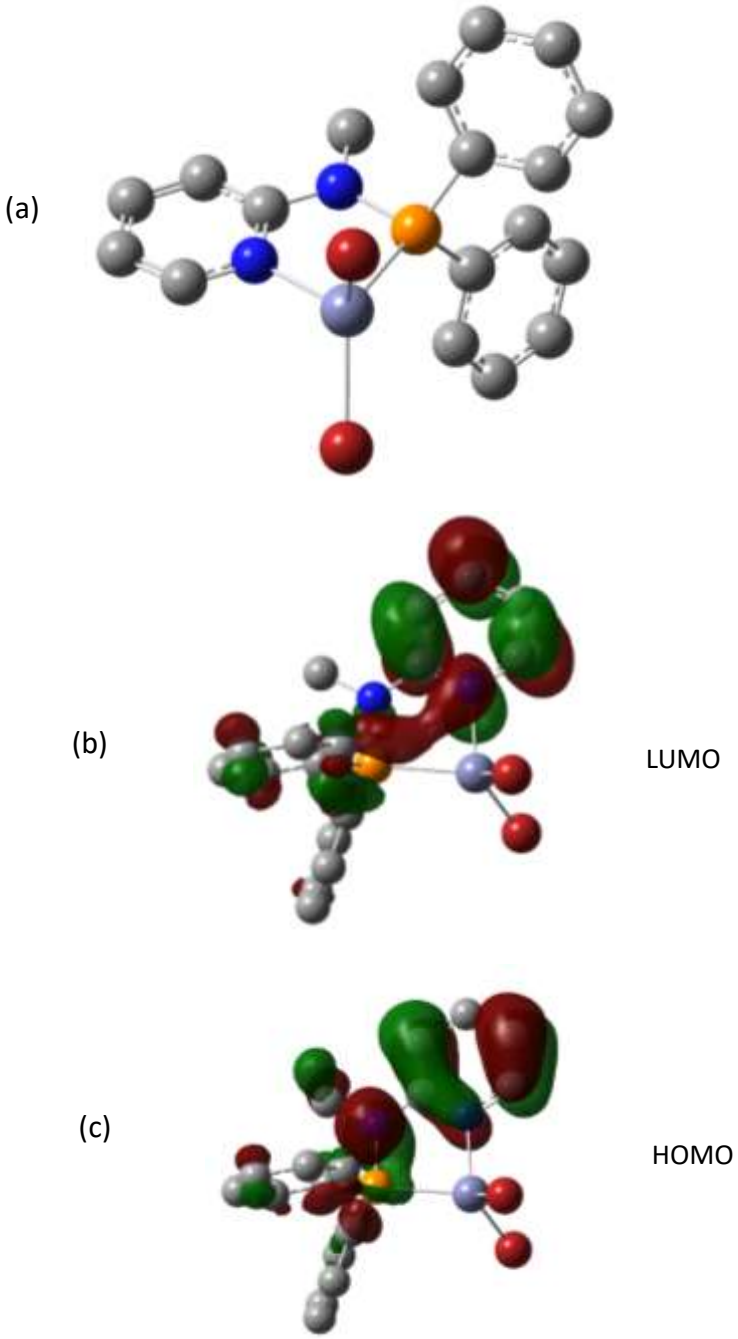

Figure 5.7. (a) DFT optimized structure of the first reduction of **5.2** to yield [Zn(2-{Ph_2PNMe}(NC_5H_3)Br_2] (**5.2**), using the B3LYP functional and def2TZVP basis set in acetonitrile (IEFPCM). Hydrogen atoms are omitted for clarity. Frequency analysis confirmed that the optimized structure was a minimum with no imaginary frequencies. (b) The LUMO (MO 128) for [Zn(2-{Ph_2PNMe}(NC_5H_3)Br_2] (**5.2**). The major fragment orbital contributions are 0.76 (py) 0.14 (Ph) 0.07 (P) (c) The HOMO (MO 127) for [Zn(2-{Ph_2PNMe}(NC_5H_3)Br_2] (**5.2**). The major fragment orbital contributions are 0.53 (py) 0.32 (NMe) 0.10 (Ph).

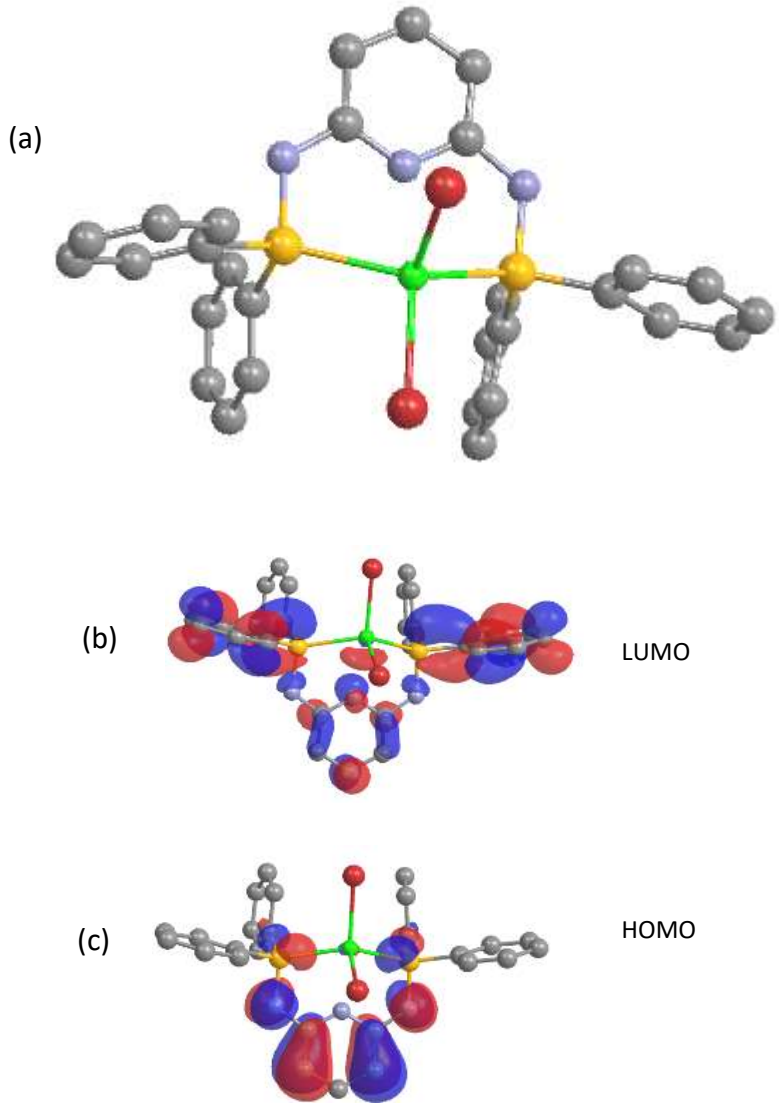

Figure 5.8. (a) DFT optimized structure of [Zn(2,6-{Ph_2PNH}$_2$(NC_5H_3)Br_2] (**5.3**) using the B3LYP functional and def2TZVP basis set in acetonitrile (PCM). Hydrogen atoms are omitted for clarity. (b)The LUMO (MO 176) for **5.3**. The major fragment orbital contributions are 0.65 (Ph), 0.15 (py), 0.14 (P), with only 0.04 (Zn). (c) The HOMO (MO 175) for [Zn(2,6-{Ph_2PNH}$_2$(NC_5H_3)Br_2] (**5.3**). The major fragment orbital contributions are 0.56 (py), 0.26 (NH), 0.08 (Ph), 0.07 (P).

The nature of the reduced complex was also examined by taking the optimized structure of **5.1, 5.2,** and **5.3**, adding an electron and performing a new DFT optimization (B3LYP/def2TZVP/PCM/CH_3CN). This led to an anionic complex (**5.1**$^-$), (**5.2**$^-$), (**5.3**$^-$) that

maintained the tetrahedral coordination environments of each of the Zn species. Furthermore, all three anions showed no significant frontier electron character on the Zn center with the added electrons residing in π orbitals on the Ph groups and the py moiety. The optimized structures displayed no imaginary vibrational frequencies. For complex **5.1**, this led to an anionic complex $[Zn(2,6\text{-}\{Ph_2PNMe\}_2(NC_5H_3)Br_2]^-$ (**5.1**$^-$) (Figure C.4, Table C.7). The optimized anionic complex maintained a tetrahedral environment on Zn with two phosphine and two bromide ligands. The anion yielded a Zn center that was less symmetrical than in the parent **5.1**. One of the Zn-P bonds showed a slight decrease in Zn-P distance with an increase in bond order compared to the other Zn-P linkage. Both Zn-Br increased slightly in bond length. Consistent with these observations, the SOMO was localized on the "shorter" Zn-P side of **5.1**$^-$. The orbital array of **5.1**$^-$ remains similar to **5.1** with the frontier orbitals dominated by ligand centered π-type orbitals. The SOMO is, as expected, localized on the phenyl substitutents (67%) (Figure C.5). The SOMO-1 (formerly HOMO) retains similar orbital characteristics distributed predominantly on py (53%) and NMe (28%) (Figure C.6). According to these computations, there is no significant frontier electron character on the Zn center and the added electrons reside in π orbitals on the Ph and py groups. The single electron reduction product **5.2**$^-$ was also successfully computationally modelled (Figure C.7, Table C.8). Compound **5.2**$^-$ displayed a SOMO that was PN ligand centered (Figure C.8-C.9). Again, computational effort makes it clear that there is no significant frontier electron character on the Zn center.

Optimization of the anion of **5.3** gave **5.3**$^-$ which like the anion **5.1**$^-$**,** displayed a Zn center that was less symmetrical than in the parent complex. One of the Zn-P bonds showed a slight decrease in Zn-P distance with an increase in bond order compared to the other Zn-P linkage. Both Zn-Br increased slightly in bond length (Figure C.10, Table C.9). Consistent with these observations, the

SOMO was localized on the phenyl substitutents of the "shorter" Zn-P side of **5.3**$^{-}$ (69%) (Figure C.11). The remaining orbital array of **5.3**$^{-}$ remained similar to **5.3** with the frontier orbitals dominated by ligand centered π-type orbitals. The SOMO-1 (formerly HOMO) retains similar orbital characteristics distributed predominantly on py (57%) and NH (27%) (Figure C.12). According to these computations, there is no significant frontier electron character on the Zn center and that the added electrons reside in π orbitals on the Ph and py groups. Note that these comments are completely analogous to the effects seen for the reduced form of [Zn(2,6 {Ph_2PNMe}$_2$(NC_5H_3)Br_2] (**5.1**).[177]

5.4.4. CO_2 reduction

An initial examination of the electrocatalytic ability of these Zn complexes toward CO_2 reduction was carried out by performing CV measurements of **5.1**, **5.2**, and **5.3** under a CO_2 atmosphere with H_2O added as a proton source. The clear increase in current under these conditions was characteristic of electrocatalytic reduction of CO_2 by complexes **5.1**, **5.3** (Figure 5.9). However**,** with [Zn(2-{Ph_2PNMe}(NC_5H_3)Br_2] (**5.2**), which displayed enhanced cathodic current in the presence of H_2O, exhibited no additional enhancements when the atmosphere was changed to CO_2 (Figure 5.10).

(a)

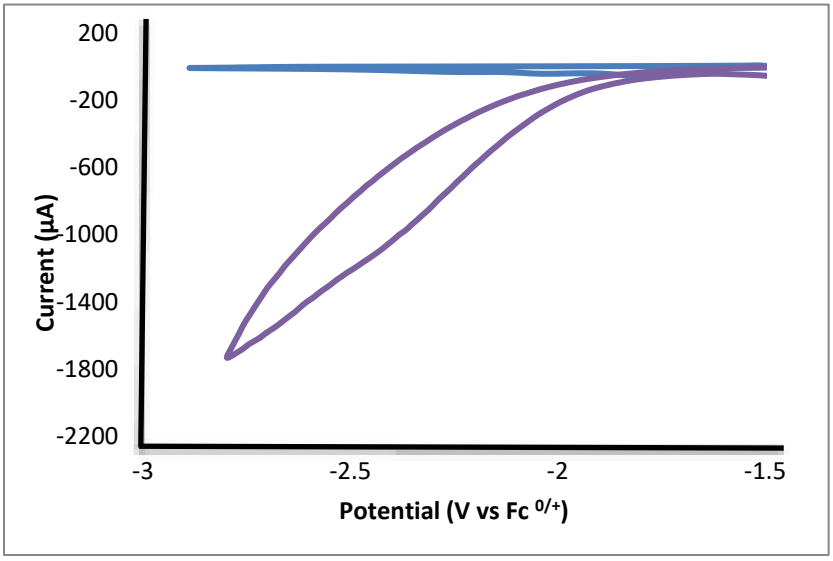

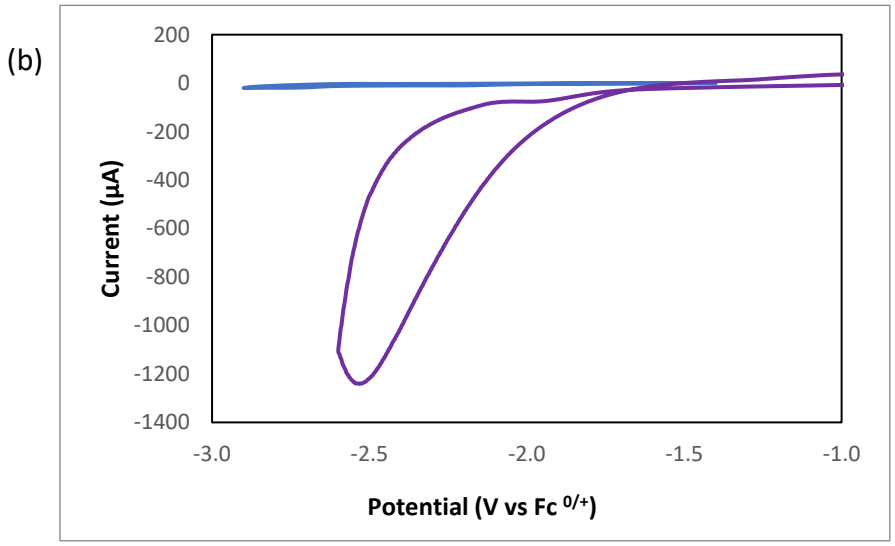

Figure 5.9. Cathodic CV measurements in CH_3CN with a GC electrode under N_2 of a) complex [Zn(2,6-{Ph_2PNMe}$_2$(NC_5H_3)Br_2] (**5.1**) (blue), 0.25M water (purple), **5.1** with 0.25M of added water (green), b) complex [Zn(2,6-{Ph_2PNH}$_2$(NC_5H_3)Br_2] (**5.3**) (blue), **5.3** with 0.25M of added water (purple).

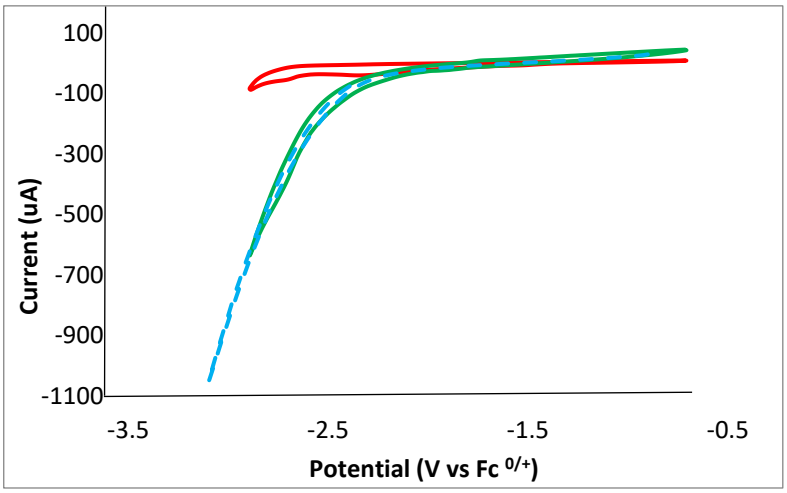

Figure 5.10. Cathodic CV measurements of complex **5.2** in CH_3CN with a GC electrode under N_2 (red), under N_2 with 700µL of added water (2.5M) (green), and under a CO_2 atmosphere with 700µL of added water (2.5M) (blue). All potentials are referenced to Fc^+/Fc.

After performing these experiments, the electrode was removed from the solution, rinsed, and immersed in fresh acetonitrile solution with electrolyte and water but containing no Zn complex. Under a CO_2 atmosphere no catalytic response during cathodic cycling was observed indicating that the electrode was innocent in this catalytic behavior.

To definitively establish the catalytic behavior of complex **5.1** and **5.3**, controlled potential electrolysis (CPE) experiments were performed and the reactor headspace was examined by gas chromatography and solution NMR analysis was employed to probe the formation of condensed phase products such as formic acid (Figure C.13). CPE measurements were carried out at -2.3V and -2.7V vs. $Fc^{+/0}$ under a CO_2 atmosphere with either 200μL or 500μL of added water. The results of these investigations, presented in Table 5.1, documented the formation of CO and H_2 as the only observed gas phase products with both **5.1** and **5.3** and HCO_2^- in solution only with **5.1**. No solution products, such as formate, were observed with **5.3**, thus indicating that **5**.**3** is selective for CO formation. These observations confirmed the unique electrocatalytic abilities of **5**.**3** as the only reported Zn-based catalyst with quantified CO formation. Furthermore, in contract to **B**, which reduced CO_2 through a methylcarbonate intermediate, **5.1** generated formate directly from CO_2 and H_2O.[108] Critical background measurements were carried out in the absence of complex **5.1** and **5.3**. These experiments yielded no CO_2 reduction products and only at more negative potential of -2.7 V was background generation of a minor amount of H_2 observed. The lack of background interference further supports the electrocatalytic behavior of **5.1** and **5.3**.

It should be further noted that initial CPE measurements of **5.2** at -2.7V in acetonitrile with added water (0.7 M) and under a CO_2 atmosphere gave 22 μmol H_2 and no indications of CO_2 reduction products.

Table 5.1. Summary of the CO_2 reduction products from controlled potential coulometry of 1mM (15mmoles) solution of compounds [Zn(2,6-{Ph_2PNH}$_2$(NC_5H_3)Br_2] (**5.3**) and [Zn(2,6-{Ph_2PNMe}$_2$(NC_5H_3)Br_2] (**5.1**) in acetonitrile under CO_2 atmosphere with added water

compound	E(V)vs $Fc^{0/+}$	Added water (µL)/(M)	CO (µmol)	HCO_2H (µmol)	FE(%)
5.3	-2.3	200/0.7	25.8	-	31
5.3	-2.3	500/1.9	65.0	-	74
5.3	-2.7	200/0.7	122.5	-	83
5.1[a]	-2.3	200/0.7	14.2	-	70
5.1[a]	-2.3	500/1.9	49	13.5	69[b]
5.1[a]	-2.7	200/0.7	24.7	-	74

[a] data from reference 177.
[b] FE for CO + HCO_2H

For comparison, the first notable feature is that both **5.1** and **5.3** were capable of electrocatalytic reduction of CO_2 to form selectively CO at -2.3 V *vs*. $Fc^{+/0}$ but the amount or rate of reduced product formation was higher for **5.3** (Figure 5.11). Perhaps not surprisingly, a more negative reduction potential (-2.7V) also results in an increased formation of reduction products. Other than the rate of reduction, the most interesting contrast between **5.1** and **5.3** is the drop in product selectivity for **5.1** with increased addition of water. Specifically, for **5.1**, HCO_2H appeared as a reduction product at 1.9M H_2O, concomitant with CO selectivity dropping to ≈78%. Finally, the results in Table 5.1 represent the first quantified CO formation measurements for homogeneous Zn-based catalysts.

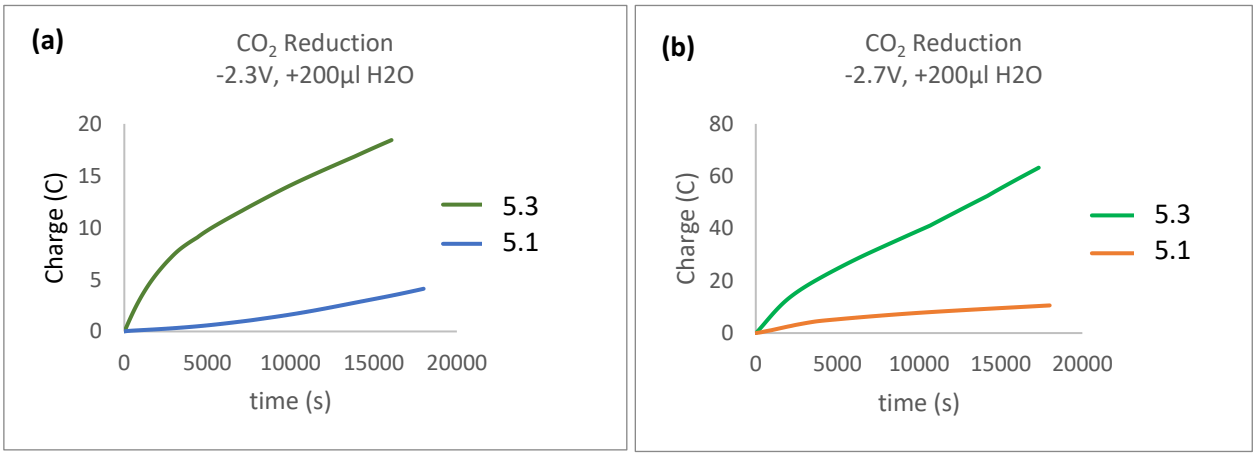

Figure 5.11. Charge versus time curves for the CPE measurements for electrocatalytic CO_2 reduction using complexes **5.1** and **5.3**. (a) measurement at -2.3V vs. $Fc^{+/0}$ with 200 mL of added water. (b) measurement at -2.7V vs. $Fc^{+/0}$ with 20mL added water.

5.4.5. Hydrogen generation from water

The hydrogen evolution reaction is a common antagonistic feature of electrocatalytic CO_2 reduction that arises from the requirement of a proton source in the CO_2 reduction process. Catalysts that reduce CO_2 to CO or formate are likely, due to the similarity in reduction potentials, to reduce protons to hydrogen (equation 5.1-5.3) making this a rival process.[182] Furthermore, the presence of CO_2 increases the acidity of the aqueous solvent mixture, further promoting proton reduction. Not surprisingly, the CO_2 electroreduction catalysis with **5.1** and **5.3** gave competitive and significant H_2 gas formation.

$2H^+ + 2e^- \rightarrow H_2$ $E^o =$ -0.41 V * (5.1)

$CO_2 + 2H^+ + 2e^- \rightarrow CO + H_2O$ $E^o =$ -0.52 V* (5.2)

$CO_2 + 2H^+ + 2e^- \rightarrow HCOOH$ $E^o =$ -0.61 V* (5.3)

*E° potentials are reported vs SHE at pH 7

Given that H_2 is a key industrial chemical and has enormous potential as a renewable and green fuel, the capability of complexes **5.1**, **5.2**, and **5.3** to electrocatalytically generate hydrogen from neutral water was next explored. At a cathodic potential of -2.3V, the same potential used for CO_2 reduction, the addition of water to solutions of **5.1**, **5.2**, and **5.3** resulted in substantial increases in the current features characteristic of a catalytic process (Figure 5.12). The onset potential for each enhancement was also measured and shown in Figure C.14. It is worth noting that no background of water reduction by GC electrode at these voltages was seen in the CV experiments shown in Figure 5.13.

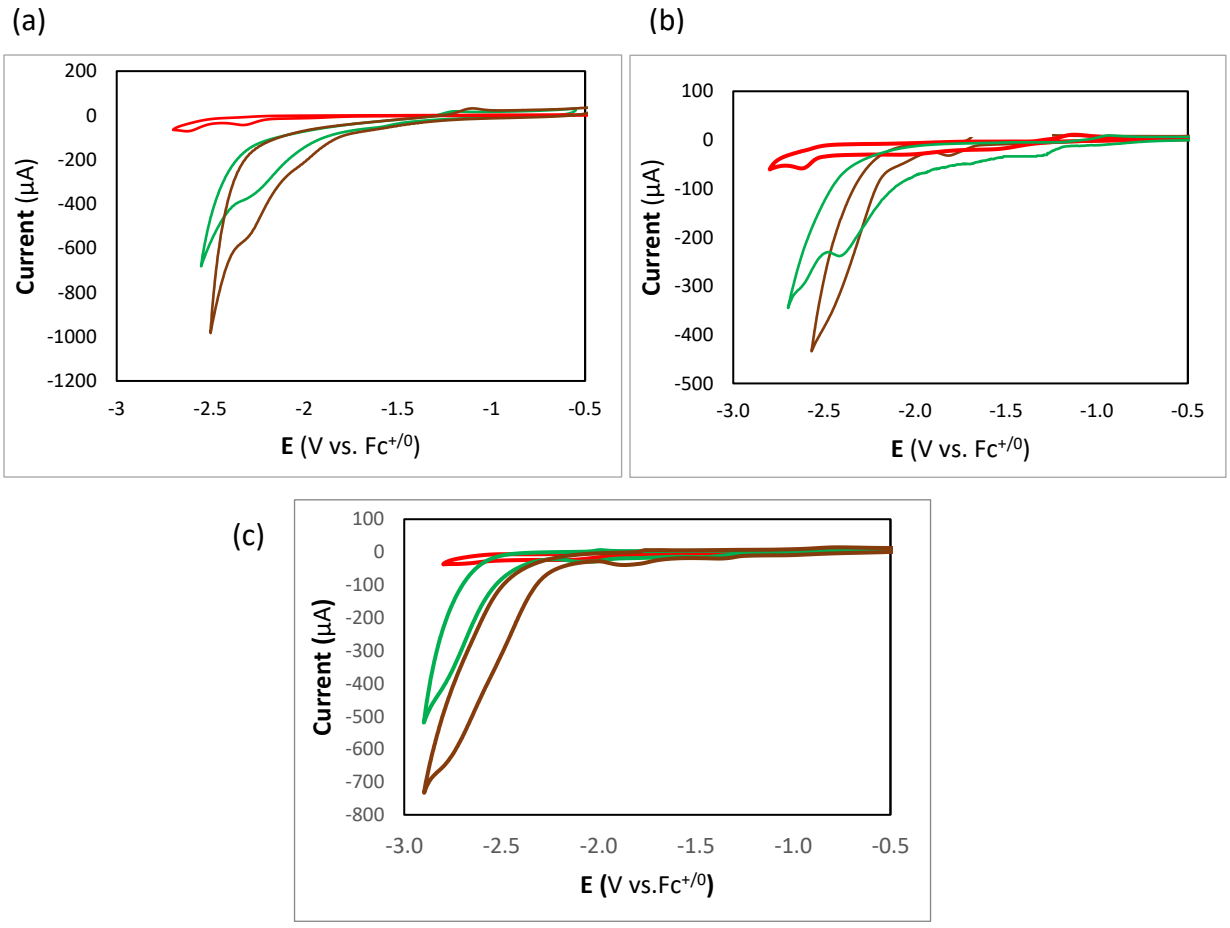

Figure 5.12. CV's of complexes [Zn(2,6-{Ph_2PNMe}$_2$(NC_5H_3)Br_2] (**5.1**), [Zn(2-{Ph2PNMe}(NC5H3)Br2] (**5.2**), and [Zn(2,6-{Ph_2PNH}$_2$(NC_5H_3)Br_2] (**5.3**) in CH_3CN with

tetrabutylammonium hexafluorophosphate (TBAHFP) supporting electrolyte using a GC working electrode, a Pt counter electrode.

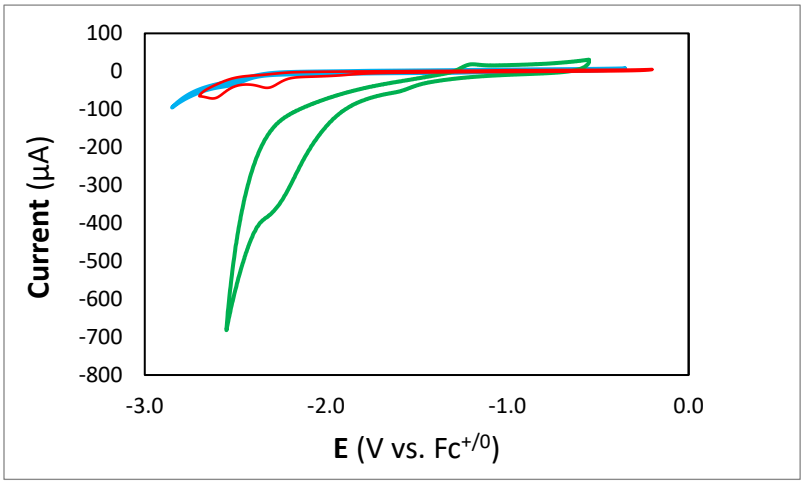

Figure 5.13. Cathodic CV measurements in CH_3CN with a GC electrode under N_2 of 0.25M water (brown), complex [Zn(2,6-{Ph_2PNMe}$_2$(NC_5H_3)Br_2] (**5.1**) (red), **5.1** with 0.25M of added water (green).

To clearly establish the catalytic behavior of these complexes and that hydrogen is, in fact, the product, controlled potential electrolysis (CPE) experiments were performed using **5.1**, **5.2**, and **5.3** with the reactor headspace examined by gas chromotography with the results presented in Table 5.2. The CPE measurements were carried out at -2.3V vs. $Fc^{+/0}$ with either 200µL (0.25M) or 800µL (1.0M) of added water.

Analysis of the reactor head space documented the formation of H_2 as the sole gas phase product. Analogous CPE measurements were made under an N_2 atmosphere in the absence of complexes. These "blank" measurements at -2.3V and 0.25M H_2O produced no H_2 and even at 1M H_2O, only a trace (1.3µmol) of H_2 was observed. Figure 5.14 also clearly shows that in the absence of Zn complexes there is only a trace number of charge passes during the CPE. Furthermore, in the presence of Zn compounds much more charge was measured, indicating catalysis. As a result,

these measurements confirmed a Faradaic efficiency for **5.1** of 88%, while for **5.2** a lower efficiency of 80% and for **5.3** the highest efficiency of 90% was seen. However, with **5.3**, at lower concentration of proton source in the solution, the efficiency dropped to 57%, which is the least among the three complexes.

Table 5.2. Controlled potential electrolysis (CPE) measurements for hydrogen generation from complexes **5.1, 5.2,** and **5.3**. All measurements were performed in acetonitrile with the indicated addition of water and at -2.3V vs $Fc^{+/0}$, In the presence of 0.1M TBAHFP as supporting electrolyte and 1mM complex.

Compound	Added water (mL)/Concentration (M)	µmol of H_2	FE%
5.1	200/0.25	32.3	77
5.1	800/1.0	42.4	88
5.2	200/0.25	22.7	81
5.2	800/1.0	35.1	80
5.3	200/0.25	9.4	57
5.3	800/1.0	20.4	90
background	***200/0.25***	0	-
	800/1.0	1.3	-

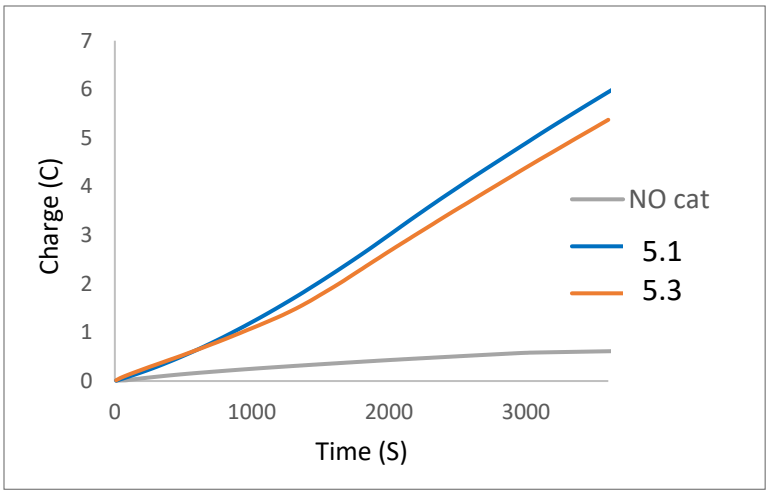

Figure 5.14. Charge versus time for CPE measurements for H_2 generation from water using catalyst **5.1** and **5.3** compared to measurement in the absence of catalyst.

Linear sweep voltammetry experiments were performed to rule out deposition of the catalyst on the surface of the GC electrode**.** A set of linear scans of a solution containing 0.5 mM of Zn complex with 0.1M water and 0.1M TBAHFP in CH_3CN were performed. After these measurements, the electrode was removed, carefully rinsed with clean solvent, and placed in a fresh CH_3CN solution containing 0.1M water and 0.1M TBAHFP and in the absence of complex. A scan of this solution showed no electrochemical activity (Figure 5.15).

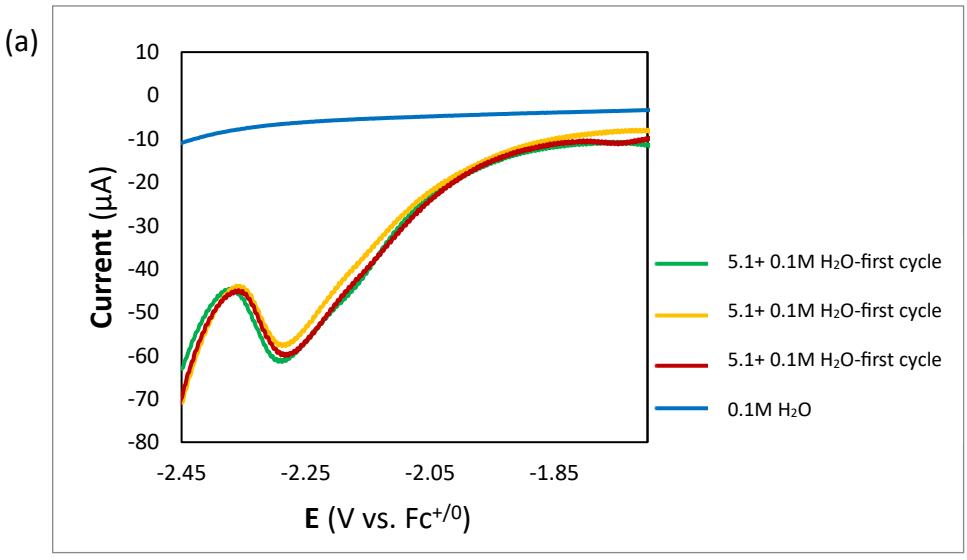

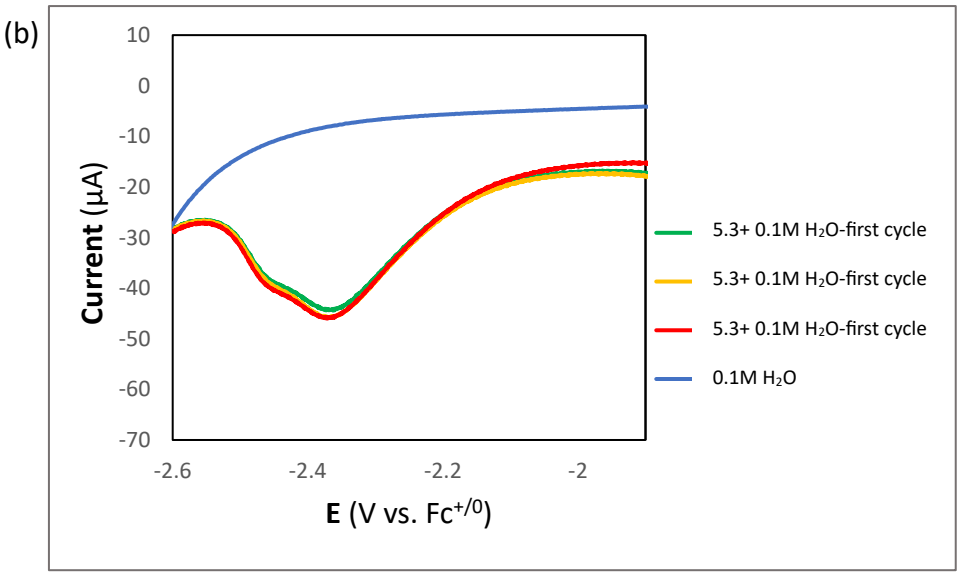

Figure 5.15. Linear Sweep Voltammetry measurements used to demonstrate that the working electrode surface remains clean during catalysis. Scans are shown for (a) **[**Zn(2,6-{Ph_2PNMe}$_2$(NC_5H_3)Br_2] **(5.1)** and (b) [Zn(2,6-{Ph_2PNH}$_2$(NC_5H_3)Br_2] **(5.3)**. In each case repeated linear scans of a solution containing 0.5 mM of Zn complex with 0.1M water in 0.1M TBAHFP in CH_3CN are shown in green, yellow and red. After these measurements, the electrode was removed, rinsed with clean solvent, and placed in a fresh solution containing no Zn complex, 0.1M water and 0.1M TBAHFP in CH_3CN and a scan is shown as blue. Scan rate = 100 mV/s.

The effect of varying the concentration of added water on the catalytic current, i_c, was also examined. Due to the competing reduction of solvent at the electrode potentials required for this reaction, the cathodic potential that allowed the observation a maximum catalytic peak current in the data was not achievable. However, at a fixed voltage of -2.3 V, measurements of the increased catalytic current (i_c) relative to the peak current in the absence of water (i_p) were carried out and this data is shown in Figures 5.16-5.18. At low concentrations, the ratio i_c/i_p, as a function of [H_2O] (Figures 5.16.b, 5.17.b, 5.18.b) displayed a linear increase in the ratio with increasing water concentration. When the [H_2O] is sufficiently large that it remains constant, the catalytic current changed from first to zero order. In this substrate concentration-independent region the current ratio can be approximated by equation 5.4 with R being the ideal gas constant, T the absolute

temperature, F the Faraday constant and v the scan rate used in the cyclic voltammetry measurement in units of V/s.[183] Since two electrons are used in the formation of H_2, n has a value of 2. This analysis allows the calculation of *k*, a value which represents the number of times a catalyst molecule produces a molecule of H_2 per second, or the turnover frequency (TOF) of this catalyst under these conditions. With a scan rate of 0.1V/s the saturation current ratio was measured to be 5 giving a TOF for catalyst **5.1** of approximatley 4.9 s^{-1}. This value drops for **5.2**, 1.7 s^{-1}, and rises for **5.3**, 70s^{-1}.

$$\frac{i_c}{i_p} = \left(\frac{n}{0.4463}\right)\sqrt{\frac{RTk}{Fv}} \qquad (5.4)$$

(a)

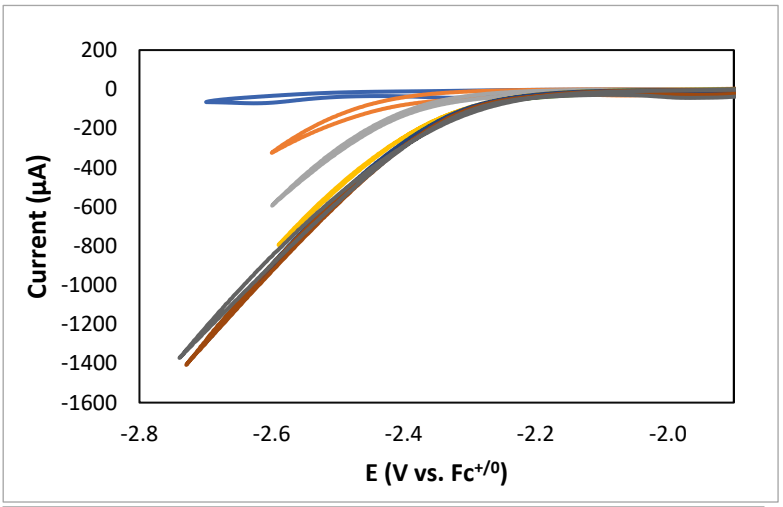

(b)

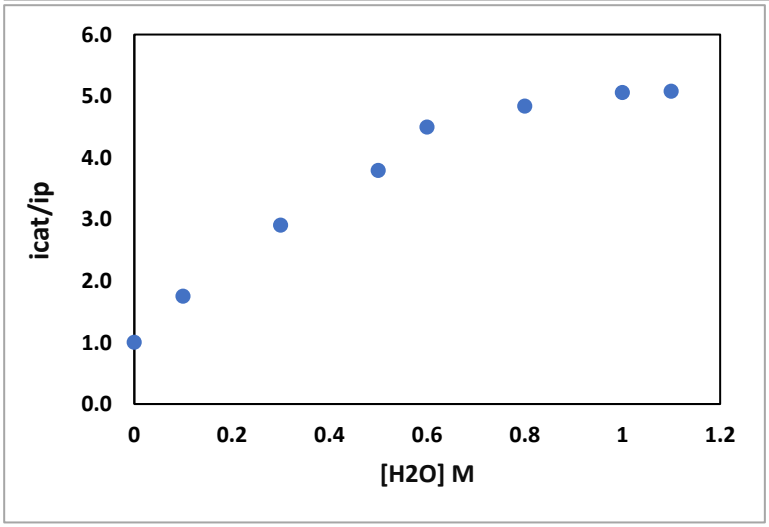

Figure 5.16. (a) Cyclic voltammograms for [Zn(2,6-{Ph_2PNMe}$_2$(NC_5H_3)Br_2] (**5.1**) (1.0 mM) under N_2 (blue) with varying amounts of added water CH_3CN/phosphate buffer (pH = 7) in CH_3CN. Scan rate 100 mV/s with GC working electrode and 0.1 M TBAHFP. (b) Plot of the ratio of the catalytic current (i_{cat}) to the peak current of the reduction at -2.3 V in the absence of water (i_p) as a function of the concentration of water.

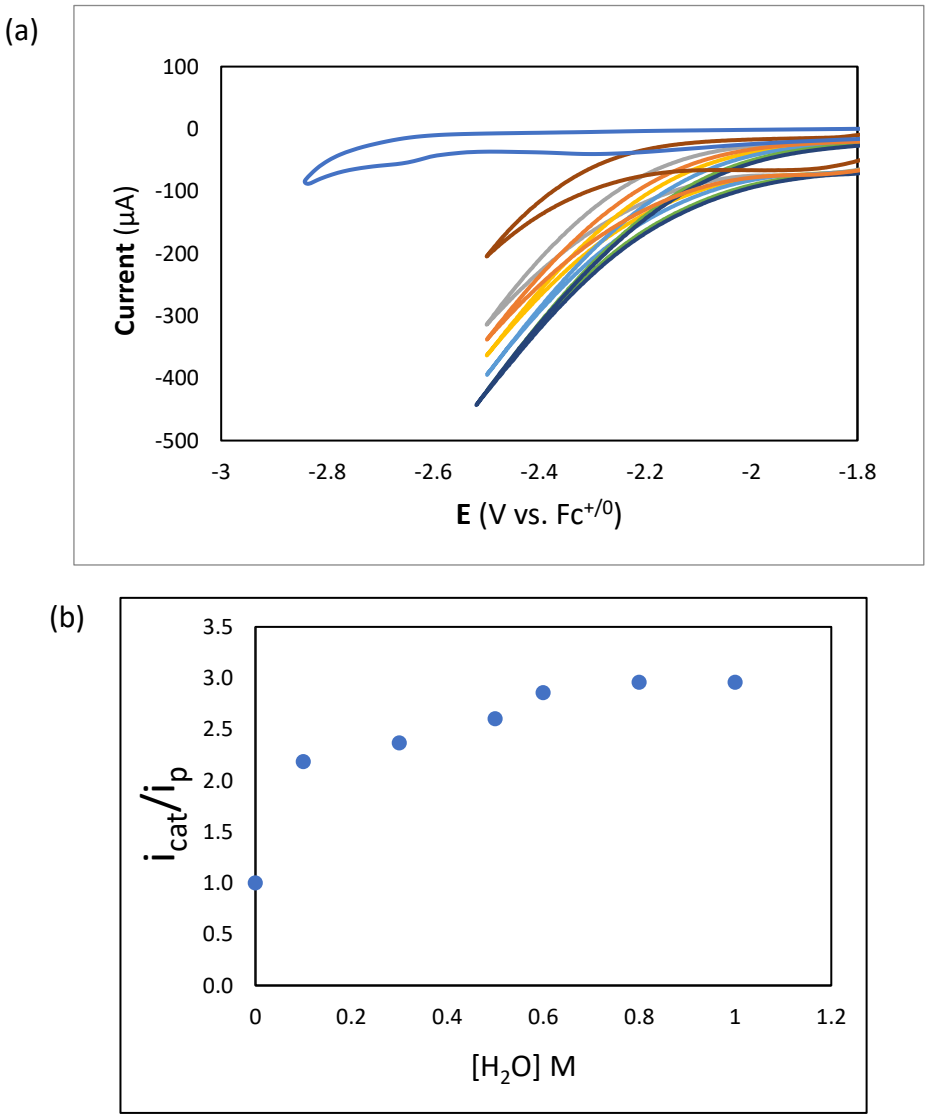

Figure 5.17. a) Cyclic voltammograms of [Zn(2-{Ph_2PNMe}(NC_5H_3)Br_2] **(5.2)** (1 mM) in the absence of water and with varying concentrations of water in CH_3CN with 0.1 M tetrabutylammonium hexafluorophosphate (TBAHFP) supporting electrolyte at 100 mV/s using a glassy carbon (GC) working electrode. (b) Corresponding plot of i_{cat}/i_p vs water concentration**.**

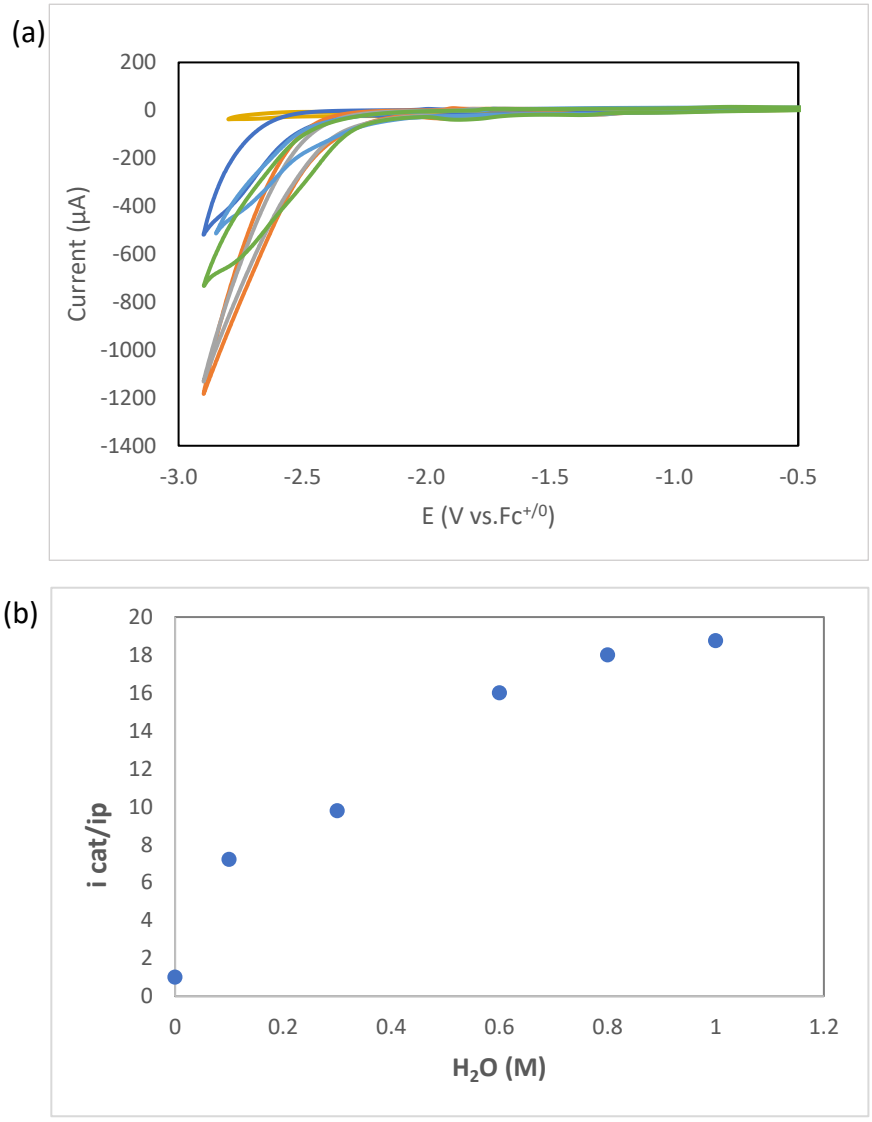

Figure 5.18. a) Cyclic voltammograms of [Zn(2,6-{Ph_2PNH}$_2$(NC_5H_3)Br_2] **(5.3)** in the absence of water and with varying concentrations of water in CH_3CN/phosphate buffer (pH = 7) mixture with 0.1 M tetrabutylammonium hexafluorophosphate (TBAHFP) supporting electrolyte at 100 mV/s using a glassy carbon (GC) working electrode. (b) Corresponding plot of i_{cat}/i_p *vs.* water concentration**.**

5.4.6. Mechanistic Proposals

A mechanistic proposal would begin with the observation that both H_2 generation and CO_2 reduction were associated with the first reduction steps for the starting materials to generate **5.1**$^-$**,** **5.2**$^-$ and **5.3**$^-$ Given that HER is simpler to envision and likely provides a foundation for a mechanistic proposal for the CO_2 reduction, a mechanism for generation of H_2 will be first

proposed. Computational examination of the intermediate species was used to support and illuminate this proposal. While an archetypal electrocatalytic HER mechanism would normally involve formation of a metal-hydride intermediate, formed through combined reduction and protonation of the metal center, the DFT computational analysis of complexes **5.1**$^{-}$**, 5.2**$^{-}$ and **5.3**$^{-}$ indicated that the partially occupied and frontier orbitals for these anionic species were ligand centered and based on π-type orbitals. This suggests that the HER catalysis from **5.1, 5.2,** and **5.3** does not involve the typical metal-H pathway, rather it could involve proton transfer mediated by the reduced ligand. Furthermore, the frontier molecular orbitals (HOMO-2 to LUMO+2) showed no significant Zn contributions. In the case of **5.1**$^{-}$ and **5.3**$^{-}$ protonation of the non-coordinated N_{py} group was computationally optimized and confirmed, by frequency analysis, to be a minimum structure, [Zn(2,6-{Ph_2PNMe}$_2$(***H***NC_5H_3))Br_2] (**(5.1)H**) (Figure 5.19, Table C.10) and [Zn(2,6-{Ph_2PNH}$_2$(***H***NC_5H_3))Br_2] (**(5.3)H**) (Figure C.16, Table C.12). Similarly, complexes **5.2** and **5.3** were protonated at N_{py} and computationally optimized to give [Zn(2-{Ph_2PNMe}(**H**NC_5H_3)Br_2] (**(5.2)H**) (Figure C.15, Table C.11). In **(5.2)H**, the protonation generated a three coordinate Zn(II) center and though Zn commonly exhibits coordination number of four, three-coordinate zinc has been observed. Importantly, alternative protonation sites were explored for both **5.1**$^{-}$**, 5.2**$^{-}$**,** and **5.3**$^{-}$ including protonation at a P center and at the NMe moiety. In all cases, the optimizations did not converge. These results support the redox activity of this PN^3P and PN^2 class of pincer ligands which is currently an open question in the literature.[184, 185] Furthermore, the frontier molecular orbitals (HOMO-2 to LUMO+2) showed no significant Zn contributions.

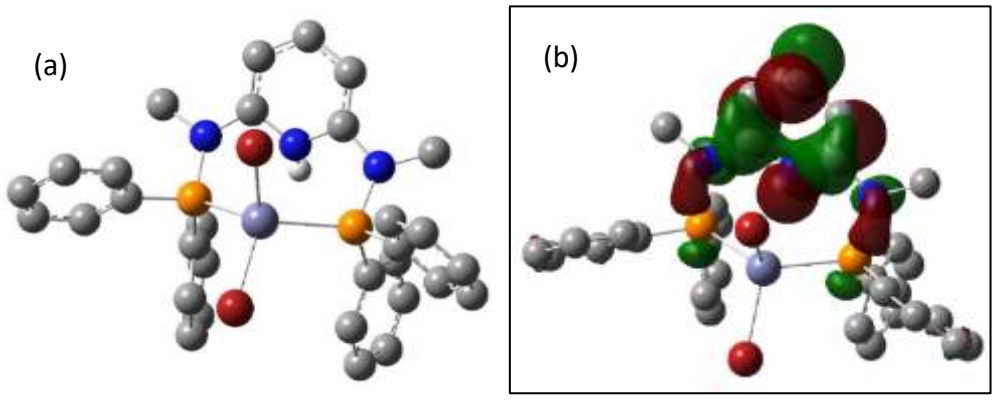

Figure 5.19. (a) DFT optimized structure of the protonated anion [Zn(2,6-{Ph_2PNMe}$_2$(HNC_5H_3))Br_2] (**(5.1)H**) using the B3LYP functional and def2TZVP basis set in acetonitrile (PCM). (b) The SOMO for **(5.1)H**, a π* orbital on py. The major fragment orbital contributions are 0.80 (pyH), 0.08 (NMe), 0.06 (P), 0.05 (Ph). In both figures, hydrogen atoms bonded to C have been omitted for clarity.

A proposed mechanism for the electrocatalytic reduction of water by complexes **5.1** and **5.3** is presented in Figure 5.20. The first step in this proposal is based on a ligand-centered reduction observed for these complexes. The combination of the unbound lone pair on Npy with the increased basicity of the reduced ligand facilitates the abstraction of a proton from water and formation of the protonated pyridyl nitrogen site to yield either **(5.1)H** and **(5.3)H**. The SOMO of this species is a pyridyl π* orbital. This species possesses both an extra electron and a proton, the components that can lead to homolytic (bimolecular) reductive elimination of H_2 and regeneration of the starting material.

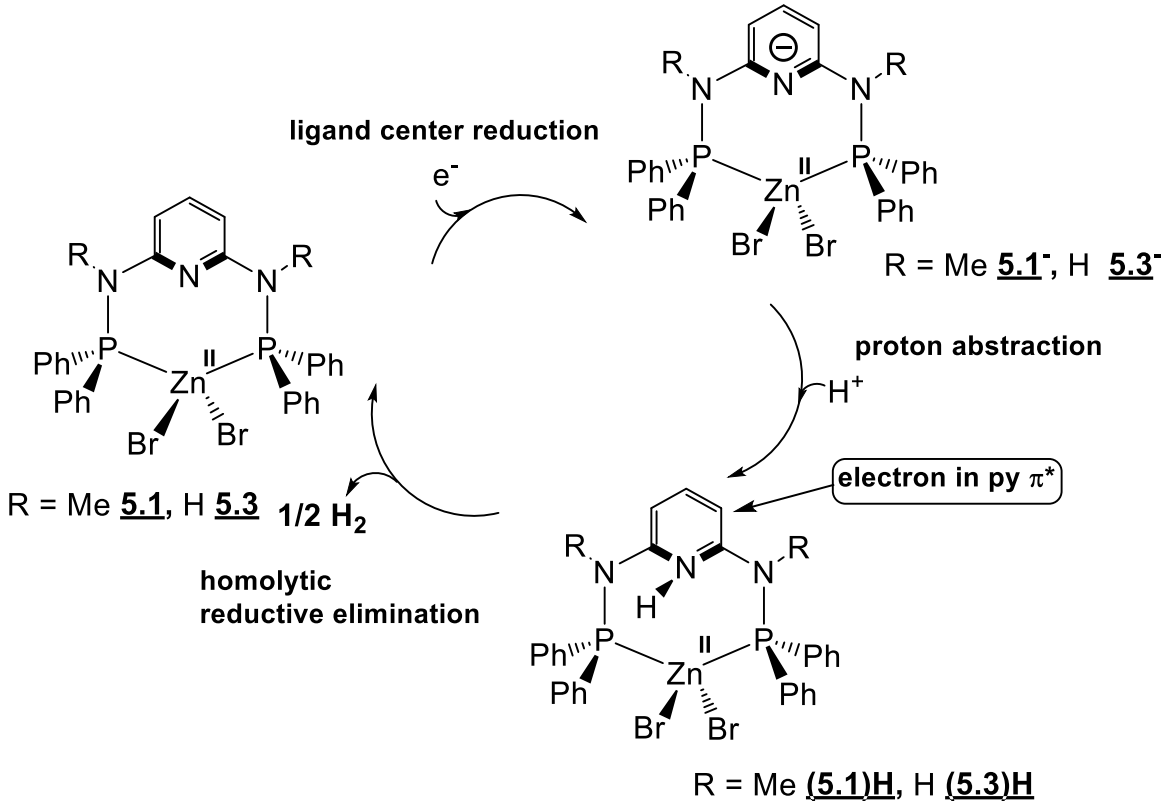

Figure 5.20. Proposed mechanism for catalytic H_2 generation using **5.1** and **5.3** as the catalyst.

Now turning to the mechanism for the electrocatalytic reduction of CO_2 by complexes **5.1** and **5.3,** a proposition is presented in Figure 5.21 which begins with the ligand-centered reduction as previously discussed. The upper portion of this mechanism leads to CO and rests on the proximity of the free pyridyl base and a Lewis acidic Zn center.[171, 173] The increased basicity of the reduced ligand together with the additional coordination by the zinc ion facilitates the binding of CO_2 and formation of pyridyl-N coordinated CO_2 intermediate (**A**).[15, 186] The bound and activated CO_2 could undergo a protonation coupled with reduction, which would lead to a metallacarboxylic acid (**B**). Metallacarboxylic acids are commonly invoked intermediates in reduction of CO_2 to yield CO. Subsequent protonation of the OH function would result in water elimination, release of CO

and closes that leg of the cycle. The proposed intermediates **A** and **B** were supported by successful computational modeling of these species (Figures 5.22, C.17, Tables C.13-C.15).

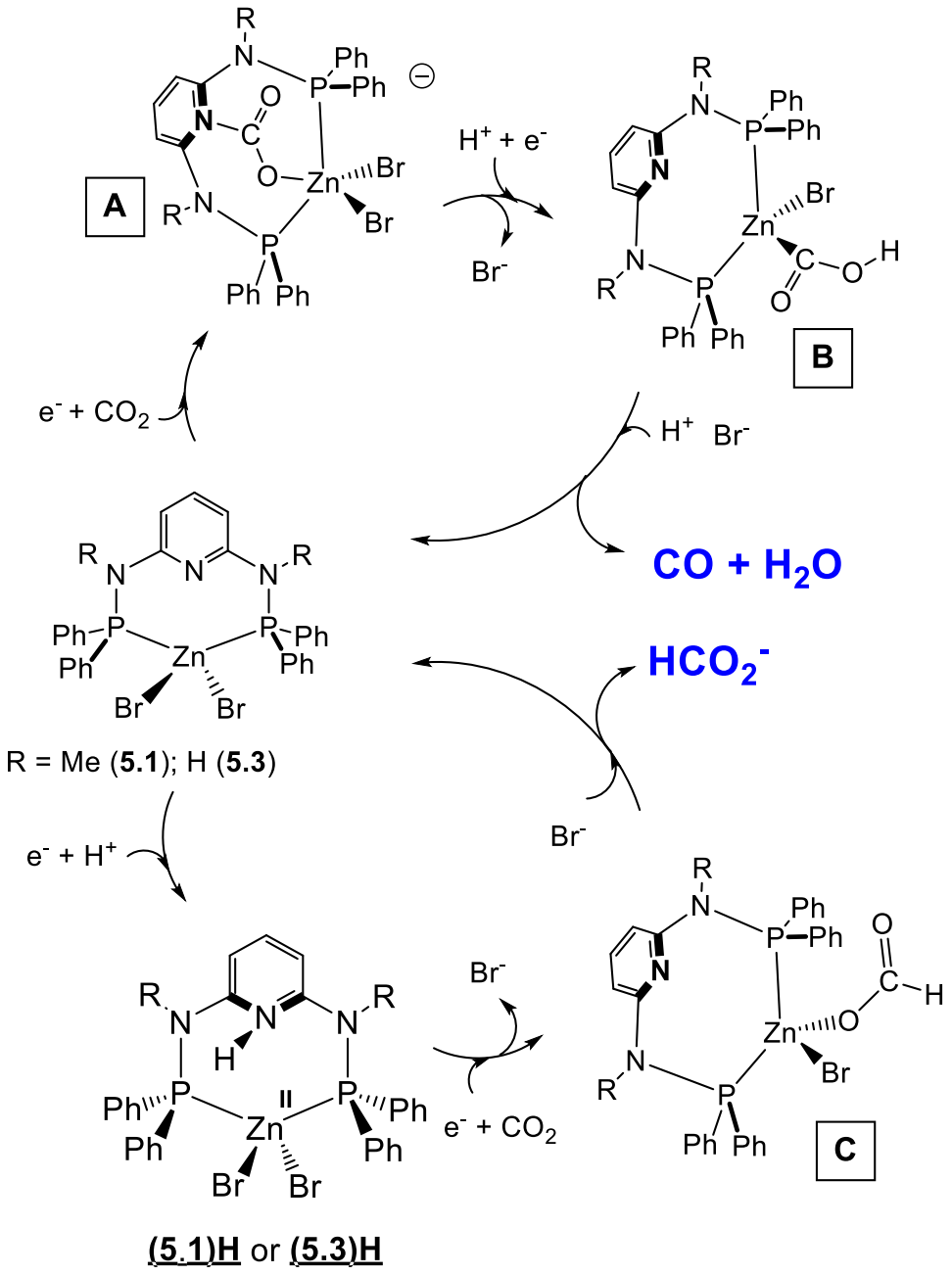

Figure 5.21. A proposed mechanism, supported by computations, for the reduction of CO_2 with complexes [Zn(2,6-{Ph_2PNR}$_2$(NC_5H_3)Br_2] (R =Me, **5.1**; R = H, **5.3**).

The lower portion of this scheme proposes an alternative formate production pathway. As shown in Figure 5.21, first reduction and proton abstraction would produce intermediates **(5.1)H** or **(5.3)H** as in the mechanism of Figure 5.20. Again the proximity of this proton near the Lewis acidic Zn(II) site allows this complex to react via metal-ligand cooperativity to capture a CO_2 and produce the formate complex (**C**), a process with literature precedent.[15, 72] As with intermediates **A** and **B**, support for complex **C** was provided by a successful computational model ((Figure 5.22, Table C.13-C.15) for complex **5.1**) ((Figure C.17, Table C.16) for complex **5.3**). Alternatively, formation of a transient Zn-H species and insertion of CO_2 could result in complex **C**.[172] Release of formate with bromide coordination completes this portion of the cycle.

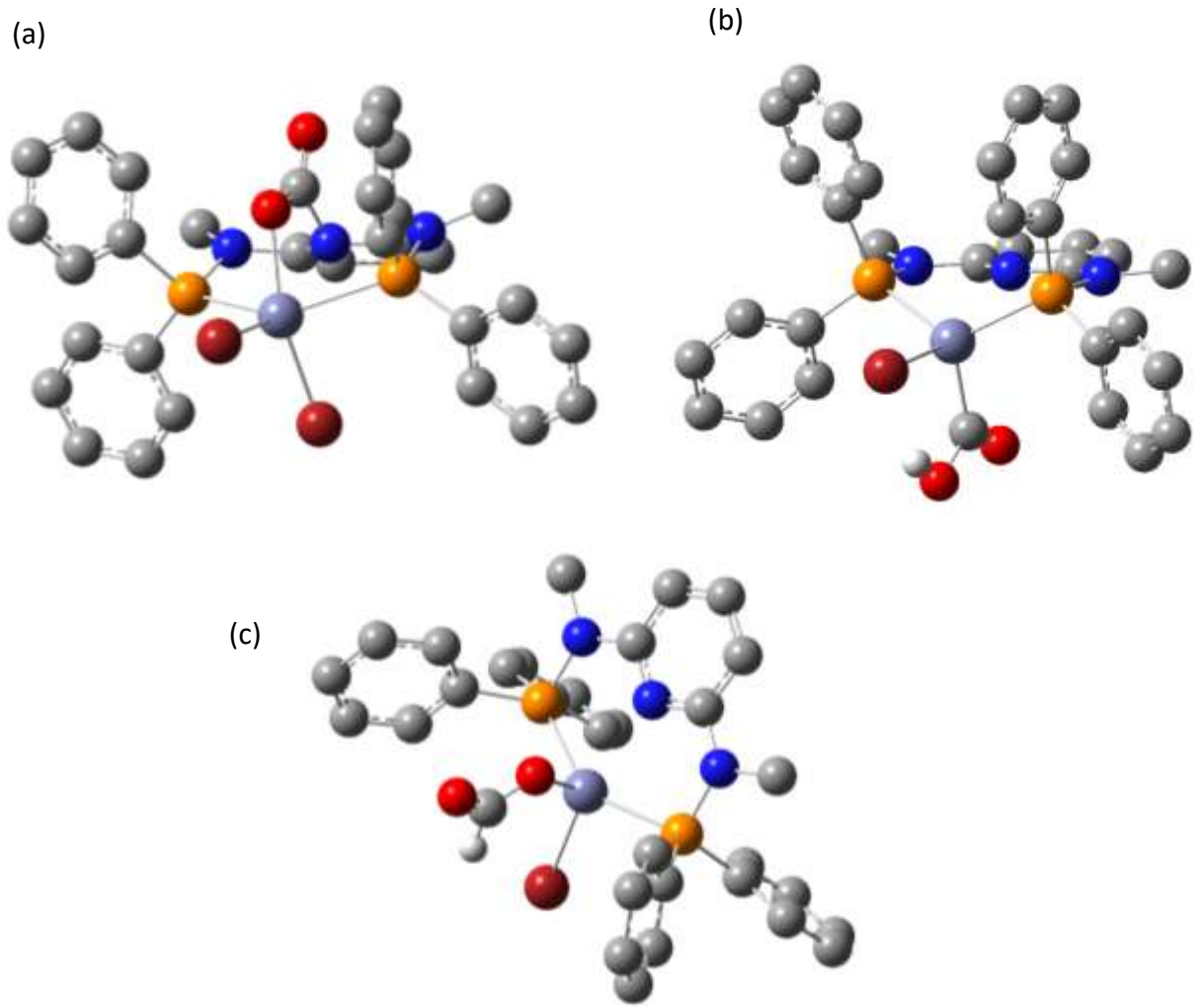

Figure 5.22. DFT optimized structures for the proposed CO_2 intermediates (a) **A**, [Zn(2,6-{Ph_2PNMe}$_2$(NC_5H_3))(CO_2)Br_2] (b) **B**, [Zn(2,6-{Ph_2PNMe}$_2$(NC_5H_3))(CO_2)Br_2] (c) **C**, [Zn(2,6-{Ph_2PNMe}$_2$(NC_5H_3))(HCO_2)Br_2], Structure was derived from compound **5.1**. These results used the B3LYP functional and def2TZVP basis set in acetonitrile (IEFPCM). Hydrogen atoms are omitted for clarity. Frequency analysis confirmed that the optimized structure was a minimum with no imaginary frequencies.

Trial for chemical reduction of complex 5.1:

In addition to computational analysis, we tried to reduce complex **5.1** using potassium as the reducing agent, in the presence of 18-crown-6, in anhydrous dichloromethane, in a glovebox (Scheme 5.2). Based on the ^{1}H and ^{31}P NMR spectrum of the product, there is evidence of ligand being released from the Zn center after the reduction. The ^{1}H NMR spectrum of the product showed two doublets at 6.5 and 6.8 ppm with equal integrations, which we attributed to the hydrogens of the meta position of pyridine (labelled as b and b') (Figure 5.23). Interestingly, these two resonances are similar to the pyridyl group in the parent complex **5.1** (δ 6.5 ppm) and with free ligand (δ 6.8 ppm. On the other hand, the ^{31}P NMR spectrum of the reduced species displayed resonances for both the parent complex and free ligand, at 24.8 and 49 ppm, along with a new signal at 27 ppm (Figure 5.24). Although these experiments are not definitive, these observations suggest that one arm of the ligand becomes unbound after first reduction giving an unsymmetrical anionic complex. Unfortunately, these observations do not provide much insight on the mechanistic features of these reactions.

Scheme 5.2. A proposed chemical reduction reaction of complex **5.1**.

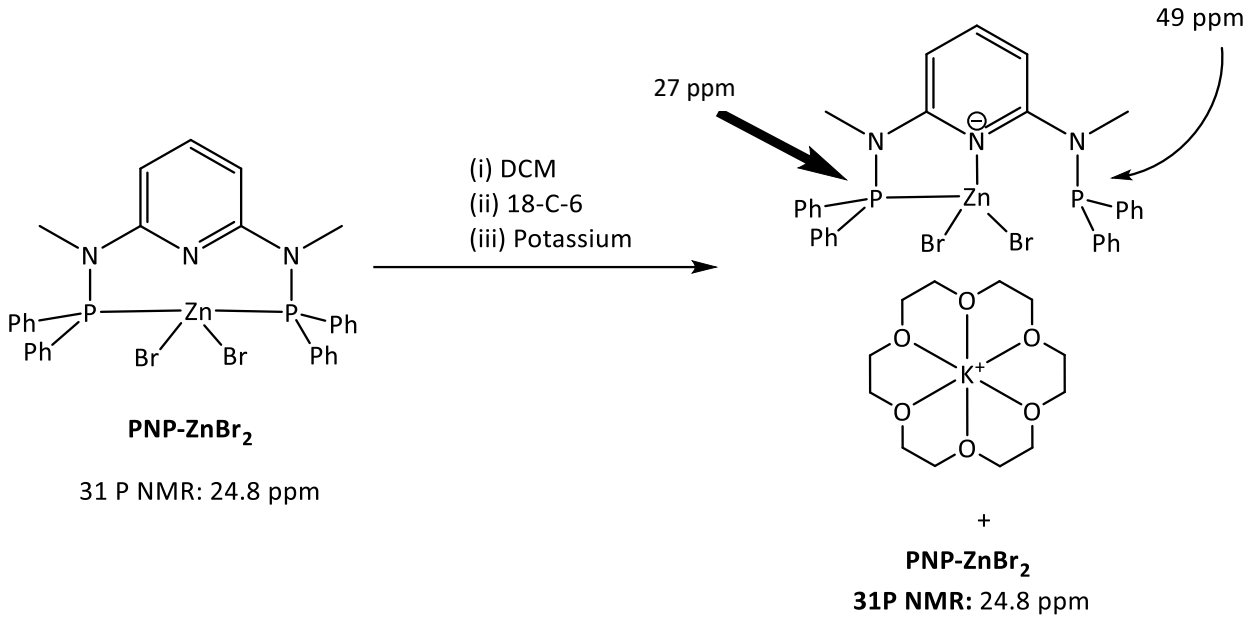

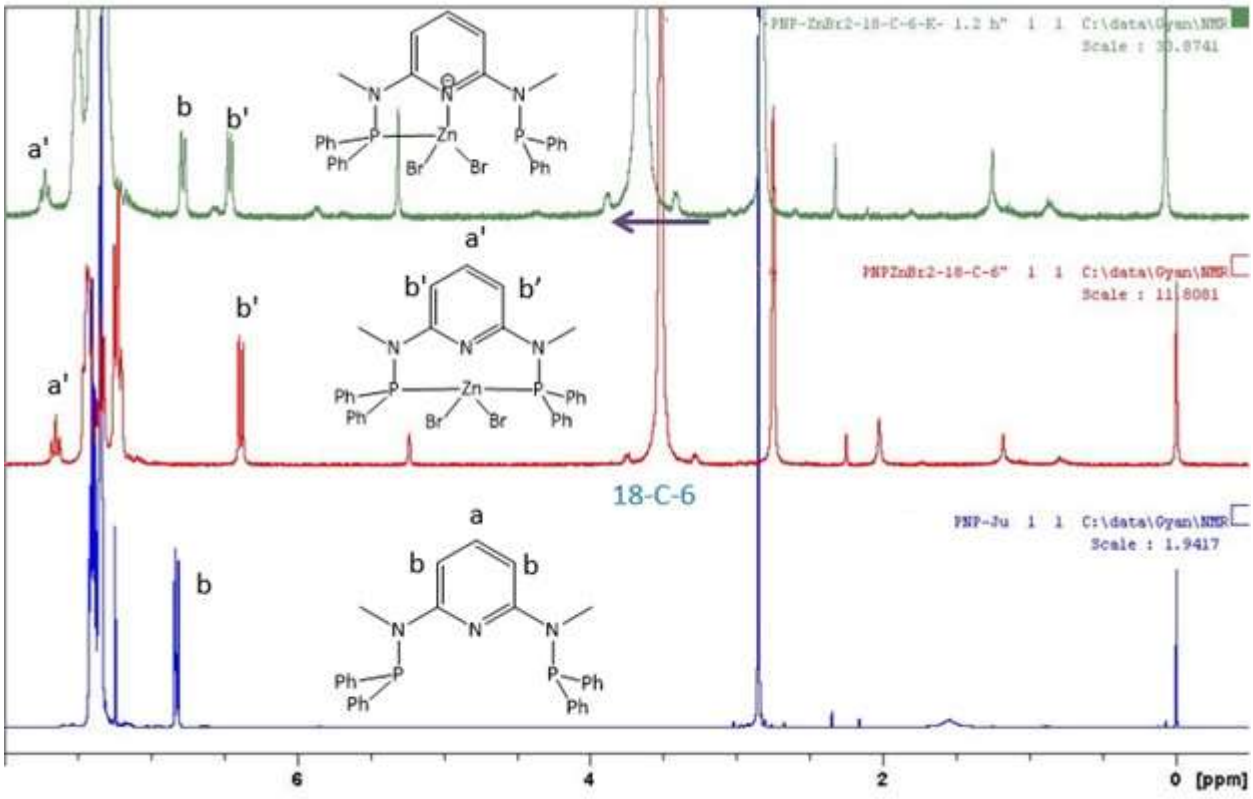

Figure 5.23. ^{1}H NMR spectrum of **reduced 5.1** (top), **5.1** (middle), and ligand (bottom).

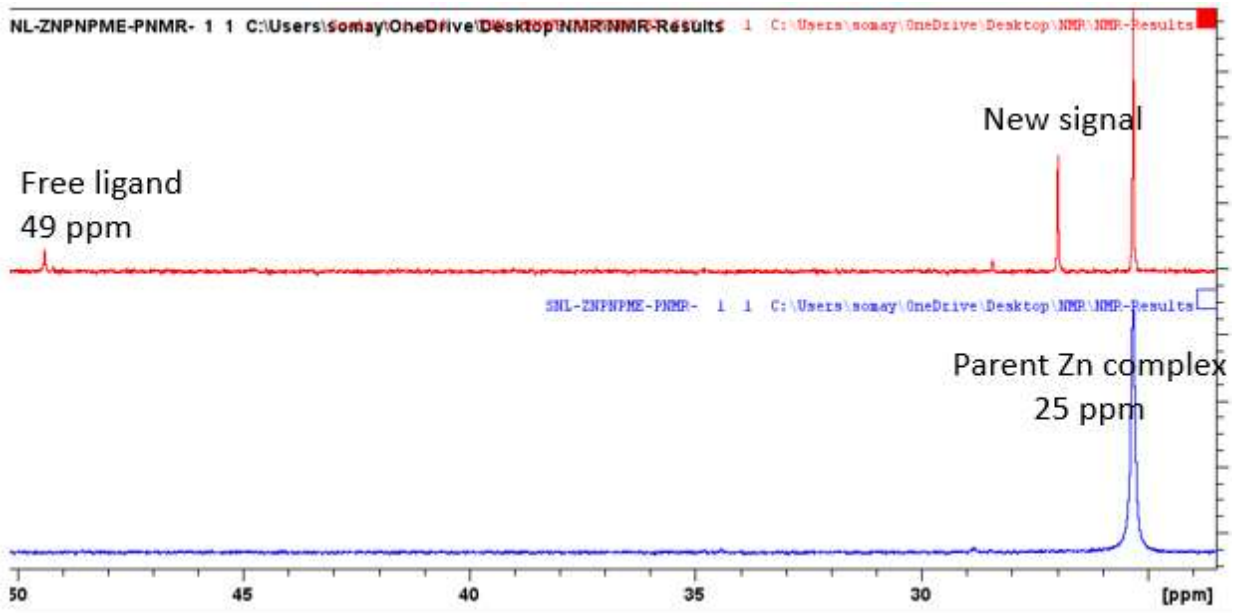

Figure 5.24. ^{31}P NMR spectrum of **reduced 5.1** (top), **5.1** (bottom).

5.5. Conclusion

This report of two unique, multifunctional Zn complexes for catalytic reduction of CO_2 to yield CO and HCO_2^- presents a fundamental process in the transformation of CO_2 into C1 products. Furthermore, these two complexes and a related bidentate "PN" ligand supported complex **5.2** efficiently generated hydrogen gas with neutral water as a feedstock is relevant for a sustainable avenue to this valuable compound and fuel. The observed reactivity is attributed to a metal-ligand synergy between a reduced, basic ligand and the Lewis acidity of the coordinated Zn(II) center. The higher rate of hydrogen production from **5.1** relative to **5.3** may correlate with the greater non-bonded Zn-Npy distance observed for **5.1**. For CO_2 reduction, complex **5.3** more favorably follows reduction at the first step leading to CO formation, while **5.1** undergoes both reduction and protonation at the first step, resulting in formation of both formate and CO. This proposition may, once again, be associated with a weak interaction between the pyridyl N and the Zn(II) center that

was manifest in the shorter Zn-Npy distance observed in the structure of **5.3**. Details provided by computational analysis help to support these propositions.

Our efforts continue to focus on investigating parameters to improve product selectivity, discovery of catalysts that are compatible with aqueous media and on exploring the role of pendant basic sites in bifunctional electroreduction.

5.6. Experimental Section

General Methods. Reactions were performed in a glovebox under a nitrogen atmosphere or using standard Schlenk techniques under an N_2 atmosphere. All solvents were sparged with nitrogen and then dried by passage through a column of activated alumina using an apparatus purchased from Anhydrous Engineering. Deuterated solvents were dried using activated molecular sieves. All other chemicals were purchased from Sigma-Aldrich and used without further purification. Ligands were synthesized based on literature procedures.[117] The complex [Zn(2,6-{Ph_2PNMe}$_2$(NC_5H_3)Br_2] **(5.1)** was prepared as reported.[177] Dried acetonitrile was purchased from Sigma-Aldrich and stored on molecular sieves in a glovebox. ^{1}H, ^{13}C{^{1}H} and ^{31}P{^{1}H} NMR spectra were recorded at 300.0, 75.0 and 121.5 MHz respectively with chemical shifts reported in ppm using the residual protons of the NMR solvent as internal standards. Elemental analysis was performed by Midwest Microlab, LLC, Indianapolis, IN.

X-ray Crystallography: The crystals were mounted on thin glass fibers using paraffin oil. Prior to data collection crystals were cooled to 200.15 K. Data were collected on a Bruker AXS SMART single crystal diffractometer equipped with a sealed Mo tube source (wavelength 0.71073 Å) APEX II CCD detector. Raw data collection and processing were performed with APEX II software package from BRUKER AXS. Semi-empirical absorption corrections based on equivalent reflections were applied. Systematic absences in the diffraction data-set and unit-cell

parameters were consistent with the assigned space group. The structures were solved by direct methods and refined with full-matrix least-squares procedures based on F2, using ShelXL[187] All non-H atoms were refined anisotropically.

Electrochemistry

All cyclic voltammetry experiments have been carried out in a three neck Pyrex cell. Samples were prepared in a glove box and sealed before removing for measurement. Cyclic voltammetry was performed using a VersaSTAT 3 (Princeton Applied Research) potentiostat. A conventional three electrode system was employed. A glassy carbon electrode (diameter = 0.4 cm) was used as the working electrode, a Pt wire as the auxiliary electrode, and an Ag wire was used as a pseudo-reference electrode. Ferrocene was used as an internal standard and added at the end of each experiment. For bulk electrocatalytic reduction experiments, a glassy carbon rod (diameter = 0.4 cm; length 2 cm) was used as the working electrode, a coiled Pt wire as the auxiliary electrode, and an Ag wire was used as a pseudo-reference electrode. The Pt electrode was separated from rest of electrolyte solution by a porous frit. Ferrocene was added as an internal reference after purging with N_2 and measured before and after water addition. Tetrabutylammonium hexafluorophosphate ($(n\text{-}Bu)_4NPF_6$, TBAHFP), the supporting electrolyte, was crystallized two times with dried methanol and dried in vacuum at 90 °C for 24 h before use and stored in the glove box. The electrolyte solution, 0.1 M $(n\text{-}Bu)_4NPF_6$ in CH_3CN, was saturated with N_2 by purging (purity $\geqslant$ 99.8%, BOC gases) for 15 minutes prior to each experiment. The concentration of catalyst was 1 mM (15 mL acetonitrile) in each experiment. Hydrogen production was measured using an Agilent 7820A gas chromatograph equipped with a thermal conductivity detector (TCD) analyzer using an Agilent select permanent gases column. The amounts of CO and H_2 were determined using a calibration curve. The liquid products from bulk electrolysis were analyzed

using ^{1}H NMR. An aliquot (100 µL) was removed from the electrochemical cell and was mixed in an NMR tube with D_2O containing a known amount of dimethyl sulfone (DMS) (400 µL) as internal standard. The sample was mixed well and the ^{1}H NMR spectra were collected. Using the ratios of the integrated values for the formic acid ($\delta \approx 8.3$ppm) and integrated values of DMS, the amount of formic acid was determined.

Computational Details: Optimized structures were obtained from density functional theory (DFT) computations using the Gaussian 09 package.[188] The B3LYP functional and def2TZVP basis set was used for all atoms. The initial optimizations began with the experimental X-ray structure as input. Optimizations for the subsequent reduction steps to generate anions began with the optimized structure from the preceding species. All optimizations used the PCM model for solvation with acetonitrile as the solvent. Frequency analysis confirmed that the optimized structures were minima with no imaginary frequencies. The canonical molecular orbitals and fragment orbital compositions were generated using the Chemissian program.

Ligand Syntheses

Synthesis of N-(diphenylphosphino)-2-methylaminopyridine (PN-Me):

A solution of 1.08 g (10.0 mmol) of 2- (methylamino)pyridine in 25 mL of diethyl ether was cooled to −78 °C. n-BuLi (10 mmol, 1.6 M in hexane, 6.25 mL) was added dropwise and the solution was stirred for 2 h. A solution of PPh_2Cl (10 mmol, 2.2 g) in 10 mL diethylether was added dropwise and the solution was allowed to warm at room temperature. This reaction mixture was stirred overnight. The reaction mixture was filtered twice and the solvent was removed to give a colorless liquid which was further kept under vacuum for 24 h at room temperature to give colorless solid. Yield; 2.28 g (78%).^{1}H NMR (162 MHz, CDCl3): δ = 2.96 (3H, d, J = 1.56 Hz), 6.75−6.79 (m, 1H), 7.39−7.55 (m, 12 H), 8.28−8.30 (m, 1H). $^{13}C\{^{1}H\}$ NMR (100 MHz, $CDCl_3$):

δ = 34.1 (d, J = 8.6 Hz), 110.5 (d, J = 41.4 Hz), 114.6 (d, J = 1.0 Hz), 128.4 (d, J = 5.8 Hz), 129.0, 131.9 (d, J = 20.4 Hz), 136.6 (d, J = 14.8 Hz), 137.0 (d, J = 3.0 Hz), 147.6 (d, J = 1.7 Hz), 161.3 (d, J = 26.9 Hz). $^{31}P\{^{1}H\}$ NMR (162 MHz, $CDCl_3$): δ = 51.0.

Synthesis of N,N′-bis(diphenylphosphino)-2,6-di(methylamino)pyridine (PN^3P-Me): n-Butyllithium (1.6 M in hexane, 8.0 mmol, 5.0 mL) was dropwise added to a toluene (100 mL) solution of N,N'-dimethyl-2,6-diaminopyridine (1.0 g, 7.3 mmol) cooled in an ice-salt bath. The mixture was stirred at room temperature for 2 h and was then cooled to –78 °C using a dry ice-acetone bath. To this mixture 1.3 mL (7.3 mmol) of chlorodiphenylphosphine was added. The resulting reaction mixture was stirred for 2 h at room temperature and refluxed for 18 h. The solution was cooled to room temperature and filtered twice with a frit. The above procedure was then repeated with the resulting yellow solution. After filtering, the solvent of resulting reaction mixture was removed under vacuum yielding a yellow oil. This oil was dissolved in acetonitrile and the mixture was heated to reflux for 10 minutes. Upon cooling at room temperature, a white precipitate formed. The acetonitrile was decanted off and the compound was dried under vacuum. Yield: 1.70 g (46%). ^{1}HNMR (162 MHz, $CDCl_3$): δ = 2.92 (6H, d, J = 1.72 Hz), 6.90 (dd, 2H, J = 2.44, 8.04), 7.38−7.49 (m, 21 H). $^{13}C\{^{1}H\}$ NMR (100 MHz, $CDCl_3$): δ = 33.9 (d, J = 8.6 Hz), 99.7 (d, J = 21.1 Hz), 128.3 (d, J = 5.8 Hz), 128.7, 132.0 (d, J = 20.7 Hz), 137.4 (d, J = 15.8 Hz), 138.2 (t, J = 3.2 Hz), 159.5 (dd, J = 2.08, 27.2 Hz). $^{31}P\{^{1}H\}$ NMR (162 MHz, $CDCl_3$): δ = 49.5.

N,N′-bis(diphenylphosphino)-2,6-diaminopyridine (PN^3P-H): 20 mmol (2.18 g) of 2,6-diaminopyridine was dried overnight in a Schlenk flask, transferred to the glove box and 40 mL of THF was added. The flask was taken from the glove box and connected to Schlenk line to purge with N_2 and cooled to -70 °C. 44 mmol of triethylamine (Et_3N) was dissolved in 10 mL THF and was added dropwise to the solution. 44 mmol (2.1 equivalent) of chlorodiphenylphosphine

(PPh_2Cl) in 10 mL THF was added dropwise over 10 minutes with stirring. The solution was allowed to warm to room temperature and set to reflux overnight. Then, the solution was transferred to glove box and filtered, washed with anhydrous hexane for three times. The solvent was removed under vacuum to afford the ligand. The ligand was stored in the glovebox. Yield: 87%. ^1H NMR (162 MHz, $CDCl_3$): δ(ppm) = 7.82-7.62 (m, 9H), 7.61-7.54 (m, 3H), 7.53-7.40 (m, 8H), 7.40-7.27 (m, 3H), 3.78-3.49 (br s, 2H, NH). $^{31}P\{^1H\}$ NMR (162 MHz, DMSO): δ(ppm) = 25.46 (s, PN). MS-ESI: (m/z): 478.4. Elemental analysis calculated for $C_{29}H_{25}N_3P_2$ (Mw. 477.1): C, 72.95; H, 5.28; N, 8.80. Found: C, 72.65; H, 5.03; N, 8.56%.

Complex Syntheses

Synthesis of [Zn(2,6-{Ph_2PNMe}$_2$(NC_5H_3)Br_2] (5.1): A solution of ligand N,N′-bis(diphenylphosphino)-2,6-di(methylamino)pyridine (0.202 g, 0.4 mmol) in 5 mL of toluene was added to a toluene suspension of $ZnBr_2$ (0.089 g, 0.4 mmol) in a glove box. The reaction mixture was stirred for 16 h at room temperature under N_2. The resulting mixture was then kept in the refrigerator and colourless precipitate was removed by filtration to give complex **5.1**. Single crystals were grown by slow diffusion of hexane into a concentrated solution of the complex in dichloromethane. Yield 0.236 g (81%). ^1H NMR (300 MHz, $CDCl_3$): δ = 2.85 (s, 6H, CH_3), 6.46 (d, 2H, J = 8.10 Hz), 7.26−7.41 (m, 13H), 7.52−7.58 (m, 7H), 7.70 (t, 1H, J = 8.1 Hz). $^{13}C\{^1H\}$ NMR (75 MHz, $CDCl_3$): δ = 33.1 (t, CH_3, J = 2.9 Hz), 99.6, 128.2 (t, J = 15.5 Hz), 128.8 (t, J = 4.7 Hz), 131.1, 133 (t, J = 7.3 Hz), 141.6 (t, J = 2.2 Hz), 156 (t, J = 6.8 Hz). $^{31}P\{^1H\}$ NMR (121.5 MHz, $CDCl_3$): δ = 22.5. Elemental Analysis calculated for $C_{31}H_{29}Br_2N_3P_2Zn$: C, 50.95; H, 4.00; N, 5.75. Found: C, 51.28; H, 4.33; N, 5.49.

Synthesis of [Zn(2-{Ph_2PNMe}(NC_5H_3)Br_2] (5.2): A solution of ligand N,N-bis(diphenylphosphino)-2- (methylamino)pyridine (0.392 g, 1.0 mmol) in 10 mL of toluene was

added to a toluene suspension of $ZnBr_2$ (0.225 g, 1.0 mmol) in a glove box. The reaction mixture was stirred for 16 h at room temperature under N_2. 50 mL of hexane was added to the resulting mixture and colourless precipitate was removed by filtration to give complex 2. Single crystals were grown by slow diffusion of hexane into a concentrated solution of the complex in dichloromethane. Yield 0.561 g (91%). ^{1}H NMR (400 MHz, $CDCl_3$): δ = 3.65 (d, 3H, CH_3, J = 3.6 Hz), 7.00 (d, 1H, J = 8.68 Hz), 7.10 (t, 1H, J = 6.38 Hz), 7.51−7.62 (m, 6H), 7.72−7.78 (m, 4H), 7.89 (t, 1H, J = 8.08 Hz), 8.42 (d, 1H, J = 2.66 Hz). ^{13}C{^{1}H} NMR (100.7 MHz, $CDCl_3$): δ = 34.3 (d, CH_3, J = 6.26 Hz), 110.2 (d, J = 2.08 Hz), 117.4 (d, J = 2.86 Hz), 125.8 (d, J = 36.36 Hz), 129.6 (d, J = 10.32 Hz), 132.5 (d, J = 1.68 Hz), 133.3 (d, J = 15.32 Hz), 142.4, 147.2 (d, J = 4.16 Hz), 156.9 (d, J = 11.88 Hz),. ^{31}P{^{1}H} NMR (162 MHz, $CDCl_3$): δ = 27.7. Elemental Analysis calculated for $C_{18}H_{17}Br_2N_2PZn$: C, 41.78; H, 3.31; N, 5.41 Found: C, 41.87; H, 3.04; N, 5.63

Synthesis of [Zn(2,6-{Ph_2PNH}$_2$(NC_5H_3)Br_2] (5.3): 0.24 g (0.5 mmol) of N,N′-bis(diphenylphosphino)-2,6-diaminopyridine in 5 mL in dichloromethane was added to 0.12 g (0.5 mmol) of $ZnBr_2$ in THF under N_2 and the solution was stirred overnight. Hexanes was then added, and a white precipitate formed and was collected. The precipitate was further washed with hexanes and then dried on a rotary evaporator. Yield was 70% (0.245 g, 0.35 mmol). Solid was then crystallized by dissolving in 1:1 CH_3CN:EtOH and diffusion of ether. ^{1}HNMR (162 MHz, d-DMSO): δ(ppm): 7.4(m, 8H), 7.3 (m, 13H), 7.2 (2H, t), 6.25 (2H, d) ^{31}P{^{1}H} NMR (162 MHz, d-DMSO): δ(ppm): 22.6

Chapter 6: Electrocatalytic reduction of nitrite by Ni(II) diaminopyridine complexes

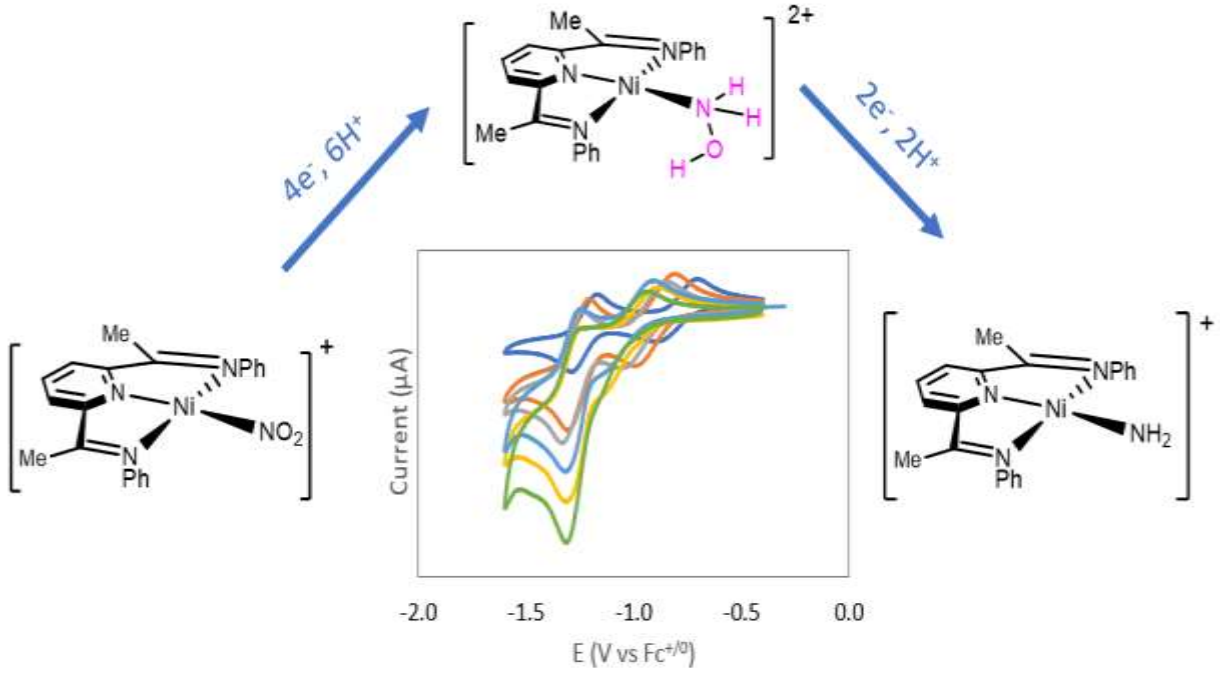

6.1. Preamble and Context

The nitrite reduction project is a new endeavour for our group that was initiated by Somayeh Norouziyan (SN). The process design, product analysis, and measurement techniques were investigated and refined by SN with the feedback from Dr. Darrin Richeson (DR). Computational work was performed by DR. The manuscript of this project is under preparation.

6.2 Abstract

Excess nitrite anions, of anthropogenic origin, in the environment disrupt the nitrogen cycle, making the electrocatalytic reduction of nitrite a significant objective. Two homogeneous Ni(II) complexes bearing a diaminopyridine ligand, $NiBr_2$-2,6-bis[(1-phenylimino)ethyl]pyridine (**6.1**) and $NiBr_2$-2, 6-bis{1-[(2,6-diisopropylphenyl)imino]-benzyl}pyridine (**6.2**) were discovered to be effective and selective for the electrocatalytic reduction of nitrite to ammonium ion and hydroxylamine using a (50/50) V/V mixture of acetonitrile/water solutions. Catalysis was observed by cyclic voltammetry at a halfwave potential of $E_{1/2} = -1.2$ V vs $Fc^{0/+}$ (0.1M TBAHFP) when the Ni complex, nitrite, and 4-morpholinepropanesulfonic acid (MOPS) buffer were present. Controlled potential coulometry at potentials -1.4 V vs $Fc^{0/+}$ in buffer yielded ammonium as the major product with good Faradaic efficiencies. The Ni complex with bulkier substitutions on the ligand displayed a higher selectivity for NH_4^+/NH_2OH. A computational examination of the catalytic mechanism of the Ni complex was used to support and elucidate the proposed chemical steps, provide some energetic details of the electron and proton transfers, and present a rationale for the selectivity of this reduction.

6.3. Introduction:

The Haber-Bosch process represents a milestone in the history of chemistry, providing mankind with a plentiful and inexpensive supply of fertilisers. Yet, growing evidence from environmental science research indicates that the excessive use of fertilisers, along with fossil-fuel combustion, has caused alarming imbalances in the nitrogen cycle, leading to NO_x accumulation in groundwater and coastal areas.[86, 189]

Nitrite is formed as an intermediate species in the biological nitrification process that converts ammonia to nitrate.[190] High nitrite concentrations are a serious water quality concern because of

its high toxicity to humans, plants, and animals.[191, 192] This environmental issue calls for efficient denitrification strategies ancillary to the widespread biological denitrification.[193, 194]

Electrocatalytic denitrification is a very promising alternative to transforming groundwater contaminants into useful products such as hydroxylamine (NH_2OH) and ammonia (NH_3) or removal by forming dinitrogen (N_2).

However, selective nitrite reduction is difficult.[86, 195] Multiple nitrite reduction products exist (equation 6.1 and 6.2), many of which have similar reduction potentials.

$$NO_2^- + 2H^+ + 1e^- \rightarrow NO + H_2O \qquad (6.1)$$
$$NO_2^- + 8H^+ + 6e^- \rightarrow NH_4^+ + 2H_2O \qquad (6.2)$$

Although nitrite can be electrochemically reduced on heterogeneous metal electrodes, catalysis is plagued by high overpotentials and low product selectivity. Moreover, catalytic activity and selectivity are strongly dependent on the electrolyte composition and pH. In this context, the amenability of molecular complexes to rational design makes them attractive for creating electrocatalysts having improved selectivity and greater efficiency.

The mechanistic control of appropriately designed molecular catalysts offers mean to address these issues. However, there are few examples of molecular electrocatalysts for nitrite reduction (Table 6.1), and very little is known about their reaction mechanisms.

The most well-investigated electrocatalyst is $[Co(cyclam)Cl_2]^+$, which produces hydroxylamine as the principal reduction product, although activity is only observed at a mercury pool working electrode and in basic media.[85] By contrast, [Co(2-TMPyP)] (2-TMPyP =tetrakis(N-methyl-2 pyridyl)porphine)[89] and $[Fe(H_2O)(TPPS)]^{3-}$ (H_2TPPS^{4-} =tetraanionic form of meso-tetrakis(*p*-sulfonatophenyl)porphyrin)[196] reduces NO_2^- to NH_3 and NH_2OH but only in acidic media; while the macrocyclic $[Fe(N_5H_2)Cl_2]^+$ (N_5H_2=pentadentate macrocycle 2,13-dimethyl-3,6,9,12,18-

pentaazabicyclo[12,3,1]octadeca-1(18),2,12,14,16-pentaene) catalyst efficiently reduces NO_2^- to NH_2OH and ammonium at near neutral pH (7.2) at -0.98 V vs Ag/AgCl.[7] In this work the importance of buffer was noted as a key to support the catalysis through pH control.

Nitrite electrocatalytic reduction is almost exclusively reported in aqueous solution with only one report in which a nonaqueous solvent was used.[197] Heterobimetallic CoMg complexes supported by diimine−dioxime ligands are reported to reduce NO_2 to N_2O selectively in organic solvent (CH_3CN) using Et_3NHCl as a proton source and [n-Bu_4N][NO_2] as the substrate. In this report the focus was on facilitating the binding of NO_2^- to the metal center and our strategy was to use an additional Lewis acidic site (Mg^{2+}) to enhance the binding affinity of NO_2^- to a low-valent Co center by analogy to the proposed role of the active-site histidine residues in nitrite reductases.

While these examples hint at a flexibility in design strategies, the structural diversity of these catalysts makes it difficult to elucidate features that are beneficial for NO_x^- reduction. However, in some of these reports it is concluded that use of redox non-innocent ligands with hydrogen-bonding functionality and flexibility in coordination mode is a key in this chemistry.[7, 87] For example, in one report,[88] an experimental and computational study revealed that the ligand 2,3-dimethyl-1,4,8,11-tetraazacyclotetradeca-1,3-diene (DIM) plays an important role by directly transferring a single electron to the bound nitrite substrate and providing intramolecular proton transfer from an amine group of the macrocycle to a nitro ligand to facilitate the key N−O bond cleavage step.

Based on these criteria, we identified the previously reported complex, [Ni(DIMPY)Br_2], as possessing some of the necessary attributes for the electrocatalytic reduction of nitrogen oxyanions.[198] The pyridinediimine moiety of this ligand provides redox non-innocent functionality which can accelerate the catalytic reaction by getting involved in the redox

reaction.[47, 137] In this chapter, using both experimental and computational studies we report on the ability of [Ni(DIMPY)Br$_2$] to facilitate the electrocatalytic reduction of NO_2^- to NH_2OH and NH_4^+. We also studied the effect of bulkier substituents on this catalysis. It is worth noting that this catalyst is among the first nitrite reduction catalysts with Ni as the metal center.[85]

Table 6.1. Homogeneous nitrite reduction catalysts.

Catalyst	Metal center	Product Selectivity	Applied Potential (V) (reference)	Other comments	Ref.
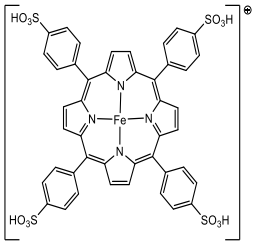	Fe(III)	NH_4^+ Up to 97%	-0.9 (SCE)	Water, pH = 6.7 phosphate buffer, Hg electrode	[196]
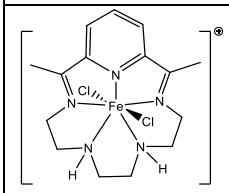	Fe(III)	NH_2OH, 91% NH_4^+, 8%	-0.98 (Ag/AgCl)	MOPS buffer pH 7.2, Hg electrode linear dependence on [MOPS], [Fe], and [NO_2^-]	[7]
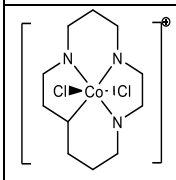	Co(III)	NH_2OH, 73% NH_4^+, 6%	-1.5 (SCE)	Hg electrode, 3M NaOH, efficiency/selectivity dependent on electrode and applied potential	[199]
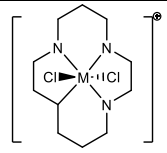 M = Co, Ni	Co(III) Ni(II)	NH_2OH	-1.5 (SCE)	Hg electrode	[85]
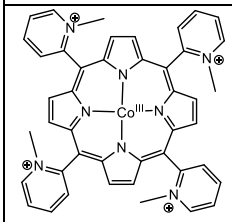	Co(III)	NH_2OH, 80% NH_4^+, 15%	-0.7 (Ag/AgCl)	pH = 5 buffer, glassy C electrode	[89]

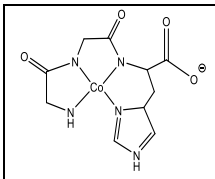	Co(III)	NH_4^+, 90%	−0.90 (Ag/AgCl)	1M MOPS buffer, pH = 7.2, Hg electrode, TON =3550 ± 420 over 5.5 h	[200]
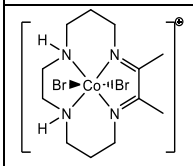	Co(III)	NH_3, 88%	-1.05V (SCE)	Aqueous	[87, 201]
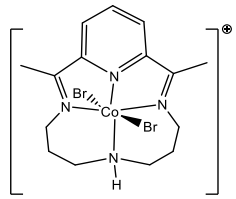	Co(III)	NH_4^+, 88%	-1.46 V (SCE)	initial pH 6.40	[88]
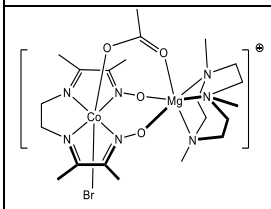	Co(III)	N_2O	-1.2V (SCE)	acetonitrile, glassy C electrode, NEt_3H^+ as proton source	[197]
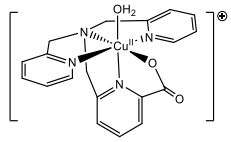	Cu(II)	NO	-0.91V ($Fc^{+/0}$)	glassy-carbon-foil electrode also contained 5 mM benzoic acid and 5 mM TBA-NO2.	[202]
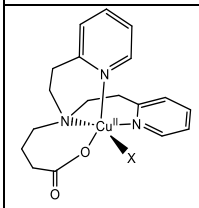	Cu(II)	NO 94-15 depend on ligand features	0.010V (Ag/AgCl)	0.1 M HEPES buffer (pH 7.4), 0.1 M NaCl, Pt disk working electrode	[203]
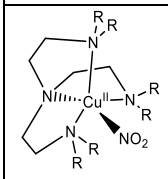	Cu(II)	NO, N_2O	Vary		[204]

6.4. Results and Discussion

6.4.1. Synthesis and Characterization

The two Ni complexes were synthesised through direct ligand addition to $NiBr_2$ in toluene at room temperature. The resulting orange (**6.1**) and yellow (**6.2**) powders were isolated by filtration in 88% (**6.1**) and 68% (**6.2**) yield and recrystallized from CH_2Cl_2. The molecular structures of these compounds were confirmed through NMR and single crystal X-ray analysis.

Scheme 6.1. Reaction scheme for the synthesis of NiDIMPY complexes.

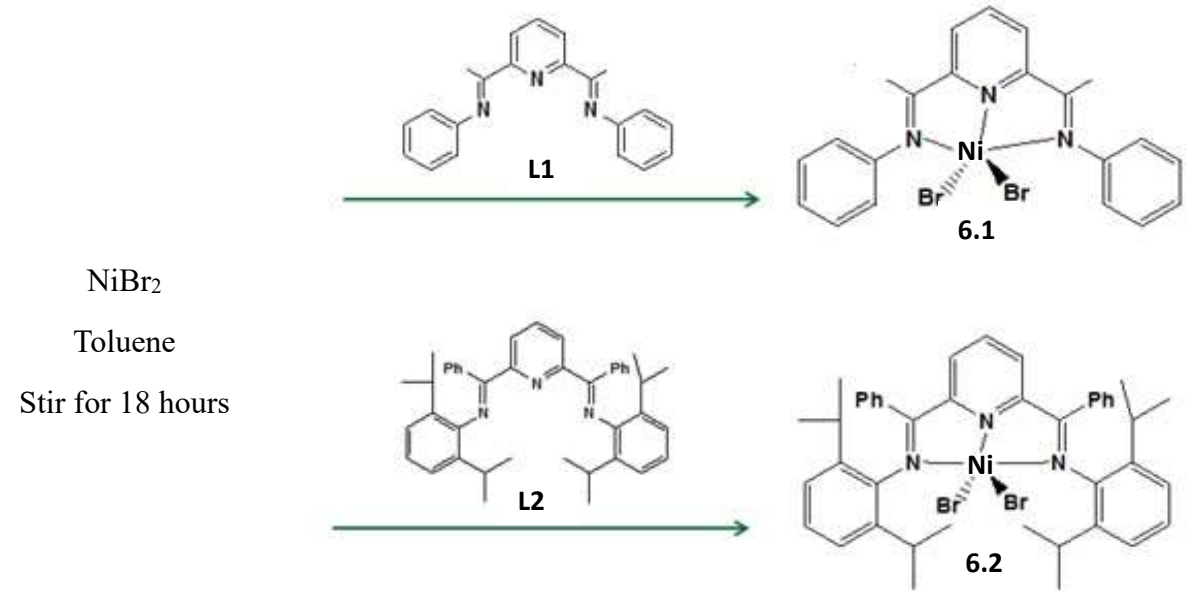

While in the solid state compound **6.1** and **6.2** were paramagnetic, consistent with a five coordinate Ni(II) center, diiminopyridine Ni(II) dihalo complexes are documented to autoionize in polar solvents to yield low spin diamagnetic, square planar d^8 species.[47, 137, 140] In fact, compounds **6.1** and **6.2** displayed diagnostic NMR spectra indicative of a symmetrical ligand coordinated with the structure $[Ni(\kappa^3\text{-}2,6\text{-}\{PhNCMe\}_2(NC_5H_3)Br]^+$ (**6.1'**$^+$) and structure $[Ni(\kappa^3\text{-}2,6\text{-}\{iprPhNCPh\}_2(NC_5H_3)Br]^+$ (**6.2'**$^+$) as represented in Scheme 6.2. Support for these observations came when attempts to computationally optimize structures **6.1** and **6.2** (DFT, B3LYP, def2-TZVP) using the PCM model for solvation in acetonitrile resulted in spontaneous dissociation of one of

the Br^- ligands and rearrangement of the Ni center to a square planar geometry. As a result, the dissociated bromide was removed, which resulted in an optimized cationic square planar d^8 complex **6.1'**$^+$ and **6.2'**$^+$ (Scheme 6.2).

Scheme 6.2. Structural Figure for compounds **6.1'**$^+$ and **6.2'**$^+$.

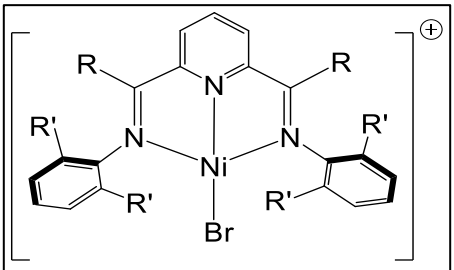

6.1'$^+$ **R=Me, R'=H**

6.2'$^+$ **R=Ph, R'=^{i}Pr**

6.4.2. XRD characterisation

We reported previously the structure of [Ni(κ^3-2,6-{PhNCMe}$_2$(NC_5H_3)Br_2] (**6.1**) to be a trigonal bipyramidal Ni(II) center displaying a neutral planar tridentate di(imino)pyridine and two bromide ligands as shown in Figure 6.1.[198] The bonding parameters were similar and consistent with other related structurally characterized species including a dichloro analogue,[137] [Ni(κ^3-2,6-{PhNCMe}$_2$(NC_5H_3)Cl_2]. We characterized **6.2** by single crystal X-ray analysis [Ni(κ^3-2,6-{ PhCN($iPr_2C_6H_3$)}$_2C_5H_3N$]. Compound **6.2** exhibits a mononuclear, distorted five-coordinate geometries with a metal dibromide unit coordinated by the three coplanar nitrogen atoms of the di(imino)pyridine ligand. The two common limiting ideal geometries for five coordinate species are trigonal bipyramidal (tbp) and square-based pyramidal (sp) metal environments and the assignment of tbp or sp metal coordination geometry can be made using a simple quantitative measure derived from calculation of structural index parameter, τ.[20, 123, 154] Application of this approach to complex **6.1** and **6.2** yielded τ parameter 0.72 and 0.02, respectively, indicating that

the coordination geometry of **6.2** can best be described as distorted square-based pyramidal (sp) with the basal plane was defined by the nitrogen donors of the bis(imino)pyridine ligand and one of the bromides identified as Br2. The pseudo-apical position is occupied by the bromo ligand labelled Br1.

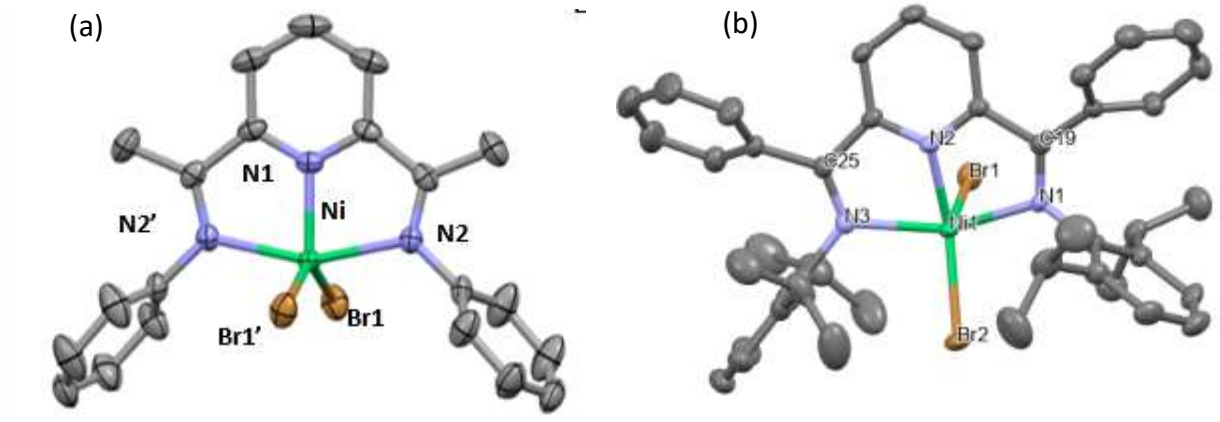

Figure 6.1. Structural representation of a) **6.1** b) **6.2**, with selected atoms labeled and hydrogen atoms omitted for clarity.

6.4.3. Computational optimizations

During computational optimization of structures **6.1** and **6.2** (DFT, B3LYP, def2-TZVP) using the PCM model for solvation in acetonitrile or water, spontaneous dissociation of one of the Br^- ligands to yield a Ni center with square planar geometries was observed. As a result, the dissociated bromide was removed and cationic square planar d^8 complex **6.1'**$^+$ and **6.2'**$^+$ (Scheme 6.2) were used in further computational optimizations. HOMO and LUMO of **6.1'**$^+$ are shown in Figure 6.2. As seen in this figure, the LUMO was dominated by a π^* orbital localized on the diiminopyridine ligand and the HOMO was essentially a lone pair on the bromide ligand.

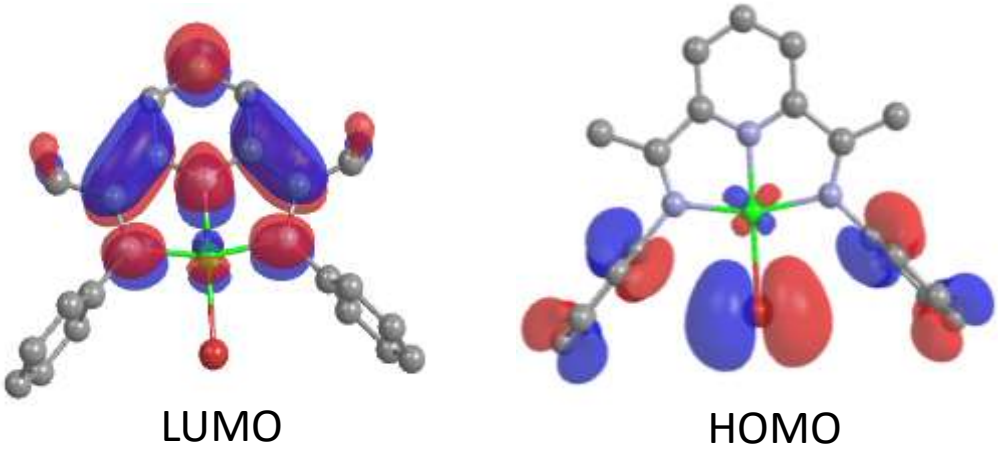

Figure 6.2. Representations of the HOMO and LUMO of complex **6.1** in water using B3LYP/def2tzvp and Polarizable Continuum Model (PCM).

6.4.4. Electrochemical characterisation

Since one of the compounds (**6.2**) was not fully soluble in water, all the electrochemistry experiments were done in a mixture of 50/50 CH_3CN/water. In addition, in chapter IV we report that the NiDIMPY complex catalyzes water to hydrogen at the second reduction, in aqueous buffer solution. In order to prevent any interference of H_2 generation with the nitrite reduction reaction, by adding CH_3CN to the solvent system we successfully moved H_2 generation to the more negative potentials. Glassy carbon was used as a working electrode. Potentials all are referenced to $Fc^{0/+}$ redox couple.

Two reversible reductions are observed in the cyclic voltammogram (CV) of both complexes, with $E_{1/2}$ values of −0.75V and −1.15V for **6.1** (Figure 6.3.a) and −0.58V and −1.08V or **6.2** (Figure 6.3.b). According to the computations and literature [47, 137], the first peak can be assigned as ligand-based reduction i.e., Ni(II)(L)/Ni(II)($L^{-\cdot}$), and the second wave can be assigned to a metal-based

reduction, i.e., Ni(II)($L^{-\cdot}$)/Ni(0)(L).

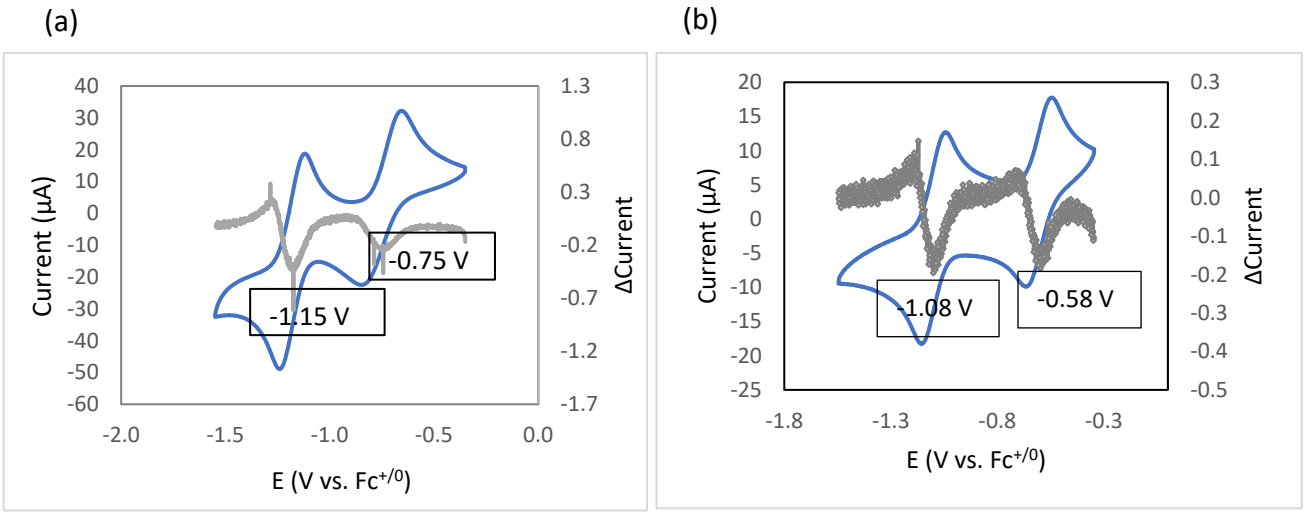

Figure 6.3. Cyclic voltammogram of 1 mM a) **6.1**, b) **6.2** in CH_3CN/water with 100 mM TBAHFP using a glassy carbon (GC) working electrode. Potentials are referenced to $Fc^{0/+}$. Two reversible reduction peaks are observed. The gray markers represent application of the method of first principles to the blue curve. Minima denote inflection points in the catalytic curve and indicate the associated onset potential and current enhancement.

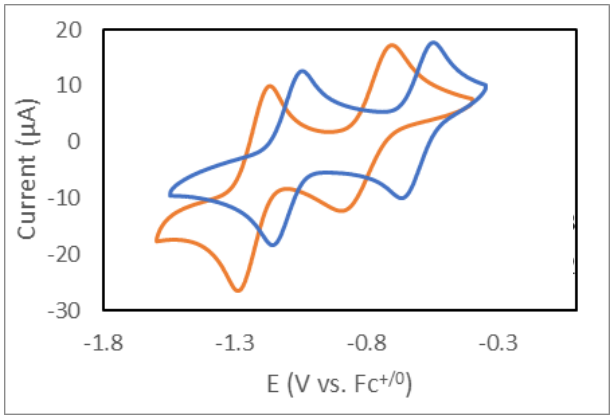

Figure 6.4. Cyclic voltammograms of (1mM) **6.1** (Orange) and **6.2** (Blue) in CH_3CN/Water with 100 mM TBAHFP using a glassy carbon (GC) working electrode.

The plots of peak current versus the square root of the scan rate for both features demonstrate a linear relationship, consistent with these processes being homogeneous according to the Randles-Ševčík equation (Figure 6.5).

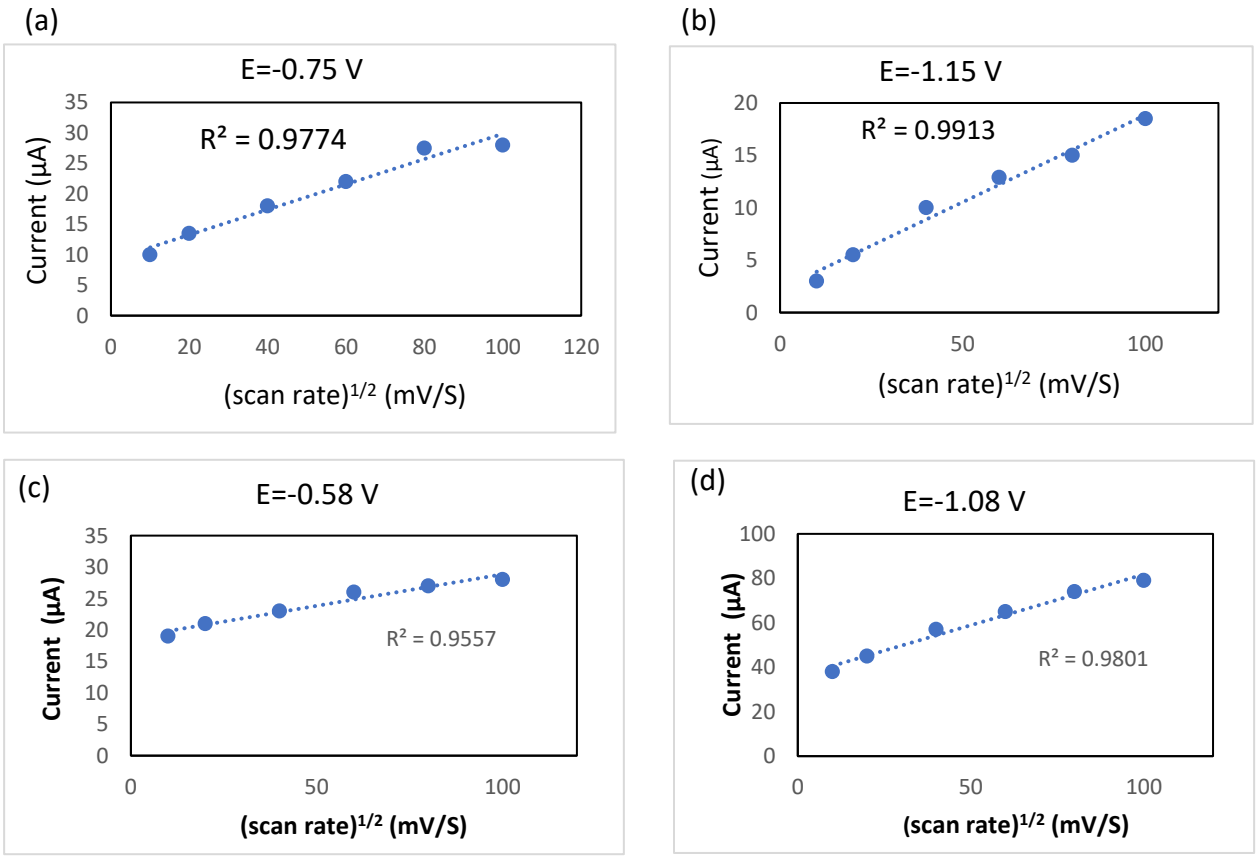

Figure 6.5. Plots of scan rate$^{1/2}$ versus current for the (a) first at -0.75 V, (b) second at -1.15 V, reduction peaks of **6.1**. (c) first at -0.58 V, (d) second at -1.08 V, reduction peaks of **6.2**.

6.4.5 Catalysis

The reactivity of these two complexes toward NO_2^- reduction was initially investigated by cyclic voltammetry (CV) in CH_3CN/H_2O. Since the NO_2^- reduction is a multielectron multiproton process, there would be a dramatic pH change during catalysis, which might affect the selectivity, products, and efficiency. Therefore, use of a buffer can help the process being more efficient and selective. We used MOPS (3-(N-morpholino)propanesulfonic acid) as the buffer firstly because it

is a noncoordinated buffer and does not interfere the reaction. Secondly, its pH range is near neutral pH (6.5-7.9) which is in the range of wastewater pH (6-8) that we would like to remove NO_2^- from. In addition to these facts, it has been reported as an efficient buffer for this catalysis.[7]

After adding NO_2^-, the second redox event for both complexes became irreversible and current enhanced with a reduction event of E_o=−1.23 V for **6.1** and E_o=-1.26 V for **6.2**, in addition to a cathodic shift in the first peak (Figure 6.6, Table 6.2). In the absence of buffered, though, no enhancement was observed, suggesting that this catalysis only occurs in a buffer solution. In the absence of catalyst, there is no sign of $NaNO_2$ reduction at the surface of glassy carbon in CH_3CN/WATER solution. However, after addition of buffer to this solution an enhancement is observed at E=-1.7 V vs $Fc^{+/0}$ and the current enhances with increasing nitrite concentration. These findings suggest that the heterogeneous reduction of nitrite by the GC electrode is enhanced in the presence of a buffer. This enhancement is likely attributed to the buffer's ability to prevent a significant fluctuation in pH throughout the reaction. While, after addition of compound **6.1** or **6.2** to the nitrite solution (CH_3CN/Buffer), the enhancement occurs at less negative potentials, correlating with the second reduction event of the Ni catalysts. Moreover, in the absence of NO_2^-, there is no background of proton reduction in the range of voltage we work at (Figure 6.6, 6.7)

Table 6.2. Reduction Potentials for **6.1** and **6.2**. CVs were performed in the mixture of CH_3CN/H_2O (50/50) with 100 mM TBAHFP, (100 mV/s) of 1mM **6.1** or **6.2**, 40 mM MOPS, in the presence and absence of nitrite.

compound	E_o First reduction	E_o new first reduction with nitrite	E_o Second reduction	E_o new second reduction with nitrite
6.1	-0.75	-0.95	-1.15	-1.23
6.2	-0.58	-0.79	-1.08	-1.26

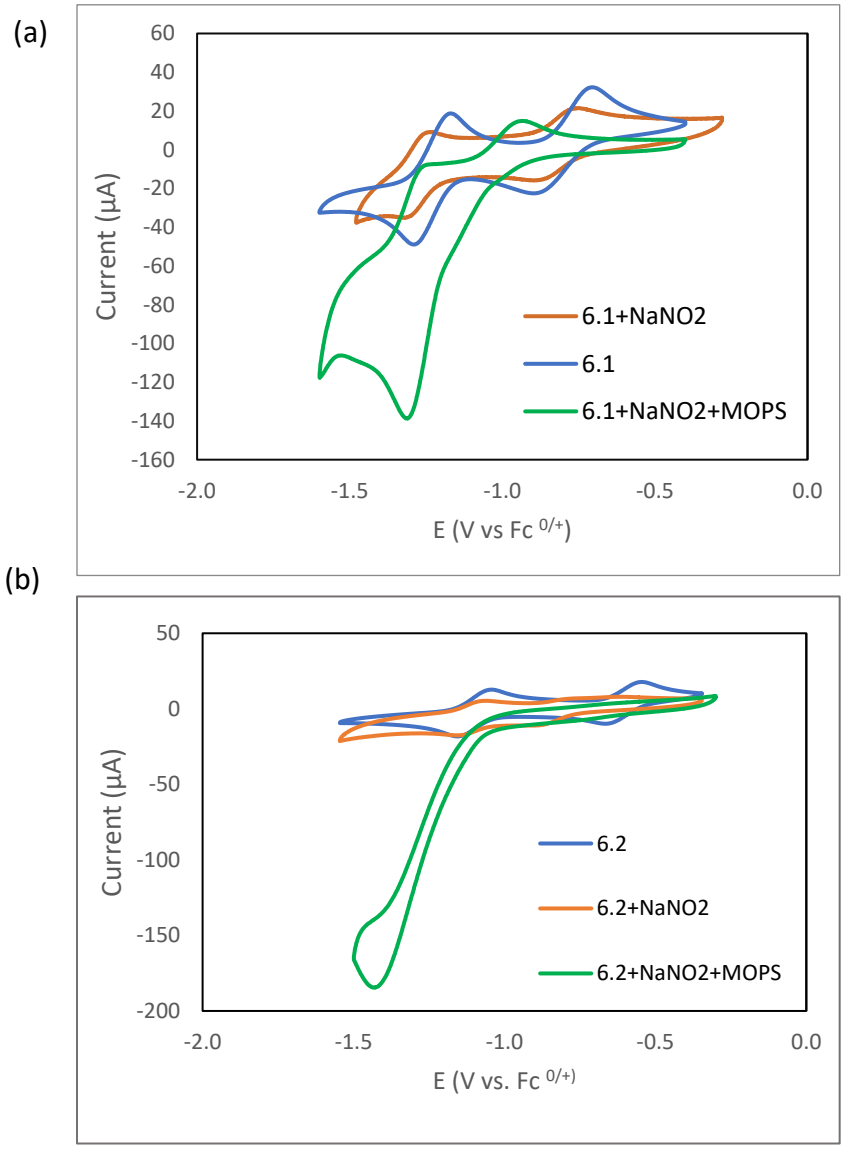

Figure 6.6. Cyclic voltammograms of a mixture of CH_3CN/H_2O (50/50) with 100 mM TBAHFP, (100 mV/s) with 1mM a): **6.1**, b): **6.2**, Ni (blue), 1mM of Ni + 100mM of $NaNO_2$ (orange), 1 mM of Ni + 100 mM of $NaNO_2$+ 40 mM MOPS (green).

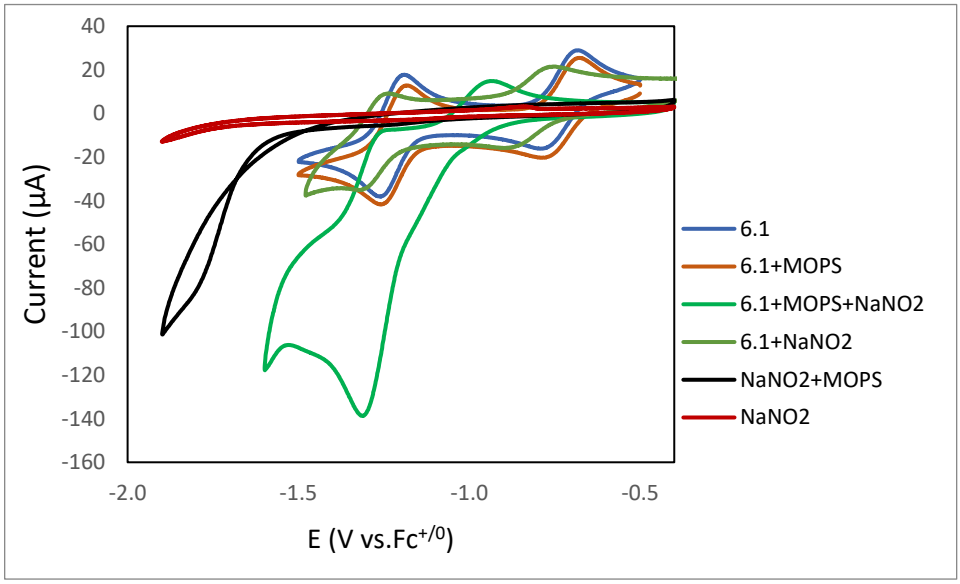

Figure 6.7. Background cyclic voltammograms in the mixture of CH_3CN/H_2O (50/50) with 100 mM TBAHFP using a glassy carbon (GC) working electrode, (100 mV/s).

The dependence of this catalysis on the concentration of each component was investigated by cyclic voltammetry. It was found that the peak current for the irreversible feature has a linear dependence on [NiDIMPY], [NO_2^-], and [MOPS] concentrations, before eventually leveling off at higher concentrations of each (Figure. 6.8-6.11). The result suggests that the rate of the reaction seems to be first order in the concentration of catalyst and nitrite.

(a)

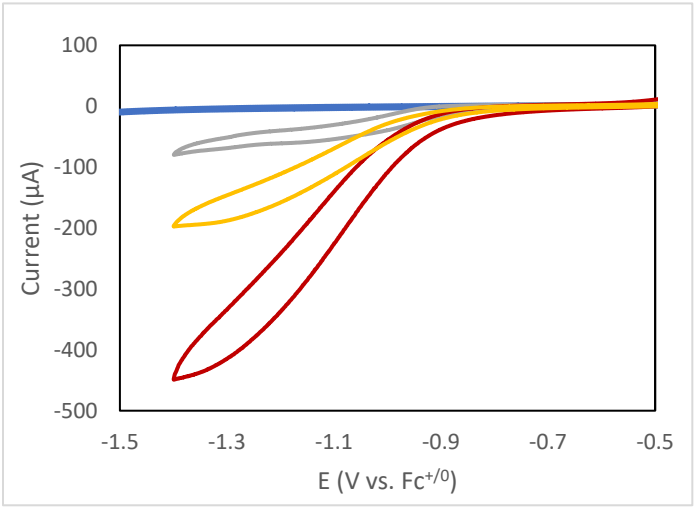

(b)

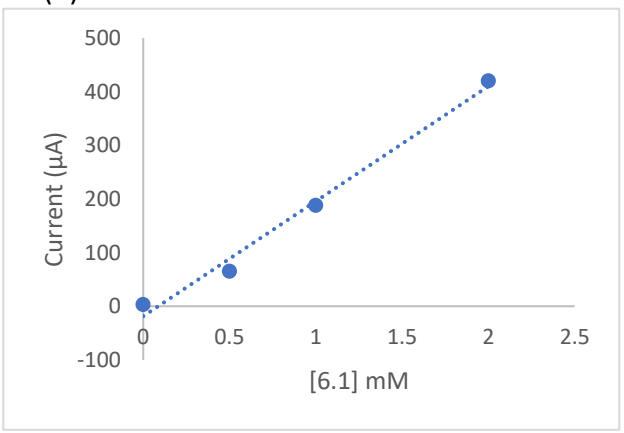

Figure 6.8. a) Cyclic voltammograms (100 mV/s) of 0.1 M TBAHFP, 40 mM MOPS, 50 mM $NaNO_2$, with **6.1** titrated from 0 to 2 mM in increments of 10 mM initially, in a mixture of CH_3CN/H_2O (50/50). b) Plot of peak current versus the concentration of **6.1** titrated.

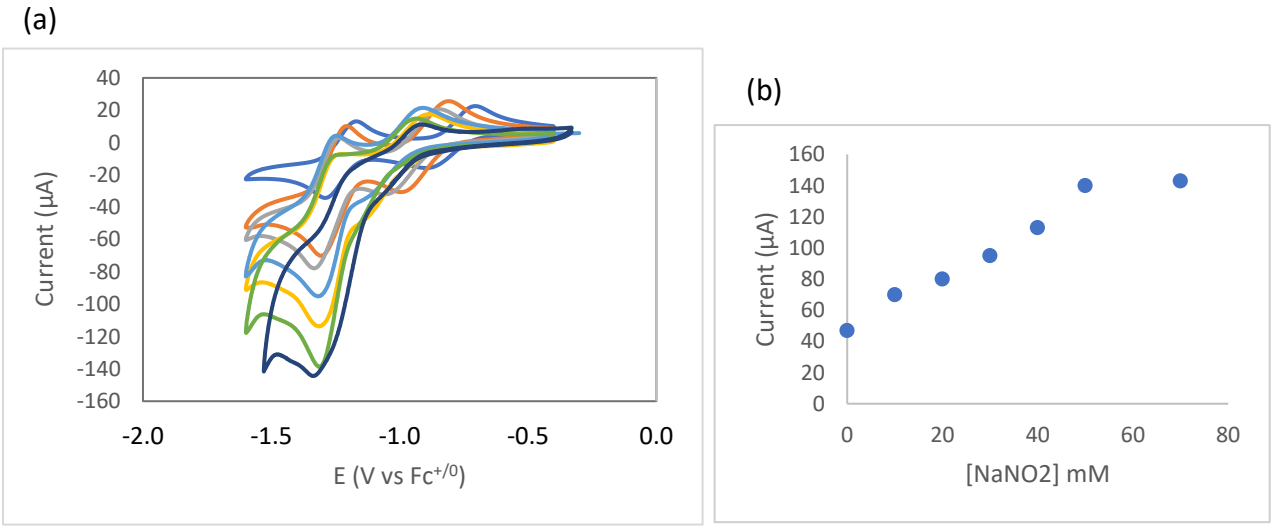

Figure 6.9. a) Cyclic voltammograms (100 mV/s) of 0.1 M TBAHFP, 40 mM MOPS, 1 mM **6.1**, with $NaNO_2$ titrated from 0 to 70 mM in increments of 10 mM initially, in a mixture of CH_3CN/H_2O (50/50). b) Plot of peak current versus the concentration of $NaNO_2$ titrated.

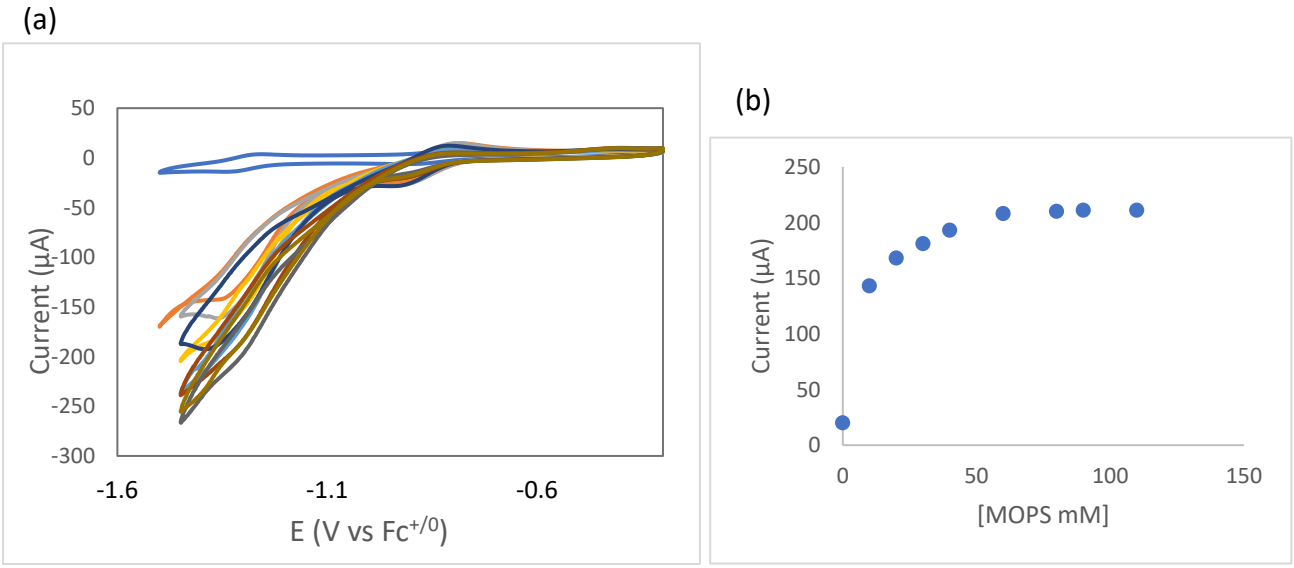

Figure 6.10. a) Cyclic voltammograms (100 mV/s) of 0.1 M TBAHFP, 50 mM $NaNO_2$, 1mM **6.1**, with MOPS titrated from 0 to 110 mM in increments of 10 mM initially, in a mixture of CH_3CN/H_2O (50/50). b) Plot of peak current versus the concentration of MOPS titrated.

(a)

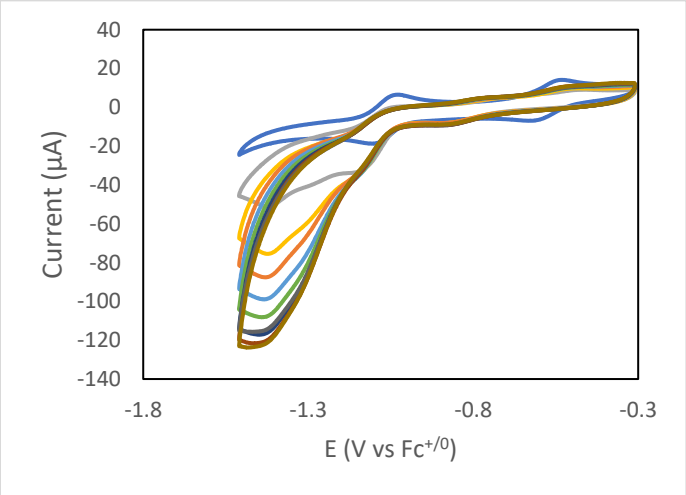

(b)

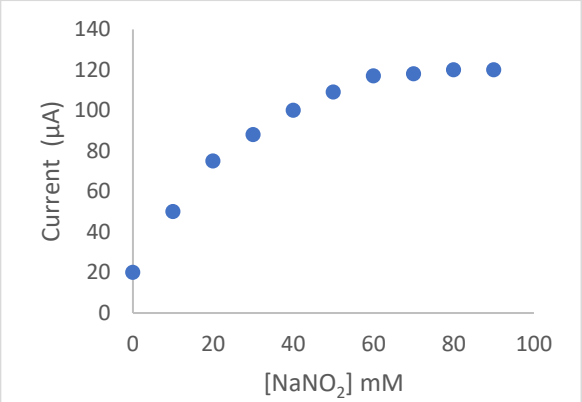

Figure 6.11. a) Cyclic voltammograms (100 mV/s) of 0.1 M TBAHFP, 40 mM MOPS, 1mM **6.2**, with $NaNO_2$ titrated from 0 to 90 mM in increments of 10 mM initially. b) Plot of peak current versus the concentration of $NaNO_2$ titrated.

Experiments to support the in-situ generation of NiL(NO_2^-)

As mentioned above, in addition to the enhancement at the second reduction peak of catalyst after addition of nitrite, a negative shift in voltage was observed at the first peak. To find out the reason, we isolated the first reversible peak of the complexes and added different concentrations of nitrite. As the NO_2^- concentration increases, the potential of the first wave shifts to more negative potentials. This observed dependence could suggest that nitrite ligand dissociation is coupled to electron transfer since nitrite is a stronger field ligand than bromide (Figure 6.12).[87]

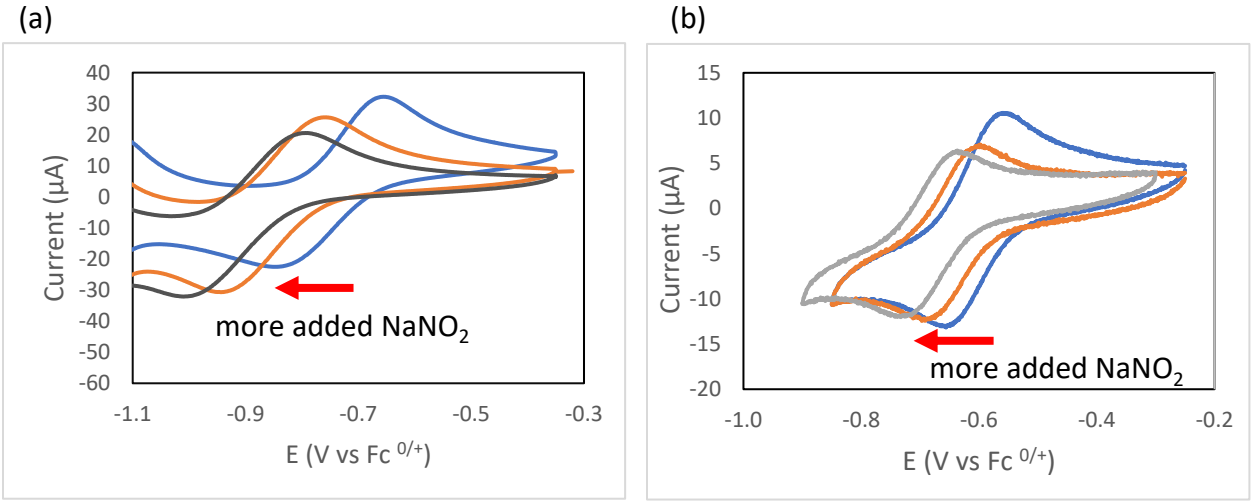

Figure 6.12. Selected cyclic voltammograms of 1 mM (a) **6.1** (b) **6.2** with different concentrations of $NaNO_2$ (scan rate = 100 mV/s, 40 mM MOPS, glassy carbon working electrode.

To confirm this hypothesis, bromide ions were replaced with nitrite through direct reaction of **6.1** and **6.3** with $AgNO_2$, in a round bottom flask covered with aluminium foil, stirred in an ice bath for two hours. The white precipitate (AgBr) was filtered off with a syringe filter, the remaining solvent was removed under vacuum and the resulting powders were dried under vacuum overnight to give a red solid, **6.3** and an orange solid **6.4**. The crystals of both compounds, suitable for X-ray analysis, were obtained by diffusing hexane in dichloromethane solutions. The single crystal XRD results (Figure 6.13) confirmed the ligand exchange in both complexes. Both bromides in **6.1** were replaced with nitrite ions, one of them bound through the N atom and the other one bound through an O atom. This new complex is labeled **6.3**. Although we also treated 2 eq of $AgNO_2$ with complex **6.2**, only one of the bromides was replaced with nitrite that was bonded to Ni through the O atom of nitrite, which could be because of steric effect due to the bulkier substituents on **6.2**. It is worth noting that only ~65% of atom Br2 is substituted with NO_2 groups (not 100% replacement, hence the disorder). This compound is labeled **6.4**.

Structure **6.3** displayed a six-coordinate Ni(II) center in a distorted octahedral environment completed by a tridentate planar diiminopyridine ligand, a κ^2-O,O-coordinated nitrite ligand and a κ^1-N-coordinated nitrite ligand. The largest angular deviation in the distorted O_h structure is due to the limited bite angle for the κ^2-NO_2 at 59.64°. If the equatorial plane is defined by the dimpy ligand, the nitrite O2 is oriented *trans* to the py group with O(2)-Ni(1)-N(2) 165.39(9)°. The remaining nitrite O1 and the κ^1 nitrite define the axis and an angle of 157.67(9) O1-Ni-N5. The two Ni-$O_{nitrite}$ bonds are similar at Ni(1)-O(1) equal to 2.140(2) Å and Ni(1)-O(2) is 2.065(2) Å. (Figure 6.13, Table D.1-D.2). The bonding and angles within the NiDIMPY segment closely resemble those of the parent NiDIMPY structure (**6.1**), as previously detailed in Chapter 3, Table B.2.

The structure obtained for **6.4** is shown in Figure 6.13. This complex, like **6.3**, also displayed a six-coordinate distorted octahedral Ni(II) center. In this case the coordination environment consisted of the planar tridentate diiminopyridine (DIMPY) ligand, a bromide ligand and a κ^2-O,O-coordinated nitrite. Again, using the diiminopyridine to define the equatorial plane placed the Ni(1)-Br(1) and Ni(1)-O(1) in the axial positions. The small bite angle for the κ^2-nitrite (59.8(5)°) produced the largest distorted angle for the octahedral Ni coordination. In **6.4** the Ni(1)-O(1) and Ni(1)-O(2) are the same within experimental error with values of 2.088(6) Å and 2.08(2) Å, respectively. The bonding and angles within the NiDIMPY segment closely resemble those of the parent NiDIMPY structure (**6.2**), as previously detailed in Chapter 4, Table 4.2. Other selected parameters, bonding and angles can be found in Table D.3-D.4.

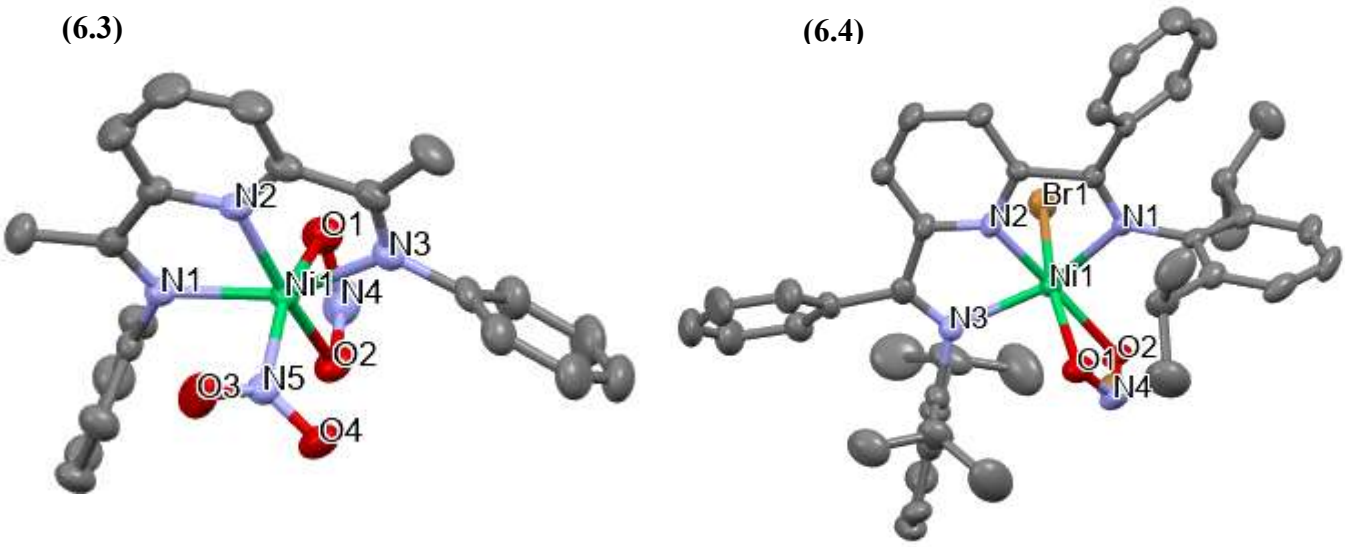

Figure 6.13. Molecular structures of **6.3** and **6.4**. Selected atoms labeled and hydrogens omitted for clarity.

A comparison of the cyclic voltammograms of **6.3** and **6.1** with added nitrite is depicted in Figure 6.14. The cyclic voltammograms reveal that the first reduction in $[NiL(NO_2)_2]^+$ (**6.3**) exhibits quasi-reversibility, unlike the reversible first peak observed in ($[NiLBr_2]^+$ (**6.1**) + nitrite). This distinction suggests that the ligand exchange, previously evident at the first peak, is no longer occurring in **6.3**. The reversibility of the peak in **6.1** indicates a ligand exchange between Br^- and NO_2^{2-}. As nitrite is now bonded as a ligand in **6.3**, the first peak manifests at a more negative voltage (Figure 6.12). Notably, the second reduction remains reversible with no change in potential. This similarity in cyclic voltammograms implies that both complexes afford access to the same active species for NO_2^- reduction (Figure 6.14 and Table 6.3).

.

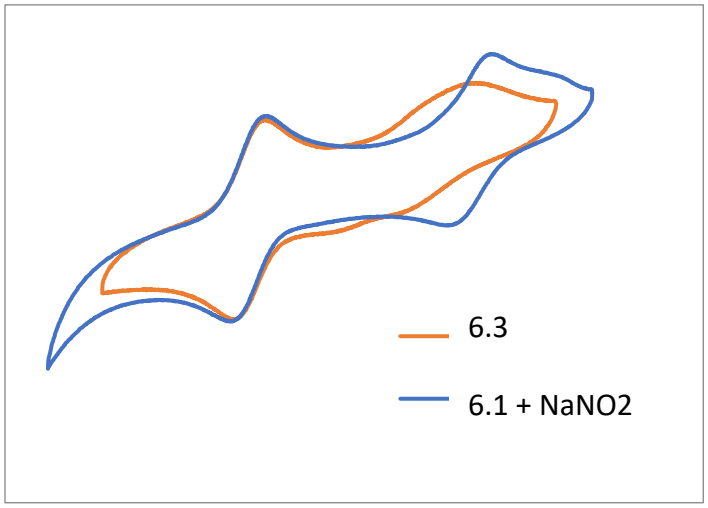

Figure 6.14. Cyclic voltammogram of (**6.1**) after adding NO_2^- to the solution (blue) and (**6.3**) (orange).

Table 6.3. Reduction Potentials (E^o) V vs $Fc^{0/+}$ for $[NiLBr_2]^+$(**6.1**) with added nitrite and $[NiL(NO_2)_2]^+$ (**6.3**).

compound	1st peak	2nd peak
6.1+$NaNO_2$	-0.61	-1.09
6.3	-0.68	-1.09

Controlled Potential Electrolysis (CPE)

CPE was carried out to determine whether the irreversible feature observed in CV corresponds to catalytic NO_2^- reduction and to identify the resulting product(s). The nitrogen cycle contains multiple transformations which could lead to several types of end products. In the gas phase, products such as nitric oxide (NO), nitrous oxide (N_2O), and nitrogen gas (N_2) could be formed and in the solution, products such as ammonia/ammonium (NH_3/NH_4^+) and hydroxylamine (NH_2OH) could be formed. Indophenol and hydroxylamine tests were used to detect the production of ammonium and hydroxylamine, respectively. ^{14}N NMR was used as a supportive test for

detection of any soluble N-containing product. Gas chromatography and Myoglobin tests were used for detection of nitrous oxide and nitric oxide gases, respectively. EI-mass spectroscopy was also used as a supportive test for detection of any gas products in this process. The procedure for these product measurement tests is detailed in the Experimental section of this chapter.

CPE was performed in a three-neck flask with 40 mL total volume. Glassy Carbon (GC), Silver (Ag) wire, Platinum (Pt) wire were used as WE, pseudo RE, and CE, respectively. A 50/50 v/v mixture of CH_3CN/Buffer aqueous solution (MOPS with pH 6.5) was used as the solvent system plus 100mM TBAHFP as the electrolyte. The reactions were carried out for 1 or 4 hours at -1.4 V (vs. $Fc^{0/+}$) in 17 mL solutions sparged with inert N_2 gas for 15 minutes.

Analysis of the product mixture after CPE, indicated the formation of NH_4^+ as the main product and a minimal amount of NH_2OH in some experiments. No N_2O, NO, or NH_3 was detected. To determine whether N_2 was produced, a CPE experiment was done using inert argon gas in place of N_2. After Gas Chromatography analysis, it was concluded that no N_2 products was formed. Using 1mM complex **6.1**, 40mM MOPS, 50mM NO_2^-, over 4h CPE, 50µmol of NH_4^+ and only 9µmol of NH_2OH were detected with FE of 48.25% and 5.78% respectively (Table 6.4, row 1). Complex **6.2** seemed more selective for NH_4^+, producing 75µmol of NH_4^+, as the sole product, with 50% FE (Table 6.4, row 3). However, at 1 hour experiment few µmol of product were observed with NH_2OH as the main product indicating that this process is slow compared to NH_4^+ production and suggesting that NH_2OH could be an intermediate in this process (Table 6.4, rows 2 and 4).

Control experiment showed that the glassy carbon electrode alone exhibited negligible background activity, passing only 12 C of charge over the 4 h period (Table 6.4, row 5 and Figure 6.15).

In the absence of buffer, a small amount of NH_4^+ (8 μmol) over 4 h was detected, probably due to hydroxide release and rise in pH over bulk experiment, confirming that this process involves proton consumption and indicating the importance of buffer in this process (Table 6.4, row 6). CPE in the absence of nitrite showed that there is no competing evolution of H_2.

On the basis of FE and TON for ammonium production, it appeared that that **6.2** was a more efficient and selective catalyst than **6.1**. We attribute this result to less electron density around the metal center in **6.2**, leading to a lower energy needed for reduction and proton transfer which is a key to an efficient process.

Although the Faradaic efficiency is not great and the calculated number for TON shows low values for this catalysis, the results are competitive with the other reported papers. Moreover, these Ni catalysts are one of the first Ni catalysts reported for nitrite electroreduction and they are among the rare examples of active catalysts for this chemistry.[85]

CPE tests with potential intermediates in the reduction of nitrite:

N_2O, NO, and NH_2OH are the common intermediates that could form in the catalytic reduction of nitrite anion. As part of an investigation into the possibility that these species were formed during catalysis, each of these species was introduced to a catalyst system. In the first experiment the cell was purged with N_2O gas for 15 min and CPE was performed for 4 h (Table 6.4, row 9). No N-containing product was measured. Similar observations were made when NO gas was used as the substrate (Table 6.4, row 10) suggesting that complex **6.1** is not able to reduce N_2O or NO gas. With this approach it must be considered that both N_2O (1.5 g/L (15 °C)) and NO (1.5 g/L (15 °C)) have rather low solubility in the water, reducing the possibility of binding these two gases to the catalyst and therefore reducing the chance of reduction. In a separate experiment 0.1M NH_2OH

was used as the substrate (Table 6.4, row 7). After 4 h CPE at -1.4V, 197μmol of NH_4^+ was measured, with 72.9% FE. It appears that this catalyst can reduce NH_2OH to NH_4^+, furthermore both the appearance of NH_2OH in previous experiments and the ability to convert NH_2OH are strong indicators that a hydroxylamine complex is formed as an intermediate in the process of nitrite reduction to ammonium using catalyst **6.1**. It is worth noting that attempts to electrocatalytically reduce NH_2OH in the absence of catalyst did not produce any ammonium product. (Table 6.4, row 8).

Table 6.4. Summary of data collected from the 1-hour and 4-hour CPE experiment at -1.4V vs $Fc^{+/0}$.

row		Time (h)	μmol of NH_4^+	FE% for NH_4^+	μmol of NH_2OH	FE% for NH_2OH	Charge	TON NH_4^+
1	1mM **6.1**+40mM MOPS+**50mM $NaNO_2$**	4	50	48.25	9	5.78	60	2.94
2	1mM **6.1**+40mM MOPS+50mM $NaNO_2$	**1**	3	11.97	8	15.96	14.5	-
3	1mM **6.2**+40mM MOPS+**50mM $NaNO_2$**	4	75	50	0	-	89	4.41
4	1mM **6.2**+40mM MOPS+50mM $NaNO_2$	**1**	0	-	11.2	30.2	14.6	-
	Background experiments							
5	40mM MOPS +50mM $NaNO_2$+**No catalyst**	4	0	-	0	-	12	-
6	1mM **6.1**+50mM NaNO2+**No MOPS**	4	8	-	0	-	8	
7	1mM **6.1**+40mM MOPS+**100mM NH_2OH**	4	197.3	72.9	-	-	160	11.6
8	40mM MOPS+**100mM NH_2OH**	4	0	-	-	-		-
9	1mM **6.1**+**N_2O**+40mM MOPS	4	0	-	0	-	14.39	-
10	1mM **6.1**+**NO**+40mM MOPS	4	0	-	0	-	13.04	-

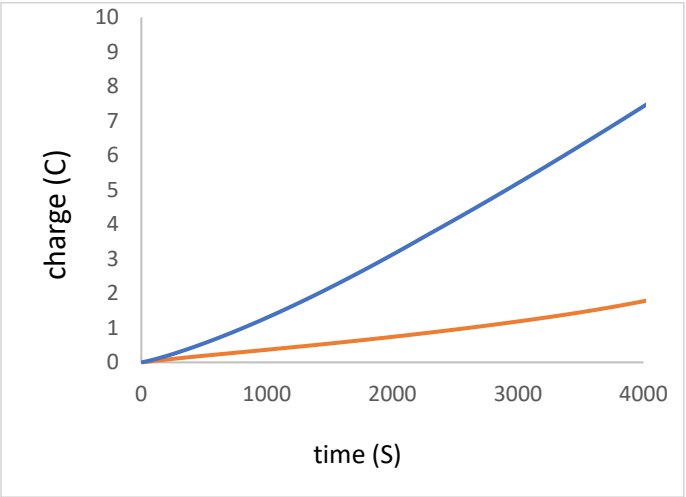

Figure 6.15. Controlled potential electrolysis of a solution containing 40 mM MOPS with 50 mM $NaNO_2$ at –1.4 V vs. $Fc^{+/0}$ (100 mV/s) with (blue) and without (orange) compound **6.1**, over 1 hour period CPE.

6.4.6. Computational Analysis & Proposed Mechanism for NO_2^- Reduction:

Nitrite reduction is a complicated multi-electron-transfer process, which involves nitrogen-containing species from +3 to -3 valence states. Dinitrogen and ammonia/ammonium, the most thermodynamically stable products, have been studied intensively. From an environmental protection perspective, harmless dinitrogen is the optimal product. For the aim of "turning waste into wealth" recyclable ammonia is the target product.

There are only a few possible pathways for the reduction of nitrite reported. These proposed mechanisms are inspired by nitrite reductase catalysis pathway which is shown in Scheme 6.3.[205] For example, Bren et al. had an insight into the mechanism through disproportionation experiments. They propose that FeN5H2 catalyzes ammonium production by disproportionation of hydroxylamine with concomitant formation of nitrous oxide and dinitrogen.[7] Smith et al. also proposed a mechanism using cyclic voltammetry and a thorough density functional theory (DFT) calculations, showing that the first step is binding nitrite to the metal center of the catalyst and that

N−O bond cleavage is the key step, facilitated by intramolecular proton transfer from an amine group of the macrocycle ligand to a nitrite ligand.[87] Gilbertson et al. also proposed the mono nitrosyl compound as intermediate for nitrite reduction reaction.[206]

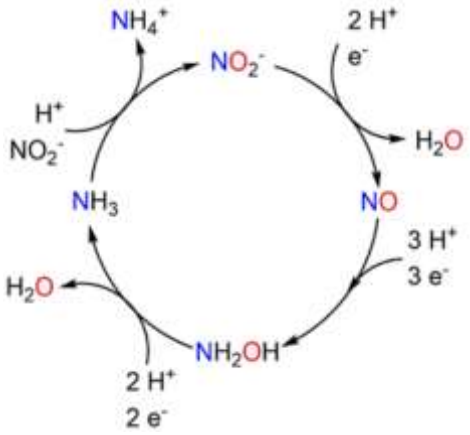

Scheme 6.3. Proposed Reaction Scheme for NO_2^- Reduction to NH_4^+ by Nitrite Reductases. complexes (ACS Catal. 2020, 10, 23, 13968–13972, Used with permission from American Chemical Society).

The well characterized mechanism for the catalytic reduction of nitrite to ammonia by cytochrome c nitrite reductase, based on a combination of experiments in conjunction with DFT computations, formed a basis for our proposed mechanism shown in Scheme 6.4.[205] To better understand, support and inform the proposed nitrite reduction reaction mechanism, density functional theory (DFT) computations were performed on these Ni complexes in water, using the polarizable continuum model (PCM) employing the B3LYP functional. Geometry optimization and vibrational frequency calculations were performed using def2-SVP as a basis set, followed by molecular energy computations with the def2-TZVP basis set.

The proposed mechanism begins with an N coordinated nitrite complex [Ni(κ^3-2,6-{Ph_2PNH}$_2NC_5H_3$)NO_2]$^+$ (**(6.1)'NO_2^+**) This species would arise from substitution of the bromide

ligand on **6.1'**$^{+}$ by nitrite. The optimized structure consists of a square planar Ni displaying symmetrical bonding of the di(imino)pyridine ligand and a Ni-NO_2 bond order calculated to be 0.66 (Figure 6.16, Table 6.5). The equal NO bonds in the nitrite ligand are consistent with a delocalized π bond between the N and O centers. The HOMO (MO 108) is dominated by the Ni d_z^2 orbital and the LUMO is localized on the di(imino)pyridine ligand and exhibited π^* symmetry. This ligand-based LUMO provides a means for the ligand to act as an electron reservoir for electrocatalysis.[20,32,33] Furthermore, the frontier molecular orbitals that display significant d-orbital contribution are consistent with a square planar Ni(II) (Figure 6.17).

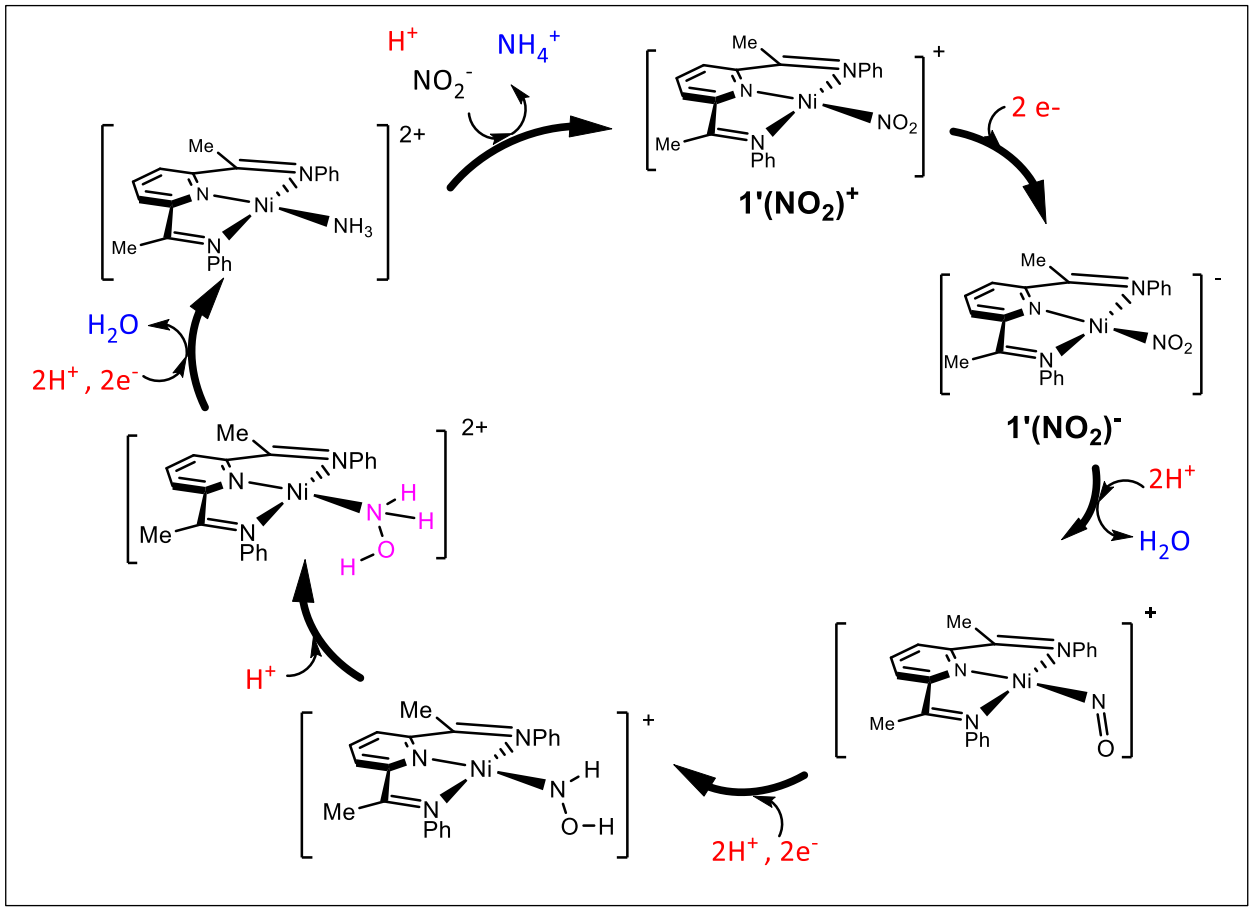

Scheme 6.4. A computationally supported proposed mechanism for the reduction of nitrite by complex **6.1**. Summary of computed thermochemistry for complexes in the proposed nitrite reduction mechanism is given in Table 6.4

Figure 6.16. DFT optimized structure of $[Ni(\kappa^3\text{-}2,6\text{-}\{Ph_2PNH\}_2NC_5H_3)NO_2]^+$ (**(6.1)'NO_2^+**) using the B3LYP functional and def2TZVP basis set in water (IEFPCM). Hydrogen atoms omitted for clarity. Frequency analysis confirmed that the optimized structure was a minimum with no imaginary frequencies.

Table 6.5. Summary of Ni-centered bonding for $[Ni(\kappa^3\text{-}2,6\text{-}\{Ph_2PNH\}_2NC_5H_3)NO_2]^+$ (**(6.1)'NO_2^+**). Values for bond length, overlap populations and Mayer bond order indices are from the B3LYP/def2TZVP/IEFPCM (water) optimization.

Bond	Length(Å)	Overlap Population	Mayer Bond order
$Ni\text{-}N_{py}$	1.866	0.15	0.59
$Ni\text{-}N_{imine}$	1.975	0.25	0.62
$Ni\text{-}N_{imine}$	1.975	0.25	0.62
$Ni\text{-}N_{nitrite}$	1.856	0.23	0.65
N-O	1.219	0.28	1.53
N-O	1.221	0.30	1.54

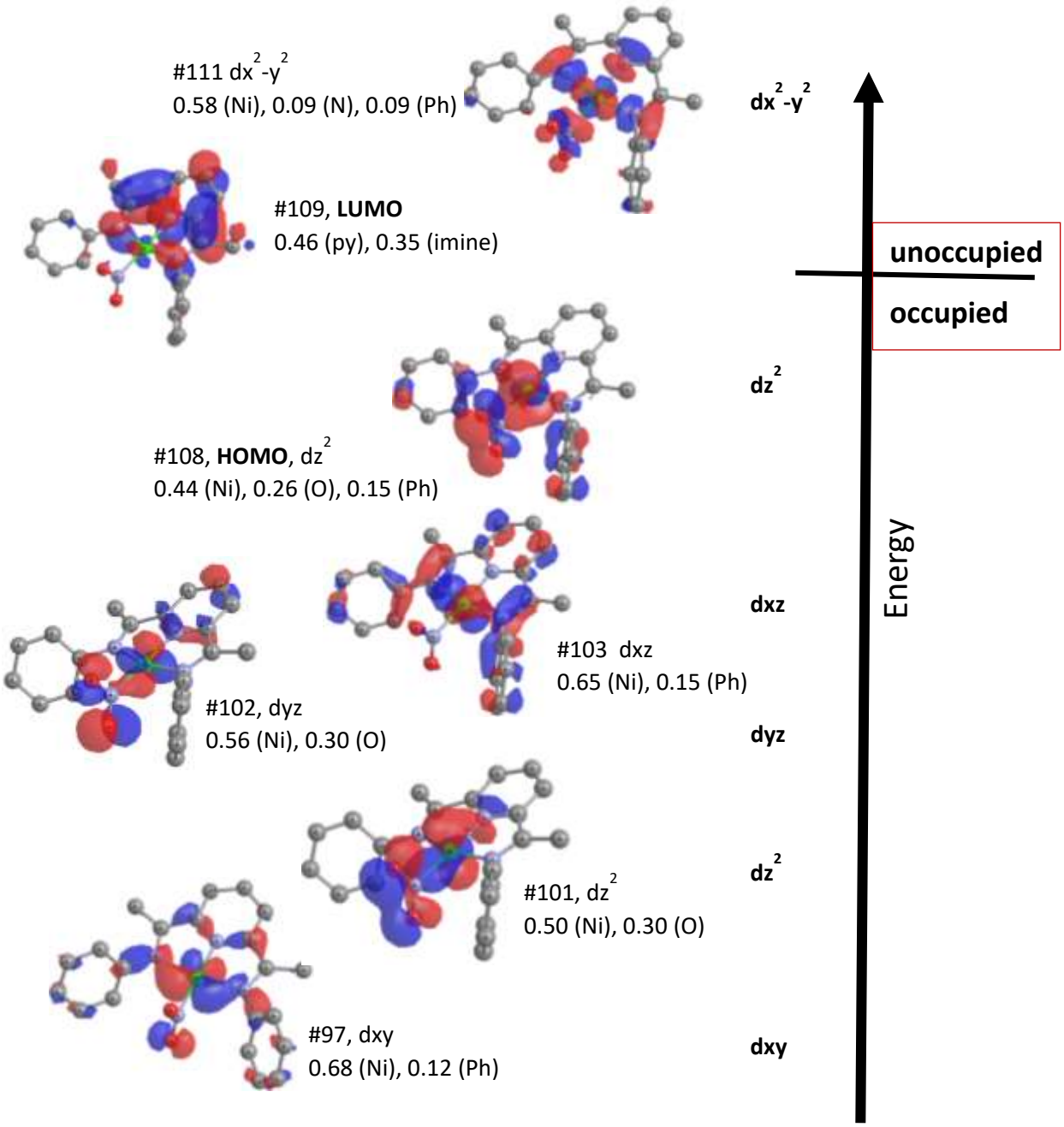

Figure 6.17. Selected, Ni-centered molecular orbitals obtained from the computational optimization of $[Ni(\kappa^3\text{-}2,6\text{-}\{Ph_2PNH\}_2NC_5H_3)NO_2]^+$ (**(6.1)'NO_2^+**) using the B3LYP functional, def2TZVP basis set and IEFPCM model for solvation in acetonitrile. Hydrogen atoms omitted for clarity. Major fragment orbital contributions were obtained from the Chemissian program.

Since catalytic activity was observed at the second reduction, this species, $[Ni(\kappa^3\text{-}2,6\text{-}\{Ph_2PNH\}_2NC_5H_3)NO_2]^-$ (**Ni(NO_2)$^-$**) was examined computationally. Both singlet and triplet species

were considered, and the triplet was calculated to be lower in energy by 5.3 kcal/mole. The resulting structure is shown in Figure D.2 with selected bonding parameters in Table D.5. The SOMOs for this triplet species (MO109 and 110, Figures D.3-D.4) were dominated by Ni d_{x2-y2} (49%) and π^* delocalized over the pyridyl and imine groups of the ligand, respectively. The MOs that are largely Ni-centered d-orbital in nature remained largely unchanged in comparison with **1'(NO$_2$)$^+$** (Figure D.5). The occupied orbital MO101 is localized on the oxygen-centers of the nitrite ligand and provide an accessible site for protonation of the **Ni(NO$_2$)$^-$**.

Addition of a second proton to the coordinated nitrite results in spontaneous loss of water during computational optimization and formation of a nitrosyl species, [Ni(κ^3-2,6-{Ph$_2$PNH}$_2$NC$_5$H$_3$)NO]$^+$ (**Ni(NO)$^+$**) as shown in Figure D.6. The calculated bonding parameters of this species given in Table D.6 and the frontier orbital distribution shown in Figure D.7 suggest a bent, formally anionic nitrosyl ligand thus making the Ni a d^8 divalent center.

Reduction and protonation of Ni(NO)$^+$ generates hydroxyamido complex [Ni(κ^3-2,6-{Ph$_2$PNH}$_2$NC$_5$H$_3$)(N(H)OH)]$^+$ (**Ni(NHOH)$^+$**). The protonation sequence is likely first at the lone electron pair on the N center represented by the HOMO of bent NO complex (Ni(NO)$^+$), shown in Figure D.9, followed by the resulting terminal oxygen site. The optimized structure of Ni(NHOH)$^+$ and selected bonding parameters are given in Figure D.8 and Table D.7 with the HOMO, LUMO and d-centered orbitals shown in Figure D.9. The computed HOMO of the hydroxyamido ligand is an N-centered lone electron pair poised for protonation to yield the hydroxyamine ligated compound [Ni(κ^3-2,6-{Ph$_2$PNH}$_2$NC$_5$H$_3$)(NH$_2$OH)]$^{2+}$ (**Ni(NH$_2$OH)$^{2+}$**).

The resulting structure and bonding of the coordinated hydroxylamine species Ni(NH$_2$OH)$^{2+}$ (Figure 6.18, Table 6.6) is consistent with the proposed structure. This compound would be the source of hydroxylamine. An occupied MO (MO97, Figure D.10) displays a major electron density

(0.56%) on the oxygen center, providing a site for protonation with release of water. The frontier orbitals for this compound are presented in Figure 6.20. Coupled with a reduction this would lead to the amido species $[Ni(\kappa^3\text{-}2,6\text{-}\{Ph_2PNH\}_2NC_5H_3)(NH_2)]^+$ (**$Ni(NH_2)^+$**) with the computationally optimized structure shown in Figure 6.19. The bonding parameters (Table 6.7) are as would be expected for a d^8 Ni complex. The frontier orbitals for this compound are presented in Figure 6.21. Perhaps most pertinent to the mechanism is the fact that the HOMO looks like N lone pair primed for protonation, release of ammonia/ammonium and closing of the proposed cycle.

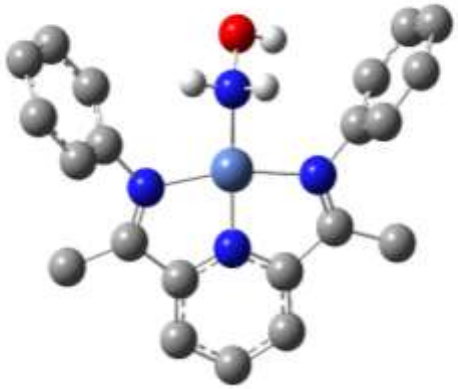

Figure 6.18. DFT optimized structure of $[Ni(\kappa^3\text{-}2,6\text{-}\{Ph_2PNH\}_2NC_5H_3)(NH_2OH)]^{2+}$ (**$Ni(NH_2OH)^{2+}$**) using the B3LYP functional and def2TZVP basis set in water (IEFPCM). Hydrogen atoms on carbon omitted for clarity. Frequency analysis confirmed that the optimized structure was a minimum with no imaginary frequencies.

Table 6.6. Summary of Ni-centered bonding for $[Ni(\kappa^3\text{-}2,6\text{-}\{Ph_2PNH\}_2NC_5H_3)(NH_2OH)]^{2+}$ ($Ni(NH_2OH)^{2+}$). Values for bond length, overlap populations and Mayer bond order indices are from the B3LYP/def2TZVP/IEFPCM (water) optimization.

Bond	Length(Å)	Overlap Population	Mayer Bond order
$Ni\text{-}N_{py}$	1.843	0.20	0.68
$Ni\text{-}N_{imine}$	1.955	0.26	0.65
$Ni\text{-}N_{imine}$	1.960	0.27	0.66
Ni-N	1.950	0.18	0.57
N-O	1.415	0.10	0.92

Figure 6.19. DFT optimized structure of $[Ni(\kappa^3\text{-}2,6\text{-}\{Ph_2PNH\}_2NC_5H_3)(NH_2)]^+$ (**Ni(NH$_2$)$^+$**) using the B3LYP functional and def2TZVP basis set in water (IEFPCM). Hydrogen atoms on carbon omitted for clarity. Frequency analysis confirmed that the optimized structure was a minimum with no imaginary frequencies.

Table 6.7. Summary of Ni-centered bonding for $[Ni(\kappa^3\text{-}2,6\text{-}\{Ph_2PNH\}_2NC_5H_3)(NH_2)]^+$ (**Ni(NH$_2$)$^+$**). Values for bond length, overlap populations and Mayer bond order indices are from the B3LYP/def2TZVP/IEFPCM (water) optimization.

Bond	Length(Å)	Overlap Population	Mayer Bond order
$Ni\text{-}N_{py}$	1.846	0.17	0.61
$Ni\text{-}N_{imine}$	1.961	0.25	0.64
$Ni\text{-}N_{imine}$	1.961	0.25	0.64
$Ni\text{-}N_{amido}$	1.809	0.25	0.86

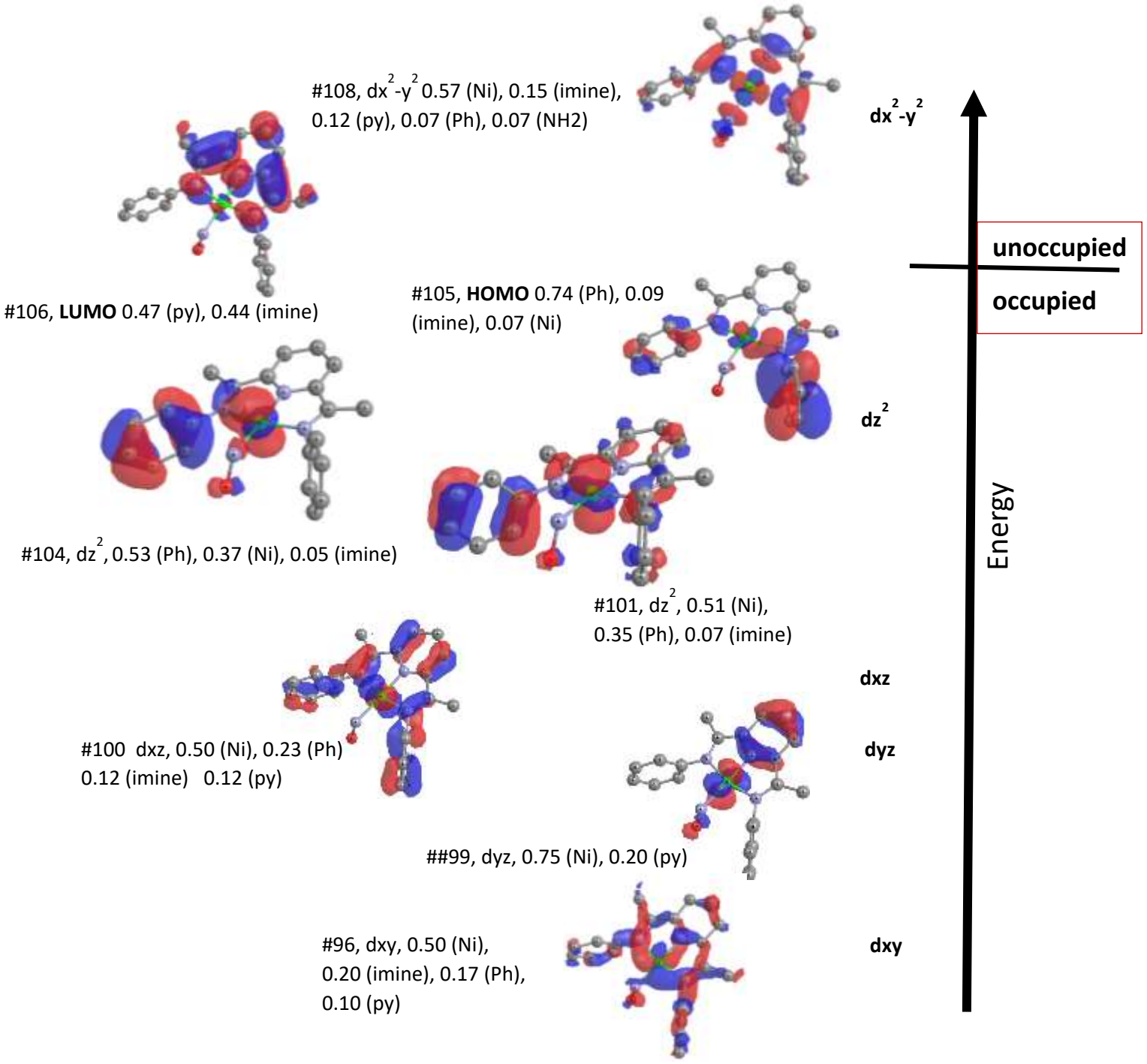

Figure 6.20. Selected, Ni-centered molecular orbitals obtained from the computational optimization of $[Ni(\kappa^3\text{-}2,6\text{-}\{Ph_2PNH\}_2NC_5H_3)(NH_2OH)]^{2+}$ (**$Ni(NH_2OH)^{2+}$**) using the B3LYP functional, def2TZVP basis set and IEFPCM model for solvation in water. Hydrogen atoms are omitted for clarity. Major fragment orbital contributions were obtained from the Chemissian program.

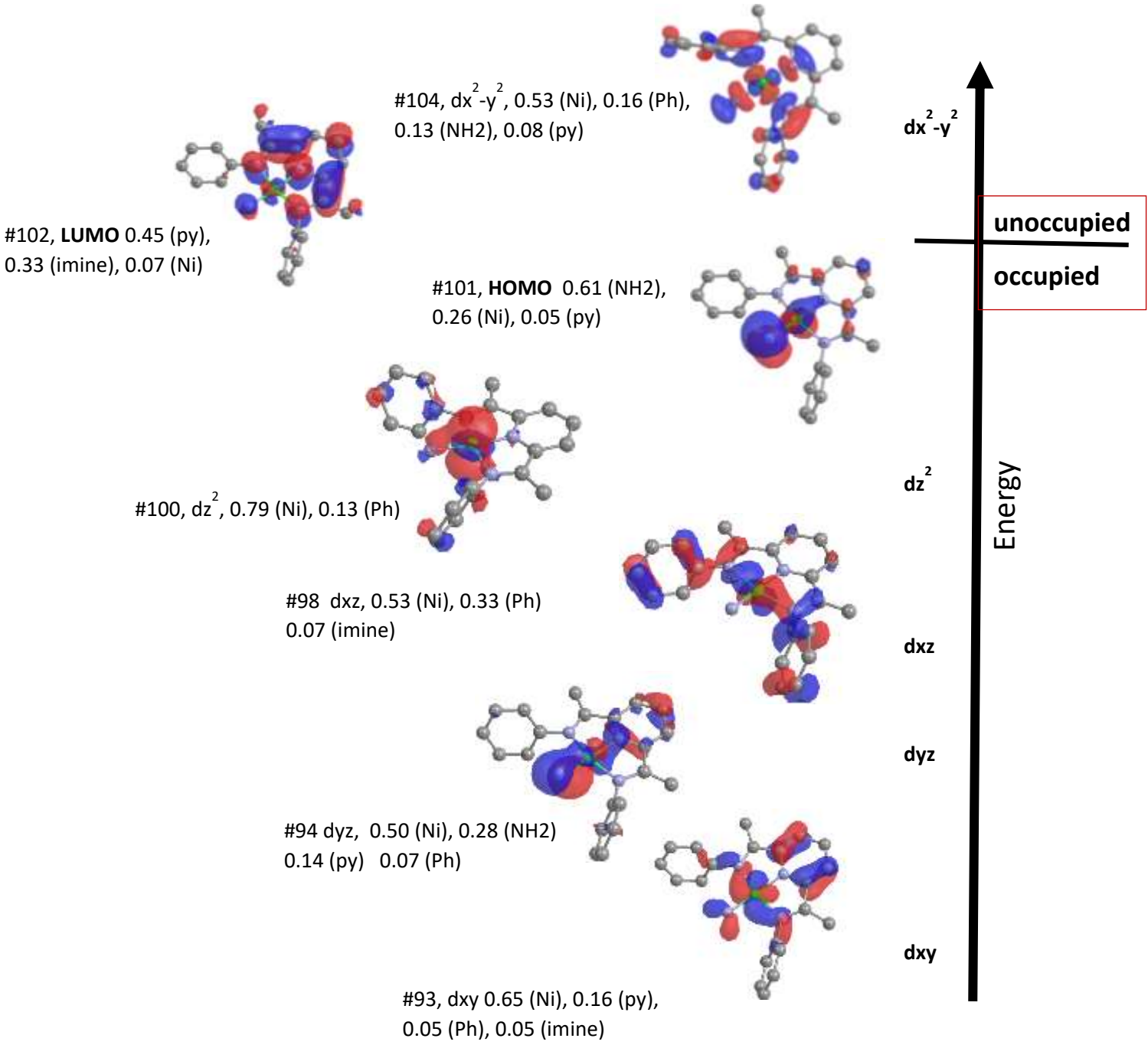

Figure 6.21. Selected, Ni-centered molecular orbitals obtained from the computational optimization of $[Ni(\kappa^3\text{-}2,6\text{-}\{Ph_2PNH\}_2NC_5H_3)(NH_2)]^+$ (**Ni(NH$_2$)$^+$**) using the B3LYP functional, def2TZVP basis set and IEFPCM model for solvation in water. Hydrogen atoms are omitted for clarity. Major fragment orbital contributions were obtained from the Chemissian program.

Table 6.8. Summary of computed thermochemistry for complexes in the proposed nitrite reduction mechanism.

Compound	Sum of electronic and thermal Enthalpies (a.u.)	Sum of electronic and thermal Free Energies (a.u.)
6.1'$(NO_2)^+$	-2687.846113	-2687.928049
Ni$(NO_2)^-$ Singlet Triplet	-2689.691655 -2689.69424	-2689.773557 -2689.782047
Ni$(NO)^+$	-2612.762566	-2612.843527
Ni$(NHOH)^+$	-2613.946868	-2614.027187
Ni$(NH_2OH)^{2+}$	-2614.404165	-2614.485435
Ni$(NH_2)^+$	-2539.242994	-2539.40815

6.5. Conclusion

In summary, we observed that the Ni(DIMPY)Br_2 complexes catalyze reduction of NO_2^- to NH_4^+ at 50% and 75% Faradaic efficiency for **6.1** and **6.2**, respectively, over 4h CPE in a mixed CH_3CN/H_2O solution in the presence of MOPS as buffer. The complex with bulkier substituents shows higher efficiency and selectivity toward NH_4^+ production; the requirement that buffer be present to observe catalysis indicates a role of buffer in the reaction, as observed for catalysts for hydrogen production in water. Following bulk CPE measurements, computations were conducted to support a proposed a mechanism for the electrochemical reduction of NO_2^-. The computations provided two distinct pathways which can be followed to show the formation of the two observed reaction products NH_2OH and NH_4^+.

Notably, Ni(DIMPY)Br_2 stands out as one of the first examples of a Ni complex that catalyzes multielectron NO_2^- reduction in aqueous solution.

There are some experiments and changes that could be explored in order to elaborate on this project such as changing the solvent system, increasing the concentrations of buffer and nitrite in CPE experiments, and assessing the effects of pH on the catalytic efficiency and selectivity. In future work, in addition to applying the mentioned changes, we plan to leverage this buffer requirement and utilize modifications of the ligand scaffold to gain insight into the mechanism of the observed reactivity and to further optimize activity. Investigation of the reduction of other oxyanion species also is planned.

6.6. Experimental Section

General:

Reagents and analytical grade solvents were purchased from Sigma Aldrich and used without further purification.

Materials

Doubly deionized water was used as a solvent in all reactions. All chemicals were used from the manufacturer without further purification. For the indophenol test: ammonium sulfate was obtained from Fisher Chemical, phenol from Acros Organics, sodium nitroferricyanide (III) dihydrate from Sigma-Aldrich, and sodium citrate dihydrate from Fisher Chemical. All the chemicals needed for synthesis of the ligands and complexes were obtained from Sigma-Aldrich. In the reactivity studies: 3-(N-morpholino)propanesulfonic acid (MOPS) was obtained from Sigma-Aldrich and sodium nitrite were obtained from Sigma-Aldrich, as well. The nitrous oxide standard used in the gas chromatography-TCD studies was of AA grade and obtained from Air Products.

Synthesis:

Synthesis of 2,6-bis[(1-phenylimino)ethyl]pyridine (L1):[158]

Aniline (5ml, 55 mmol) was added to a solution of 2,6-diacetylpyridine (0.489 g, 3 mmol) in absolute propan-2-ol (50 mL). The reaction mixture was refluxed for 2 h and then allowed to cool down to room temperature. The crude product precipitated as a yellow powder. Pure product was obtained in 90% yield upon recrystallization from methanol. ^{1}H NMR (60 MHz, $CDCl_3$); δ 8.32 (m, py, 3 H), 7.1 (m, Ph, 10 H), and 2.41 (s, CH_3, 6 H) ppm.

Synthesis of $NiBr_2$-2,6-bis[(1-phenylimino)ethyl]pyridine (6.1):[159, 207]

$NiBr_2$ powder (34 mg, 0.160 mmol) was added to a clear yellow solution of L1 (100 mg, 0.165 mmol) in a mixture of 2 mL of toluene, and 4 mL of hexanes. The reaction mixture was allowed to stir for 4 hours, gradually becoming orange. Solution was then held at -20°C overnight, over which time a bronze precipitate formed. Solution was filtered, washed with 5 x 2 mL hexanes, and allowed to dry under vacuum. A fine orange powder was isolated in 68% yield. red block-like crystals suitable for X-ray analysis were grown by diffusion of saturated dichloromethane solution in hexanes.

Synthesis of 2,6-Bis{[2,6-di(isopropyl)phenyl)imino]benzyl}pyridine (L2): [159]

A mixture of 2,6-dibenzoylpyridine (5.0 g, 17.4 mmol), 2,6 diisopropylaniline (7.5 g, 38.3 mmol), and p-toluenesulfonic acid (0.2 mg) in toluene (50 mL) were placed in a round bottom flask equipped with a Dean–Stark trap. Under a nitrogen atmosphere, the reaction mixture was heated to reflux in an oil bath at 140˚C for 48 h then cooled to room temperature and the solvent was removed under vacuum to give a dark yellow oil. Hexanes were added and a small quantity of a white solid was removed by filtration. The filtrate was removed under vacuum yielding a dark yellow oil. Methanol (~400 mL) was added to this oil and the mixture was stirred for several minutes, causing the product to precipitate as a yellow solid which was filtered off and rinsed with methanol. The filtrate was reduced to about half the initial volume under vacuum, and then placed in a refrigerator, causing additional product to precipitate, which was filtered off and rinsed with methanol. The product was obtained as a yellow powder. Yield: 7.2 g (68%). ^{1}H NMR (d6-dimethyl sulfoxide, 162 MHz) δ 7.82 (br t, 1 H, py, p CH), 7.55–7.20 (br m, 12 H, Ar–H), 6.94 (br s, 6H, Ar–H), 2.90 (m, 4H, iPr), 1.00 (d, 24H, iPr) ppm.

Synthesis of $NiBr_2$-2, 6-Bis{1-[(2,6-diisopropylphenyl)imino]-benzyl}pyridine (6.2):[159]

$NiBr_2$ powder (34 mg, 0.160 mmol) was added to a clear yellow solution of L2 (100 mg, 0.165 mmol) in 6 mL of toluene. The reaction mixture was allowed to stir for 4 hours, gradually becoming brown. Solution was then held at -20°C overnight, over which time a light brown precipitate formed. Solution was filtered, washed with 5 x 2 mL hexanes, and allowed to dry under vacuum. A light brown powder was isolated in 78% yield. Brown needle-like crystals suitable for X-ray analysis were grown from saturated dichloromethane solution by diffusion of hexane and storing at -20°C for several hours. ^{1}H NMR (d-chloroform, 162 MHz) δ 8.46 (d, 2 H, py, m CH), 7.91 (t, 1 H, py, p CH), 7.18-7.03 (br m, 16 H, Ar–H), 2.75 (m, 4H, iPr), 1.14 (d, 24H, iPr) ppm. Molecular structure of complex 6.2 plus angles and bond distances are reported in chapter 4.

Preparation of [NiL1(NO_2)$_2$] (6.3):[87]

A 25 mL flask (wrapped with aluminum foil) was charged with $AgNO_2$ powder (7.5 mg, 0.491 mmol, 2 eq) and a solution of [NiL1Br_2] (6.1) (13.0 mg, 0.0245 mmol, 1 eq) in methanol (10 mL). The resulting solution of mixture was stirred in an ice bath for 2 h until the yellow solution changed to pale orange. The off-white precipitate (AgBr) was removed through filtration and the pale orange solution was collected (7.2 mg, 65%). Crystals of [NiL1(NO_2)$_2$] suitable for single crystal X-ray diffraction were obtained by slow diffusion of hexane into a dichloromethane solution of the complex.

Preparation of [NiL2(NO_2)Br] (6.4):

A 25 mL flask (wrapped with aluminum foil) was charged with $AgNO_2$ powder (7.5 mg, 0.491 mmol, 2 eq) and a solution of [NiL2Br_2] (6.2) (22.2 mg, 0.0245 mmol, 1 eq) in methanol (10 mL). The resulting solution of mixture was stirred in an ice bath for 2 h until the yellow solution changed to pale orange. The off-white precipitate (AgBr) was removed through filtration and the pale orange solution was collected (10.4 mg, 48%). Crystals of [NiL2(NO_2)Br] suitable for single

crystal X-ray diffraction were obtained by slow diffusion of hexane into a dichloromethane solution of the complex.

X-ray Crystallography: The crystals of $Ni(NO_2)_2$-2,6-bis[(1-phenylimino)ethyl]pyridine (**6.3**) and $Ni(NO_2)$Br-2,6-Bis{1-[(2,6-diisopropylphenyl)imino]-benzyl}pyridine (**6.4**) were mounted on thin glass fibers using paraffin oil. Prior to data collection crystals were cooled to 200.15 °K. Data were collected on a Bruker Smart ApexII single crystal diffractometer equipped with a sealed tube Mo source (wavelength 0.71073 Å) and an ApexII CCD detector. Raw data collection and processing were performed with the Apex3 software package from Bruker. Initial unit cell parameters were determined from 60 data frames from select ω scans collected at the different sections of the Ewald sphere. Semi-empirical absorption corrections based on equivalent reflections were applied.[208] Systematic absences in the diffraction data-set and unit-cell parameters were consistent with the assigned space group. The initial structural solution was determined using ShelXT direct methods,[121] and refined with full-matrix least-squares procedures based on F^2 using ShelXL.[122] Hydrogen atoms were placed geometrically and refined using a riding model. All scattering factors are contained in several versions of the ShelXL program library, with the latest version used being v.6.12 at the time of this writing.

Electrochemistry:

Electrochemical experiments were carried out in a single compartment cell, with 40 mL approximate volumes, using a VersaSTAT 3 (Princeton Applied Research) potentiostat. Samples were prepared in an open air, sealed, and connected to a Schlenk line and maintained under a nitrogen atmosphere. A conventional three electrode system was employed consisting of a glassy carbon working electrode (diameter = 0.3 cm), a Pt wire as the auxiliary electrode, and an Ag wire as a pseudo-reference electrode. Ferrocene was added as a reference compound and potentials were

referred to the redox potential of ferrocenium ion (Fc^+)/ferrocene (Fc) as an internal standard. Dried acetonitrile was purchased from Sigma Aldrich and stored on molecular sieves in the glovebox. Tetrabutylammoniumhexafluorophosphate, $[(n\text{-}Bu)_4N]PF_6$ (TBAHFP), the supporting electrolyte, was crystallized two times with ethanol, dried under vacuum at 90 °C for 24 h before used and stored in a glovebox. Deionized (DI) water was used. The typical concentration of catalyst was 1 mM in each experiment.

Other Physical Measurements:

Gas chromatography for detection of gas products (H_2, N_2O) was conducted on a Shimadzu gas chromatograph- 2014 equipped with a thermal conductivity detector (TCD). Helium carrier gas (purity ≥ 99.995%) was utilized with an isothermal 6-minute run at 30 ºC on an Agilent HP-PLOT Q column. UV-vis spectra were recorded with a Cary 100 spectrophotometer. The ^1H NMR spectra were recorded at 400 MHz respectively with chemical shifts reported in ppm using the residual protons of the NMR solvent as internal standards. Mass spectrometric measurements were used for detection of NO, which were performed at the Chemistry Mass Spectrometry Facility at the University of Ottawa, Ontario on a Micromass Quattro triple quadrapole mass spectrometer equipped with an electrospray ionization source.

CPE Experiments with possible intermediates:

All the background experiments were performed in sealed 40-mL three neck cell. 4 h CPE was performed in the presence of 40 mM MOPS, 1mM **6.1**, under NO, N_2O, and under N_2 for the reaction containing 50.0 mM NH_2OH. The indophenol test was used to analyze for the presence of NH_4^+ as a product.

Equations:

Turnover number (TON) was estimated using the following equation:

TON = n product / n catalyst

where n product = moles of hydroxylamine or ammonium produced and n catalyst = moles of catalyst

added.

Turnover frequency (TOF) can then be estimated as follows:

TOF = TON / t

Where TON = turnover number and t = time

Randles-Sevcik equation:

$i_p = 0.496(FAC)\sqrt{(DF\nu/RT)}$

The Randles-Sevcik equation which describes the peak current of a mass-transport limited event establishes a relationship of peak current being proportional to the square root of the scan rate. In the Randles-Sevick equation, i_p describes peak current observed in CV, F is Faraday's constant, A is the surface area of the electrode in cm^2, C is the concentration of electroactive species in mol/cm^3, D is the diffusion coefficient of the electroactive species in cm^2/s, ν is the scan rate in V/s, R is the ideal gas constant, and T is the absolute temperature.

Product Measurement Techniques:

Significant time and efforts were done on trouble shooting these techniques since it was the first time these techniques had being used in our group. All these techniques were followed based on different nitrite reduction papers. Many instruments were used to characterise and quantify the possible products here, such as UV-Vis, ^{14}N NMR, EI-Mass spectroscopy, and gas chromatography. All the used techniques in addition to the procedure for each test are listed below.

Indophenol blue test:

This technique is a spectrophotometry method to detect and quantify Ammonium in the solution. It is s based on the formation of an indophenol blue pigment during the reaction of phenol and hypochlorite in the presence of ammonia.[7, 209]

Procedure:

1mL of reagent A (100 mL aqueous solution of 11.1 mL liquefied phenol in ethyl alcohol) and 25mL of sample solution are added into a test tube. After the tube is vigorously shaken, 1 mL of reagent B (0.5% w/v nitroprusside aqueous solution) is added into the test tube and is shaken. 2.5 ml of reagent D (12.5ml of 5% sodium hypochlorite in 50ml reagent C (50g trisodium citrate plus 2.5 g sodium hydroxide in 250 water)) is added to the test tube and vigorously shaken. This solution is moved to a 50ml volumetric flask, and the volume is filled with water. The color of the solution is developed at room temperature for 1 hour and the absorbance at 640 nm was measured at room temperature (Figure 6.23). A calibration curve for ammonia quantification is constructed using standard ammonium chloride solution (Figure 6.22, Figure D.1.b). The amount of ammonium after electrolysis is quantified according to this calibration curve. Control experiments reveal that color development does not occur in the presence of any of the species present in the electrocatalysis experiments, i.e. catalyst, electrolyte, etc.

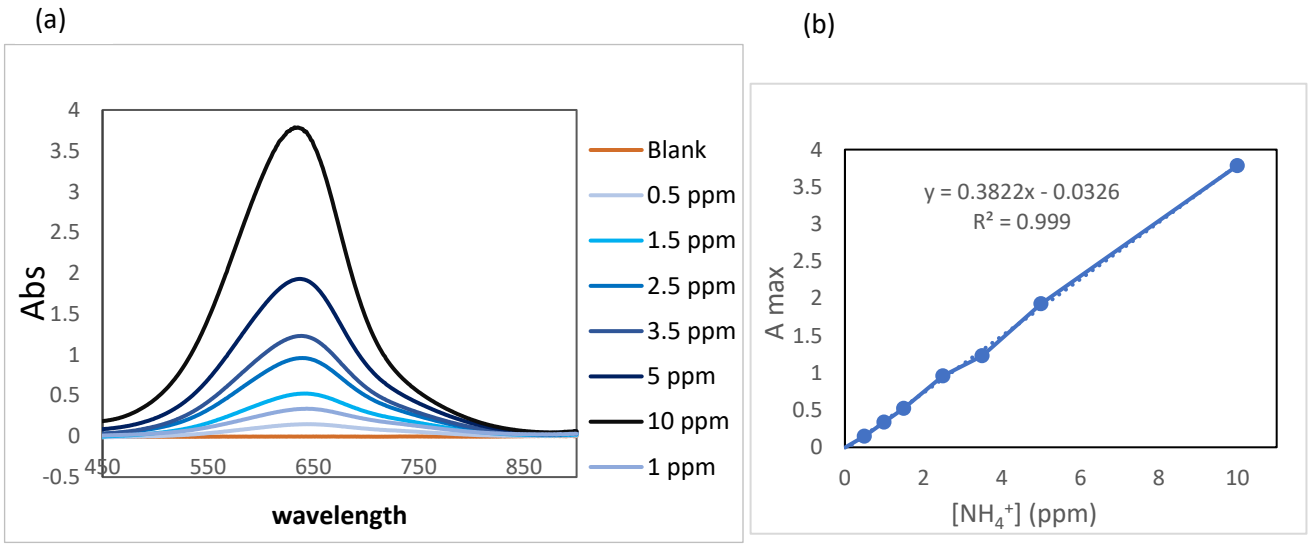

Figure 6.22. a) UV-vis spectra of the NH_4Cl standards for the indophenol blue test containing 0 to 10 µM ammonium. b) Calibration curve for the indophenol blue test.

Figure 6.23. Sample solution color before (right) and after (left) indophenol test.

Hydroxylamine test:

This spectroscopic method is based on oxidation of NH_2OH to N_2O by Fe(III) using ferric ammonium sulfate as oxidation agent, resulting in orange pigment.[210]

Procedure:

1ml of reagent A (0.96 mL of 1 M sodium acetate solution in 1.14 mL of 1M acetic acid solution) is added to 25 mL of sample in a test tube and is vigorously shaken. 1ml of Reagent B (0.0192 g of ferric ammonium sulfate in 10 mL 0.1 M HCl) is added to the test tube and is shaken. 1ml of reagent C (0.018 g of 1,10 phenanthroline in 10 mL 1M aceticacid solution) and shaken again. The color of the solution is developed at room temperature for 30 minutes and the absorbance at 510 nm measured at room temperature (Figure 6.25). A calibration curve for hydroxylamine quantification is constructed using standard hydroxylamine solution. The amount of NH_2OH after electrolysis is quantified according to this calibration curve (Figure 6.24, Figure D.1.a). Control experiments reveal that color development does not occur in the presence of any of the species present in the electrocatalysis experiments, i.e. catalyst, electrolyte, etc.

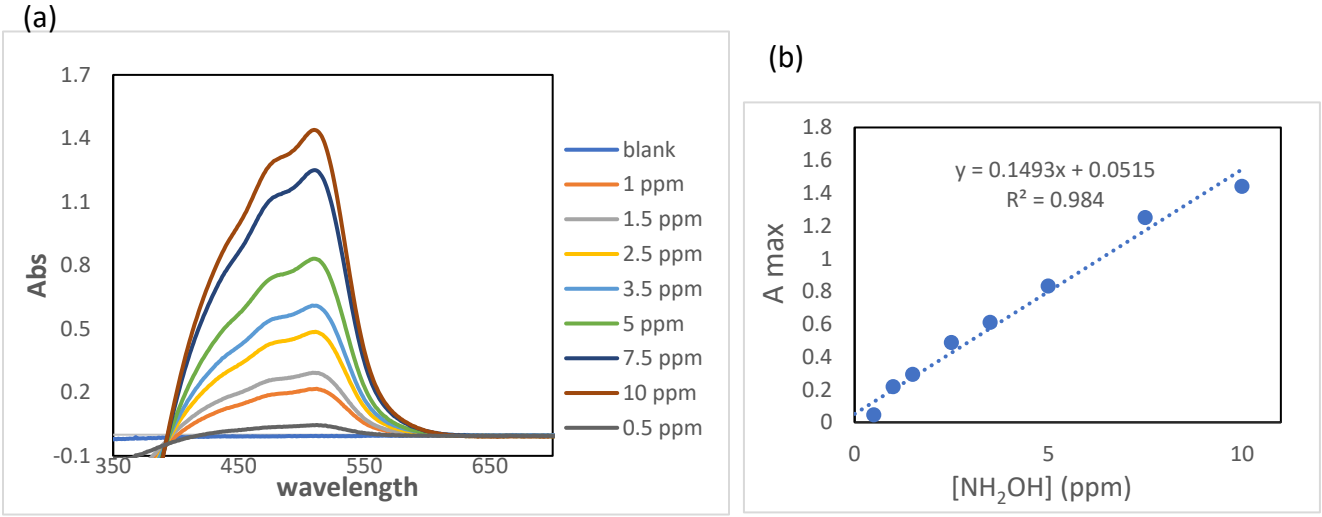

Figure 6.24. a) UV-vis spectra of the (NH_2OH) standards for the hydroxylamine test containing 0 to 10 μM hydroxylamine. b) Calibration curve for the hydroxylamine test.

Figure 6.25. Sample solution color before (left) and after (right) hydroxylamine test.

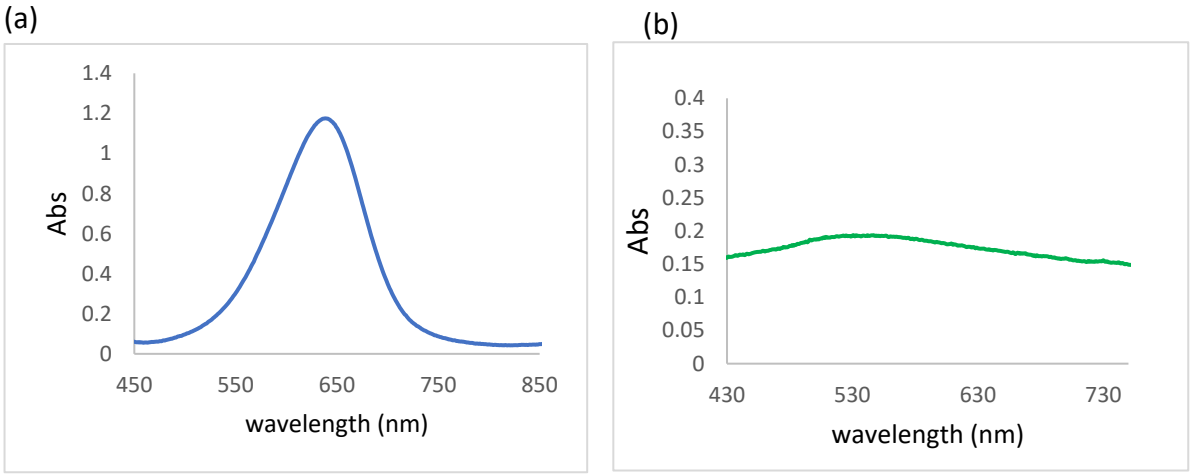

Figure 6.26. a) UV-vis spectra of detected (NH_4^+) as product at 640 nm b) UV-vis spectra of detected (NH_2OH) as product at 510 nm, measured after the CPE experiment shown in table 4, row 1.

Myoglobin Test for NO:

After accounting for NH_2OH and NH_4^+, a significant portion of the charge is unaccounted for. One possibility for the unaccounted charge is the formation of other products. Nitric oxide was first considered as a possibility as it is a proposed intermediate of NO_2^- reduction by nitrite reductases.

This test is based on the reaction of Fe(II) myoglobin (Mb(II)) with NO and shift in the absorption of the product.[7, 211]

Procedure:

Flowing N_2 gas was utilized to bubble the headspace of the CPE cell after overnight electrolysis through a solution containing 500 µM Fe(II) myoglobin (Mb(II)) in 100 mM phosphate buffer at pH 7.4, for 20minutes (Figure 6.28). Following CPE, a 50x dilution of the Mb(II) solution before (pre CPE) and after (post CPE) flowing the headspace gas were then assessed by absorption spectroscopy. As it is shown in Figure 6.27, no shift in the Soret or Q bands of Mb was observed confirming the lack of formation of the Mb-NO adduct. In order to show the changes we would have on the absorption if we had NO in the headspace of the CPE solution, we flow some NO gas to the Mb(II) solution. As you see a new peak shows up at 360nm and the main peak shifts from 409 to 413nm.

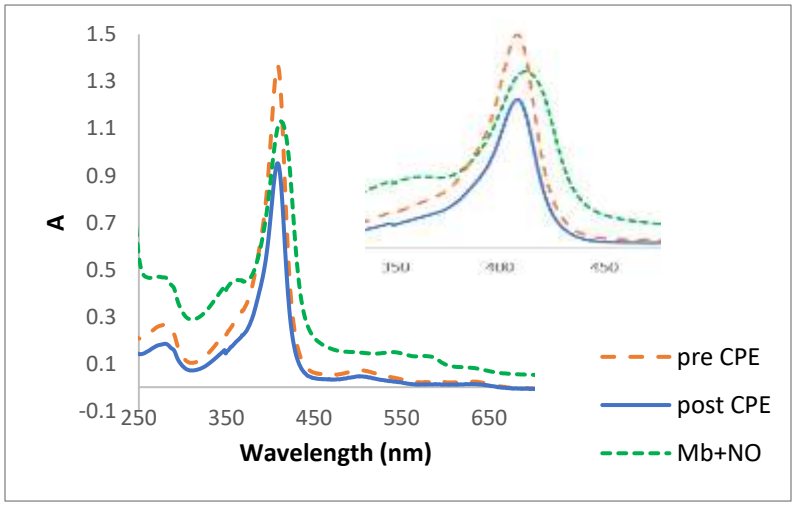

Figure 6.27. UV-vis spectra of a 50x dilution of the 500 µM myoglobin (Mb) in 100 mM phosphate buffer at pH 7.4 solution used for the Mb test for NO.

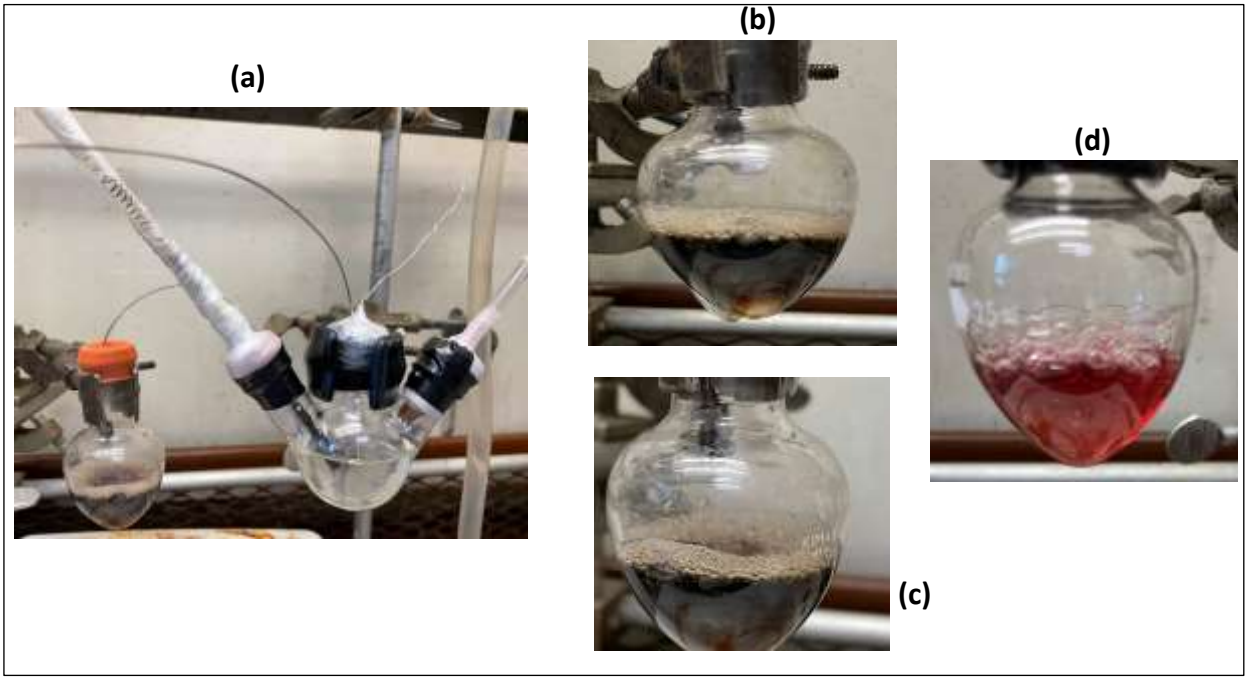

Figure 6.28. a) myoglobin test set up, b) Mb(II) solution before CPE, c) Mb(II) solution after CPE, d) Mb(II) solution reacted with standard NO gas.

Gas chromatography:

Gas chromatography was used for detection of N_2O gas. By injection of standard N_2O gas in gas chromatography, the retention time of 3.2-3.4 min was observed (Figure 6.29.a). Injecting the headspace of electrolysis cell after 4h experiment, no peak was observed at this area. another peak close to this area was observed which belongs to air in the second column of the instrument (Figure 6.29.b). We also used gas chromatography to detect H_2 production as a competitive reaction. The retention time for H_2 gas is 5.36. No H_2 was detected in the presence of nitrite in the electrolysis cell.

(a)

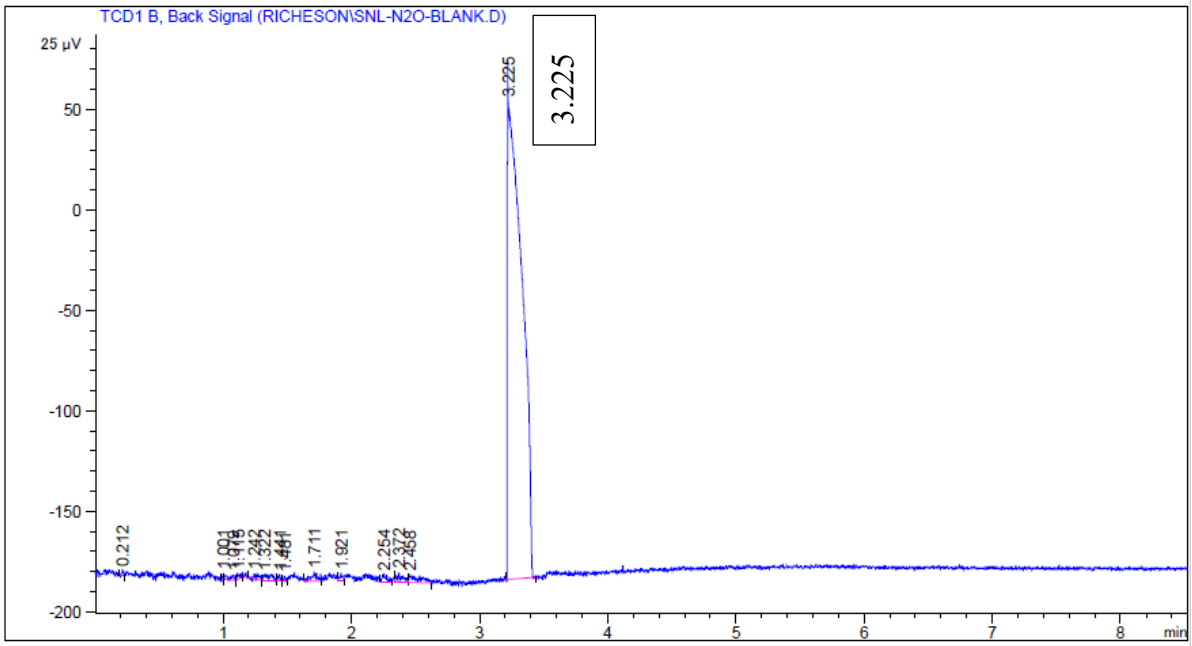

(b)

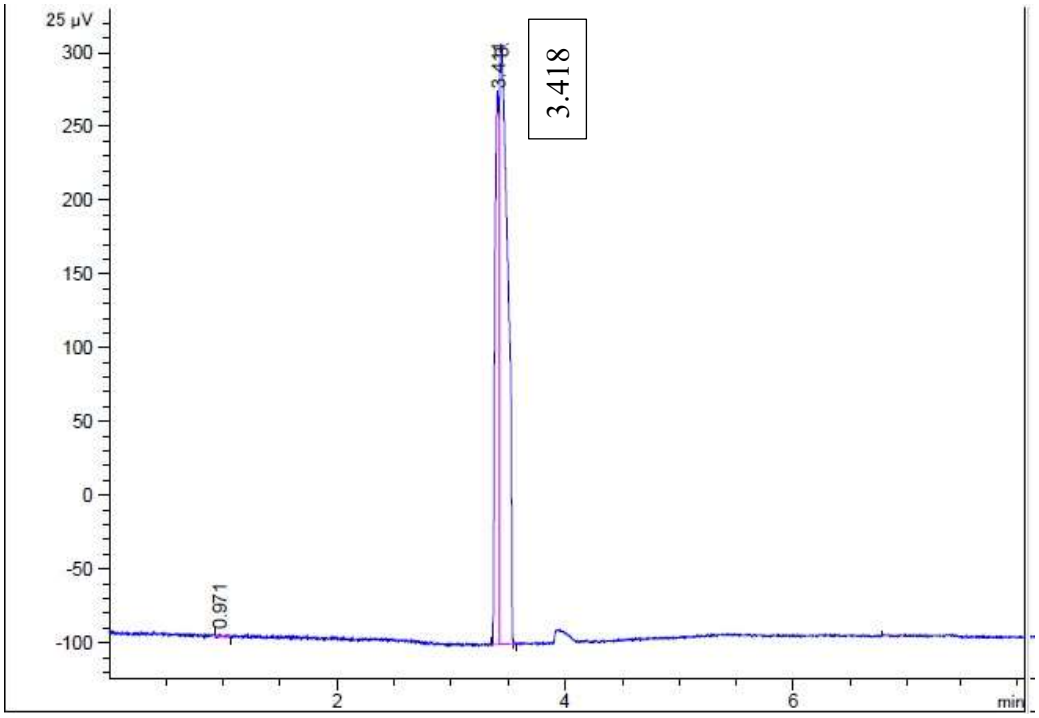

Figure 6.29. Gas chromatography spectrum of (a) standard N_2O gas, and (b) after CPE experiment. The peak at 3.4 belongs to CO_2 gas in the Gas chromatography column.

Electron impact- mass spectroscopy:

EI-mass spectroscopy is a very accurate method that was used as a supportive technique to detect any possible N-containing product in the headspace of the cell after CPE. Based on the literature, possible gas products could be N_2O, NO, NH_3. After 4h CPE, none of these products were detected using this technique. However, after an overnight CPE, a peak at 30.0 which belongs to NO was observed (Figure 6.30). This observation and the myoglobin test result suggest that NO is made after a long CPE and the concentration is very low so that we could not measure it with myoglobin test.

This technique has not been used in the literature for product measurement for nitrite reduction reactions and we are the first group using it.

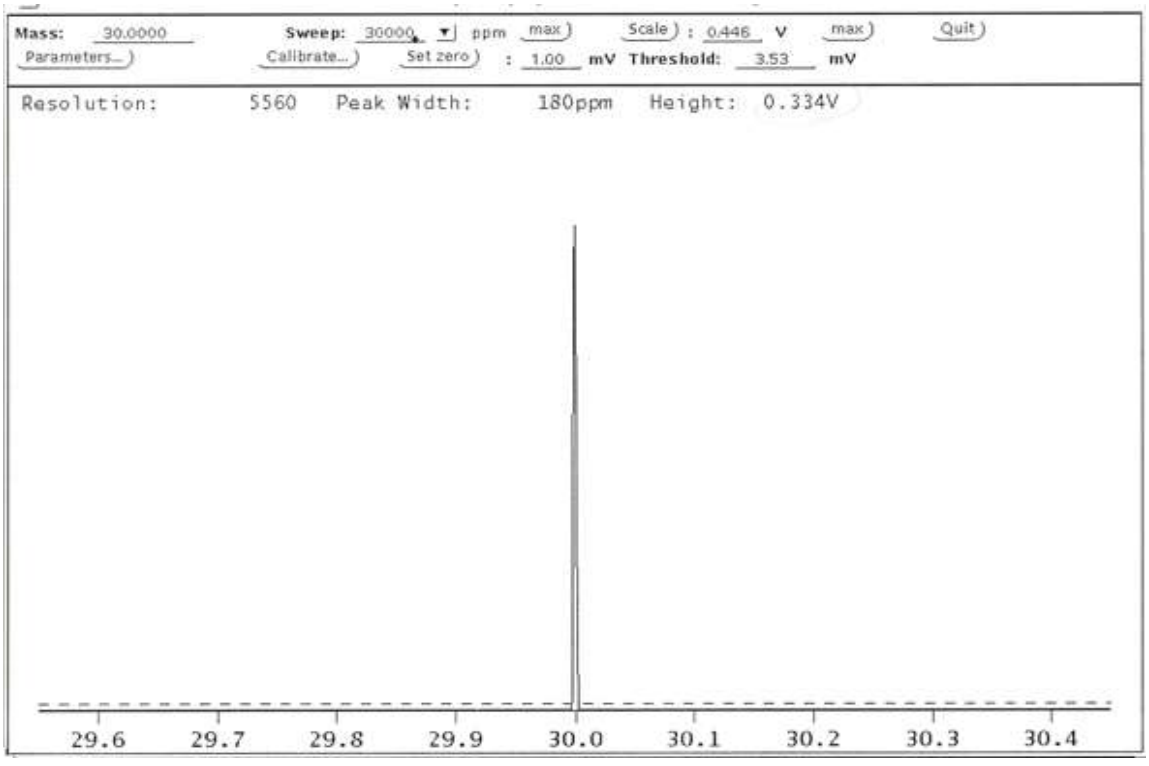

Figure 6.30. Mass spectrum of gas products after CPE experiment (1mM **6.1**, 0.5M $NaNO_2$, 0.1M MOPS, 18h). the peak at 30 shows NO gas.

^{14}N NMR:

This technique was used as a supportive method for detection of any possible N-containing products in the solution such as NH_4^+, NH_2OH. Both of these products have a known peak at 358 ppm (sharp peak) and 276 ppm (broad peak), respectively.

Procedure:

^{14}N nuclear magnetic resonance spectroscopy (NMR) was carried out using a Bruker Avance 500 instrument operating for the ^{1}H nucleus and 36.1 MHz for the ^{14}N nucleus.

Nitromethane ($MeNO_2$) was used as an external standard. For each sample, 500 scans were obtained with a relaxation delay (d1) of 10 seconds to allow for sufficient relaxation of $^{14}NH_4^+$ nuclei. Quantification of NH_4^+ is performed via addition of a capillary tube containing 1.0 M $MeNO_2$ to the NMR tube where indicated. A calibration curve was made by comparing the peak areas of standards with known [NH_4^+] compared to the peak area of the 1.0 M $MeNO_2$ standard within the capillary tube (Figure 6.31).[7] This test only was used in one or two experiments, in order to confirm the presence of ammonium as the product (Figure 6.32). This test was mostly used in the next project reported in chapter 7.

(a)

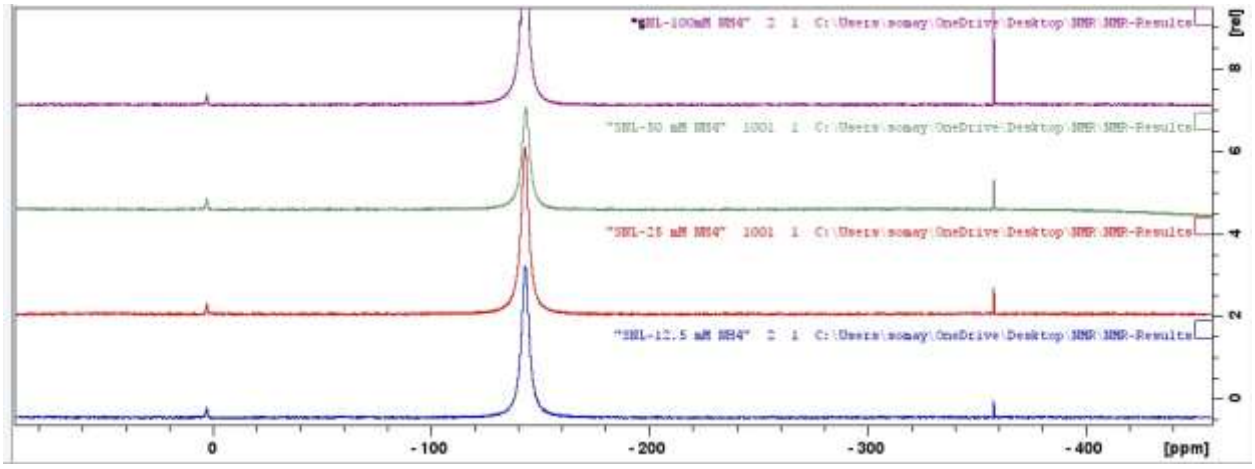

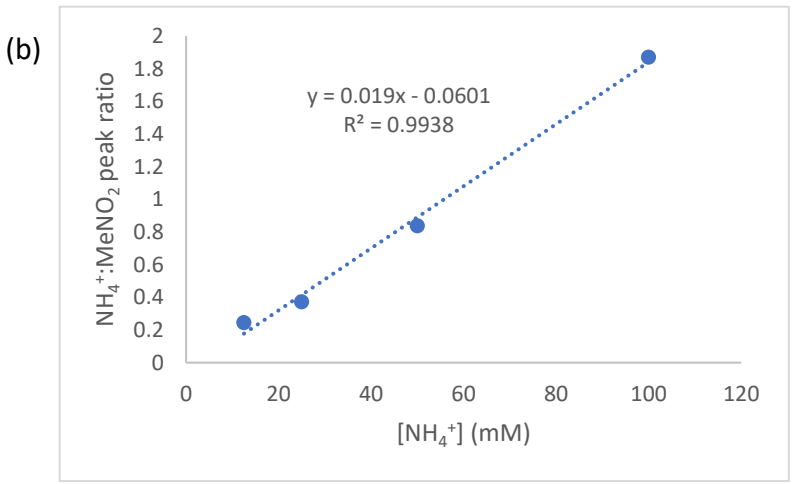

Figure 6.31. a) ^{14}N NMR of standards containing 12.5 to 100 mM NH_4^+ with capillary tubes containing 1.0 M $MeNO_2$. b) calibration curve made by plotting the ^{14}N NMR peak ratio of NH_4^+ to $MeNO_2$ for the NH_4^+ standards shown in a.

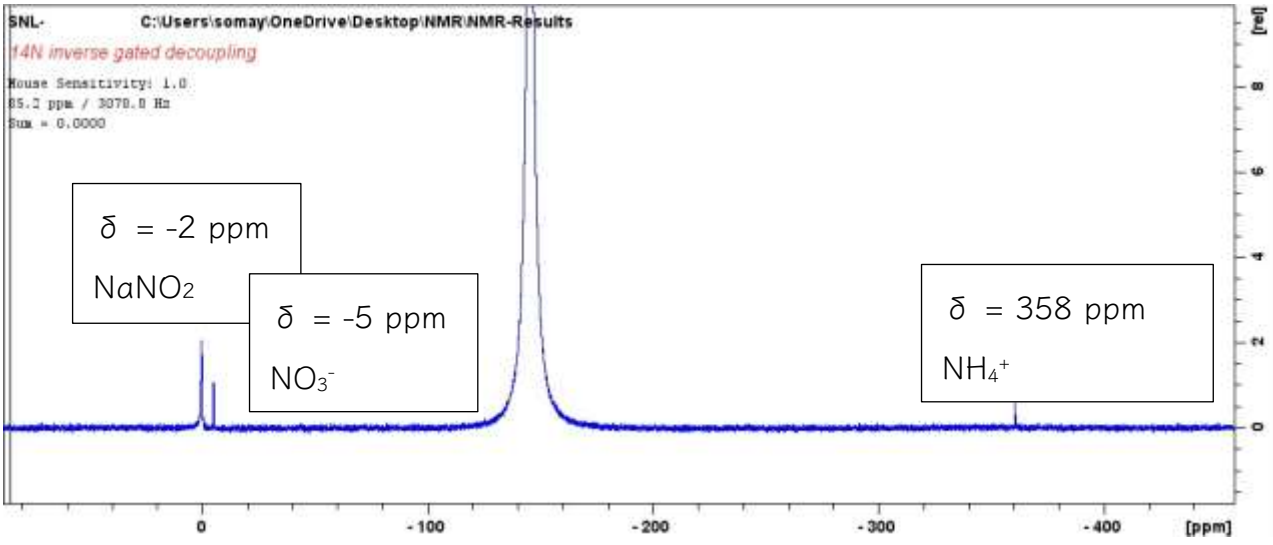

Figure 6.32. ^{14}N NMR (500 MHz) of aqueous solutions obtained either following the CPE experiment shown in table 4, row 1. The sharp peak observed at δ =-358 ppm is attributed to NH_4^+, the peak at δ =-2 attributed to $MeNO_2$, and the peak at δ =-5ppm attributed to NO_3^- as an oxidation product of nitrite.

Chapter 7: Electrocatalytic Nitrite Reduction in Neutral Water with Ni(II) and Co(II) Macrocycle Complexes: Catalytic Evaluation and Mechanistic Elucidation

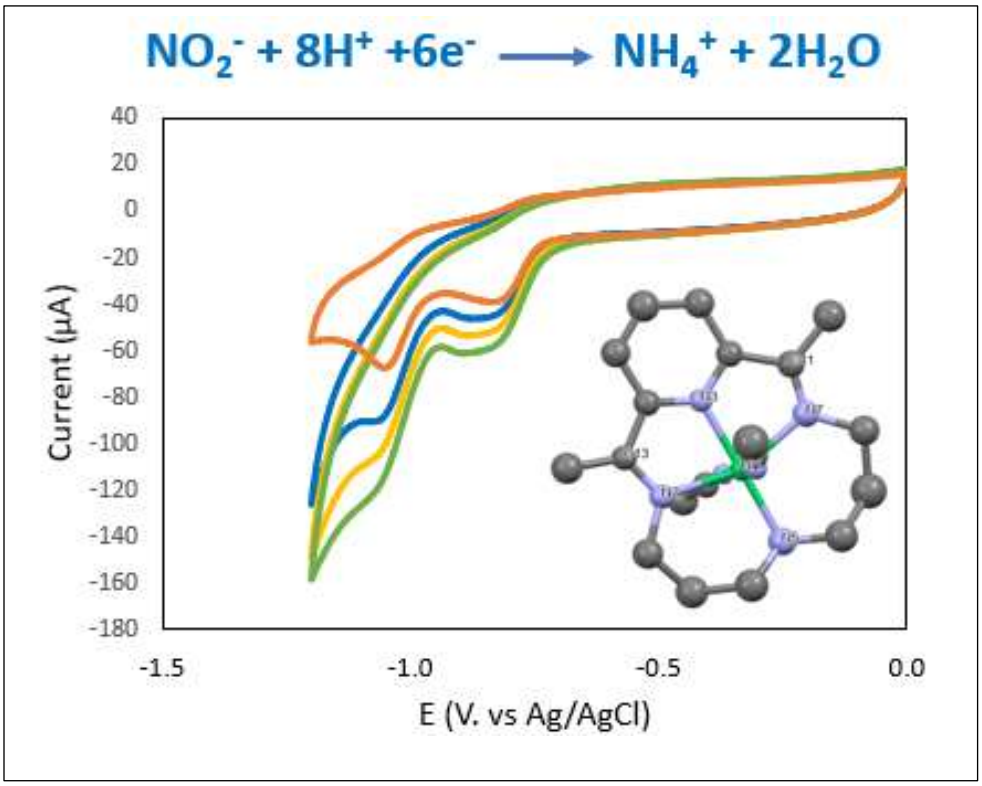

7.1 Preamble and Context

This chapter is a continuation of the work in the previous chapter. The proposal is to incorporate the diminopyridine group into a macrocycle that displays additional amine coordination sites and to examine this change on the ability of the complex to catalyze nitrite reduction reactions. This project was initiated by Somayeh Norouziyan (SN). Selected ^{14}N NMR spectra were measured by Jonathan Ferguson (JF). Synthesis of complex **Ni3** and related electrochemistry was performed by Jake Thibodeau (JT). The manuscript of this project is under preparation.

7.2 Abstract

Nitrite anions, of anthropogenic origin, in the environment disrupt the nitrogen cycle making the electrocatalytic reduction of nitrite a significant objective. Homogeneous Ni(II) and Co(II) complexes bearing a macrocyclic supporting ligand consisting of a tridentate redox active di(imino)pyridine moiety coupled with amine donor sites are effective and selective for the electrocatalytic reduction of nitrite to ammonium ion and hydroxylamine in buffered (pH 7.2) aqueous solutions. Controlled potential coulometry at potentials of -0.98 and -1.2 V vs Ag/AgCl in aqueous solutions buffered with 4-morpholinepropanesulfonic acid (MOPS) yielded ammonium as the major product with Faradaic efficiencies ranging from 50-85%. The Ni complex with a pentadentate ligand, showed an unsymmetrical macrocyclic structure, due to the preference of Ni for octahedral geometry. This complex displayed a higher selectivity for NH_4^+/NH_2OH than the Co complex with the pentadentate ligand and the Ni with tetradentate ligand. A computational examination of the catalytic mechanism of the Ni complex was used to support and elucidate the proposed chemical steps, to provide some energetic details of the electron and proton transfers, and to present a rationale for the selectivity of this reduction.

7.3 Introduction

Due the substantial increase in world population over the last few centuries, the need for more agricultural resources has skyrocketed. To feed the population's constant and growing need for food, the Haber-Bosch process was invented and industrialized for the primary use of synthesizing ammonia for use in fertilizers.[76] However, because the Haber-Bosch process is producing such large amounts of ammonia, there has been a dramatic increase in man-made nitrogen content being introduced into the global nitrogen cycle. While the Haber-Bosch process is a necessity to meet the demands of a growing population, there have been detrimental side effects on the planet's ecosystems due to the unnatural increase in nitrogen content in the nitrogen cycle. Because of this, ecosystems can begin to experience eutrophication resulting in damage to aquatic life and bodies of water and potentially to humans.[14] These concerns have attracted the attention of scientists and stimulated research into methods to address the excessive amount of manmade nitrogen content added to the environment such as the electroreduction of nitrogen oxyanions. (e.g. NO_3^- and NO_2^-). These efforts also aid in understanding the nitrogen cycle and the transformations that occur within it.[212]

Recently, several nitrite-reducing transition metal catalysts, particularly using Fe and Co metal complexes, have been reported (Table 6.1) With the importance of sustainably managing the concentration of wastewater contaminants such as nitrite and nitrate, molecular catalysts are a promising route to explore. Specifically, exploring catalysts for the reduction of nitrite (NO_2^-) and the elucidation of its reaction mechanisms would bring valuable insight into the global nitrogen cycle.[7]

Ligand Selection

A common characteristic of 3d metal-centered complexes that participate in homogeneous NO_x reduction reactions is the use of a redox active moiety in the ligand design. Additionally,

intramolecular proton shuttles, typically as secondary amines which are bound to the metal, are incorporated into the ligand. Together, these two features are speculated to reduce reaction barriers and promote catalytic nitrite reduction.[86, 88] A recently published literature review of advancements in the field of electrocatalytic nitrite reduction listed a variety of different metal-ligand frameworks providing different product selectivity with no clear trend as to how it was achieved. Thus, the rational design of catalysts, is necessary and of great importance for selective homogeneous nitrogen oxyanion reduction catalysis.[9]

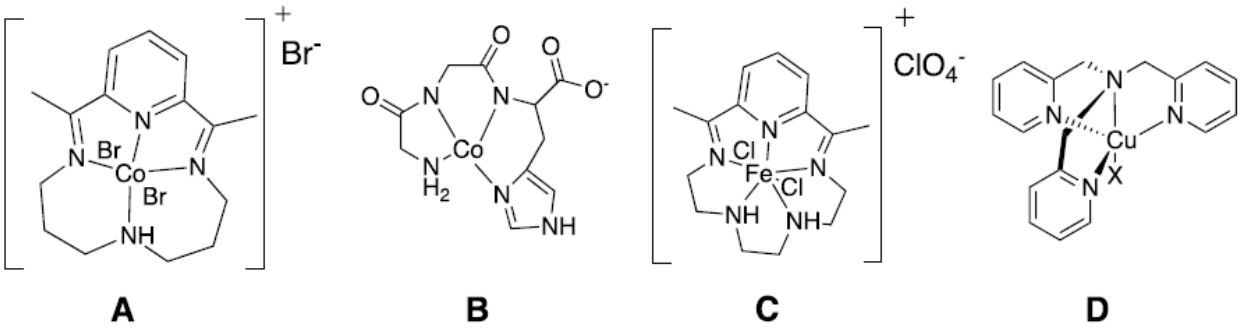

Scheme 7.1. Selected reported homogeneous nitrite reducing electrocatalysts that incorporate an intramolecular proton shuttle and redox active moiety (excluding D which has only a redox-active moiety).

When selecting a potential ligand to explore electrocatalytic nitrite reduction, several factors were considered such as synthetic difficulty, whether the resulting catalyst would be homogeneous or heterogeneous, and an associated target reaction product.

Macrocycle ligands designed around the diiminopyridine core are quite well-known. The redox chemistry with these ligands is most developed for the ligands L1 and L3 shown in Scheme 7.2.[213, 214] For L2, the hydrogen evolution chemistry was reported for Mn, Fe, Co, Zn with focus on Co.[215, 216] This was followed by the photochemical H_2 production from Co.[217] Complexes of L2 with Fe and Co have been studied for CO_2 reduction.[218] The Ni(II) complex of L1 is reported and

has been studied for the H_2 generation.[219-221] The L1 ligand was reported for the preparation of a Co complex that was employed for CO_2 reduction.[222] Interestingly, some of these macrocyclic ligands have been reported to be less effective in preparation of Ni(II) complexes and this same effect has been observed for Cu chemistry. The researchers have suggested that these observations originate in the preference of these metals for octahedral coordination geometry.[214]

Scheme 7.2. Some macrocyclic ligand structures.

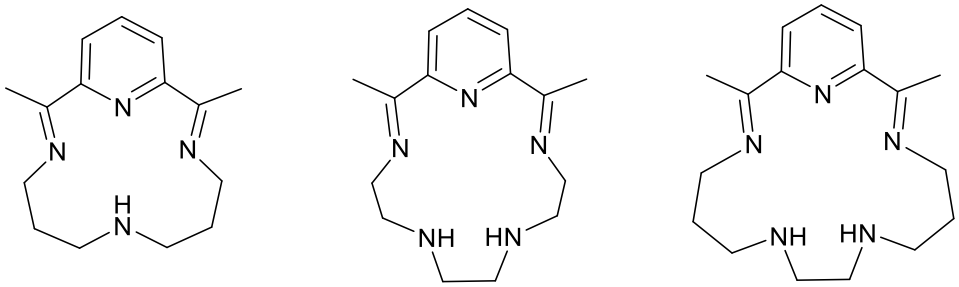

In related literature reports the authors maintain that the diiminopyridine moiety of the tetra or pentaaza macrocycle provided a redox non-innocent functionality and the secondary amine donor provided an intramolecular proton shuttle with the macrocycle being sufficiently flexible to allow for mono- or bidentate binding of targeted cation or anion to the metal center and that these features were key in these types of catalysis.[88] In 2020, Bren and coworkers reported an Fe(II) complex supported by L2 as an active catalyst for nitrite reduction with high efficiency.[7] These reports inspired our efforts to explore the Nitrite Reduction Reaction (NRR) of these macrocycle ligand with other first row metal centers. We also wished to compare these results with the reactivity of the NiDIMPY complexes, reported in chapter 6, and therefore, we chose Ni(II) as the first choice of metal center. Hence, in this chapter, three Ni complexes with tetradentate and pentadentate macrocycle ligands are reported as active electrocatalysts for NRR. To the best of our knowledge, except Ni cyclam complex[85] and NiDIMPY complex reported in chapter 6, there are no other Ni-

base electrocatalysts reported for this reduction. Furthermore, we added a Co complex with pentadentate macrocycle to our list of catalysts as a comparison to Ni and Fe[7] analogs and the reported Co-tetradentate macrocycle, **A**[88] (Scheme 7.1).

7.4 Results & Discussion

7.4.1. Synthesis and Structural Characterization of Complexes

The general approach to the preparation of the macrocycles is the reaction of diacetylpyridine with the appropriate primary diamine in equimolar proportions in the presence of a metal salt as a templating agent.[223] Various solvents were used, most commonly MeOH or EtOH. The optimum reaction temperatures and reaction periods, found by experiment, varied widely from 30 min at 20°C to 48 h at 65°C.[214] The importance of the metal ion is shown by the fact that in its absence only viscous oils were obtained, these having indefinite composition and properties suggestive of an oligomeric/polymeric constitution. However, not all metal ions have proved to be effective as templates for bigger macrocycles. It is surprising that neither Ni(II) nor Cu(II) are templates for any of the L2 and L3 macrocycles since both ions are commonly used as templates in the synthesis of tetradentate 'N4' macrocycles.[224] Single crystal X-ray structure determinations of a wide range of metal complexes of the potentially pentadentate macrocycles by Nelson and coworkers have shown that the preferred conformation of the 15-membered and the 16-membered rings (L2 and L3) is that in which the five donor atoms define a pentagonal plane but that the more flexible 17-membered rings may adopt a variety of conformations. Thus, 7-coordinate (pentagonal bipyramidal) geometries have been demonstrated for Mg(II), Mn(II), Fe(III), Fe(II), Zn(II), Cd(II) and Sn(IV), and 6-coordinate (pentagonal pyramidal) structures for Co(II), Ag(I), Cd(II) and Hg(II) complexes containing L2, L3.[225-231] In a few cases, however, octahedral rather than pentagonal-based geometries are obtained.

For synthesising the Ni complex with the L1 macrocyclic ligand (**Ni1**), we followed the metal templated reaction between Ni(II)Cl_2 and a stoichiometric amount of 2,6-diacetylpyridine and 3,3'-diaminodipropylamine, followed by anion exchange with perchlorate, which resulted in a purple precipitate of complex Ni{(2,12-dimethyl-3,7,11,17-tetraazabicyclo[11.3.1]heptadeca-1(17),13,15-triene)$(MeCN)_2$}ClO_4 **(Ni1),** (Scheme 7.3). Crystallization was achieved by layering diethyl ether on a solution of **Ni1** dissolved in acetonitrile.

Scheme 7.3. Synthesis of **Ni1**.

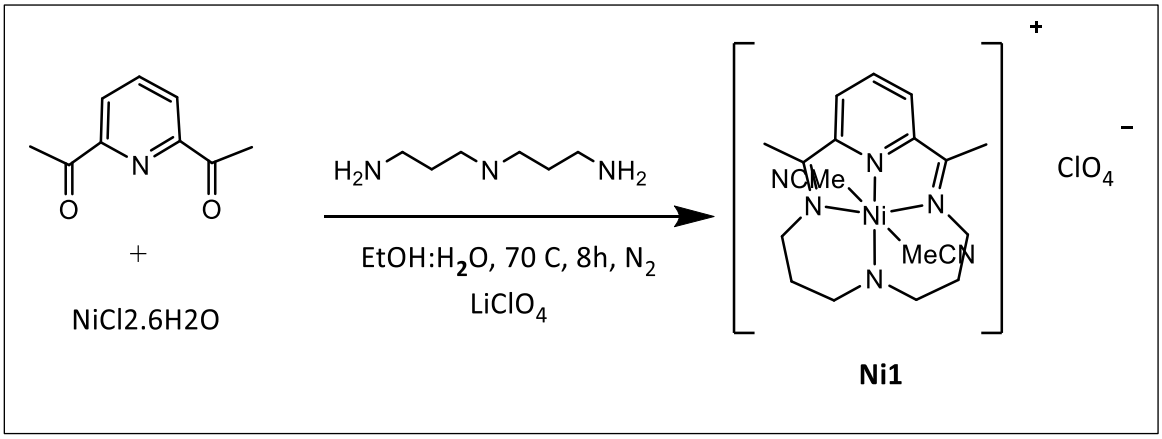

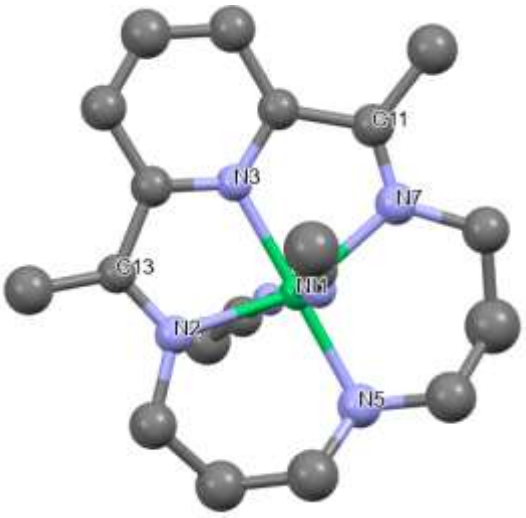

Figure 7.1. depicts the results of the X-ray structural analysis of complex **Ni1** showing only the cationic metal complex portion of the structure. The perchlorate counterion is not shown.

The single crystal X-ray analysis of **Ni1** complex gave the structure shown in Figure 7.1, consisted of the expected tetradentate macrocyclic ligand in addition to two coordinated CH_3CN molecules (which are the crystallization solvent), leading to a nickel center that adopts a distorted octahedral geometry, as seen in Tables E.1 and E.2. [219, 220] The main distortions are due to the limited bite angle of the pyridyl N3 center with the imine N centers (N2, N7). For example the bite angle N(2)-Ni(1)-N(3) is 78.4 (3)°. This also led to a reduced angle for N(2)-Ni(1)-N(7) of 156.8(8)°. The bond angle between N(3)-Ni(1)-N(5) is 178.9(5)°. Interestingly, the bond between the Ni metal center and acetonitrile anion has an average length of 2.1(4)Å which is longer than the length of Ni with other nitrogen centers of the L1 ligand. It seems likely that the bound acetonitrile dissociates when **Ni1** is dissolved in a solvent.

Attempts to employ the template procedure to obtain Ni(II) complex with L2 were not successful. Several approaches were explored but the product was invariably the distorted octahedral complex **Ni2** represented in Scheme 7.4. It appears that rather than preparation of a Ni complex of L2, a new more flexible macrocycle derived from L2 by addition of ROH (solvent) across one of the azomethine bonds (L4) results (**Ni2**) (Scheme 7.4 and 7.5). If the reaction is carried out in the presence of water, hydrolysis occurs to give an octahedral complex of the ring-opened ligand (L5). Molecular models and various structural analysis show that L2 cannot fold so as to occupy five octahedral positions.

In contrast the Co(II) complex with L2 (**Co2**), was successfully prepared with the template method, as reported in the literature[216, 218] and confirmed by UV-Vis, FT-IR, elemental and electrochemical analysis (Scheme 7.4).

Scheme 7.4. Synthesis of **Ni2** and **Co2.**

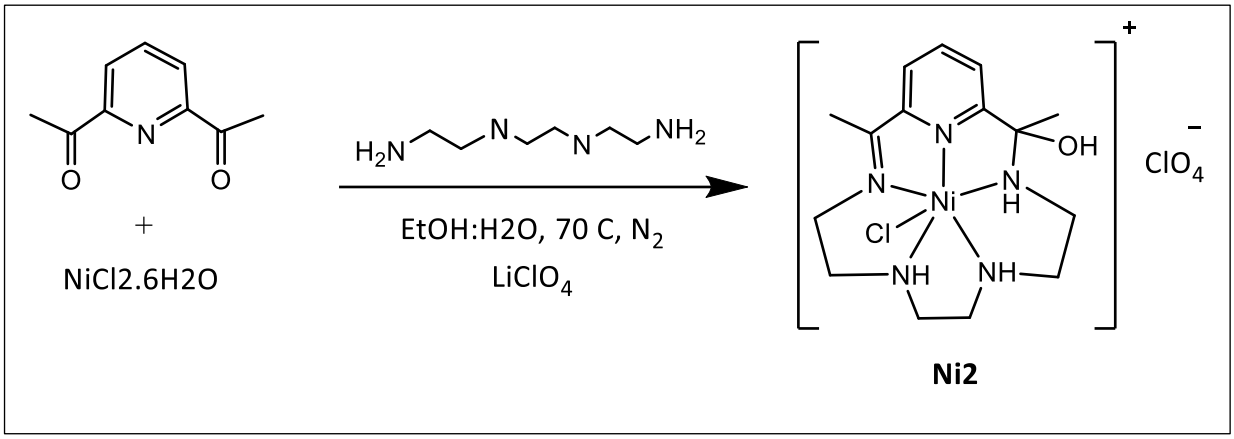

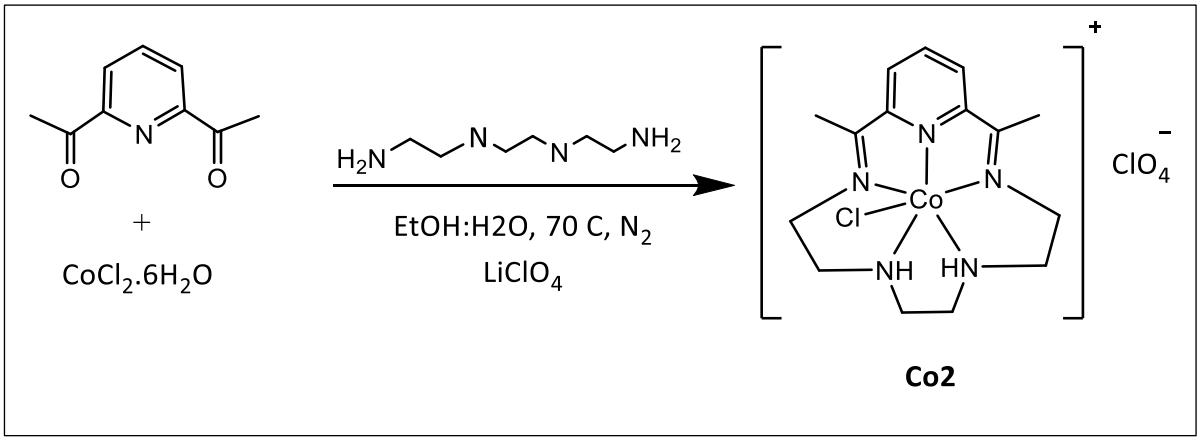

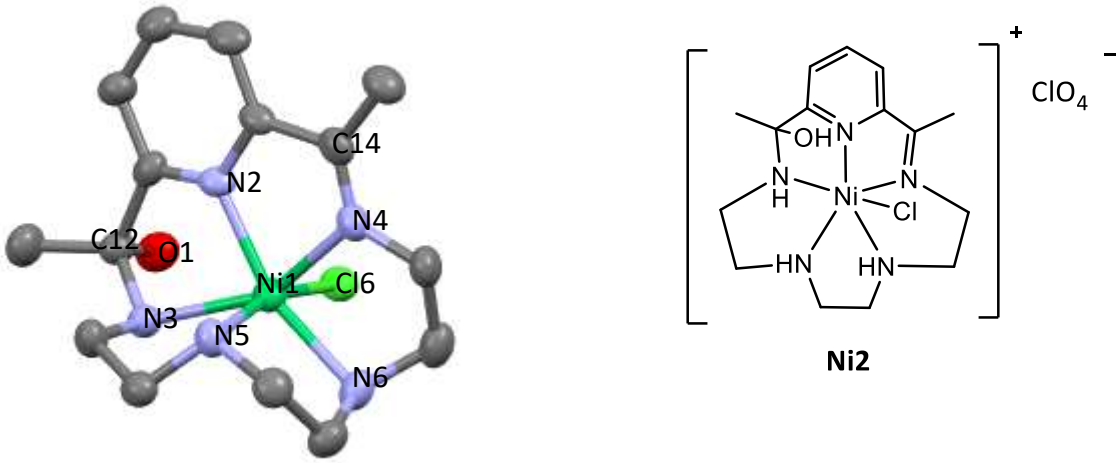

Figure 7.2. depicts the results of the X-ray structural analysis of complex **Ni2** showing only the cationic metal complex portion of the structure. The perchlorate counterion is not shown.

Scheme 7.5. Some macrocyclic ligand structures made by Ni(II) and Cu(II).

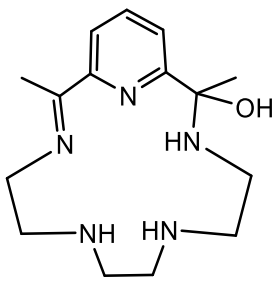

L4

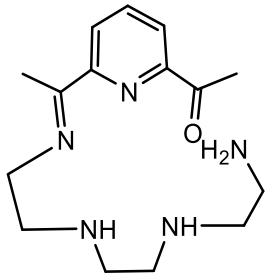

L5

The **Ni2** complex, shown in Figure 7.2, consisted of the expected pentadentate macrocyclic ligand that was coordinated to the Ni center in a distorted octahedral arrangement as seen in Table E.3 and E.4. Ni is coordinated through six bonds, five of them to N and one to Cl. The average bond angle between N(2)-Ni(1)-N(3) and N(2)-Ni(1)-N(4) is 78.4(3)°. This value is a bit higher for N(5)-Ni(1)-N(6) and N(4)-Ni(1)-N(6), which is 82.3°. The bond length between C(12)-O(1) is 1.425(9) Å. Due to the presence on O attached to C(12), the bond length between C(12)-N(3) is longer than C(14)-N(4) which is 1.48(1) Å and 1.26(2) Å, respectively. One chloride anion is coordinated to the Ni center perpendicular to the plane defined by the ligand. Interestingly, the bond between the Ni metal center and chloride anion has a length of 2.468(2) Å which is rather long. We speculated that the chloride is bound only in the solid state and dissociates immediately upon **Ni2** dissolving in a solvent.

Increasing the size of the pentadentate macrocycles to the 17-membered ring (L3) leads to a considerable increase in flexibility allowing a readier response to the geometrical preferences of the central metal ion. The reported synthesis employs a transmetallation of the Ag(I) complex in [AgL3][ClO_4] with Ni(II) in dry ROH (R = Me or Et) the product is an octahedral complex of the new more flexible macrocycle. Thus, L3 can fold so as to occupy five octahedral sites when

complexed to Ni(II) (Scheme 7.6). [232] Although this complex was characterized by UV-Vis and FT-IR, no crystal structure was reported.

Scheme 7.6. Synthesis of **Ni3.**

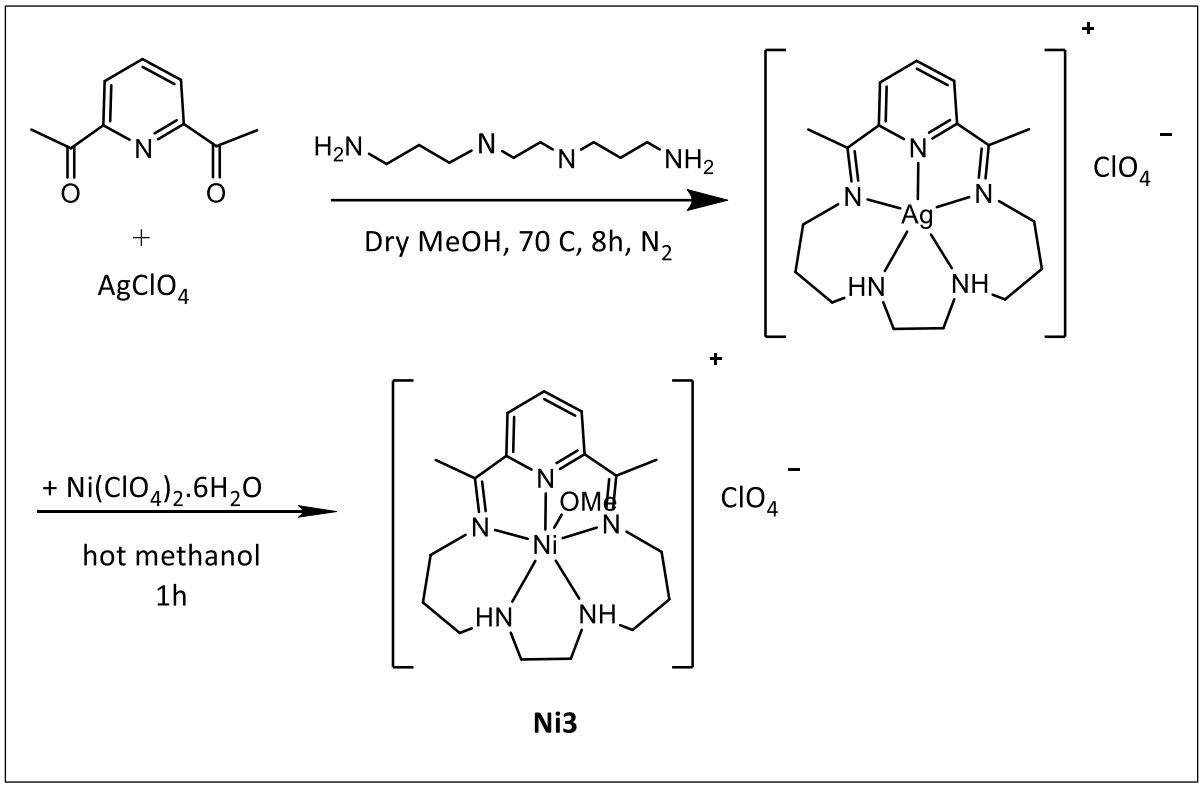

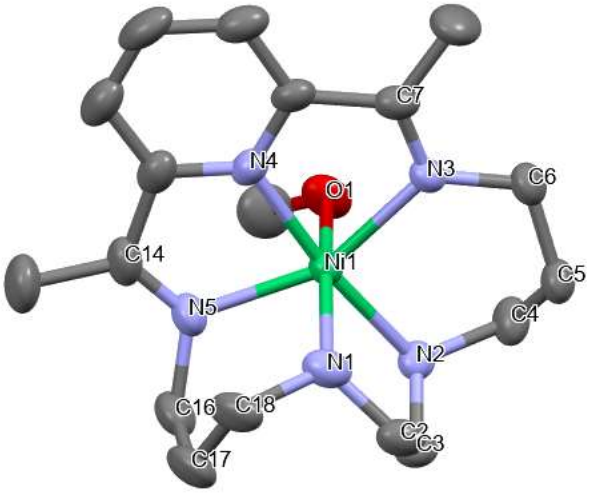

Figure 7.3. depicts the results of the X-ray structural analysis of complex **Ni3** showing only the cationic metal complex portion of the structure. The perchlorate counterion is not shown.

Single crystal X-ray structure of **Ni3** complex is shown in Figure 7.3, confirming the proposed structure that consists of the expected pentadentate macrocyclic ligand that is coordinated to the Ni center in a distorted octahedral arrangement as seen in Tables E.5 and E.6. The pentaaza ligand is coordinated to the Ni through all five nitrogen centers. Within this ligand the N2, N3, N4 and N5 define a four-coordinate slightly distorted plane. The limitations of the bite angles for the pyridyl N (N4) and the imine N (N3, N5) do lead to some distortion. The coordinated N2 center is oriented trans to the N4 at an angle of 172.8°. Overall, the result is a NiN4 plane that can be used to define the equator or the distorted octahedron. The flexibility of the pentaaza ligand allows for the N1 center of the ligand to coordinate approximately perpendicular to the NiN4 plane (average N-Ni-N angle of 92°). The remaining coordination site is occupied by a O coordinated methoxide group originating from the crystallization solvent and is also approximately perpendicular to the NiN4 plane. This $(MeO)^-$ ligand is trans to N1 with a O(1)-Ni(1)-N(1) angle of 166.5°.

7.4.2. Electrochemical characterization

With compounds **Ni1**, **Ni2**, **Co2**, and **Ni3** in hand, we set out to perform the electrochemical characterization and examine their ability to electrocatalytically reduce nitrite. For all the electrochemical characterization, the Ag/AgCl (3M KCl) reference electrode was used. The initial characterization was carried out in acetonitrile. This approach provides a better comparison with the electrochemistry of the other Ni complexes reported in this thesis. Moreover, the electrochemistry of these complexes in organic solvent is often more straightforward.

Ni1 displays two reversible reduction peaks at E_p = -0.6 V and E_p = -1.18 V (Figure 7.4a). For both peaks the ΔE_p = 0.1 V. This value is higher than the ideal number of 0.059V for a reversible redox event, but it is close to the ΔE_p that we measured for the $Fc^{0/+}$ redox reactions in the same solvent system. This difference is attributed to the resistance in the electrochemical cell (Chapter 2, Figure

A.15). **Ni2** shows a reversible peak at E_p= -0.88V, and an irreversible one at E_p = -1.24V vs. Ag/AgCl (Figure 7.4b). In the case of complex **Co2** a redox peak at E_p = -1 is observed with ΔE_p of 0.3V, showing that it is not reversible (Figure 7.4c). Finally, **Ni3** has a similar CV to **Ni1**, showing two reversible peaks at E_p = -0.93 V and E_p = -1.6 V (Figure 7.4b). According to the literature, the initial reduction product in macrocyclic complexes affords a M^I species formulated as $[M^I(L)]$ and the second reduction process is a ligand-reduced species $[M^I(L^{-\cdot})]^+$.[88, 216, 218] All the reduction potentials are listed in Table 7.1 for a better comparison.

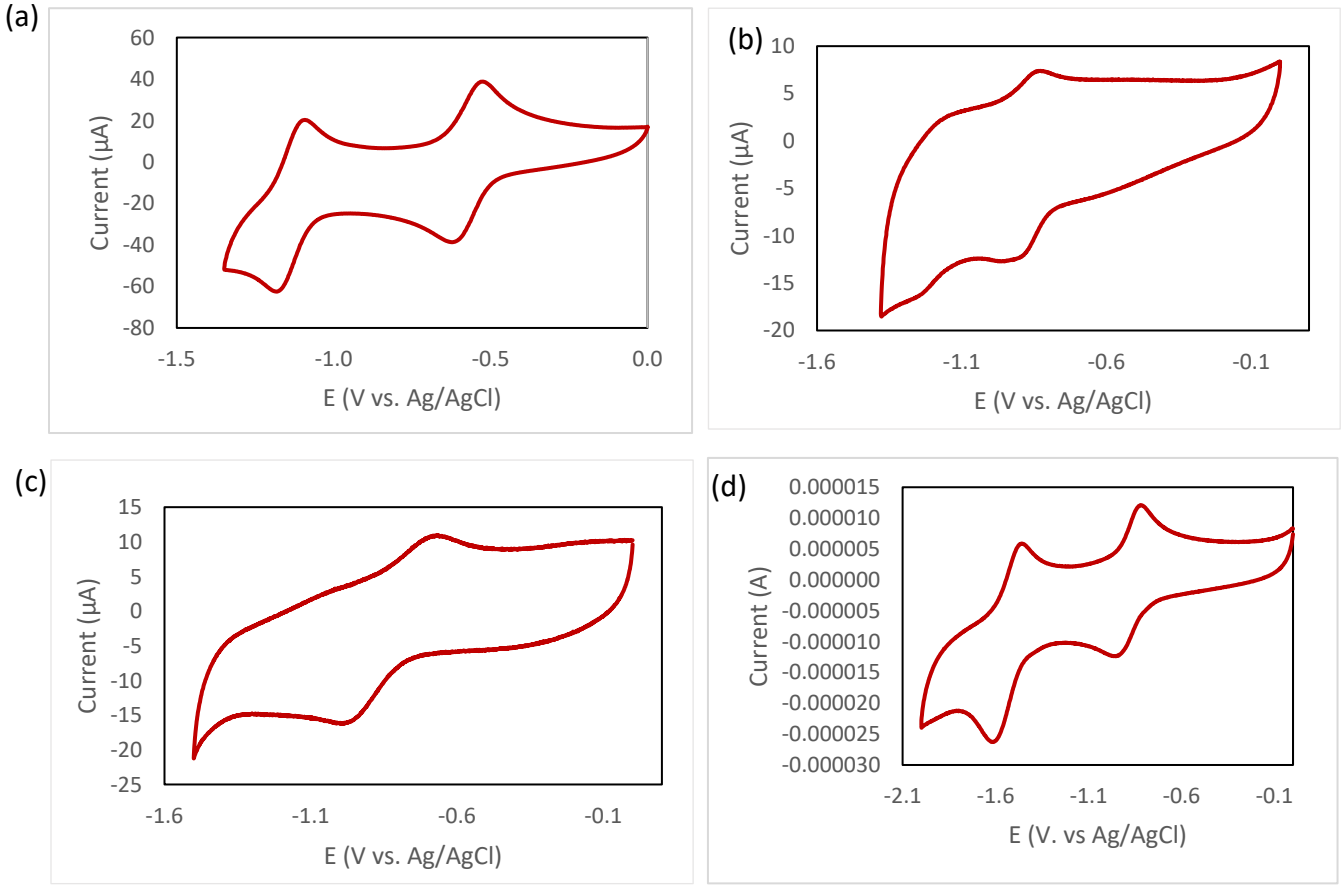

Figure 7.4. Cyclic voltammogram of (0.5mM) a) **Ni1** b) **Ni2** c) **Co2** d) **Ni3** in CH_3CN with 100mM TBAHFP using a glassy carbon (GC) working electrode. All potentials are referenced to Ag/AgCl (3M KCl).

Having confirmed the fundamental electrochemistry of these complexes in acetonitrile, the electrochemical features were next examined in aqueous solution, a more applicable solvent for nitrite reduction. Furthermore, given the requirement of multiple proton transfer events and the documented influence of pH on the nitrite reduction products, an aqueous buffer system was chosen to mitigate large pH changes during the catalytic transformation. The selection of the buffer was based on two criteria; the first was a buffer that was centered at pH 7 and the second was to focus on a buffer with a "non-coordinating" conjugate base to minimize interference on the catalyst. These attributes led to the selection of the "Good's buffer" derived from 4-morpholinepropanesulfonic acid (MOPS) with a pKa of 7.20.

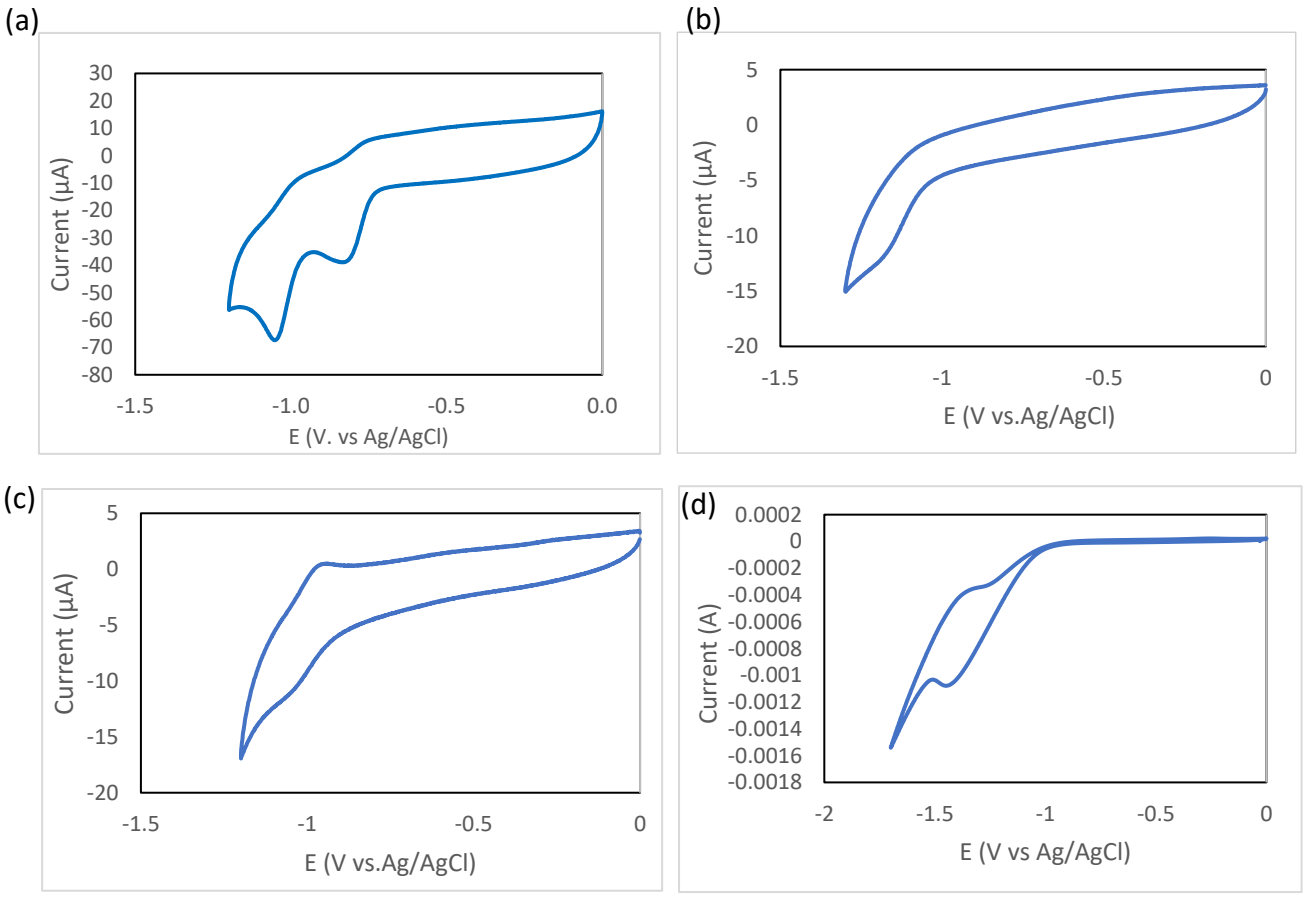

Figure 7.5. Cyclic voltammogram of (0.5mM) a) **Ni1** b) Ni2 c) **Co2** d) **Ni3**, in H_2O with 100mM KCl, using a glassy carbon (GC) working electrode. Potentials are referenced to Ag/AgCl (3M KCl).

Table 7.1. Reduction potentials of complexes reported in this chapter. All potentials are referenced to Ag/AgCl (3M KCl).

	E(V) in CH_3CN		E(V) in H_2O	
compound	First reduction	Second reduction	First reduction	Second reduction
Ni1	-0.6	-1.18	-0.81	-1.04
Ni2	-0.88	-1.24	-1.12	_
Co2	-1	_	-1.05	_
Ni3	-0.93	-1.6	-1.44	_

The stability and homogeneity of these reductions were assessed by measuring the scan rate dependence of the current for the first and second reduction peaks for complex **Ni1, Ni2**, **Co2,** and **Ni3** in water. The results of these measurements are shown in Figure 7.6. The linear relationship obtained for the square root of the scan-rate versus peak current is consistent with the Randles-Ševčík equation and supports diffusion-controlled processes.

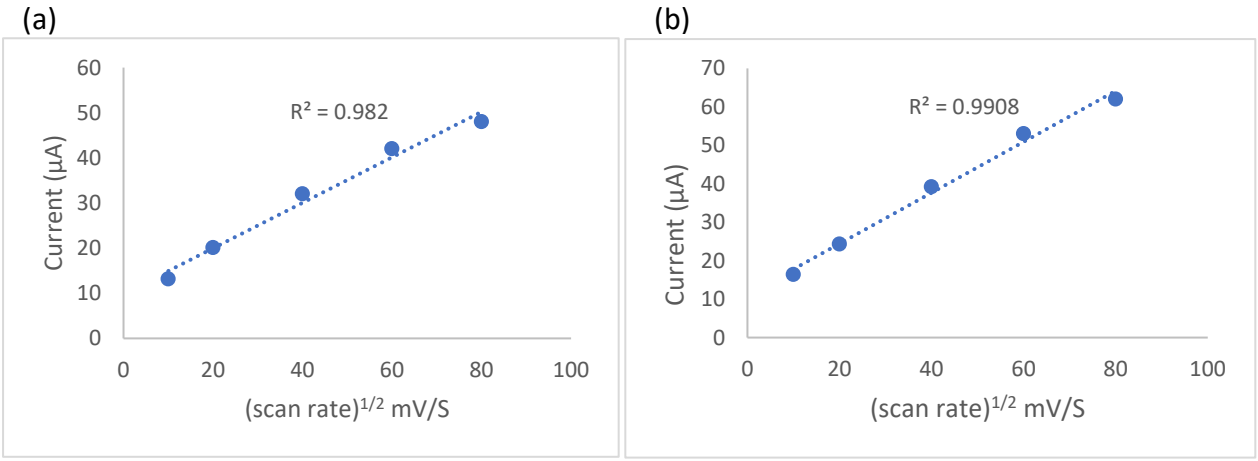

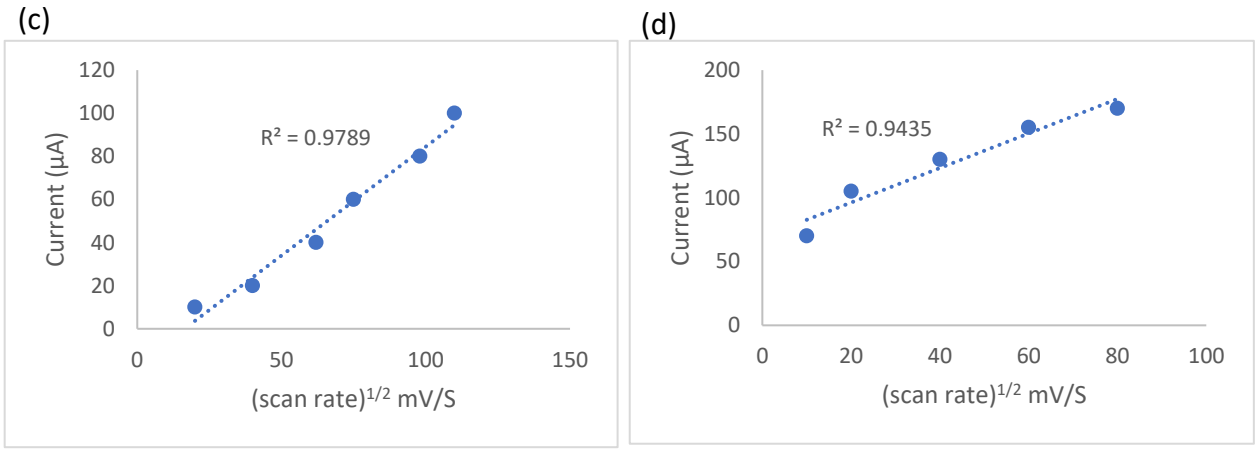

Figure 7.6. Scan rate dependence of the first and second reduction peak for complex a) second peak of **Ni1** at -1.04V, b) first peak of **Ni2** at -1.12V**, c)** first peak of **Co2** at -1.05V, d) first peak of **Ni3** at -1.44V, in water with 0.1 M KCl as the supporting electrolyte and 50mM MOPS buffer.

With these features established, the effect of incremental addition of $NaNO_2$ to a reaction cell containing 100 mM MOPS buffer and **Ni1** was investigated. After the initial addition of $NaNO_2$ into the system, there is a significant current enhancement at the second reduction event indicative of a catalytic process taking place. Continued additions beyond 80 mM $NaNO_2$ to the reaction system resulted in only small current increases (Figure 7.7). At 100mM it reaches saturation point and there was no further observed current enhancement.

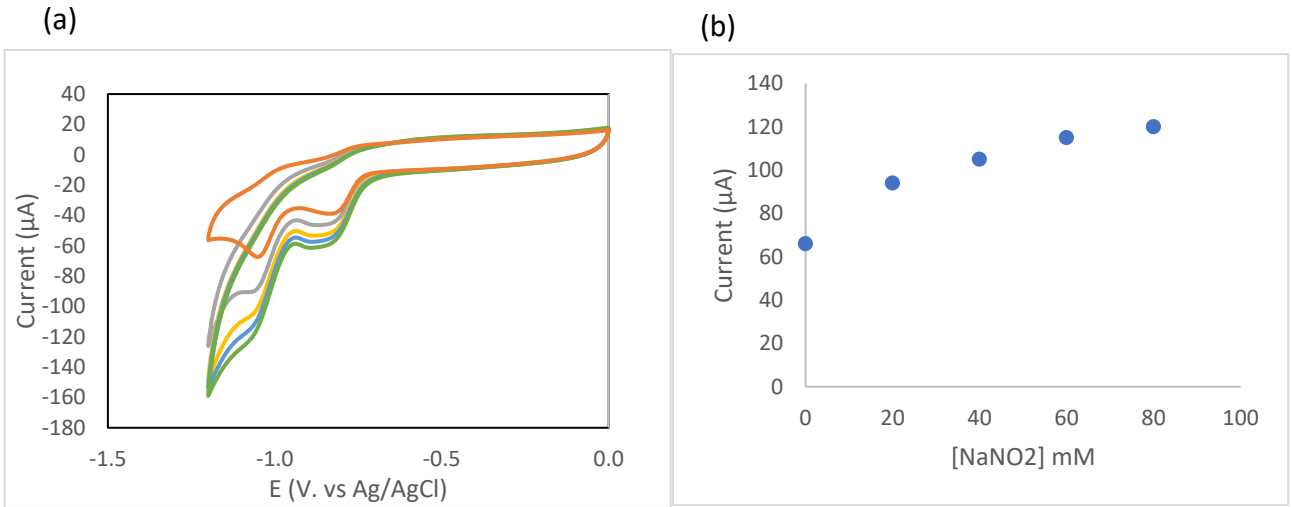

Figure 7.7. a) Cyclic voltammograms (100 mV/s) of 0.1 M KCl, 30 mM MOPS, 0.5 mM **Ni1**, with $NaNO_2$ titrated from 0 to 80 mM, b) Plot of peak current versus the concentration of $NaNO_2$ titrated.

Further assessment of the reaction conditions was carried out through several control experiments, which were used to demonstrate the requirement of complex, MOPS buffer, and substrate (sodium nitrite) in the catalysis system. A cyclic voltammogram with all the background experiments is shown in Figure 7.8. This figure documents that there is no enhancement in current before -1.4V in the absence of **Ni1** in the mixture of MOPS and nitrite. By adding **Ni1** to this solution an enhancement is observed. It is interesting that in the absence of MOPS, after addition of nitrite to the **Ni1** solution no enhancement in the catalysts peak was observed (Figure 7.8, yellow curve). It indicates the important role of buffer in the catalysis. This makes sense because there is a direct relationship between pH and reduction potential. These blank experiments also suggest that there is no competitive reaction such as HER happening in this voltage range.

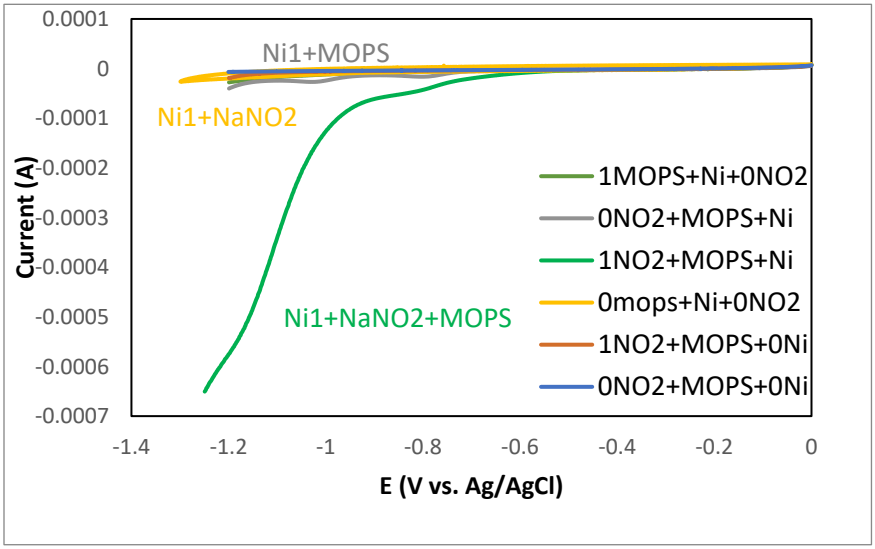

Figure 7.8. Cyclic voltammograms (100 mV/s) in water with 0.1 M KCl or $NaNO_2$ or MOPS or **Ni1** added as indicated in the legend. The third scan is shown for each experiment.

In the blank experiments, it was observed that the reduction of nitrite by the glassy carbon (GC) electrode in the MOPS solution occurs at -1.45 V vs. Ag/AgCl, as illustrated in the Gray

voltammogram (Figure 7.9). Additionally, in the absence of both nitrite and catalyst, an enhancement at -1.6 V vs. Ag/AgCl was noted, indicative of water reduction by the GC electrode, as depicted in the Orange voltammogram (Figure 7.9). These findings affirm that there is no discernible background interference in the catalytic processes under investigation.

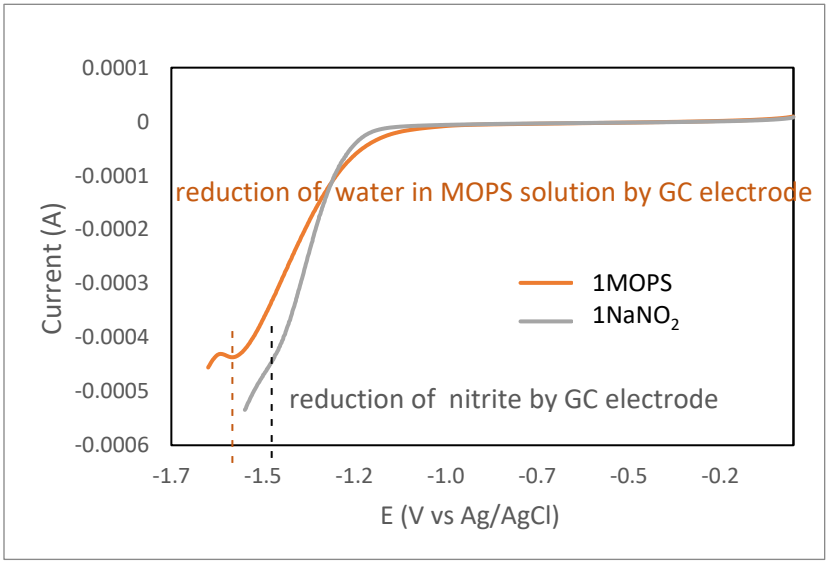

Figure 7.9. Background cyclic voltammograms in aqueous solution with 100 mM KCl and 1M MOPS pH=7, in the absence of **Ni1** (gray) and $NaNO_2$ (orange), using a glassy carbon (GC) working electrode, (100 mV/s). Water reduction with **Ni1** in an aqueous MOPS solution pH=7, happens at -1.6 V, and in the absence of catalyst nitrite reduction happens at -1.5 V.

Figures 7.10 and 7.11 indicate the linear dependence of catalysis to the concentration of MOPS and **Ni1** until it reaches to the saturation point. These results could suggest a first order kinetics with respect to the concentrations of MOPS and catalyst in this reaction.

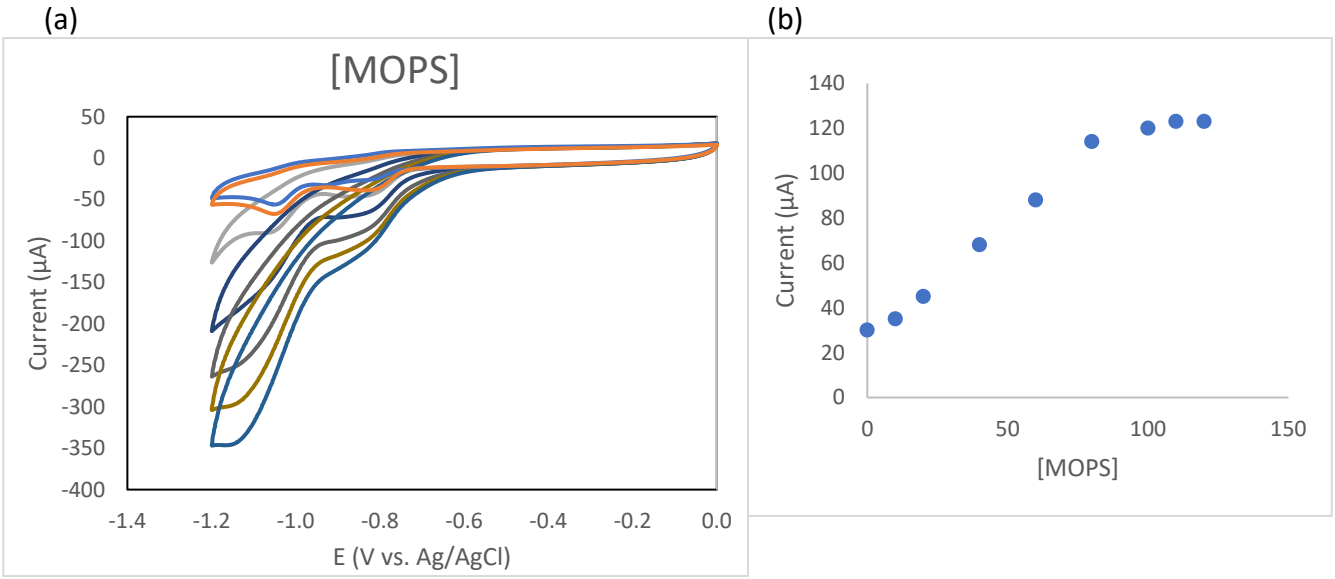

Figure 7.10. a) Cyclic voltammograms (100 mV/s) of 0.1 M KCl, 100 mM $NaNO_2$, 0.5 mM **Ni1**, with MOPS titrated from 0 to 120 mM, b) Plot of peak current versus the concentration of MOPS titrated.

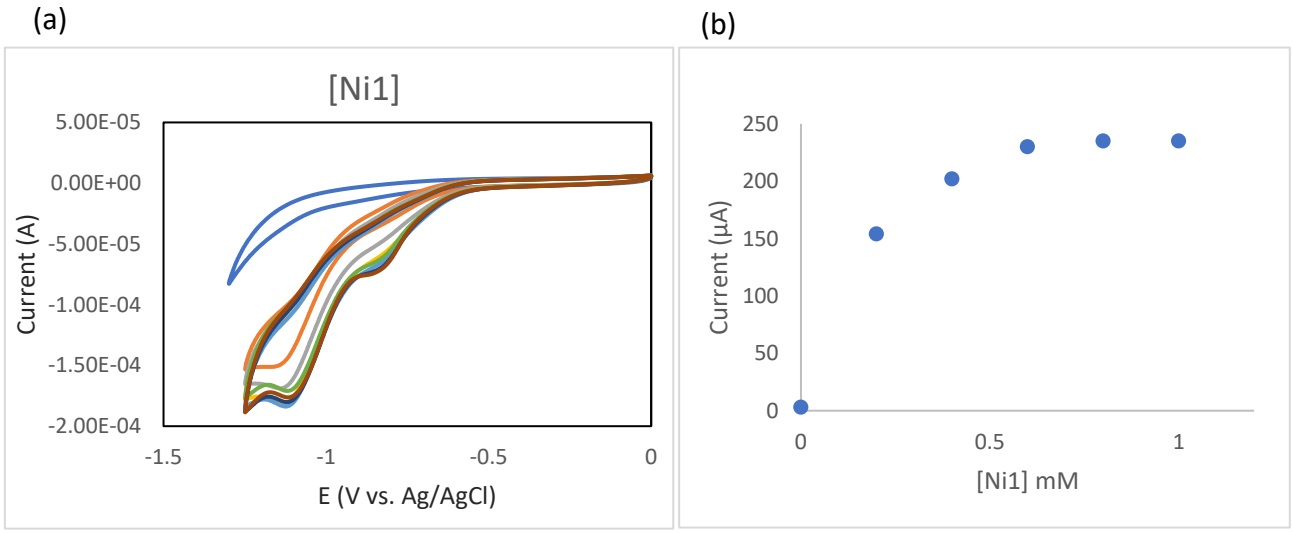

Figure 7.11. a) Cyclic voltammograms (100 mV/s) of 0.1 M KCl, 30 mM MOPS, 100 mM $NaNO_2$, with **Ni1** titrated from 0 to 1 mM in increments of 0.2 mM initially, b) Plot of peak current versus the concentration of **Ni1** titrated.

The parallel set of experiments with **Ni2**, **Co2**, and **Ni3** were also performed, and similar observations were seen for **Ni2** and **Co2.** The peak current for the irreversible feature in **Ni2** and

Co2 showed a linear dependence on [233], [NO_2^-], and [MOPS] before eventually leveling off at higher concentrations of each (Figure 7.12-7.17). However with **Ni3** the observations were different. After addition of nitrite to the **Ni3**-MOPS solution, the reduction peak gradually shifts anodically, from -1.38 V to -0.9 V. By increasing nitrite concentration this peaks first goes to the lower current and then to the higher currents (Figure 7.18). Moreover, the potential for the peak seen for **Ni3** is very close to the potential of the nitrite reduction by GC electrode and this would likely lead to conflicting background generation of reduction products. The results obtained with this complex require further investigation and due to time constraints was not further investigated for this thesis.

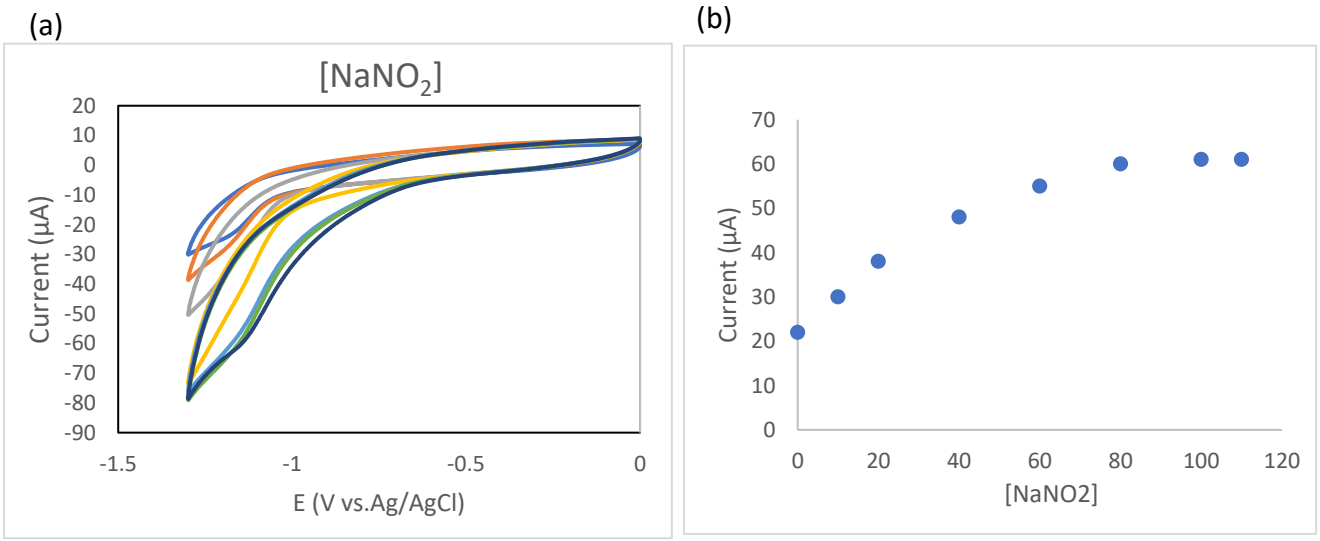

Figure 7.12. a) Cyclic voltammograms (100 mV/s) of 0.1 M KCl, 30 mM MOPS, 0.5 mM **Ni2**, with **$NaNO_2$** titrated from 0 to 110 mM, b) Plot of peak current versus the concentration of **$NaNO_2$** titrated.

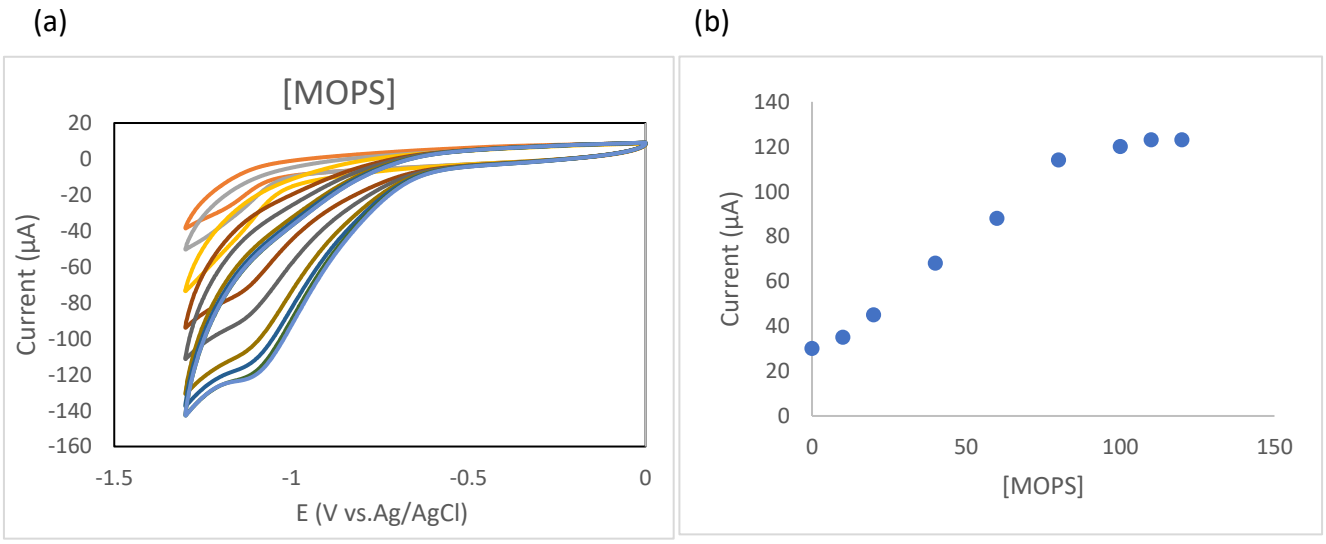

Figure 7.13. a) Cyclic voltammograms (100 mV/s) of 0.1 M KCl, 100 mM $NaNO_2$, 0.5 mM **Ni2**, with MOPS titrated from 0 to 120 mM, b) Plot of peak current versus the concentration of MOPS titrated.

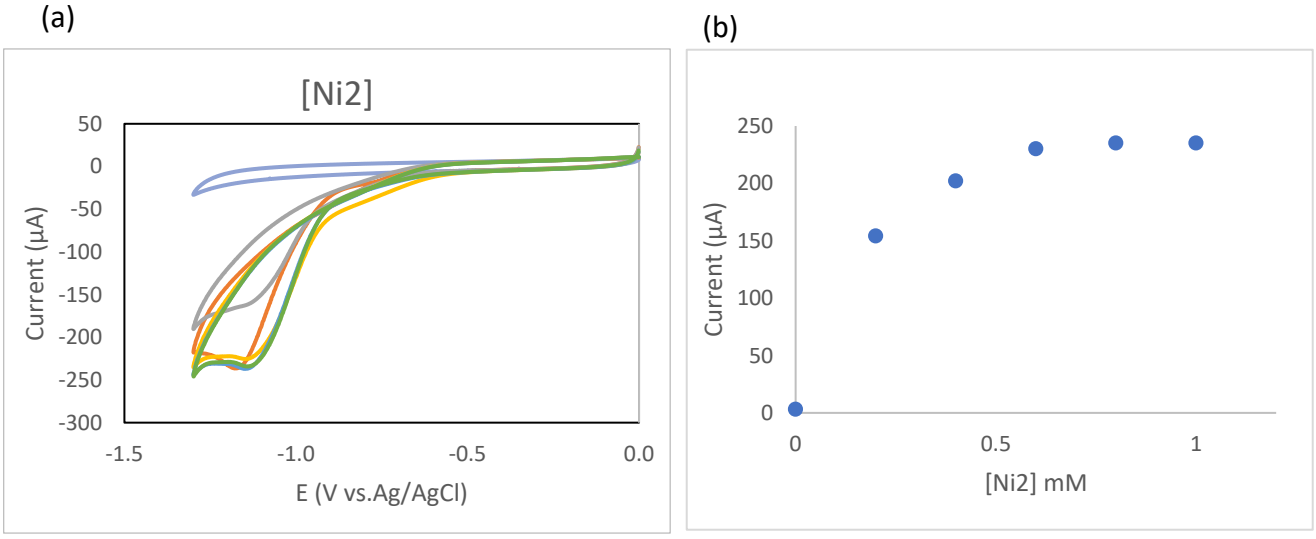

Figure 7.14. a) Cyclic voltammograms (100 mV/s) of 0.1 M KCl, 30 mM MOPS, 100 mM $NaNO_2$, with **Ni2** titrated from 0 to 1 mM in increments of 0.2 mM initially, b) Plot of peak current versus the concentration of **Ni2** titrated.

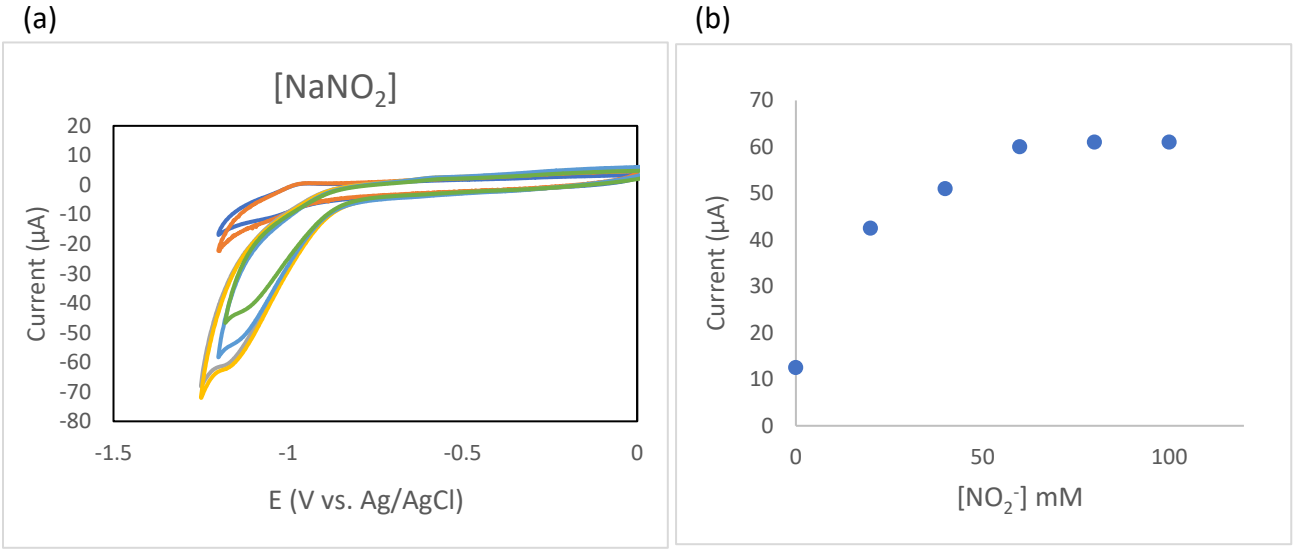

Figure 7.15. a) Cyclic voltammograms (100 mV/s) of 0.1 M KCl 30 mM MOPS, 0.5 mM **Co2**, with $NaNO_2$ titrated from 0 to 100 mM in increments of 20 mM initially, b) Plot of peak current versus the concentration of $NaNO_2$ titrated.

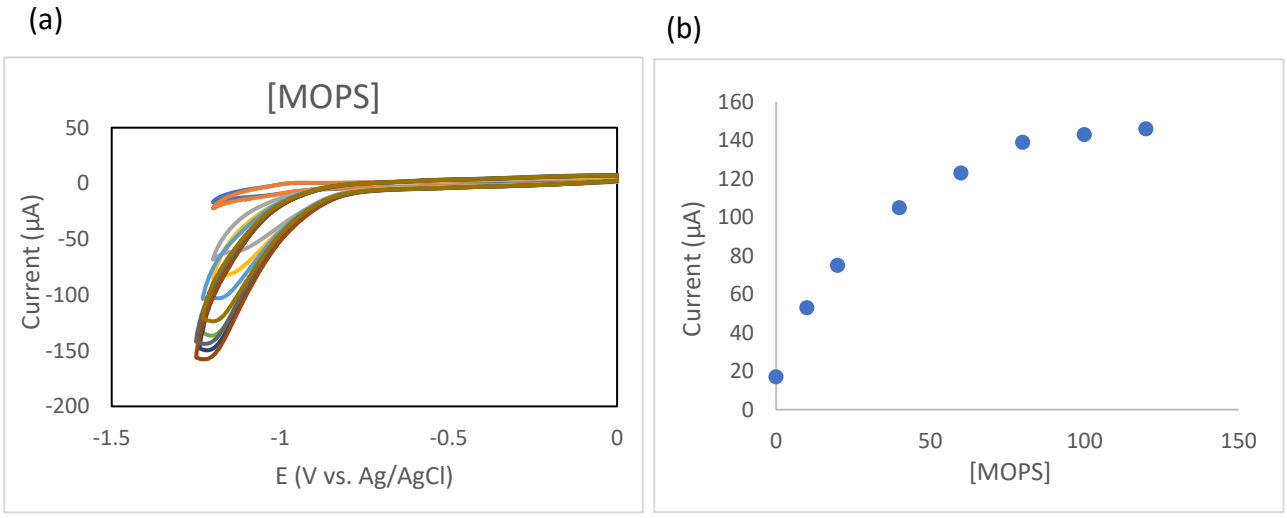

Figure 7.16. a) Cyclic voltammograms (100 mV/s) of 0.1 M KCl, 100 mM $NaNO_2$, 0.5 mM **Co2**, with MOPS titrated from 0 to 120 mM, b) Plot of peak current versus the concentration of MOPS titrated.

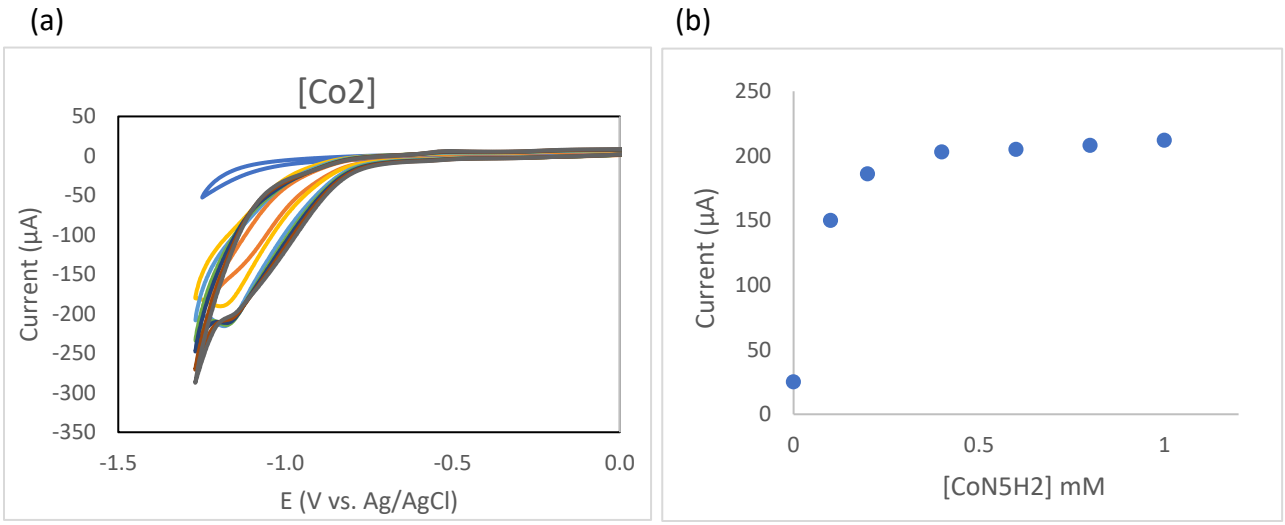

Figure 7.17. a) Cyclic voltammograms (100 mV/s) of 0.1 M KCl, 30 mM MOPS, 100 mM $NaNO_2$, with **Co2** titrated from 0 to 1 mM, b) Plot of peak current versus the concentration of **Co2** titrated.

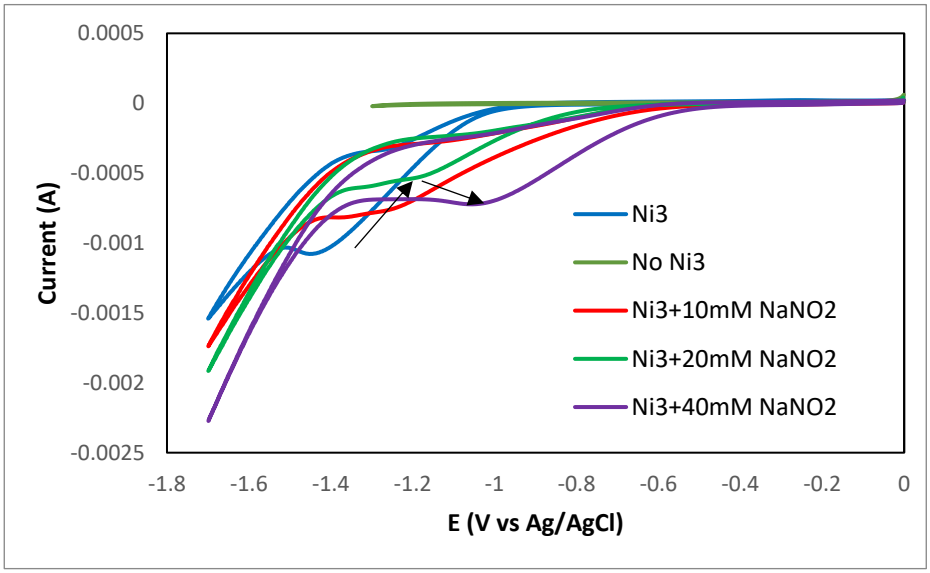

Figure 7.18. a) Cyclic voltammograms (100 mV/s) of 0.1 M KCl 30 mM MOPS, 0.5 mM **Ni3**, with $NaNO_2$ titrated from 0 to 100 mM in increments of 10 mM initially, b) Plot of peak current versus the concentration of $NaNO_2$ titrated.

Control experiments varying the reaction condition also demonstrate similar results to **Ni1** with **Ni2** and **Co2**, confirming the requirement of complex **Ni2** and **Co2**, MOPS buffer, and sodium nitrite in the reaction system to catalysis take place (Figure 7.19-20).

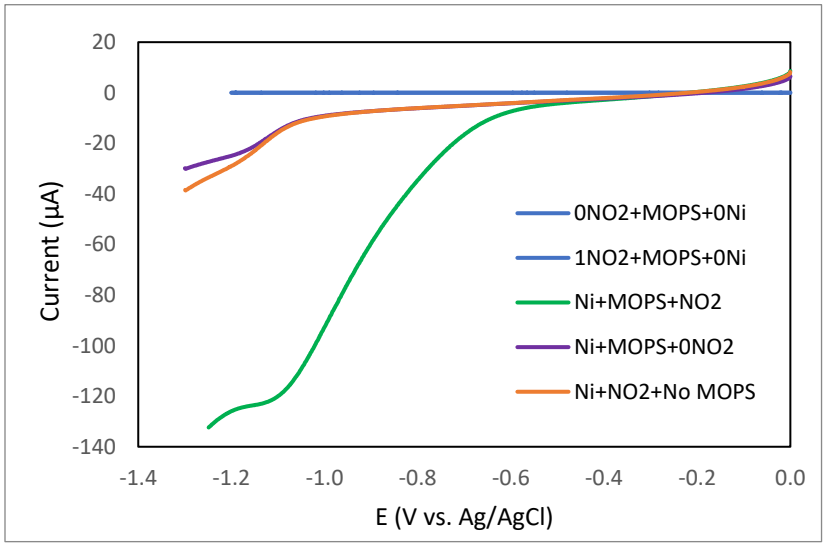

Figure 7.19. Linear Sweep voltammograms (100 mV/s) in water with 0.1M KCl or $NaNO_2$ or MOPS or **Ni2** added as indicated in the legend. The third scan is shown for each experiment.

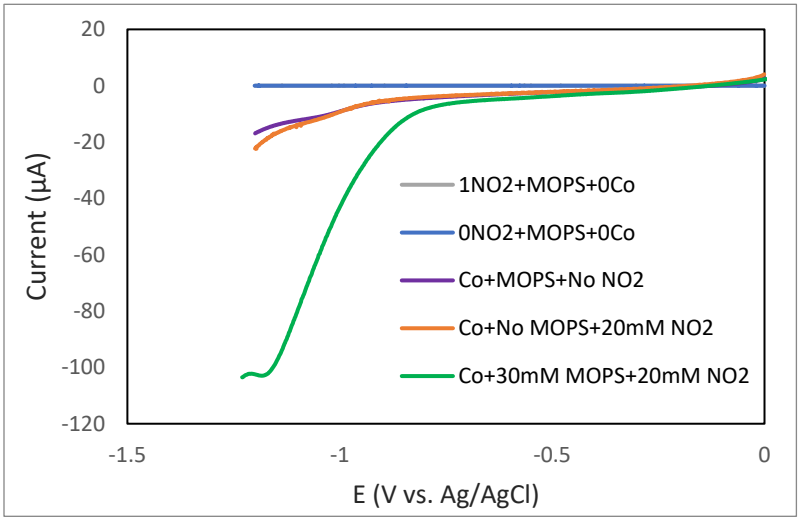

Figure 7.20. Linear Sweep voltammograms (100 mV/s) in water with 0.1M KCl or $NaNO_2$ or MOPS or **Co2** added as indicated in the legend. The third scan is shown for each experiment.

Scan rate dependence measurements were run on complex **Ni1**, **Ni2,** and **Co2** under catalytic conditions consisting of 100 mM MOPS buffer and 10 mM $NaNO_2$ (Figure 7.21). The plot of the square root of the scan-rate vs. peak current displayed a linear relationship, which is consistent with a diffusion-controlled process.

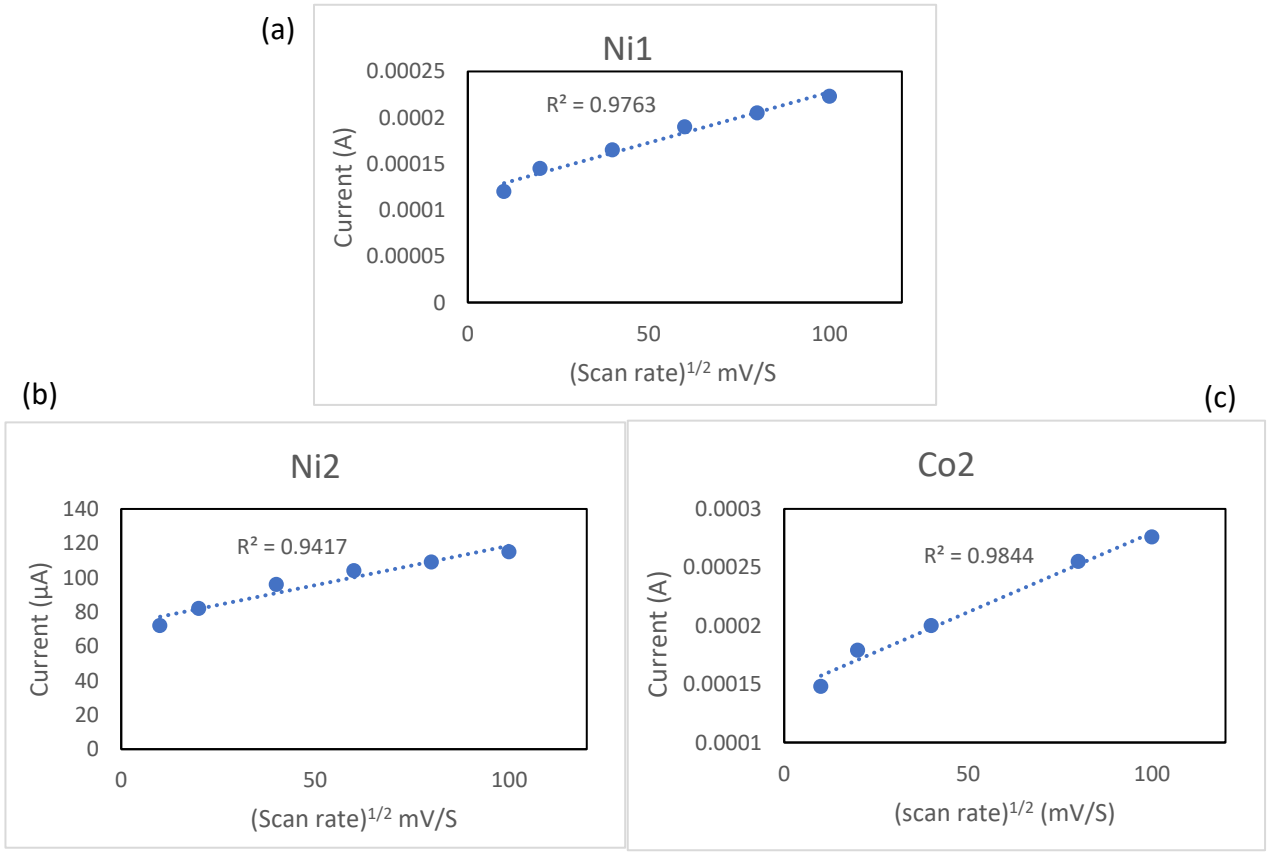

Figure 7.21. Plots of scan rate$^{1/2}$ versus current for the first peak in the presence of 30mM MOPS, 100mM $NaNO_2$, 0.1M KCl and 1mM a) **Ni1**, b) **Ni2**, c) **Co2**, at half wave potential.

To investigate the effect of pH on this catalysis, a solution of catalyst and nitrite in a MOPS buffered solution with initial pH of 7 was prepared. The pH of this solution was changed by adding µl aliquots of 0.1N NaOH. After each addition the pH was recorded. The results are shown in

Figures 7.22 and 7.23. The solution pH impacts peak current, with lower pH translating to a higher current response and less negative potential for this catalysis. This makes sense because lower pH, means more H^+ is accessible, then the protonation will take place faster.

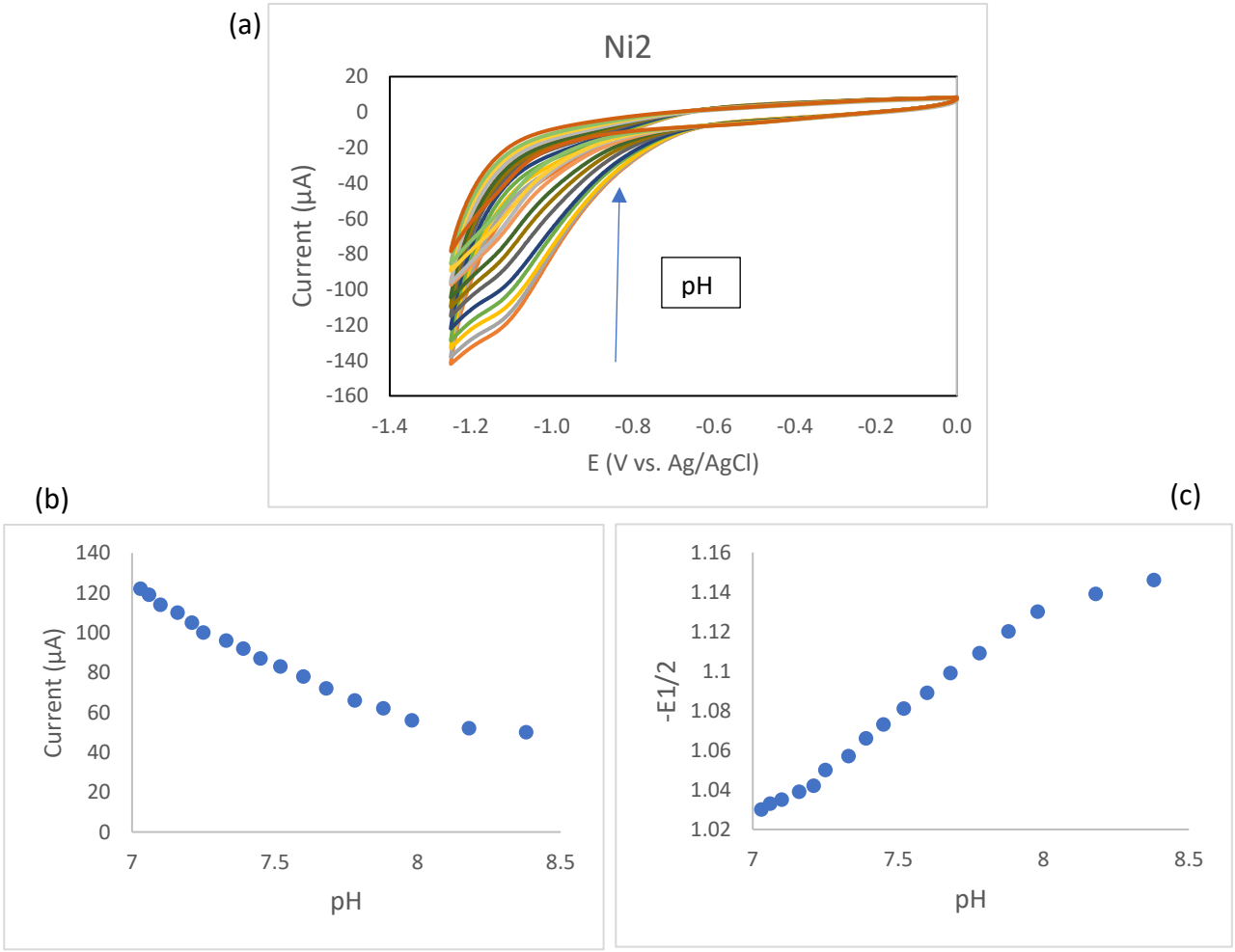

Figure 7.22. a) Cyclic voltammograms (100 mV/s) of 0.1 M KCl, 100 mM $NaNO_2$, 30 mM MOPS, and 0.5mM **Ni2** as pH is varied from 7.0 to 8.4 by addition of sub-µL amounts of NaOH. b) Plot of peak current versus pH. C) plot of onset potential versus pH.

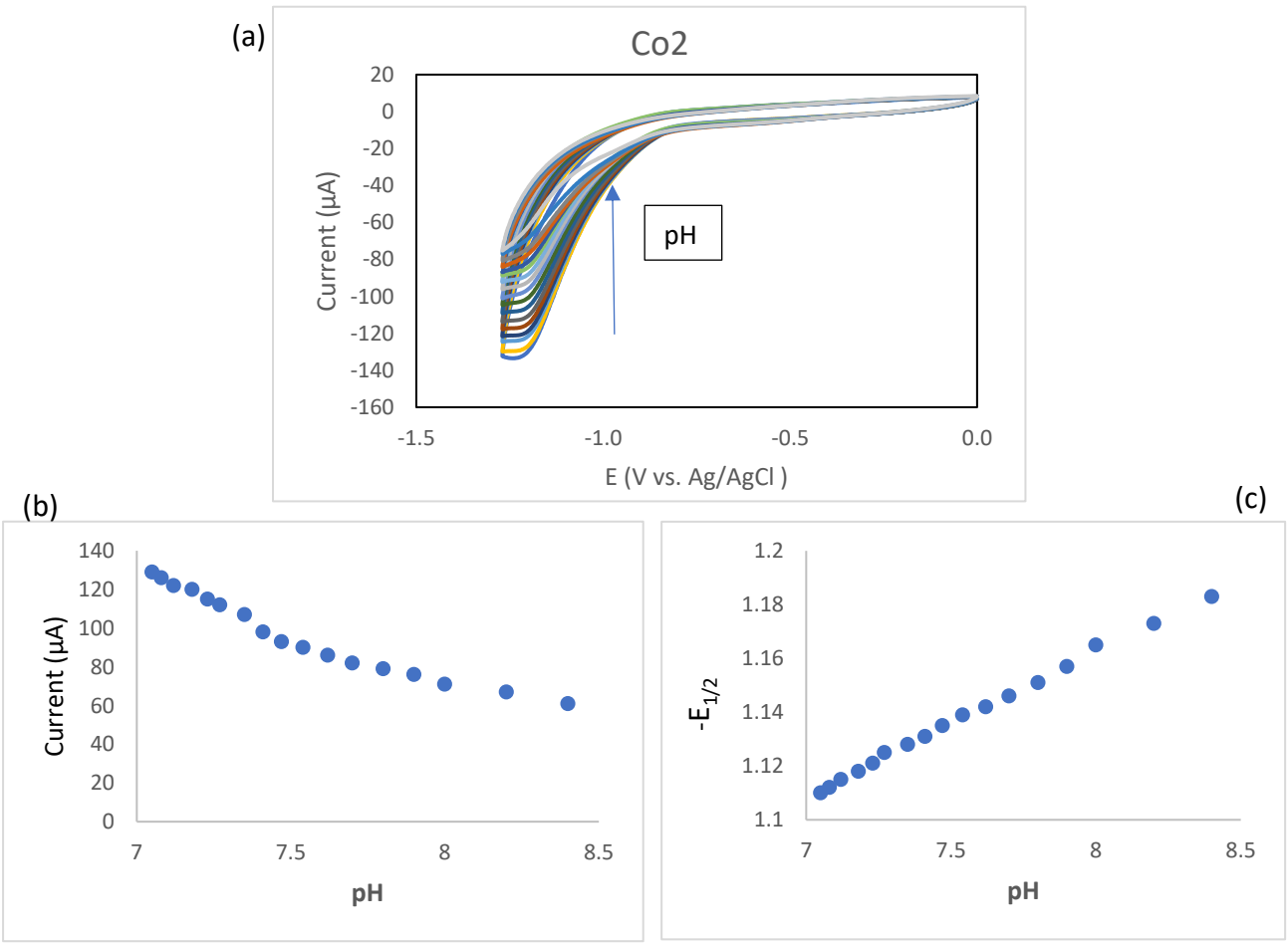

Figure 7.23. a) Cyclic voltammograms (100 mV/s) of 0.1 M KCl, 100 mM NaNO2, 30 mM MOPS, and 0.5mM **Co2** as pH is varied from 7.0 to 8.4 by addition of sub-µL amounts of NaOH. b) Plot of peak current versus pH. C) plot of half-peak potential versus pH.

7.4.3. Controlled Potential Electrolysis (CPE)

Controlled potential electrolysis (CPE) was carried out to determine whether the irreversible feature observed in CV corresponds to catalytic NO_2^- reduction and to identify the resulting product(s). CPE was performed in the presence of 500 µM of the catalyst complexes in a 1M KCl and 1M MOPS buffer aqueous solution with pH 7.2 containing 1M $NaNO_2$ and over 1 and 5h period, at -1.2V with **Ni1**, which correlate with the second reduction peak, and at−0.98 V vs. Ag/AgCl with **Ni2** and **Co2**, which corresponds to the first reduction peak. As noted above, a higher concentration of MOPS was chosen for CPE experiments since the time of reaction is longer

than in CV. pH was chosen near neutral pH, a bit basic, to avoid any possible side reactions, such as HER. Other experiments in the absence of each substrate also were performed as background experiments. Indophenol and hydroxylamine tests were used to detect the production of ammonium and hydroxylamine, respectively. ^{14}N NMR was used as a supportive test for detection of any product in the solution. Gas chromatography and myoglobin tests were used for detection of nitrous oxide and nitric oxide gases, respectively. Electron Impact-mass spectroscopy was also used as a supportive test for detection of any possible gas products in the headspace of the electrochemical cell. Because the electrolysis was conducted under an atmosphere of N_2, the formation of N_2 as a nitrite reduction product was not assessed.

Following CPE, product identification was conducted. Analysis of the product mixture indicated the formation of NH_4^+ and NH_2OH as products (Table 7.2). Using 500µM **Ni1**, 1M MOPS with pH=7.2, 1M NO_2^-, over 1h CPE, at -1.2V, 3µmol of NH_4^+ and 19.3µmol of NH_2OH were detected with Faradaic efficiency of 9.9% and 44.8%, respectively. With **Ni2** under the same conditions, 5.4µmol of NH_4^+ and 21.16µmol of NH_2OH were obtained. Carrying out analogous CPE experiments with **Co2** resulted in selective formation of NH_2OH, producing 53.94µmol, as the sole product, with 98.6% Faradaic efficiency. By increasing CPE time to 5h, **Ni2** and **Co2** generated more NH_4^+ (68% with **Ni2** and 62% with **Co2**) at the expense of NH_2OH. However, NH_4^+ was the sole product of **Ni1** with an efficiency of 50%. The observation of increased Faradaic efficiency for NH_4^+ and decreased FE for NH_2OH with time for these catalysts is accounted by relatively slow conversion of NH_2OH to NH_4^+. To determine if a similar slow step is active here, a constant potential of −0.98 V was applied to 1.0 M NH_2OH and 1.0 M MOPS (pH 7.2) in the presence and absence of **Co2** for 5h. With **Co2** catalyst, consumption of NH_2OH was observed, resulting in formation of NH_4^+ (Figures 7.24). However, in the absence of catalyst, no NH_4^+ was

measured, and only 3C charge was passed over 5h CPE, indicating that **Co2** is active toward electrocatalytic reduction of NH_2OH and glassy carbon electrode is not.

No NO or N_2O were detected by the myoglobin test and gas chromatography measurements, respectively. However, after an overnight CPE experiment with catalyst **Ni1** and using Electron Impact mass spectroscopy which is much more sensitive than these methods, both NO and N_2O were detected, suggesting that these could be intermediates or side-products in this process (Figure E.1-E.3). The presence of NH_4^+ also was confirmed by ^{14}N NMR (Figure 7.26-7.28). We quantified the amount of ammonium by ^{14}N NMR using the calibration curve. The achieved amount was close to what we measured by the indophenol test.

According to the CV measurements, in the absence of MOPS no enhancement was seen after addition of nitrite to the catalyst solution (Figure 7.8, 7.19, 7.20). To confirm this observation, CPE without using buffer solution was performed. Bulk electrolysis also is consistent with CV, generated only 34C charge in the absence of buffer compared to 141C charge produced when we used buffer (Figure 7.25). This result indicates the important role of buffer in this reaction, as has been observed for catalysts for hydrogen production in water.[234, 235] Moreover, the pH measurement before and after CPE in the absence of buffer showed a significant change in pH from 7.2 to 9.1. This change was much less (from 7.2 to 7.9) when buffer was used. This result also confirms that this catalysis process involves proton consumption and using buffer could help to prevent the significant change in pH.

Table 7.2. Summary of data collected from CPE experiments in the presence of 1 M MOPS buffer, pH 7.2, and 100 mM $NaNO_2$.

row	compound	E	Time (h)	NH_4^+ (µmol)	FE	TON	NH_2OH (µmol)	FE	TON	Charge	pH1	pH2
1	**Ni1**	-1.2	1	3	9.9	0.35	19.3	44.8	2.3	17.5		

2	**Ni2**	-0.98	1	5.4	14.6	0.63	21.16	38.1	2.5	21.4	7.2	7.3
3	**Co2**	-0.98	1	0	-	0	53.94	98.6	6.4	21.1	7.2	7.3
4	**Ni1**	-1.2	5	68.1	50	8	0	-	-	100		
5	**Ni2**	-0.98	5	94	68	11	62.6	30.2	7.3	93	7.2	7.8
6	**Co2**	-0.98	5	137	62	16	139	41.9	16.3	141	7.2	7.9
7	**Ni1**	-1.2	16	374	84.4	44	0	-	-	256		
8	-	-0.98	5	0	-	-	-	5.7	-	13		
9	-	-1.2	5	0	-	-	13			21		
10	**Co2**-no buffer	-0.98	5	0	-	-	0	-	-	34	7.2	9.1

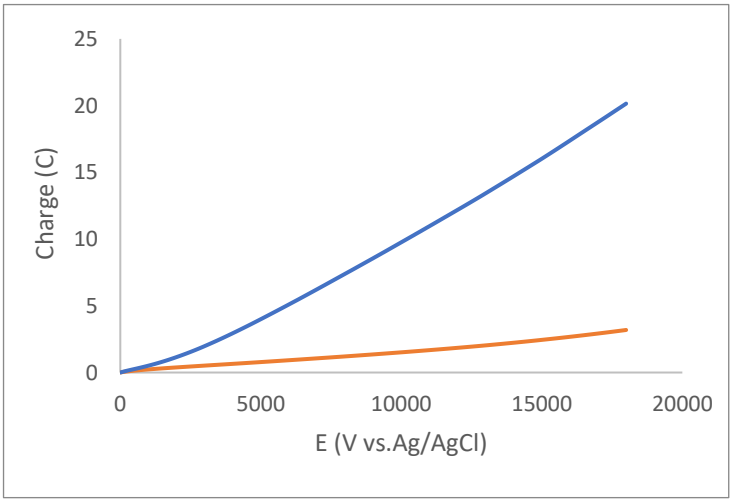

Figure 7.24. Charge-time plot of the CPE reaction of direct reduction of NH_2OH to NH_4^+ at –0.98 V vs. Ag/AgCl (100 mV/s) of a solution containing 1M KCl, 1 M NH_2OH and 1 M MOPS pH 7.2, with (blue) and without (orange) 500 µM **Co2**, over 5 hours period CPE.

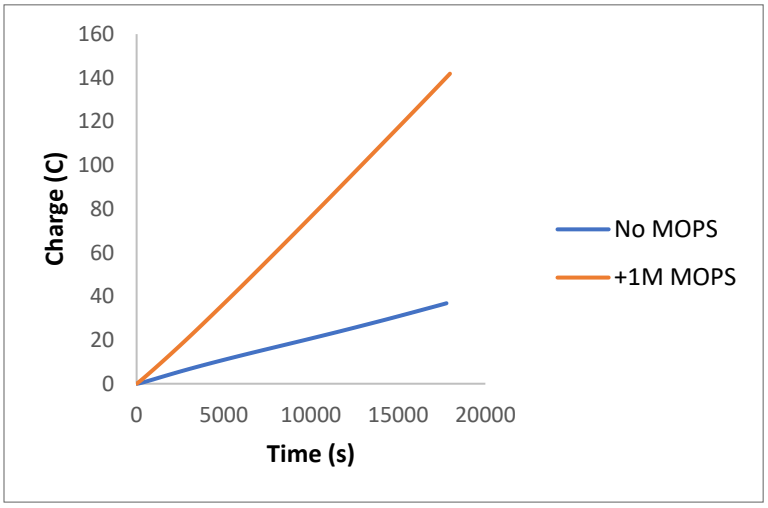

Figure 7.25. CPE at –0.98 V vs. Ag/AgCl of a solution containing 1 M KCl, 1 M $NaNO_2$ and 0.5 mM **Co2**, with 1M (orange) and without (blue) MOPS buffer solution, over 5 hours period CPE.

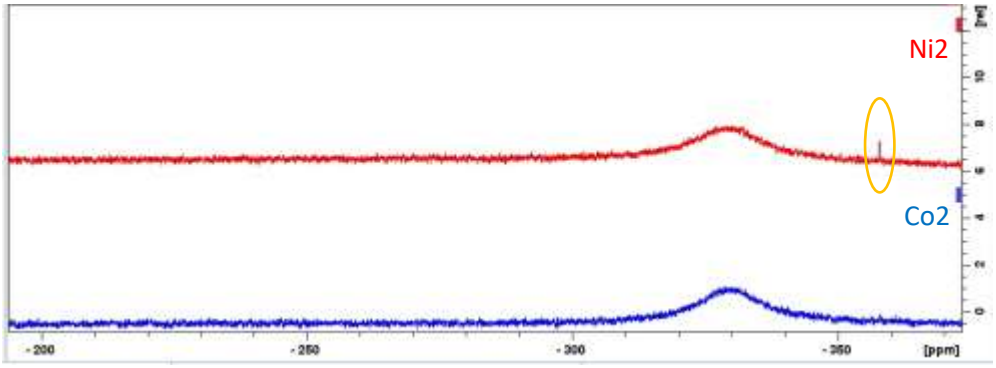

Figure 7.26. ^{14}N NMR of the reaction shown in Table 7.2 row 2 (red), row 3 (blue). The broad peak at -330 ppm was assigned to MOPS, and the sharp peak at -358 ppm was assigned to NH_4^+.

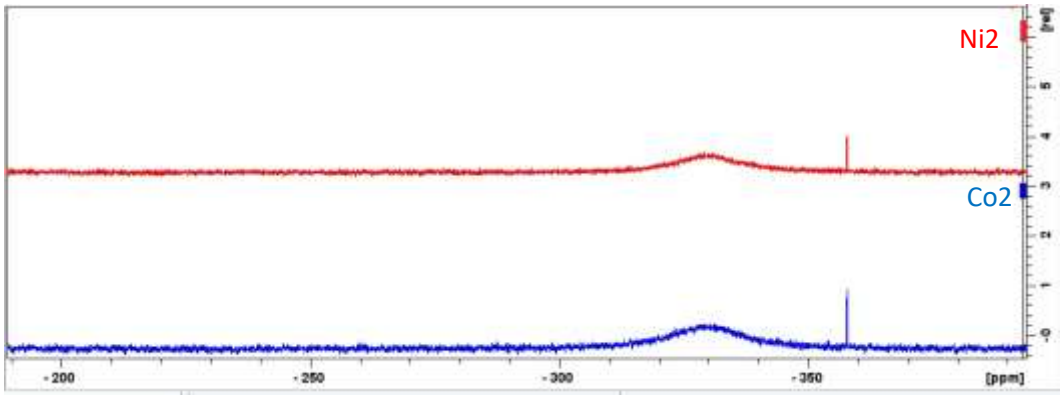

Figure 7.27. ^{14}N NMR of the reaction shown in Table 7.2, row 5 (red), row 6 (blue). The peak at -358 ppm was assigned to NH_4^+.

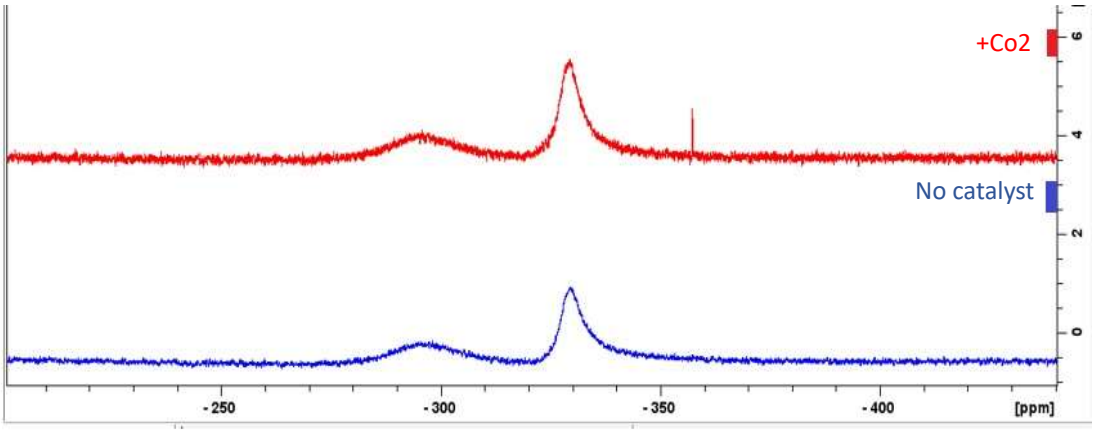

Figure 7.28. ^{14}N NMR spectrum used for quantification of [NH_4^+] from the direct reduction of NH_2OH studies by **Co2** (red) over five hours. The glassy carbon electron under these condition does not reduce NH_2OH (blue). The peak at -358 ppm was assigned to NH_4^+. The peak at -330 ppm was assigned to MOPS and the broad peak at -295 ppm was assigned to the remaining NH_2OH.

The results for **Ni2** and **Co2** that are reported in Table 7.2 can be compared with the reported nitrite reduction chemistry of the Fe complex, **C** shown in Scheme 7.1,[7] Complex **C** and **Co2** have the same pentaazamacrocyclic ligand but **C** was an Fe(III) center. Under similar experimental conditions **Co2** gave preferential NH_2OH production with slower NH_4^+ production. At the short

CPE time (1h) **Co2** selectively reduces NO_2^- to NH_2OH with higher efficiency. In the case of **Ni2,** although an analogous complex was targeted, the resulting pentaazamacrocycle added ROH across one of the imine groups as shown in Scheme 7.4 and Figure 7.2. Interestingly, **Ni2** showed a high efficiency for NH_4^+ production. We attributed this to the **Ni2** complex being more flexible (due to the presence of amine in one arm instead of the π-conjugated imine) and facilitating proton transfer reactions. Furthermore, this behavior parallels that of **Ni1**. However, it is important to bear in mind that since the ligand structure in **Ni2** differs from that of **Co2** and **Fe2**, the direct comparison between these complexes is difficult.

Both **Ni1** and **Ni2** complexes also showed a better performance as NO_2RR catalysts than NiDIMPY complexes that are reported in chapter 6. This could be an effect of using flexible macrocyclic ligand which have more open space to binds to nitrite ions. While DIMPY is more rigid as a pincer ligand with less open space. Moreover, presence of secondary amines in these macrocyclic ligands, can act as intramolecular proton shuttles. These two features are speculated to reduce reaction barriers and promote the catalytic nitrite reduction.

It is also worthwhile to compare the nitrite reduction performance of **Co2** to the reported reactivity of the Co(III) complex with a tetraazamacrocyclic supporting ligand, $[Co(CR)Br_2]^+$ (CR = (dimethyl-3,7,11,17-tetraazabicyclo-[11.3.1]-heptadeca-1(17),2,11,13,15-pentaene)).[88] It appears that **Co2** with pentadentate ligand, displays higher efficiency in NH_4^+ production. While this result may be an effect of the extra NH in the macrocycle of **Co2** or due to a larger more flexible macrocyclic ligand, it is important to note that the NO_2^- reduction using $[Co(CR)Br_2]^+$ was reported in unbuffered solutions and this may also affect catalytic performance.

In another experiment the dependence of charge to the applied potential for this process in the presence and absence of catalyst was measured to confirm that the presence of catalyst is a key for

the reaction to take place. The result is shown in Figure 7.29. CPE experiments were performed at potentials ranging from -0.8 V to -1.4 V vs Ag/AgCl (0.1 M KCl) in increments of 5 mV, containing 1.0 M MOPS, 1.0 M $NaNO_2$, in the presence and absence of 500 µM **Co2**, at pH 7.2. A significant enhancement starts from -1V, when there is catalyst in the solution; this voltage indicates where the catalysis starts from. While in the absence of catalyst, little amount of charge passes through the solution, even at -1.4V.

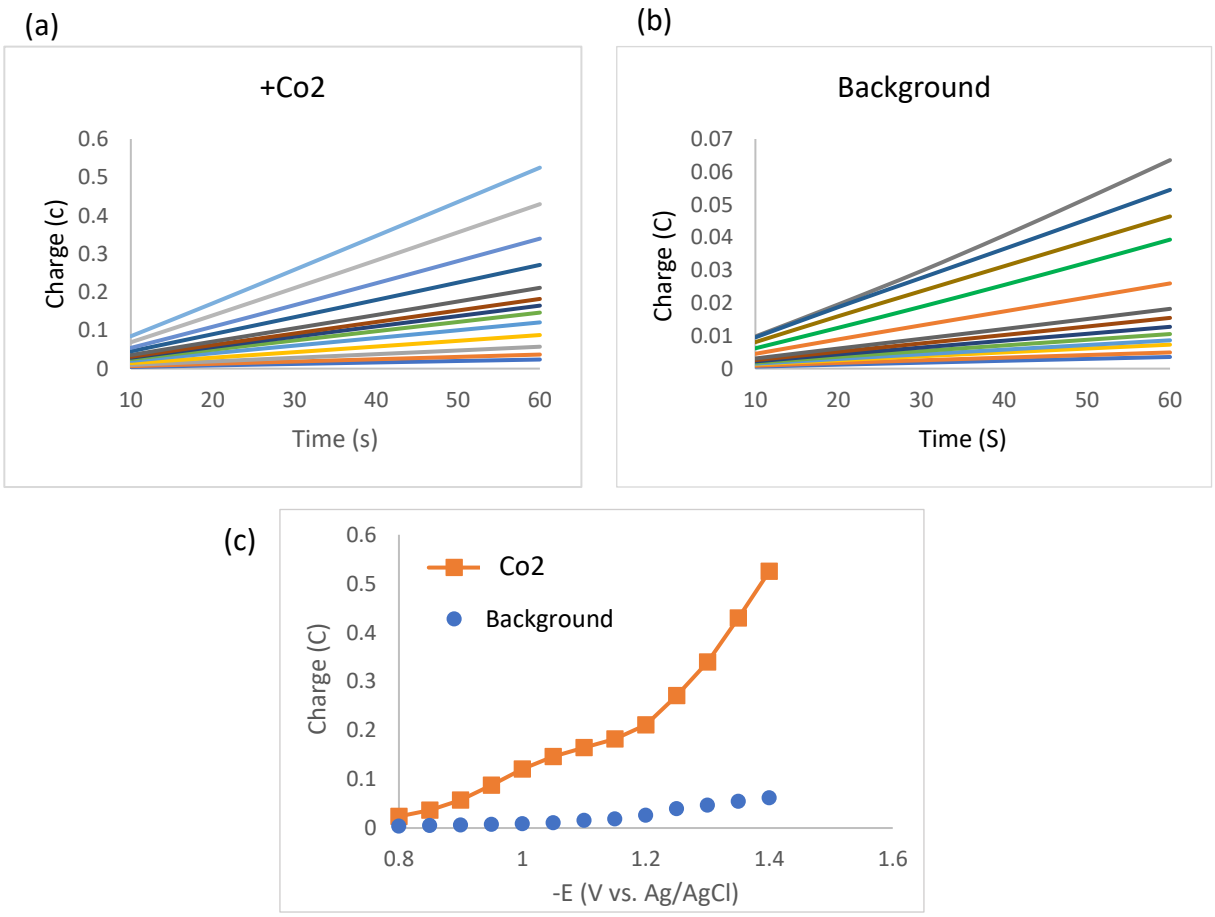

Figure 7.29. Ladder plot showing nitrite reduction by **Co2**. CPE experiments were performed at potentials ranging from -0.8 V to -1.4 V vs Ag/AgCl (0.1 M KCl) in increments of 5 mV. a) CPE experiments are shown for the sample containing 1.0 M MOPS, 1.0 M $NaNO_2$, and 500 µM **Co2** at pH 7.2. b) CPE experiments are shown for the sample containing 1.0 M MOPS, 1.0 M $NaNO_2$ at pH 7.2. c) Plot of charge versus potential for the sample with 0.5mM **Co2** (orange square) and without **Co2** (blue circle).

7.5. Mechanism:

Members of our group have recently carried out a computational exploration of the mechanism of Ni (II) tetraazamacrocyles in the reduction of nitrite. The results for this investigation are summarized in Scheme 7.7. This mechanism is initiated with coordination of nitrite through the N center followed by reduction and protonation steps that afford an NO complex as an intermediate. Subsequent reduction and protonation results in formation of hydroxylamine and ammonium as products. For this Ni complex, the calculated Gibbs free energy for release of hydroxylamine as product was -6.23 kcal/mol. On the other hand, the addition of a proton to the oxygen center of the hydroxylamine occurs at a relative Gibbs free energy of -29.25 kcal/mol yielding the amido species. This observation was used to rationalize the favored production of ammonium over the release of hydroxylamine. This clearly confirms that NH_4^+ is a more favored NO_2RR product using Ni macrocycles. In the future work we are planning to study DFT analysis of the analogous cobalt complex for a better comparison.

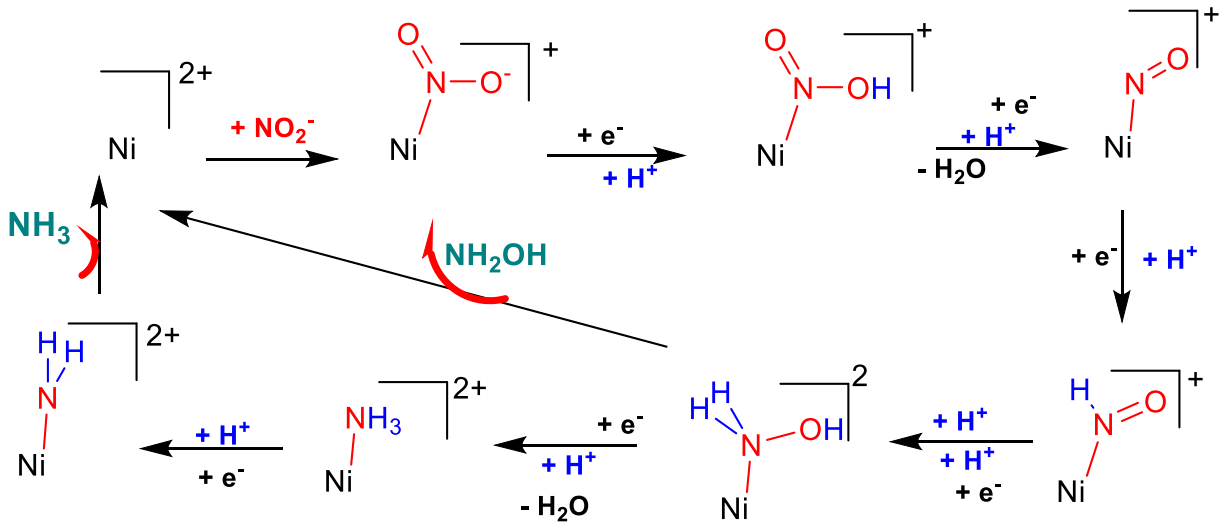

Scheme 7.7. Computationally supported proposed mechanism for the reduction of nitrite by **Ni1**.

7.6 Conclusion:

In summary, this study delved into the impact of ligand and metal center variations on the catalytic effectiveness of first-row metal complexes in nitrite reduction reactions. We initiated the investigation by incorporating the diminopyridine group into a macrocycle ligand with additional amine coordination sites, followed by expanding the ring size and altering the metal center.

The introduction of three new electrocatalysts for nitrite reduction, particularly the Ni(II) tetra and pentaazamacrocycle (**Ni1** and **Ni2**), demonstrated significant advancements in the electrocatalytic reduction of aqueous nitrite, contributing to the limited pool of reported Ni complexes in this catalytic domain. Additionally, **Co2** proved to be an effective electrocatalyst for NO_2^- reduction, offering a unique Co(II) pentaazamacrocycle that stands as a valuable comparison to a growing number of reported Co(III) catalysts.

The cyclic voltammetry experiments highlighted distinct product selectivity among the investigated complexes. At shorter electrolysis times, hydroxylamine was the major product, while the Ni complexes exhibited superior selectivity and higher Faradaic efficiency for NH_4^+ at longer times compared to the Co analog. The comparative analysis of our results with similar structures in the literature suggests that a more flexible macrocycle offers enhanced catalytic activity. Remarkably, within the subset of three metals utilizing the L2 ligand (iron, cobalt, and nickel), nickel stands out as a more selective catalyst for ammonium production in nitrite reduction reactions. It's important to acknowledge, however, that due to the slightly different structure of the nickel complex compared to the other two, direct comparisons become challenging.

Furthermore, our investigation revealed that the Ni macrocycle complexes studied in this chapter outperformed the Ni DIMPY complexes from the previous chapter in terms of efficiency in nitrite reduction. This enhanced efficiency is attributed to the greater flexibility of macrocycles and the

presence of additional coordination sites and the possibility of the hydrogens of amine act as proton shuttle, facilitating a more efficient nitrite reduction reaction.

This comprehensive exploration addresses specific aspects of nitrite electrocatalytic reduction, offering insights on both practical and fundamental levels to comprehend methods for controlling electrocatalysis. Given the time constraints, this chapter serves as an initial foray into these effects, aiming to stimulate innovative ideas and approaches in the design of nitrite reduction catalysts.

7.7 Experimental Section:

Materials

Doubly deionized water was used as a solvent in all reactions and procedures with a resistivity of 18.2 MΩ. All chemicals were used from the manufacturer without further purification. For the indophenol test: ammonium sulfate was obtained from Fisher Chemical, phenol from Acros Organics, sodium nitroferricyanide (III) dihydrate from Sigma-Aldrich, and sodium citrate dihydrate from Fisher Chemical. All the chemicals needed for synthesis of the ligands and complexes were obtained from Sigma-Aldrich. In the reactivity studies: 3-(N-morpholino)propanesulfonic acid (MOPS) was obtained from Sigma-Aldrich and sodium nitrite were obtained from Sigma-Aldrich, as well. The nitrous oxide standard used in the gas chromatography-TCD studies was of AA grade and obtained from Air Products.

Preparation and characterisations of Ni(II)(2,12-dimethyl-3,7,11,17-tetraazabicyclo [11.3.1]heptadeca-1(17),2,11,13,15-pentaene)$(MeCN)_2$ (Ni1)[220]

This preparation followed the reported process for synthesis. In a round bottom flask, 1.63 g (0.01 mol) of 2,6-diacetylpyridine was added to 140 mL of aqueous ethanol that contains 70 mL of ethanol. The solution was heated to 50°C and stirred until all the diacetyl dissolved. Then, 0.01 mol of $NiCl_2(6H_2O)$ was added to the solution. The solution was mixed for 30 minutes with heating at 70°C. To the mixture, 0.01 mol of 3,3'-diamino-N-dipropylamine was added followed by the addition of 0.8 mL of acetic acid. The mixture was stirred at 70 °C for 8 hours. The solvent was reduced by half on a rotary evaporator and left to cool to room temperature. The solution was cooled with an ice bath and 0.04 mol of $LiClO_4$ was added and stirred for 2 hrs. The mixture was filtered through sintered glass, washed with a minimum amount of ethanol followed by several washes with diethyl ether. The purple powder was dried under vacuum. Compound Ni1 was

crystallized by layering a concentrated acetonitrile solution of **Ni1** with diethyl ether**.** Fourier-transform infrared spectroscopy following synthesis shows a new band appears centered at 1630 cm^{-1}. The experimental elemental analysis for $C_{19}H_{27}N_6Ni$ was determined to be: C 46.98%; H 5.68%; N 14.23%.

Preparation and Characterization of Ni(II)(2- methyl-hydroxyl, 13-methyl -3,6,9,12,18-pentaazabicyclo [12.3.1] octadeca-1(18),12,14,16-tetraene(ClO_4) (Ni2):[7, 236]

In a round bottom flask, 1.296 g (0.01 mol) $NiCl_2$ and 1.63 g (0.01 mol) of 2,6-diacetylpyridine are added to 140 mL of aqueous ethanol that contains 70 mL of ethanol. The contents were stirred for 30 minutes with heating at 70 ˚C. To the mixture, 1.54 g (0.01 mol) of triethylenetetraamine was added followed by the addition of 0.8 mL of acetic acid. The mixture was stirred at 70 ˚C for 8 hours. The solvent was reduced by half and 4.26 g (0.04 mol) of $LiClO_4$ was added and stirred for 2 hrs. The mixture was filtered on a sintered glass, washed with ethanol followed by washing with diethyl ether. An orange-pink fine powder was obtained. The compound was crystallized by slow diffusion of ether into acetonitrile. Fourier-transform infrared spectroscopy following synthesis shows a new band appears centered at 1632 cm^{-1} that is a good match with literature values for the imine bonds of these heterocyclic complexes [2,3][236]. The experimental elemental analysis for $C_{15}H_{21}ClN_5Ni$ was determined to be: C 45.8%; H 5.99%; N 17.02%.

Preparation and Characterization of Co(II)(2,13-dimethyl-3,6,9,12,18-pentaazabicyclo [12.3.1]octadeca- 1(18),2, 12, 14, 16-pentaene)(Cl) (Co2):[216]

In a round bottom flask, 1.298 g (0.01 mol) $CoCl_2$ and 1.63 g (0.01 mol) of 2,6-diacetylpyridine are added to 140 mL of aqueous ethanol that contains 70 mL of ethanol. The contents were stirred for 30 minutes with heating at 70 ˚C. To the mixture, 1.54 g (0.01 mol) of triethylenetetraamine is added followed by the addition of 0.8 mL of acetic acid. The mixture was stirred at 70 ˚C for 8

hours. The solvent was reduced by half and 4.26 g (0.04 mol) of $LiClO_4$ was added and stirred for 2 hrs. The mixture was filtered on a sintered glass, washed with ethanol followed by washing with diethyl ether. A yellow-orange fine powder was obtained. The compound was crystallized by slow diffusion of ether into acetonitrile. An electronic absorption spectrum of the purified product in water shows five absorptions at λ1 = 286 nm (ε = 1925 $M^{-1}cm^{-1}$), λ2 = 296 nm (2360 $M^{-1}cm^{-1}$) λ3 = 306 nm (ε = 2015 $M^{-1}cm^{-1}$), λ4 = 367 nm (405 $M^{-1}cm^{-1}$) and λ5 = 422 nm (371 $M^{-1}cm^{-1}$). Fourier-transform infrared spectroscopy following synthesis shows a new band appears centered at 1653 cm^{-1}[7]. The experimental Elemental analysis for $C_{15}H_{21}ClCoN_5$ was determined to be: C 45.20%; H 5.38%; N 17.88%.

Preparation and Characterization of Ag(I) (2,15-dimethyl-3,6,10,13,17-pentaazabicyclo [13.3.1] enneadeca-1(20), 2, 14, 16, 18-pentaene)(ClO_4) (AgL3):[237]

In a round bottom flask, 2.073 g (0.01 mol) $AgClO_4$ and 1.63 g (0.01 mol) of 2,6-diacetylpyridine were added to 70 mL of dry methanol. The contents were stirred for 30 minutes with heating at 70 ˚C. To the mixture, 1.74 g (0.01 mol) of 1,2-bis(3-aminopropylamino)ethane was added. The mixture was stirred at 70 ˚C for 8 hours. The yellow precipitate was filtered off and the resulting solution was reduced by half. Upon cooling yellow crystals of AgL3 were precipitated. The crystals were collected, washed with cold methanol, and dried. The compound was crystallized by slow diffusion of ether into acetonitrile.

Preparation and Characterization of Ni(II)(2,15-dimethyl-3,6,10,13,17-pentaazabicyclo [13.3.1] enneadeca -1(20), 2, 14, 16, 18-pentaene)(ClO_4) (Ni3):[236]

In a round bottom flask, 1 eq of AgL3 in methanol solution was added to a hot mixture of 1eq $Ni(II)Cl_2$ in methanol and stirred for 2h. The color of the solution gradually turned to brown. The precipitate was filtered off and the resulting solution was rotovapped. The resulting pinkish brown

powder was washed with cold methanol and dried under vacuum overnight. The compound was crystallized by slow diffusion of ether into acetonitrile.

Electrochemistry:

Electrochemical experiments were carried out in a single compartment cell, with 40 mL approximate volumes, using a VersaSTAT 3 (Princeton Applied Research) potentiostat. Samples were prepared in an open air, sealed, and connected to a Schlenk line and maintained under a nitrogen atmosphere. A conventional three electrode system was employed consisting of a glassy carbon working electrode (diameter = 0.3 cm), a Platinum wire as the auxiliary electrode, and an Ag/AgCl (3M KCl) reference electrode. Deionized (DI) water was used as solvent. Anhydrous potassium chloride purchased from Sigma Aldrich was used as supporting electrolyte. Dry and crystallized tetrabutylammonium hexafluorophosphate, $[(n\text{-}Bu)_4N]PF_6$ (TBAHFP) and dried acetonitrile, both purchased from Sigma Aldrich were used as the supporting and solvent, respectively. The typical concentration of catalyst was 0.5 mM in each experiment unless it was otherwise specified.

X-ray Crystallography:

The crystals of **Ni1**, **Ni2**, and **Ni3** were mounted on thin glass fibers using paraffin oil. Prior to data collection crystals were cooled to 200.15 K. Data were collected on a Bruker Smart and Kapa ApexII single crystal diffractometer equipped with a sealed tube Mo source (wavelength 0.71073 Å) and an ApexII CCD detector. Raw data collection and processing were performed with the Apex3 software package from Bruker. Initial unit cell parameters were determined from 60 data frames from select ω scans collected at the different sections of the Ewald sphere. Semi-empirical absorption corrections based on equivalent reflections were applied. Systematic absences in the diffraction data-set and unit-cell parameters were consistent with the assigned space group. The

initial structural solution was determined using ShelXT direct methods, and refined with full-matrix least-squares procedures based on F2 using ShelXL. Hydrogen atoms were placed geometrically and refined using a riding model. All scattering factors are contained in several versions of the ShelXL program library, with the latest version used being v.6.12 at the time of this writing.

Other Physical Measurements:

Gas chromatography for detection of gas products (H_2, N_2O) was conducted on a Shimadzu Gas chromatography- 2014 equipped with a thermal conductivity detector (TCD). Helium carrier gas (purity ≥ 99.995%) was utilized with an isothermal 6-minute run at 30 ºC on an Agilent HP-PLOT Q column. UV-vis spectra were recorded with a Cary 100 spectrophotometer. Mass spectrometric measurements was used for detection of possible gas products such as NO, N_2O, which were performed at the Chemistry Mass Spectrometry Facility at the University of Ottawa, Ontario on a Micromass Quattro triple quadrapole mass spectrometer equipped with an electrospray ionization source.

^{14}N nuclear magnetic resonance spectroscopy (NMR) was carried out using a Bruker Avance 500 instrument operating at 500 MHz for the ^{1}H nucleus and 36.1 MHz for the ^{14}N nucleus. Nitromethane ($MeNO_2$) was used as an external standard. For each sample, 550 scans were obtained with a relaxation delay (d1) of 10 seconds to allow for sufficient relaxation of $^{14}NH_4^+$ nuclei. Quantification of NH_4^+ is performed via addition of a capillary tube containing 1.0 M $MeNO_2$ to the NMR tube where indicated. A calibration curve was made by comparing the peak areas of standards with known [NH_4^+] compared to the peak area of the 1.0 M $MeNO_2$ standard within the capillary tube.

Myoglobin Test for NO: Flowing N_2 gas was utilized to bubble the headspace of the CPE cell after 5 hours electrolysis (0.5mM Ni2, 1M MOPS, 1M $NaNO_2$, at –0.98 V vs. Ag/AgCl) through a solution containing 500 µM Fe(II) myoglobin (Mb(II)) in 100 mM phosphate buffer at pH 7.4. Following CPE, a 50x dilution of the Mb(II) solution was then assessed by absorption spectroscopy.

Equations:

Turnover number (TON) was estimated using the following equation:

TON = n product / n catalyst

where n product = moles of hydroxylamine or ammonium produced and n catalyst = moles of catalyst

added.

Faradaic efficiency (FE) was calculated from the following equation:

FE (%) = (ne × F × 100%) / QT

Where ne = the moles of electrons required to generate the measured moles of a species of interest from NO_2^- (6 moles of electrons per mole of ammonium, 4 moles of electrons per mole of hydroxylamine, F = Faraday's constant (96485.3 C/mol e-), and QT = the total charge passed during the CPE experiment in coulombs.

Randles-Sevcik equation:

$i_p = 0.496(FAC)\sqrt{(DFv/RT)}$

The Randles-Sevcik equation which describes the peak current of a mass-transport limited event establishes a relationship of peak current being proportional to the square root of the scan rate. In the Randles-Sevick equation, i_p describes peak current observed in CV, F is Faraday's constant, A is the surface area of the electrode in cm^2, C is the concentration of electroactive species in mol/cm^3, D is the diffusion coefficient of the electroactive species in cm^2/s, ν is the scan rate in V/s, R is the ideal gas constant, and T is the absolute temperature.

Chapter 8: Conclusion

This thesis centered on the utilization of non-innocent ligands anchored to a 3d metal center, with a particular focus on complexes of nickel. The primary objective was an in-depth exploration of the catalytic efficacy of these complexes across three pivotal realms of electrocatalysis: hydrogen generation, carbon dioxide reduction, and nitrite reduction. The ultimate aim was to contribute to sustainability by enhancing our understanding and harnessing the catalytic potential of these ligands within these diverse electrochemical processes.

The first project focused on developing a robust and air-stable Ni(II) complex using PN^3P type pincer ligands with diverse substituents. These newly introduced catalysts demonstrated high Faradaic efficiency (90%) in electrocatalytic water reduction to hydrogen. Computational analyses highlighted the significance of a unique ligand-based electron transfer mechanism, showcasing the cooperative role of the PN^3P ligand as an electron reservoir for successful catalysis.

To delve deeper into the role of the PN^3P ligand as a non-innocent ligand in catalysis, in another project, we chose zinc, a redox-innocent metal, as the metal center. The resulting Zn-PN^3P and Zn PN^2 complexes exhibited efficient HER, generating H_2 with high Faradaic efficiency using neutral water as a feedstock. This reaffirmed the crucial role of these non-innocent ligands in catalysis. Additionally, we demonstrated that the unique Zn-PN^3P complexes play a key role in the conversion of CO_2 into C1 products (CO and HCO_2^-). The observed reactivity is attributed to a metal-ligand synergy between a reduced, basic ligand and the Lewis acidity of the coordinated Zn(II) center.

Recognizing the significance of the PN^3P ligand, we further explored the effects of using a redox-active ligand in terms of solubility, efficiency, and sustainability. For this purpose, DIMPY pincer ligands, structurally similar to the PN^3P framework, and known as redox-active species, were chosen. The research in Chapters 3 and 4 focused on studying the HER of Ni complexes with

DIMPY pincer ligands, particularly delving into the mechanism with various substrates featuring different pKa values in non-aqueous conditions. The study revealed that these Ni(II) complexes serve as effective catalysts for H_2 production at various cathodic potentials, with the process exhibiting distinct pathways depending on substrate acidity and pKa values. The study extended to aqueous solutions. A water-soluble Ni(II)DIMPY complex, was found to be a pre-catalyst for hydrogen production in neutral water with great Faradaic efficiency, marking a rare example of HER in pH 7 water. Experimental results, corroborated by DFT computational analysis, underscored the ligand's crucial role as an electron reservoir in the reduction step, unveiling distinct reaction pathways for the two hydrogen formation routes.

In Chapter 6, we explored a novel catalytic target, the reduction of nitrite to ammonium, an intriguing and actively researched area in recent literature. As a multielectron multi-proton process, choosing a non-innocent ligand that could help the reduction and protonation was the reason for choosing DIMPY complexes of Ni and testing their catalysis toward nitrite reduction. We observed catalytic reduction of NO_2^- to NH_4^+ and NH_2OH, with an average Faradaic efficiency of 50% in a CH_3CN/H_2O solution. The inclusion of a buffer was found to be crucial for reaction efficiency, and bulkier substituents on complexes increased efficiency and selectivity towards NH_4^+ production. Computational analysis elucidated two distinct pathways originating from the nitrite complex, established experimentally as the precatalyst, leading to the formation of the observed reaction products NH_2OH and NH_4^+.

Addressing the observed low Faradaic efficiency with NiDIMPY complexes in Chapter 6, we hypothesized that the limited flexibility of the pincer ligand might be a hindrance. To explore a more flexible alternative, DIMPY-based macrocycle ligands were employed in Chapter 7. The resulting Ni catalysts exhibited exceptional activity in the reduction of NO_2^- to NH_4^+, with the 17-

membered ring showing particularly great efficiency. Comparisons with analogous Co(II) complexes provided insights into the impact of metal variation, with the Ni complex displaying higher selectivity for NH_4^+ production over the Co analog, emphasizing the influence of structural flexibility. In this chapter, Ni macrocycle complexes surpassed the efficiency of Ni(II)DIMPY complexes from Chapter 6 in nitrite reduction. This improvement is credited to the enhanced flexibility of the macrocycle framework and the presence of a secondary amine, acting as a proton shuttle for a more efficient reduction process. Overall, this research contributes valuable insights into the electrocatalytic reduction of aqueous nitrite, underlining the importance of catalyst design and optimization. The findings suggest the potential of Ni macrocycle complexes for further development as nitrite reduction catalysts.

The thesis demonstrates several notable **strengths**, beginning with the introduction of highly efficient catalysts for diverse catalytic targets. The use of earth-abundant metals, such as nickel, and water as both a proton source and solvent enhance the sustainability of the electrocatalytic processes explored. Particularly, the research significantly contributes valuable insights into the electrocatalytic reduction of aqueous nitrite, expanding our understanding of this area. Overall, the thesis lays a promising foundation for the development of sustainable and efficient electrocatalytic processes for hydrogen production, CO_2 reduction, and nitrite reduction.

However, certain **weaknesses** should be acknowledged. First, there is a notable lack of experimental evidence for the proposed mechanisms, posing a limitation in fully understanding the catalytic processes. Additionally, the thesis would benefit from a more in-depth study of the roles of various parameters, including the metal center, ligand size, and the influence of a buffer, particularly in Chapters 6 and 7. Lastly, a more comprehensive kinetic study is needed to provide a thorough understanding of the reaction kinetics and dynamics involved in the catalytic processes

explored. In the future, addressing these weaknesses will further strengthen the overall scientific impact of the research.

Each chapter of this thesis thoroughly examines various parameters to assess the efficacy of catalysts, comparing findings with existing literature. For nitrite reduction catalysts introduced in this study, their performance aligns within the spectrum of literature findings. Notably, in the realm of CO_2 reduction, the distinctive aspect of this study lies in the utilization of Zn, as a redox-innocent metal center, rendering unexpected insights. While our catalysts may not outperform others in terms of H_2 production efficiency, our findings contribute significant value to the understanding of this domain.

Future research in electrocatalysis for water, CO_2, and nitrite should prioritize the development of advanced catalyst designs and materials to enhance efficiency. Tailoring catalysts for specific reactions, exploring earth-abundant elements, and optimizing performance under various conditions are key areas for investigation. Understanding the intricate mechanisms governing electrocatalytic processes, particularly the impact of ligand modifications and the role of non-innocent ligands, offers opportunities for fine-tuning performance. The integration of computational methods to predict and guide experimental efforts will expedite the discovery of efficient catalysts. Collaborative interdisciplinary research is essential for addressing the complexities of electrocatalysis and advancing sustainable solutions for hydrogen generation, carbon dioxide reduction, and nitrite reduction.

Building upon the insights gained from the current research, **future investigations** in electrocatalysis should prioritize understanding the role of ligand flexibility by designing and synthesizing ligands with superior flexibility to optimize catalytic activity. Systematic exploration of modifications to the ligand scaffold will be crucial in understanding their impact on catalytic

efficiency. Expanding the scope of applications by targeting the reduction of various oxyanion species beyond nitrite such as nitrate would broaden the relevance of electrocatalysis. Leveraging the identified buffer requirement in nitrite reduction presents an exciting opportunity to fine-tune electrocatalyst performance and control reaction kinetics and selectivity. The effect of using a different working electrode on the reduction potential and efficiency of the reaction would be interesting to study. In summary, these proposed directions aim to address specific challenges and lay the foundation for sustainable advancements in electrocatalytic processes.

References

1. Vitousek, P.M., H.A. Mooney, J. Lubchenco, and J.M. Melillo, *Human domination of Earth's ecosystems.* Science, 1997. **277**(5325): p. 494-499.
2. Singh, S. and P.C. Ramamurthy, *Nitrates in the environment: A critical review of their distribution, sensing techniques, ecological effects and remediation.* Chemosphere, 2022. **287**: p. 131996.
3. Trewavas, A., *Fertilizer: no-till farming could reduce run-off.* Nature, 2004. **427**(6970): p. 99-99.
4. Sun, Z., Ma, T., Tao, H., Fan, Q. and Han, B., *Fundamentals and challenges of electrochemical CO_2 reduction using two-dimensional materials.* Chem, 2017. **3**(4): p. 560-587.
5. Wu, J., Y. Huang, W. Ye, and Y. Li, *CO_2 reduction: from the electrochemical to photochemical approach.* Advanced Science, 2017. **4**(11): p. 1700194.
6. Genovese, C., C. Ampelli, S. Perathoner, and G. Centi, *Mechanism of C–C bond formation in the electrocatalytic reduction of CO_2 to acetic acid. A challenging reaction to use renewable energy with chemistry.* Green Chemistry, 2017. **19**(10): p. 2406-2415.
7. Stroka, J.R., B. Kandemir, E.M. Matson, and K.L. Bren, *Electrocatalytic multielectron nitrite reduction in water by an iron complex.* ACS Catalysis, 2020. **10**(23): p. 13968-13972.
8. Meng, S.-L. and C. Zhang, *Cobaloximes: selective nitrite reduction catalysts for tandem ammonia synthesis.* Energy & Environmental Science, 2023. **16**(4): p. 1590-1596.
9. Zhang, X. and B. Zhang, *Recent advances in electrocatalytic nitrite reduction.* Chemical Communications, 2022. **58**(17): p. 2777-2787.
10. Kroneck, P.M., *Nature's nitrite-to-ammonia expressway, with no stop at dinitrogen.* JBIC Journal of Biological Inorganic Chemistry, 2022: p. 1-21.
11. Jangam, A. and S. Kawi, *Conversion of CO_2 to C1 chemicals: catalyst design, kinetics and mechanism aspects of the reactions.* Catalysis Today, 2020. **358**: p. 3-29.
12. Al-Tamreh, S.A. and EI. Naas, *Electroreduction of carbon dioxide into formate: A comprehensive review.* ChemElectroChem, 2021. **8**(17): p. 3207-3220.
13. Sagar, S., R.K. Kanaparthi, M.K. Tiwari, and S. Saha, *Recent Progress of Electrocatalysts and Photocatalysts Bearing First Row Transition Metal for Hydrogen Evolution Reaction (HER).* Photophysics, Photochemical and Substitution Reactions-Recent Advances, 2020.
14. Wang, Y. and B. Zhang, *Nitrate electroreduction: mechanism insight, in situ characterization, performance evaluation, and challenges.* Chemical Society Reviews, 2021. **50**(12): p. 6720-6733.
15. Francke, R., B. Schille, and M. Roemelt, *Homogeneously catalyzed electroreduction of carbon dioxide—methods, mechanisms, and catalysts.* Chemical Reviews, 2018. **118**(9): p. 4631-4701.
16. Jin, X. and R. Cao, *Comparing electrocatalytic hydrogen and oxygen evolution activities of first-row transition metal complexes with similar coordination environments.* Journal of Energy Chemistry, 2021. **63**: p. 659-666.
17. Johnson, D., Z. Qiao, and A. Djire, *Progress and challenges of carbon dioxide reduction reaction on transition metal based electrocatalysts.* ACS Applied Energy Materials, 2021. **4**(9): p. 8661-8684.

18. Feng, Y., L. Chen, and Z.-Y. Yuan, *Recent developments and prospects for engineering first-row transition metal-based catalysts for electrocatalytic NO x− reduction to ammonia.* Inorganic Chemistry Frontiers, 2023.
19. Lyaskovskyy, V. and B. De Bruin, *Redox non-innocent ligands: versatile new tools to control catalytic reactions.* ACS Catalysis, 2012. **2**(2): p. 270-279.
20. Ouanounou, S. and D. Richeson, *Structural and electronic trends for five coordinate 1 st row transition metal complexes: Mn (II) to Zn (II) captured in a bis (iminopyridine) framework.* Dalton Transactions, 2016. **45**(36): p. 14327-14334.
21. De Bruin, B., P. Gualco, and N.D. Paul, *Redox Non-innocent Ligands: Reactivity and Catalysis.* Ligand Design in Metal Chemistry: Reactivity and Catalysis, 2016: p. 176-204.
22. Elgrishi, N. and J.L. Dempsey, *A practical beginner's guide to cyclic voltammetry.* Journal of Chemical Education, 2018. **95**(2): p. 197-206.
23. Pletcher, D., Greff R, Peat R, Peter LM, Robinson J, *Instrumental methods in electrochemistry*. 2001: Elsevier.
24. Zhu, J., Hu, L., Lee, L. Y. S., & Wong, K. Y., *Recent advances in electrocatalytic hydrogen evolution using nanoparticles.* Chemical Reviews, 2019. **120**(2): p. 851-918.
25. Eliaz, N. and E. Gileadi, *Physical electrochemistry: fundamentals, techniques, and applications*. John Wiley & Sons, 2019.
26. Boudart, M., *Kinetics of chemical processes: butterworth-Heinemann series in chemical engineering*. Elsevier, 2014.
27. Boudart, M., *Turnover rates in heterogeneous catalysis.* Chemical Reviews, 1995. **95**(3): p. 661-666.
28. Trasatti, S. and O. Petrii, *Real surface area measurements in electrochemistry.* Journal of Electroanalytical Chemistry, 1992. **327**(1-2): p. 353-376.
29. Kozuch, S. and J.M. Martin, *"Turning over" definitions in catalytic cycles*. 2012, ACS Catalysis. p. 2787-2794.
30. Cheng, Y., H. Wang, T. Qian, and C. Yan, *Interfacial engineering of carbon-based materials for efficient electrocatalysis: Recent advances and future.* Journal of Energy Chemistry, 2022. **4**(3): p. 100074.
31. Thoi, V.S., Y. Sun, J.R. Long, and C.J. Chang, *Complexes of earth-abundant metals for catalytic electrochemical hydrogen generation under aqueous conditions.* Chemical Society Reviews, 2013. **42**(6): p. 2388-2400.
32. Karunadasa, H.I., C.J. Chang, and J.R. Long, *A molecular molybdenum-oxo catalyst for generating hydrogen from water.* Nature, 2010. **464**(7293): p. 1329-1333.
33. Theerthagiri, J. and A.P. Murthy, *Fundamental aspects and recent advances in transition metal nitrides as electrocatalysts for hydrogen evolution reaction: A review.* Current Opinion in Solid State and Materials Science, 2020. **24**(1): p. 100805.
34. Kaeffer, N. and V. Artero, *The dark side of molecular catalysis: diimine–dioxime cobalt complexes are not the actual hydrogen evolution electrocatalyst in acidic aqueous solutions.* ACS Catalysis, 2016. **6**(6): p. 3727-3737.
35. Chakrabarti, S. and L.M. Mirica, *Characterization of paramagnetic states in an organometallic nickel hydrogen evolution electrocatalyst.* Nature Communications, 2023. **14**(1): p. 905.

36. Mejia-Rodriguez, R. and M.Y. Darensbourg, *The hydrophilic phosphatriazaadamantane ligand in the development of H_2 production electrocatalysts: iron hydrogenase model complexes.* Journal of the American Chemical Society, 2004. **126**(38): p. 12004-12014.
37. Wang, Z. and J. Liu, *Diiron azadithiolates with hydrophilic phosphatriazaadamantane ligand as iron-only hydrogenase active site models: Synthesis, structure, and electrochemical study.* Inorganica Chimica Acta, 2007. **360**(7): p. 2411-2419.
38. Fisher, B.J. and R. Eisenberg, *Electrocatalytic reduction of carbon dioxide by using macrocycles of nickel and cobalt.* Journal of the American Chemical Society, 1980. **102**(24): p. 7361-7363.
39. Collin, J.P., A. Jouaiti, and J.P. Sauvage, *Electrocatalytic properties of (tetraazacyclotetradecane) nickel (2+) and Ni_2 (biscyclam) 4+ with respect to carbon dioxide and water reduction.* Inorganic Chemistry, 1988. **27**(11): p. 1986-1990.
40. Pool, D.H. and D.L. DuBois, *$[Ni(PPh_2NAr_2)_2(NCMe)][BF_4]_2$ as an electrocatalyst for H_2 production: PPh_2NAr_2 = 1,5-(di(4-(thiophene-3-yl)phenyl)-3,7-diphenyl-1,5-diaza-3,7-diphosphacyclooctane).* Journal of Organometallic Chemistry, 2009. **694**: p. 2858-2865.
41. DuBois, M.R. and D.L. DuBois, *The roles of the first and second coordination spheres in the design of molecular catalysts for H 2 production and oxidation.* Chemical Society Reviews, 2009. **38**(1): p. 62-72.
42. Kilgore, U.J. and D.L. DuBois, *$[Ni\ (PPh_2NC_6H_4X_2)_2]^{2+}$ complexes as electrocatalysts for H_2 production: effect of substituents, acids, and water on catalytic rates.* Journal of the American Chemical Society, 2011. **133**(15): p. 5861-5872.
43. Helm, M.L., and D.L. DuBois, *A synthetic nickel electrocatalyst with a turnover frequency above 100,000 s− 1 for H_2 production.* Science, 2011. **333**(6044): p. 863-866.
44. Jain, A., Shaw, W.J., *Incorporating peptides in the outer-coordination sphere of bioinspired electrocatalysts for hydrogen production.* Inorganic Chemistry, 2011. **50**(9): p. 4073-4085.
45. McNamara, W.R. and R. Eisenberg, *Cobalt-dithiolene complexes for the photocatalytic and electrocatalytic reduction of protons in aqueous solutions.* Proceedings of the National Academy of Sciences, 2012. **109**(39): p. 15594-15599.
46. Begum, A., G. Moula, and S. Sarkar, *A Nickel (II)–Sulfur-Based Radical-Ligand Complex as a Functional Model of Hydrogenase.* Chemistry–A European Journal, 2010. **16**(41): p. 12324-12327.
47. Luca, O.R. and R.H. Crabtree, *A tridentate Ni pincer for aqueous electrocatalytic hydrogen production.* New Journal of Chemistry, 2012. **36**(5): p. 1149-1152.
48. Muthuramalingam, S., M. Velusamy, and R. Mayilmurugan, *Fixation of atmospheric CO 2 as C1-feedstock by nickel (II) complexes.* Dalton Transactions, 2021. **50**(23): p. 7984-7994.
49. Kortlever, R. and M.T.M. Coper, *Catalysts and reaction pathways for the electrochemical reduction of carbon dioxide.* The Journal of Physical Chemistry Letters, 2015. **6**(20): p. 4073-4082.
50. Sordakis, K. and M. Beller, *Homogeneous catalysis for sustainable hydrogen storage in formic acid and alcohols.* Chemical Reviews, 2018. **118**(2): p. 372-433.
51. Zhong, H., Kawanami, H., *Formic acid-based liquid organic hydrogen carrier system with heterogeneous catalysts.* Advanced Sustainable Systems, 2018. **2**(2): p. 1700161.

52. Grice, K.A. and C.P. Kubiak, *Recent studies of rhenium and manganese bipyridine carbonyl catalysts for the electrochemical reduction of CO_2*, in *Advances in Inorganic Chemistry*. 2014, Elsevier. p. 163-188.
53. Hawecker, J., J.-M. Lehn, and R. Ziessel, *Electrocatalytic reduction of carbon dioxide mediated by Re(bipy)(CO)$_3$Cl (bipy= 2, 2'-bipyridine).* Journal of the Chemical Society, Chemical Communications, 1984(6): p. 328-330.
54. Sullivan, B.P., Meyer, T.J., *One-and two-electron pathways in the electrocatalytic reduction of CO_2 by fac-Re(bpy)(CO)$_3$ Cl (bpy= 2, 2'-bipyridine).* Journal of the Chemical Society, Chemical Communications, 1985(20): p. 1414-1416.
55. Bourrez, M., F. Molton, S. Chardon-Noblat, and A. Deronzier, *[Mn (bipyridyl)(CO)$_3$Br]: an abundant metal carbonyl complex as efficient electrocatalyst for CO_2 reduction.* Angewandte Chemie International Edition, 2011. **50**(42): p. 9903-9906.
56. Narouz, M.R., P. De La Torre, L. An, and C.J. Chang, *Multifunctional Charge and Hydrogen-Bond Effects of Second-Sphere Imidazolium Pendants Promote Capture and Electrochemical Reduction of CO_2 in Water Catalyzed by Iron Porphyrins.* Angewandte Chemie International Edition, 2022. **61**(37): p. e202207666.
57. Dodge, H.M., Liu. C., Miller, A.J.M., *Polyketones from carbon dioxide and ethylene by integrating electrochemical and organometallic catalysis.* ACS Catalysis, 2023. **13**(7): p. 4053-4059.
58. Fors, S.A. and C.A. Malapit, *Homogeneous Catalysis for the Conversion of CO_2, CO, CH_3OH, and CH_4 to C^{2+} Chemicals via C–C Bond Formation.* ACS Catalysis, 2023. **13**(7): p. 4231-4249.
59. Kumbhakar, S., Maji, S., *Synthesis, characterization, structural and photophysical properties of heteroleptic ruthenium complexes containing 2-(1H-benzo [d] imidazol-2-yl) quinoline ligand towards electrocatalytic CO_2 reduction.* Journal of Chemical Sciences, 2022. **134**(3): p. 71.
60. Mohamed, E.A., Z.N. Zahran, and Y. Naruta, *Efficient heterogeneous CO_2 to CO conversion with a phosphonic acid fabricated cofacial iron porphyrin dimer.* Chemistry of Materials, 2017. **29**(17): p. 7140-7150.
61. Tan, X., X. Sun, and B. Han, *Ionic liquid-based electrolytes for CO_2 electroreduction and CO_2 electroorganic transformation.* National Science Review, 2022. **9**(4): p. nwab022.
62. Pugliese, E., Halime, Z., Aukauloo, A., *Dissection of Light-Induced Charge Accumulation at a Highly Active Iron Porphyrin: Insights in the Photocatalytic CO_2 Reduction.* Angewandte Chemie International Edition, 2022. **61**(14): p. e202117530.
63. Zhu, J.-Y., Chen, Y., *Iridium nanotubes as bifunctional electrocatalysts for oxygen evolution and nitrate reduction reactions.* ACS Applied Materials & Interfaces, 2020. **12**(12): p. 14064-14070.
64. Liao, L.-L., Yu, D.G., *Electrochemical ring-opening dicarboxylation of strained carbon–carbon single bonds with CO2: Facile synthesis of diacids and derivatization into polyesters.* Journal of the American Chemical Society, 2022. **144**(5): p. 2062-2068.
65. Tam, S.M., Webster, R.B., *Competition between Reversible Capture of CO_2 and Release of $CO_2^{\bullet-}$–Using Electrochemically Reduced Quinones in Acetonitrile Solutions.* The Journal of Physical Chemistry C, 2021. **125**(22): p. 11916-11927.
66. Pal, R., Trovitch, R.J., Baik, M.H., *Reaction of a Molybdenum Bis (dinitrogen) Complex with Carbon Dioxide: A Combined Experimental and Computational Investigation.* Inorganic Chemistry, 2021. **60**(11): p. 7708-7718.

67. Wang, J., Hu, W., Han, X., *Defective bimetallic selenides for selective CO_2 electroreduction to CO.* Advanced Materials, 2022. **34**(3): p. 2106354.
68. Nandhakumar, P., Yang, H., *Di (Thioether Sulfonate)-Substituted Quinolinedione as a Rapidly Dissoluble and Stable Electron Mediator and Its Application in Sensitive Biosensors.* Advanced Healthcare Materials, 2022. **11**(2): p. 2101819.
69. Sato, R. and Y. Amao, *Carbonic anhydrase/formate dehydrogenase bienzymatic system for CO_2 capture, utilization and storage.* Reaction Chemistry & Engineering, 2022. **7**(1): p. 181-191.
70. Tan, X., H. Li, and S. Yang, *Single-Atom Catalysts-Enabled Reductive Upgrading of CO_2.* ChemCatChem, 2021. **13**(23): p. 4859-4877.
71. Dhabarde, N., Subramanian, V.R., *Review of photocatalytic and photo-electrocatalytic reduction of CO_2 on carbon supported films.* International Journal of Hydrogen Energy, 2022. **47**(72): p. 30908-30936.
72. Cronin, S.P., Grapperhaus, C.A., *Exploiting Metal–Ligand Cooperativity to Sequester, Activate, and Reduce Atmospheric Carbon Dioxide with a Neutral Zinc Complex.* Inorganic Chemistry, 2020. **59**(7): p. 4835-4841.
73. Chen, J.G., Schrock, R.R., Crooks, R.M., *Beyond fossil fuel–driven nitrogen transformations.* Science, 2018. **360**(6391): p. eaar6611.
74. Guo, W., Xu, Q., *Electrochemical nitrogen fixation and utilization: theories, advanced catalyst materials and system design.* Chemical Society Reviews, 2019. **48**(24): p. 5658-5716.
75. Glibert, P.M., R. Maranger, D.J. Sobota, and L. Bouwman, *The Haber Bosch–harmful algal bloom (HB–HAB) link.* Environmental Research Letters, 2014. **9**(10): p. 105001.
76. Smith, C., A.K. Hill, and L. Torrente-Murciano, *Current and future role of Haber–Bosch ammonia in a carbon-free energy landscape.* Energy & Environmental Science, 2020. **13**(2): p. 331-344.
77. Van Langevelde, P.H., I. Katsounaros, and M.T. Koper, *Electrocatalytic nitrate reduction for sustainable ammonia production.* Joule, 2021. **5**(2): p. 290-294.
78. Fu, X., Kang, Y., *Alternative route for electrochemical ammonia synthesis by reduction of nitrate on copper nanosheets.* Applied Materials Today, 2020. **19**: p. 100620.
79. Garcia-Segura, S., M. Lanzarini-Lopes, K. Hristovski, and P. Westerhoff, *Electrocatalytic reduction of nitrate: Fundamentals to full-scale water treatment applications.* Applied Catalysis B: Environmental, 2018. **236**: p. 546-568.
80. Wang, Y., Zhang, B., *Electrochemical synthesis of nitric acid from air and ammonia through waste utilization.* National Science Review, 2019. **6**(4): p. 730-738.
81. Yao, Y., Shao, M., *A spectroscopic study of electrochemical nitrogen and nitrate reduction on rhodium surfaces.* Angewandte Chemie, 2020. **132**(26): p. 10565-10569.
82. Hu, H.-Y., N. Goto, and K. Fujie, *Effect of pH on the reduction of nitrite in water by metallic iron.* Water Research, 2001. **35**(11): p. 2789-2793.
83. Clark, Senftle, T.P., Wong, M.S., *Mechanistic insights into pH-controlled nitrite reduction to ammonia and hydrazine over rhodium.* ACS Catalysis, 2019. **10**(1): p. 494-509.
84. Braley, S.E., Jakubikova, E., Smith, J.M., *Buffer Assists Electrocatalytic Nitrite Reduction by a Cobalt Macrocycle Complex.* Inorganic Chemistry, 2022. **61**(33): p. 12998-13006.

85. Taniguchi, I., N. Nakashima, K. Matsushita, and K. Yasukouchi, *Electrocatalytic reduction of nitrate and nitrite to hydroxylamine and ammonia using metal cyclams.* Journal of Electroanalytical Chemistry and Interfacial Electrochemistry, 1987. **224**(1-2): p. 199-209.
86. Xu, S., Jakubikova, E., Smith, J.M., *A flexible, redox-active macrocycle enables the electrocatalytic reduction of nitrate to ammonia by a cobalt complex.* Chemical Science, 2018. **9**(22): p. 4950-4958.
87. Xu, S., Jakubikova, E., Smith, J.M., *Intramolecular hydrogen bonding facilitates electrocatalytic reduction of nitrite in aqueous solutions.* Inorganic Chemistry, 2019. **58**(14): p. 9443-9451.
88. Partovi, S., Z. Xiong, K.M. Kulesa, and J.M. Smith, *Electrocatalytic reduction of nitrogen oxyanions with a redox-active cobalt macrocycle complex.* Inorganic Chemistry, 2022. **61**(24): p. 9034-9039.
89. Cheng, S.-H. and Y.O. Su, *Electrocatalysis of nitric oxide reduction by water-soluble cobalt porphyrin. Spectral and electrochemical studies.* Inorganic Chemistry, 1994. **33**(25): p. 5847-5854.
90. Wang, M., L. Chen, and L. Sun, *Recent progress in electrochemical hydrogen production with earth-abundant metal complexes as catalysts.* Energy & Environmental Science, 2012. **5**(5): p. 6763-6778.
91. Wang, J.-W., W.-J. Liu, D.-C. Zhong, and T.-B. Lu, *Nickel complexes as molecular catalysts for water splitting and CO_2 reduction.* Coordination Chemistry Reviews, 2019. **378**: p. 237-261.
92. Luo, G.-G., Zhang, Q. *Recent progress in ligand-centered homogeneous electrocatalysts for hydrogen evolution reaction.* Inorganic Chemistry Frontiers, 2019. **6**(2): p. 343-354.
93. Greene, B.L., Wu, C.H., Vansuch, G.E., Adams, M.W. and Dyer, R.B., *Proton inventory and dynamics in the Ni_a-S to Ni_a-C transition of a [NiFe] hydrogenase.* Biochemistry, 2016. **55**(12): p. 1813-1825.
94. Pantani, O., E. Anxolabehere-Mallart, A. Aukauloo, and P. Millet, *Electroactivity of cobalt and nickel glyoximes with regard to the electro-reduction of protons into molecular hydrogen in acidic media.* Electrochemistry Communications, 2007. **9**(1): p. 54-58.
95. Jacques, P.-A., V. Artero, J. Pécaut, and M. Fontecave, *Cobalt and nickel diimine-dioxime complexes as molecular electrocatalysts for hydrogen evolution with low overvoltages.* Proceedings of the National Academy of Sciences, 2009. **106**(49): p. 20627-20632.
96. McCrory, C.C., C. Uyeda, and J.C. Peters, *Electrocatalytic hydrogen evolution in acidic water with molecular cobalt tetraazamacrocycles.* Journal of the American Chemical Society, 2012. **134**(6): p. 3164-3170.
97. Stubbert, B.D., J.C. Peters, and H.B. Gray, *Rapid water reduction to H_2 catalyzed by a cobalt bis (iminopyridine) complex.* Journal of the American Chemical Society, 2011. **133**(45): p. 18070-18073.
98. Das, A., Han, Z., Brennessel, W.W., Holland, P.L. and Eisenberg, R., *Nickel complexes for robust light-driven and electrocatalytic hydrogen production from water.* ACS Catalysis, 2015. **5**(3): p. 1397-1406.
99. Zhang W, Hong J, Zheng J, Huang Z, Zhou J, Xu R. *Nickel–thiolate complex catalyst assembled in one step in water for solar H_2 production.* Journal of the American Chemical Society, 2011. **133**(51): p. 20680-20683.

100. Han, J., Zhang, W., Zhou, T., Wang, X. and Xu, R., *Nickel-complexes with a mixed-donor ligand for photocatalytic hydrogen evolution from aqueous solutions under visible light.* Royal Society of Chemistry Advances, 2012. **2**(22): p. 8293-8296.
101. Wiese, S., Raugei, S., DuBois, D.L., *Hydrogen production using nickel electrocatalysts with pendant amines: ligand effects on rates and overpotentials.* ACS Catalysis, 2013. **3**(11): p. 2527-2535.
102. Tsay, C., Yang, J.Y., *Electrocatalytic hydrogen evolution under acidic aqueous conditions and mechanistic studies of a highly stable molecular catalyst.* Journal of the American Chemical Society, 2016. **138**(43): p. 14174-14177.
103. Xue, D., Q.-X. Peng, S.-Z. Zhan, *Synthesis and electrochemical properties of a water soluble nickel (II) complex supported by N-phenylpyridin-2-ylmethanimine ligand.* Inorganic Chemistry Communications, 2017. **82**: p. 11-15.
104. Xue, D., Q.-X. Peng, D. Li, S.-Z. Zhan, *Synthesis, characterization and electro-catalytic properties of a water-soluble nickel (II) complex supported by picolinic acid ions.* Polyhedron, 2017. **126**: p. 239-244.
105. Lauck, M.T.J., *Cobaltocenium Amides-Photoinduced Electron Transfer Processes in Donor-Acceptor Amides*. 2019, Dissertation, Mainz, Johannes Gutenberg-Universität, 2020.
106. Gan, L., Groy, T.L., Tarakeshwar, P., Mazinani, S.K., Shearer, J., Mujica, V. Jones, A.K., *A nickel phosphine complex as a fast and efficient hydrogen production catalyst.* Journal of the American Chemical Society, 2015. **137**(3): p. 1109-1115.
107. Solis, B.H., Hammes-Schiffer, S., *Nickel phlorin intermediate formed by proton-coupled electron transfer in hydrogen evolution mechanism.* Proceedings of the National Academy of Sciences, 2016. **113**(3): p. 485-492.
108. Haddad, A.Z., Garabato, B.D., Kozlowski, P.M., Buchanan, R.M., Grapperhaus, C.A., *Beyond metal-hydrides: non-transition-metal and metal-free ligand-centered electrocatalytic hydrogen evolution and hydrogen oxidation.* Journal of the American Chemical Society, 2016. **138**(25): p. 7844-7847.
109. Cronin, S.P., Grapperhaus, C.A., *Utilizing charge effects and minimizing intramolecular proton rearrangement to improve the overpotential of a thiosemicarbazonato zinc HER catalyst.* Inorganic Chemistry, 2019. **58**(19): p. 12986-12997.
110. Chen, L., Zhang, P., Wang, N., *Bioinspired Design of Positioned Amine Assists Hydrogen Evolution from Neutral Water by Nickel Tripyridine-Diamine.* ChemCatChem, 2020. **12**(15): p. 3853-3856.
111. Zhang, P., Wang, M., Yang, Y., Zheng, D., Han, K. and Sun, L., *Highly efficient molecular nickel catalysts for electrochemical hydrogen production from neutral water.* Chemical Communications, 2014. **50**(91): p. 14153-14156.
112. Wang, X., L. Yao, Y. Pan, and K.-W. Huang, *Synthesis of group 10 metal complexes with a new unsymmetrical PN3P-pincer ligand through ligand post-modification: Structure and reactivity.* Journal of Organometallic Chemistry, 2017. **845**: p. 25-29.
113. Li, H., Huang, K.W., *A Pseudodearomatized PN^3P^* Ni–H Complex as a Ligand and σ-Nucleophilic Catalyst.* The Journal of Organic Chemistry, 2018. **83**(24): p. 14969-14977.
114. Li, H., Gonçalves, T.P., Zhao, Q., Gong, D., Lai, Z., Wang, Z., Zheng, J., Huang, K.W., *Diverse catalytic reactivity of a dearomatized PN^3P^*–nickel hydride pincer complex towards CO_2 reduction.* Chemical Communications, 2018. **54**(81): p. 11395-11398.

115. Li, H., B. Zheng, and K.-W. Huang, *A new class of PN^3-pincer ligands for metal–ligand cooperative catalysis.* Coordination Chemistry Reviews, 2015. **293**: p. 116-138.
116. Lupp, D., Huang, K.-W., *The Importance of Metal–Ligand Cooperativity in the Phosphorus–Nitrogen PN3P Platform: A Computational Study on Mn-Catalyzed Pyrrole Synthesis.* Organometallics, 2019. **39**(1): p. 18-24.
117. Rao, G.K., Richeson, D., *Electro-and Photocatalytic Generation of H2 Using a Distinctive CoII "PN3P" Pincer Supported Complex with Water or Saturated Saline as a Hydrogen Source.* Chemistry–A European Journal, 2017. **23**(66): p. 16763-16767.
118. Benito-Garagorri, D., Kisala, J., Kirchner, K., *Achiral and chiral transition metal complexes with modularly designed tridentate PNP pincer-type ligands based on N-heterocyclic diamines.* Organometallics, 2006. **25**(8): p. 1900-1913.
119. Mastalir, M., Bedford, R.B., *Air-stable triazine-based Ni (II) PNP pincer complexes as catalysts for the Suzuki–Miyaura cross-coupling.* Organic Letters, 2016. **18**(13): p. 3186-3189.
120. Pool, D.H., DuBois, D.L., *[Ni (PPh_2NAr_2)$_2$ (NCMe)][BF_4]$_2$ as an electrocatalyst for H_2 production: PPh_2NAr_2= 1, 5-(di (4-(thiophene-3-yl) phenyl)-3, 7-diphenyl-1, 5-diaza-3, 7-diphosphacyclooctane).* Journal of Organometallic Chemistry, 2009. **694**(17): p. 2858-2865.
121. Sheldrick, G.M., *A short history of SHELX.* Acta Crystallographica Section A: Foundations of Crystallography, 2008. **64**(1): p. 112-122.
122. Hübschle, C.B., G.M. Sheldrick, and B. Dittrich, *ShelXle: a Qt graphical user interface for SHELXL.* Journal of Applied Crystallography, 2011. **44**(6): p. 1281-1284.
123. Addison, A., T. Rao, and J. Reedijk, *J. van Rijn, GC Verschoor, Synthesis. structure, and spectroscopic properties of copper (ll) compounds containing nitrogen-sulphur donor ligands; the crystal and molecular structure of aqua [1, 7-bis (N-methylhenzimidazol-2'-yl)-2, 6-dithiaheptane] copper (ll) perchlorate.* Journal of Chemical Society Dalton Transaction, 1984: p. 1349-1356.
124. Wiedner, E.S., Bullock, R.M., *Molecular catalysts with diphosphine ligands containing pendant amines.* Chemical Reviews, 2022. **122**(14): p. 12427-12474.
125. Tong, L., L. Duan, A. Zhou, and R.P. Thummel, *First-row transition metal polypyridine complexes that catalyze proton to hydrogen reduction.* Coordination Chemistry Reviews, 2020. **402**: p. 213079.
126. Roy, S., M. Bacchi, G. Berggren, and V. Artero, *A Systematic Comparative Study of Hydrogen-Evolving Molecular Catalysts in Aqueous Solutions.* ChemSusChem, 2015. **8**(21): p. 3632-3638.
127. Zee, D.Z., T. Chantarojsiri, J.R. Long, and C.J. Chang, *Metal–polypyridyl catalysts for electro-and photochemical reduction of water to hydrogen.* Accounts of Chemical Research, 2015. **48**(7): p. 2027-2036.
128. Bernhardt, P.V. and L.A. Jones, *Electrochemistry of macrocyclic cobalt (III/II) hexaamines: electrocatalytic hydrogen evolution in aqueous solution.* Inorganic Chemistry, 1999. **38**(22): p. 5086-5090.
129. Beyene, B.B., S.B. Mane, and C.-H. Hung, *Highly efficient electrocatalytic hydrogen evolution from neutral aqueous solution by a water-soluble anionic cobalt (II) porphyrin.* Chemical Communications, 2015. **51**(81): p. 15067-15070.

130. Zhang, P., Sun, L., *Electrocatalytic hydrogen evolution from neutral water by molecular cobalt tripyridine–diamine complexes.* Chemical Communications, 2013. **49**(82): p. 9455-9457.
131. Beley, M., J.P. Collin, R. Ruppert, and J.P. Sauvage, *Electrocatalytic reduction of carbon dioxide by nickel cyclam2+ in water: study of the factors affecting the efficiency and the selectivity of the process.* Journal of the American Chemical Society, 1986. **108**(24): p. 7461-7467.
132. Rao, G.K., Richeson, D., *Electrocatalytic generation of H_2 from neutral water in acetonitrile using manganese polypyridyl complexes with ligand assistance.* Dalton Transactions, 2017. **46**(20): p. 6518-6522.
133. Frey, M., *Hydrogenases: hydrogen-activating enzymes.* ChemBioChem, 2002. **3**(2-3): p. 153-160.
134. Lubitz, W., H. Ogata, O. Rudiger, and E. Reijerse, *Hydrogenases.* Chemical Reviews, 2014. **114**(8): p. 4081-4148.
135. Flisak, Z. and W.-H. Sun, *Progression of diiminopyridines: from single application to catalytic versatility.* ACS Catalysis, 2015. **5**(8): p. 4713-4724.
136. Chen, L., Sun, S.G., *Anxolabe' hère-Mallart, E.; Robert, M.; Lau, T.-C. Dual Homogeneous and Heterogeneous Pathways in Photo-and Electrocatalytic Hydrogen Evolution With Nickel (II) Catalysts Bearing Tetradentate Macrocyclic Ligands.* ACS Catalysis, 2015. **5**: p. 356-364.
137. Chen, Z., Sun, S.G., *Nickel Complexes with Non-innocent Ligands as Highly Active Electrocatalysts for Hydrogen Evolution.* Chinese Journal of Chemistry, 2018. **36**(12): p. 1161-1164.
138. Charlene, T., *Electrocatalytic Hydrogen Evolution under Acidic Aqueous Conditions and Mechanistic Studies of a Highly Stable Molecular Catalyst.* 2016.
139. Alyea, E. and P. Merrell, *Synthesis and characterization of metal complexes of terdentate NNN donor. txt ligands derived fromo 2, 6-diacetylpyridine. Nickel (II) complexes with 2, 6-diacetylpyridinebis (imines).* Inorganica Chimica Acta, 1978. **28**: p. 91-97.
140. Luca, O.R., Crabtree, R.H., *Study of an S= 1 Ni (II) pincer electrocatalyst precursor for aqueous hydrogen production based on paramagnetic ^1H NMR.* Dalton Transactions, 2013. **42**(24): p. 8802-8807.
141. Rountree, E.S., B.D. McCarthy, T.T. Eisenhart, and J.L. Dempsey, *Evaluation of homogeneous electrocatalysts by cyclic voltammetry*. 2014, ACS Publications. p. 9983-10002.
142. Appel, A.M. and M.L. Helm, *Determining the overpotential for a molecular electrocatalyst*. 2014, ACS Publications. p. 630-633.
143. Fourmond, V., P.-A. Jacques, M. Fontecave, and V. Artero, *H2 evolution and molecular electrocatalysts: determination of overpotentials and effect of homoconjugation.* Inorganic Chemistry, 2010. **49**(22): p. 10338-10347.
144. Cook, T.R., Teets, T.S. and Nocera, D.G., *Solar energy supply and storage for the legacy and nonlegacy worlds.* Chemical Reviews, 2010. **110**(11): p. 6474-6502.
145. Wang, T., Xie, H., Chen, M., D'Aloia, A., Cho, J., Wu, G. and Li, Q., *Precious metal-free approach to hydrogen electrocatalysis for energy conversion: From mechanism understanding to catalyst design.* Nano Energy, 2017. **42**: p. 69-89.

146. Huo, P., Peters, J.C. and Miller III, T.F., *Breaking the correlation between energy costs and kinetic barriers in hydrogen evolution via a cobalt pyridine-diimine-dioxime catalyst.* ACS Catalysis, 2016. **6**(9): p. 6114-6123.
147. Du, P. and R. Eisenberg, *Catalysts made of earth-abundant elements (Co, Ni, Fe) for water splitting: recent progress and future challenges.* Energy & Environmental Science, 2012. **5**(3): p. 6012-6021.
148. Chirik, P.J., *Preface: forum on redox-active ligands.* Inorganic Chemistry, 2011. **50**(20): p. 9737-9740.
149. Chen, X., Lu, J. and Zhuang, L., *Highly efficient molecular cobalt electrode for (photo) electrochemical hydrogen evolution.* The Journal of Physical Chemistry C, 2014. **118**(36): p. 20791-20798.
150. Luca, O.R. and R.H. Crabtree, *Redox-active ligands in catalysis.* Chemical Society Reviews, 2013. **42**(4): p. 1440-1459.
151. McCarthy, B.D. and J.L. Dempsey, *Decoding proton-coupled electron transfer with potential–p K a diagrams.* Inorganic Chemistry, 2017. **56**(3): p. 1225-1231.
152. Brown, J., J. Ovens, and D. Richeson, *Elucidating Two Distinct Pathways for Electrocatalytic Hydrogen Production Using CoII Pincer Complexes.* ChemSusChem, 2022. **15**(5): p. e202102542.
153. Baffert, C., V. Artero, and M. Fontecave, *Cobaloximes as functional models for hydrogenases. 2. Proton electroreduction catalyzed by difluoroborylbis (dimethylglyoximato) cobalt (II) complexes in organic media.* Inorganic Chemistry, 2007. **46**(5): p. 1817-1824.
154. Muetterties, E.t. and L. Guggenberger, *Idealized polytopal forms. Description of real molecules referenced to idealized polygons or polyhedra in geometric reaction path form.* Journal of the American Chemical Society, 1974. **96**(6): p. 1748-1756.
155. Addison, A.W., van Rijn, J. and Verschoor, G.C., *Synthesis, structure, and spectroscopic properties of copper (II) compounds containing nitrogen–sulphur donor ligands; the crystal and molecular structure of aqua [1, 7-bis (N-methylbenzimidazol-2'-yl)-2, 6-dithiaheptane] copper (II) perchlorate.* Journal of the Chemical Society, Dalton Transactions, 1984(7): p. 1349-1356.
156. Magoński, J., Z. Pawlak, and T. Jasiński, *Dissociation constants of substituted phenols and homoconjugation constants of the corresponding phenol–phenolate systems in acetonitrile.* Journal of the Chemical Society, Faraday Transactions, 1993. **89**(1): p. 119-122.
157. Kozak, A., Dąbrowska, A. and Chmurzyński, L., *A potentiometric study of acid–base properties of the (phenol+ phenolate) systems in acetonitrile and,(acetonitrile+ cyclohexane) solvent system.* The Journal of Chemical Thermodynamics, 2003. **35**(1): p. 77-89.
158. Mentes, A., J. Fawcett, and R.D. Kemmitt, *2, 6-Bis [1-(phenylimino) ethyl] pyridine.* Acta Crystallographica Section E: Structure Reports Online, 2001. **57**(5): p. o424-o425.
159. Esteruelas, M.A., Oliván, M. and Oñate, E., *Preparation, structure, and ethylene polymerization behavior of bis (imino) pyridyl chromium (III) complexes.* Organometallics, 2003. **22**(3): p. 395-406.
160. Elgrishi, N., M.B. Chambers, X. Wang, and M. Fontecave, *Molecular polypyridine-based metal complexes as catalysts for the reduction of CO_2.* Chemical Society Reviews, 2017. **46**(3): p. 761-796.

161. Bonin, J., A. Maurin, and M. Robert, *Molecular catalysis of the electrochemical and photochemical reduction of CO_2 with Fe and Co metal based complexes. Recent advances.* Coordination Chemistry Reviews, 2017. **334**: p. 184-198.
162. Takeda, H., C. Cometto, O. Ishitani, and M. Robert, *Electrons, photons, protons and earth-abundant metal complexes for molecular catalysis of CO_2 reduction.* ACS Catalysis, 2017. **7**(1): p. 70-88.
163. Queyriaux, N., Jane, T., Massin, J., Artero V., and M. Chavarot-Kerlidou, *Recent developments in hydrogen evolving molecular cobalt (II)–polypyridyl catalysts.* Coordination Chemistry Reviews, 2015. **304**: p. 3-19.
164. Losse, S., J.G. Vos, and S. Rau, *Catalytic hydrogen production at cobalt centres.* Coordination Chemistry Reviews, 2010. **254**(21-22): p. 2492-2504.
165. Kissling, S., Altenbuchner, P.T., Niemi, T., Repo, T. and Rieger, B., *Zinc-Catalyzed Transformation of Carbon Dioxide.* Zinc Catalysis: Applications in Organic Synthesis, 2015, p. 179-206.
166. Enthaler, S., "Rise of the zinc age in homogeneous catalysis?." ACS Catalysis*, 2013. **3**(2): p. 150–158.*
167. Power, P.P., *Main-group elements as transition metals.* Nature, 2010. **463**(7278): p. 171-177.
168. Klaus, S., M.W. Lehenmeier, C.E. Anderson, and B. Rieger, *Recent advances in CO_2/epoxide copolymerization—New strategies and cooperative mechanisms.* Coordination Chemistry Reviews, 2011. **255**(13-14): p. 1460-1479.
169. Kato, M. and T. Ito, *Facile carbon dioxide uptake by zinc (II)-tetraazacycloalkane complexes. 1. Syntheses, characterizations, and chemical properties of (monoalkyl carbonato)(tetraazacycloalkane) zinc (II) complexes.* Inorganic Chemistry, 1985. **24**(4): p. 504-508.
170. Kato, M. and T. Ito, *Facile carbon dioxide uptake by zinc (II)-tetraazacycloalkane complexes. 2. X-ray structural studies of (. mu.-monomethyl carbonato)(1, 4, 8, 11-tetraazacyclotetradecane) zinc (II) perchlorate, bis (. mu.-monomethyl carbonato) tris [(1, 4, 8, 12-tetraazacyclopentadecane) zinc (II)] perchlorate, and (monomethyl carbonato)(1, 4, 8, 11-tetramethyl-1, 4, 8, 11-tetraazacyclotetradecane) zinc (II) perchlorate.* Inorganic Chemistry, 1985. **24**(4): p. 509-514.
171. Dobrovetsky, R. and D.W. Stephan, *Catalytic reduction of CO_2 to CO by using zinc (ii) and in situ generated carbodiphosphoranes.* Angewandte Chemie International Edition, 2013. **52**(9): p. 2516-2519.
172. Sattler, W. and G. Parkin, *Zinc catalysts for on-demand hydrogen generation and carbon dioxide functionalization.* Journal of the American Chemical Society, 2012. **134**(42): p. 17462-17465.
173. Donovan, E.S., Barry, B.M., Wirtz, M.N., Geiger, W.E. and Kemp, R.A., *Facilitated carbon dioxide reduction using a Zn (II) complex.* Chemical Communications, 2016. **52**(8): p. 1685-1688.
174. Thompson, E.J. and L.A. Berben, *Electrocatalytic Hydrogen Production by an Aluminum (III) Complex: Ligand-Based Proton and Electron Transfer.* Angewandte Chemie International Edition, 2015. **54**(40): p. 11642-11646.
175. Sherbow, T.J., J.C. Fettinger, and L.A. Berben, *Control of Ligand p K a Values Tunes the Electrocatalytic Dihydrogen Evolution Mechanism in a Redox-Active Aluminum (III) Complex.* Inorganic Chemistry, 2017. **56**(15): p. 8651-8660.

176. Rauch, M., Kar, S., Kumar, A., Avram, L., Shimon, L.J. and Milstein, D., *Metal–Ligand Cooperation Facilitates Bond Activation and Catalytic Hydrogenation with Zinc Pincer Complexes.* Journal of the American Chemical Society, 2020. **142**(34): p. 14513-14521.
177. Berro, P., Norouziyanlakvan, S., and Richeson, D., *Electrocatalytic reduction of CO_2 to CO and HCO_2^- with Zn (ii) complexes displaying cooperative ligand reduction.* Chemical Communications, 2021. **57**(73): p. 9292-9295.
178. Norouziyanlakvan, S., Rao, G.K. and Richeson, D., *Electrocatalytic H_2 Generation from Water Relying on Cooperative Ligand Electron Transfer in "PN^3P" Pincer-Supported NiII Complexes.* Chemistry–A European Journal, 2021. **27**(54): p. 13518-13522.
179. Burt, J., W. Levason, and G. Reid, *Coordination chemistry of the main group elements with phosphine, arsine and stibine ligands.* Coordination Chemistry Reviews, 2014. **260**: p. 65-115.
180. Stucky, G.D. and R.E. DeSimone, *Crystal and molecular structure of 4-methylpyridinium triphenylphosphine tribromozincate.* Inorganic Chemistry, 1971. **10**(8): p. 1808-1812.
181. Sattler, W. and G. Parkin, *Synthesis, structure, and reactivity of a mononuclear organozinc hydride complex: Facile insertion of CO_2 into a Zn–H bond and CO_2-promoted displacement of siloxide ligands.* Journal of the American Chemical Society, 2011. **133**(25): p. 9708-9711.
182. Lehn, J.-M. and R. Ziessel, *Photochemical generation of carbon monoxide and hydrogen by reduction of carbon dioxide and water under visible light irradiation.* Proceedings of the National Academy of Sciences, 1982. **79**(2): p. 701-704.
183. Yang, J.Y., Smith, S.E., Liu, T., Hoffert, W.A., Kassel, W.S., DuBois, M.R., DuBois, D.L. and Bullock, R.M., *Two pathways for electrocatalytic oxidation of hydrogen by a nickel bis (diphosphine) complex with pendant amines in the second coordination sphere.* Journal of the American Chemical Society, 2013. **135**(26): p. 9700-9712.
184. Semproni, S.P., C. Milsmann, and P.J. Chirik, *Four-coordinate cobalt pincer complexes: electronic structure studies and ligand modification by homolytic and heterolytic pathways.* Journal of the American Chemical Society, 2014. **136**(25): p. 9211-9224.
185. Gayton, J.N., Li, Q., Hill, G. and Delcamp, J.H., *Pyridyl CO_2 Fixation Enabled by a Secondary Hydrogen Bonding Coordination Sphere.* American Chemical Society Omega, 2020. **5**(20): p. 11687-11694.
186. Deria, P., Li, S., Zhang, H., Snurr, R.Q., Hupp, J.T. and Farha, O.K., *A MOF platform for incorporation of complementary organic motifs for CO_2 binding.* Chemical Communications, 2015. **51**(62): p. 12478-12481.
187. Farrugia, L.J., *WinGX and ORTEP for Windows: an update.* Journal of Applied Crystallography, 2012. **45**(4): p. 849-854.
188. Frisch, M., & Clemente, F. MJ Frisch, GW Trucks, HB Schlegel, GE Scuseria, MA Robb, JR Cheeseman, G. Scalmani, V. Barone, B. Mennucci, GA Petersson, H. Nakatsuji, M. Caricato, X. Li, HP Hratchian, AF Izmaylov, J. Bloino and G. Zhe. *Gaussian, 9.*
189. Rafiqul, I., C. Weber, B. Lehmann, and A. Voss, *Energy efficiency improvements in ammonia production—perspectives and uncertainties.* Energy, 2005. **30**(13): p. 2487-2504.
190. Maia, L.B. and J.J. Moura, *How biology handles nitrite.* Chemical Reviews, 2014. **114**(10): p. 97.
191. Matassa, S. and W. Verstraete, *Can direct conversion of used nitrogen to new feed and protein help feed the world?* 2015, ACS Publications.

192. Galloway, J.N. and J. Cosby, *The nitrogen cascade.* Bioscience, 2003. **53**(4): p. 341-356.
193. Fowler, D., and M. Coyle, *The global nitrogen cycle in the twenty-first century.* Philosophical Transactions of the Royal Society B: Biological Sciences, 2013. **368**(1621): p. 20130164.
194. Sebilo, M. and Mayer, B., *Long-term fate of nitrate fertilizer in agricultural soils.* Proceedings of the National Academy of Sciences, 2013. **110**(45): p. 18185-18189.
195. Amanullah, S. and Day, A., *Biochemical and artificial pathways for the reduction of carbon dioxide, nitrite and the competing proton reduction: effect of 2nd sphere interactions in catalysis.* Chemical Society Reviews, 2021. **50**(6): p. 3755-3823.
196. Barley, M.H. and T.J. Meyer, *Electrocatalytic reduction of nitrite to ammonia based on a water-soluble iron porphyrin.* Journal of the American Chemical Society, 1986. **108**(19): p. 5876-5885.
197. Uyeda, C. and J.C. Peters, *Selective nitrite reduction at heterobimetallic CoMg complexes.* Journal of the American Chemical Society, 2013. **135**(32): p. 12023-12031.
198. Norouziyanlakvan, S., J. Ferguson, and D. Richeson, *Electrocatalytic hydrogen production from neutral water using an aqueous Ni (II) pincer complex.* Catalysis Science & Technology, 2022. **12**(24): p. 7494-7500.
199. Li, H.L., W.C. Anderson, J.Q. Chambers, and D.T. Hobbs, *Electrocatalytic reduction of nitrate in sodium hydroxide solution in the presence of low-valent cobalt-cyclam species.* Inorganic Chemistry, 1989. **28**(5): p. 863-868.
200. Guo, Y. and Bren, K.L., *Cobalt metallopeptide electrocatalyst for the selective reduction of nitrite to ammonium.* Journal of the American Chemical Society, 2018. **140**(49): p. 16888-16892.
201. Xiang, Y., D.-L. Zhou, and J.F. Rusling, *Electrochemical conversion of nitrate to ammonia in water using Cobalt-DIM as catalyst.* Journal of Electroanalytical Chemistry, 1997. **424**(1-2): p. 1-3.
202. Cioncoloni, G. and Symes, M.D., *Proton-coupled electron transfer enhances the electrocatalytic reduction of nitrite to NO in a bioinspired copper complex.* ACS Catalysis, 2018. **8**(6): p. 5070-5084.
203. Hunt, A.P., and N. Lehnert, *Nitric oxide generation on demand for biomedical applications via electrocatalytic nitrite reduction by copper BMPA-and BEPA-carboxylate complexes.* ACS Catalysis, 2019. **9**(9): p. 7746-7758.
204. Woollard-Shore, J.G., J.P. Holland, M.W. Jones, and J.R. Dilworth, *Nitrite reduction by copper complexes.* Dalton Transactions, 2010. **39**(6): p. 1576-1585.
205. Einsle, O. and F. Neese, *Mechanism of the six-electron reduction of nitrite to ammonia by cytochrome c nitrite reductase.* Journal of the American Chemical Society, 2002. **124**(39): p. 11737-11745.
206. Kwon, Y.M. and J.D. Gilbertson, *Nitrite reduction by a pyridinediimine complex with a proton-responsive secondary coordination sphere.* Chemical Communications, 2016. **52**(73): p. 11016-11019.
207. Manuel, T.D. and J.-U. Rohde, *Reaction of a Redox-Active Ligand Complex of Nickel with Dioxygen Probes Ligand-Radical Character.* Journal of the American Chemical Society, 2009. **131**(43): p. 15582-15583.
208. Blessing, R.H., *An empirical correction for absorption anisotropy.* Acta Crystallographica Section A: Foundations of Crystallography, 1995. **51**(1): p. 33-38.

209. Weatherburn, M., *Phenol-hypochlorite reaction for determination of ammonia.* Analytical Chemistry, 1967. **39**(8): p. 971-974.
210. Hu, B. and S.T. Mei. *Spectrophotometric determination of hydroxylamine in biological wastewater treatment processes.* International journal of environmental science and technology, 2018. **15**: p. 323-332.
211. Rapson, T.D. and H. Dacres, *Micromolar biosensing of nitric oxide using myoglobin immobilized in a synthetic silk film.* Biosensors and Bioelectronics, 2014. **62**: p. 214-220.
212. Braley, S.E., D.C. Ashley, E. Jakubikova, and J.M. Smith, *Electrode-adsorption activates trans-[Cr (cyclam) Cl_2]$^+$ for electrocatalytic nitrate reduction.* Chemical Communications, 2020. **56**(4): p. 603-606.
213. Nelson, S., S. McFall, M. Drew, and A.b. Othman. *The Coordination Chemistry of Some Pentadentate Macrocyclic Ligands*. In Proceedings of the Royal Irish Academy. Section B: Biological, Geological, and Chemical Science. 1977: P. 523-532.
214. Nelson, S., *Developments in the synthesis and coordination chemistry of macrocyclic Schiff base ligands.* Pure and Applied Chemistry, 1980. **52**(11): p. 2461-2476.
215. Cook, D.H. and D.E. Fenton, *Calcium, strontium, and barium complexes of pyridyl-containing macrocyclic Schiff bases.* Journal of the Chemical Society, Dalton Transactions, 1979(2): p. 266-272.
216. Wang, J.W. and K. Sakai, *A molecular cobalt hydrogen evolution catalyst showing high activity and outstanding tolerance to CO and O_2.* Angewandte Chemie International Edition, 2019. **58**(32): p. 10923-10927.
217. Gueret, R. and M.N. Collomb, *Cobalt (II) Pentaaza-Macrocyclic Schiff base complex as catalyst for light-driven hydrogen evolution in water: electrochemical generation and theoretical investigation of the one-electron reduced species.* Inorganic Chemistry, 2019. **58**(14): p. 9043-9056.
218. Chen, L. and M. Robert, *Molecular catalysis of the electrochemical and photochemical reduction of CO_2 with earth-abundant metal complexes. Selective production of CO vs HCOOH by switching of the metal center.* Journal of the American Chemical Society, 2015. **137**(34): p. 10918-10921.
219. Karn, J.L. and D.H. Busch, *Nickel (II) Complexes of the Tetradentate Macrocycle 2, 12-Dimethyl-3, 7, 11, 17-Tetraazabi cyclo (11.3. 1) Heptadeca-1 (17), 2, 11, 13, 15-Pentaene.* Nature, 1966. **211**(5045): p. 160-162.
220. Chen, L., Anxolabéhère-Mallart, E. and M. Robert, *Dual homogeneous and heterogeneous pathways in photo-and electrocatalytic hydrogen evolution with nickel (II) catalysts bearing tetradentate macrocyclic ligands.* ACS Catalysis, 2015. **5**(1): p. 356-364.
221. Ghosh, M., T. Weyhermüller, and K. Wieghardt, *Electronic structure of the members of the electron transfer series [NiL] z (z= 3+, 2+, 1+, 0) and [NiL (X)] n (X= Cl, CO, P $(OCH_3)_3$) species containing a tetradentate, redox-noninnocent, Schiff base macrocyclic ligand L: an experimental and density functional theoretical study.* Dalton Transactions, 2010. **39**(8): p. 1996-2007.
222. Lacy, D.C., C.C. McCrory, and J.C. Peters, *Studies of cobalt-mediated electrocatalytic CO_2 reduction using a redox-active ligand.* Inorganic Chemistry, 2014. **53**(10): p. 4980-4988.
223. Nelson, S.M., C.V. Knox, M. McCann, and M.G. Drew, *Metal-ion-controlled transamination in the synthesis of macrocyclic Schiff-base ligands. Part 1. Reactions of 2,*

6-diacetylpyridine and dicarbonyl compounds with 3, 6-dioxaoctane-1, 8-diamine. Journal of the Chemical Society, Dalton Transactions, 1981(8): p. 1669-1677.
224. Cairns, C., S. McFall, S. Nelson, and M. Drew, *Nickel (II) complexes of quinquedentate macrocyclic ligands and the crystal and molecular structure of the ring-opened hydrolysis product [11-(6-acetyl-2-pyridyl)-3, 7, 10-triazadodec-10-enylamine-NN' N "N‴ N ""]-aquanickel (II) diperchlorate.* Journal of the Chemical Society, Dalton Transactions, 1979, (3): p.446-453
225. Drew, M. and S. Nelson. *Crystal and molecular-structure of Znb (NCS) 2.1-2$C_2H_4C_{12}$.* Acta Crystallographica Section A. 1975.
226. Drew, M.G., A.H. bin Othman, P.D. Mcllroy, and S.M. Nelson, *Seven-co-ordination in metal complexes of quinquedentate macrocyclic ligands. Part II. Synthesis, properties, and crystal and molecular structures of some iron (III) derivatives of two 'N 5' macrocycles.* Journal of the Chemical Society, Dalton Transactions, 1975(23): p. 2507-2516.
227. Nelson, S., S. McFall, and M. Drew, AH binOthman and NB Mason. *Crystal structures of four complexes of quinquedentate macrocyclic ligands with novel co-ordination geometries containing five-co-ordinate silver (I), six-co-ordinate cadmium (II), six-co-ordinate mercury (II), and seven-co-ordinate cadmium (II).* Journal of the Chemical Society, Chemical Communications, 1977(6): p. 167-168.
228. Drew, M.G., J. Nelson, and S.M. Nelson, *Intramolecular ligand rearrangement in the isomerisation of a seven-co-ordinate to a six-co-ordinate nickel (II) complex of a multidentate Schiff base. The crystal and molecular structures of the six-co-ordinate product.* Journal of the Chemical Society, Dalton Transactions, 1981(8): p. 1691-1696.
229. Drew, M., AH binOthman, SG McFall, PDA McLlroy, SM Nelson. *Seven-co-ordination in metal complexes of quinquedentate macrocyclic ligands. Part 5. Synthesis and properties of pentagonal-bipyramidal and pentagonal-pyramidal manganese (II) complexes and crystal and molecular structure of {2, 15-dimethyl-3, 7, 10, 14, 20-penta-azabicyclo [14.3. 1] eicosa-1 (20), 2, 14, 16, 18-pentaene} bis (isothiocyanato) manganese (II).* Journal of the Chemical Society, Dalton Transactions, 1977, (5): p. 438-446.
230. Drew, M.G., A.H. bin Othman, and S.M. Nelson, *Seven-co-ordination in metal complexes of quinquedentate macrocyclic ligands. Part IV. Crystal and molecular structures of two pentagonal bipyramidal iron (II) complexes.* Journal of the Chemical Society, Dalton Transactions, 1976(14): p. 1394-1399.
231. Drew, M.G., S.G. McFall, and S.M. Nelson, *Pentagonal-pyramidal cadmium (II) and mercury (II) complexes of the quinquedentate macrocyclic ligand 2, 15-dimethyl-3, 7, 10, 14, 20-penta-azabicyclo [14.3. 1] eicosa-1 (20), 2, 14, 16, 18-pentaene.* Journal of the Chemical Society, Dalton Transactions, 1979(4): p. 575-581.
232. Nelson, S.M., Mcfall, S.G., Drew, M.G., *Crystal structures of four complexes of quinquedentate macrocyclic ligands with novel co-ordination geometries containing five-co-ordinate silver (I), six-co-ordinate cadmium (II), six-co-ordinate mercury (II), and seven-co-ordinate cadmium (II).* Journal of the Chemical Society, Chemical Communications, 1977(6): p. 167-168.
233. Caricato, M., G. Scalmani, G.W. Trucks, and M.J. Frisch, *Coupled cluster calculations in solution with the polarizable continuum model of solvation.* The Journal of Physical Chemistry Letters, 2010. **1**(15): p. 2369-2373.

234. Alvarez-Hernandez, J.L., A.E. Sopchak, and K.L. Bren, *Buffer pKa impacts the mechanism of hydrogen evolution catalyzed by a cobalt porphyrin-peptide.* Inorganic Chemistry, 2020. **59**(12): p. 8061-8069.
235. Le, J.M., Bren, K.L., *Tuning mechanism through buffer dependence of hydrogen evolution catalyzed by a cobalt mini-enzyme.* Biochemistry, 2020. **59**(12): p. 1289-1297.
236. Cairns, C., S.G. McFall, S.M. Nelson, and M.G. Drew, *Nickel (II) complexes of quinquedentate macrocyclic ligands and the crystal and molecular structure of the ring-opened hydrolysis product [11-(6-acetyl-2-pyridyl)-3, 7, 10-triazadodec-10-enylamine-NN′ N ″N‴ N ⁗]-aquanickel (II) diperchlorate.* Journal of the Chemical Society, Dalton Transactions, 1979(3): p. 446-453.
237. Cabral, J.D.O., Cabral, M.F., Drew, M.G.B., Nelson, S.M. and Rodgers, A., *Silver (I) and Cadmium (II) complexes of pentadentate macrocyclic ligands containing phosphorus donor atoms.* Inorganica Chimica Acta, 1977. **25**: p. L77-L79.

Appendix A

Table A.1. Crystal data and structure refinement for $[Ni\{\kappa^3\text{-}(Ph_2PNH)_2(NC_5H_3)Br]^+Br^-]$

Empirical formula	$C_{29}H_{25}BrN_3NiP^+ Br^-$	
Formula weight	695.99	
Temperature	200(2) K	
Wavelength	0.71073 Å	
Crystal system	Orthorhombic	
Space group	Pbca	
Unit cell dimensions	a = 15.7344(7) Å	α= 90°.
	b = 15.7246(7) Å	β= 90°.
	c = 23.0171(9) Å	γ = 90°.
Volume	5694.8(4) $Å^3$	
Z	8	
Density (calculated)	1.623 Mg/m^3	
Absorption coefficient	3.624 mm^{-1}	
F(000)	2784	
Crystal size	0.248 x 0.19 x 0.156 x mm^3	
Theta range for data collection	1.769 to 33.189°.	
Reflections collected	10883	

Independent reflections	7683 [R(int) = 0.0403]	
Completeness to theta = 25.242°	99.9 %	
Refinement method	Full-matrix least-squares on F^2	
Data / restraints / parameters	10883 / 7 / 334	
Goodness-of-fit on F^2	1.000	
Final R indices [I>2sigma(I)]	R1 = 0.0338	wR2 = 0.0709
R indices (all data)	R1 = 0.0649	wR2 = 0.0825

Table A.2. Selected bond lengths [Å] and angles [°] for $[Ni\{\kappa^3\text{-}(Ph_2PNH)_2(NC_5H_3)Br]^+Br^-$]

Bond Distances (Å)			
C(25)-N(2)	1.362(2)	C(13)-P(2)	1.8036(19)
C(25)-N(1)	1.369(2)	Br(1)-Ni(1)	2.2799(3)
C(29)-N(2)	1.364(2)	N(1)-P(1)	1.6828(17)
C(29)-N(3)	1.370(2)	N(2)-Ni(1)	1.8857(15)
C(7)-P(1)	1.7979(19)	N(3)-P(2)	1.6817(17)
C(1)-P(1)	1.805(2)	Ni(1)-P(1)	2.1705(5)
C(2)-C(3)	1.391(4)	Ni(1)-P(2)	2.1686(5)
C(19)-P(2)	1.802(2)		

Bond Angles [°]			
C(25)-N(1)-P(1)	118.49(13)	N(1)-P(1)-C(1)	106.64(9)
C(25)-N(2)-C(29)	118.81(16)	C(7)-P(1)-C(12)	107.85(10)
C(25)-N(2)-Ni(1)	120.53(12)	N(1)-P(1)-Ni(1)	98.87(6)
C(29)-N(2)-Ni(1)	120.66(13)	C(7)-P(1)-Ni(1)	117.35(7)
C(29)-N(3)-P(2)	117.95(13)	C(1)-P(1)-Ni(1)	117.60(7)
N(2)-Ni(1)-P(1)	86.17(5)	N(3)-P(2)-C(19)	106.93(10)
N(2)-Ni(1)-P(2)	85.88(5)	N(3)-P(2)-C(13)	107.03(9)
P(1)-Ni(1)-P(2)	171.91 (2)	C(19)-P(2)-C(13)	104.07(9)
N(2)-Ni(1)-Br(1)	177.31(5)	N(3)-P(2)-Ni(1)	99.21(6)
P(1)-Ni(1)-Br(1)	93.428(16)	C(19)-P(2)-Ni(1)	120.08(7)
P(2)-Ni(1)-Br(1)	94.586(17)	C(13)-P(2)-Ni(1)	118.31(6)
N(1)-P(1)-C(7)	107.12(9)		

Table A.3. Crystal data and structure refinement for [Ni{κ^3-$(Ph_2PNMe)_2(NC_5H_3)Br_2$].

Empirical formula	$C_{31}H_{29}Br_2N_3NiP_2$	
Formula weight	724.04	
Temperature	200(2) K	
Wavelength	0.71073 Å	
Crystal system	Monoclinic	
Space group	P 21/c	
Unit cell dimensions	a = 12.941(4) Å	α= 90°.

	b = 16.192(4) Å	β= 100.835(4)°.
	c = 13.831(4) Å	γ = 90°.
Volume	2846.6(13) $Å^3$	
Z	4	
Density (calculated)	1.689 Mg/m^3	
Absorption coefficient	3.629 mm^{-1}	
F(000)	1456	
Crystal size	0.450 x 0.420 x 0.240 x mm^3	
Theta range for data collection	1.602 to 29.466°.	
Reflections collected	7433	
Independent reflections	6250 [R(int) = 0.0403]	
Completeness to theta = 25.242°	99.9 %	
Refinement method	Full-matrix least-squares on F^2	
Data / restraints / parameters	7433 / 0 / 354	
Goodness-of-fit on F^2	1.000	
Final R indices [I>2sigma(I)]	R1 = 0.0382	wR2 = 0.1175

R indices (all data)	R1 = 0.0480	wR2 = 0.1235

Table A.4. Selected Bond lengths [Å] and angles [°] for [Ni{κ^3-$(Ph_2PNMe)_2(NC_5H_3)Br_2$].

Bond Distances (Å)			
Br(1)-Ni(1)	2.3100(6)	C(20)-P(2)	1.820(3)
Br(2)-Ni(1)	2.7961(9)	C(26)-P(2)	1.813(3)
P(1)-Ni(1)	2.1432(9)	C(1)-N(1)	1.471(4)
P(2)-Ni(1)	2.1687(9)	C(2)-N(2)	1.368(4)
N(1)-P(1)	1.696(3)	C(2)-N(1)	1.381(4)
N(2)-Ni(1)	1.911(2)	C(6)-N(2)	1.362(4)
N(3)-P(2)	1.709(3)	C(6)-N(3)	1.386(4)
C(8)-P(1)	1.805(3)	C(7)-N(3)	1.466(4)
C(14)-P(1)	1.813(3)		
Bond Angles [°]			
N(2)-Ni(1)-P(1)	83.60(8)	N(3)-P(2)-C(26)	107.84(14)
N(2)-Ni(1)-P(2)	86.00(8)	N(3)-P(2)-C(20)	104.85(14)
P(1)-Ni(1)-P(2)	154.35(3)	C(26)-P(2)-C(20)	108.64(14)
N(2)-Ni(1)-Br(1)	172.14(8)	N(3)-P(2)-Ni(1)	99.36(10)
P(1)-Ni(1)-Br(1)	92.53(3)	C(26)-P(2)-Ni(1)	122.49(11)
P(2)-Ni(1)-Br(1)	94.74(3)	C(20)-P(2)-Ni(1)	111.82(10)
N(2)-Ni(1)-Br(2)	84.88(8)	C(2)-N(1)-C(1)	120.1(3)
P(1)-Ni(1)-Br(2)	100.01(3)	C(2)-N(1)-P(1)	114.8(2)
P(2)-Ni(1)-Br(2)	102.34(3)	C(1)-N(1)-P(1)	123.2(2)

Br(1)-Ni(1)-Br(2)	102.56(2)	C(6)-N(2)-C(2)	119.5(2)
N(1)-P(1)-C(8)	104.99(14)	C(6)-N(2)-Ni(1)	120.3(2)
N(1)-P(1)-C(14)	106.21(14)	C(2)-N(2)-Ni(1)	119.9(2)
C(8)-P(1)-C(14)	109.07(14)	C(6)-N(3)-C(7)	118.6(3)
N(1)-P(1)-Ni(1)	99.79(9)	C(6)-N(3)-P(2)	117.5(2)
C(8)-P(1)-Ni(1)	125.77(10)	C(7)-N(3)-P(2)	123.7(2)
C(14)-P(1)-Ni(1)	108.99(10)		

Table A.5. Crystal data and structure refinement for [Ni{κ^2-(Ph_2PNMe)(NC_5H_3)Br_2].

Empirical formula	$C_{18}H_{17}Br_2N_2NiP$	
Formula weight	510.80	
Temperature	200(2) K	
Wavelength	0.71073 Å	
Crystal system	Monoclinic	
Space group	P 21/c	
Unit cell dimensions	a = 12.2791(18) Å	α= 90°.
	b = 9.1902(14) Å	β= 107.860(5)°.
	c = 17.705(3)Å	γ = 90°.
Volume	1901.7(5) $Å^3$	
Z	4	
Density (calculated)	1.784 Mg/m^3	
Absorption	5.308 mm^{-1}	

coefficient		
F(000)	1008.0	
Crystal size	0.358 x 0.217 x 0.123 x mm^3	
Theta range for data collection	1.742 to 25.060°.	
Reflections collected	3181	
Independent reflections	2229 [R(int) = 0.0403]	
Completeness to theta = 25.242°	94.4 %	
Refinement method	Full-matrix least-squares on F^2	
Data / restraints / parameters	3181 / 183 / 218	
Goodness-of-fit on F^2	1.107	
Final R indices [I>2sigma(I)]	R1 = 0.0679	wR2 = 0.1789
R indices (all data)	R1 = 0.1046	wR2 = 0.1652

Table A.6. Selected Bond lengths [Å] and angles [°] for [Ni{κ^2-(Ph_2PNMe)(NC_5H_3)Br_2].

Bond Distances (Å)			
Br(1)-Ni(1)	2.3371(16)	P(1)-C(13)	1.808(10)
Br(2)-Ni(1)	2.3101(16)	N(1)-C(1)	1.350(13)
Ni(1)-N(1)	1.935(8)	N(1)-C(5)	1.359(12)
Ni(1)-P(1)	2.107(3)	N(2)-C(5)	1.389(14)
P(1)-N(2)	1.684(8)	N(2)-C(6)	1.473(12)
P(1)-C(7)	1.800(10)		
Bond Angles (°)			
N(1)-Ni(1)-P(1)	86.3(3)	N(1)-C(5)-N(2)	116.3(9)
N(1)-Ni(1)-Br(2)	170.2(2)	N(1)-C(5)-C(4)	120.8(10)
P(1)-Ni(1)-Br(2)	84.57(9)	N(2)-C(5)-C(4)	122.9(9)
N(1)-Ni(1)-Br(1)	96.6(2)	N(2)-C(6)-H(6A)	109.5
P(1)-Ni(1)-Br(1)	170.43(10)	N(2)-C(6)-H(6B)	109.5
Br(2)-Ni(1)-Br(1)	93.00(6)	N(2)-P(1)-C(7)	104.6(5)
N(2)-P(1)-C(13)	104.7(4)	C(5)-N(2)-C(6)	118.9(9)
C(7)-P(1)-C(13)	106.5(5)	C(5)-N(2)-P(1)	116.9(6)
N(2)-P(1)-Ni(1)	101.5(3)	C(6)-N(2)-P(1)	124.0(8)
C(7)-P(1)-Ni(1)	116.8(3)	N(1)-C(1)-C(2)	123.3(11)
C(13)-P(1)-Ni(1)	120.7(3)	N(1)-C(1)-H(1)	118.4
C(1)-N(1)-C(5)	118.0(9)	C(18)-C(13)-P(1)	116.8(7)
C(1)-N(1)-Ni(1)	123.0(7)	C(14)-C(13)-P(1)	123.7(8)
C(5)-N(1)-Ni(1)	119.0(7)	N(2)-C(6)-H(6C)	109.5

Computational Results

Starting species **2.1**$^{+}$:

Complex **2.1** consisted of a cationic Ni species **2.1**$^{+}$ and an uncoordinated bromide counter anion. The descriptions for the computational results on cation **2.1**$^{+}$ and the reduction products are based on the following orientation of complex [Ni(κ^3-2,6-{Ph_2PNH}$_2$$NC_5H_3$)Br]$^{+}$ relative to the Cartesian axes shown.

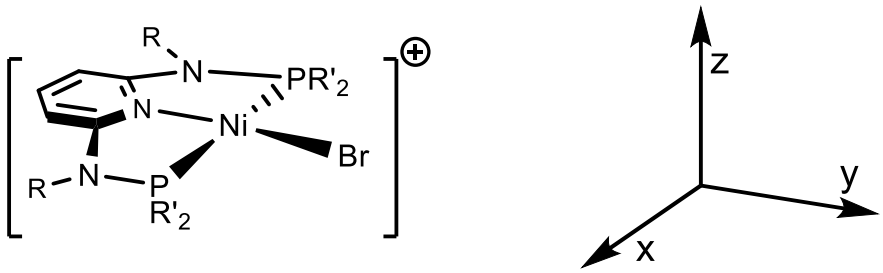

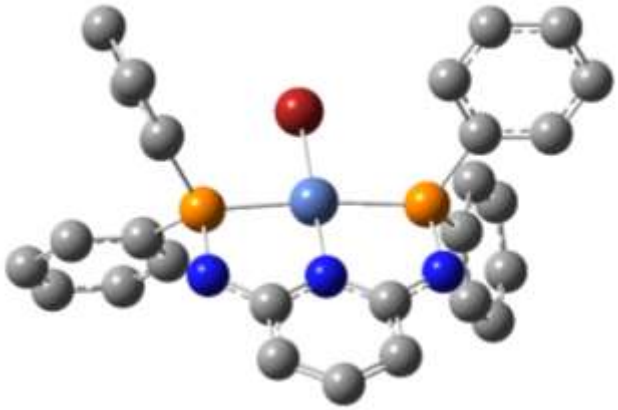

Figure A.1. DFT optimized structure of [Ni(κ^3-2,6-{Ph_2PNH}$_2$$NC_5H_3$)Br]$^{+}$ using the B3LYP functional and def2TZVP basis set in acetonitrile (IEFPCM). Hydrogen atoms eliminated for

clarity. Frequency analysis confirmed that the optimized structure was a minimum with no imaginary frequencies.

Table A.7. Comparison of selected structural parameters of the single crystal X-ray diffraction structure of the cation $[Ni(\kappa^3\text{-}2,6\text{-}\{Ph_2PNH\}_2NC_5H_3)Br]^+$ (**2.1**$^+$) and the optimized cation (B3LYP, def2TZVP) using the IEFPCM model for solvation with acetonitrile as the solvent.

Bond	Experimental	Computed Distance b3lyp/def2tzvp
Ni-Br	2.299	2.3129
Ni-N	1.9101	1.9239
Ni-P	2.173, 2.181	2.2144

Table A.8. Summary of Ni-centered bonding for $[Ni(\kappa^3\text{-}2,6\text{-}\{Ph_2PNH\}_2NC_5H_3)Br]^+$ (**2.1**$^+$). Values for bond length, overlap populations and Mayer bond order indices are from the B3LYP/def2TZVP/IEFPCM (acetonitrile) optimization.

Bond	Length(Å)	Overlap Population	Mayer Bond order
Ni-Br	2.313	0.26	0.83
Ni-P	2.214	0.31	0.85
Ni-N	1.924	0.20	0.61

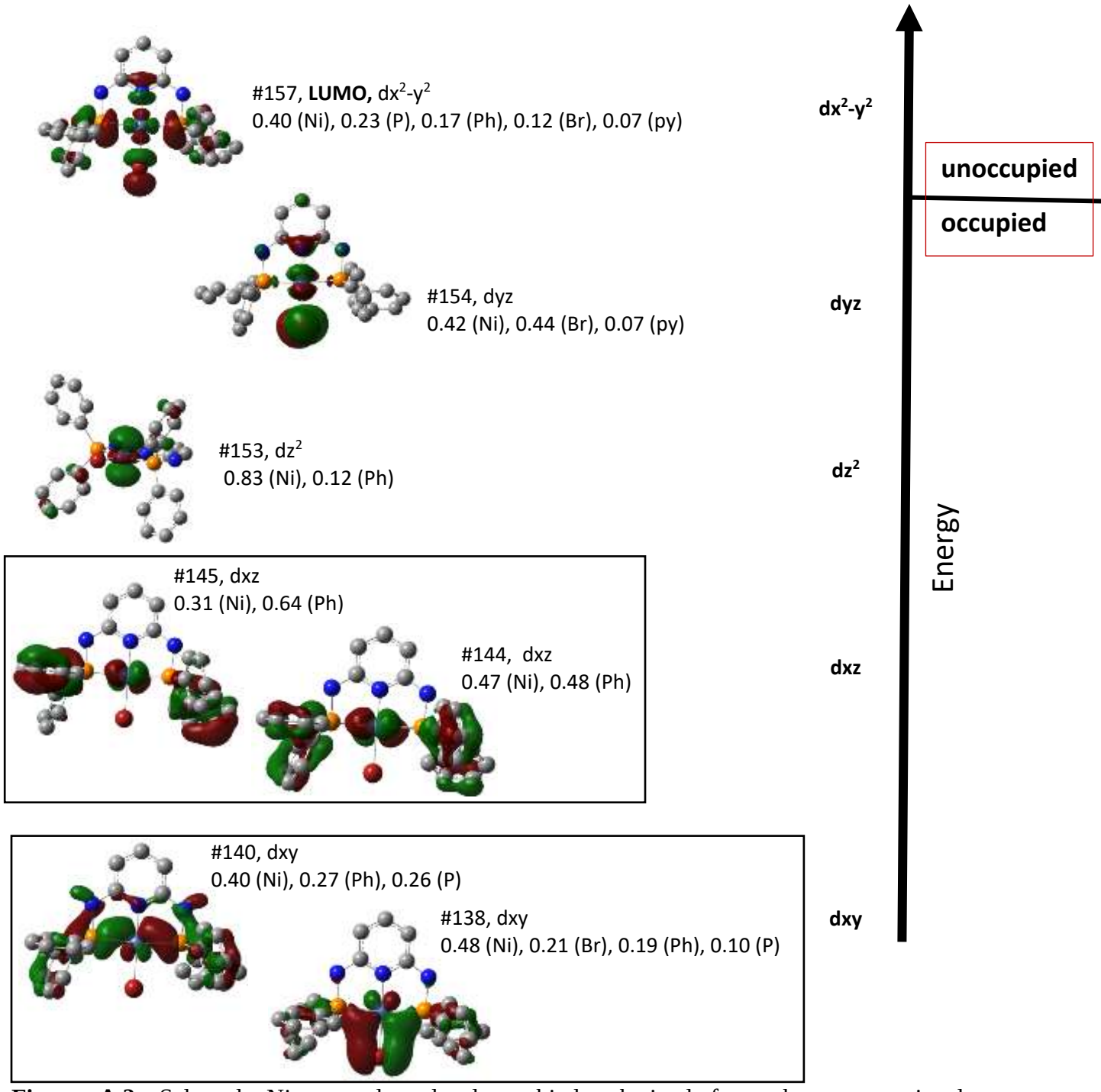

Figure A.2. Selected, Ni-centered molecular orbitals obtained from the computational optimization of $[Ni(\kappa^3\text{-}2,6\text{-}\{Ph_2PNH\}_2NC_5H_3)Br]^+$ (**2.1**$^+$) using the B3LYP functional, def2TZVP basis set and IEFPCM model for solvation in acetonitrile. Major fragment orbital contributions were obtained from the Chemissian program.

First Reduction (**2.1**):

The first reduction event adds one electron to **2.1**$^{+}$ resulting in a neutral complex [Ni(κ^3-2,6-{Ph_2PNH}$_2$$NC_5H_3$)Br] **2.1** which was successfully optimize to a square planar neutral species shown in Figure 2.S3.

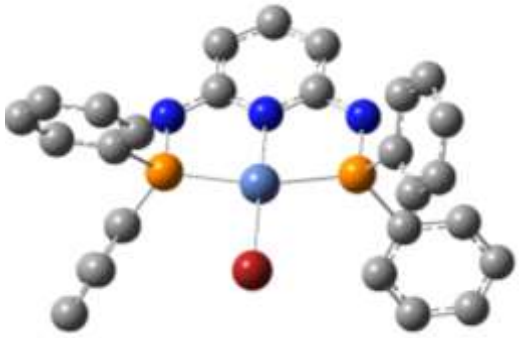

Figure A.3. DFT optimized for the addition of a single electron to **2.1**$^{+}$ to give the neutral species, [Ni(κ^3-2,6-{Ph_2PNH}$_2$$NC_5H_3$)Br] (**2.1**).Hydrogen atoms eliminated for clarity. Frequency analysis confirmed that the optimized structure was a minimum with no imaginary frequencies.

Table A.9. Summary of Ni-centered bonding for [Ni(κ^3-2,6-{Ph_2PNH}$_2$$NC_5H_3$)Br] (**2.1**). Values for bond length, overlap populations and Mayer bond order indices are from the B3LYP/def2TZVP/IEFPCM (acetonitrile) optimization.

Bond	Length(Å)	Overlap Population	Mayer Bond order
Ni-Br	2.615	0.14	0.43
Ni-P	2.307	0.28	0.73
Ni-N	2.115	0.13	0.36

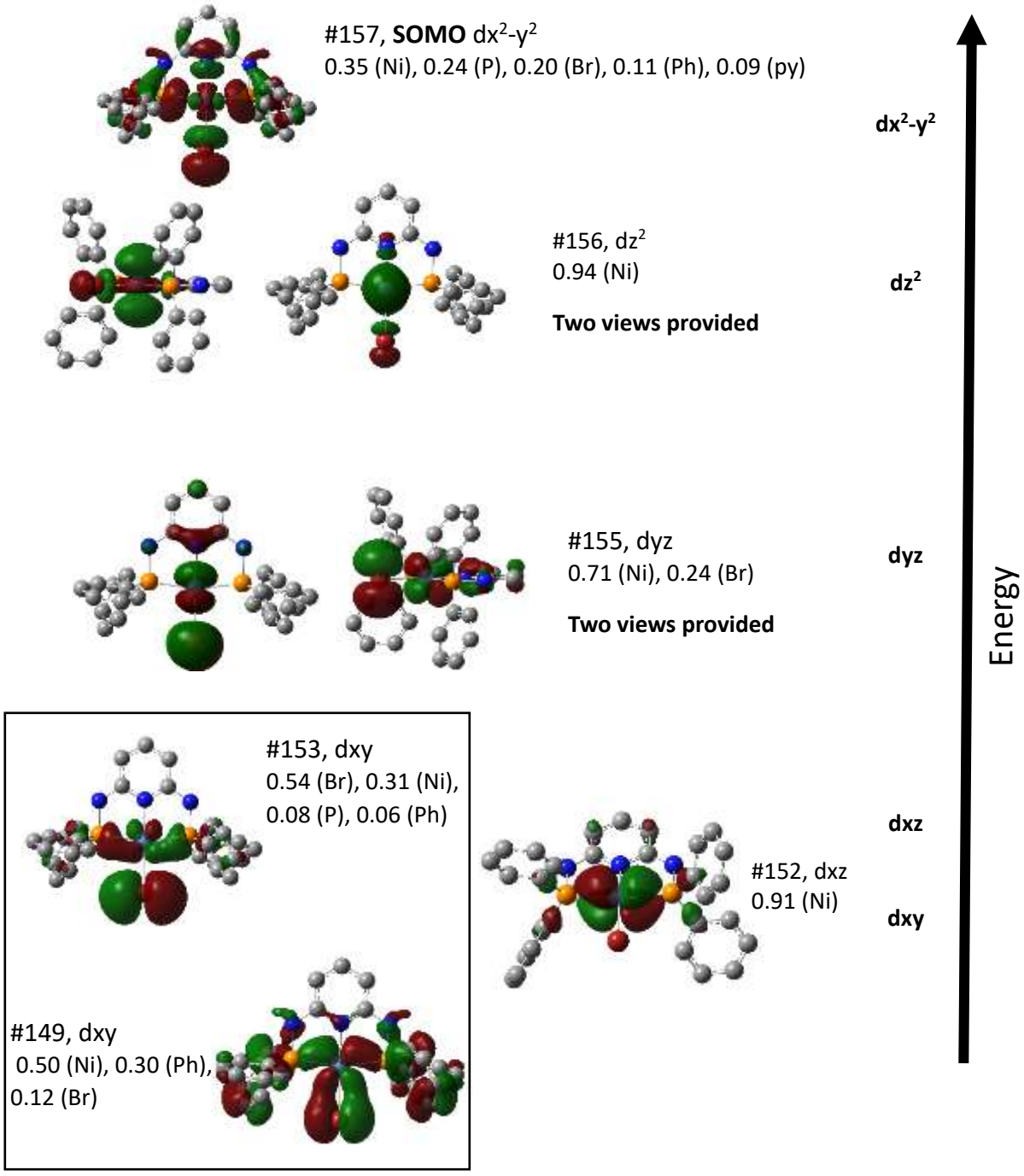

Figure A.4. Selected, Ni-centered molecular orbitals obtained from the computational optimization of the first reduction product, [Ni(κ^3-2,6-{Ph_2PNH}$_2$$NC_5H_3$)Br] (**2.1**), using the B3LYP functional, def2TZVP basis set and IEFPCM model for solvation in acetonitrile. Major fragment orbital contributions were obtained from the Chemissian program.

Second Reduction (**2.1**$^{-}$):

The addition of an electron to [Ni(κ^3-2,6-{Ph_2PNH}$_2$$NC_5H_3$)Br] **2.1** (second reduction of **2.1**$^{+}$) leads to the proposed anion, [Ni(κ^3-2,6-{Ph_2PNH}$_2$$NC_5H_3$)Br]$^{-}$ (**2.1**$^{-}$). This anion could exhibit either a singlet and triplet ground state, both were optimized and the singlet state was found to be lower in energy and was used in all subsequent analysis. The optimization outcome for **2.1**$^{-}$ showed substantial structural changes with the most obvious being deviation of the Ni geometry from square planar. In particular, the bromo ligand shifted perpendicular to the PN^{3}PNi plane as shown in Figure 2.S5. At the same time increase in the Ni-Br bond length and decrease in the Ni-Br bond order (Table 2.2). This electron was added to MO #157 (Figure 2.S6) which has become the HOMO for **2.1**$^{-}$. This orbital remains σ* in character and Ni dx^2-y^2 based. The HOMO-1 (52% Ni) retained the dz^2 character but because of the structural changes is σ* for Ni-Br.

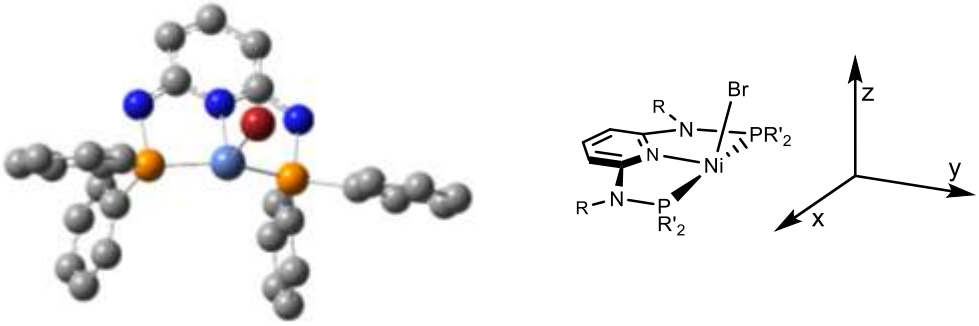

Figure A.5. DFT optimized structure for the complex [Ni(κ^3-2,6-{Ph_2PNH}$_2$$NC_5H_3$)Br]$^{-}$ (**2.1**$^{-}$) using the B3LYP functional and def2TZVP basis set. Frequency analysis confirmed that the optimized structure was a minimum with no imaginary frequencies. Hydrogen atoms eliminated for clarity. The associated drawing provides the orientation of the Cartesian axes used in the discussion of this complex and is similar to that used throughout the computational presentation.

Table A.10. Summary of Ni-centered bonding for [Ni(κ^3-2,6-{Ph_2PNH}$_2$$NC_5H_3$)Br]$^{-}$ (**2.1**$^{-}$) using Values for bond length, overlap populations and Mayer bond order indices are from the B3LYP/def2TZVP/IEFPCM(acetonitrile) optimization.

Bond	Length(Å)	Overlap Population	Mayer Bond order
Ni-Br	2.735	0.07	0.26

Ni-P	2.141	0.34	1.13
Ni-N	2.017	0.12	0.31

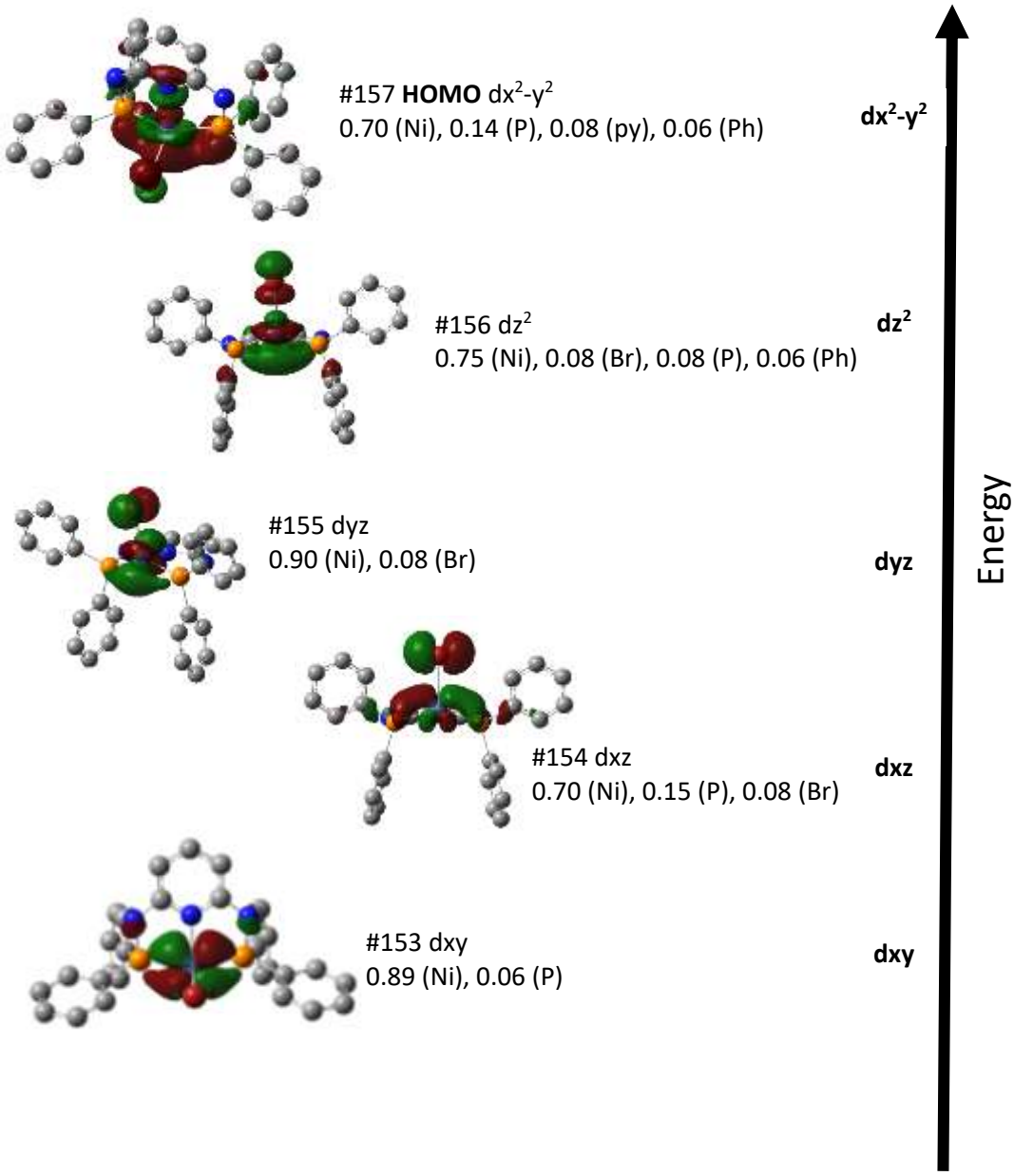

Figure A.6. Selected, Ni-centered molecular orbitals obtained from the computational optimization of the second reduction product [Ni(κ^3-2,6-{Ph_2PNH}$_2$$NC_5H_3$)Br]$^-$ (**2.1**$^-$) using the B3LYP functional, def2TZVP basis set and IEFPCM model for solvation in acetonitrile. Major fragment orbital contributions were obtained from the Chemissian program.

Third Reduction (**A**$^-$):

The addition of an electron to [Ni(κ^3-2,6-{Ph_2PNH}$_2$$NC_5H_3$)Br]$^-$ (**2.1**$^-$) (third reduction of **2.1**$^+$) leads to the proposed anion, [Ni(κ^3-2,6-{Ph_2PNH}$_2$$NC_5H_3$)]$^-$ (**A**$^-$) shown in Figure 2.S7. This species underwent spontaneous dissociation of a bromide anion and conversion to planar **A**$^-$. Along with loss of a bromo ligand, the bond length of the Ni-P and Ni-N decreased slightly and the bond order increased (Table 2.S10). A comparison with the cationic starting material given in Table S8 suggests that the Ni-P and Ni-N bonding interactions in **A**$^-$ are restored to near their original starting points.

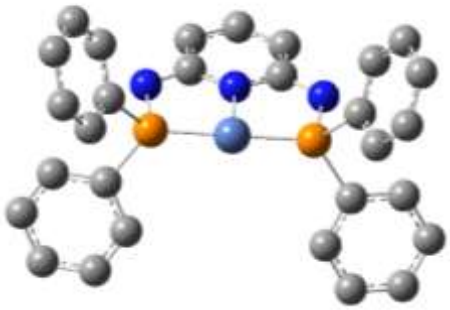

Figure A.7. DFT optimized structure for the complex [Ni(κ^3-2,6-{Ph_2PNH}$_2$$NC_5H_3$)]$^-$ (**A**$^-$) using the B3LYP functional and def2TZVP basis set. Hydrogen atoms eliminated for clarity. Frequency analysis confirmed that the optimized structure was a minimum with no imaginary frequencies.

Table A.11. Summary of Ni-centered bonding for [Ni(κ^3-2,6-{Ph_2PNH}$_2$$NC_5H_3$)]$^-$ (**A**$^-$) Values for bond length, overlap populations and Mayer bond order indices are from the B3LYP/def2TZVP/IEFPCM(acetonitrile) optimization.

Bond	Length(Å)	Overlap Population	Mayer Bond order
Ni-P	2.111	0.36	1.19
Ni-P	2.109	0.37	1.20
Ni-N	1.937	0.18	0.40

Computation on **2.2** resulting in **2.2**$^+$:

The first significant observation during optimization of the electronic structure of **2.2** carried out with the IEFPCM model for solvation with acetonitrile, was the spontaneous apical Br^- ligand dissociation. This led to direct formation of $\mathbf{2.2}^+$, the analogue with $\mathbf{2.1}^+$ and is consistent with the observed similarity in the voltametric behavior of **2.1** and **2.2** in acetonitrile (Figure 2.11).

The resulting optimized structure of $\mathbf{2.2}^+$ is shown in Figure 2.S8 with selected bonding parameters in Table A.12-A.13. The descriptions for the computational results on $\mathbf{2.2}^+$ and the reduction products is based on the following orientation of complex $[Ni(\kappa^3\text{-}2,6\text{-}\{Ph_2PNMe\}_2NC_5H_3)Br]^+$ ($\mathbf{2.2}^+$) relative to the Cartesian axes.

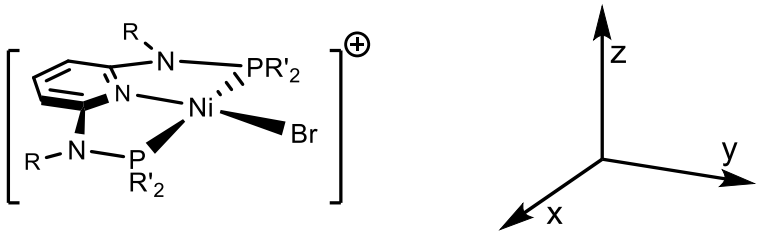

As described, the addition of one electron to $\mathbf{2.2}^+$ results in complex **2.2**, $[Ni(\kappa^3\text{-}2,6\text{-}\{Ph_2PNMe\}_2NC_5H_3)Br]$. The second electron addition resulted in spontaneous bromide loss to yield $[Ni(\kappa^3\text{-}2,6\ \{Ph_2PNMe\}_2NC_5H_3)]$, **B**. Addition of an electron to **B** led to the anion $[Ni(\kappa^3\text{-}2,6\text{-}\{Ph_2PNMe\}_2NC_5H_3)]^-$, $\mathbf{B}^-$, the analogue of $\mathbf{A}^-$, which was derived from $\mathbf{2.1}^+$ reduction as described above.

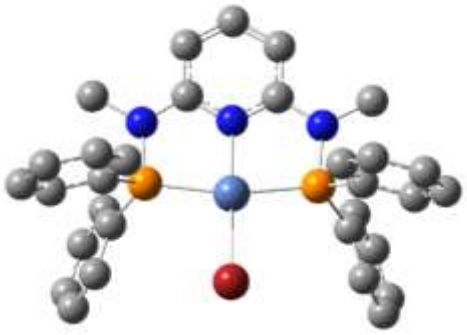

Figure A.8. DFT optimized structure of [Ni(κ^3-2,6-{Ph_2PNMe}$_2$$NC_5H_3$)Br]$^+$ (**2.2**$^+$) using the B3LYP functional and def2TZVP basis set with solvation with acetonitrile modeled with the IEFPCM model. Hydrogen atoms eliminated for clarity. Frequency analysis confirmed that the optimized structure was a minimum with no imaginary frequencies.

Table A.12. Selected optimized bond length parameters of the cation [Ni(κ^3-2,6-{Ph_2PNMe}$_2$$NC_5H_3$)Br]$^+$ (**2.2**$^+$) and comparison with computed parameters for [Ni(κ^3-2,6-{Ph_2PNH}$_2$$NC_5H_3$)Br]$^+$ (**2.1**$^+$).

Bond	**2.2**$^+$ Computed Distance b3lyp/def2tzvp	**2.1**$^+$ Computed Distance b3lyp/def2tzvp
Ni-Br	2.345	2.3129
Ni-N	1.918	1.9239
Ni-P	2.204	2.2144

Table A.13. Summary of Ni-centered bonding for [Ni(κ^3-2,6-{Ph_2PNMe}$_2$$NC_5H_3$)Br]$^+$ (**2.2**$^+$). Values for bond length, overlap populations and Mayer bond order indices are from the B3LYP/def2TZVP/IEFPCM (acetonitrile) optimization.

Bond	Length(Å)	Overlap Population	Mayer Bond order
Ni-Br	2.345	0.27	0.82
Ni-P	2.204	0.31	0.86
Ni-P	2.204	0.31	0.86
Ni-N	1.918	0.20	0.62

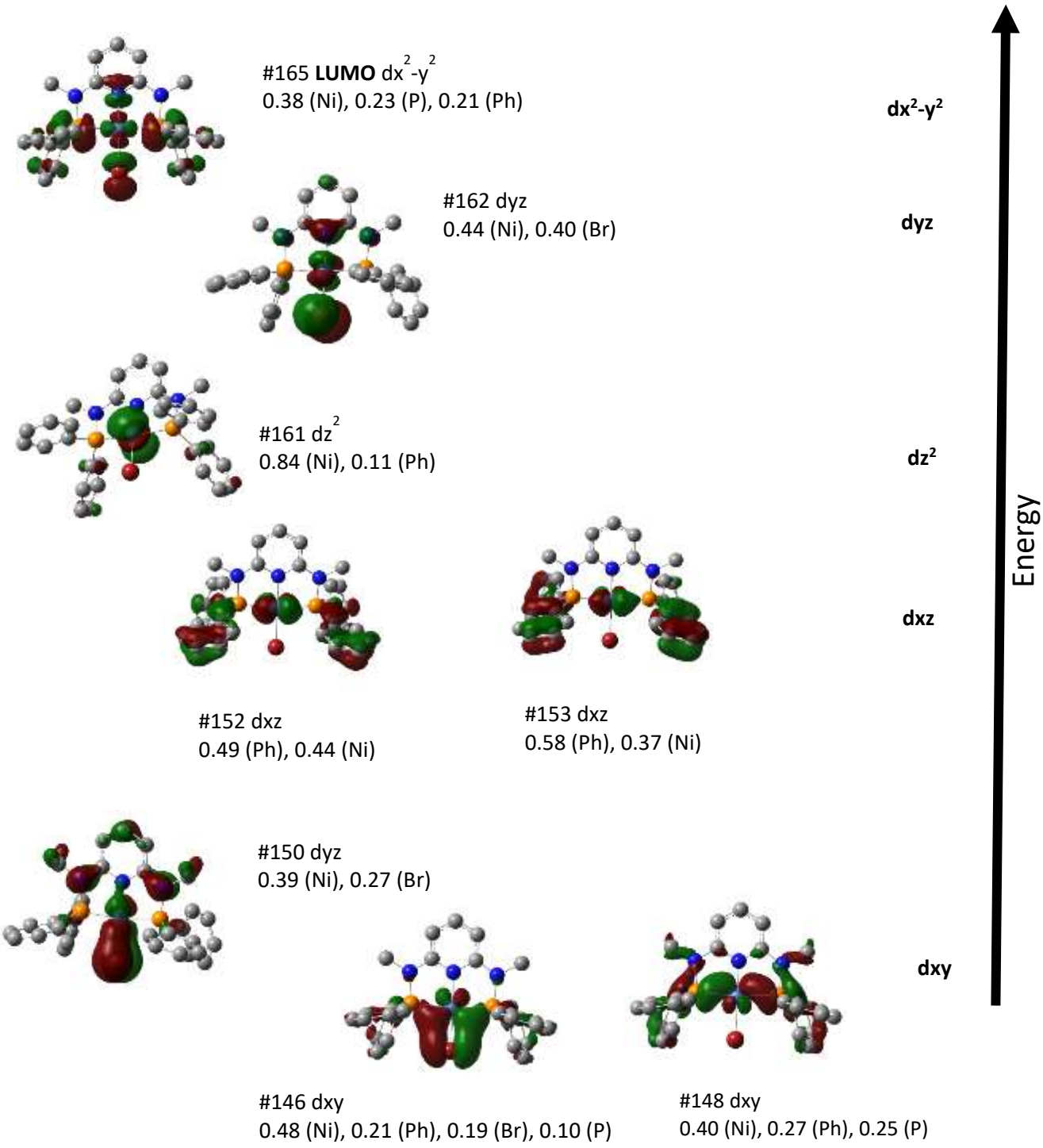

Figure A.9. Selected, Ni-centered orbitals obtained from the computational optimization of [Ni(κ^3-2,6-{Ph_2PNMe}$_2$$NC_5H_3$)Br]$^+$ (**2.2**$^+$) using the B3LYP functional and def2TZVP basis set and IEFPCM model for solvation in acetonitrile. Major fragment orbital contributions were obtained from the Chemissian program.

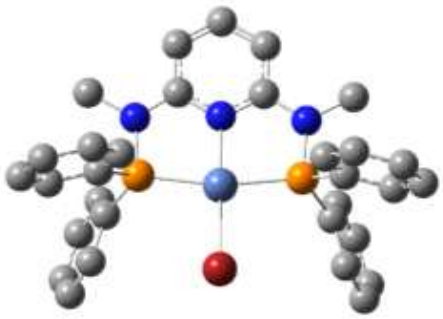

Figure A.10. DFT optimized for the neutral complex [Ni(κ^3-2,6-{Ph_2PNMe}$_2$$NC_5H_3$)Br] (**2.2**), the first reduction product of **2.2**$^+$, using the B3LYP functional and def2TZVP basis set with solvation with acetonitrile modeled with the IEFPCM model. Hydrogen atoms eliminated for clarity. Frequency analysis confirmed that the optimized structure was a minimum with no imaginary frequencies.

Table A.14. Summary of Ni-centered bonding for [Ni(κ^3-2,6-{Ph_2PNMe}$_2$$NC_5H_3$)Br] (**2.2**). Values for bond length, overlap populations and Mayer bond order indices are from the B3LYP/def2TZVP/IEFPCM (acetonitrile) optimization.

Bond	Length(Å)	Overlap Population	Mayer Bond order
Ni-P	2.268	0.2947108	0.7661646
Ni-Br	2.641	0.1507122	0.4264591
Ni-N	2.100	0.1316221	0.3780663

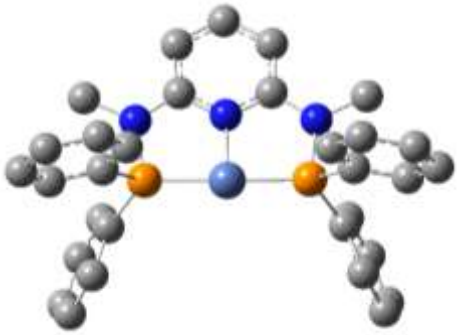

Figure A.11. DFT optimized for the neutral complex [Ni(κ^3-2,6-{Ph_2PNMe}$_2$$NC_5H_3$)] (**B**), the reduction product of **2.2**. During optimization, the bromo ligand spontaneously dissociated and the complex [Ni(κ^3-2,6-{Ph_2PNMe}$_2$$NC_5H_3$)] (**B**) was optimized using the B3LYP functional and def2TZVP basis set with solvation with acetonitrile using the IEFPCM model. Hydrogen atoms eliminated for clarity. Frequency analysis confirmed that the optimized structure was a minimum with no imaginary frequencies.

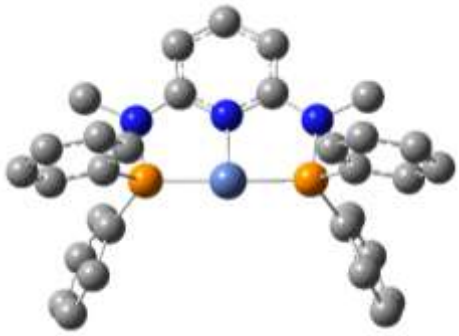

Figure A.12. DFT optimized structure of the addition of one electron to **B** (i.e. the third reduction product of **2.2**$^{+}$) to yield [Ni(κ^3-2,6-{Ph_2PNMe}$_2$$NC_5H_3$)]$^-$ (**B**$^-$). Optimization used the B3LYP functional and def2TZVP basis set with solvation with acetonitrile modeled with the IEFPCM model. Hydrogen atoms eliminated for clarity. Frequency analysis confirmed that the optimized structure was a minimum with no imaginary frequencies.

Table A.15. Summary of Ni-centered bonding for [Ni(κ^3-2,6-{Ph_2PNMe}$_2$$NC_5H_3$)]$^-$ (**B**$^-$). Values for bond length, overlap populations and Mayer bond order indices are from the B3LYP/def2TZVP/IEFPCM(acetonitrile) optimization.

Bond	Length(Å)	Overlap Population	Mayer Bond order
Ni-N	1.918	0.18	0.41
Ni-P	2.099	0.38	1.20
Ni-P	2.100	0.37	1.21

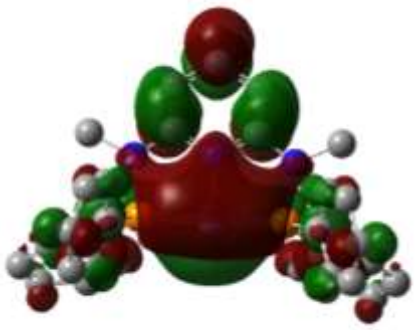

Figure A.13. Representation of the SOMO obtained from the computational optimization of [Ni(κ^3-2,6-{Ph_2PNMe}$_2$$NC_5H_3$)]$^-$ (**B**$^-$) using the B3LYP functional and def2TZVP basis set and IEFPCM model for solvation in acetonitrile. Major fragment orbital contributions were obtained from the Chemissian program.

Table A.16. Summary of Ni-centered bonding for the neutral complex [Ni(κ^3-2,6-{Ph_2PNMe}$_2NC_5H_3$)H] (**Ni-H**), the proposed hydride intermediate in the catalytic cycle. Values for bond length, overlap populations and Mayer bond order indices are from the B3LYP/def2TZVP/IEFPCM (acetonitrile) optimization.

Bond	Length(Å)	Overlap Population	Mayer Bond order
Ni-H	1.604	0.41	0.87
Ni-P	2.291	0.15	0.67
Ni-N	2.071	0.13	0.37

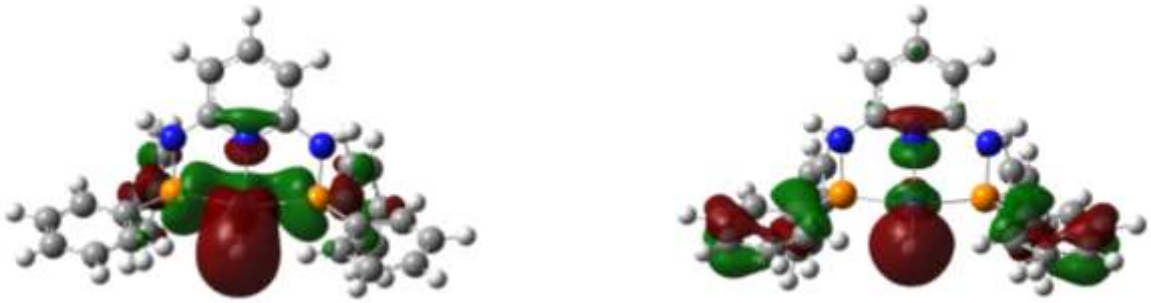

Figure A.14. The two major Ni-H bonding molecular orbitals for the neutral complex [Ni(κ^3-2,6-{Ph_2PNMe}$_2NC_5H_3$)H] (**Ni-H**), the proposed hydride intermediate in the catalytic cycle. Results of a DFT optimized structure using the B3LYP functional and def2TZVP basis set with solvation with acetonitrile using the IEFPCM model. On the left is a representation of the SOMO that has 0.27 H s, 0.30 Ni d_{yz} and d_z^2 and 0.22 P fragment orbital contribution. On the right is a filled bonding orbital that is 0.41 Ph, 0.25 Ni, 0.24 H, and 0.10 py fragment contributions.

Table A.17. Summary of Ni-centered bonding for the anionic complex [Ni(κ^3-2,6-{Ph_2PNMe}$_2NC_5H_3OH$]$^-$ (**Ni-OH$^-$**), a proposed intermediate in the catalytic cycle. Values for bond length, overlap populations and Mayer bond order indices are from the B3LYP/def2TZVP/IEFPCM (acetonitrile) optimization.

Bond	Length(Å)	Overlap Population	Mayer Bond order
Ni-O	2.077	0.09	0.34
Ni-P	2.141	0.37	1.20
Ni-P	2.147	0.32	1.15
Ni-N	2.051	0.09	0.30

(a)

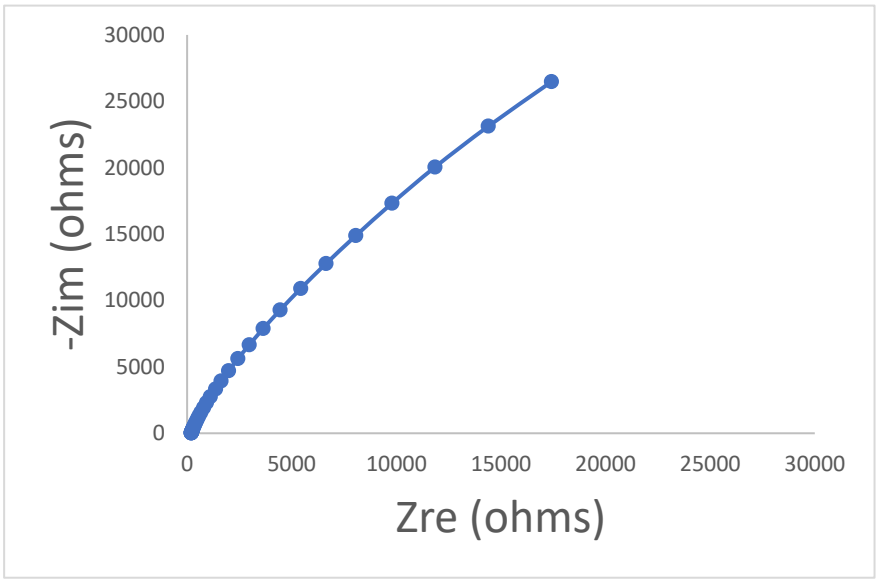

(b)

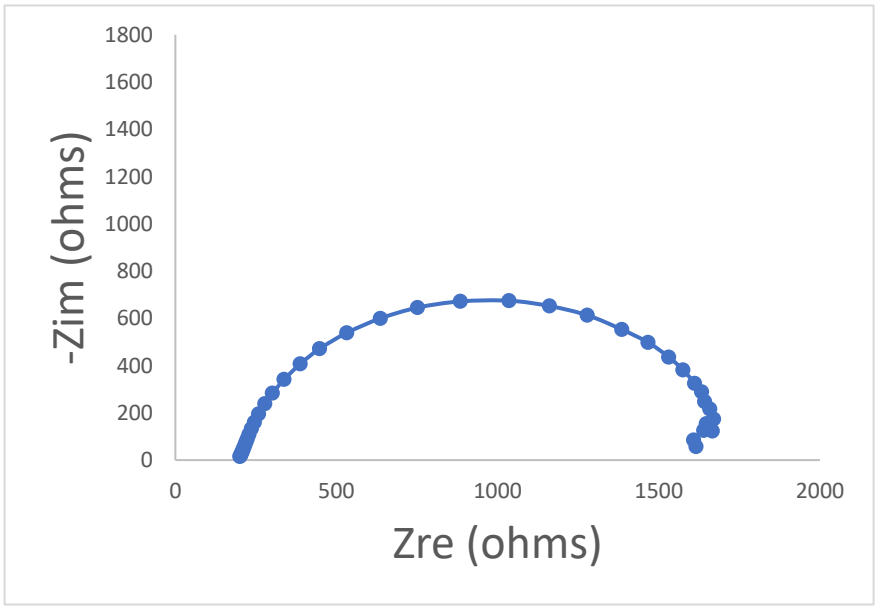

Figure A.15. Nyquist plots from EIS measurements on electrochemical cells containing [Ni(2,6-{Ph_2PNH}$_2$(NC_5H_3)Br]$^+$Br$^-$ (**2.1**) (1.0 mM) in CH_3CN solution with 0.28M water and 0.1 M tetrabutylammonium hexafluorophosphate (TBAHFP) supporting electrolyte using a glassy carbon (GC) working electrode and a Pt counter electrode. (a) measured at 0 V, Z_{re} = 201.6 Ω (b) measured at -2V, Z_{re} = 200.6Ω.

Appendix B:

Table B.1. Crystal data and structure refinement for (**3.1**).

Compound	
Empirical formula	$C_{21}H_{19}Br_2NiN_3$
Formula weight	531
Temperature(K)	203(2)
λ (Å)	0.71073
Crystal system	Monoclinic
Space group	C 2/c
a (Å)	15.9809(5)
b (Å)	8.5994(3)
c (Å)	15.5441(5)
α (deg)	90.00
β (deg)	102.998(1)
γ (deg)	90.00
V (Å3)	2081.43(12)
Z	4
DX (calc) (g/cm^3)	1.697
Mu (mm-1)	4.782
R1a	0.0244
wR2b	0.0650

Table B.2. Selected Bond lengths [Å] and angles [°] for (**3.1**).

Bond lengths [Å]		**Bond angles [°]**	
Br(1)-Ni(1)	2.3967	N(1)-Ni(1)-N(2)	78.1
Ni(1)-N(1)	1.947	Br(1)-Ni(1)-N(1)	112.41
Ni(1)-N(2)	2.114	Br(1)-Ni(1)-N(2)	96.40
N(1)-C(3)	1.338	Br(1)-Ni(1)-Br(1)'	135.18
N(2)-C(4)	1.278(4)	Ni(1)-N(1)-C(3)	118.8
N(2)-C(6)	1.436(4)	Ni(1)-N(2)-C(4)	114.7
C(1)-C(2)	1.381	Ni(1)-N(2)-C(6)	123.7
C(2)-C(3)	1.388(4)	C(4)-N(2)-C(6)	121.5(3)
C(4)-C(5)	1.491(5)	C(3)-C(4)-C(5)	119.8(3)

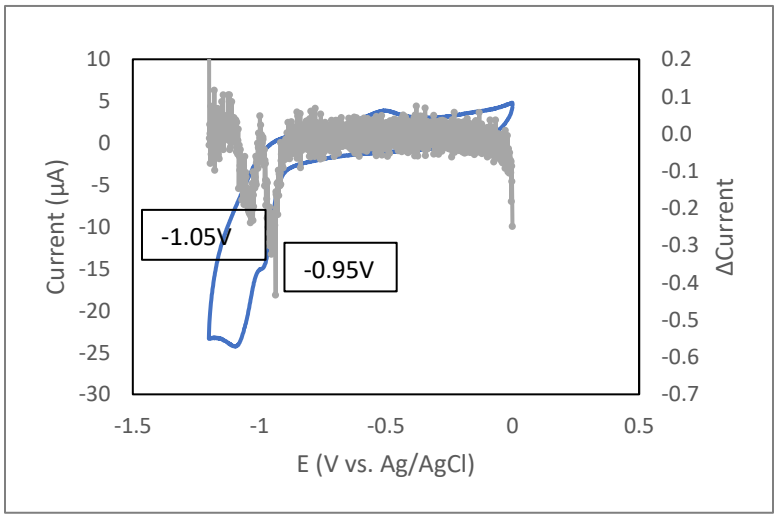

Figure B.1. Cyclic voltammogram of complex $[Ni(\kappa^3\text{-}2,6\text{-}\{PhNCMe\}_2(NC_5H_3)(OH_2)]^{2+}$ (**3.1'(OH$_2$)$^{2+}$**) (1mM) in presence of 100mM KBr in phosphate buffer pH=7, using a glassy carbon (GC) working electrode, Ag/AgCl reference electrode. Two irreversible reduction peaks and an oxidation peak were observed with $E_{1/2}$ of -0.95 V and -1.05 V, and -0.5 V versus Ag/AgCl. The gray markers represent application of the method of first principles to the blue curve. Minima

denote inflection points in the catalytic curve and indicate the associated onset potential and current enhancement.

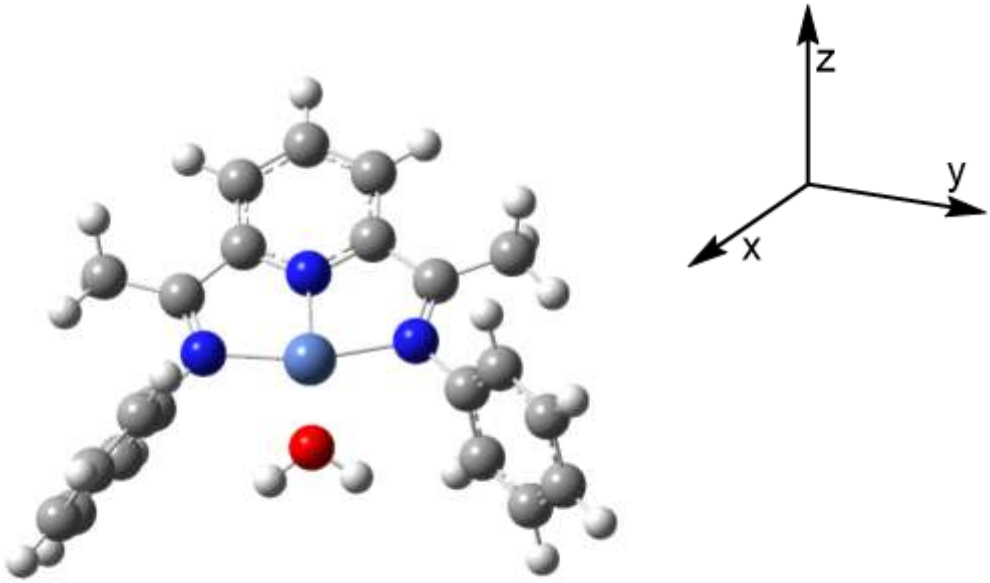

Figure B.2. Computationally optimized $[Ni(\kappa^3\text{-}2,6\text{-}\{PhNCMe\}_2(NC_5H_3)(OH_2)]^{2+}$ (**3.1'$(OH_2)^{2+}$**) (DFT, B3LYP, def2-TZVP, PCM in water).

Table B.3. Selected bond parameters for computationally optimized $[Ni(\kappa^3\text{-}2,6\text{-}\{PhNCMe\}_2NC_5H_3)(OH_2)]^{2+}$ (**3.1'$(OH_2)^{2+}$**)

bond	Length(Å)	Mayer Bond order
Ni-N_{py}	1.820	0.73
Ni-N_{imine}	1.948	0.68
Ni-N_{imine}	1.947	0.68
Ni-O	1.932	0.38

Table B.4. Selected bond parameters for computationally optimized $[Ni(\kappa^3\text{-}2,6\text{-}\{PhNCMe\}_2NC_5H_3)(OH_2)]$ (**3.1'(OH_2)**). The product of the second reduction of (**3.1'$(OH_2)^{2+}$**).

Bond	Length(Å)	Mayer Bond order
Ni-N_{py}	1.913	0.60
Ni-N_{imine}	2.087	0.46
Ni-N_{imine}	2.127	0.41
Ni-O	2.101	0.20

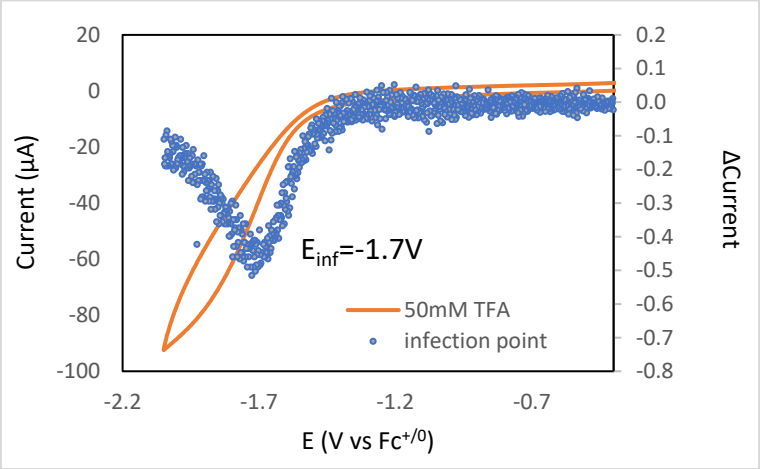

Figure B.3. Background cyclic voltammogram showing current enhancements related to the reduction of the TFA by the GC electrode. Solution contained 0.1M TBAHFP, and 50mM TFA. The CV was performed at a scan rate of 100mV/s. The blue markers represent application of the method of first principles to the orange curve. Minima denote inflection points in the catalytic curve and indicate the associated onset potential and current enhancement.

Figure B.4. The structure obtained for the optimization of $[Ni(\kappa^3\text{-}2,6\text{-}\{PhNCMe\}_2NC_5H_3)(H)]^+$ (**Ni(II)H**), Obtained using the B3LYP functional, def2TZVP basis set and PCM model for solvation in water. This species was obtained after the protonation of $[Ni(\kappa^3\text{-}2,6\text{-}\{PhNCMe\}_2(NC_5H_3)(OH_2)]^{2+}$ as described in the text.

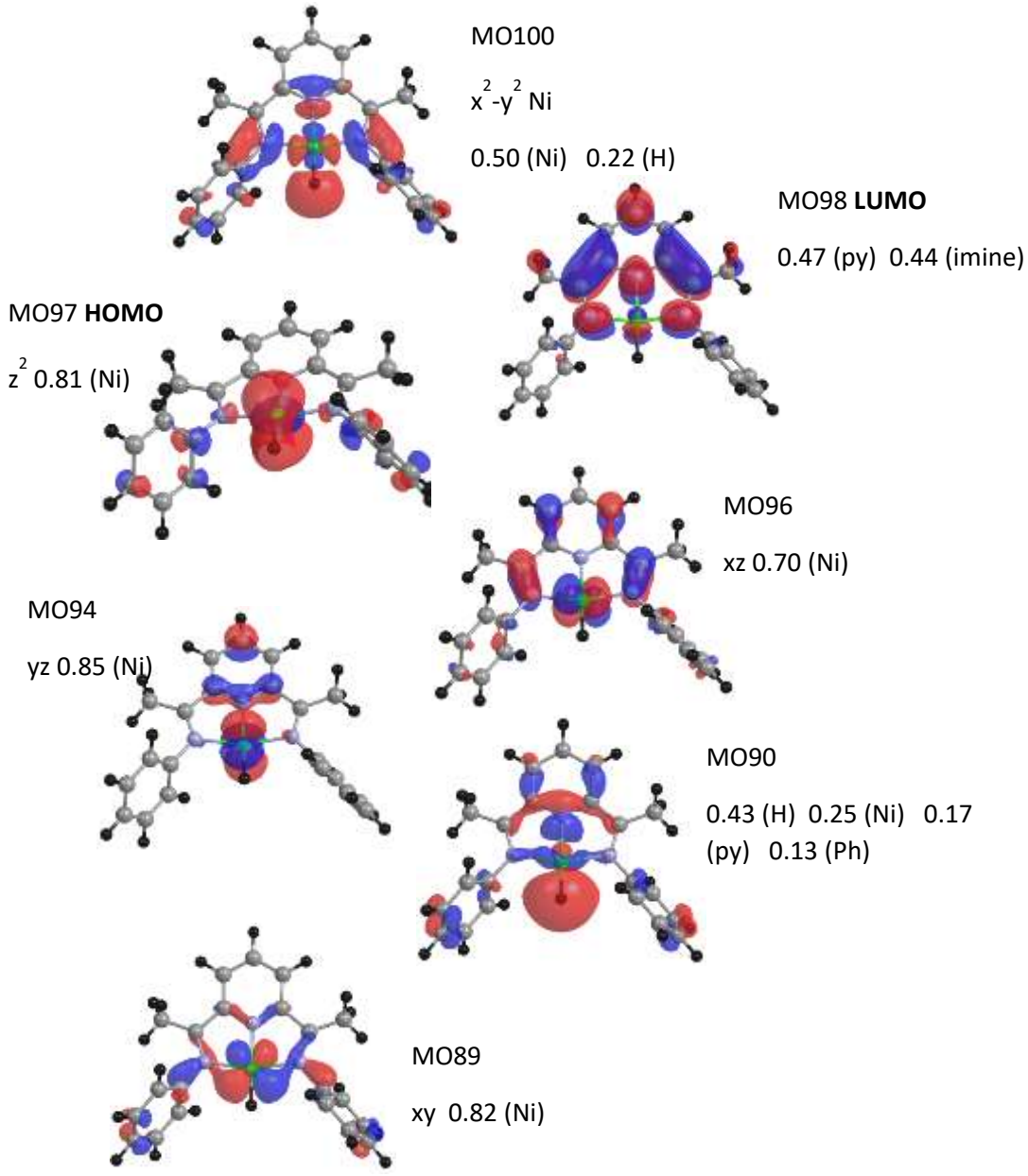

Figure B.5. Selected molecular orbitals, focusing on the Ni d orbitals, obtained for the optimization of $[Ni(\kappa^3\text{-}2,6\text{-}\{PhNCMe\}_2NC_5H_3)(H)]^+$ (**Ni(II)H**), Obtained using the B3LYP functional, def2TZVP basis set and PCM model for solvation in water. Major fragment orbital contributions were visualized using the Chemissian program using a 0.03 isosurface.

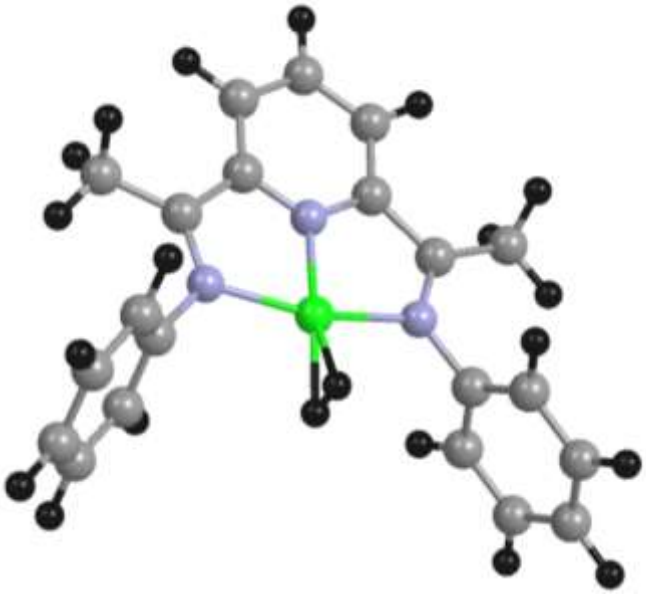

Figure B.6. The structure obtained for the optimization of $[Ni(\kappa^3\text{-}2,6\text{-}\{PhNCMe\}_2NC_5H_3)(H_2)]^{2+}$ (**Ni(II)(H)$_2$**). Obtained using the B3LYP functional, def2TZVP basis set and PCM model for solvation in water. This species was obtained after the protonation of $[Ni(\kappa^3\text{-}2,6\text{-}\{PhNCMe\}_2(NC_5H_3)H]^+$ as described in the text.

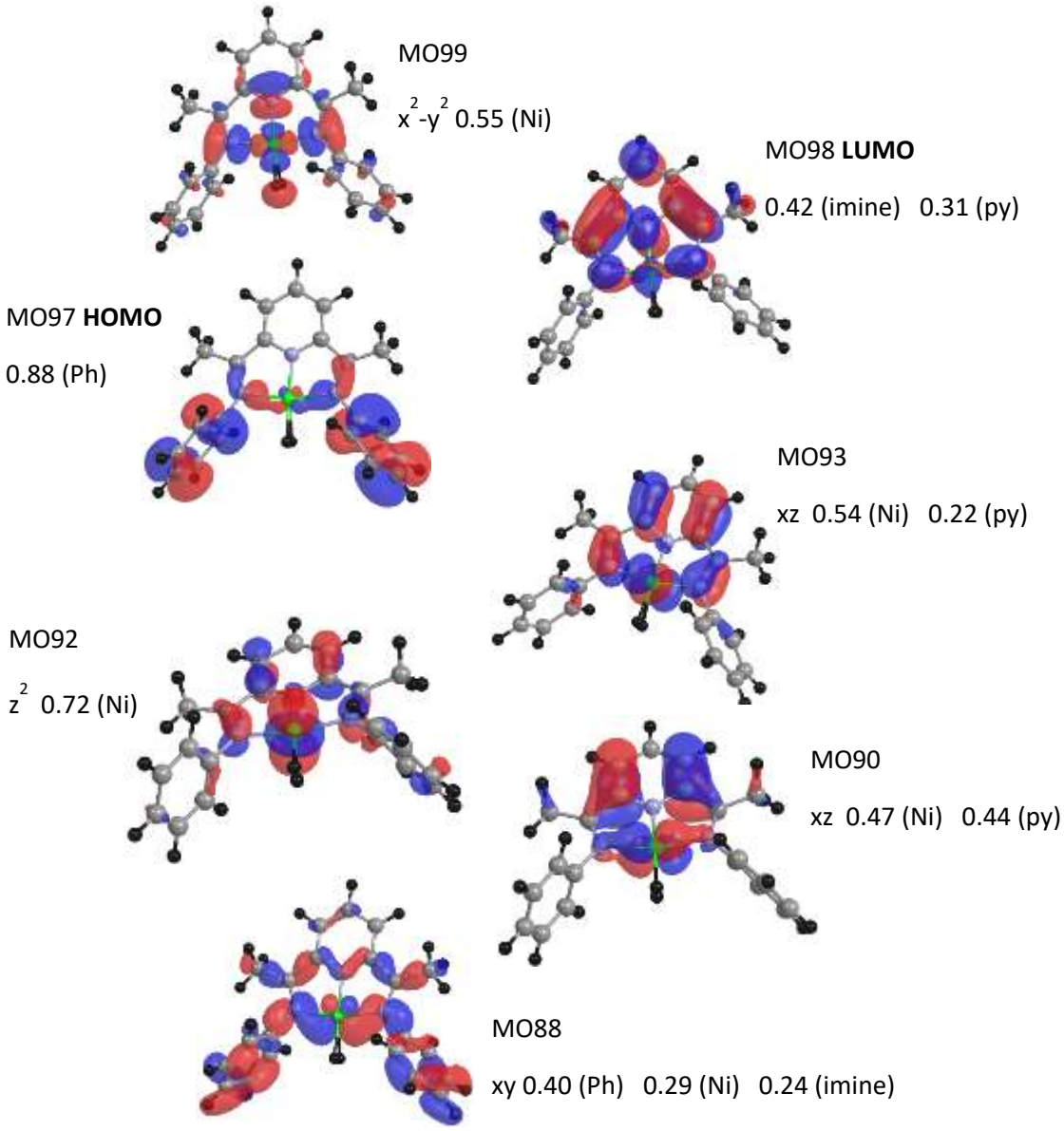

Figure B.7. Selected molecular orbitals, focusing on the Ni d orbitals, obtained for the optimization of $[Ni(\kappa^3\text{-}2,6\text{-}\{PhNCMe\}_2NC_5H_3)(H_2)]^{2+}$ (**Ni(II)(H)$_2$**. Obtained using the B3LYP functional, def2TZVP basis set and PCM model for solvation in water. Major fragment orbital contributions were visualized using the Chemissian program using a 0.03 isosurface.

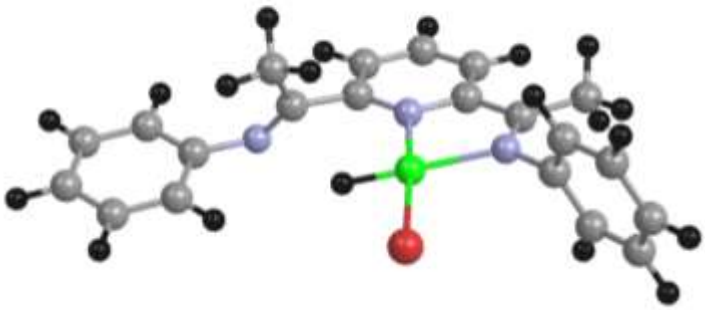

Figure B.8. The structure obtained for the optimization of $[Ni(\kappa^2\text{-}2,6\text{-}\{PhNCMe\}_2NC_5H_3)(H)Br]^+$ (**Ni(II)BrH**), Obtained using the B3LYP functional, def2TZVP basis set and PCM model for solvation in acetonitrile. This species was obtained after the protonation of $[Ni(\kappa^3\text{-}2,6\text{-}\{PhNCMe\}_2(NC_5H_3)Br]^+$ (**3.1'**$^+$) as described in the text.

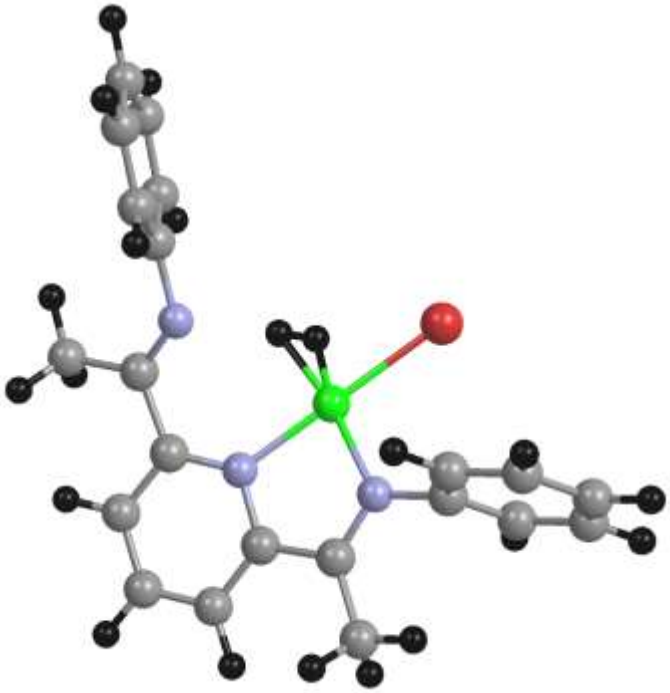

Figure B.9. The structure obtained for the optimization of $[Ni(\kappa^2\text{-}2,6\text{-}\{PhNCMe\}_2NC_5H_3)Br(H_2)]^+$ (**Ni(II)Br(H$_2$)**), Obtained using the B3LYP functional, def2TZVP basis set and PCM model for solvation in acetonitrile. This species was obtained after the protonation of $[Ni(\kappa^2\text{-}2,6\text{-}\{PhNCMe\}_2NC_5H_3)(H)Br]^+$ (**Ni(II)BrH**), as described in the text.

Appendix C:

Table C.1. Crystal data and structure refinement for **5.1** and **5.2**

	5.1	**5.2**
Empirical formula	$C_{31}H_{29}Br_2N_3P_2Zn$	$C_{18}H_{17}Br_2N_2PZn$
Formula weight	730.70	517.49
Temperature (K)	200(2)	200(2)
Wavelength (Å)	0.71073	0.71073
Crystal system	Hexagonal	Monoclinic
Space group	P 61	P 2_1
a (Å)	10.6902(2)	9.2997(12)
b (Å)	10.6902(2)	17.268(2)
c (Å)	46.4469(9)	12.0322(15
α (deg)	90	90
β (deg)	90	92.223(2)
γ (deg)	120	90
Volume (Å 3)	4596.83(19)	1930.8(4)
Z	6	4
Density (calculated) (Mg/m3)	1.584	1.780
Absorption coefficient (mm-1)	3.539	5.495
Reflections collected	19945	19945
Independent reflections	9485 [R(int) = 0.0266]	9485 [R(int) = 0.0266]
Final R indices [I>2sigma(I)]	R1 = 0.0421, wR2 = 0.1026	R1 = 0.0302, wR2 = 0.0583

R indices (all data)	R1 = 0.0467, wR2 = 0.1047	R1 = 0.0478, wR2 = 0.0633

.

Table C.2. Selected Bond lengths [Å] and angles [°] for [Zn(2,6-{Ph2PNMe}2(NC5H3)Br2] (**5.1**)

Bond	[Å]		Bond	[Å]
Zn(1)-Br(2)	2.3868(15)		Zn(1)-P(2)	2.425(3)
Zn(1)-Br(1)	2.4016(13)		P(1)-N(1)	1.709(8)
Zn(1)-P(1)	2.424(3)		P(2)-N(3)	1.713(9)
Angle	[°]		Angle	[°]
Br(2)-Zn(1)-Br(1)	115.50(5)		C(2)-N(1)-P(1)	116.3(6)
Br(2)-Zn(1)-P(1)	108.50(8)		C(1)-N(1)-P(1)	123.2(7)
Br(1)-Zn(1)-P(1)	107.52(8)		C(2)-N(1)-C(1)	120.2(8)
Br(2)-Zn(1)-P(2)	109.68(8)		C(6)-N(3)-C(7)	119.7(9)
Br(1)-Zn(1)-P(2)	101.92(8)		C(6)-N(3)-P(2)	116.9(7)
P(1)-Zn(1)-P(2)	113.76(9)			

Table C.3. Selected Bond lengths [Å] and angles [°] for the two molecules of [Zn(2-{Ph_2PNMe}(NC_5H_3)Br_2] (**5.2**) in the asymmetric unit.

Bond	[Å]		Bond	[Å]
N(1)-Zn(1)	2.067(4)		N(3)-Zn(2)	2.091(4)
P(1)-Zn(1)	2.4030(13)		P(2)-Zn(2)	2.4045(13)
Br(1)-Zn(1)	2.3400(8)		Br(3)-Zn(2)	2.3302(8)
Br(2)-Zn(1)	2.3368(8)		Br(4)-Zn(2)	2.3485(8)

Angle	[°]		Angle	[°]
N(1)-Zn(1)-Br(2)	110.18(11)		N(3)-Zn(2)-Br(3)	107.25(12)
N(1)-Zn(1)-Br(1)	109.79(12)		N(3)-Zn(2)-Br(4)	111.23(11)
Br(2)-Zn(1)-Br(1)	118.26(3)		Br(3)-Zn(2)-Br(4)	117.82(3)
N(1)-Zn(1)-P(1)	81.58(11)		N(3)-Zn(2)-P(2)	80.53(11)
Br(2)-Zn(1)-P(1)	110.57(4)		Br(3)-Zn(2)-P(2)	124.86(4)
Br(1)-Zn(1)-P(1)	120.21(4)		Br(4)-Zn(2)-P(2)	108.36(4)

Table C.4. Crystal data and structure refinement for [Zn(2,6-{Ph_2PNH}$_2$(NC_5H_3)Br_2] (**5.3**)

Empirical formula	$C_{58}H_{50}Br_4N_6P_4Zn_2$ {$(C_2H_5)_2O$} {CH_3CN}
Formula weight	1520.47
Temperature (K)	200(2)
Wavelength (Å)	0.71073
Crystal system	Monoclinic
Space group	P 21/c
a (Å)	18.323(2)
b (Å)	19.036(2)
c (Å)	19.746(2)
α (deg)	90
β (deg)	93.162(2)
γ (deg)	90
Volume ($Å^3$)	6876.9(14)
Z	4
Density (calculated) (Mg/m^3)	1.469
Absorption coefficient (mm^{-1})	3.159
Reflections collected	74867
Independent reflections	14168 [R(int) = 0.0683]
Final R indices [I>2sigma(I)]	R1 = 0.0452, wR2 = 0.0452
R indices (all data)	R1 = 0.1091, wR2 = 0.1010

Table C.5. Selected Bond lengths [Å] and angles [°] for the two molecules of [Zn(2,6-{Ph_2PNH}$_2$(NC_5H_3)Br_2] (**5.3**) in the asymmetric unit.

Bond Distances[Å]			
Br(1)-Zn(1)	2.4637(8)	Br(4)-Zn(2)	2.4120(9)
Br(2)-Zn(1)	2.4087(8)	Br(3)-Zn(2)	2.3979(9)
N(2)-Zn(1)	2.472(4)	N(5)-Zn(2)	2.525(4)
P(1)-Zn(1)	2.4510(14)	P(3)-Zn(2)	2.4443(15)
P(2)-Zn(1)	2.4527(14)	P(4)-Zn(2)	2.4364(15)
Bond Angles [°]			
Br(2)-Zn(1)-P(1)	108.89(4)	Br(3)-Zn(2)-Br(4)	111.25(3)
Br(2)-Zn(1)-P(2)	101.40(4)	Br(3)-Zn(2)-P(4)	107.65(5)
P(1)-Zn(1)-P(2)	132.11(5)	Br(4)-Zn(2)-P(4)	104.37(4)
Br(2)-Zn(1)-Br(1)	110.55(3)	Br(3)-Zn(2)-P(3)	105.53(4)
P(1)-Zn(1)-Br(1)	101.81(4)	Br(4)-Zn(2)-P(3)	101.43(4)
P(2)-Zn(1)-Br(1)	101.10(4)	P(4)-Zn(2)-P(3)	126.20(5)
Br(2)-Zn(1)-N(2)	93.13(10)	Br(3)-Zn(2)-N(5)	90.58(10)
P(1)-Zn(1)-N(2)	71.47(10)	Br(4)-Zn(2)-N(5)	158.11(10)
P(2)-Zn(1)-N(2)	70.66(10)	P(4)-Zn(2)-N(5)	68.73(10)
Br(1)-Zn(1)-N(2)	156.18(10)	P(3)-Zn(2)-N(5)	69.83(10)

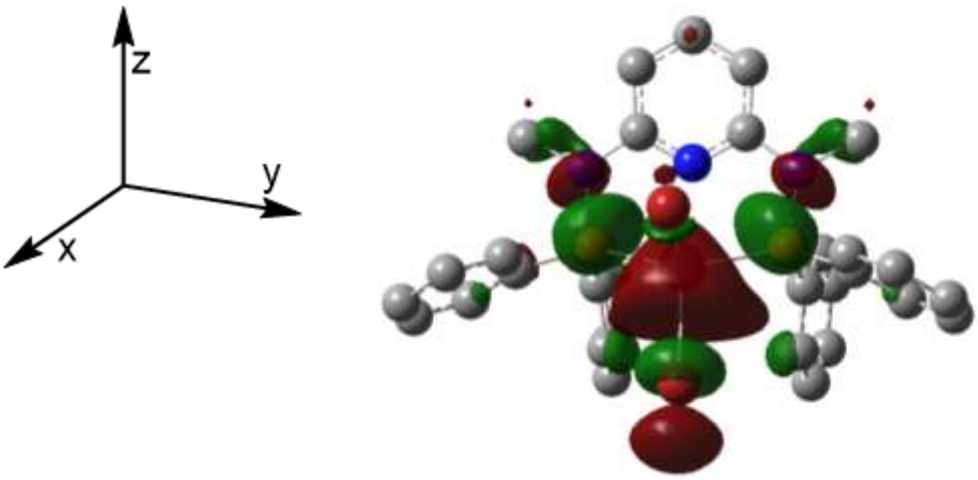

Figure C.1. The lowest energy unoccupied MO with substantial Zn fragment orbital contribution (MO 194) for **5.1.** The fragment orbital contributions are 0.51 (Zn), 0.21 (P)and 0.12 (Ph).

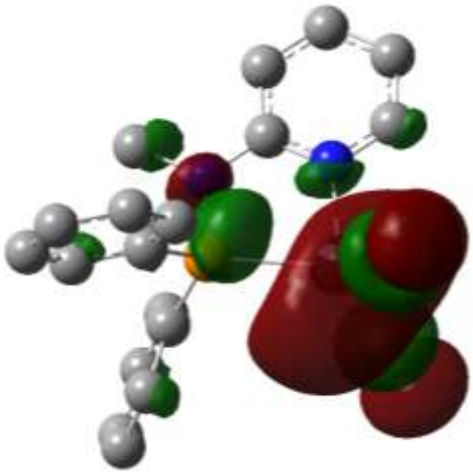

Figure C.2. The lowest energy unoccupied MO with substantial Zn fragment orbital contribution (MO 134) for (**5.2**). The major fragment orbital contributions are 0.73 (Zn) 0.07 (P) 0.06 (py) 0.05 (Ph)

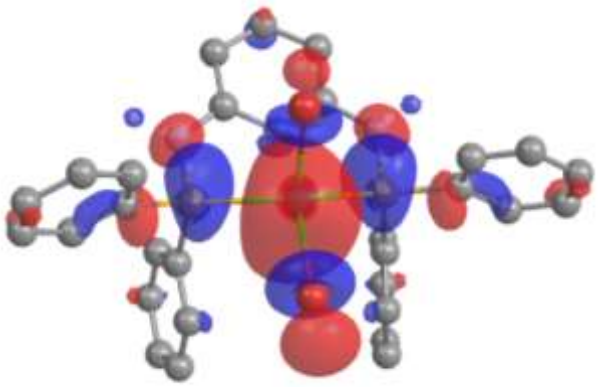

Figure C.3. The lowest energy unoccupied MO (MO 186) with substantial Zn fragment orbital contribution for (**5.3**). The fragment orbital contributions are 0.56 (Zn), 0.16 (Ph), 0.13 (P), 0.06 (Br), 0.06 (NH).

Table C.6. Summary of computed Zn-centered bonding from the optimization of [Zn(2,6-{Ph2PNH}2(NC5H3)Br2] (5.3). Values for bond length, overlap populations and Mayer bond order indices are from the B3LYP/def2TZVP/PCM (acetonitrile) optimization.

Bond	Length(Å)	Overlap Population	Mayer Bond order
Zn-P	2.542	0.25	0.59
Zn-P	2.542	0.25	0.59
Zn-Br plane	2.494	0.24	0.64
Zn-Br apex	2.475	0.24	0.67
Zn-N	2.745	0.03	0.06

First reduction, the computational optimization:

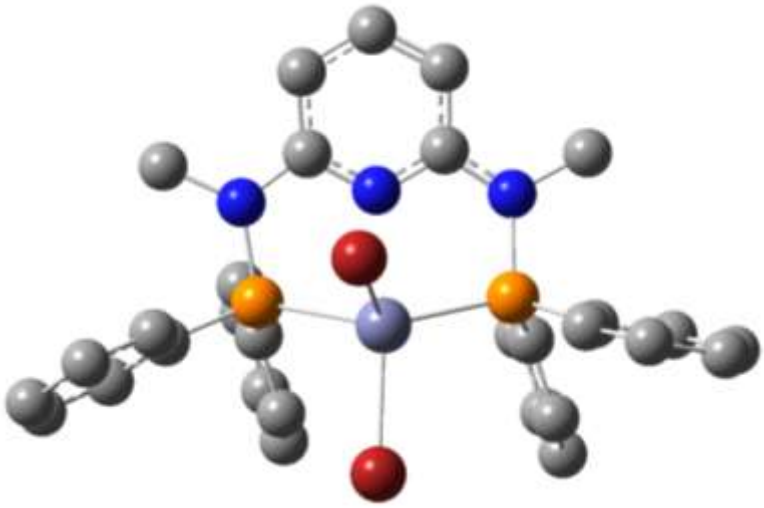

Figure C.4. DFT optimized result for the addition of a single electron to **5.1** to give the anionic species, $[Zn(2,6\text{-}\{Ph_2PNMe\}_2(NC_5H_3)Br_2]^-$ (**5.1**$^-$). Hydrogen atoms are eliminated for clarity. Frequency analysis confirmed that the optimized structure was a minimum with no imaginary frequencies.

Table C.7. Summary of Zn-centered bonding for the anion $[Zn(2,6\text{-}\{Ph_2PNMe\}_2(NC_5H_3)Br_2]^-$ (**5.1**$^-$**).** Values for bond length, overlap populations and Mayer bond order indices are from the B3LYP/def2TZVP/IEFPCM (acetonitrile) optimization.

Bond	Length(Å)	Overlap Population	Mayer Bond order
Zn-P	2.524	0.22	0.54
Zn-P	2.445	0.32	0.72
Zn-Br	2.518	0.22	0.63
Zn-Br	2.559	0.21	0.58
Zn-N	2.672	0.04	0.09

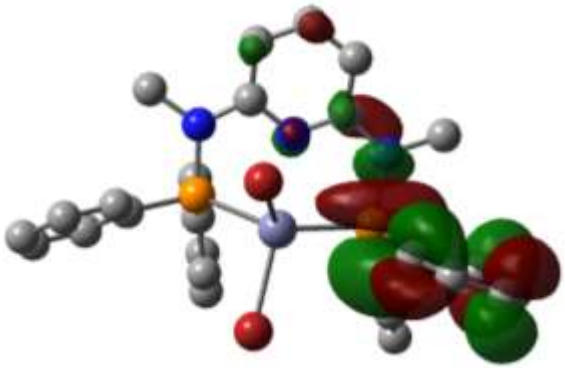

Figure C.5. The SOMO (MO 184) for [Zn(2,6-{Ph_2PNMe}$_2$(NC_5H_3)Br_2]$^-$ (**5.1**$^-$). The major fragment orbital contributions were Ph (0.67) P (0.21), py (0.07).

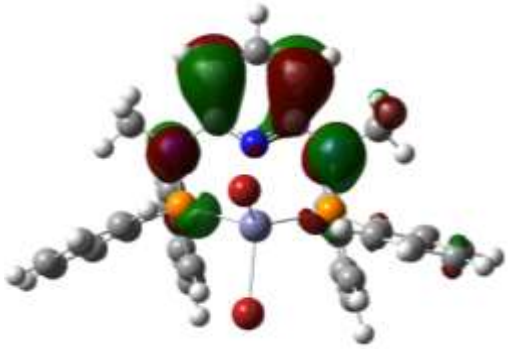

Figure C.6. The SOMO-1 (MO 183) for [Zn(2,6-{Ph_2PNMe}$_2$(NC_5H_3)Br_2]$^-$ (**5.1**$^-$). The major fragment orbital contributions were 0.53 (py) 0.28 (NMe) 0.08 (Ph) 0.05 (P).

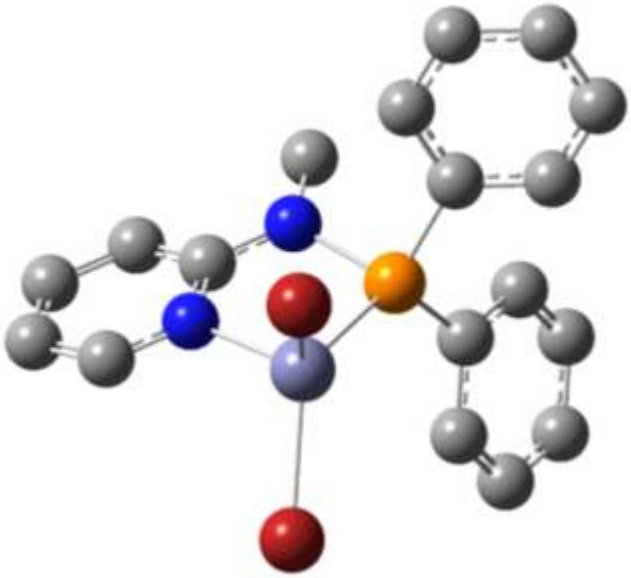

Figure C.7. DFT optimized structure of the first reduction of **5.2** to yield [Zn(2-{Ph_2PNMe}(NC_5H_3)Br_2]$^-$ (**5.2**$^-$), using the B3LYP functional and def2TZVP basis set in acetonitrile (IEFPCM). Hydrogen atoms eliminated for clarity. Frequency analysis confirmed that the optimized structure was a minimum with no imaginary frequencies.

Table C.8. Summary of Zn-centered bonding for the anion [Zn(2-{Ph2PNMe}(NC5H3)Br2]- (**5.2**$^-$**).** Values for bond length, overlap populations and Mayer bond order indices are from the B3LYP/def2TZVP/IEFPCM (acetonitrile) optimization.

Bond	Length(Å)	Overlap Population	Mayer Bond order
Zn-Br	2.477	0.25	0.67
Zn-Br	2.472	0.27	0.71
Zn-P	2.412	0.32	0.71
Zn-N	2.102	0.20	0.47

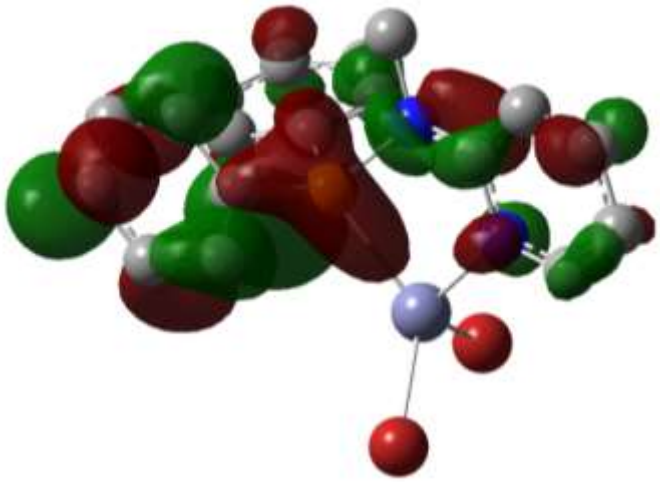

Figure C.8. The SOMO (MO 128) for [Zn(2-{Ph_2PNMe}(NC_5H_3)Br_2]$^-$ (**5.2**$^-$), The major fragment orbital contributions are 0.56 (Ph), 0.25 (P), 0.14 (py).

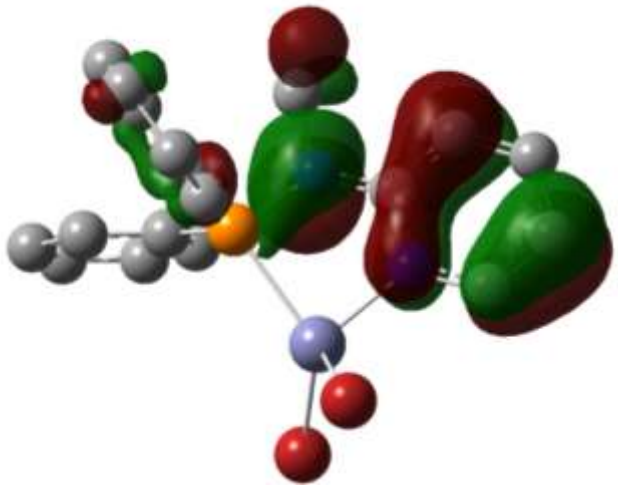

Figure C.9. The SOMO-1 ((MO 127, formerly the HOMO) for [Zn(2-{Ph_2PNMe}(NC_5H_3)Br_2] (**5.2**$^-$). retains similar character to the starting neutral species. The major fragment orbital contributions are 0.52 (py), 0.37 (NMe), 0.08 (Ph).

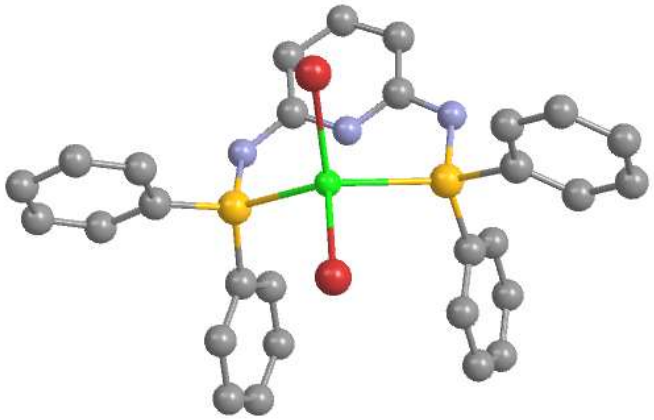

Figure C.10. DFT optimized result for the addition of a single electron to **5.3** to give the anionic species, [Zn(2,6-{Ph_2PNH}$_2$(NC_5H_3)Br_2]$^-$ (**5.3**$^-$). Hydrogen atoms are eliminated for clarity. Frequency analysis confirmed that the optimized structure was a minimum with no imaginary frequencies.

Table C.9. Summary of computed Zn-centered bonding for the anion [Zn(2,6-{Ph_2PNH}$_2$(NC_5H_3)Br_2]$^-$ (**5.3**$^-$). Values for bond length, overlap populations and Mayer bond order indices are from the B3LYP/def2TZVP/IEFPCM (acetonitrile) optimization.

Bond	Length(Å)	Overlap Population	Mayer Bond order
Zn-N	2.691	0.04	0.09
Zn-P	2.565	0.23	0.53
Zn-P	2.472	0.33	0.71
Zn-Br	2.508	0.22	0.63
Zn-Br	2.545	0.21	0.58

The orbital array for the first reduction product, $[Zn(2,6\text{-}\{Ph_2PNH\}_2(NC_5H_3)Br_2]^-$ (**5.3**$^-$), was similar to the frontier orbitals of **5.3** and were dominated by π-type molecular orbitals. The SOMO and SOMO-1 for **5.3**$^-$ were localized on the phenyl substitutents as shown in Figures 5.S11 and 5.S12.

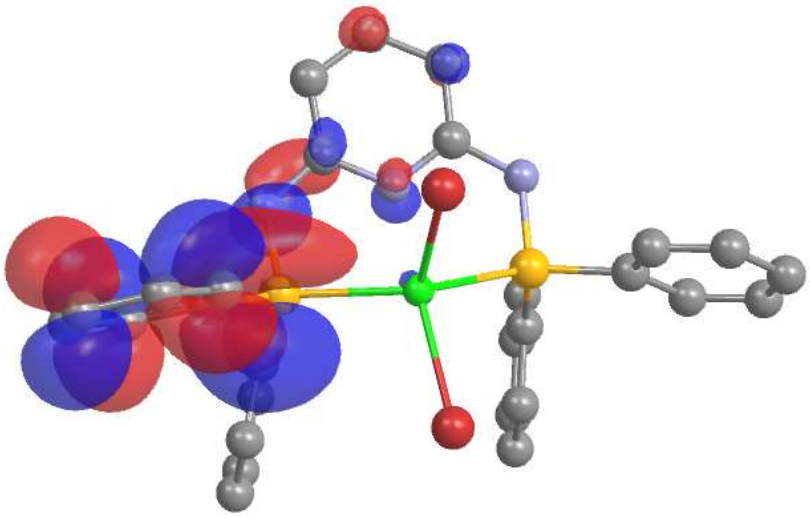

Figure C.11. The SOMO (MO 176) for $[Zn(2,6\text{-}\{Ph_2PNH\}_2(NC_5H_3)Br_2]^-$ (**5.3**$^-$). The major fragment orbital contributions were Ph (0.69) P (0.20), py (0.07).

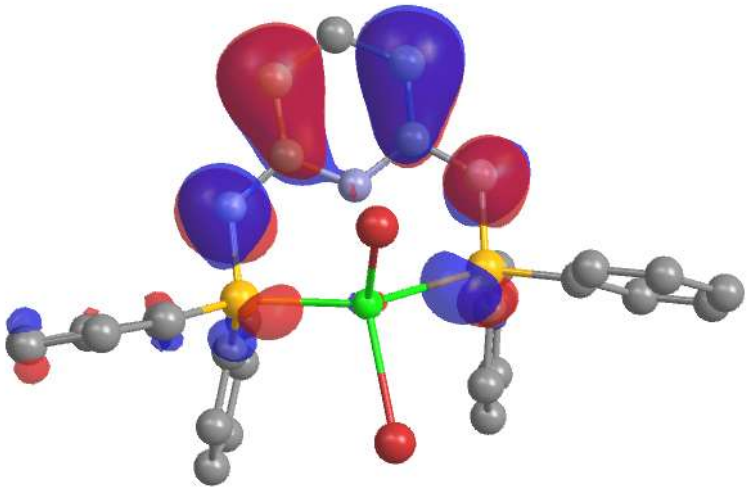

Figure C.12. The SOMO-1 (MO 175) for $[Zn(2,6\text{-}\{Ph_2PNH\}_2(NC_5H_3)Br_2]^-$ (**5.3**$^-$). The major fragment orbital contributions were 0.57 (py) 0.27 (NH) 0.08 (Ph) 0.06 (P).

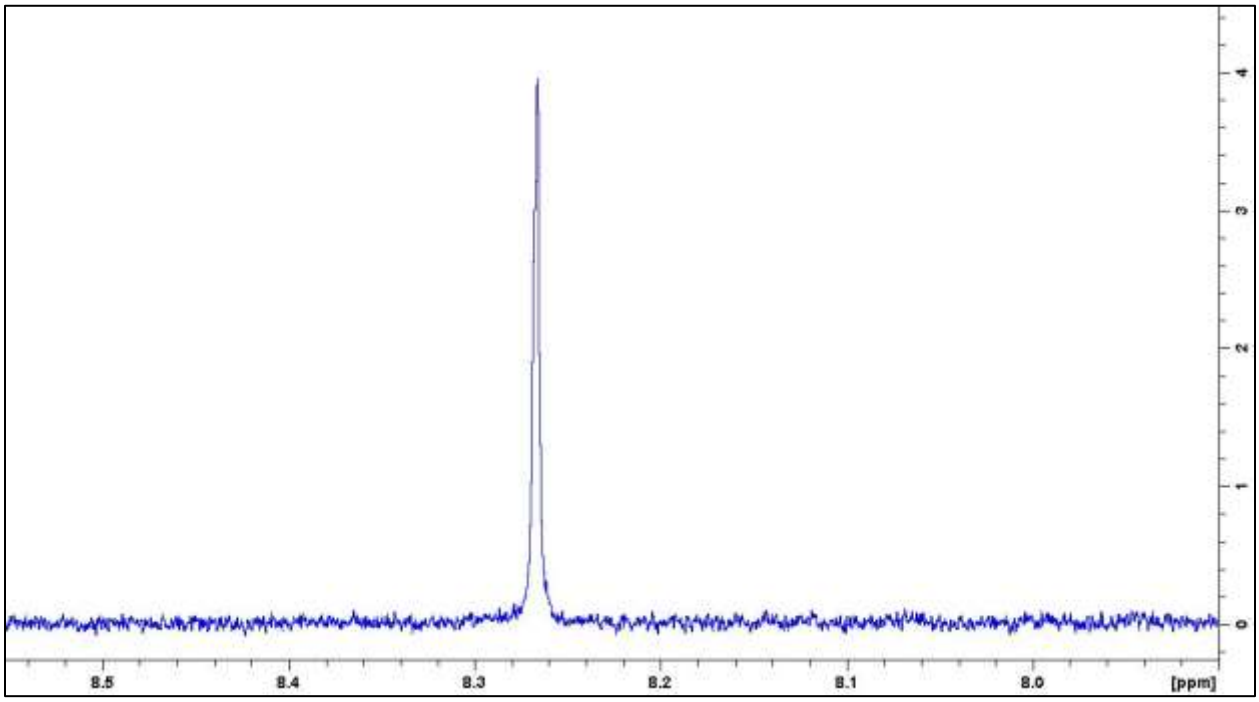

Figure C.13. An example of the NMR peak for formate/formic acid used in the analysis. This particular sample is from the bulk electrolysis of **5.1** with 1.9 M H_2O for 5 hours at -2.7 V vs Fc^+/Fc.

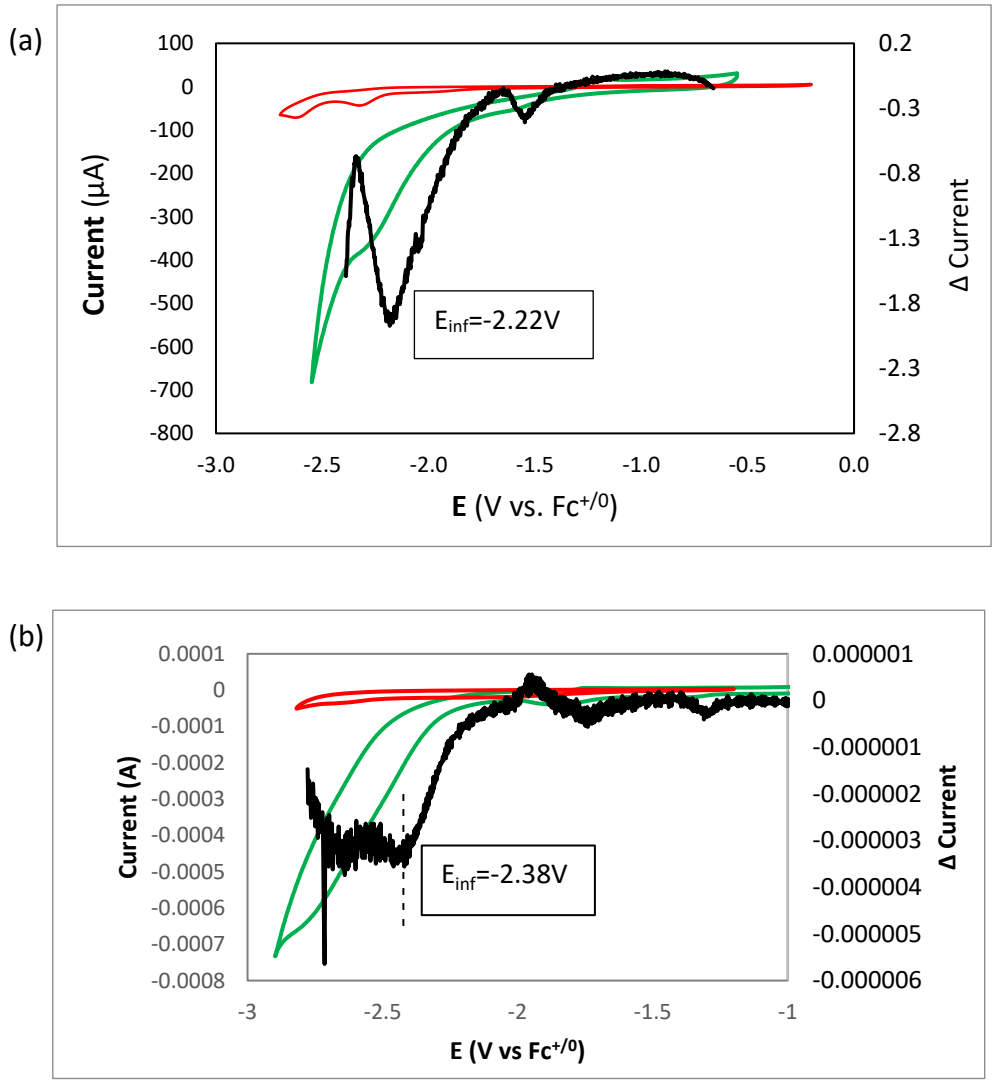

Figure C.14. Cathodic CV measurements in CH_3CN with a GC electrode under N_2 of a) complex **[Zn(2,6-{Ph_2PNMe}$_2$(NC_5H_3)Br_2] (5.1)** (red), **5.1** with 0.25M of added water (green), inflection point (black), b) complex **[Zn(2,6-{Ph_2PNH}$_2$(NC_5H_3)Br_2] (5.3)** (red), **5.3** with 0.4M of added water (green), inflection point (black).

Table C.10. Summary of Zn-centered bonding for [Zn(2,6-{Ph_2PNMe}$_2$(HNC_5H_3))Br_2] (**(5.1)H**) Values for bond length, overlap populations and Mayer bond order indices are from the B3LYP/def2TZVP/IEFPCM (acetonitrile) optimization.

Bond	Length(Å)	Overlap Population	Mayer Bond order

Zn-N_{py}	2.923	0.05	0.05
Zn-P	2.518	0.24	0.57
Zn-Br	2.457	0.24	0.66
Zn-Br	2.464	0.25	0.67
N_{py}-H	1.026	0.26	0.85

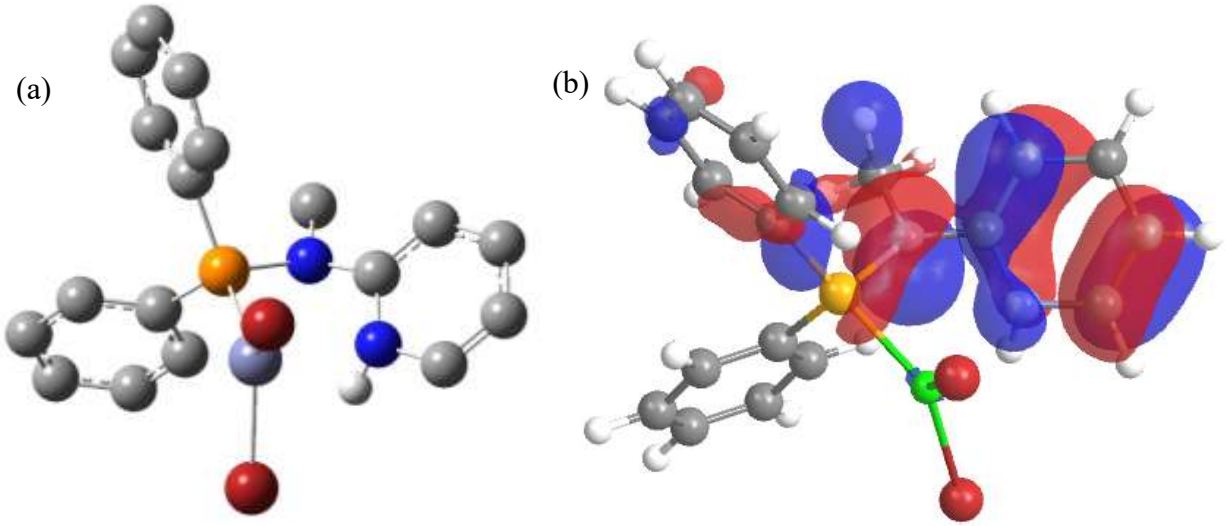

Figure C.15. a) DFT optimized structure of the protonated anion (**5.2**$^-$) to yield [Zn(2-{Ph_2PNMe}(**H**NC_5H_3)Br_2] ((**5.2)H**) using the B3LYP functional and def2TZVP basis set in acetonitrile (IEFPCM). Hydrogen atoms bonded to C have been omitted for clarity. Frequency analysis confirmed that the optimized structure was a minimum with no imaginary frequencies. b) The SOMO-1 ((MO 127) for The major fragment orbital contributions are 0.49 (pyH) 0.35 (NMe) 0.10 (Ph).

Table C.11. Summary of Zn-centered bonding for the protonated anion [Zn(2-{Ph_2PNMe}(**H**NC_5H_3)Br_2] ((**5.2)H**). Values for bond length, overlap populations and Mayer bond order indices are from the B3LYP/def2TZVP/IEFPCM (acetonitrile) optimization.

Bond	Length(Å)	Overlap Population	Mayer Bond order
Zn-Br	2.403	0.28	0.76
Zn-Br	2.430	0.29	0.76
Zn-P	2.489	0.30	0.66
Zn-N_{py}	2.561	0.07	0.14
H-N_{py}	1.025	0.30	0.86

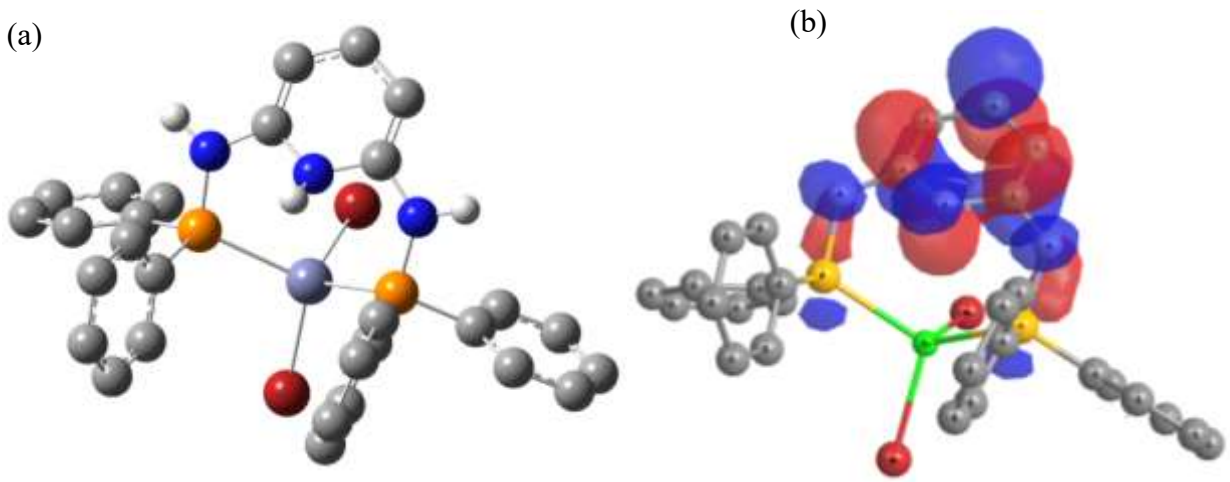

Figure C.16. a) DFT optimized structure of the protonated anion (**5.3**$^{-}$) to yield [Zn(2,6-{Ph_2PNH}$_2$(**H**NC_5H_3))Br_2] ((**5.3)H**) using the B3LYP functional and def2TZVP basis set in acetonitrile (IEFPCM). Hydrogen atoms bonded to C have been eliminated for clarity. b) SOMO (MO 176) for the optimized [Zn(2,6-{Ph_2PNH}$_2$(**H**NC_5H_3))Br_2] ((**5.3)H**) The major fragment orbital contributions are 0.78 (pyH) 0.08 (NMe) 0.06 (P) . All hydrogen atoms have been omitted for clarity.

Table C.12. Summary of Zn-centered bonding for [Zn(2,6-{Ph_2PNH}$_2$(HNC_5H_3))Br_2] (**(5.3)H**) Values for bond length, overlap populations and Mayer bond order indices are from the B3LYP/def2TZVP/IEFPCM (acetonitrile) optimization.

Bond	Length (Å)	Overlap Pop	Bond order
Zn-Npy	3.010	0.04	0.04
Zn-P	2.533	0.25	0.59
Zn-Br	2.476	0.23	0.64
Zn-Br	2.473	0.24	0.66
N_{py}-H	1.019	0.27	0.86

Table C.13. Summary of Zn-centered bonding and N-pyridyl- CO_2 for intermediate **A** derived from **5.1**, [Zn(2,6-{Ph_2PNMe}$_2$(NC_5H_3))(CO_2)Br_2] (shown in Figure 5.19.a) . Values for bond length, overlap populations and Mayer bond order indices are from the B3LYP/def2TZVP/IEFPCM (acetonitrile) optimization.

Bond	Length(Å)	OverlapPop	Bond order
Zn-Br	2.567	0.21	0.57
Zn-Br	2.493	0.26	0.67
Zn-O	2.196	0.15	0.31

Zn-P	2.711	0.15	0.35
$C(CO_2)$-N_{py}	1.547	0.08	0.73

Table C.14. Summary of Zn-centered bonding for metallacarboxylic acid intermediate **B** derived from **5.1**, [Zn(2,6-{Ph_2PNMe}$_2$(NC_5H_3))(CO_2H)Br] (shown in Figure 5.19.b) . Values for bond length, overlap populations and Mayer bond order indices are from the B3LYP/def2TZVP/IEFPCM (acetonitrile) optimization.

Bond	Length(Å)	OverlapPop	Bond order
Zn-Br	2.708	0.15	0.45
Zn-P	2.526	0.23	0.54
Zn-C	2.079	0.34	0.86

Table C.15. Summary of Zn-centered bonding for metallacarboxylic acid intermediate **C** derived from **5.1**, [Zn(2,6-{Ph_2PNMe}$_2$(NC_5H_3))(HCO_2)Br] (shown in Figure 5.19.c) . Values for bond length, overlap populations and Mayer bond order indices are from the B3LYP/def2TZVP/IEFPCM (acetonitrile) optimization.

Bond	Length(Å)	OverlapPop	Bond order
Zn-Br	2.533	0.20	0.56
Zn-N_{py}	2.330	0.19	0.34
Zn-P	2.551	0.21	0.50
Zn-O	1.995	0.21	0.57

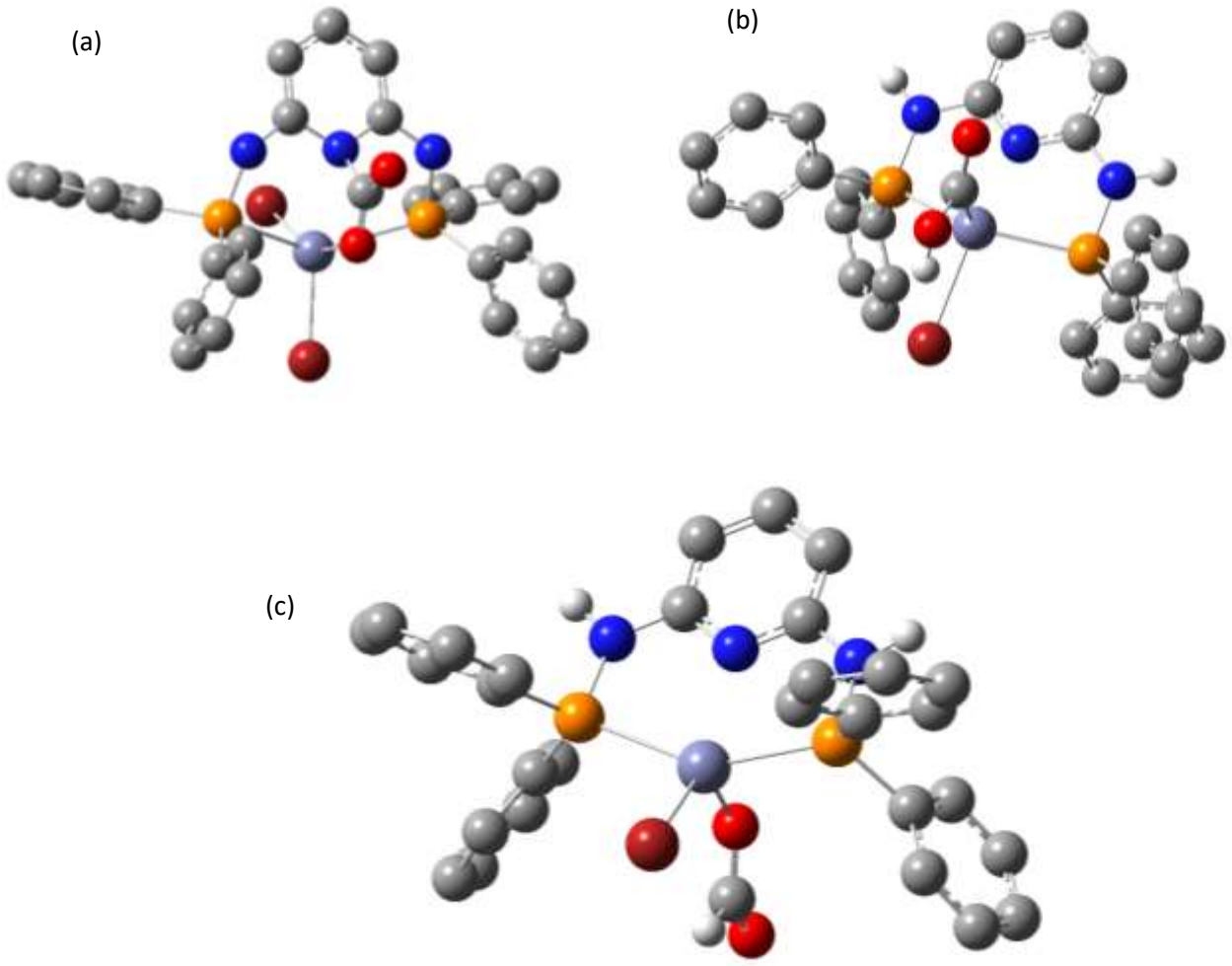

Figure C.17. DFT optimized structures for the proposed CO_2 intermediates (a) **A**, [Zn(2,6-{Ph_2PNH}$_2$(NC_5H_3))(CO_2)Br_2], (b) **B**, [Zn(2,6-{Ph_2PNH}$_2$(NC_5H_3))(CO_2)Br_2], (c) **C**, [Zn(2,6-{Ph_2PNH}$_2$(NC_5H_3))(HCO_2)Br_2], Structure was derived from compound **5.3**. These results used the B3LYP functional and def2TZVP basis set in acetonitrile (IEFPCM). Hydrogen atoms been eliminated for clarity. Frequency analysis confirmed that the optimized structure was a minimum with no imaginary frequencies.

Table C.16. Summary of Zn-centered bonding and N-pyridyl- CO_2 for intermediate **A** derived from **5.3**, [Zn(2,6-{Ph_2PNH}$_2$(NC_5H_3))(CO_2)Br_2] (shown in Figure 5.S14.a). Values for bond length, overlap populations and Mayer bond order indices are from the B3LYP/def2TZVP/IEFPCM (acetonitrile) optimization.

Bond	Length(Å)	OverlapPop	Bond order
Zn-Br	2.531	0.22	0.61

Zn-Br	2.483	0.25	0.67
Zn-P	2.765	0.14	0.32
Zn-O	2.142	0.15	0.34
$C(CO_2)$-N_{py}	1.544	0.10	0.75

Appendix D

Table D.1. Crystal data and structure refinement for (**6.3**).

Compound	
Empirical formula	$C_{21}H_{19}O_4NiN5$
Formula weight	464.12
Temperature(K)	208(2)
λ (Å)	0.71073
Crystal system	Monoclinic
Space group	P 21/n
a (Å)	12.8438(7)
b (Å)	12.5427(6)
c (Å)	13.3978(7)
α (deg)	90.00
β (deg)	102.919(2)
γ (deg)	90.00
V (Å3)	2103.70(19)
Z	4
DX (calc) (g/cm^3)	1.465
Mu (mm^{-1})	0.960
R1a	0.0365
wR2b	0.0909

Table D.2. Selected Bond lengths [Å] and angles [°] for (**6.3**).

Bond lengths [Å]		**Bond angles [°]**	
Ni(1)-O(1)	2.140(2)	O(1)-Ni(1)-O(2)	59.64(8)
Ni(1)-O(2)	2.065(2)	O(1)-Ni(1)-N(1)	89.56(8)
Ni(1)-N(1)	2.102(2)	O(2)-Ni(1)-N(1)	98.05(8)

Ni(1)-N(2)	1.971(2)	O(2)-Ni(1)-N(2)	165.39(9)
Ni(1)-N(5)	2.017(3)	N(1)-Ni(1)-N(2)	77.46(9)
O(2)-N(4)	1.267(4)	N(1)-Ni(1)-N(3)	154.98(9)
O(3)-N(5)	1.237(3)	N(1)-Ni(1)-N(5)	93.48(9)
O(4)-N(5)	1.245(3)	Ni(1)-O(1)-N(4)	92.5(2)
N(1)-C(1)	1.433(3)	Ni(1)-O(2)-N(4)	95.6(2)
N(1)-C(8)	1.283(3)	Ni(1)-N(1)-C(1)	122.5(2)

Table D.3. Crystal data and structure refinement for (**6.4**).

Compound	
Empirical formula	$C_{44}H_{49}Br_{1.35}Cl_2N_{3.65}NiO_{1.30}$
Formula weight	887.19
Temperature(K)	200(2)
λ (Å)	0.71073
Crystal system	triclinic
Space group	P1
a (Å)	9.5505(3)
b (Å)	9.6152(3)
c (Å)	13.7760(4)
α (deg)	93.303(2)
β (deg)	107.506(2)
γ (deg)	113.688(2)
V (Å3)	1081.50(6)
Z	1
DX (calc) (g/cm^3)	1.362
Mu (mm-1)	1.855
R1a	0.0496

wR2b	0.909

Table D.4. Selected Bond lengths [Å] and angles [°] for (**6.4**).

Bond lengths [Å]		**Bond angles [°]**	
Br(1)-Ni(1)	2.4684(7)	N(2)-Ni(1)-N(3)	77.0(2)
Ni(1)- N(2)	1.976(6)	N(2)-Ni(1)-O(1)	110.6(6)
Ni(1)-N(3)	2.182(6)	N(2)-Ni(1)-O(2)	170.1(4)
Ni(1)-N(1)	2.200(6)	N(1)-Ni(1)-C(1)	127.9(4)
Ni(1)- O(1)	2.088(6)	O(1)-Ni(1)-O(2)	59.8(5)
Ni(1)- O(2)	2.08(2)	O(2)-Ni(1)-N(1)	99.5(4)
N(1)- C(1)	1.460(9)	O(1)-Ni(1)-N(1)	88.4(3)
N(1)-C(19)	1.28(1)	N(3)-Ni(1)-Br(1)	94.4(2)
N(2)- C(20)	1.33(1)	N(1)-Ni(1)-Br(1)	96.1(1)

(a)

(b)

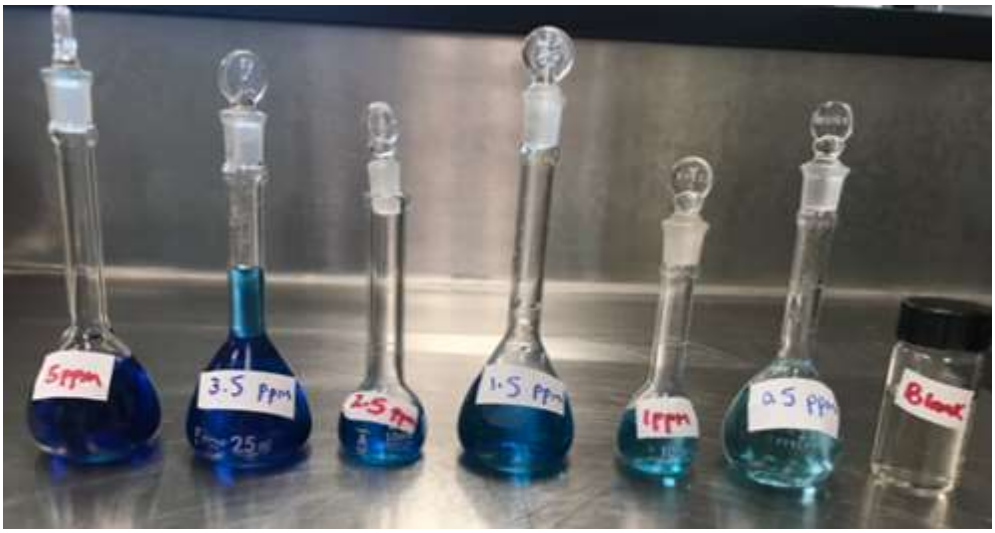

Figure D.1. Figures of the solutions were prepared for calibration curve for a) hydroxylamine and b) indophenol test.

Computational support for the proposed mechanism:

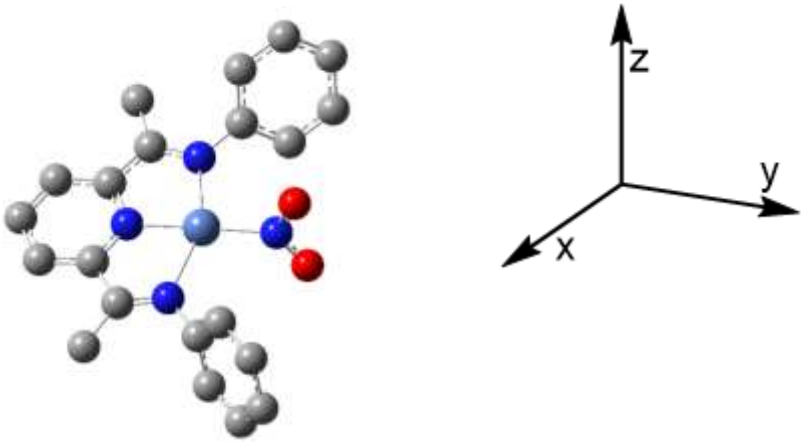

Figure D.2. DFT optimized structure of $[Ni(\kappa^3\text{-}2,6\text{-}\{Ph_2PNH\}_2NC_5H_3)NO_2]^-$ **$(Ni(NO_2)^-)$** in the triplet state using the B3LYP functional and def2TZVP basis set in water (IEFPCM). Hydrogen atoms omitted for clarity. Frequency analysis confirmed that the optimized structure was a minimum with no imaginary frequencies.

Table D.5. Summary of Ni-centered bonding for $[Ni(\kappa^3\text{-}2,6\text{-}\{Ph_2PNH\}_2NC_5H_3)NO_2]^-$ $(Ni(NO_2)^-)$ in triplet state. Values for bond length, overlap populations and Mayer bond order indices are from the B3LYP/def2TZVP/IEFPCM (water) optimization.

Bond	Length(Å)	Overlap Population	Mayer Bond order
Ni-N_{py}	1.937	0.16	0.54
Ni-N_{im}	2.141	0.17	0.40
Ni-N_{im}	2.208	0.14	0.32
Ni-$N_{nitrite}$	1.974	0.24	0.55
N-O	1.250	0.21	1.45
N-O	1.250	0.21	1.45

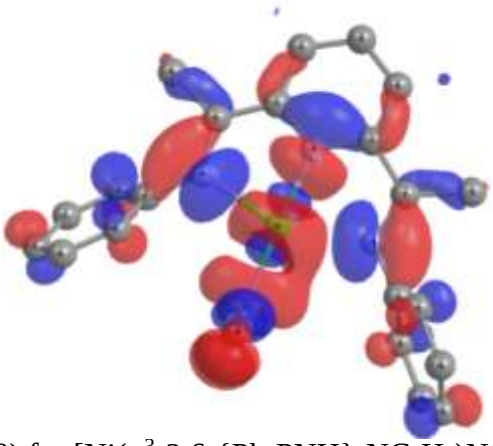

Figure D.3. SOMO (MO 109) for [Ni(κ^3-2,6-{Ph_2PNH}$_2$$NC_5H_3$)$NO_2$]$^-$ **(Ni(NO_2)$^-$)** in the triplet state using the B3LYP functional and def2TZVP basis set in water (IEFPCM). Hydrogen atoms omitted for clarity. The major orbital fragment allocation: 0.49 (Ni), 0.17 (imine), 0.16 (NO_2), 0.11 (py), and 0.07 (Ph).

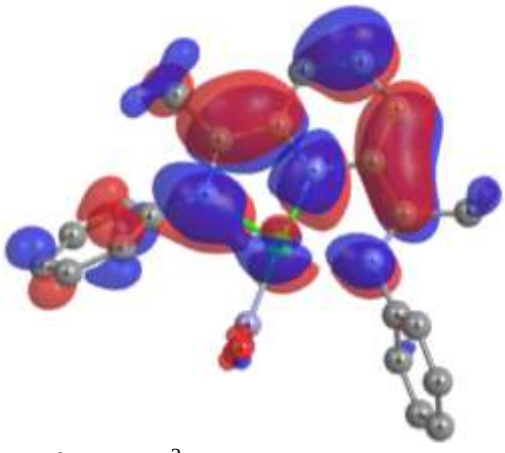

Figure D.4. SOMO (MO 110) for [Ni(κ^3-2,6-{Ph_2PNH}$_2$$NC_5H_3$)$NO_2$]$^-$ **(Ni(NO_2)$^-$)** in the triplet state using the B3LYP functional and def2TZVP basis set in water (IEFPCM). Hydrogen atoms

omitted for clarity. The major orbital fragment allocation: 0.46 (py), 0.40 (imine), 0.07 (Ph), 0.06 (Ni).

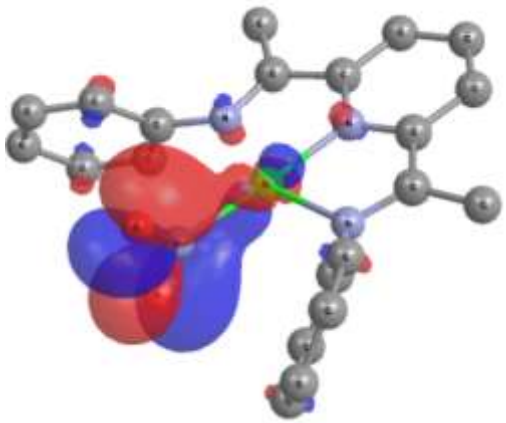

Figure D.5. Molecular orbital 110 for $[Ni(\kappa^3\text{-}2,6\text{-}\{Ph_2PNH\}_2NC_5H_3)NO_2]^-$ (**$Ni(NO_2)^-$**) in the triplet state using the B3LYP functional and def2TZVP basis set in water (IEFPCM). Hydrogen atoms omitted for clarity. The major orbital fragment allocation: 85 (NO_2).

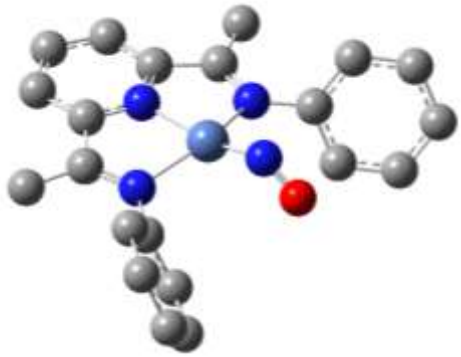

Figure D.6. DFT optimized structure of $[Ni(\kappa^3\text{-}2,6\text{-}\{Ph_2PNH\}_2NC_5H_3)NO]^+$ **($Ni(NO)^+$)** using the B3LYP functional and def2TZVP basis set in water (IEFPCM). Hydrogen atoms omitted for clarity. Frequency analysis confirmed that the optimized structure was a minimum with no imaginary frequencies.

Table D.6. Summary of Ni-centered bonding for $[Ni(\kappa^3\text{-}2,6\text{-}\{Ph_2PNH\}_2NC_5H_3)NO]^+$ ($Ni(NO)^+$). Values for bond length, overlap populations and Mayer bond order indices are from the B3LYP/def2TZVP/IEFPCM (water) optimization.

Bond	Length(Å)	Overlap Population	Mayer Bond order
$Ni\text{-}N_{py}$	1.941	0.19	0.49
$Ni\text{-}N_{imine}$	2.038	0.20	0.50

$Ni\text{-}N_{imine}$	2.040	0.19	0.50
$Ni\text{-}N_{nitrosyl}$	1.694	0.26	1.22
N-O	1.173	0.25	1.72

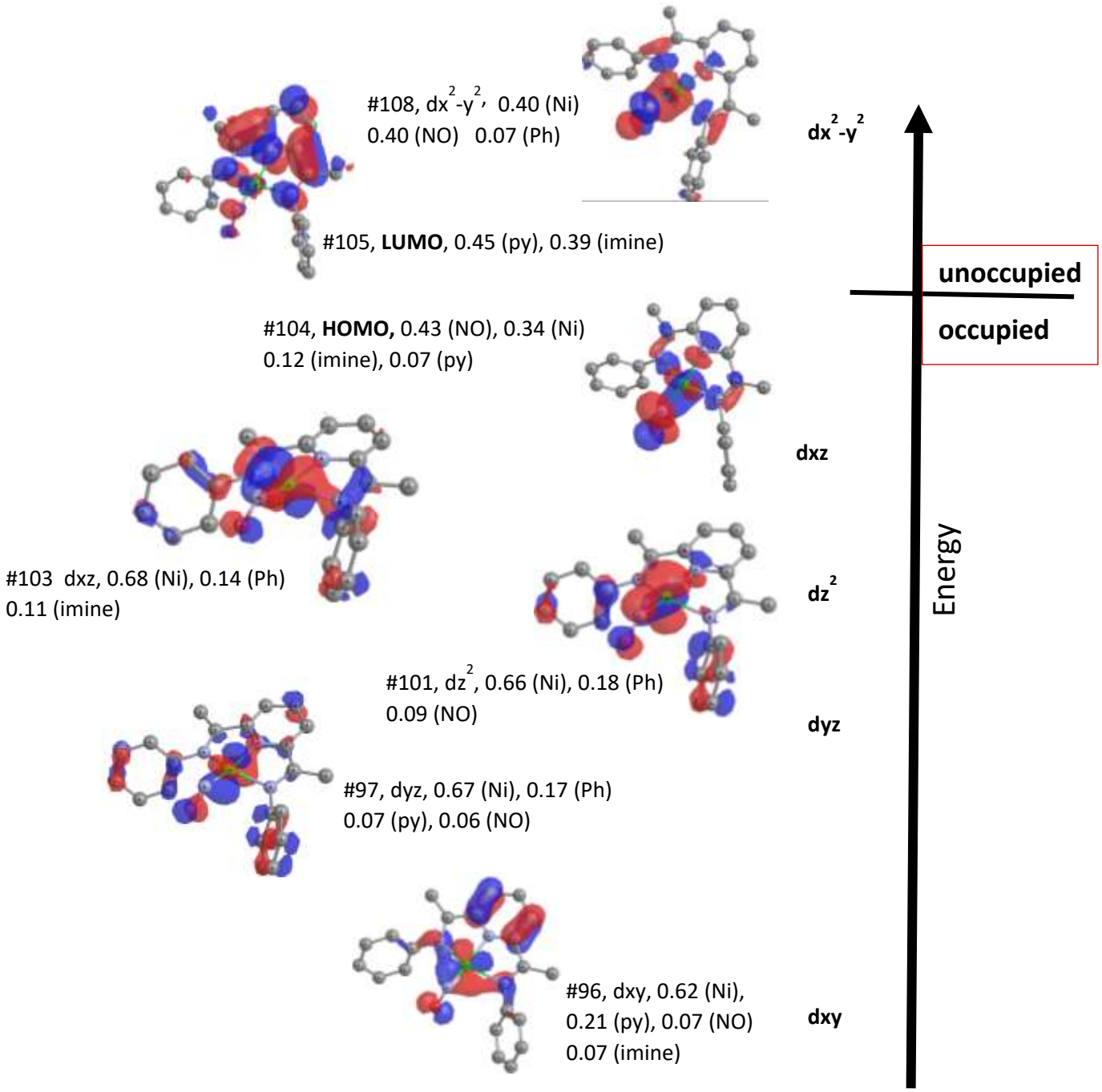

Figure D.7. Selected, Ni-centered molecular orbitals obtained from the computational optimization of $[Ni(\kappa^3\text{-}2,6\text{-}\{Ph_2PNH\}_2NC_5H_3)NO]^+$ **$(Ni(NO)^+)$** using the B3LYP functional,

def2TZVP basis set and IEFPCM model for solvation in water. Hydrogen atoms have been omitted for clarity. Major fragment orbital contributions were obtained from the Chemissian program.

Figure D.8. DFT optimized structure of [Ni(κ^3-2,6-{Ph_2PNH}$_2$$NC_5H_3$)(**N(H)OH**)]$^+$ **(Ni(NHOH)$^+$)** using the B3LYP functional and def2TZVP basis set in water (IEFPCM). Hydrogen atoms on carbon omitted for clarity. Frequency analysis confirmed that the optimized structure was a minimum with no imaginary frequencies.

Table D.7. Summary of Ni-centered bonding for [Ni(κ^3-2,6-{Ph_2PNH}$_2$$NC_5H_3$)(N(H)OH)]$^+$ (**Ni(NHOH)$^+$**). Values for bond length, overlap populations and Mayer bond order indices are from the B3LYP/def2TZVP/IEFPCM (water) optimization.

Bond	Length(Å)	Overlap Population	Mayer Bond order
Ni-N_{py}	1.874	0.18	0.59
Ni-N_{imine}	2.007	0.25	0.59
Ni-N_{imine}	1.969	0.26	0.62
Ni-N	1.832	0.25	0.88
N-O	1.424	0.06	0.86

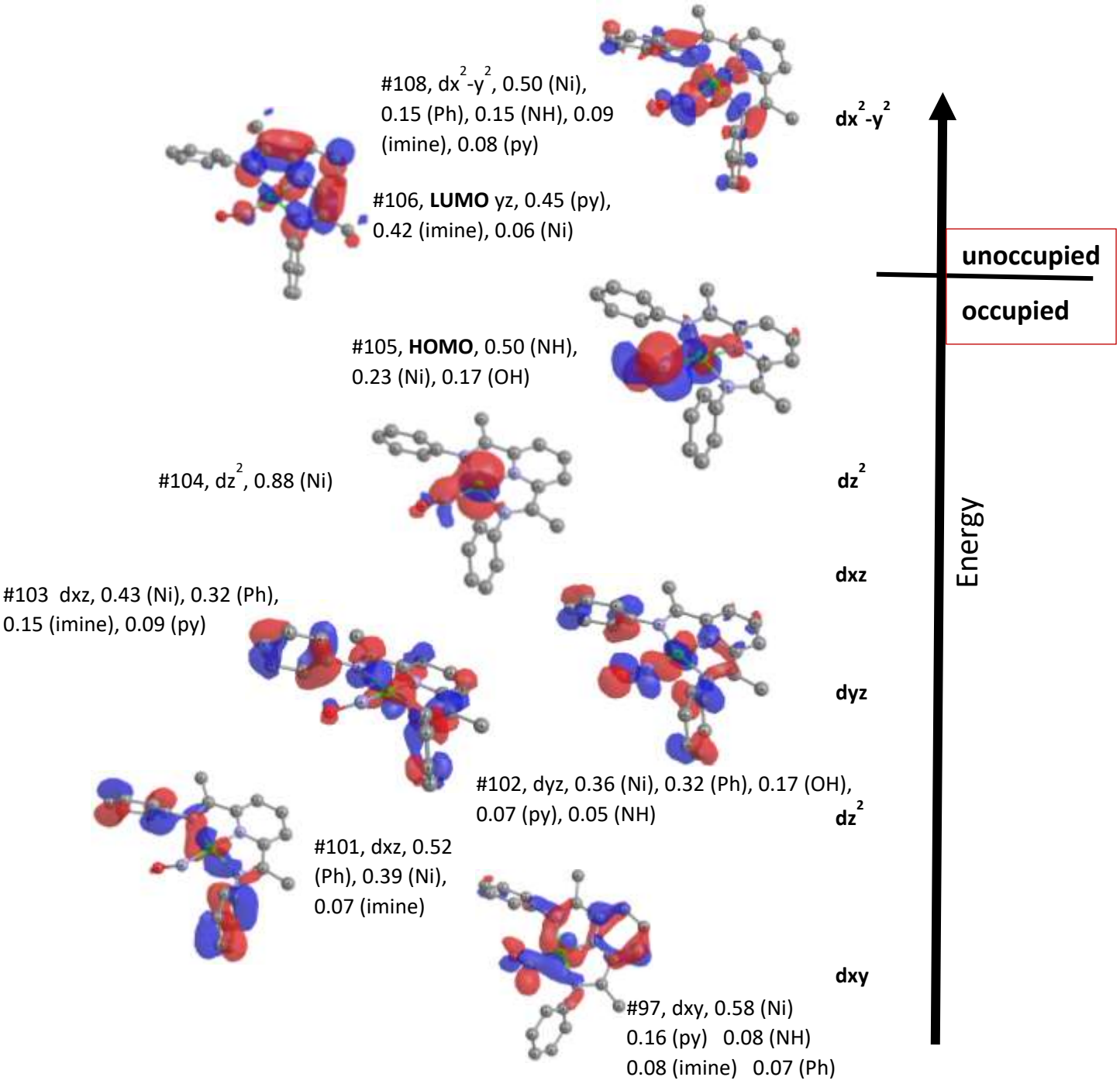

Figure D.9. Selected, Ni-centered molecular orbitals obtained from the computational optimization of $[Ni(\kappa^3\text{-}2,6\text{-}\{Ph_2PNH\}_2NC_5H_3)(N(H)OH)]^+$ **(Ni(NHOH)$^+$)** using the B3LYP functional, def2TZVP basis set and IEFPCM model for solvation in water. Hydrogens atoms omitted for clarity. Major fragment orbital contributions were obtained from the Chemissian program.

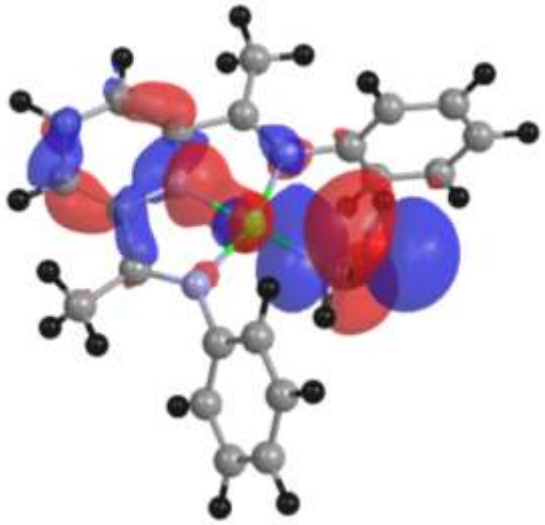

Figure D.10. Molecular orbital #97 for $[Ni(\kappa^3\text{-}2,6\text{-}\{Ph_2PNH\}_2NC_5H_3)(NH_2OH)]^{2+}$ (**Ni(NH2OH)$^{2+}$**) using the B3LYP functional and def2TZVP basis set in water (IEFPCM). The major orbital fragment allocation: 0.56 (OH), 0.19 (NH_2), 0.11 (Ni), 0.09 (py).

Appendix E:

Table E.1. Crystal data and structure refinement for (**Ni1**).

Compound	
Empirical formula	$C_{19}H_{21}Cl_2N_4NiO_4$
Formula weight	368
Temperature(K)	203(2)
λ (Å)	0.71073
Crystal system	Triclinic
Space group	P2(1)/c
a (Å)	15.9466(4)
b (Å)	9.8281(2)
c (Å)	16.6598(4)
α (deg)	90.00
β (deg)	93.593(2)
γ (deg)	90.00
V (Å3)	2605.87
Z	1
p (calc) (Mg/m3)	1.394
Mu (mm-1)	2.451
R1a	0.0812
wR2b	0.1797

Table E.2. Selected Bond lengths [Å] and angles [°] for (**Ni1**).

Bond lengths [Å]		**Bond angles [°]**	
Ni(1)- N(2)	2.059(4)	N(2)-Ni(1)-N(3)	78.4(0)
Ni(1)-N(3)	1.960(2)	N(2)-Ni(1)-N(5)	100.8(9)

Ni(1)-N(5)	2.066(0)	N(3)-Ni(1)-N(5)	178.9(5)
Ni(1)-N(4)	2.118(0)	N(2)-Ni(1)-N(7)	156.8(8)
Ni(1)-N(8)	2.160(9)	N(3)-Ni(1)-N(5)	178.9(5)
N(5)-C(17)	1.466(3)	C(13)-N(2)-C(15)	121.8(9)
N(2)-C(15)	1.449(8)	C(11)-N(7)-C(20)	122.7(9)
N(2)-C(13)	1.311(2)	C(15)-C(16)-C(17)	117.2(4)
C(15)-C(16)	1.529(5)	N(4)-Ni(1)-N(8)	176.6(4)

Table E.3. Crystal data and structure refinement for (**Ni2**).

Compound	
Empirical formula	$C_{17}H_{21}Cl_3N_5NiO_4$
Formula weight	524.45
Temperature(K)	200(2)
λ (Å)	0.71073
Crystal system	Triclinic
Space group	P -1
a (Å)	8.3711(8)
b (Å)	11.4503(11)
c (Å)	13.0200(12)
α (deg)	64.774(2)
β (deg)	82.214(2)
γ (deg)	83.183(2)
V (Å3)	1115.97
Z	1
p (calc) (Mg/m3)	1.561
Mu (mm-1)	1.26
R1a	0.1167

wR2b	0.2574

Table E.4. Selected Bond lengths [Å] and angles [°] for (**Ni2**).

Bond lengths [Å]		**Bond angles [°]**	
Cl(6)-Ni(1)	2.468(2)	N(2)-Ni(1)-N(6)	160.8(2)
Ni(1)-N(2)	2.0157(7)	N(2)-Ni(1)-N(5)	100.6(2)
Ni(1)-N(3)	2.233(6)	N(2)-Ni(1)-N(3)	76.1(2)
N1(i)-N(4)	2.030(6)	N(2)-Ni(1)-N(4)	78.4(3)
Ni(1)-N(5)	2.117(7)	N(4)-Ni(1)-N(5)	94.3(3)
Ni(1)-N(6)	2.126(7)	N(5)-Ni(1)-N(6)	82.2(2)
N(3)-C(16)	1.48(1)	Cl(6)-Ni(1)-N(5)	165.1(2)
N(5)-C(17)	1.49(1)	Cl(6)-Ni(1)-N(2)	92.6(2)
N(6)-C(21)	1.47(1)	Cl(6)-Ni(1)-N(6)	87.6(2)
N(3)-C(12)	1.48(1)	O(32)-C(12)-N(3)	107.4(6)
C(12)-O(32)	1.425(9)	C(17)-N(25)-C(20)	112.1(6)

Table E.5. Crystal data and structure refinement for (**Ni3**).

Compound	
Empirical formula	$C_{18}H_{31}Cl_2N_5NiO_9$
Formula weight	591.09
Temperature(K)	200(2)
λ (Å)	0.71073
Crystal system	Triclinic
Space group	P 21/c
a (Å)	9.9524(5)

b (Å)	16.5098(6)
c (Å)	15.1274(7)
α (deg)	90.00
β (deg)	90.825(1)
γ (deg)	90.00
V (Å3)	2485.36(19)
Z	4
p (calc) (Mg/m3)	1.580
Mu (mm-1)	1.053
R1a	0.0474
wR2b	0.1261

Table E.6. Selected Bond lengths [Å] and angles [°] for (**Ni3**).

Bond lengths [Å]		**Bond angles [°]**	
O(1)-Ni(1)	2.113(2)	O(1)-Ni(1)-N(1)	166.5(1)
Ni(1)-N(1)	2.132(3)	O(1)-Ni(1)-N(2)	85.60(9)
Ni(1)-N(2)	2.074(2)	O(1)-Ni(1)-N(3)	88.92(9)
Ni(1)-N(4)	1.992(2)	N(1)-Ni(1)-N(2)	83.3(1)
Ni(1)-N(5)	2.098(3)	N(1)-Ni(1)-N(3)	100.1(1)
O(1)-C(1)	1.416(5)	N(2)-Ni(1)-N(4)	172.8(1)
N(1)-C(18)	1.485(5)	N(1)-Ni(1)-N(4)	101.5(1)
N(1)-C(2)	1.479(4)	Ni(1)-O(1)-C(1)	126.5(2)
N(2)-C(3)	1.476(4)	C(7)-N(3)-C(6)	118.8(2)
N(2)-C(4)	1.492(4)	C(14)-N(5)-C(16)	122.9(3)
C(4)-C(5)	1.514(4)	N(1)-C(18)-C(17)	115.0(3)

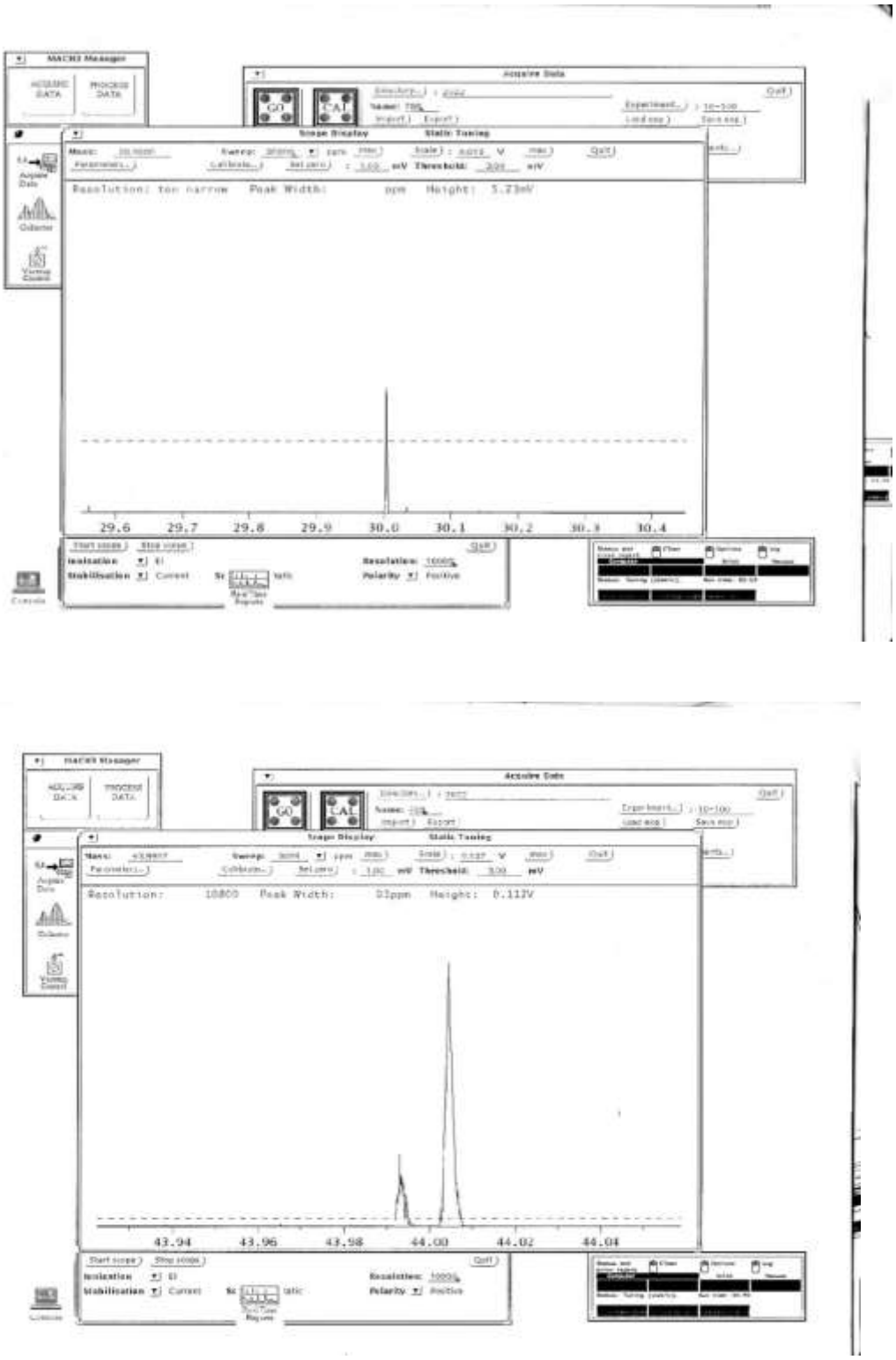

Figure E.1. Mass spectrum of gas products after CPE experiment shown in Table 7.2, row 7. The peak at 30.0 shows NO gas and the peak at 44.01 shows N_2O gas.

(a)

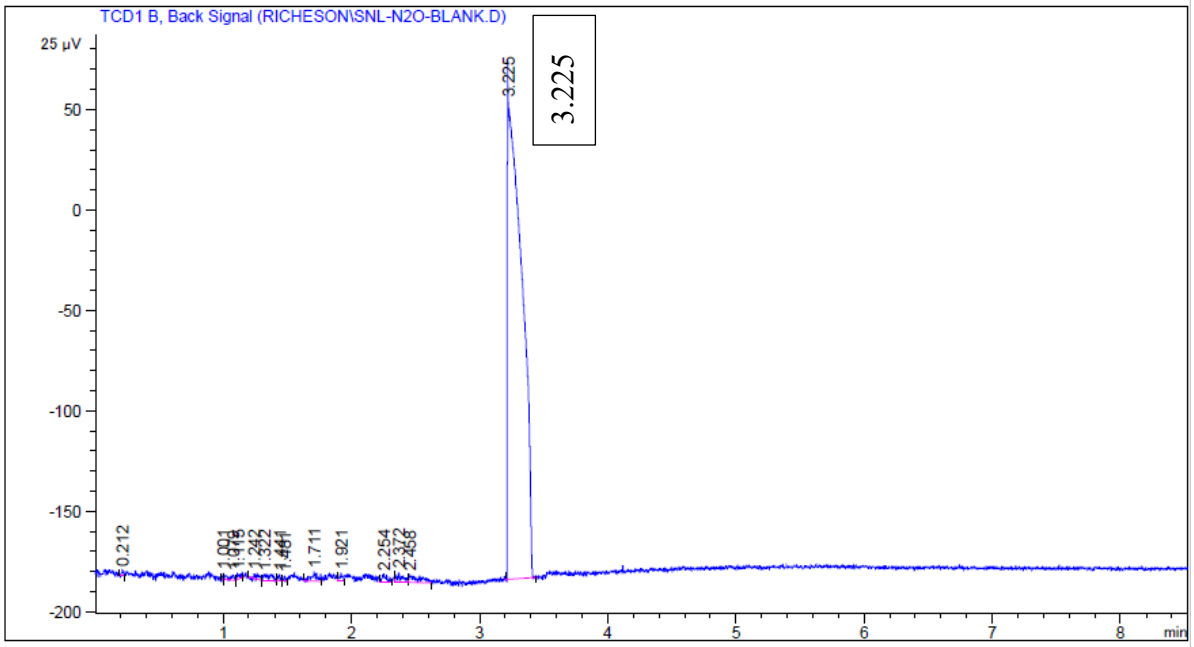

(b)

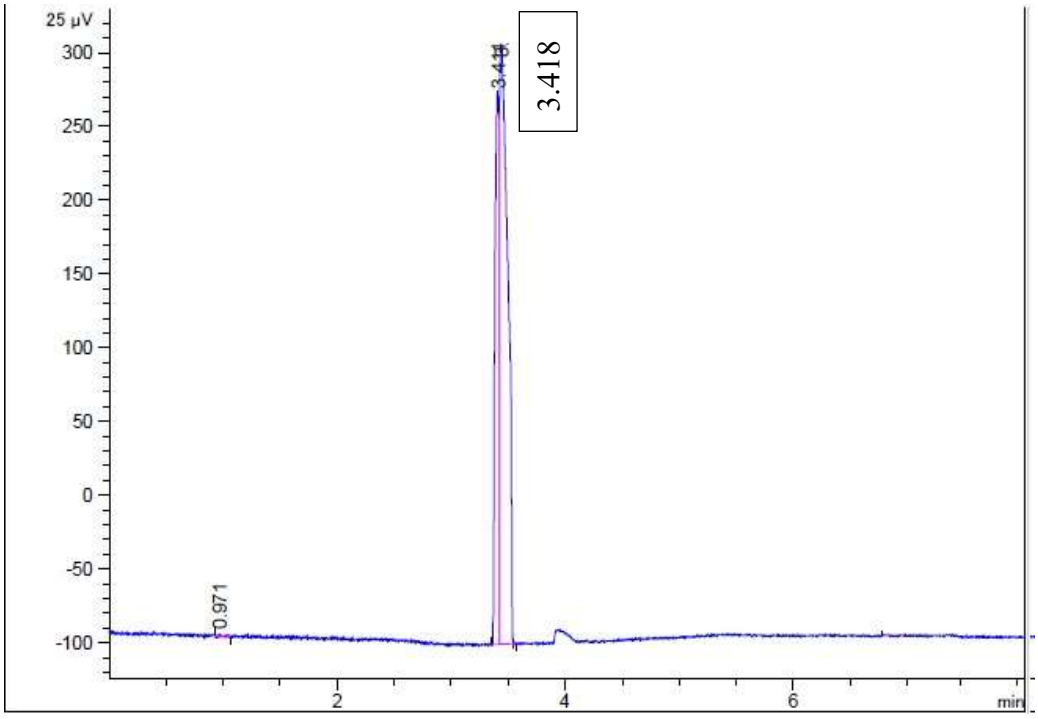

Figure E.2. Gas chromatography spectrum of (a) standard N_2O gas, and (b) after CPE experiment, table 7.2, row 4. The peak at 3.4 belongs to CO_2 gas in the gas chromatography column.

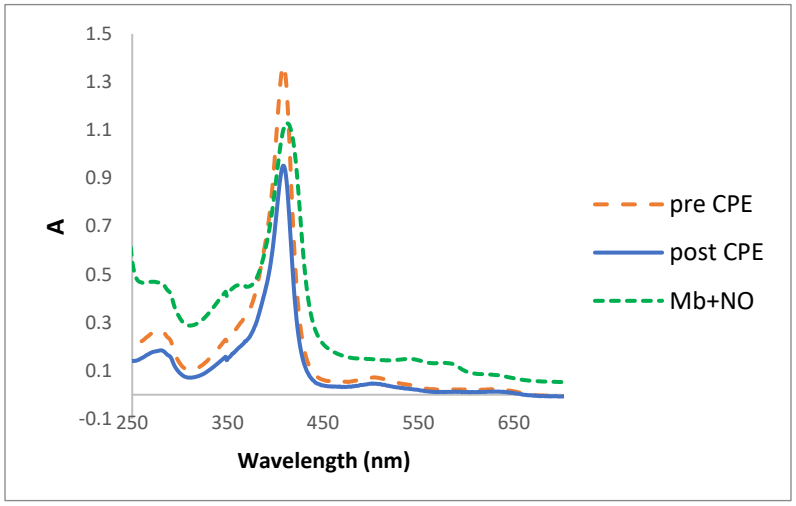

Figure E.3. UV-vis spectra of a 50x dilution of the 500 μM myoglobin (Mb) in 100 mM phosphate buffer at pH 7.4, solution used for the Mb test for NO.